

University of Nottingham

UK | CHINA | MALAYSIA

An Investigation into Laser Sintering of nano-Hydroxyapatite Coated Powders for Bone Tissue Applications

by

Dominic Hui (BSc)

Submitted in accordance with the requirements for the degree of Doctor of Philosophy

Faculty of Engineering

March 2019

Declaration of Authorship

I, Dominic Hui (BSc), declare that this thesis titled, 'An Investigation into Laser Sintering of nano-Hydroxyapatite Coated Powders for Bone Tissue Applications' and the work presented in it are my own. I confirm that:

- This work was done wholly or mainly while in candidature for a research degree at this University.
- Where any part of this thesis has previously been submitted for a degree or any other qualification at this University or any other institution, this has been clearly stated.
- Where I have consulted the published work of others, this is always clearly attributed.
- Where I have quoted from the work of others, the source is always given. With the exception of such quotations, this thesis is entirely my own work.
- I have acknowledged all main sources of help.
- Where the thesis is based on work done by myself jointly with others, I have made clear exactly what was done by others and what I have contributed myself.

Signed: 

Date: 21 March 2019

Acknowledgements

I would like to express my sincere thanks and gratitude to my supervisors, Associate Professor Ruth Goodridge, Professor David Grant and Associate Professor Colin Scotchford for their continued support, encouragement and guidance throughout the entirety of my studies.

I would also like to offer my special thanks to the technical staff in the Woflson building, Nanoscale and Microscale Research Centre and in the Additive Manufacturing labs, in particular Julie Thompson for teaching me everything I needed to know about cell culturing. It was a real joy to work in your lab, and to Denise McLean for her assistance on the Transmission Electron Microscopy machine. I would also like to thank Mark East, Mark Hardy and Joe White for their support and training on the laser sintering machines.

To David, George, and Julian, for all the emotional support, camaraderie and laughter you guys brought along the way.

To my family, for their endless love and encouragement which has enabled me to remain focused.

To Alice, for always believing in me, for spending countless hours reading through my work, for never letting my head drop during the hard times. I couldn't have done it without you.

Abstract

Exploratory routes were undertaken to deposit Nanoparticles (NPs) such as nano-hydroxyapatite (nHA) onto control substrate particles namely Polyamide 12 (PA12) and biodegradable particles such as Poly Lactic Acid (PLA). This was to exploit the benefits of additive manufacturing for the production of an osteoconductive nanocomposite for the potential use in bone tissue applications. This was achieved by adapting a previously developed method that was used to deposit multi-walled carbon nanotubes (MWCNT) onto PA12 particles by Bai et al. [1]. The advantages of using this coating method include its relative simplicity and the ability to produce large quantities of powder over a relatively short period. Furthermore, this method was shown to leave nanoparticles exposed on the surface of the final part without the need for post processing, which may be highly advantageous for guiding cell-material interaction. The overall aim was to produce a nanocomposite which was suitable as a bone substitute material and served to further expand the current range of materials available for laser sintering, specifically for biomedical applications, and provide further insight into the effects that nanocoated powders can have on the laser sintering process.

Nanoparticle loadings from 0.5 to 5.0 wt% were tested to establish the maximum surface coverage of the polymer particles. The resulting nanocoated powders were subject to morphological and physical examination using scanning electron microscopy, laser diffraction size analysis, powder rheometry and scanning differential calorimetry, to assess the suitability of the powders for laser sintering.

The nanocoated powders were initially processed in a commercial (Formiga P100) laser sintering system operating at 10.6μm. However, given the large volume of powder required for each test (minimum of 1-2 kg per run), a consumer (Sintratec) laser sintering machine was also used for the investigation. The laser wavelength used in the consumer system (445 nm) was not suitable for the processing of PA12 powders. Therefore, MWCNT (0.5 wt% for PA12 powders and 1.0 wt% for PLA powders) in addition to nHA was used to coat the powders to enable their processing. The PA12-nHA nanocomposites containing 0.5 wt% and 1.0 wt% nHA ,which were processed on

the commercial system, exhibited a significant increase in tensile modulus (18% and 13% respectively) and tensile strength (33% and 9% respectively) when compared to the neat PA12 parts. However, as the loading was increased from 1.0 to 1.5 wt% the presence of nHA on the surface of the polymer particles led to significant processing issues in both systems. Part warping became more pronounced as the nHA content was increased, which ultimately led to build failure as the parts were pulled off the powder bed by the re-coating mechanism. It was found that part warping could be reduced by decreasing the overall energy density imparted onto the powder bed from 0.11 J mm^2 to 0.032 J mm^2 for PA12-nHA powders in the commercial system and 0.19 J mm^2 to 0.12 J mm^2 for PA12-MWCNT-nHA powders in the consumer system. However, if lowered too much, the resulting parts had a high degree of porosity, poor handleability and poor overall mechanical properties. The PLA-MWCNT-nHA powders on the other hand displayed an opposite trend, requiring a higher energy density input (from 0.10 J mm^2 to 0.19 J mm^2) to prevent significant warping. However, parts produced were mechanically weak with poor handlability. As such, a heat treatment process was also investigated to improve the final part density of the PLA nanocomposites. This proved successful by substantially increasing the tensile modulus of the part by 44% for parts containing 2.0 wt% nHA and 327% for parts containing 5 wt% nHA. A post processing heat treatment may be an effective method for improving the consolidation of parts processed from powders which are sensitive to the effects of warping, and this have a narrow processing window.

In-vitro cellular assessment of the nanocomposite materials, produced by laser sintering, indicated cytocompatibility after 7 days of direct culture. This was established using Alamar Blue and Hoechst DNA 33258 assays and cellular morphological assessment via scanning electron microscopy. Osteoconductivity analysis, via Alkaline Phosphatase (ALP) and Osteocalcin assays using an immortalised version of Human Mesenchymal Stem Cells (hiMSCs) cultured directly onto the nanocomposites, revealed an improvement in the osteoconductive response for materials containing the highest loading of nHA after 21 days. Thus, the powders investigated in this work were capable of being processed by laser sintering and the resulting nanocomposites were cytocompatible and demonstrated a higher bioactive potential when compared to the base polymer material.

Contents

Declaration of Authorship i

Acknowledgements ii

Abstract iii

List of Figures xi

List of Tables xv

Abbreviations xvii

1 Introduction 1
1.1 Thesis Structure . . . 4

2 Literature Review 6
2.1 Function of Human Bone . . . 6
2.2 Composition of Bone . . . 7
2.3 Histology and Microstructure of Bone . . . 9
2.4 Mechanical Properties of Bone . . . 10
2.5 Bone Substitute Materials . . . 13
2.5.1 Ceramics and Glasses . . . 15
2.5.2 Metals . . . 21
2.5.3 Polymers . . . 22
2.5.3.1 Non-degradable . . . 23
2.5.3.2 Biodegradable . . . 25
2.5.3.3 Natural . . . 25
2.5.3.4 Synthetic . . . 25
2.5.3.5 Composites . . . 28
2.5.3.6 Nano-composites . . . 30
2.6 Common Production Methods for Bone Substitute Materials . . . 34
2.7 Additive Manufacturing . . . 37
2.8 Laser Sintering . . . 43
2.9 Consolidation of Powders by Laser Sintering . . . 47

2.10 Materials used in Laser Sintering . . . 50
2.11 Biomedical polymers for Laser Sintering . . . 55
2.12 Polymer Powder Characteristics . . . 59
2.13 Gap in the Knowledge . . . 62
2.14 Key Hypotheses . . . 63

3 Experimental Methods 66
3.1 Powder Production . . . 68
3.1.1 Production of PA12-nHA powders for Commercial Laser Sintering Machine (Formiga P100) . . . 72
3.1.2 Production of PA12-MWCNT-nHA Powders for Processing in a Consumer Laser Sintering Machine (Sintratec) . . . 73
3.1.3 Production of PLA-MWCNT-nHA powders for Processing in a Consumer Laser Sintering Machine (Sintratec) . . . 73
3.2 Powder characterisation . . . 74
3.2.1 Particle sizing . . . 74
3.2.2 Powder Flowabilty and Bulk properties - Specific Energy . . . 75
3.2.3 Powder Flowabilty and Bulk properties - Aeration . . . 76
3.2.4 Powder Flowabilty and Bulk properties - Permeability . . . 76
3.2.5 Powder Flowabilty and Bulk properties - Compressibility . . . 77
3.2.6 Differential Scanning Calorimetry . . . 78
3.2.7 Melt Rheology . . . 80
3.2.8 Attenuated total reflectance - Fourier transform infrared spectroscopy (ATR-FTIR) . . . 81
3.2.9 UV-Vis spectroscopy . . . 83
3.2.10 X-ray diffraction . . . 83
3.2.11 Scanning Electron Microscopy - Powder morphology . . . 84
3.2.12 Scanning Electron Microscopy - Fractured samples . . . 85
3.2.13 Scanning Electron Microscopy - Biological samples . . . 85
3.2.14 Transmission Electron Microscopy . . . 86
3.3 Laser Sintering of Nano-coated Powders . . . 86
3.3.1 Determination of Powder Bed Temperature . . . 86
3.3.2 Processing Parameters (Formiga P100) . . . 86
3.3.3 Processing Parameters (Sintratec) . . . 87
3.3.4 Heat Treatment of PLA nanocomposites . . . 89
3.3.5 Tensile Testing . . . 89
3.3.6 Compression Testing of PLA Nanocomposites . . . 89
3.3.7 Dynamic Mechanical Analysis . . . 90
3.3.8 Density Measurements . . . 91
3.4 Cell Study . . . 91
3.4.1 Defrosting of cells . . . 92
3.4.2 General Cell Maintenance . . . 92
3.4.3 Cell Seeding . . . 93
3.4.4 Sample Preparation . . . 94

3.4.5 Cytotoxicity study - Alamar Blue Assay (nanoparticles) 94
3.4.6 Cytotoxicity Study – Hoechst 33258 DNA Assay (Nanoparticles) 95
3.4.7 Cytotoxicity Study - Alamar Blue (Laser Sintered Nanocomposites) 96
3.4.8 Cytotoxicity Study – Hoechst 33258 DNA Assay (Laser Sintered Nanocomposites) 97
3.4.9 Osteoconductivity studies 97
3.4.10 Osteoconductivity Study - Alkaline Phosphatase Assay 97
3.4.11 Osteoinductivity Study - Osteocalcin Assay 98
3.4.12 Osteogenesis Study – Alizarin Red Staining 99
3.4.13 Cell Culturing on Laser Sintered Nanocomposite Scaffold 100
3.4.14 Statistics 101

4 Powder Characterisation 103
4.1 Nanoparticle morphology and sizing - nHA 104
4.2 Particle Sizing 105
4.2.0.1 Particle sizing - PA12-nHA powders 105
4.2.0.2 Particle sizing - PLA-MWCNT-nHA powders 107
4.3 Powder morphology and surface coverage 108
4.3.0.1 Powder Morphology and Surface Coverage - PA12-nHA and PA12-MWCNT-nHA powders 108
4.3.0.2 Powder Morphology and Surface Coverage - PLA-MWCNT-nHA powders 115
4.4 Powder Flowability and Powder Bulk Properties 121
4.4.1 Specific Energy - PA12-nHA and PA12-MWCNT-nHA Powders 122
4.4.2 Specific Energy - PLA-MWCNT-nHA powders 123
4.4.3 Aeration - PA12-nHA Powders 124
4.4.4 Aeration - PLA-MWCNT-nHA powders 125
4.4.5 Permeability - PA12-nHA powders 126
4.4.6 Permeability - PLA-MWCNT-nHA powders 127
4.4.7 Compressibility - PA12-nHA powders 128
4.4.8 Compressibility - PLA-MWCNT-nHA powders 130
4.5 Thermal Characterisation 132
4.5.1 Differential Scanning Calorimetry 132
4.5.2 Standard DSC - PA12-nHA powders 132
4.5.3 Standard DSC - PLA-MWCNT-nHA powders 133
4.5.4 The Effect of Different Cooling Rates on PA12-nHA Powders . 136
4.5.5 The Effect of Different Cooling Rates on PLA-MWCNT-nHA Powders 137
4.5.6 Isothermal DSC - PA12-nHA powders 140
4.5.7 Isothermal DSC - PLA-MWCNT-nHA powders 141
4.5.8 Crystallisation kinetics - PA12-nHA powders 143
4.5.9 Crystallisation kinetics - PLA-MWCNT-nHA powders 147
4.6 Melt rheology 150

4.7 ATR-FTIR . . . 151
4.8 UV-Vis Spectroscopy . . . 152
4.9 XRD . . . 154
4.9.1 XRD - PA12-nHA powders . . . 154
4.9.2 XRD - PLA-MWCNT-nHA powders . . . 155
4.10 Discussion . . . 157

5 Laser Sintering of nano-coated powders 176
5.1 Processing of PA12-nHA in the Formiga P100 laser sintering machine . 177
5.1.1 Determination of the powder bed temperature of PA12-nHA powders . . . 177
5.1.2 Laser sintering parameters for PA12-nHA powders . . . 178
5.2 Processing of PA12-MWCNT-nHA in the Sintratec laser sintering machine 185
5.2.1 Determination of the powder bed temperature of PA12-MWCNT-nHA powders . . . 185
5.2.2 Laser sintering parameters for PA12-MWCNT-nHA powders . . 188
5.3 Processing of PLA-MWCNT-nHA in the Sintratec laser sintering machine 195
5.3.1 Determination of the powder bed temperature of PLA-MWCNT-nHA powders . . . 195
5.3.2 Laser sintering parameters for PLA-MWCNT-nHA powders . . 196
5.4 SEM of single layers from the Sintratec machine . . . 201
5.5 Discussion . . . 202

6 Characterisation of Laser Sintered Nanocomposites 215
6.1 Characterisation of PA12 Laser Sintered Nanocomposite Samples . . . 216
6.2 Density Measurements of PA12 Nanocomposites Processed In a Commercial Machine (Formiga P100) . . . 216
6.2.1 Density Measurements of PA12 Nancomposites Processed In a Consumer Machine (Sintratec) . . . 217
6.2.2 Tensile Measurements of PA12 Nanocomposites Processed In a Commercial Machine (P100) . . . 218
6.2.3 Tensile Measurements of PA12 Nanocomposites Processed In a Consumer Machine (Sintratec) . . . 219
6.3 SEM of Fracture Surfaces . . . 219
6.3.1 SEM of PA12 Nanocomposites Processed In a Commercial Machine . . . 219
6.4 Characterisation of PLA Based Nanocomposite Samples . . . 223
6.5 Density Measurements of PLA Nanocomposites Processed In a Consumer Machine (Sintratec) . . . 223
6.5.1 Density Measurements of the Heat Treated PLA Nanocomposite Samples . . . 224
6.6 Dimensional Change of PLA Samples Following Heat Treatment . . . 225
6.6.1 Tensile Measurements of PLA Nanocomposites Processed In a Consumer Machine (Sintratec) . . . 226

6.6.2 Tensile Measurements of Heat Treated PLA Nancomposite Samples . . . 227
6.6.3 Compression Testing of PLA Nanocomposite Samples . . . 230
6.7 Dynamic Mechanical Analysis of PLA Nanocomposite Samples . . . 231
6.7.1 SEM of PLA Nanocomposites Processed In a Consumer Machine (Sintratec) . . . 233
6.7.2 SEM of Heat-Treated PLA Nanocomposite Samples . . . 236
6.8 Discussion . . . 236

7 Cellular Assessment of Nano-Particles and Laser Sintered Nanocomposites 247
7.1 Cytotoxicity of Nano-Particles . . . 248
7.1.1 nHA Alamar Blue . . . 248
7.1.2 nHA Hoechst 33258 DNA Assay . . . 250
7.1.3 MWCNT Alamar Blue . . . 252
7.1.4 MWCNT Hoechst 33258 DNA Assay . . . 253
7.1.5 MWCNT-nHA Alamar Blue . . . 254
7.1.6 MWCNT-nHA Hoechst 33258 DNA Assay . . . 256
7.2 Cytotoxicity of Laser Sintered Nanocomposites . . . 257
7.2.1 Cytotoxicity of PA12-nHA Nanocomposite - Alamar Blue . . . 257
7.2.2 Cytotoxicity of PA12-nHA Nanocomposite - Hoechst 33258 DNA Assay . . . 259
7.2.3 Cytotoxicity of PA12-MWCNT-nHA Nanocomposite - Alamar Blue . . . 260
7.2.4 Cytotoxicity of PA12-MWCNT-nHA Nanocomposite - Hoechst 33258 DNA Assay . . . 262
7.2.5 Cytotoxicity of PLA-MWCNT-nHA Nanocomposite - Alamar Blue 263
7.2.6 Cytotoxicity of PLA-MWCNT-nHA Nanocomposite - Hoechst 33258 DNA Assay . . . 264
7.3 Bioactivity Assessment of laser sintered Nanocomposite Materials . . . 266
7.3.1 Bioactivity of Nanocomposite Samples - Hoechst 33258 DNA Assay . . . 266
7.3.2 Bioactivity of the Nanocomposite Samples - Alkaline Phosphatase Assay . . . 268
7.3.3 Bioactivity of Nanocomposite Samples - Osteocalcin Assay . . . 269
7.3.4 Bioactivity of Nanocomposite Samples - Alizarin Red Assay . . . 271
7.4 SEM Imaging . . . 272
7.4.1 SEM Imaging of hiMSC Cultured on PA12-MWCNT-nHA Nanocomposite Samples . . . 272
7.4.2 SEM Imaging of hiMSC Cultured on PLA-MWCNT-nHA Nanocomposite Samples . . . 275
7.4.3 SEM Imaging of hiMSC Cultured on a Nanocomposite Scaffold 277
7.5 Discussion . . . 279

8 General Discussion,Conclusion and Suggestions for Future Work 288

8.1 General Discussion 288
8.2 Conclusion 294
8.3 Suggestions for Future Work 298

A Publications **301**

Bibliography **302**

List of Figures

2.1 Microstructure of cancellous bone . . . 9
2.2 Microstructure of trabecular bone . . . 10
2.3 Strain rate sensitivity of cortical bone . . . 11
2.4 Wear damage of metals and ceramics on UHMPE . . . 16
2.5 Bioglass and the development of HCA . . . 20
2.6 Effect of particle size on tensile strength on PP/$CaCO_3$ composite . . . 32
2.7 Effect of particle size on tensile strength of epoxy composite . . . 33
2.8 AM skull implant . . . 40
2.9 Implants made by AM . . . 40
2.10 Intramedullary rod made using AM . . . 41
2.11 Comparison of FDM vs laser sintering . . . 44
2.12 Depiction of a typical laser sintering system . . . 45
2.13 Effect of laser power on the tensile properties of PA12 parts . . . 46
2.14 Energy density and particle consolidation . . . 47
2.15 Cross section of a laser sintered PA12 part . . . 48
2.16 Phase and transition temperatures of commonly used thermoplastics . 51
2.17 Change in specific volume of semi-crystalline and amorphous polymers with temperature . . . 52
2.18 DSC trace of a PA12 powder . . . 53
2.19 DSC trace of a powder with no laser sintering processability . . . 54
2.20 Relationship between molecular weight and melt viscosity of Poly styrene 54
2.21 SEM images of polystyrene parts . . . 55

3.1 CNT chiral structures . . . 68
3.2 Flow diagram for powder production . . . 71
3.3 Directional movement of the FT4 rheomter blade through a powder bulk 75
3.4 CAD model of tensile test piece produced on the Sintratec . . . 88
3.5 CAD model of a scaffold produced for cell testing . . . 101

4.1 TEM images of nHA rods . . . 105
4.2 Size distribution of coated PA12 powders . . . 106
4.3 Size distribution of coated PLA powders . . . 108
4.4 SEM images of PA0 and PA4H particles . . . 109
4.5 SEM images of PA0, PA1H, PA4H and PA10H particles . . . 110
4.6 SEM image of a PA05M5H particle . . . 111
4.7 SEM showing the distribution of nHA on a PA1H particle . . . 112

4.8 SEM of the surface of a PA05M particle . . . 113
4.9 SEM of PA2H and PA05M5H particle . . . 114
4.10 SEM image of a PL0 particle . . . 116
4.11 SEM image of a PL1M particle . . . 118
4.12 SEM image of a PL1M5H particle . . . 120
4.13 The surface of a PL1M5H particle . . . 121
4.14 Specific energy of PA0, PA2H and PA4H powders . . . 122
4.15 Specific energy of asPL0, PL0 sieved, PL1M and PL1M5H powders . . . 123
4.16 Aerated energy of coated PA12 powders . . . 125
4.17 Aerated energy of coated PLA powders . . . 126
4.18 Permeability of coated PA12 powders . . . 127
4.19 Permeability of coated PLA powders . . . 128
4.20 Compressibility of coated PA12 powders . . . 129
4.21 Conditioned bulk density of coated PA12 powders . . . 130
4.22 Compressibility of coated PLA powders . . . 131
4.23 Conditioned bulk density of coated PLA powders . . . 132
4.24 DSC curves of coated PA12 powders using a standard ramp and cooling rate . . . 133
4.25 DSC curves of coated PLA powders using a standard ramp and cooling rate . . . 135
4.26 DSC curves of the 1st, 2nd and 3rd cycle of a PL0 powder . . . 135
4.27 Non-isothermal crystallisation curves of coated PA12 powders . . . 137
4.28 Non-isothermal crystallisation curves of coated PLA powders . . . 139
4.29 Isothermal crystallisation curves for coated PA12 powders . . . 140
4.30 Isothermal crystallisation curves for coated PLA powders . . . 142
4.31 Avrami plots for coated PA12 powders . . . 145
4.32 Arrhenius plots for coated PA12 powders . . . 146
4.33 Avrami plots for coated PLA powders . . . 148
4.34 Arrhenius plots for coated PLA powders . . . 149
4.35 Shear viscosity of coated PLA powders . . . 150
4.36 ATR-FTIR spectrum of coated PA12 powders . . . 151
4.37 UV-Vis spectrum of coated PA12 powders . . . 153
4.38 UV-Vis spectrum of coated PLA powders . . . 154
4.39 XRD pattern for coated PA12 and PA12-nHA nanocomposite . . . 155
4.40 XRD pattern for coated PLA powders . . . 156
4.41 XRD pattern for preheated PLA powders . . . 157
4.42 Powder force diagram . . . 161
4.43 Cohesivity diagram of coated particles . . . 162
4.44 Non-isothermal crystallisation curves for PA12 Amado et al. [2] . . . 167
4.45 Illustration of wetting and nucleus cap formation on the surface of the nanoparticle . . . 169
4.46 Plot of ΔG vs r for homogenous and heterogenous nucleation . . . 170

5.1 PA0H powder being spread across the build platform of the Formiga P100. . . . 178

5.2 Processing window for coated PA12 powders in the Formiga P100 . . . 181
5.3 Warped PA12 samples . . . 182
5.4 Example of tensile test piece and discs for cell testing . . . 183
5.5 The average dimensional error for samples produced on the Formiga P100 . . . 184
5.6 Example of PA05M5H powder overheating . . . 187
5.7 Processing windows for coated PA12 powders processed in the Sintratec 190
5.8 PA05M2H powders being processed at different settings . . . 191
5.9 PA05M5H powder curl development . . . 192
5.10 Average dimensional error of samples produced on the Sintratec . . . 193
5.11 Example of change of powder melt viscosity . . . 194
5.12 Example of PL1M powder degradation . . . 197
5.14 PL1M5H scaffold for cellular studies . . . 198
5.13 Processing windows for coated PLA powders in the Sintratec . . . 199
5.15 Average dimensional error of PLA samples produced in the Sintratec . 200
5.16 SEM of single layers: PA05M, PA05M5H, PL1M and PL1M5H . . . 202
5.17 Contour map displaying the temperature variation across the build platform of the Sintratec . . . 209
5.18 Build chamber of the Sintratec . . . 210
5.19 Formiga P100 build platform temperature ditribution . . . 211
5.20 Surface temperature distribution of icoPP powder . . . 212
5.21 Simulated termperature variation of PA12 nd icoPP powders . . . 213

6.1 SEM image of PA0 fracture surface . . . 220
6.2 High resolution SEM imfage of PA1.5H fracture surface . . . 221
6.3 SEM images of the fracture surfaces of (a) and (b) PA05H, (c) and (d) of PA1H and (e) and (f) PA1.5H nanocomposites taken at low and high magnification. . . . 222
6.4 Dimensional measurements of PLA samples following heat-treatment . 226
6.5 Comparison of tensile properties of PLA and heat-treated PLA samples 229
6.6 DMA analysis of heat-treated PLA samples . . . 232
6.7 Loss modulus of heat-treated PLA samples . . . 232
6.8 Tan delta of heat-treated PLA samples . . . 233
6.9 SEM fracture surface of PLA-MWCNT-nHA samples . . . 235
6.10 SEM fracture surface of heat-treated PLA-MWCNT-nHA samples . . . 236
6.11 Schematic showing consolidation of a powder layer . . . 240
6.12 Graph showing weight loss of PLA at different isothermal temperatures 241

7.1 Alamar Blue - cytotoxicity of nHA particles . . . 250
7.2 Hoechst 33258 DNA Assay - cytotoxicity of nHA particles . . . 251
7.3 Alamar Blue - cytotoxicity of MWCNT . . . 253
7.4 Hoechst 33258 DNA Assay - cytotoxicity of MWCNT . . . 254
7.5 Alamar Blue - cytotoxicity of MWCNT-nHA . . . 256
7.6 Hoechst 33258 DNA Assay - cytotoxicity of MWCNT-nHA . . . 257
7.7 Alamar Blue - cytotoxicity of PA12-nHA samples . . . 259

7.8 Hoechst 33258 DNA Assay - cytotoxicity of PA12-nHA samples 260
7.9 Alamar Blue - cytotoxicity of PA12-MWCNT-nHA samples 261
7.10 Hoechst 33258 DNA Assay - cytotoxicity of PA12-MWCNT-nHA samples 263
7.11 Alamar Blue - cytotoxicity of PLA-MWCNT-nHA samples 264
7.12 Hoechst 33258 DNA Assay - cytotoxicity of PLA-MWCNT-nHA samples 265
7.13 PA12 and PLA nancomposite samples - Hoechst 33258 DNA Assay . . 267
7.14 PA12 and PLA nancomposite samples - ALP Assay 269
7.15 PA12 and PLA nancomposite samples - Osteocalcin Assay 270
7.16 PA12 and PLA nancomposite samples - Alizarin Red Assay 272
7.17 SEM hiMSC cells cultured on PA12-MWCNT-nHA samples 274
7.18 SEM hiMSC cells cultured on PLA-MWCNT-nHA samples 276
7.19 SEM images of hiMSCs cultured on of PA0 and PL1M5H scaffolds . . 278

8.1 Image showing (a) Formlabs Fuse 1 and (b) SinterIt Lisa, consumer laser sintering machines which both feature a fully enclosed design [3] [4]. 291
8.2 Top image shows a cross section of a normal, healthy, vertebrae where as the image underneath is of an osteoporotic. Note the reduction in cancellous bone density and inwards bowing of the osteoporotic vertebrae [5]. 293

List of Tables

2.1 Mechanical properties of cortical bone . . . 12
2.2 Ca/P ratio of biomedical ceramics . . . 17
2.3 Composition of bioglass . . . 20
2.4 AM processes . . . 38
2.5 Commercially available powders for laser sintering . . . 65

3.1 Properties of CNTs . . . 68
3.2 Laser sintering parameters used to test PA12-nHA powders in the Formiga P100 . . . 87
3.3 Laser sintering parameters used to test PA12-MWCNT-nHA powders in the Sintratec . . . 88
3.4 Laser sintering parameters used to test PLA-MWCNT-nHA powders in the Sintratec . . . 88
3.5 Parameters used for DMA testing . . . 90

4.1 Size distribution of coated PA12 powders . . . 106
4.2 Size distribution of coated PLA powders . . . 107
4.3 Aerated energy of coated PA12 powders . . . 124
4.4 Aerated energy of coated PLA powders . . . 126
4.5 The peak melting and crystallisation temperatures of coated PA12 powders using standard ramp and cooling rate . . . 133
4.6 The peak melting and crystallisation temperatures of coated PLA powders using standard ramp and cooling rate . . . 134
4.7 Peak crystallisation temperatures of coated PLA powders during Non-isothermal cooling . . . 138
4.8 Crystallisation time of coated PA12 powders . . . 141
4.9 Crystallisation time of coated PLA powders . . . 141
4.10 The activation energy and avrami constant of coated PA12 powders . . . 143
4.11 The avrami exponent and activation energy of coated PLA powders . . . 147
4.12 ATR-FTIR peak assignment for coated PA12 powders . . . 152

5.1 Results of the powder spreading test for coated PA12 powders in the Formiga P100 . . . 177
5.2 Parameters used for the testing of PA12-nHA powders in the Formiga P100 . . . 179
5.3 Results of the powder bed temperature test for coated PA12 powders in the Sintratec . . . 186

5.4 Parameters used for the testing coated PA12 powders in the Sintratec . 188
5.5 Results of the powder spreading test for coated PLA powders 196
5.6 Parameters used for testing coated PLA powders in the Sintratec . . . 196

6.1 Summary of processing parameters used for PA12-nHA and PA12-MWCNT-nHA powders 216
6.2 Density measurements of PA12-nHA samples 217
6.3 Density measurements of PA12-MWCNT-nHA samples 218
6.4 Tensile test data for PA12-nHA samples 218
6.5 Tensile test data for PA12-MWCNT-nHA samples 219
6.6 Summary of the Sintratec parameters used for PLA-MWCNT-nHA . . 223
6.7 Density measurements of PL1M-MWCNT-nHA samples 224
6.8 Density measurements of heat treated PLA samples 224
6.9 Tensile test data of heat-treated PLA samples 227
6.10 Tensile test data for heat-treated PLA samples 227
6.11 Compressive properties of heat-treated PLA samples 230
6.12 Comparison of tensile and compressive properties of various polymer composites/nanocomposites 246

Abbreviations

AB	Alamar Blue
AE	Aerated energy
ALP	Alkaline Phosphatase
AM	Additive Manufacturing
AR	Aeration ratio
ATR-FTIR	Attenuated total reflectance - Fourier transform infrared spectroscopy
CNT	Carbon nanotube
Ca-P	Calcium phosphate
DSC	Differential Scanning Calorimetry
DMA	Dynamic Mechanical Analysis
DMEM	Dulbecco's Modified Eagle's Medium
ECM	Extracellular Matrix
EDX	Energy dispersive x-ray spectroscopy
FEG ESEM	Field emission gun environmental scanning electron microscopy
EoB	Elongation at break
FDM	Fused deposition modelling
FN	Fibronectin
HA	Hydroxyapatite
HDPE	High density polyethylene
HOBs	Human osteoblasts
IM	Injection moulding
MC3T3	Fibroblast cell line
MG-63	Osteosarcoma cell line
MWCNT	Multi-walled carbon nanotubes

NPs	Nanoparticles
nHA	nano-Hydroxyapatite
OCN	Osteocalcin
OSP	Osteopontin
PA12	Polyamide-12
PA05H	PA12 with 0.5 wt% nHA
PA1H	PA12 with 1.0 wt% nHA
PA1.5H	PA12 with 1.5 wt% nHA
PA2H	PA12 with 2.0 wt% nHA
PA4H	PA12 with 4.0 wt% nHA
PA10H	PA12 with 10.0 wt% nHA
PA05M2H	PA12 with 0.5 wt% MWCNT and 2.0 wt% nHA
PA05M5H	PA12 with 0.5 wt% MWCNT and 5.0 wt% nHA
PCL	Polycarprolactone
PEEK	Polyether ether ketone
PGA	Poly (glycolic acid)
PLA	Poly (lactic acid)
asPL0	as-received Poly (lactic acid)
PL1M	PLA with 1.0 wt% MWCNT
PL1M2H	PLA with 1.0 wt% MWCNT and 2.0 wt% nHA
PL1M5H	PLA with 1.0 wt% MWCNT and 5.0 wt% nHA
PLGA	Poly (co-glycolic acid)
POE	Poly (orthoesters)
PU	Polyurethanes
PVA	Poly (vinyl alcohol)
SEM	Scanning Electron Microscopy
SE	Specific Energy
SLA	Steriolithography
Tc	Crystallisation temperature
TEM	Transmission electron microscopy
Tg	Glass transition temperature

Tm	Melting temperature
UHMWPE	Ultra high molecular weight polyethylene
UV-vis	UV-visible light spectroscopy
XRD	X-ray diffraction crystallography
β-**TCP**	β-Tri-calcium phosphate

Chapter 1

Introduction

Additive manufacturing (AM)is a broad term which refers to a range of advanced manufacturing methods which aims to build three dimensional (3D) structures generated from computer aided design (CAD), in a layer by layer process. The implications of this is significant in regards to the generation of biomaterial structures for orthopaedic applications.

Implants and devices that support migration, proliferation and differentiation of bone cells require a well interconnected, porous, 3D structure with modest mechanical strength, typically less than 2 MPa, in order to support the surrounding tissue whilst bone mineralisation occurs. Eventually the load will be transferred from the structure to the newly mineralised bone [6–13]. Typical methods for the manufacture of bone substitute materials include solvent casting, sol–gel, gas foaming, particulate leaching and melt extrusion (for fully dense structures) [14–36]. However, these techniques are generally limited to simple shapes and some require the use of toxic solvents or binders. They generally produce materials that are not ideally tailored to fit to the individual patient, can be time consuming to produce and carry further disadvantages, including batch to batch variation. The ability to construct highly complex, 3D structures from a variety of degradable and non-degradable polymers makes powder based additive manufacturing processes, such as laser sintering, very promising. A laser (typically CO_2) acts on a preheated powder bed to selectively melt the surface of the polymer particles, fusing them together. Each consolidated layer corresponds to a 'sliced' image

of a CAD model to be built [37]. When a layer is complete the build platform lowers and a new layer of polymer powder is spread over the previous layer. This process is repeated until the build is complete. Laser sintering has several key advantages over the typical methods mentioned such as greater control over internal and external geometries, part to part reproducibility and no requirement for expensive moulds or potentially toxic binders [38–41]. Laser sintering also solves a persistent problem within the orthopaedic field where standard 'off the shelf' implants are often not sufficient for use in patients afflicted with complex conditions. By combining advanced imaging technology such as CT and MRI, it is now possible to translate patient specific data into 3D models which can be used to manufacture prosthetics and implants which match the unique requirements of individual patients. Laser sintering is well suited for this niche, especially for small-sized non-standard implants such as those used in the spine, craniofacial and dental areas [42–45].

The NHS reported that almost a million procedures were related to problems with bones and joints in 2009-2010 [46] and in the US there were 6 million reported bone fractures (2007) [47]. A typical long bone surgery can cost in the region of £14,500 [46]. Currently, metallic components are the preferred choice for bone substitute materials. Dependent on their application, such as for a hip replacement in a total hip arthroplasty or a fracture fixation device, their high elastic modulus can result in a large mismatch in mechanical properties between metallic implants and the bone which they support. This leads to a phenomenon known as stress shielding and can lead to osteoporosis, delayed bridging and re-fracture when the device is removed [48]. This, in combination with their longevity within the body, can lead to aseptic loosening of the device and ultimately lead to the failure of the implant and further complications for the patient. Revision procedures require additional hospital stays and are costly, around £1,200-400 per day, per bed [46]. This has therefore led to the development of biodegradable, materials with the aim of providing sufficient mechanical support whilst allowing bone cells to integrate with the material and synthesise new bone tissue. The material will degrade, leaving behind the newly synthesised bone, thus avoiding some of the potential complications associated with permanent devices.

Synthetic, degradable polymers such as poly lactic acids (PLA) have been explored in detail for orthopaedic applications due to their well understood degradation mechanism and biocompatibility. However, some of the disadvantages of PLA for use in these applications include its poor ductility with low impact resistance [49]. Hydrolysis is the major degradation mechanism for PLA, whilst the degradation product of PLA is lactic acid is decomposed in the body, the accumulation of lactic acid at the implant site due to "burst" release as a result of bulk degradation of PLA will lead to a localised drop in the local pH. This can trigger immune responses, which can lead to chronic inflammation and other foreign body reactions in addition to accelerated degradation of the material [50]. Due to these reasons and the general lack of bioactive properties and poor mechanical properties associated with neat polymers a common approach is to reinforce PLA with inorganic fillers. Nanoparticles (NPs) have caused much excitement in the research community, with experiments showing enhanced biological and mechanical properties when used as a reinforcing phase, as opposed to micron sized particles [51]. A popular choice of nano filler for bone tissue engineering applications is hydroxyapatite (HA: $Ca_{10}(PO_4)_6(OH)_2$) due to its similar chemical composition to natural bone, which promotes osteoblast adhesion, proliferation and differentiation [52]. HA therefore proves to be an attractive option for use in biodegradable orthopaedic implants and may act to as a buffer to the lactic acid accumulation [53]. PLA and nHA is a potential combination that has been explored for many different types of processing methods [34, 36, 54–59].

Powders for laser sintering are generally limited to polyamides such as Polyamide 12 (PA12). Due to its physical, thermal and chemical properties, it is well understood and relatively easy to process via laser sintering. There have been attempts to explore PLA/nHA and other degradable polymer/NP powders for laser sintering and the common methods for the production of these powders include: solid-in-oil-in-water emulsion/solvent (S/O/W) techniques, the mixing of filler with polymer melts, which are then extruded and cut into pellets before being cryogenically milled to powder and dry blending powders with a filler. However, common problems associated with these methods include: the agglomeration of nano-fillers, which can lead to poor mechanical properties compared to the neat polymer, the need for toxic solvents and the

angular shaped particles with wide size distributions (associated with grinding/milling methods) which often make the powder unsuitable for laser sintering.

An alternative approach to powder production was developed by Bai et al. [1], which involved coating individual PA12 particles with multi-walled carbon nanotubes (MWCNT). The advantages of this method were its relative simplicity, the ability to produce large quantities of powder over a relatively short period and maintaining the near spherical morphology of the original particle. Furthermore, the nanoparticles were exposed on the surface of the final part without the need for post processing which may be highly advantageous for guiding cell-material interaction. However, there are a number of challenges to ensuring suitable distribution and deposition of different morphologies of nanoparticle in particular to that related to nHA as well as the influence on the laser sintering processing, mechanical properties of the final part in addition to the resultant cell surface interactions.

To explore this further, PA12 was selected as a carrier particle for investigating the production of nHA coated powders for laser sintering via Bai's method, owing to its wide use in laser sintering. PLA was also included due to the large body of work surrounding it's usage in orthopaedic applications despite some of the draw backs previously mentioned. Due to the significant advantages that AM technologies have over common production methods for biomaterial structures, the processing of nHA coated powders will be explored via laser sintering. The presence of nHA on the outer surface will increase the bioactivity of the resulting nanocomposites, and the presence of the nHA will also serve to increase the mechanical properties of the final part. This will expand the current range of biomedical materials available for laser sintering and provide further insight into the effects that nanocoated powders can have on the laser sintering process.

1.1 Thesis Structure

This thesis is separated into eight Chapters. In Chapters 1 and 2, the background and literature surrounding the field is presented. Furthermore, these Chapters highlight the

gap in the current knowledge and present the subsequent research objectives.

Chapter 3 provides detailed information relating to the materials used for the powder production process, including the techniques used to characterise the coated powders. Furthermore, it also presents the methodology used to process the coated powders in the laser sintering machine, and the mechanical and cellular testing used for the subsequent nanocomposites.

Chapter 4 assesses the degree of surface coverage and NP distribution achieved via the alternative powder production method, and the suitability of the coated powders for laser sintering. Powder characteristics such as size distribution, morphology, surface coverage, the ability of the powder to flow during powder deposition and whether the presence of nano particles affects the thermal characteristics and optical properties of the powder are analysed and discussed.

Chapter 5 assesses the impact that nanoparticles have on the laser sintering characteristics of the powder through investigation in both a commercial and consumer laser sintering machine. The processing parameters for the powders will be determined to provide detailed view of the processing windows for each powder composition, and will thus indicate the feasibility of processing the coated powders via laser sintering.

In Chapter 6, the mechanical properties of the nanocomposites produced via laser sintering were explored to assess whether the material possessed sufficient mechanical properties to act as a bone substitute material and whether the presence of the NP influenced the mechanical properties of the part.

Chapter 7 explores the cytocompatability of the nanocomposite materials and assess whether the nanocomposites can elicit an improved osteoconductive response to the material through in vitro assays. In Chapter 8, a general discussion of the wider implications of the work in this thesis, a summary of the overall results in relation to the research objectives and suggestions for future work.

Chapter 2

Literature Review

2.1 Function of Human Bone

The human body is comprised of 213 bones, excluding sesamoid bones and can be divided into four categories: long bones, short bones, flat bones and irregular bones. Bone can be considered as a highly specialised tough and rigid form of connective tissue that serves four major roles [60]

1. To provide a rigid structure that can assist in locomotion by acting as insertion sites for muscles and by acting as an intricate lever system that transfers the magnitude and direction of the forces generated by skeletal muscles and ligaments;

2. Bone also acts as a structural framework for the attachment of soft tissue and organs;

3. To protect the internal organs and bone marrow from external forces;

4. To also act as a mineral reservoir facilitating the storage and provision of calcium to the human body, in addition to serving as a reservoir for growth factors and cytokines, and providing the location of new blood cell formation via haemopoesis within the bone marrow space [61].

2.2 Composition of Bone

Bone can be regarded as a composite material consisting of 35% organic phase such as 90% Type I Collagen, 5% non-collagenous proteins and 2% lipids [62] [63] The organic phase of bone consists mainly of fibrous Type I Collagen. Collagen is formed from polypeptide chains that are wound together in a twist to form a triple helical fibril. Each chain contains approximately 1000 amino acids with every third residue being glycine which facilitates the hydrogen bonding and cross-linking between adjacent fibrils and therefore provide structural stability. Collagen fibres are made up of bundles of several microfibrils that are themselves composed of clusters of five collagen molecules [62] [64]. Observation of bone under polarised light microscopy has revealed that collagen fibres are arranged parallel to adjacent fibres forming a lamellar bone structure. This structure can be further subdivided into five layers in which the fibres consecutively rotate 30 degrees to the previously layer [65]. Depending on the anatomical location and its specific role, i.e. resistance to compression, shear or tension, the orientation of the collagen fibres can differ. For example, collagen orientated at 45 degrees between longitudinal and transverse lamellae has been shown to provide increased resistance to shear forces [66].

Bone also serves as a major reservoir for calcium and contains 99% of the total amount of calcium present in the body. Bone mineral is mainly in the form of Hydroxyapatite (HA; $Ca_{10}(PO_4)_6(OH)_2$) and exists as hexagonal, nanoapatite crystals with a plate like morphology ranging from 20 - 50 nm in length and 12 - 20 nm in width. They are present in discrete spaces within collagen fibrils, often aligning parallel to the collagen fibre, and provide bone with tremendous strength and toughness. The stoichiometric ratio of Ca/P of geological HA is 1.67. However, in natural bone this ratio varies due to the presence of impurities. There is also an age dependent variation in the chemical composition, size, and amount of HA [63] [67].

The non-collagenous proteins form the rest of the composition of bone and play a crucial role in the development, mineralisation, and homoeostasis of bone tissue. This has been demonstrated through the use of radioisotype labelling and immunohistochemistry and studies have shown that the precipitation of HA does not occur in supersaturated

calcium phosphate solutions without the presence of non-collagenous proteins which act as nucleators [63]. Non-collagenous proteins include post translationally modified phosphorylated proteins such as bone sialoprotein and proteoglycans. Bone sialoprotein (BSP) may act to bind calcium ions and thus act as sites for mineral nucleation [68]. Fibronectin is a ubiquitous cell attachment protein that co-ordinates the migration, interaction, and differentiation of osteoblast precursor cells. Thrombospondin also aids in calcium binding and contains the arginylglycylaspartic acid (RGD) peptide, which is a common sequence that mediates cell attachment [69]. Alkaline phosphatase (ALP) has been reported to be involved in the mineralisation process by providing localised concentrations of phosphate ions. The accumulation of ALP often precedes calcification and is therefore commonly used as an early indicator for osteoblast differentiation [69]. On the other hand, Osteocalcin is the most abundant form of non-collagenous protein present in bone and is produced by osteoblasts although its function is not fully understood. The γ – carboxyglutamic acid residues bind calcium and it has been suggested that osteocalcin may act to retard or control calcification and has therefore been commonly used as a marker for late stage differentiation of the osteoblast lineage [69] [70]. Similar to osteocalcin, matrix Gla Protein (MGP) is a vitamin κ-dependent γ – carboxyglutamic acid (Gla) protein and has also been identified as a calcification inhibitor in cartilage which may act as a regulatory inhibitor of bone morphogenic protein-2 (BMP-2) by binding to its receptor site. Studies have shown that MGP deficiency in mice results in premature calcification of bone [69] [71]. Mineralised bone tissue also contains small amounts of lipids and proteolipids which have been reported to have an influence on bone cell survival by directly acting on the mineralisation process by forming complexes with calcium phosphate ions [69] [72].

The extra-cellular matrix (ECM) forms the clear majority of bone tissue and provides a structural framework for cells to reside. It is composed of a three-dimensional (3D) arrangement of polysaccharides such as; collagens, elastins and fibrogens [73].

2.3 Histology and Microstructure of Bone

Compact bone is arranged in units called osteons or harversian systems (10 - 500μm) [74]. Blood vessels, lymphatic vessels and nerves penetrate the compact bone through perforating canals. These canals form junctions with the medullary cavity, periosteum and central harversian canal which runs longitudinally through the bone. Surrounding the central harversian canals is a hard-calcified matrix that is arranged in concentric rings (lamellae) of 3 - 20μm [74]. Between the lamellae are small spaces called lacunae which contain the mature osteoblasts, called osteocytes. Further small gaps protruding radially from the lacunae are called canaliculi. The long cytoplasmic extensions occupy these spaces and allow communication between different osteocytes. Furthermore, the canal system allows effective flow of nutrients and waste products in and out of the compact bone since diffusion is slow. The microstructural arrangement of compact bone can be seen in Figure 2.1.

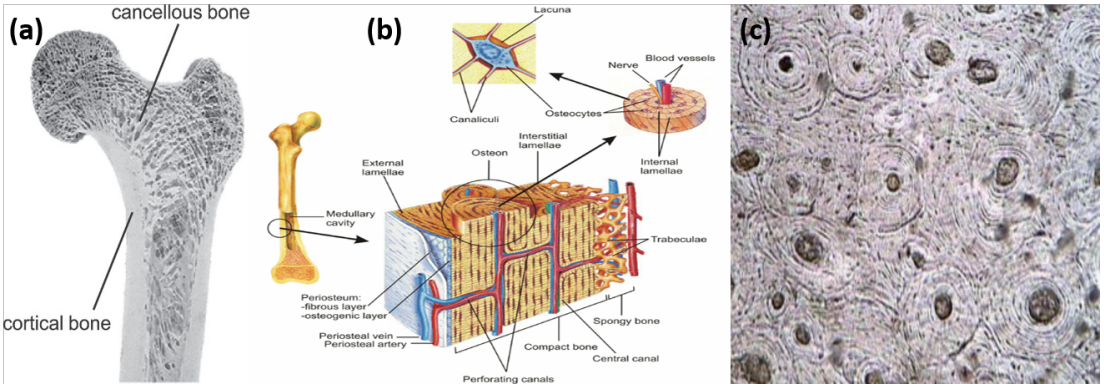


FIGURE 2.1: Cross section of human femur showing cortical and cancellous bone [75] (a), the microstructural arrangement of compact bone [76] (b) and the histological cross section of human cortical bone (c). The Osteon units can be clearly seen with Haversian systems located within the centre of the osteons [77].

Spongy bone on the other hand, bone has a less densely packed structure compared to compact bone and unlike compact bone it does not contain osteons but instead consists of trabeculae (75 - 200 μm) that contain fewer harversian canals [74]. The trabeculae are arranged in an irregular network of thin columns giving an open network that is occupied by red bone marrow or myeloid tissue and is a site for haemopoiesis. Spongy bone is the main composition in short, flat and irregularly shaped bones. It also forms the majority of the epiphyses of long bones. Due to it irregular and open

structure, spongy bone reduces the overall weight of a bone giving rise to the notion that bone is a light weight composite structure [78]. The microstructure of spongy bone can be seen in Figure 2.2.

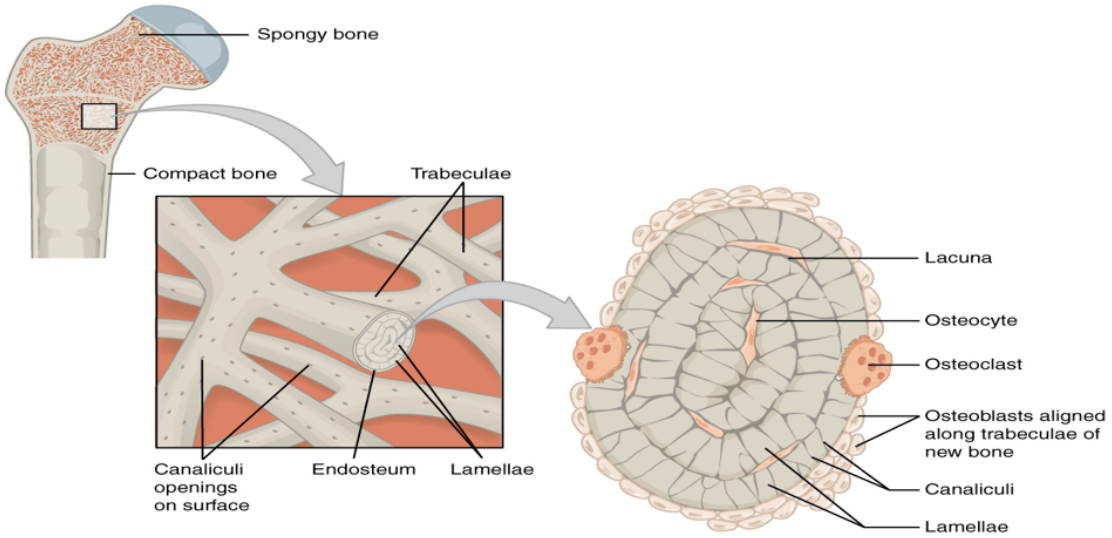


FIGURE 2.2: The microstructural arrangement of trabecular bone.

2.4 Mechanical Properties of Bone

Their complex material and microstructural arrangement provides bone with high mechanical stiffness and toughness. The presence of collagen offers tensile strength and the mineral phase imparts compressional and shear strength. Therefore, the composite system reacts differently under different loading regimes, and rates. For example, cortical bone is stronger and stiffer when the force applied is parallel to the longitudinal direction of the osteons. The Young's modulus of cortical specimens has been shown to be in the order of 14 - 20 GPa when tested in the longitudinal direction [79]. However, it is weakest when forces are applied transversally. Tests of cortical specimens in the transverse direction have yielded results in the region of 5.4 GPa [80] [81]. Cancellous bone on the other hand, due to its lower density 0.2 g cm^{-1} and porosity of up to 90%, have weaker mechanical properties compared to cortical bone. The arrangement of its structure means that it has isotropic properties and thus the properties under tension and compression are comparative [81] [82]. The mechanical properties of cortical bones from a variety of different species have been investigated. Models including

horses, pigs, sheep and humans have been utilised and despite the variations between species there is a similar trend in mechanical properties and remodelling characteristics are similar throughout the animal kingdom [83]. Another factor to consider is the anatomical site, since studies have shown that cancellous bone properties vary significantly between different sites [84] [85]. Table 2.1 reports the mechanical properties of bone from various different species under different loading regimes and highlights the difference between loading mechanism and anatomical location of the bone.

Furthermore, bone is extremely strain rate sensitive due to its viscoelastic nature. Ductility is reduced with increased strain rate however the tensile modulus and strength increases. The reported optimum strain rate for energy absorption is 0.1 - 1 s^{-1} as seen in Figure 2.3 [82]. Cortical bone is up to 2 decades stiffer than cancellous bone but sustains less strain than cancellous bone before failure. It has been reported that cancellous bone can sustain strains of up to 75% whereas cortical bone fails at strain exceeding 2% [82].

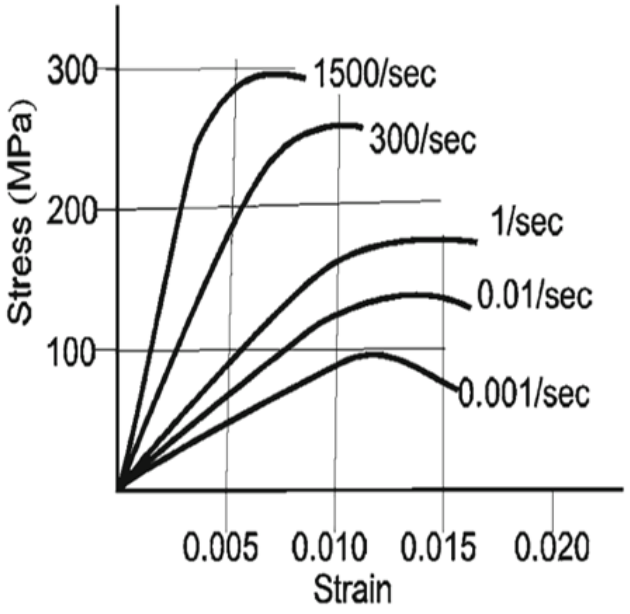


FIGURE 2.3: Strain rate sensitivity of cortical bone [82].

Age is another important factor to consider as this influences the degree of mineralization. Adolescent bones can absorb as much as 45% more energy before failure compared to adults however the stiffness of the bones can be as much as 32% weaker than that of adult bones [82]. Disease can also affect the mechanical properties of

TABLE 2.1: Mechanical properties of wet cortical bone in various modes of loading. [82].

Bone	Horses	Cattle	Pigs	Human (20-39 years)
Ultimate Tensile Strength (MPa)				
Femur	121 ±1.8	113 ±2.1	88 ±1.5	124 ±1.1
Tibia	113	132 ±2.8	108 ±3.9	174 ±1.2
Humerus	102 ±1.3	101 ±0.7	88 ±7.3	125 ±0.8
Radius	120	135 ±1.6	100 ±3.4	152 ±1.4
Elongation (%)				
Femur	0.75 ±0.008	0.88 ±0.020	0.68 ±0.010	1.41
Tibia	0.70	0.78 ±0.008	0.76 ±0.028	1.50
Humerus	0.65 ±0.005	0.76 ±0.006	0.70 ±0.033	1.43
Radius	0.71	0.79 ±0.009	0.73 ±0.032	1.50
Young's Modulus (GPa)				
Femur	25.5	25.0	14.9	17.6
Tibia	23.8	24.5	17.2	18.4
Humerus	17.8	18.3	14.6	17.5
Radius	22.8	25.9	15.8	18.9
Compressive Strength (MPa)				
Femur	145 ±1.6	147 ±1.1	100 ±0.7	107 ±4.3
Tibia	163	159 ±1.4	106 ±1.1	-
Humerus	154	144 ±1.3	102 ±1.6	-
Radius	156	152 ±1.5	107 ±1.6	-
Contraction (%)				
Femur	2.4	1.7 ±0.02	1.9 ±0.02	1.85 ±0.04
Tibia	2.2	1.8 ±0.02	1.9 ±0.02	-
Humerus	2.0 ±0.03	1.8 ±0.02	1.9 ±0.02	-
Radius	2.3	1.8 ±0.02	1.9 ±0.02	-
Compressive Modulus (GPa)				
Femur	9.4 ±0.47	8.7	4.9	-
Tibia	8.5	-	5.1	-
Humerus	9.0	-	5.0	-
Radius	8.4	-	5.3	-
Shear Strength (MPa)				
Femur	99 ±1.5	91 ±1.6	65 ±1.9	54 ±0.6
Tibia	89 ±2.7	95 ±2.0	71 ±2.8	-
Humerus	90 ±1.7	86 ±1.1	59 ±2.0	-
Radius	94 ±3.3	93 ±1.8	64 ±3.2	-
Torsional Modulus (GPa)				
Femur	16.3	16.8	13.5	3.2
Tibia	19.1	17.1	15.7	-
Humerus	23.5	14.9	15.0	-
Radius	15.8	14.3	8.4	-

bone. For example, Osteoporosis, a metabolic disease, can lead to a reduction in bone tissue leading to low strength and stiffness due to increased porous voids, therefore reducing the ability of bone to absorb energy before fracture. Osteoporosis is particularly prevalent in elderly women. It is estimated that 25% of women aged 50 – 76 have some form of bone loss due to osteoporosis. Fractures occurring to the vertebral bodies and the femur are common [82].

2.5 Bone Substitute Materials

Despite the innate ability of bone to self repair, in cases of complex and severe fractures or damage caused by disease, the ability of bone to repair and restore its normal functions via natural routes is compromised. In such cases a bone substitute must be used to bridge the damaged sites. The primary criteria for any bone substitute material is to be biocompatible with the host tissue. Although definitions of biocompatibility vary they have generally been described as the ability to support normal cellular activity without eliciting any adverse systemic or local effects on the host tissue [86]. However, the ideal bone substitute material should go beyond the ability to be solely passive in nature. Rather, it should facilitate in the recruitment, adhesion and migration of osteoprogenitor cells to the site of healing (osteoconductive), and should promote the differentiation of those osteoprogenitor cells into mature osteoblasts. These osteoblasts can then synthesise new bone, ECM, which is then followed by mineralisation and calcification of the ECM (osteoinduction) to form bone [87]. In addition to this, the substitute material must have the ability to accommodate the formation of new blood vessels, via angiogenesis and vasculogenesis, that penetrate the implanted material to provide a vital system for the provision of oxygen and nutrients and the removal of waste metabolic products [88].

Traditionally, natural materials have been used for bone augmentation procedures. Autografts are bone grafts that have been harvested and transplanted to a bone defect site within the same individual and can be considered as the most predictable osteogenic graft for bone tissue regeneration and are regarded as being highly osteoconductive

and osteoinductive [89]. The most common sites for harvesting autografts is from the mandible, the maxilla, the calvaria, the iliac crest and from the tibia and can be in the form of blocks or it can be ground to produce coarse powders [89] [90]. Autografts harvested from cancellous bone tissue have the ability to revascularise sooner, up to five days post transplantation, compared to cortical bone tissue due to their spongy/-porous nature [91]. Cortical grafts, on the other hand, have high initial strength after implantation. However, this decreases over time, at six months post implantation the mechanical strength can be up to 50% weaker than normal bone [89]. Despite some of their highly advantageous properties, autografts require additional surgery for the procurement of graft material which can lead to increases in operative time and cost. These procedures also carry a risks such as: fracture at the donor site, donor site morbidity, and postoperative pain and rehabilitation for the patient. Furthermore, only a limited volume of graft material can be harvested at any one time, thereby limiting these techniques to use in minor procedures.

Allografts, on the other hand, are bone graft materials that have been harvested from non-genetically identical members of the same species. While allografts are subject to multiple treatments prior to implantation, the risk of disease transmission cannot be eliminated. It has been estimated that the risk of human immunodeficiency virus (HIV) transmission can be 1 in 1.6 million with allograft implantation and cases of cross-infections and transmission of bovine spongiform encephalopathy have been documented from the use of allografts [92–95]. However, these minor risks are far outweighed by the advantages that allografts can provide. Large quantities of graft material can be harvested and use of off-the-shelf products eliminates the drawbacks associated with secondary surgical sites. Allografts can be harvested from fresh or frozen iliac cancellous bone which possesses the highest osteoconductive and osteoinductive potential. They can also be harvested from freeze-dried bone allografts which have been used extensively for treating periodontal defects. However, it is mechanically weaker when compared to fresh or frozen allografts. Demineralised freeze-dried bone allografts are commonly used in the maxillofacial and periodontal procedures and have the advantage of rapid resorption and exposure of osteoinductive proteins after demineralisation [89].

Xenografts are derived from non-human species. Commercially available bovine bone is processed to yield natural bone mineral without the organic component. Xenografts derived from bovine sources pose a risk of carrying diseases, however the key advantages of this method is the higher osteoconductive potential compared to synthetically derived materials and the availability of graft material. However, xenografic materials are often brittle and lack toughness. Fracture of these materials often occurs during screw fixation processes which can lead to difficulties during the surgical procedure and non-ideal bone healing conditions [89].

To minimise the risk of disease transmission, and any potentially adverse immune responses, and to overcome some of the inherent problems associated with autografts, synthetic bone substitute materials are becoming more common in clinical practice. The major advantages of these include: their relatively high abundance; no risk of disease transmission; low antigenicity; highly tailorable properties; no need for surgical harvesting of material, and therefore reduced costs. These materials will be discussed further, in the following sections.

2.5.1 Ceramics and Glasses

Due to their chemical and structural stability, ceramics have good biocomaptability with host bone tissue in addition to having a high corrosion resistance to bodily fluids. Ceramics also exhibit high tensile and compressive modulus and strength in addition to being extremely hard. Polycrystalline aluminium oxide (Al_2O_3) or alumina was the first ceramic used in orthopaedic and dental surgery. Alumina has been implemented in the femoral heads of total hip joint prostheses as articulating surfaces which rotate against acetabular cups, and has been shown to produce significantly less wear debris when compared to polymer or metallic systems due to their higher hardness. Wear debris can cause adverse immune reactions and ultimately lead to aseptic loosening and failure of the implant [96]. As seen in Figure 2.4, in a study that compared the wear damage of articulating surfaces made from stainless steel, cobalt chrome, titanium, alumina and zirconia on the articulating surface of an acetabular cup made from ultra-high-molecular-weight-polythylene (UHMWPE). The results showed that the ceramic

based materials produced the least amount of wear damage on the UHMWPE surfaces compared to metallic systems [97].

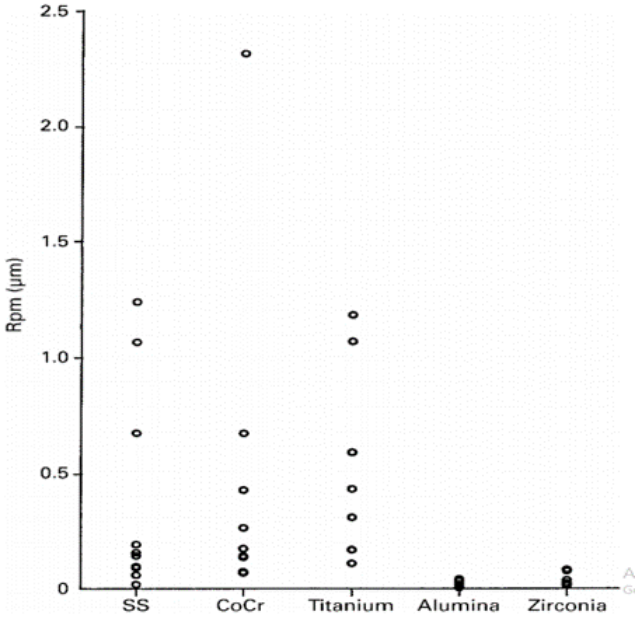


FIGURE 2.4: Distribution of damage (Rpm) caused by stainless steel (SS) cobalt chrome (CoCr), titanium, alumina and zirconia on UHMPE surfaces [97].

Eventually the use of alumina as articulating surfaces in total joint prostheses was superseded by zirconia due to its higher fracture toughness and flexural strength [96]. Alumina and zirconia ceramics are inert materials which do not interact with the host tissue and therefore do not form physical bonds to them. For cases such as articulating surfaces this is a desirable trait, however for implants that require biological fixation to achieve stability, biological inertness is not desirable. The host tissue response to biologically inert materials is to encapsulate them in a non-adherent fibrous tissue, thus isolating them from their local environment. This fibrous layer can prevent direct chemical or biological bonds from forming between the bone and implant interface, which can ultimately lead to implant failure through motion. Therefore, for materials that require stable biological fixation and integration with the hosts bone tissue, bioactive materials are required.

Calcium phosphate based ceramics and their derivatives are the most popular choice for use as bioactive, bone substitute materials. They have been used extensively since the 1960s and can be applied as powders or granules for bone and tooth cements; the

TABLE 2.2: Ca/P ratio of calcium phosphate based ceramics used in medical applications [96].

Material	Abbreviation	Formula	Ca/P ratio
Tetracalcium phosphate	TTCP	$Ca_4(PO_4)_2$	2.0
Hydroxyapatite	HA	$Ca_{10}(PO_4)_6(OH)_2$	1.67
Tricalcium phosphate (α, $alpha$', β, γ	TCP	$Ca_3(PO_4)_2$	1.50
Octacalcium phosphate	OCP	$Ca_8H_2(PO_4)_6.5H_2O$	1.33
Dicalcium phosphate dihydrate (brushite)	DCPD	$CaHPO4.2H_2O$	1.0
Dicalcium phosphate (monite)	DCP	$CaHPO_4$	1.0
Calcium pyrophosphate (α, β, γ)	CCP	$Ca_2P_2O_7$	1.0
Calcium pyrophosphate dihydrate	CPPD	$Ca_2P_2O_7.2H_2O$	1.0
Heptcalcium phosphate	HCP	$Ca_7(P_5O_{16})_2$	0.7
Tetracalcium dihydrogen phosphate	TDHP	$Ca_4H_2P_6O_{20}$	0.67
Calcium phosphate monohydrate	CPM	$Ca(H_2PO_4)_2.H_2O$	0.5

production of small, low weight bearing, implants; as porous scaffolds for cell ingrowth and new bone development; and have been applied as biocompatible and bioactive coatings on metal implants [98]. They can be synthesised by mixing calcium and phosphate solutions under acidic or alkaline conditions. Only compounds with a Ca/P ratio of ≥ 1 are suitable for implantation, as anything < 1 will lead to rapid dissolution within the body. Table 2.2 Shows the various ratios of Ca/P based ceramics currently used in orthopaedics [96] [99].

If the Ca/P ratio is < 1.67, β-tricaclium phosphate (TCP) and other phases such as tetracalcium phosphate (TTCP) are present with HA. If the Ca/P ratio is > 1.67, calcium oxide (CaO) will be present with the HA phase [96] [99]. In-vitro studies investigating the differentiation of MSC cells grown on calcium phosphate ceramics have found positive affects on osteoinduction Lee et al. [100] studied the differentiation of human MSC cells grown on electro spun scaffolds with and without HA, it was shown that the expression of ALP, OCN and BSP was elevated on scaffolds with HA [100]. In another study Eslaminejad et al. showed increased levels of OCN and OPN content in rat BMSCs cultured on alginate-gelatin-β-TCP scaffolds [101]. When comparing the osteoinductive potential of different calcium phosphates, Hu et al. showed that HA induced higher expression of OCN, OPN and type I collagen in rabbit BMSCs compared to Amorphous calcium phosphates (ACP) [102]. Similarly, Brugge et al. showed that the amorphous calcium phosphates may inhibit the mineralisation of rat BMSCs compared to crystalline calcium phosphates [103]. This suggests that the crystallinity

of the phases present has a strong effect on the osteoinductivity of calcium phosphate ceramics. Yuan et al. compared TCP, HA and BCP ceramics and found a higher expression of OCN and BSP in human BMSCs grown on TCP compared to HA and BCP [104]. The studies have suggested a hierarchy exists for the osteoinductive potential of calcium phosphate based ceramics TCP $>$ BCP $\approx$ HAP $>$ ACP [99]. To support the regeneration of bone tissue, the resorption of calcium phosphates must match the rate of new bone synthesis. As mentioned above, the Ca/P ratio greatly affects the dissolution rate of the material. As TCP has a lower Ca/P ratio compared to HA it dissolves significantly faster than HA. Therefore, HA is commonly the choice of calcium phosphate based ceramic used in bone substitute materials and has been extensively investigated over the years. For example, Tripathi et al. [105] produced porous HA based scaffolds, and the biological interaction was investigated using human osteoblast like SAOS2 cells. SEM imaging showed that the cells had attached and spread over the surface of the scaffold, adopting rounded morphology and extended filopodia by day 7. By day 10 the cells had adopted a more flattened/spread morphology with extended lamellopodia and formed a continuous cell layer which covered the entire surface of the HA scaffold. An MTT assay demonstrated that proliferation was stimulated across 7 days with high cell viability indicative of good cytocompatibility. ALP results also increased across the 7 day period. Enhanced protein uptake was also observed on the HA scaffolds with a four-fold increase in protein attachment compared to the control disc . Prado et al. [106] implanted HA into the distal epiphysis of the femur of a rat that had ovarietomy-induced osteoporosis in order to evaluate the osteogenic properties of HA. Radiography and morphometric analysis suggested good biocompatibility of the hydroxyapatite implant. Histological analysis showed good bone formation around the HA implant in addition to proliferation of connective tissue with increase in bone volume in the defect site . Chang et al. [107] assessed the histological response of bone ingrowth within porous HA implants. After implantation, into the defect sites created in the proximal tibia of New Zealand rabbits, active osteoinduction was observed with evidence of new bone formation within the porous HA implant. Furthermore, the extent of the histological changes was seen to correlate with pore geometry, with optimum bone growth occurring in cylindrical pores with 300 μm pore size. HA based

bone cements have also seen significant use in the treatment of craniofacial defects. A clinical study conducted by Burstein et al. [108] reviewed the post-operative outcome of HA based cements used to treat orbital cranial reconstruction in over 150 patients across a 7-year period. It reported a 92% satisfaction rate over a minimum 1- year follow-up, indicating the success of the clinical usage of HA based cements for the treatment of craniofacial defects.

Bioactive glass was first pioneered by Hench et al. [109] in 1971. Bioglass® is a series of specialised glasses consisting of Na_2-O-CaO-SiO_2 with addition of P_2O_5, B_2O_3 and CaF_2 [96]. Upon immersion in biological fluid, a hydroxy-carbonate apatite (HCA) layer is formed on the surface through a series of chemical reactions which is summarised in Figure 2.5. The reaction takes place in a series of 12 steps with the first five occurring on the surface of the bioactive glass due to fast ion exchange of alkali ions such as Na^+ or K^+ with hydrogen ions from body fluids (stage 1). Following this, the glass network breaks down through the loss of soluble SiO_2 in the form of $Si(OH)_4$ which results in the breakdown of Si-O-Si bonds and the formation of Si-OH (Silanols) at the glass-solution interface (stage 2). Following this, a condensation reaction occurs resulting in the repolymerisation of a SiO_2 rich layer which is depleted in alkali cations (stage 3). Chemisorption of Ca^{2+} and PO_4^{3-} through the SiO_2 layer occurs which results in the growth of an amorphous CaO-$P_2O_5 4$ rich film (stage 4). The amorphous CaO-P_2O_5 layer begins to crystallise through the incorporation of OH_-, CO_3^{2-} of F^- ions from solution to form a mixed hydroxyl, carbonate, fluorapatite layer. A series of reactions then leads to the adsorption of growth factors on the HCA surface resulting in a sequence of cellular attachment, proliferation and differentiation before, ultimately, new bone formation [110].

The resulting HCA layer is chemically and structurally the same as the mineral phase of natural bone and therefore direct bonding to host tissue can be achieved. Bioglass® 45S5 was the original composition (46.1 mol.% SiO_2, 24.4 mol.% Na_2O, 26.9 mol.% CaO and 2.6 mol.% P_2O_5) and has been used in over a million patients as middle ear implants, orbital floor implants and in the treatment of jaw bone defects and is found in a range of commercialised products [112] [113]. For example, as an active repair agent in toothpaste NovaMin® (GlaxoSmithKline, UK), that can mineralise dentin tubules to

TABLE 2.3: Composition of bioglass and glass ceramics [111].

Bioglass	SiO_2	P_2O_5	CaO	CaF	Na_2O	Others	Properties
42S5.6	42.1	2.6	29.0	-	26.3	-	Mol %
46S5.2	46.1	2.6	26.9	-	24.4	-	Mol %; best tissue bonding of bioglass formulas
49S4.9	49.1	2.6	25.3	-	23.8	-	Mol %
5254.6	52.1	2.6	23.8	-	21.5	-	Mol %
55S4.3	55.1	2.6	22.2	-	20.1	-	Mol %
60S3.8	60.1	6	19.6	-	17.7	-	Mol %; no phosphate film formed
45S5	45	6	24.5	-	24.5	-	Original bioglass formulation, binds to bone and soft tissue
45S5F	45	6	12.25	12.25	24.5	-	-
45S5.4F	45	6	14.7	9.8	24.5	-	-
40S5B5	40	6	24.5	-	24.5	$5B_2O_3$	-
52S4.6	52	6	21	-	21	-	-
55S4.3	55	6	19.5	-	19.5	-	-
8625	-	-	-	-	-	Fe_2O_3	Highly biocompatible, does not bind with tissue, fibrous encapsulation; absorbs infrared radiation, can be laser sealed, used for RFD tag encapsulation.

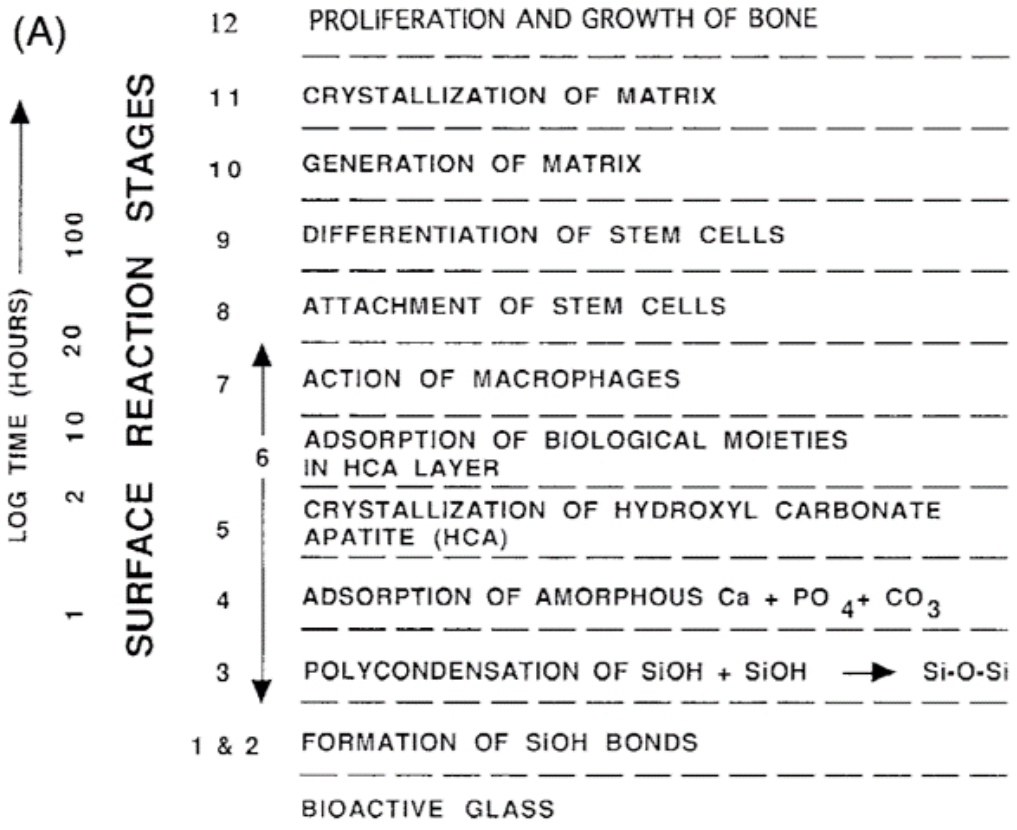


FIGURE 2.5: Sequence of reactions involved during the formation of bonds between bone and bioactive glass [110].

reduce tooth sensitivity. Middle ear prosthesis (MEP®) is made from bioglass® 4565 which has been melt casted. Endosseous Ridge Maintenance Implant (ERMI®) is a cone of bioglass 45S5 inserted into fresh tooth extraction site for the repair of tooth roots and to provide support for dentures. PerioGlas® (now NovaBone Products LLC, Alachua, FL) has been used in the treatment of jaw bone defects from periodontal

disease. A particulate based bioglass® 45S5 synthetic bone graft is pushed into defect sites to provide sufficient anchoring of titanium implants. Other particulate based products include Biogran® (BIOMET 3i, Palm Beach Gardens, FL) and BonAlive® (BonAlive Biomaterials, Turku, Finland) [114] [112]. By altering the composition, the solubility and biological response of the glass can be altered [96]. Table 2.3 summarises the range of compositions available and some of their biological properties.

2.5.2 Metals

Metals have a long history of use in orthopaedic applications such as the fixation of long bone fracture and non-unions, stabilisation of spinal fractures, replacement of damaged joints caused by disease or physical damage and in maxillofacial implants [115]. Their mechanical properties such as high strength, modulus and fatigue life make them, currently, the only material that can withstand the high dynamic loads which the body is often subject to. Metallic materials are often based on alloy systems as opposed to being commercially pure. Standard surgical implant materials include, stainless steel 316 L, cobalt based alloys ASTM F75 and ASTM F799 and titanium alloys such as Ti-6Al-4V (ASTM F67 and F136), these materials have been widely used in the fabrication of artificial hip stems [116]. It is widely accepted that in order to achieve clinical success the implants must be capable of forming a stable interface with the host bone tissue. However, metallic implants do not generally bond to bone tissue, which can lead to fibrous capsule formation and adversely affect the function of the implant [116] [117]. However, surface modification can overcome this issue and improve the bioactivity of the implant surface. For example, calcium phosphate based ceramic coatings have often been utilised to improve the biological interface between the implant surface and bone tissue [118] [110]. However, there has been concern over metallic ion release through corrosion that can lead to adverse inflammatory reactions and could result in tissue damage and secondary infection. Implant infections have been shown to be a significant cause for morbidity and even mortality in patients that have received metallic implants [115]. Studies have highlighted concerns over the long term presence of Ti-6Al-4V implants, as elemental vanadium has been shown to

be cytotoxic. In a study conducted by Gomes et al. it was shown that ion release from Ti-6Al-4V alloys can cause DNA and nuclear damage through generation of highly toxic reactive oxygen species through the reaction between metallic compounds and biological molecules such as DNA [119] [120]. Another issue that arises when using metallic implant materials is a phenomenon known as stress shielding. Stress shielding occurs through stiffness mismatch between bone and the metal implant. As theorised by Julius Wolff in the 19th century, bone in a healthy person is capable of adapting to loads under which it is subject to. Changes in loading regimes over a prolonged period can cause the bone to remodel itself to become more resistant to the direction of that load [121] [122]. When a stiffer implant is used, compared to the natural bone which it is intended to support, the bone is subjected to a lower stress and will therefore remodel itself to adapt to those changes in loading. This can lead to bone resorption and eventually loosening of the implant [123]. Furthermore, the current metallic materials available do not degrade and are therefore permanent once implanted. Device removal and corrective surgery is sometimes required and can therefore lead to increased patient suffering and costs. Although degradable metals are now being looked at such as magnesium based alloys, there are associated risks with magnesium toxicity [116]. Therefore, currently metallic based materials are not the ideal candidate for bone substitute materials.

2.5.3 Polymers

Polymers are an interesting candidate as bone substitute materials, they are composed of covalently bonded, repeating, monomer units that can be either the same (homopolymer) or different (copolymer). Their structures can either be amorphous, with a randomly organised polymer chains, or have a crystalline, highly ordered chain structure. Generally they display properties of both and are therefore semi-crystalline. These properties, in addition to their molecular chain length or molecular weight (Mw), influence their physical and thermal characteristics. Typically, they possess good toughness, high fatigue life, good impact absorbing properties and can be highly biocompatible. Furthermore, these properties can be tuned for the required application by altering

their chemical composition and structure. Polymers for bone tissue related applications generally fall into two categories: non-degradable and degradable [89]. These materials will be explored in further detail in the following section.

2.5.3.1 Non-degradable

Non-degradable polymers are derived from synthetic sources and have been extensively investigated. They include polymers such as: poly(methyl methacrylate) (PMMA); polyaryletherketones (PAEK); and ultra-high-molecular-weight polyethylene (UHMWPE). PMMA is a synthetic thermoplastic resin produced by the polymerisation of methyl methacrylate (MMA) and possesses good processability, handling properties and biocompatibility in addition to good mechanical properties, low moisture absorption and thermal stability up to 65°C [124]. It has been used for the surgical fixation of artificial joints for over 50 years. It was primarily used as a cement and was first implemented in 1958 by Dr. John Charnley who applied dental acrylic for a total hip arthroplasty [125, 126]. However, PMMA suffers from volumetric shrinkages and through long term loading of the implant, the production of PMMA wear particles from metallic surfaces can lead to a local inflammatory response and if left untreated it can lead to chronic complications. The addition of barium sulphate and zirconium oxides were used to improve radio opaqueness, however this posed an increased risk of the implant loosening [125, 127].

Ultra-high-molecular-weight polyethylene is one of the most widely used polymers in orthopaedic applications [124]. Its molecular weight can range from 3 million g/mol to 10 million g/mol, therefore exhibiting good wear and impact resistance. This makes it widely used for articulating surfaces of total joints such as acetabular and tibial components in hip and knee joints [124] [128]. However, despite their good wear resistance, 10% of implanted UHMWPE used in total knee and hip replacements fail after 10 years [128]. This is primarily as a result of pitting, delamination and abrasion, due to the mismatch in surface hardness from opposing metallic or ceramic surfaces of the femoral components in hip and knee devices. This can result in wear particles and

inflammatory responses which, if they are chronic, can lead to osteolysis [128] [129] [130].

Polypropylene is a thermoplastic polymer commonly used in injection moulding and can be characterised by its low density (0.9 g/cm3), relatively high thermal stability, ease of processing and corrosion resistance. It is therefore a potential candidate for light weight orthopaedic implants and has been explored for use in bone fixation devices in veterinary science as intramedullary rods and orbital reconstructions [131, 132].

Polysulfones (PS) is a sulphur containing thermoplastic which possesses good chemical resistance, thermal stability (with wide glass transition temperature typically 190 - 290°C), strength and flexibility. Polysulfone composites with HA have been explored for use in as bone substitute materials [133, 134].

Polyamide (PA) is characterised by the presence of repeating amide groups thus having a similar backbone structure to natural polypeptide sequences [135], PA is commercially referred to as Nylon. Several different types of polyamide exist, each being denoted by a specific number (e.g. PA12 or PA66) which refers to the number of carbon atoms present in the molecular chain and thus determines their properties [136]. PA is less vulnerable to chemical modification and direct binding of antibodies to the surface of the material thus making it inert and highly biocompatible. Furthermore, due to its high tensile strength, flexibility and toughness, its clinical uses are diverse. These applications have included: sutures, implants for ligament and tendon repair, catheter balloons and dialysis membranes [135, 137]. Although these materials may offer promise they lack the ability to degrade within the human body. Long term exposure to these materials may elicit undesirable, chronic, inflammation which may require further corrective surgery to remove the implant. Therefore, the ideal permanent bone substitute material for low weight bearing applications, such as fracture fixation devices, the material should also be biodegrable with by-products that can be tolerated within the body and removed through normal metabolic processes.

2.5.3.2 Biodegradable

Biodegardable polymers can either be derived from natural or synthetic sources.

2.5.3.3 Natural

Natural polymers are a logical choice for bone substitute materials and are primarily formed from the constituents of the ECM. As discussed previously collagen is the most abundant protein in animals and forms a third of the total protein content in humans and forms 89% of the organic matrix and 32% of the volumetric composition of bone [138]. Due to its favourable cell adhesion properties and ease of processability into sheets, tubes, foams and powders, collagen has been used in a variety of commercialised products. For example, Bio-Glide® (GeistlichPharma AG, Wolhusen, Switzerland) is a resorbable collagen membrane for the use in guided bone regeneration [139] [140]. In 1993, the first collagen based implant for bone, Collagraft^{TM} (collagen corp, USA) was released and was based on highly purified Type I collagen. INFUSE® is another bone graft material (Medtronic Sofamor Danek, Inc., USA) which incorporates recombinant human bone morphogenetic protein-2 (rhBMP-2) in a collagen sponge carrier and has been applied as lumbar spine fusion devices, tibial fracture plates, maxillofacial and dental regenerative grafting procedures. OssiMend^{TM} Bone Graft Matrix (Collagen Matrix, Inc. New Jersey, USA) combines calcium phosphate minerals with collagen and has been used in spinal surgery [141]. Other applications include the regeneration of cartilage, skin and blood vessel, corneal bandages, contact lenses and drug delivery devices [142, 143].

2.5.3.4 Synthetic

Despite their promise the down sides of natural polymers include poor mechanical properties, low reproducibility due to dependency of the natural source, water solubility or high hydrophilicity which can lead to swelling of the materials, immunogenicity, and potential risk of transmitting animal-originated pathogens [142]. Therefore, investigations into synthetically derived biodegradable polymers have been significant in recent

years and they are currently the largest subset of biodegradable polymers available. One such material that has been studied significantly is Polylactic acid (PLA). PLA is a chiral molecule with four stereoisomeric forms D-PLA, L-PLA as well as racemic D,L-PLA and meso-PLA. This enables products derived from Lactic acid to exhibit a wide range of properties and degradation profiles that can be specifically tailored for the desired application [144]. The L/D ratio of D,L-PLA influences what type of crystal structure is present [145]. For example, matrices containing over 93% L-PLA are semi-crystalline [145]. The densely packed crystalline regions retards water penetration thus reducing its degradation rate (typically $>$ 24 months). However, between 50 - 93%, L-PLA a completely amorphous structure is present with a less densely packed and degrades faster. These are commonly employed in the fabrication of devices which are subject to low levels of mechanical stresses such as absorbable sutures. These can be tailored to degrade between 1 - 12 months, therefore, providing sufficient support to hold a wound closed as it heals. In practice L-PLA is more frequently employed as it degrades via a hydrolytic enzymatic pathway yielding L+ lactic acid which is a naturally occurring stereoisomer of lactic acid and is more readily tolerated within the body [146]. Furthermore, due to its semi-crystalline structure it has improved mechanical stiffness (2.7GPa), toughness and degradation profiles which are best suited for orthopaedic implant devices [147]. PLA already has FDA approval and is currently used in biodegradable sutures and drug delivery vehicles [148]. Some PLLA based orthopaedic products currently on the market include: Phantom Thread Soft Tissue Fixation Screw®, Phantom Suture Anchor®, Bio screw®, Bio-Anchor® and the Clearfix Meniscal Dart® to name a few. Their degradation profiles have been tailored based on the degree of crystallinity, molecular weight and co-polymerisation with other polymers [149].

In addition to PLA, Polyglycolic acid (PGA) has also been extensively researched as a bone substitute material. PGA is a highly crystalline (45 - 55%) polymer which possesses a high melting point (220 - 225°C) and is most commonly formed through the ring-opening polymerisation of cyclic glycolide monomers. PGA degrades through hydrolysis and esterases, the glycolic acid by-products can be excreted directly in urine or may react to form glycine which can subsequently form pyruvic acid and enter the

tricarboxylic acid cycle [58]. Due to its high tensile modulus (7 GPa) and strength and fibre forming capabilities it has been used in commercial surgical sutures since the 1960s such as Dexon® and Suretak^{TM} . It has also been used in fracture fixation devices such as, SmartPins^{TM} and Bionix^{TM} implants by Smith and Nephew, Craniomaxillofacial fixation, LactoSorb^{TM}; Screws and Plates by Biomet and meniscus repair, SD sorb^{TM} by Surgical Dynamics [58] [59]. However, PGA is more acidic and hydrophilic than PLA and is thus more hydrolytically unstable and degrades at a faster rate compared to PLA. PGA is therefore, not used in its pure form in these devices, rather, it is co-polymerised with PLA monomers to achieved the desired mechanical and degradation profiles for its intended application [58].

Poly-carprolactone (PCL) is a semi-crystalline polymer with a low melting temperature, (58 - 63°C) and low glass transition temperature (-60°C) which allows for easy processing. It is prepared by the ring opening polymerisation of ϵ-caprolactone [58] [141]. The degradation rate of PCL is three times slower than P(DL)LA, however it can be adjusted by alteration of the crystallinity of the polymer by co-polymerising it with DL-Lactide. The versatility of PCL and its co-polymers means it has been widely investigated for bone and cartilage repair in addition to surgical sutures such as Monocryl® [58] [141] [150]. However, PCL has limited bioregulatory activity and is susceptible to bacteria mediated degradation and has thus limited its use [151].

Polypropylene fumarate (PPF) is an unsaturated linear polyester and is produced by the reaction of diethyl fumarate and propylene glycol through a bis(hydroxypropyl)lfumarate diester intermediate [152]. When cross linked through fumarate double bond its forms a degradable network that can possess high mechanical strength and has therefore been investigated as a bone substitute material. The rate of degradation can also be adjusted through the type of cross linking present and through co-polymerisation [153]. Studies conducted on a rat tibial defect site have shown good osteoblast proliferation and woven bone formation in addition to low inflammatory responses thus indicating that PPF has good bone biocompatibility [141] [154]. During degradation via hydrolytic ester chain scission, propylene glycol and fumaric acid are produced and are well tolerated within the body. PPF can also be injected into a liquid form and crosslinked in-situ making PPF suitable for minimally persistent procedures for

orthopaedic applications [141] [154]. Cross linkable polyanhydrides are also being explored as injectable devices, which can be cured via UV, for the treatment of irregular shaped bone defects. They have been shown to provide sufficient mechanical support to facilitate bone regeneration whilst also being degradable overtime [155] [156].

Polyhydroxyalkanoates (PHA) are aliphatic polyesters that have been produced by microorganisms through unbalanced growth conditions [157] [158] [141]. PHAs are semi-crystalline with melting temperature range of 160 - 180°C. Several co-polymers of PHA exist, including poly 3-hydroxybutylvalerate (PHB), Poly(3-hydroxybutyrate-co-3-hydroxyvalerate)(PHBV), poly 4-hydroxybutarate (P4HB) and poly 3-hydroxyoctanoate (PHO) [158]. PHA and associated composites have been utilised in a range of orthopaedic applications including; meniscus repair devices, tacks, screws, bone plates, articular cartilage repair devices, bone marrow scaffolds, spinal fusion devices and as ligament and tendon grafts [158] [159]. Due to the production method, pyrogenic contaminants can be purified with PHA which can pose risks for implantation devices and must therefore be removed using oxidising agents such as hydrogen peroxide or benzoyl peroxide to reduce the endotoxin levels [158] [160].

2.5.3.5 Composites

Although polymers possess good biocompatibility once implanted and have highly tuneable properties they still generally lack the necessary mechanical stiffness and bioactive potential for a bone substitute material. Therefore, reinforcement of a relatively low modulus polymer with an inorganic phase can yield materials that possess stronger mechanical and bioactive properties compared to the native polymer matrix [53]. Applications of biocomposites have seen prolific use in musculoskeletal applications and bone regeneration over the past few decades [53]. Such applications include bone plates, screws, bone replacement materials and cements. Much of the biocomposite research conducted today focuses on polymer-ceramic based composites. They are an attractive option given their potential to reduce costs and risks associated with re-corrective surgery and removal of permanent devices [53]. As mentioned previously calcium phosphate based ceramics are by far the most popular choice of additive/

filler. Bonfield et al. [161] was the first to develop a reinforced polymer composite with micron sized (8.77μm) HA acting as a bioactive filler for use as a bone analogue material to replicate skeletal tissue. HAPEX^{TM} is a HA reinforced polyethylene composite and was the first HA based composite (40% HA content) to be commercialised. It is currently used in middle ear and orbital floor implants with and possesses a tensile modulus of approximately 4.45 GPa, which is significantly higher than base PE polymer. The presence of HA also promotes integration of the implant with the hosts bone [161] [162]. Other HA reinforced devices include HYAFF11-HA^{TM} and HA-PMMA bone cements [161].

Composite systems utilising carbon fibre has also been explored for bone augmentation devices due to their incredibly high stiffness (up to 500 GPa [163]) and light weight nature, they also improve the radioluscency of the composite material. Carbon fibre/PEEK composites have garnered much attention recently due to their bioinertness and high mechanical and fatigue strength, comparable to metallic based systems, and have been explored for use as hip stems [164]. To improve the bioactivity, intramedullary nails have been fabricated using a mixture of carbon fibre/ polyamide 12/ hydroxyapatite (CF/PA12/HA). Numerical simulation has predicted improved bone density of these implants compared to traditional titanium based implants [165] [164]. However, concerns have arisen in regards to the effects that CF wear debris can have on the surrounding tissue and requires further investigation.

As mentioned, biodegradable polymers are the most desirable form of matrix materials and there has been much focus on the utilisation of these polymers in composite systems. For example, composite foams consisting of PLGA and short HA fibres have been produced in a two-stage process of particulate leaching followed by compression moulding. Porosimetry revealed the mean pore size to range from 24 $\pm$ 4 to 52 $\pm$6 μm for polymer fibre ratios of 5:8 and 1:0 respectively. The compressive and yield strength of the composite foams also increased with increasing HA content [55]. HA granules have also been incorporated into blends of PCL and poly(D, L-lactic-co-glycolic acid) these composites were produced through phase separation techniques. The tensile properties of the resulting composites showed a dramatic increase reaching a third of that of trabecular bone when 10% HA was used. Histological and SEM analysis also

revealed that rabbit bone marrow stromal cells, cultured on the composites, were well supported and penetrated the scaffold material by 8 weeks with collagen production being present to a depth of 500 μm [56]. Attawia et al. [166] has shown that osteoblasts grown on porous PLGA/HA composite scaffolds proliferated by 145% in 24 h compared to neat polymer material, highlighting the increased bioactivity that composite materials can provide over base polymers. Immunofluorescence and confocal laser microscopy had also revealed that the cells had begun migrating to the interior of the composite scaffold. Zhang et al. [57] has also investigated the production of highly porous PLA and PLGA/ HA scaffolds via thermally induced phase separation techniques. A significant increase (83%) in compressive strength and modulus were observed for the reinforced composite compared to the neat polymers. In-vitro cell studies on the composites also showed that osteoblasts penetrated deep into the scaffold compared to cells cultured on pure polymeric materials, indicating the osteoconductive nature of the scaffold. Furthermore, for the six-week cultivation period cell numbers were consistently higher on the composites compared to the neat polymer. In addition, bone specific markers such as bone sialoprotein and osteocalcin were detected at increased quantities on the composite materials. Histological analysis also confirmed the osteoinductive potential of the composites through increased quantities of tissue formation that was more uniformly distributed throughout the composite scaffolds compared to the neat polymer which only showed new tissue formation isolated to the surface.

2.5.3.6 Nano-composites

Recently an exciting field of research has developed with nano-composites. Due to their high specific surface area to volume ratio and their nano-topography, Nanoparticles (NPs) have attracted much attention in the field of bone tissue engineering, with enhanced bioactivity when compared to their microscaled counterparts. For example, in-vitro studies by Webster et al. [52] demonstrated that osteoblast adhesion was significantly higher on surfaces containing nanoscale particles (24 nm alumina, 39 nm titania and 67 nm HA) compared to micron sized particles. Protein analysis also showed

that surfaces containing NPs had greater levels of adsorbed vitronectin which is crucial for anchorage dependent cells. Morphological studies on human osteoblast cells (HOB) that were cultured on nano-silicon/HA patterned surface showed that HOBs were capable of growing in the presence of these nanoparticles with long filopodia extending between the NP patterned tracks. Confluent areas of cells and well organised fibre-like extracellular matrices were observed after a 7 day culture period. Nanosized spherical nodules attached within the newly deposited ECM were also observed and through energy dispersive x-ray (EDX) analysis found that these nodules contained Ca and P therefore indicating that these nodules were in fact a calcification front for further bone mineralisation [167]. Pukanszky et al. [168] have also shown that the effect of particle size has a dramatic effect on the strength of various composite systems. For example, the strength of a Polypropylene (PP)/$CaCO_3$ composite composed of varying reinforcement particle sizes ranging from 10 nm - 58 μm, was shown to increase with decreasing particle size. Figure 2.6 highlights that for a given particulate volume fraction the composite strength increases with decreasing particle size. It has been found that the smaller particles have a higher total surface area compared to particles of a larger diameter and thus strength increases with increasing surface area due to a more efficient stress transfer mechanism between the interface of the matrix and reinforcing particle [169].

Similarly PA6/silica nanocomposites made from 12, 25 and 50 nm silica reinforcing particles supports this evidence with the smaller particles providing a greater degree of reinforcement through an increase in strength. Furthermore another study of the mechanical properties of Kaolin filled nylon 6,6 composites, also found that strength increases with a mean decreasing particle size (0.4 - 4.8μm)[169]. Figure 2.7 shows that the tensile strength of an epoxy silica composite is also significantly affected by the mean particle size within a micro-scale range and indicates a large improvement in tensile strength with decreasing particle size. This is further supported by tensile test results with epoxy/alumina trihydrate composites with the highest tensile strength recorded at 58 $\pm$3.4 MPa (1 μm, 10 vol%) and the lowest 27.2 $\pm$12.4 MPa (12μm, 10 vol%). Other systems such as $Mg(OH)_2$/ ethylene-propyl-ene-diene terpolymer (EPDM) also shows that for the same particle loading (40 wt%) nano sized $Mg(OH)_2$

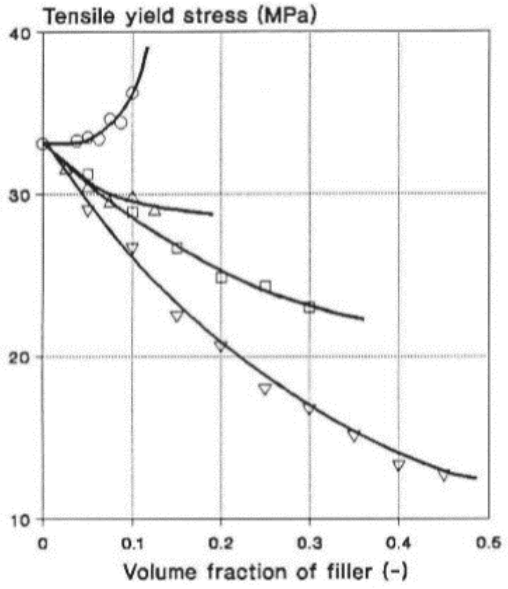


FIGURE 2.6: Effect of particle size on the tensile yield stress of PP/$CaCO_3$ composite: (circle) 0.01 μm, (triangle) 0.08 μm, (square) 1.3 μm and (Inverted-triangle) 58 μm [168].

particle fillers (50 - 100 nm) imparted stronger reinforcement (9 MPa) than micron sized fillers (2.03 μm, 5MPa) [169].

The advantages of using nano-fillers has also been discussed in the work by Griffith and Weibull (Griffith,1920; Weibull, 1951). They claimed that the smaller the reinforcement is the stronger it becomes (typically 1 - 5 wt% [170]). They theorise that as the material size is decreased the probability of critical flaw size also decreases which enables the material to approach its intrinsic strength. In a study conducted using graphene nano platelets (GNP) at 0.1wt% in a bisphenol-A -based epoxy; under uniaxial tensile testing the young's modulus increases from 2.85 GPa (baseline epoxy, no filler) to 3.74 GPa. A significant increase of 31%, whilst the tensile strength increases by 40% from 55MPa to 78 MPa [171]. However, ensuring that the particles are well dispersed and well bonded to the matrix is vital [172]. Research has highlighted the difficulties in using nanofillers, with particle agglomeration being the main issue when TiO_2 nanoparticles were incorporated into a PLGA matrix [173]. The effect of agglomeration increased with increasing nanofiller volume fraction owing to their larger specific surface area and has thus led to a decrease in mechanical properties with increasing particle loading [53]. For example in a study involving PVC/nano $CaCO_3$ composites

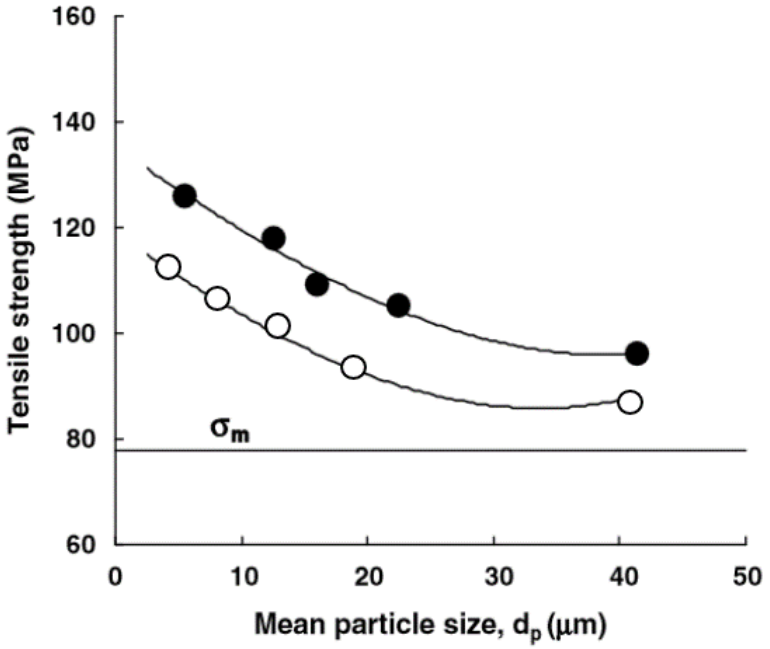


FIGURE 2.7: Effect of particle size on tensile strength of epoxy composite (black circles) 64 wt% silica particles, (white circles) 55 wt% silica particles. Solid line represents pure matrix strength [169].

at various weight ratios it was found that at 5 wt% nanoparticle loading the composite exhibited an increase in tensile strength and peaked at 61 MPa however at higher loadings the tensile strength in fact decreased. At 30 wt% the tensile strength fell to 57 MPa (close to that of 100% PVC) and this was attributed to poor filler-polymer interaction and agglomeration of the nanoparticles [174]. Therefore, investigations looking at improving the dispersion of nanoparticles within polymer matrices are still ongoing. High shear mixing has been used to exfoliate the NPs and has also been applied to silicate- nanoclay particles in an unsaturated polymer through high shear rates of 1000 s^{-1} improvements in NP dispersion were achieved [175]. However, this technique may not be suitable for heat sensitive materials and therefore other methods such as coating the nanoparticles with dispersants have also been trialled [176].

2.6 Common Production Methods for Bone Substitute Materials

Sponge and foam materials have been produced either by solvent casting/ salt leaching methods and have been utilised in bone and cartilage tissue engineering applications and in drug delivery systems. These techniques have used resorbable polymers such as PLLA, gelatin and copolymer blends like PLGA/PVA [14–19]. Fabrication involves salt crystals which are placed into a mould, a polymer is poured over the salt which flows into the empty spaces. Using a solvent, the salt is then leached from the scaffold leaving behind a porous structure. Choice of salt grain sizes determines the sizes of the pores generated in the overall construct. Gas foaming techniques have also been explored for creating porous scaffolds. The polymer is vigorously stirred forming an aerated foam and then set. The technique is commonly combined with solvent casting/particulate leaching to form open porous structures. For example, PLLA, PLGA and PDLLA have been fabricated via this route to produce materials with controlled porosity up to 97% and has been utilised in drug delivery and for tissue engineering constructs [20–22]. Another technique involves fusing micron sized spheres of polymer/ ceramic to form an interconnected porous structure. These particles are commonly prepared via solvent evaporation technique where the polymer is dissolved in a water immiscible solvent and a dispersion is formed with small droplets of polymer. The solvent is evaporated off leaving behind microspheres [23]. Copolymer blends of PLGA and PLGA with HA have been fabricated via this route resulting in high density constructs and due to the large surface area available could potentially be applicable to bone repair materials and as an in-vitro model for evaluating anticancer agents [177] [178] [179] [180]. Particle aggregation techniques have also been utilised in fabricating porous scaffolds and involves the random packing of the particles with subsequent thermal processing to fuse the particles together forming a 3D porous structure with inherent porosity. Gelatin microparticles have been utilised to form 3D scaffolds for applications in cartilage engineering through this method [181]. Sintered PLGA microspheres have also been explored in creating structures with a mean pore size of 210 μm, 35% porosity and a compressive modulus of 232 MPa [182]. An alternative method involves

liquid phase separation and has also been employed in the production of highly porous microcellular foams and membranes from low density polystyrene, PEG and PLLA and poly urethane scaffolds with pores sizes of up to 150 μm [24–27]. A single homogenous polymer solution is created at an elevated temperature and is converted, by the removal of thermal energy, into two separated phases. With one phase being polymer rich and the other being polymer-lean. Freeze drying of the phase separated polymer solution leads to microcellular structures because of the removal of solvent. Controlling the thermodynamic state of the polymer solution, depending on whether the quenching end point is located in the metastable region between bimodal and spinodal curves or in an unstable region below the spinodal curve, a poorly interconnected bead like structure can be achieved or subsequently a well-interconnected open porous structure can be achieved. The polymer concentration, quenching route, and quenching depth the pore size and distribution can be controlled [183]. Advantages of such techniques includes simplicity and control of pore size and geometry. However, pore interconnectivity is often low and difficult to control. Use of toxic solvents also poses health risks. Furthermore, these techniques are generally limited to simple shapes such as flat sheets or tubes with scaffold thicknesses of only around 3 mm in addition these techniques are very time consuming [28] [14]. Furthermore, batch to batch variation between samples and mechanically weak structures limits these production methods to low stress applications.

In the production of fully dense polymeric materials techniques such as melt extrusion are commonly employed. This involves the melting of thermoplastics at high temperature and extruding them through a die or into a cast. The molten plastic is then cooled leaving behind a fully dense structure. Conventional extrusion using twin screw extruders have been used to fabricate nano-composites from a range of degradable and non-degradable materials such as HDPE/UHMWPE reinforced with HA which has seen commercialization as a bone replacement material (HAPEX) [29]. Zirconia and β-TCP have also been utilized as inorganic filler material in polyethylene nano-composites produced by melt extrusion [30]. Melt extrusion of polyamides reinforced with nHA for bone tissue engineering applications have also been studied with

improvements in tensile modulus and compressive modulus in addition to even distribution of nHA throughout the polymer matrix [184] [185]. PEEK based composites using tri-calcium phosphates have shown to be favourable materials for the attachment of cells and has been demonstrated using fibroblasts and human osteoblasts [31] [32]. PEEK/CNT have also been explored for their thermal properties. It was found that even with the addition of small loading of CNT (1 wt%) increased the crystallization temperature of PEEK by 10°C and raised the crystallinity of the matrix by 6%. TGA analysis also demonstrated a significant increase in thermal stability by raising the degradation temperature by 45°C for a 1 wt% loading of CNT [33]. Resorbable composites utilising PLA/ HA have been fabricated using twin screw extruder. However, results have shown that due to the high temperatures involved during the mixing of the HA and polymer melt degradation of the material was seen with a decrease in molecular weight from 100 KDa to 49 KDa which could be confirmed with the presence of degradation products within the machinery, this led to a subsequent loss in mechanical properties of the composite with a reduction in tensile strength (66 MPa) compared to virgin PLA (73 MPa) [34]. PLA/ Aluminium oxide based composites have also been explored and demonstrated uniform distribution of aluminium oxide particles, the thermal stability of the composite was on par with virgin PLA with degradation occurring above 350°C for both materials. However, a decrease in molecular weight, associated with the high temperature conditions during processing, was also observed resulting in decreased mechanical performance [35]. PCL/HA composites produced by conventional melt extrusion techniques have shown improvements in modulus with increased filler content and processing conditions. It was found that dry blending the PLA with HA prior to melt extrusion lead to the greatest improvement in elastic modulus 550 MPa at 30 wt% HA. However ultimate tensile strength decreased with increasing filler content due to poor interaction between the polymer matrix and HA filler [36].

Due to the limitations of such techniques in the fabrication of complex structures the use of additive manufacturing as a method for the production of bone substitute materials will be explored in the following section.

2.7 Additive Manufacturing

Additive manufacturing (AM) is a broad term used to describe a collection of advanced manufacturing techniques that produce physical three-dimensional (3D) objects derived from computer generated models. The term is often used interchangeably with 3D Printing. According to Wohlers Associates the industry generated $ 5.165 billion in revenue in 2015 and by 2020 it is projected to be a $ 17 billion industry [186]. Three of the leading sectors in this field include the automotive, medical and aerospace industries [187–189]. To date there are numerous techniques that can be described as AM processes and in 2012 the ASTM International committee, F42 on Additive Manufacturing Technologies, published a list that categorised the AM processes; this can be seen in Table 2.4. Compared to traditional, subtractive methods, such as milling, cutting, drilling or moulding processes, AM adds material in a layer-by-layer manner. Therefore, AM offers the ability to create structures with complex internal and external geometries and thus offers greater design freedom compared to the traditional manufacturing methods. Furthermore, for low volume production, AM removes the need for machine tooling and allows for the production of highly customised products through improved resource efficiency during manufacturing as a result of the bottom-up approach [190]. Life cycle analysis of goods produced by AM show that savings are estimated to be in the region of $100-370 billion by 2025 arising from reductions in material input and handling, in addition to shorter supply chain as parts can be made on site which eliminates transportation costs and reduces lead time [190]. Furthermore, storage costs for inventory can also be eliminated as items can be made to order [187, 190–192].

In the medical implants sector coupling of AM and advanced imaging technology such as CT and MRI, it is now possible to translate patient specific data into 3D models which can be used to print prosthetics and implants that match the unique requirements for individual patients. AM is well suited for this niche, especially for small-sized non-standard implants such as those used in the spine, craniofacial and dental areas [42–45]. AM first saw commercial success in the medical field with the production of customised dental implants and prosthetics in the early 2000s and has rapidly expanded with the

TABLE 2.4: Summary of AM processes as categorised by the 2012 ASTM international Committee [196].

Classification	Technology	Description	Materials	Developers (country)
Binder Jetting	3D printing Ink Jetting S-Print M-Print	Creates objects by depositing a binding agent to join powdered material.	Metals, polymer, ceramics	ExOne (USA) VoxelJet (Germany) 3D Systems (USA)
Direct Energy Deposition	Direct metal deposition Laser deposition Laser consolidation Electron beam direct Melting	Parts built by using focused thermal energy to fuse materials as they are deposited onto a substrate.	Metal:powders and wires	DM3D (USA) NRC-IMI (Canada) Irepa LAser (France) Trumpf (Germany) Sciaky (USA)
Material Exrusion	Fused deposition modelling	Builds parts in layers by dispensing materials through a nozzle	Polymer	Stratasys (USA) Delta Micro Factory (China)
Material Jetting	Polyjet Ink-jetting Thermojet	Build parts by depositing small droplets which are then cured by exposure to light.	Photopolymer and wax	3D Systems (USA) Stratasys (USA) LUXexcel (Netherlands) 3D Systems (USA)
Powder Bed Fusion	Direct metal laser sintering Selective laser melting Electron beam melting selective laser sintering	Creates objects using thermal energy to fuse regions of a powder bed.	Metals, polymers, ceramics	EOS (Germany) Reinshaw (UK) Phenix Systems (France) Matsura Machinery (Japan) ARCAM (Sweden)
Sheet Lamination	Ultrasonic consolidation Laminated object manufacture	Parts built by trimming sheets of material and binding them together in layers.	Hybrids, metallic, ceramic	Fabrisonic (USA) CAM-LEM (USA)
VAT Photopolymerisation	Steriolithography Digital light processing	Parts built by using light to selectively cure layers of a material in a vat of photopolymer.	Photopolymers, ceramics	3D Systems (USA) EnvisionTEC (Germany) DWS Sri (Italy) Lithoz (Austria)

inclusion of bone, ears, wind pipe, jaw, blood vessels, organs and drug delivery devices [42, 43, 193, 194]. Today 99% of hearing aids manufactured are custom made using AM [42]. The ability to produce custom implants and prosthetics solves a persistent problem in orthopaedics where standard implants are often not sufficient for some patients and complex cases. Surgeons may need to modify implants by having to either shave away plastic/metal or they may need to perform extra bone graft surgery to ensure that the implant is fitted correctly. This is a frequent issue in neurosurgery where standard cranial implants do not exist [42] [43]. However, Materialise is one of several companies that has been attempting to address the issue. They have utilised AM to design custom, titanium cranial plates (as seen in Figure 2.8) that fit large defect sites by utilising patients own MRI scan data and then processing this data in computer-aided-design (CAD) software to produce a custom fit cranial plate. These plates also incorporate a complex porous geometry to facilitate bone integration with the implant and provides ideally placed fixation points based on location and bone density of the implant site [42]. Maxillofacial implants, created by AM at the BIOMED research institute was the first titanium mandibular prosthesis to be implanted and in 2013 Oxford Performance Materials received FDA approval for AM produced PEEK skull plate which was successfully implanted [195].

It is clear that AM provides an exciting avenue of research in the production of medical devices, especially within the field of orthopaedics. However, the adoption of AM mainstream in this area is still relatively slow. The choice of approved implantable materials is currently limited and identifying which AM process is most suitable for a given application still needs further investigation. Therefore, the regulatory framework for AM produced medical devices has not been established, however strides are being made with the FDA publishing a draft guidance for the design and manufacture of implantable 3D-printed medical devices [43]. Another significant issue hindering the adoption of AM mainstream is the high initial cost of machines and the lack of knowledge for the processes themselves compared to well established, traditional methods. This has a considerable impact on the design process chain [197]. The speed of manufacture is another issue. Depending on the complexity of design and the requirement for tight tolerances and surface finish, AM processes can take substantially longer than traditional methods for the production of large number of simple parts [197]. Furthermore, the notion that AM provides "complexity for free" is not true in practice. For some AM processes, such as, fuse deposition modelling (FDM), stereolithography (SLA) and metal based powder bed fusion (PBF), complex shapes with large overhangs will require additional support structures to facilitate their production. For PBF and SLA which utilise powder and light curable resins, respectively, will require the removal of excess material from hollow cavities and thus drainage systems must be considered during the design stage, all of which add to pre- and post-production steps. As touched upon earlier, AM technologies are not normally suited to high through put mass production, rather its greatest advantages are seen in low quantity, highly bespoke items such as those found within the medical sector [197].

As mentioned, there is plethora of AM techniques available. The most common and most easily accessible is FDM, a melt extrusion based process. It has been utilised in the field of hard tissue regeneration with the primary material under investigation for this application being biodegradable PCL and PCL based composites such as PCL-TCP and PCL-HA. These materials have been investigated to produce scaffolds for bone and cartilage regeneration. For example, Zein et al. [200] investigated FDM to produce scaffolds with honeycomb-like, porous structures. PCL scaffolds were produced with

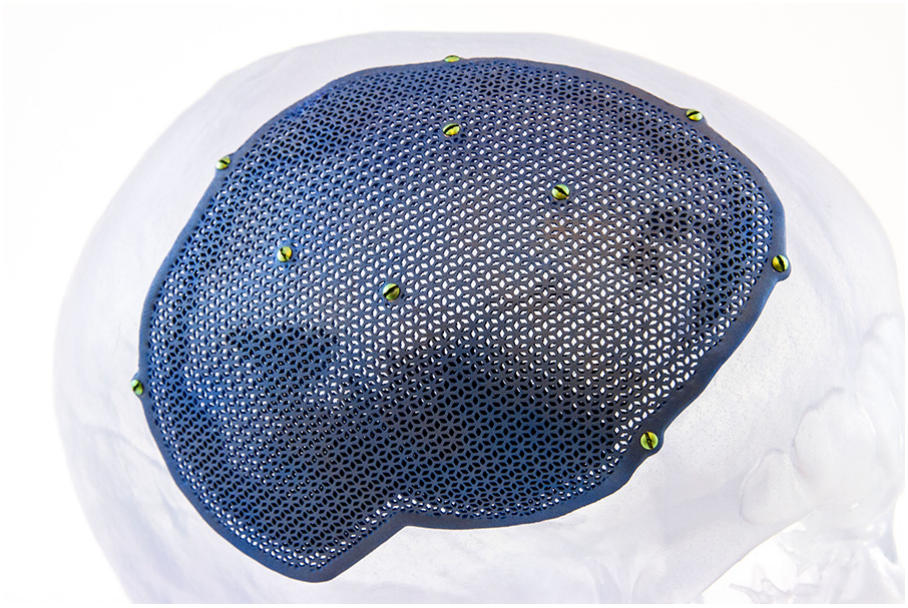


FIGURE 2.8: Image of a Titanium skull implant produced by AM providing a good fit over a large defect site [198]

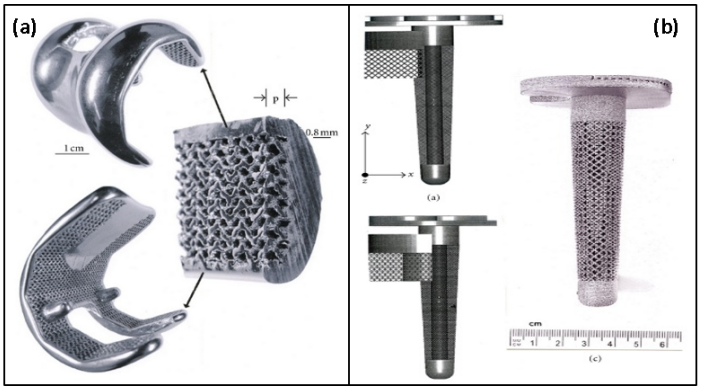


FIGURE 2.9: Image of (a) Femoral component of knee implant made by EBM, cross section shows functionally graded structure to maximise strength-weight and (b) tibial component with open porous structure for bio-integration [199].

a range of pore sizes from 160 to 700 μm, and porosities ranging from 48 to 77% . However, the mechanical properties such as compressive modulus, ranging from 4 to 77 MPa, and a compressive strength ranging from 0.4 to 3.6 MPa, was relatively low to be considered for use as hard tissue replacement [200]. Rai et al. [201] demonstrated good hMSCs viability and differentiation when cultured on PCL-TCP scaffolds in-vitro through fluorescent imaging, DNA quantification and ALP production. However, in-vivo studies using femoral critical -sized defects in nude rats showed that only 50% of hMSCs implanted on the scaffold, responded favourably, which was determined by new bone volume [201]. On the other hand, scaffolds made from PCL-TCP, with MSCs

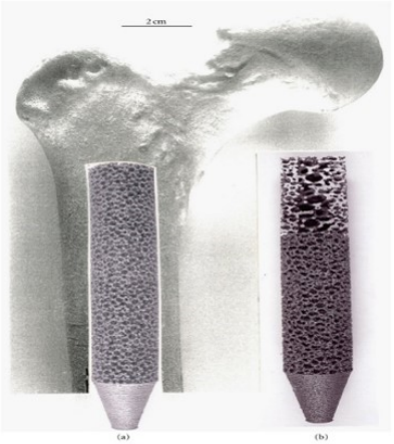


FIGURE 2.10: Image of a intramedullary rod manufactured by EBM with porous outer structure and dense core [199].

pre-loaded onto them, was used to treat a critical size defects in a dog mandible and was shown to facilitate early revascularization and faster bone regeneration over an 8 week period [202]. Xu et al. [203] prepared PCL-HA scaffolds using FDM. A CT model obtained from a segment of a goat femur was used as a guide for the design of a structure with cortical and cancellous bone-like features. The structures demonstrated good cytocompatibility with osteoblast like MC3T3-E1 cells and in-vivo bone formation with compressive strengths comparable to that of the adult goat femur of 15.43 MPa and 18.17 MPa respectively. However due to the layer wise deposition of material the tensile modulus was significantly lower at 80.16 MPa compared to $>$132.22 MPa of the adult goat femur [203].

SLA, on the other hand, is another wide spread AM technique, which utilises photo curable resins. Compared to FDM, the resolution achievable is significantly higher as the galvanometer systems used to drive the laser optics can position the laser spot with an accuracy of upto 25 μm, in X and Y, the resolution on a FDM printer is largely determined by nozzle size which typically range from 0.2 - 0.4 mm [204]. This greater resolution enables the production of highly intricate shapes with well-defined architectures. However, the use of SLA in the production of hard tissue scaffolds has been limited, although successful attempts have been made with the use of photo-crosslinkable PCL which produced scaffolds with a porosity of $\approx$70.5% and an average pore size of 465 μm in addition to polypropylene fumarate (PPF) [205] [206]. However,

the cellular functionality and viability of cells cultures on the scaffolds remains untested and there is currently a lack of in-vitro and in-vivo tests in literature demonstrating the potential of SLA in the production of hard tissue [205]. Therefore, the adoption of SLA within the orthopaedic implant sector has been extremely limited. Furthermore, the reliance on photocurable resins is a major drawback in regards to the adoption of SLA for biomedical implants. The major categories of photoinitiators include radical photopolymerisation, hydrogen abstraction and cationic photopolymerization the latter of which is not used in medical applications due to generation of toxic by-products [205, 207, 208]. Therefore, the selection of photocurable resins that are suitable and commercially available, remains extremely limited.

Much of the AM produced orthopaedic implants are currently focused around metal based PBF methods, for example knee and hip implants, as seen in Figure 2.9, fabricated using electron beam melting (EBM) from Co-29Cr-6Mo alloy, the greater design freedom that AM offers allowed for the production of functionally graded systems which combines the best properties of denser materials with those of more porous ones. The low porosity regions provide strength, whilst high porosity promotes cellular infiltration, proliferation and differentiation within the implant to achieve bio-integration with the hosts bone tissue [209] [210]. These functionally graded implants were printed as monolithic structures, a complexity that cannot be achieved with conventional manufacturing methods such as casting [199]. Intramedullary rods for the upper femur have also been fabricated by EBM, as seen in Figure 2.10, with Ti-6Al-4V with a central solid rod for stiffness and outer mesh of porous foam like structure to promote vascularisation and bone tissue ingrowth [199]. Studies conducted on Ti-6Al-4V scaffolds prepared by EBM has demonstrated good In-vitro cytocompatibility and in-vivo ossintegration with elevated cell counts and ALP production over time and increased depth of bone ingrowth when implanted into segmental defects made in a goat metatarsus [211]. Laser melting (LM) and laser ablation methods have also been implemented in the production of custom artificial hip stems from Ti-6Al-4V, following post heat treatment, metallic implants made from LM can have a tensile modulus ($>$1 GPa) that exceeds conventional forging, milling and casting processes in addition to having a comparable elongation at break of 15%. This high stiffness is required to support

the strong loads femoral bones are subject to [212–214]. Metal based PBF implants have also been successfully implemented in; total shoulder replacements, acetabular cages, knee replacements and as fracture fixation devices in the contralateral wrist with good clinical results [215–219]. However, as discussed in section 2.5.2, metallic materials are not always best suited as bone replacement materials due to their very high stiffness which may lead to stress shielding, longevity within the body and risks posed with chronic immune reaction and corrosion leading to release of potentially harmful metal ions. Similar to FDM and SLA processes metal based PBF also requires additional support structures for large overhangs, typically greater than 45°, support material then requires manual removal which can be difficult in areas where there are thin walled structures. The surface then requires post finishing to preserve the carefully engineered surfaces which further adds to post processing time and costs. Initial costs of metallic powder based machines are significantly higher than that of FDM and SLA based systems and are typically in the region of a $ 1 million. Feed stock of metallic powder and powder handling stations with ventilation systems are also a significant factor to consider when compared to filament and resin based systems.

Although, PBF methods have some significant draw backs, it is still the AM method of choice when manufacturing orthopaedic implants offering high resolution and good mechanical properties. The following section discusses a polymer based PBF method which holds significant promise in addressing some of the short comings of the other AM techniques discussed.

2.8 Laser Sintering

Laser sintering is a powder based, free-form, fabrication technique that builds objects in a multi layered bottom-up process and was first developed in the mid 1980's at The University of Texas by Dr. Carl Deckard and commercialised by Nova Automation, soon to become DTM corporation in 1989. A laser, typically CO_2 in an industrial machine such as the EOS Formiga P100, or a low cost diode for consumer applications, acts on a preheated powder bed to selectively melt the surface of polymer particles fusing

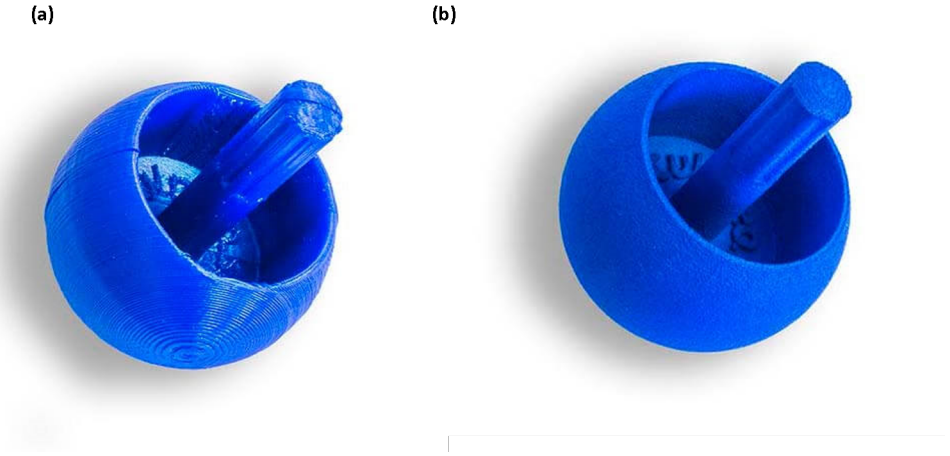


FIGURE 2.11: Comparison of a spinning top produced by (a) FDM and (b) laser sintering. Layer lines and surface blemishes can be seen on the FDM print compared to the smoother, higher resolution, print achieved by laser sintering [220].

them together. The fused layers correspond to a sliced image of a CAD model. Each time a slice is completed the build platform lowers and a new layer of polymer powder is dispensed over the previous layer to be built (Figure 2.12). Layers as thin as 0.05-0.3 mm can be achieved [39]. Through this layer- by- layer process solid 3D objects can be built without the need for additional support structures to facilitate their construction [40]. The lack of support structures enables highly complex shapes to be manufactured with little to no post processing being required.

The main parameters that control dimensional accuracy and subsequently the mechanical strength of laser sintered parts include laser power (W), laser spot diameter (mm), scan speed (mm/s) and scan spacing (mm) [39] [221]. Nelson et al. [222] [223] related these three independent parameters to develop the energy density equation (ED (J mm^2)) given by [224]:

$$ED = \frac{Q}{Lss \times SS} \tag{2.1}$$

where,

Q is laser power (W),

LSS is laser scan speed (mm s^{-1}),

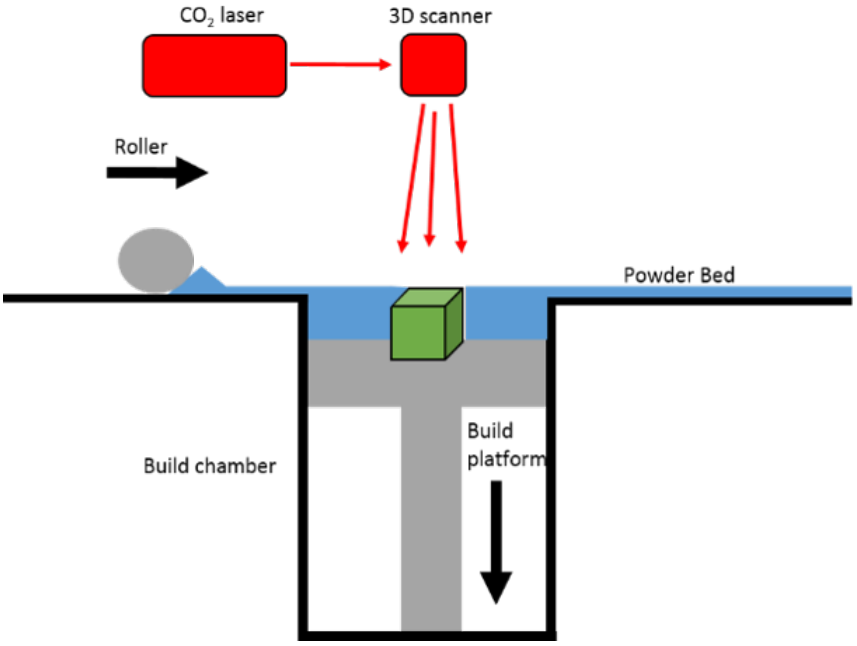


FIGURE 2.12: Depiction of a typical laser sintering system. A CO_2 laser selectively melts the polymer particles. As each layer is built the platform lowers and a roller/wiper mechanism deposits an new layer of powder.

SS is scan spacing (mm)

These parameters must be optimised depending on the polymer powder to be processed and the specific geometrical and structural requirements of the 3D object to be built. By varying the ED it is possible to tune the degree of particle fusion and this can have a profound effect on mechanical properties of the sintered part as demonstrated in Figure 2.13 and Figure 2.14 [225]. Increasing the ED, to an optimum point, will lead to increased particle fusion thus reducing material delamination and leading to denser parts [37]. Going beyond the optimum ED input, for the chosen material, will lead to polymer degradation and thus reduce the mechanical performance of the final part, in addition to a reduction in final part accuracy due to additional particle fusion beyond the perimeters of the laser scan path.

However, there are some limitations, the ED equation does not consider other important factors such as powder bed temperature, scan strategy, direction of gas flow and laser offsets [226]. Furthermore, absorption of the incident laser is not 100% efficient, factors such as; powder optical properties, additive content and type of laser used will have a significant affect on the absorption characteristics. Particle size also has large

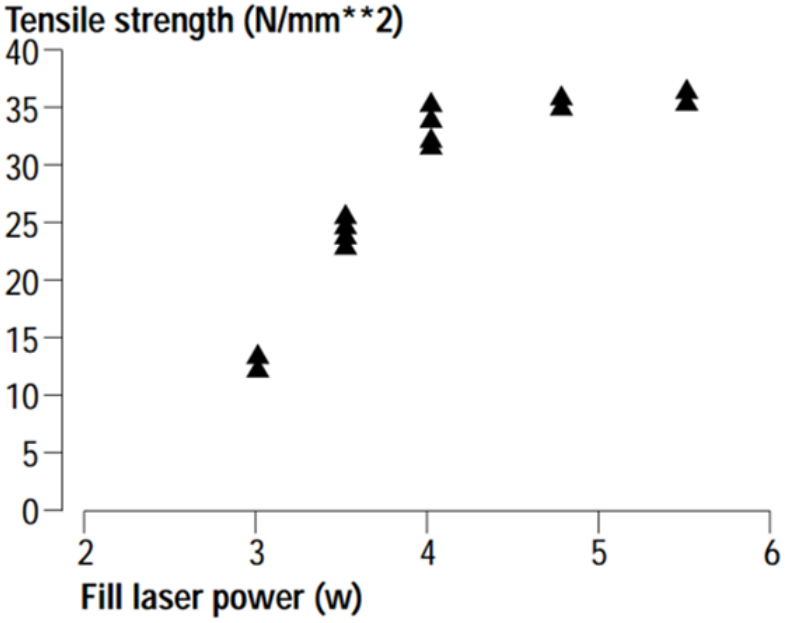


FIGURE 2.13: A graph showing the variation in tensile strength vs laser power for a part made from polyamide 12 [230].

influence on the relative amount of energy that is absorbed by the incoming laser [227]. Despite this the equation still holds relevance as an approximation for calculating the energy transferred to the powder bed however is should not form the sole basis for process optimisation [228].

As mentioned, the powder temperature is an important factor to consider. Too low a temperature results in a high thermal gradient between the sintered and un-sintered material which can lead to warping at the edges and corners of the final build this is known as 'curling'. This phenomenon can lead to distortions either during or after the build. In build curling commonly leads to blockage of the re-coating mechanism and resulting in failed builds. On the other hand, too high a temperature causes powder agglomeration resulting in 'caking' which subsequently affects dimensional accuracy [41]. The choice of powder bed temperature is highly dependent on the material of choice. In general, it should be kept just below the melting onset temperature (Tm) for semi-crystalline polymers or below the glass transition temperature (Tg) for amorphous materials, this reduces the large thermal gradients that are associated to part warping [229].

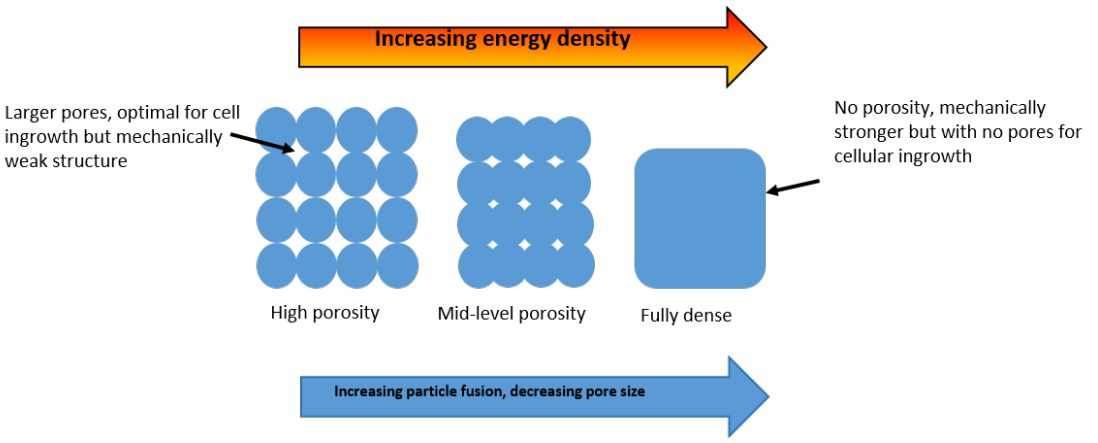


FIGURE 2.14: A schematic showing that higher energy density will result in a greater degree of particle fusion resulting in denser structures. In biomedical applications porosity can be exploited for cellular ingrowth and channels for the transfer of nutrients and waste into and out of the structure. However high porosity leads to mechanically weak structures.

2.9 Consolidation of Powders by Laser Sintering

The consolidation of an assembly of particles under the influence of thermal energy, more than approximately half of the absolute melting temperature, is generally referred to as sintering and is commonly associated with a reduction in the surface area of a packed powder [231]. This occurs through the formation of inter-particle bonds via 'necking' between adjacent particles though atomic motion at the sintering temperature. The driving force for this is the lowering of the free energy which leads to consolidation of the particles into a solid structure and is done in the absence of external pressure [232] [233]. Solid state sintering occurs below the materials melting temperature and involves the diffusion of atoms between adjacent particles which leads to neck formation and growth over time [232]. This form of consolidation mechanism is rarely applied in additive manufacturing due to the slow speeds involved in the diffusion process. The high velocity of a scanning laser during the laser sintering process does not provide sufficient time for diffusion of atoms to occur. Therefore, the consolidation of polymer particles via laser sintering generally occurs by either two main mechanisms; liquid phase sintering (partial melting) and full melting. Technologies utilising the partial melting mechanism are commonly referred to as laser sintering, whereas full melting is commonly referred to as laser melting [232]. Partial melting

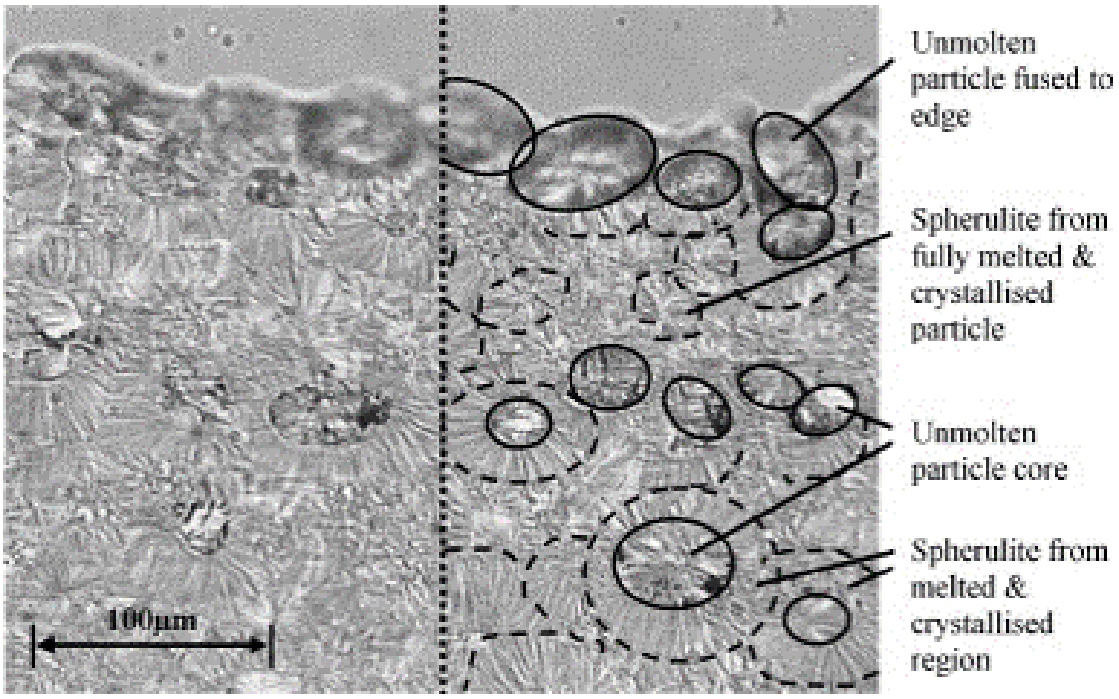


FIGURE 2.15: Cross section of PA12 part that has been laser sintering, revealing regions of un-molten cores and spherulite formation [235].

occurs when the heat energy supplied to the polymer particle is not sufficient to completely melt it, rather, the outer surface of the particle melts and the inner core remains solid. The consolidation of adjacent particles occurs via liquid neck formation and is driven by capillary forces of the liquid phase. Full melting on the other hand involves the complete melting of the polymer particle into the liquid phase [232] [234]. In practice a combination of partial and full melting is likely to occur, in the laser sintering of polymers. Zarringham et al. [235] studied the micro-structure of laser sintered PA12 parts through light optical microscopy. A cross section of a sintered part revealed a mixture of molten and un-molten cores surrounded by spherulties, indicative of the re-crystalisation process associated with the melting and cooling of a polymer. This can be seen in Figure 2.15. They stipulated that the presence of un-molten cores had a significant influence on the mechanical properties of the final part as they form an inter-crystal-form composite like structure. A weak inter-crystal-form interface could lead to weak parts due to crack formation and propagation under relatively low stress leading to the rupture of the core from the matrix [235].

The degree of crystallinity within a thermoplastic polymer can significantly influence

the type of consolidation mechanism present during laser sintering. For semi-crystalline polymers, the nature of their highly ordered molecular regions means that they possess a sharp melting region and therefore do not gradually soften as temperature increases. They, instead, remain hard until sufficient heat energy is absorbed and then rapidly transition to a viscous liquid. For this reason, depending on the parameters used, partial and full melting mechanisms occur. Amorphous polymers on the other hand, have a disordered and random molecular structure, upon heating above the Tg the polymer will soften and the degree of softening increases with temperature. The viscosity is significantly higher than that of fully molten semi-crystalline polymers, therefore, the sintering rate is significantly less than that of semi-crystalline polymers. This leads to a lower degree of consolidation resulting in higher porosity and weaker mechanical properties and is therefore not applicable for parts which require strength [232].

The first physical model used to describe the consolidation of two identical spherical particles by viscous flow was proposed by Frenkel in 1945:

$$\frac{\gamma}{\alpha} = \left(\frac{3\Gamma t}{2\eta\alpha}\right)^{\frac{1}{2}} \tag{2.2}$$

Where,

α is the particle radius,

t is the sintering time,

γ is the sintering neck radius,

η is the viscosity,

Γ is the surface tension of the material

However, Frenkel's model is limited to Newtonian flow and only in the early stages of sintering when particle diameter remains constant [236]. In 1949 Eshelby et al. corrected it to satisfy the continuity equation and established the Frenkel-Eshelby model:

$$\frac{\gamma}{\alpha} = \left(\frac{\Gamma t}{\mu \alpha}\right)^{\frac{1}{2}} \tag{2.3}$$

Qualitative assessments of Frenkel's model have been conducted by numerous authors [236, 237]. However, due to the multitude of factors involved in laser sintering the theoretical models currently available are not fully capable of modelling the coalescence of polymer particles during processing. However, they do provide an approximation that can be utilised in deciding which polymer to use.

2.10 Materials used in Laser Sintering

In theory any thermoplastic can be processed by laser sintering, however in practice some thermoplastics behave more favourably than others when processed via laser sintering. To date only a limited number of commercially available thermoplastics can be processed by laser sintering. These generally fall under the categories of semi-crystalline and amorphous. When heated to high temperatures these thermoplastics undergo a transition from a solid/glassy structure to a softer rubbery solid until finally forming a viscous melt. Different polymers vary in temperature at which these transitions occur, as depicted in Figure 2.16. Semi-crystalline polymers have a Tg in the region of -100°C to 50°C and a Tm between 100°C and 400° which is accompanied by a significant change in volume, as seen in Figure 2.17. On the other hand, amorphous polymers do not have a distinctive Tm range but instead have a Tg around 100°C, above which they transition to a rubbery solid and eventually to a liquid state [229]. Different molecular weights influence the value of Tg and Tm and re-crystallization temperatures and thus explain the difference of processability for different polymers via laser sintering.

Above the Tm the relatively low viscosity of semi-crystalline polymers favours the consolidation of particles with densities comparable to fully dense moulded polymers. Consolidation of amorphous polymers occurs at temperatures above Tg forming a more viscous state compared to semi crystalline polymers at the same temperature [238].

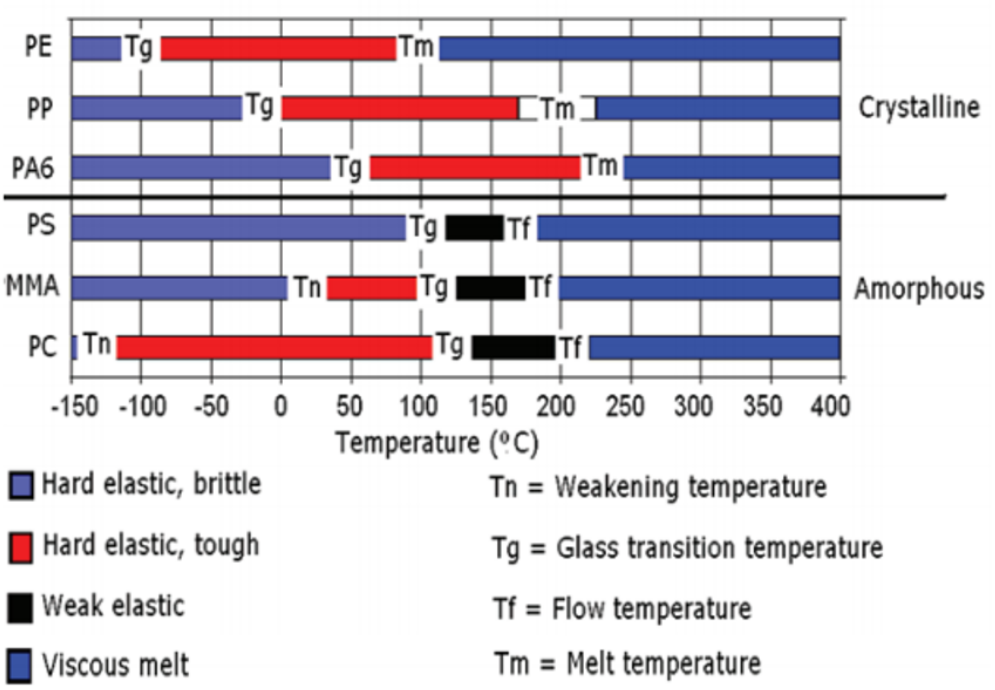


FIGURE 2.16: Phase and transition temperatures of commonly used thermoplastics [238].

Semi-crystalline polymers that can be processed by laser sintering typically have a large separation between melting and crystallisation temperatures. Due to the volumetric shrinkages involved when molten polymer cools, which is caused by the re-ordering of the molecular chains, if the crystallisation and melting temperatures of the polymer are close together, rapid re-crystallisation can occur leading to part warping due to the stresses imparted by shrinkage. This can significantly impact upon dimensional accuracy of the final part or lead to premature warping during the build [230]. Therefore, in laser sintering there is a strong desire to delay polymer re-crystallisation [238]. The testing of different grades of polyamide (PA) have shown considerable differences in dimensional accuracy. This has been attributed to the differences in % crystalinity within the polymer which affected the onset Tm and Tc temperatures of the different grades of PA [239]. Figure 2.18 shows the DSC profile of PA12 polymer that is well suited for laser sintering, exhibiting a large separation of the melting peak and crystallisation peak where as Figure 2.19 shows the DSC trace of a polymer which is more challenging to process due to the overlap of the melting and crystallisation peak and is prone to significant warping [229].

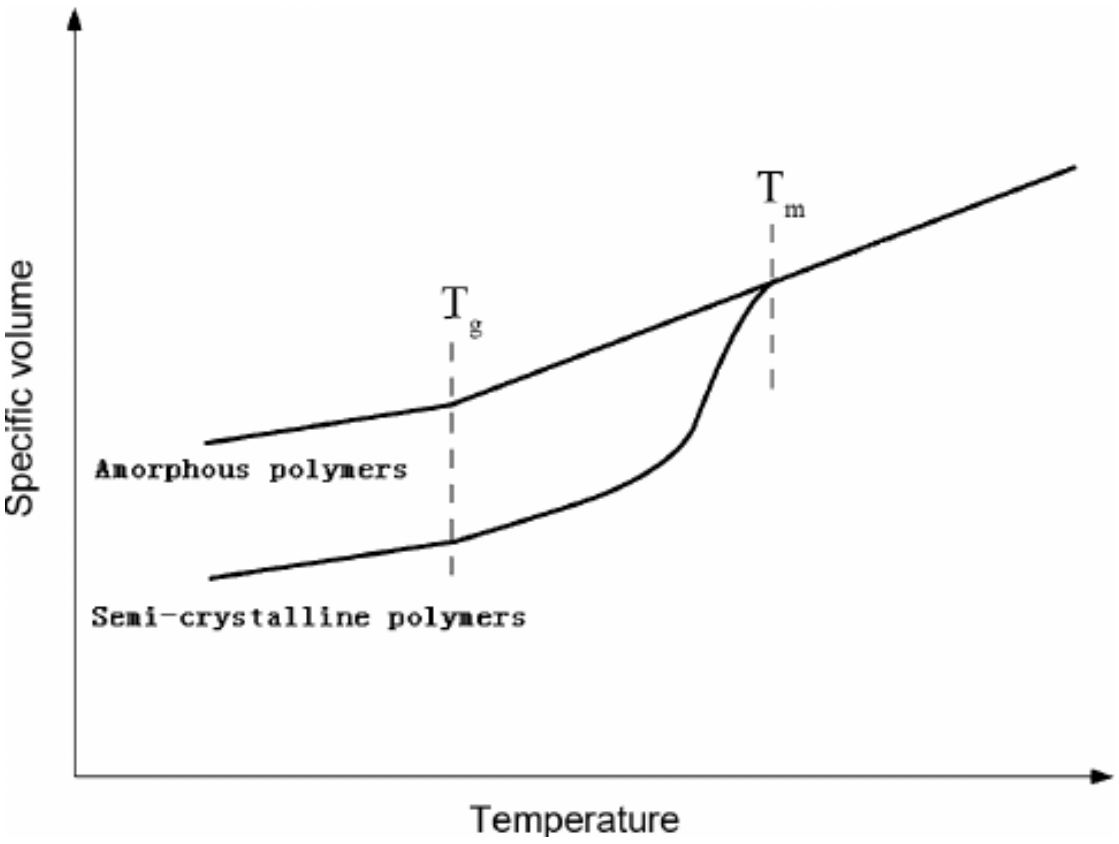


FIGURE 2.17: Change in specific volume of semi-crystalline and amorphous polymers with temperature [240].

The melt viscosity of the polymer is also a significant factor that determines a polymers suitability for laser sintering. The weight-average molecular weight (Mw) directly affects the melt viscosity through the relation defined in equation 2.4:

$$\eta_0 = k(Mw)^n \tag{2.4}$$

Where,

η_0 is the melt viscosity (Pa s),

Mw is the molecular weight,

k and n are constants related to the critical molecular weight (Mc). When Mw is $<$ Mc then n $= 1$ and when Mw $>$ Mc then n $= 3.4$ [239]

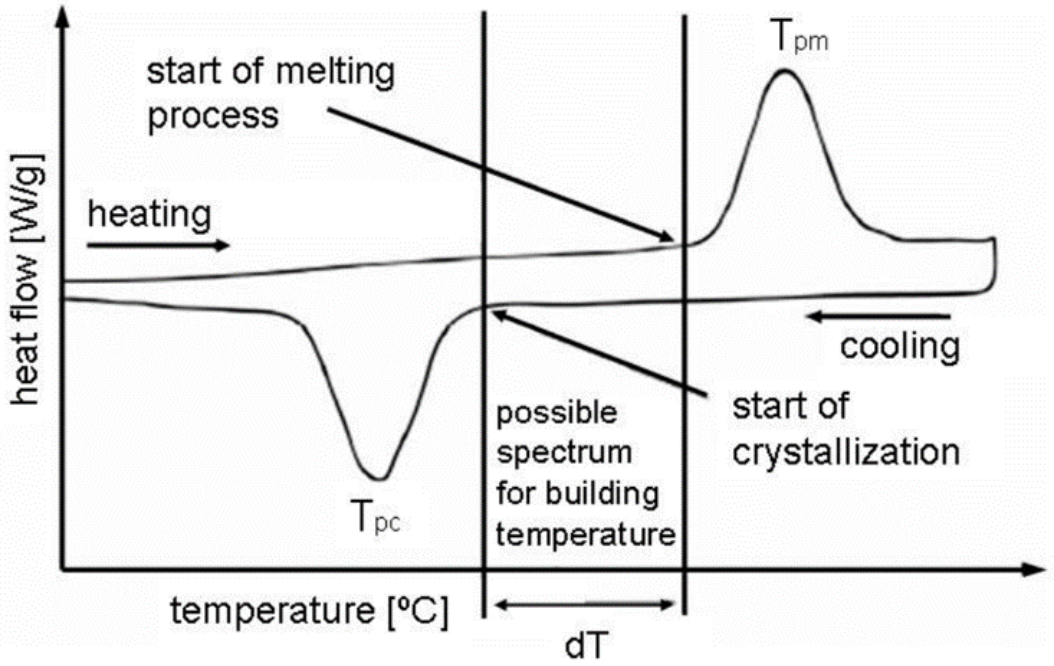


FIGURE 2.18: DSC trace for PA12, that is well suited for laser sintering, with no overlap of melting and crystallisation peaks [229].

Figure 2.20 shows the relationship between the Mw of different grades of polystyrene and their melt viscosities. Another method of quantifying melt viscosity is via the Melt Flow Index (MFI), and is a measure of the ease at which molten polymer can flow through an orifice with a given force over 10 minutes. MFI is expressed as either mass flow g/10 min or volume flow in $cm^3/10$ min, generally the higher the MFI the lower the melt viscosity of the polymer [241]. Shi et al. [239] observed the processing of polystyrene powders (PS) with different MFIs of 3 $cm^3/10$ min and 8 $cm^8/10$ min. The PS powder with the lowest MFI (highest viscosity) produced samples that were less dense compared to the PS powder with higher MFI. SEM imaging also showed higher porosity and lower particle-particle fusion associated with the PS powder with the lower MFI as seen in Figure 2.21. As discussed previously, the Frenkel model of sintering (equation 2) states that dimensionless neck formation between two adjacent particles (x/r) increases as melt viscosity decreases (η_O). Therefore the melt viscosity plays a crucial role in determining the degree of particle fusion. Due to the speed at which the laser scans and the time needed for high viscosity particles to coalesce, polymers with very high melt viscosities are either not suited for laser sintering or require post heat treatment to produce denser parts [229].

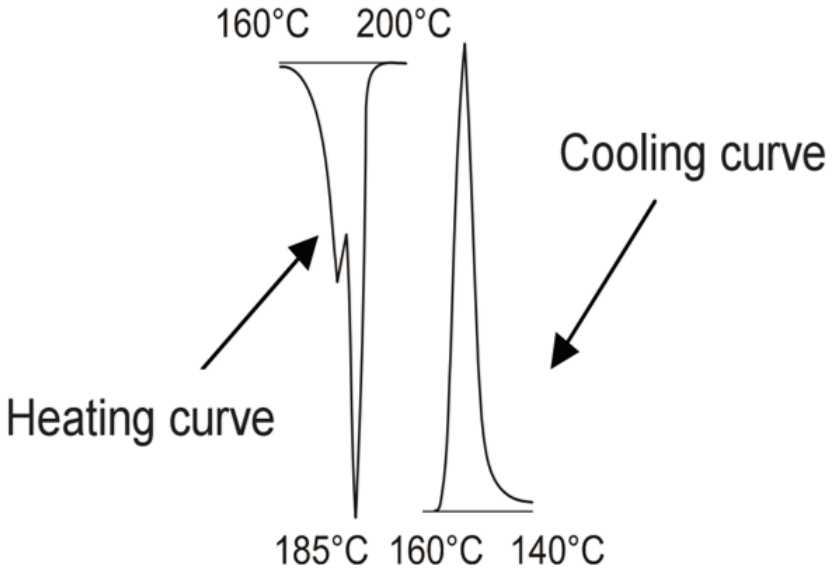


FIGURE 2.19: DSC curve of a commercial blend with little processability due to overlapping melting and crystallisation peaks [238].

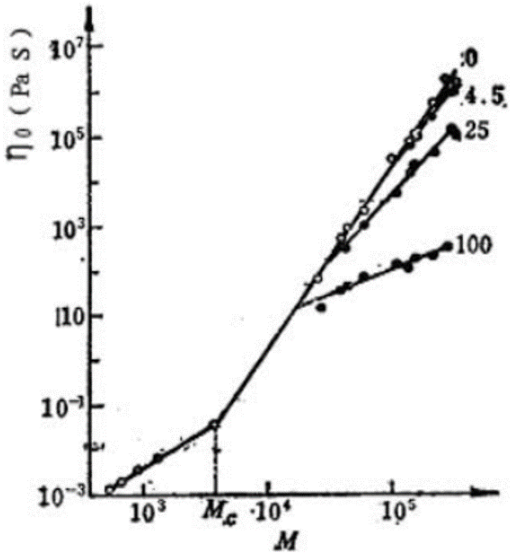


FIGURE 2.20: Relationship between molecular weight and melt viscosity of PS [239].

Due to the range of requirements needed, the number of commercially available polymers is extremely limited with PA12 being the most popular choice as it possesses a narrow melting and crystallisation temperature range and a suitable melt viscosity, therefore giving it a relatively wide processing window. These thermal and chemical characteristics make PA12 relatively easy to process via laser sintering [229] [41]. Table 2.5 shows the major commercially available polymers for laser sintering.

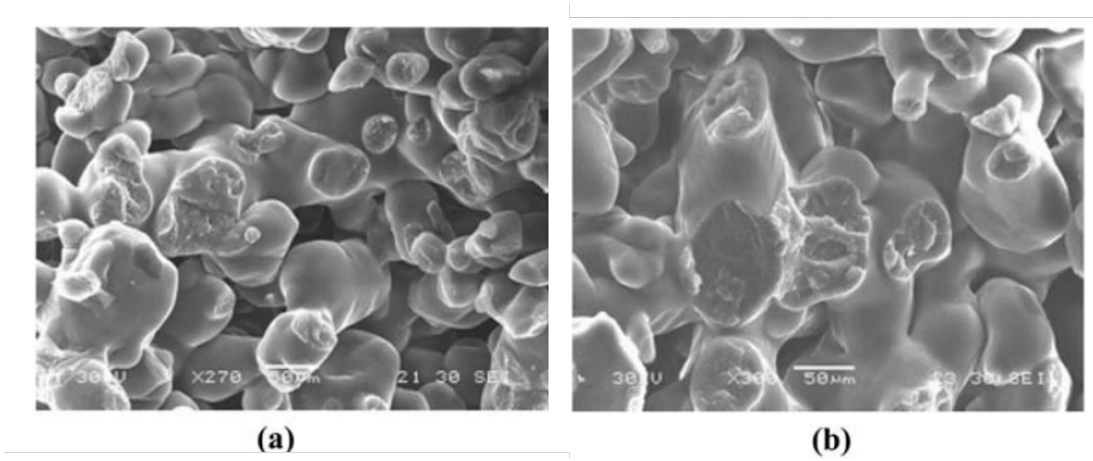


FIGURE 2.21: SEM images of the fracture surfaces of (a) PS with a higher MFI and decreased levels of particle fusion compared to (b) PS with a lower MFI [239].

2.11 Biomedical polymers for Laser Sintering

Laser sintering is an exciting route in the manufacture of biomedical implants and much research has been conducted on taking existing polymers and increasing their biofunctionality by incorporating other additives to produce composite materials. For example, hydroxyapatite reinforced polyethylene and polyamide composites for customised maxillofacial implants manufactured by laser sintering has been explored. A structure which provided a suitable surface for cellular attachment, proliferation, differentiation and mineralisation of primary human osteoblasts was successfully produced by Zhang et al. [245]. Composite structures with a high HA content, above 30 wt%, demonstrated a highly uniform distribution of HA particles in the polymer matrix which enhanced cellular proliferation and maturation indicated by increased alkaline phosphatase activity and osteocalcin production [245].

Due to its flexibility and natural lubrication PVA has been used extensively in the treatment of defects under compressive loads such as cartilage, and also makes an attractive material choice in the fabrication of maxillofacial implants via laser sintering. Test specimens formed from 90 wt% PVA and 10 wt% HA were used to study potential osteoconductive performance by submersion in simulated body fluid (SBF). SEM showed formation of hydroxy-carbonate apatite layer, thus providing favourable environment for the attachment and proliferation of osteoblasts and their precursors [246]. The production of PVA/HA powder was performed via two methods, spray

drying and physical blending. The spray drying method yielded a small amount of composite powder, 150 - 200 g per 9 l of suspension. Laser sintering of the spray dried powder, led to charring of PVA with limited fusion between the particles thus leading to very fragile samples that were extremely difficult to handle. This was associated with the high HA content with insufficient PVA to act as a binder. On the other hand, physically blended PVA/HA powders performed better during laser sintering with the maximum limit of 30 wt% HA. Particle fusion did occur with interconnected micro-pores, however dispersion of HA on the surface of the PVA was poor [246].

Hao et al. [247] compared the bioactive potential of high density polyethylene (HDPE)/HA composites structures produced by laser sintering and injection moulding (IM). Composite powders were produced by physical blending before compounding in a twin-screw extruder and milling. It was found that by altering the laser power whilst keeping scan speed and scan spacing fixed, the surface roughness and pore morphology could be altered. Low laser powers produced rough open pores on the surface and a highly interconnected porous structure within, ranging from 45 to 54% porosity which was favourable for cellular penetration. Specimens produced from IM, on the other hand, had a smooth surface texture and no interconnected porous structure. Another advantage that laser sintering has compared to IM was the surface exposure HA on the laser sintered specimens thus being immediately visible to cells potentially improving osteoconductivity, whereas IM specimens showed no HA present on the surface instead it remained buried beneath the surface. Sample geometries were limited to only single and multi-layered block, and as a result of production method, the composite powders had a rough and uneven morphology, with a wide particle size distribution. In order to expose HA particles on the surface of the laser sintered parts a higher laser power was needed to vaporise the HDPE [247]. The degradation of HDPE through excessive energy input could negatively impact the mechanical properties of the final part as discussed previously [225].

Another study conducted by Shuai et al. [248], in regards to laser sintering of PVA/ calcium silicate based composites, also showed that use of high laser power led to exposure of the calcium silicate, however PVA degradation through excessive thermal decomposition led to a reduction in polymer crystallinity.

PEEK based composites are an attractive candidate as bone substitute materials due to their strength and compatibility. The production of PEEK/β-TCP and PEEK/bioglass composites via laser sintering have been explored by Wilmowsky et al. [249]. Results showed that the powders were processable with multi-layered discs shaped samples being produced. Human osteoblasts were seeded onto the discs and cultured for 7 days. Surface exposure of bioglass was evident through SEM examination and osteoblasts were seen making direct contact with the exposed particles. The composites also demosntrated cytocompatability with a homogeneous layer of cells growing on the surface of the discs. However, to process the powders the laser sintering machine required heavy modification to enable the heating up to 310°C and to ensure uniform heat distribution over the build platform. Furthermore, the as received PEEK powder had a broad particle size distribution from 5 - 110 μm and an irregular morphology. Therefore, powder flowability was significantly hindered and required the addition of 1 wt% carbon black to improve flow. The powders were produced by physically blending PEEK and inorganic filler, although surface exposure was observed it was not extensive and was not well distributed [249].

In addition to non-resorbable thermoplastics there has been much research into resorbable composite materials for laser sintering. Poly-ϵ-caprolactone/HA based composites have been considered for hard tissue engineering and the feasibility of using laser sintering to construct scaffolds with reproducible and well defined architectures has been demonstrated [250]. Scaffolds based on PCL/tricalcium phosphates (TCP) have also been produced by laser sintering. It was seen that by increasing macroporosity, stiffness of scaffolds was seen to drop. However, by introducing geometrical changes, stiffness could be increased. Cylindrical scaffolds were produced with varying microarchitecture designs with 42 - 80% designed porosity and pore sizes ranging from 500 - 560 μm. In-vivo tests performed using critical size defects in sheep tibia showed mineralised callus formation around the defect. However, PCL required cryogenic milling resulting in wide particle distributions and irregular shapes and a high loading (50%) of TCP was required to elicit an improved biological response [251]. The incorporation of needle shaped nano HA with PCL has also been explored with laser sintering. The scaffolds produced exhibited porosities ranging from 78% and 70%

and a compressive strength of 1.38 MPa to 3.17 MPa. The powders were produced by physical blending and resulted in the agglomeration of the nano-fillers, however, in-vitro studies using human bone marrow stromal cells showed enhanced levels of human bone morphogenic protein-2 release from the cells. Furthermore in-vivo studies using rabbit models were also conducted with the nano-HA/PCL scaffolds with enhanced bone formation compared to pure PCL [252]. PLA/HA based composites are also currently being explored due to their highly tuneable degradation profile. Preliminary work to establish laser sintering parameters on an experimental machine has been conducted with reports of a laser power of 10 - 15 W and scan speed of 100 mm/s were suitable for producing multi-layered, basic components, from a 2:1 ratio PLA/HA blend with a highly interconnected porous network throughout the structure [253]. The experimental laser sintering set-up did not have an automated powder delivery system and required manual powder spreading in addition to no bed heating apparatus. Inconsistencies in powder layer deposition and surrounding temperature can influence the parameters and thus affect the success of a build [253]. Human fetal femur derived cells seeded onto the surface of PLA specimens fabricated from laser sintering demonstrated excellent cell viability, growth and osteogensis in-vitro and in-vivo on a murine model [254]. Zhou et al. [54] have also explored incorporating spherical nHA with PLA and fabricating complex objects with a tetragonal porous structure with built in rectangular channels. Focused ion beam milling revealed that the spherical nHA were evenly distributed on the surface and within the PLA/nHA particles. Preliminary nanoindentation tests on the coated PLA showed a higher hardness compared to pure PLA (figure not reported). However, the powder was produced via the solid-in-oil-in-water (S/O/W) method and was thus labour intensive and resulted in a low yield of powder [54].

The ability of laser sintering to produce scaffolds with defined macro and micro architecture, using a range of resorbable and non-resorbable polymer and polymer/ceramic composites, that can support cellular infiltration, growth and mineralisation of osteogenic cells, has been demonstrated and therefore shows an exciting opportunity for the production of bioactive bone substitute materials.

2.12 Polymer Powder Characteristics

In laser sintering, the ability to deposit smooth uniform layers is crucial to the overall ability to produce multi-layered parts in addition to the final part properties [255]. The particle size distribution is another important factor to consider with regards to the processability of the powders. Particle size can affect the flowability, surface finish, part accuracy and overall density. Too small a particle size can lead to spreading difficulties due to static forces and may lead to part growth due to increased heat transfer [256] [41]. Conversely too large a particle size can lead to poor surface finish and a shift of the processing window, requiring increased laser power to consolidate the particles due to the lower transfer of heat. Therefore, particles should ideally have a relatively narrow size distribution between 45 - 90 μm [256]. Shi et al. [239] observed an inverse relationship between particle size and density of a laser sintered part. PS particle sizes of $>$150 μm produced samples with the lowest density of 0.34 g/cm^3 whereas PS particles with a size $<$75 μm produced samples with a higher density of 0.43 g/cm^3. It was also noted that a stair stepping effect was more pronounced on parts made from larger particle sizes thus indicating that particle size has a significant affect on dimensional accuracy. However, too small a particle size $<$75 μm made powder spreading difficult due to the cohesive nature of fine particles and it was determined that a suitable range of 70 - 100 μm is most suitable for laser sintering [239].

As discussed in the previous section, the conventional methods for composite and nanocomposite powder production include: solid-in-oil-in-water emulsion/solvent (S/O/W) techniques; the mixing of filler with polymer melts which is then extruded and cut into pellets before being cryogenically milled to form powders, spray drying of polymer/NP solutions and dry blending. For example, nanocomposite powders made from poly(hydroxybutyrate-co-hydroxyvalerate) (PHBV) micro-spheres and calcium phosphate particles were fabricated via the oil-in-water and solid-in-oil-in-water (S/O/W) emulsion evaporation methods. PHBV was first dissolved in chloroform and then added to an aqueous phase containing 1% (W/V) of poly(vinyl alcohol) (PVA), the resulting emulsion was stirred and evaporated off. Ca-P particles used for the composite were dispersed in a PHBV-chloroform solution to form a solid-in-oil nanosuspension. Then

the addition of the PVA solution formed an emulsion of Ca-P/PHBV microspheres. The resulting particles were spherical in morphology with an average diameter of 48 μm and had Ca-P nanoparticles encapsulated within [257]. These powders were then successfully used to fabricate porous structures via laser sintering with highly controlled and reproducible porous architecture with good dimensional accuracy [257]. PCL microspheres have also been prepared via S/O/W method to produce scaffolds with controlled pore size ranges [258]. Similarly, S/O/W technique was also used to prepare PLLA/ carbonated hydroxyapatite (CHAp) nanocomposite micro-spheres for laser sintering by Zhou et al. [54]. The resulting micro-spheres had a size range of 5 - 30 μm which was on the lower recommended region of suitable powder sizes for laser sintering. However, the powders were successfully processed with CHAp nano-spheres which were well dispersed within the nanocomposite structure [54]. However, issues associated with S/O/W techniques include the need for large quantities of toxic solvents and that it is labour intensive with a low yield of powder. HA and HDPE powders, on the other hand, have been prepared through dry blending to produce mixtures with 30 - 40 vol % and then compounded in a twin-screw extruder to produce HA-HDPE composite before being pelletised and then powdered in a centrifugal mill. However, the resulting powders had a rough and angular morphology with HA buried beneath the surface of the polymer particles [247]. The need for liquid nitrogen and powerful grinding machines followed by separation of particles into suitable sizes for laser sintering makes grinding and milling of powders an expensive process. As mentioned previously, the production of poly vinyl alcohol (PVA) and HA composite powders have been explored by both physical blending and through spray drying. The results showed that physically blended powders had a poor distribution of HA on the surface of the polymers particles where as the spray drying process, which first requires dissolution of the PVA in solvent before stirring with HA, did produce spherical particles but was labour intensive, producing a low yield of powder. For every 9 litres of suspension only 150 - 200g of usable powder was obtained [246]. Wahab et al. [259] have also used spray drying to produce PA 6/cerium oxide, PA 6/zirconia and PA6/clay nanocomposites. The results showed that the method yielded spherical particles but with a small particle size, with an average size between 5 - 40 μm, smaller than the reported

optimum size range [239]. The PA 6/ cerium oxide powders exhibited poor dispersion whereas the PA 6/zirconia and PA 6/clay powders did display good distribution at 5 wt% loading. However, production of the powders required the use of formic acid, to dissolve the PA 6, and continuous stirring for 7 hours at a concentration of 30g/ litre to yield the desired, near spherical, powder morphology [259].

Therefore the major drawbacks associated with these methods include: the agglomeration of the nanofillers, which can lead to poor mechanical properties compared to the neat polymer, the angular shaped particles with wide size distributions, the need for expensive and toxic solvents and labour intensiveness of the process which produce a low powder yield. Bai et al. [260] adopted an alternative approach to producing nano-composite powders and was able to produce PA12 powders that were individually coated in MWCNT at loadings of 0.1 - 0.4 wt%. By taking, as received, PA12 powder and heating it in water, at temperatures of $\approx 100^{\circ}$C, coupled with strong mechanical stirring and addition of a MWCNT/water dispersion, the surface of the PA12 became soft enough to allow MWCNT to adhere. This method resulted in individually coated PA12 particles with a good distribution and surface coverage of MWCNT. This relatively simple, yet novel method allowed for the production of large quantities ($\approx$500g) per batch, of MWCNT coated PA12 powders, without affecting the original powders size or morphology. Once processed by laser sintering the nanocomposites exhibited over a 40% increase in Young's modulus and an 8% increase in UTS. Furthermore, the elongation at break was also comparable to neat PA12, indicating a good dispersion of the MWCNT in the polymer matrix. This improvement in tensile properties was also accompanied by a 16% increase in flexural modulus and a 11% increase in flexural strength [260].

Therefore the method adopted by Bai et al. [260] is an attractive method for the production of nano-coated powders and serves as a good platform for investigating the effects of different additions of NPs and at different loadings and shall be the powder production method utilised in this thesis.

2.13 Gap in the Knowledge

The literature has also highlighted a number of key issues that are yet to be addressed in laser sintering. The need for the correct chemical and thermal properties in addition to being able to be processed into powder with suitable morphologies and sizes for laser sintering currently makes the range of commercially available powders limited with PA12 being the most predominant polymer used commercially. Material choice is not only limited, but powder feedstock for laser sintering is currently expensive. The difficulties associated with producing powders in-house through cryogenic milling or S/O/W include labour intensiveness with low yields in addition to wide particle sizes with irregular morphologies and inadequate surface coverage of inorganic additives once processed. Achieving good dispersion of NPs is crucial to the overall performance of composite device. Therefore the method adopted by Bai et al. [1, 260] may provide a possible alternative route in the production of nano-coated powders which addresses these issues. However, only a low wt% of NPs was studied, the effects of higher loadings, to maximise the biological response to the material, has not yet been investigated in the production of coated powders in this way. In addition to material cost, the initial cost of a laser sintering system is significant. A commercial machine such as the Formiga P100 (EOS) costs in the region of £250,000. Therefore much research has been conducted on experimental machines which require retrofitting with expensive CO_2 lasers. The advantages of such machines over commercial machines is the less material is used consumed, however this limits researchers to relatively basic structures and inconsistent results.

In light of this, the main research objectives and key hypotheses to be studied were identified:

- Adapt the coating method adopted by Bai et al. [1], for the coating of PA12 and PLA powders with alternative nano-particles such as nHA.
- Investigate how different loadings of nHA may impact the powder morphology, flowability and thermal characteristics of the coated powders and to assess what influence this may have on powder processability during laser sintering.

- Investigate the feasibility of processing the nHA coated powders in a commercial (EOS Formiga P100) and consumer laser sintering system (Sintratec). Determine the optimum laser sintering parameters needed to successfully process the coated powders for the production of nanocomposites for mechanical and cellular testing. Assess whether the presence of nHA at different loadings affects the laser sintering performance of the powders, if so how? The hypothesis is that a higher loading of nHA will require increased energy input due to the nHA acting as a thermal barrier and thus reducing the rate of heat transfer through the powder bulk.

- Assess whether the nancomposites produced on the commercial and consumer laser sintering systems are suitable as a bone substitute material by way of examination of the mechanical properties of the nanocomposite and the behaviour that osteoblast-like cells exhibit when cultured directly onto the surface of the material. The hypothesis is that the addition of nHA will increase the osteogenic response to the laser sintered sample, due to direct exposure of nHA on the surface of the material which will facilitate improved cell material interaction.

2.14 Key Hypotheses

- The addition of nHA to the outer surface of PA12 and PLA particles will not significantly impact upon the overall size and morphology of the powder. However, the increased surface roughness will result in greater inter-particle friction and decrease the ease with which particles can pass over one another. This will lead to a less densely packed powder bulk, and a higher degree of porosity in the laser sintered sample.

- The addition of nHA on the surface of the powder will not alter the melting temperature. However, the temperature at which re-crystallisation occurs will be reduced and the crystallisation rate of the polymer melt will increase as a result of the nHA. This alteration to the re-crystallisation behaviour of the

coated powders will increase the powders' sensitivity to warping during laser sintering processing.

- The nHA coating will affect the laser sintering parameters, due to the nHA acting as a thermal barrier and reducing the thermal transfer through the powder bulk. As a result, a greater input of energy density will be required to fuse the powder particles.

- The presence of nHA will increase the mechanical stiffness of the resulting nanocomposite due its high, inherent, elastic modulus when compared to the base polymer. This will also be aided by the high degree of nHA dispersion within the nanocomposite structure, as a result of the powder coating method used.

- The nHA, MWCNT and MWCNT-nHA, when in free suspension and when immobilised onto the surface of PA12 and PLA, will be cytocompatible with osteosarcoma cell lines. Furthermore, the addition of nHA on the surface of the powders will increase the osteogenic response of human mesenchymal stem cells to the laser sintered material when compared to the base polymer. The increased osteogenic response will be partly due to the cells' ability to directly interact with the nHA.

TABLE 2.5: List of commercially available polymer powders for laser sintering and their properties. Adapted from [1] [242] [243] [244]

Material	Trade Name	Manufacturer	Tensile Modulus (GPa)	Tensile Strength (MPa)	Elongation (%)	Part density (g cm^3)
PA12	PA2200	EOS	1.7	50	20	0.93
	DuraForm PA	3D Systems	1.6	43	14	1.0
	PA640	ALM	1.7	48	14	1.0
PA12 Composites)	PA3200 GF (glass filled)	EOS	3.2	51	9	1.22
	Aluminide (aluminium)	EOS	3.8	48	4	1.36
	CarbonMide (carbon filled)	EOS	3.4	56	6.3	1.04
	DuraForm HST (fibre filled)	3D Systems	5.7	51	4.5	1.20
	DuraForm GF (glass filled)	3D Systems	5.9	38.1	2	-
	PA614-GS (glass spheres)	ALM	3.2	51	9	0.82
	PA 614-CF (carbon fibre and glass)	ALM	3.8	33	3	0.82
	PA601-CF (carbon fibre)	ALM	2.9	66	3.6	1.07
	PA 605-A (aluminium)	ALM	3.7	43	3.3	1.07
PA11	PA1101	EOS	1.6	48	45	0.99
	DuraForm EX	3D Systems	1.5	48	47	1.01
	PA 860	ALM	1.4	58	51	0.96
PA11 Composite	PA 840-GSL (fibre)	ALM	3.4	48	4	0.87
PEEK	EOS PEEK HP3	EOS	4.2	90	2.8	1.31
PS	PrimeCast 101	EOS	1.6	5.5	0.4	0.77
	PS 200	ALM	1.6	2.8	-	0.86
Elastomeric	DuraForm TPU	3D Systems	7.4	1.8	110	0.44
	DuraForm Flex	3D Systems	5.3	2.1	220	0.78
	TPE 210	ALM	8	-	110	1.03

Chapter 3

Experimental Methods

A laser sintering grade of Polyamide 12 (PA12; PA2200) powder was obtained from EOS Gmbh, Germany and an untested, experimental grade of PLA powder was specially manufactured by A.Schulmans (SCHULASINT^{TM} XX00505) for this study. Due to the limited quantity and availability of this specialist powder, the PLA was tested in a consumer laser sintering machine (Sintratec).

The PA12 and PLA powders were both coated with nano-Hydroxyapatite (nHA) to improve the osteoconductive and mechanical properties of the final parts. An aqueous solution of rod shaped nHA (15 wt%) was obtained from Promethean Particles Ltd, UK. The nHA had a typical length and diameter of 400 nm and 30 nm respectively. This was assessed by SEM and TEM (section 3.2.14.)

The Sintratec uses a laser diode (445 nm - visible light region). To absorb the laser energy, the PA12 and PLA powders were coated in a dual phase mixture of MWCNT and nHA. The Sintratec was supplied with a blend of PA12 with 1 wt% of carbon black (CB). However, CB is the by-product of incomplete combustion of hydrocarbons and is primarily used as a reinforcing additive in the production of car tyres; it is also used as a pigment in printing ink, paper and plastics [261]. However, the International Agency for Research on Cancer (IRAC) has considered carbon black as "probably carcinogenic" [262], and cytoxicity and genotoxicity studies have demonstrated the potential of excessive DNA damage to human cells [262–266]. There has also been a documented

correlation between CB exposure and a higher risk of developing cardiovascular diseases [267–269]. For the purposes of this work the nanocomposites manufactured by laser sintering are intended to be implanted into the human body for long term/permanent use. This is defined as being greater than 30 days of continuous use by the EU Medical Device Regulation 2017/745 [270] and in accordance to BS EN ISO 10993 - Biological Evaluation of Medical Devices [271]. Therefore, an alternative to CB, in the form of carbon nanotubes was used.

In this work, an aqueous solution of multi-walled carbon nanotubes (MWCNT - 10 wt%) was obtained from Nanostructured and Amorphous Materials, Inc, USA, with a purity of over 90%, diameter $>$ 50 nm and a length of 10-20 μm.

Carbon Nanotubes (CNTs) are an allotrope of carbon, essentially consisting of a rolled-up layer of graphene which forms a cylindrical tube. They can possess a length:diameter ratio of up to 1.32 $\times$ 108:1, the largest of any other material available, and can be considered as nearly one-dimensional (1D) structures [272]. The lattice structure of graphene is a hexagonal arrangement of carbon atoms. Each carbon atom is covalently bonded to three neighbouring carbon atoms. The 2s, 2px and 2py orbitals are hybridised into three sp2 orbitals forming σ-bonds with adjacent carbon atoms in the same plane. The remaining valence electron in the 2pz orbitals hybridises with the other 2pz orbital forming a delocalised π-bonds out of plane. Due to graphene's sp2 bonds being considerably stronger than the sp3 bonds present in diamond, and due to the delocalised electrons present in the 2pz orbitals, CNTs possess remarkable mechanical, electrical and thermal properties [273] [274]. Multi-walled carbon nanotubes are formed from multiple concentric layers of graphene (MWCNT) with a shell separation of $\approx$0.34 nm [275]. The properties of CNTs can be significantly altered dependent on how the graphene sheet is orientated on rolling. The type of rolling can be specified by a chiral vector. There are three unique geometries of carbon nanotubes; armchair, zig-zag and chiral, this is illustrated in Figure 3.1. The mechanical properties of SWCNT and MWCNT can also vary considerably, this is shown in Table 3.1.

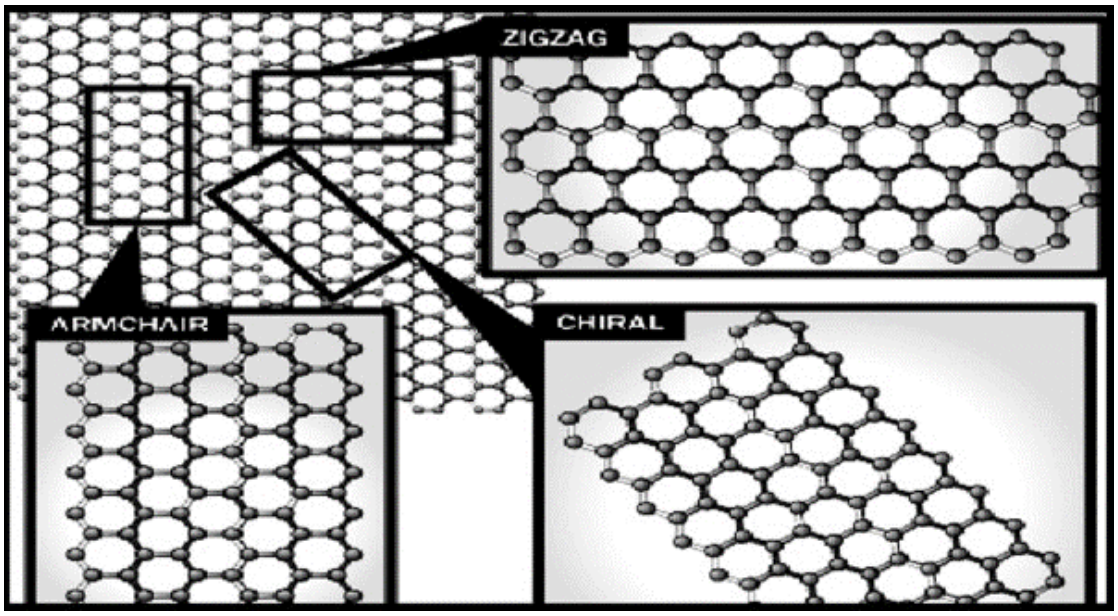


FIGURE 3.1: Schematic diagram showing the formation of different CNT chiral structures [272].

TABLE 3.1: Theoretical and experimental properties of CNT and MWCNT adapted from [276].

Material	**Young's Modulus (GPa)**	**Tensile Strength (GPa)**	**Elongation at Break (%)**	**Density (g cm^{-3})**	**Thermal Conductivity (W m^{-1} k^{-1})**
SWCNT	$\approx$ 1000	50 - 500	16	0.8	3000
MWCNT	$\approx$ 300 - 1000	10 - 60	-	1.8	3000

The use of CNTS in musculoskeletal biomaterials is an exciting prospect with well over 500 papers investigating the use of CNTS in synthetic bone replacement material being documented over the past decade [277]. Some studies have demonstrated biocompatibility of CNTs and improvied osteoconductive performance in-vitro due to the unique properties of CNTs [277–280]. This will be explored in more detail in chapter 7.

3.1 Powder Production

Nano-coated powders were to be tested in a commercial laser sintering machine (Formiga P100) and in a consumer laser sintering machine (Sintratec). The powders were prepared using a modified patented method, described by Jiaming Bai [1]. Briefly, the method involved suspending PA12 powders in water, the suspension is

heated above the glass transition temperature (Tg) of PA12, this softened the surface of the powder particles. Nanoparticles were then added to the suspension and mixed at temperature, which allowed the nanoparticles to adhere onto the surface of the PA12.

In this work, PA12 powders coated with nHA were to be used in the Formiga P100. For PA12 and PLA powders that were to be used in the Sintratec, the powders were coated in a dual mixture of MWCNT and nHA, using the same production method-subject to a slight modification. The quantity of nHA used to coat PA12 was initially calculated using the method prescribed by Jiaming Bai [1].

Assuming that PA12 particle is a sphere, the surface area for one particle:

$$S_{PA} = 4\pi R_{PA}^2 \tag{3.1}$$

Assuming nHA is a cylinder, the shadow area for on nHA particle on the PA12 surface is:

$$S_{nHA} = 2R_{nHA} \times L_{nHA} \tag{3.2}$$

The number of nHA to fully cover one PA12 particle:

$$N = \frac{S_{PA}}{S_{nHA}} \tag{3.3}$$

PA12 powder/nHA volume ratio:

$$\frac{V_{PA}}{V_{nHA}} = \frac{\frac{4}{3}\pi {R^3}_{PA}}{N \times \pi R_{nHA}^2 \times L} \tag{3.4}$$

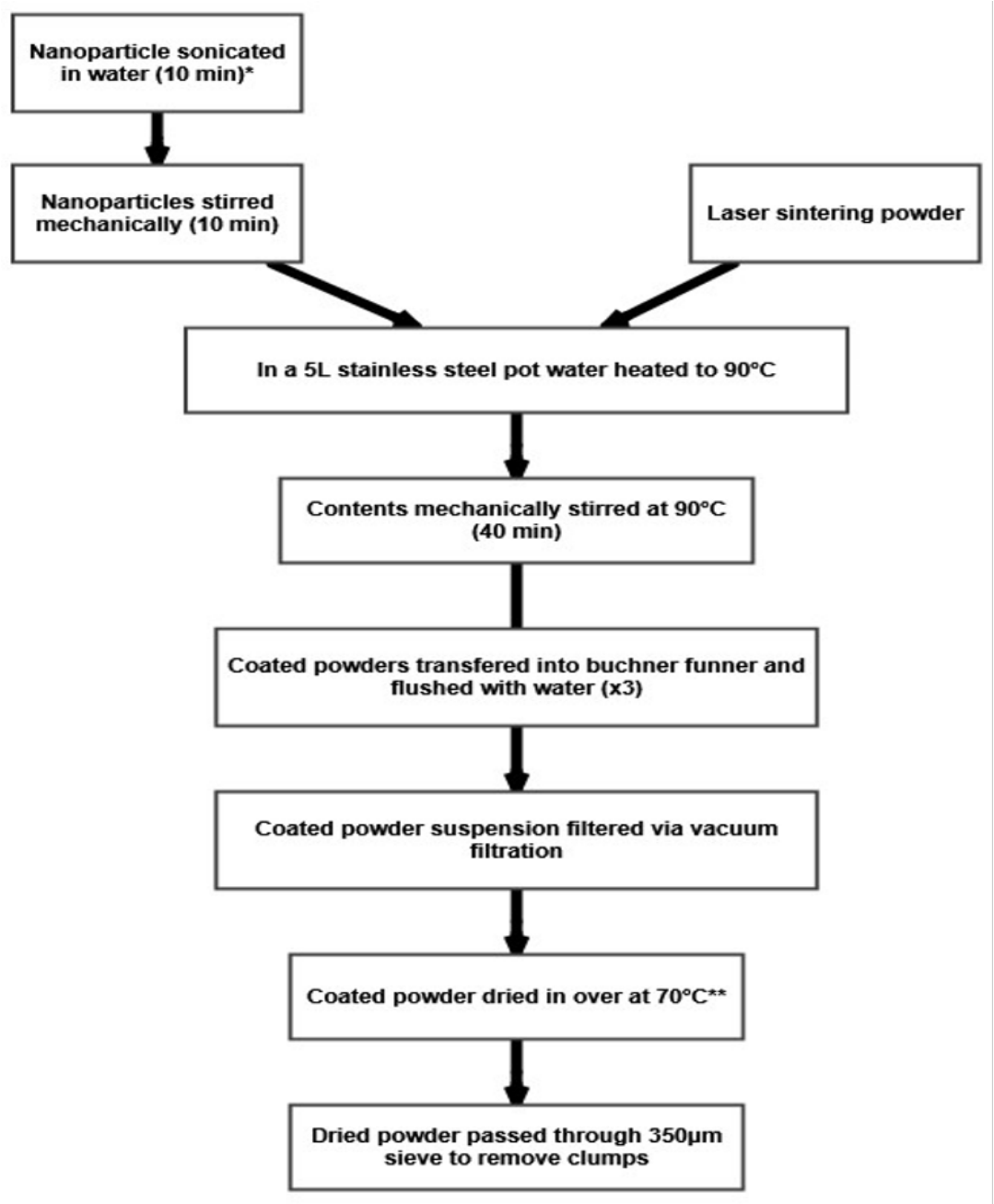
PA12 powder/nHA weight ratio:

$$\frac{m_{PA}}{m_{nHA}} = \frac{V_{PA} \times \rho_{PA}}{V_{nHA} \times \rho_{nHA}} \tag{3.5}$$

Therefore,

$$\frac{m_{PA}}{m_{nHA}} = \frac{S_{nHA}}{S_{PA}} \frac{\frac{4}{3}\pi R_{PA}^3}{\pi R_{nHA}^2 \times L} \times \frac{\rho_{PA}}{\rho_{nHA}} \tag{3.6}$$

Approximately 2.5 wt% was needed for complete coverage. Preliminary testing using 2 and 4 wt% powders led to significant processing issues in the Formiga P100. Therefore the decision was taken to reduce the nHA content for powders that were intended to be use in the Formiga P100 laser sintering machine. An overview of the powder production method can be seen in Figure 3.2. The following subsections describe the processes in more detail.



* For dual NP variants, nanoparticles suspensions are sonicated separately before being mixed together to form a dispersed NP suspension

** For PLA powder variants, powders are dried in a vacuum oven

FIGURE 3.2: Process flow diagram for powder production.

3.1.1 Production of PA12-nHA powders for Commercial Laser Sintering Machine (Formiga P100)

Individual PA12 particles were coated with nHA at six different loadings: 0.5, 1.0, 1.5, 2.0, 4.0 and 10.0 wt%. For the preparation of a 1 kg batch of nanocoated powder, 2 L of tap water was initially heated to 95°C in a 5 L stainless steel vessel using a digital hotplate (SD500, Bibby Scientific). Whilst the water was heating, the nHA slurry was measured and poured into a 500 ml glass beaker, to which 300 ml of deionised water was added. The slurry was mixed for 10 min using an overhead mechanical stirrer (Pro40, SciQuip) set to 1000 rpm with a foil lid placed over the top of the beaker to prevent overspill. Once the nHA/water suspension had formed, the beaker was then placed in a sonicating bath (Bransonic® 5510 Ultrasonic Cleaner) for 15 min to disperse the nanoparticles. Once the water in the steel vessel had reached the desired temperature, the overhead mechanical stirrer was set to 500 rpm and used to stir the water, to which the pre-weighed PA12 powder was then added. The dispersed nHA/water suspension was added to the PA12/water suspension and mixed at 80-90°C for 40 min to allow the nHA to attach onto the surface of the PA12 particles. A foil lid was used to retain the heat and prevent spillage. The temperature was monitored using a digital thermometer and care was taken to ensure the water did not boil, as in previous incidences boiling severe over spill from the mixing vessel. After mixing, the coated powder was transferred and filtered through a vacuum filtration system which comprised of a 240 mm buchner funnel (Fisher Scientific), 2 L filter flask (Fisher Scientific) and a vacuum pump (Capex 8C, Bennett Scientific). The coated powder was flushed three times with fresh water to remove any unadhered NPs. The washed nanocoated powder was then dried in an oven overnight at 80°C. Moisture analysis was then conducted (MX-70 at 100°C) to confirm that the powder was sufficiently dry (0.01% moisture). As mentioned, preliminary work using PA12-nHA powders showed that loadings of 4.0 and 10.0 wt% nHA could be prepared but could not be processed via laser sintering, this is discussed in chapter 5. However, the 4.0 and 10 wt% nHA powders were analysed alongside: 0.5,1.0, 1.5 and 2.0 wt% powders to demonstrate the effects of higher nHA loadings on the physical, chemical and thermal characteristics

of the powder and laser sintering characteristics. Uncoated PA12 (0 wt%) was used as a control and underwent the same production steps as the coated powders but with no nHA added. The PA12 powders coated with: 0, 0.5, 1.0, 1.5, 2.0, 4.0 and 10.0 wt% nHA will be hereinafter referred to as: PA0, PA05H, PA1H, PA1.5H, PA2H, PA4H and PA10H, respectively.

3.1.2 Production of PA12-MWCNT-nHA Powders for Processing in a Consumer Laser Sintering Machine (Sintratec)

The production of PA12-MWNCT-nHA powders followed the same method as described for PA12-nHA powders, with a slight modification, in this case MWCNT and nHA were dispersed separately before being added to the PA12/water suspension (Figure 3.2). A loading of 0.5 wt% MWCNT and a nHA loading of 2.0 and 5.0 wt% was used. The decision to use these loadings was based on preliminary testing on the Sintratec machine with good processing observed using 0.5 wt% MWCNT. The decision to explore 2.0 and 5.0 wt% nHA was based on cellular test results reported in chapter 7. Powder containing 0.5 wt% MWCNT only was also produced using the same production method to serve as a control. The PA12 powders containing 0.5 wt% MWCNT with either 2.0 or 5.0 wt% nHA will be hereinafter referred to as PA05M, PA05M2H and PA05M5H, respectively.

3.1.3 Production of PLA-MWCNT-nHA powders for Processing in a Consumer Laser Sintering Machine (Sintratec)

The production of PLA-MWNCT-nHA powders followed the same method described for PA12-nHA-MWCNT powders, with a slight modification, in this case after flushing and filtering, the coated PLA powders were dried in a vacuum oven (Heraeus Vacutherm VT6025, ThermoFisher Scientific) at 30°C, 1.5 bar overnight with desiccating silica gel packs to absorb the condensate. The MWCNT and nHA were dispersed separately before being added to the PLA/water suspension. A loading of 1.0 wt%

MWCNT and nHA was added at 2.0 and 5.0 wt%. The decision to use these loadings was based on preliminary testing on the Sintratec machine with good processing observed using 1.0 wt% MWCNT. Powders coated with 1 wt% MWCNT only were also produced using the same production method to serve as a control. The decision to explore 2.0 and 5.0 wt% nHA was based on cellular test results reported in chapter 7. The PLA powders containing 1.0 wt% MWCNT and 2.0 and 5.0 wt% nHA will be hereinafter referred to as PL1M, PL1M2H and PL1M5H.

3.2 Powder characterisation

3.2.1 Particle sizing

Particle size can effect the flowability, packing density and processing performance of the powder. Therefore the size distribution of the powders, both as-received and following NP coating, was measured using a laser diffraction based analyser (Mastersizer 3000, Malvern Instruments). A feed rate of 25% and a vacuum pressure of 1 bar was used for the measurements. The obscuration range of the laser beam was set at a minimum of 0.5 and a maximum of 6.5. A total of 10 measurements were taken for each powder composition, at 5 s per reading. The results of the 10 readings were then averaged. Prior to analysis, powders were dried overnight in an oven at 80°C and checked using the moisture analyser. For the PA12 based powders, PA0 was used as the control whilst PA4H and PA05M5H were assessed based on them being the "worst case" scenario for alteration to particle size. For PLA based powders, PL0 was used as the control and PL1M, PL1M5H powders were assessed. Due to their larger particle size, PL0 powder was also analysed after passing through a 150 μm sieve.

3.2.2 Powder Flowabilty and Bulk properties - Specific Energy

The powder flowability and bulk properties of the following powders were analysed on a Freeman FT4 powder rheometer: PA12-nHA powders (PA0, PA2H, PA4H), PLA-MWCNT-nHA powders (PL1M and PL1M5H), as received PLA powder (asPL0) and PLA powder that had been passed through a 150μm sieve were analysed .

The specific energy (SE) is a measure of how powder will flow in an unconfined, low stress environment and is calculated from the work done in moving the rheometer blade through the powder from the bottom of the vessel to the top, as depicted in Figure 3.3. The result calculated was then normalised against mass [281]. The powders were measured using the stability and variable flow rate test programme with the supplied 25 mm x 25 ml split vessel and 23.5 mm rheometer blade. This test sequence was repeated three times and the results for the SE were averaged and plotted on a graph. The formulae for calculating the SE is given as [281]:

$$SE = \frac{\frac{\textit{Up energy cycle 6 + Up energy cycle 7}}{2}}{\textit{split mass}}(mJ/g) \tag{3.7}$$

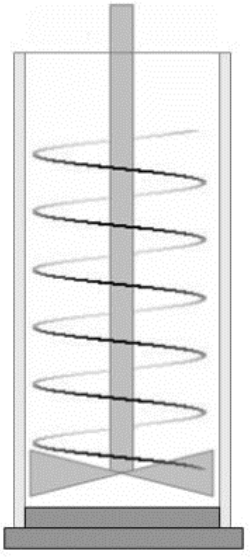


FIGURE 3.3: Diagram showing the directional movement of the rheomter blade through the powder, adapted from [281].

This was calculated by the FT4 data analysis software available in the rheometer following collation of the data for the three tests.

Another parameter given, when using the stability and variable flow rate test, was the conditioned bulk density. This was measured after the conditioning and powder splitting step of the testing procedure.

3.2.3 Powder Flowabilty and Bulk properties - Aeration

As air occupies the spaces between the particles, how the particles interact with air affects the flow properties of the powder. The aeration test programme introduced air into the base of the powder column. The reduction in flow energy was quantified by the work done in moving the rheometer blade through the powder at different air velocities. The test was repeated 3 times for each powder using a 25 mm x 35 ml vessel and a 23.5 mm rheometer blade. An aeration velocity of 0 – 1 mm s^{-1} was used for PA12 powders and a velocity of 0 - 2 mm s^{-1} was used for PLA based powders. The aeration ratio (AR) and aerated energy (AE) was calculated on the FT4 data analysis programme. The aeration ratio is given by:

$$AR = \frac{\textit{Energy (Air velocity 0)}}{\textit{Energy (Air velocity n)}} \tag{3.8}$$

And the aerated energy was given by:

$$\textit{AE (mJ)} = \textit{Energy (Air velocity n)} \tag{3.9}$$

3.2.4 Powder Flowabilty and Bulk properties - Permeability

Permeability is a measure of how easily air can be transmitted through the powder bulk, the permeability test programme was used to measure assess this property. The measurements were repeated 3 times using a 25 mm x 10 ml split vessel with the aeration base, 23.5 mm blade and piston, and an applied normal stress of 0.08 - 1 kPa. The data was recorded as pressure drop across the powder vs normal stress, and was converted to permeability vs applied normal stress, using the FT4 data analysis

programme by applying Darcy's Law [281]:

$$Q = \frac{kA}{\mu}\frac{P_a - P_b}{L} \tag{3.10}$$

Where,

Q = air velocity per unit time ($cm^{-3}s^{-1}$),

k = permeability (cm^2),

A = Cross-sectional area of powder bed (cm^2)

P_a-P_b = pressure drop across powder bed (Pa),

μ = Air viscosity (Pa.s) (for air at sea level = 1.74 x 10^{-5} Pa.s),

L = length of powder bed (cm),

Rearranging gives:

$$k = \frac{q\mu L}{\Delta P} \tag{3.11}$$

Where,

q = air flow rate (cm s^{-1}),

ΔP = pressure drop across powder bed (mbar)

3.2.5 Powder Flowabilty and Bulk properties - Compressibility

The compressibility can indicate the degree of cohesiveness within the powder bulk. This is assessed by measuring the density of the powder bulk as a function of applied normal stress. This was assessed using the compressibility programme using an applied normal stress of 0.08 – 1 kPa. A 25 mm x 10 ml split vessel, 23.5 mm blade and piston was used. The test was carried out 3 times for each powder composition and the results were analysed using the FT4 data analysis programme. The compressibility was equal to the percentage change in volume after compression (%).

3.2.6 Differential Scanning Calorimetry

The thermal properties such as melting temperature and crystallisation temperature of the PA12-nHA and PLA-MWCNT-nHA, powders were analysed on a Perkin Elmer DSC800 using a temperature ramping programme - 30°C to 200°C to 30°C at 10°C min^{-1}. Nitrogen was used as the purge gas and was set to a flow rate of 20 ml min^{-1} and the IntraCooler unit was allowed to reach -100°C before testing was conducted. Typical masses analysed were in the range of 7 - 10 mg, in an aluminium pan and lid crimped over the top. The heat flow vs temperature was plotted and the peak melting temperature and peak crystallisation temperature was calculated using the Pyris Software. The test was repeated three times and the results were averaged. The first heating cycle was assessed. The thermal history of PL0 was also studied by subjecting it to a different heat and cooling cycle. First the powder was heated from 30°C to 200°C, and then cooled to 30°C followed by reheating to 200°C. This performed using a heating and cooling rate of 10°C min^{-1}. The second cooling cycle, cooled the powder rapidly from 200°C to 30°C at 80°C min^{-1}.

Isothermal and non-isothermal analysis was also conducted on PA0, PA4H, PL0, PL1M and PL1M5H, to assess their crystallisation behaviour. These powders were chosen to demonstrate the effects on cyrytsallsation behaviour of powders having no nHA to having high nHA loadings. The Perkin Elmer DSC800 was used with nitrogen as the purge gas and set to a flow rate of 20 ml min^{-1}, while the IntraCooler was allowed to reach -100° before the test was conducted. Powders were weighed (7 - 10 mg) in an aluminium pan, with a lid crimped over the top. The powders were initially heated to 200°C using the standard temperature ramp programme of 10°C min^{-1} and held for 5 min to ensure the powder was fully molten. The samples were then cooled back to 30°C using various cooling rates of 10, 5, 2 and 1°C min^{-1}. The heat flow was recorded on the pyris software and plotted against temperature. For the isothermal crystallisation study the powders were heated to 200°C using the method as described previously and held for 5 min to ensure the powder had fully melted prior to conducting the test. The PA0 and PA4H samples were then cooled to 160, 163, 165 and 168°C and held at each temperature for 15 min. The PL0, PL1M and PL1M5H were cooled

to 127, 130, 133, 135, 137, 140 and 143°C and held for 15 min. A cooling rate of 10°C min^{-1} was used for each powder composition. Using the pyris software, the Avrami crystallisation kinetics model was applied on the isothermal data. This was based on the product of two functions $k(T)$ and $f(x)$ [282]. The first function $k(T)$ gives the temperature-dependent term which is the Arrhenius equation [282]:

$$k(T) = Zexp\left(\frac{-E_a}{RT}\right) \tag{3.12}$$

where,

$E_a =$ activation energy (kJ mol^{-1}),

$Z =$ pre-exponential factor,

$R =$ gas constant

$T =$ absolute temperature (K)

The rate function which gives the dependence of the reaction rate is based on the Avrami equation [282]:

$$f(x) = (1 - x)^n \tag{3.13}$$

where,

$n =$ reaction order

$x =$ fraction reacted

The pyris software solved these equations through collation of the data under isothermal conditions at several different temperatures. Under isothermal conditions, the equations are simplified and lnZ and n was determined by linear regression at each of the selected temperatures. The same data was also analysed by iso-conversion by fitting data from each of the isothermal curves at the same value of x [282]. The activation energy was calculated from the iso-conversion data by linear regression for each degree of the reaction evaluated. Pyris used a modified rate function based on

the the growth of crystallites around the nuclei, derived from the Avrami equation [282]:

$$f(x) = n(1-x)[-ln(1-x)][(n-1)/n] \tag{3.14}$$

where,

$n =$ Avrami constant

$x =$ fraction crystallised

3.2.7 Melt Rheology

As polymer powders do not experience shear stress when processed by laser sintering, the zero-shear viscosity of PL0, PL1M and PL1M5H samples was assessed. This was done using the Kinexus rheometer (Malvern Instruments), with a parallel plate geometry. Approximately 20 g of powder was poured onto the centre of the plate and the secondary 40 mm plate was lowered onto the powder, the assembly was then heated to 190°C to melt the powder. The plate was lowered further to a gap height of 5 mm, this process of heating and lowering the plate was repeated until a gap height of 0.5 mm was reached. The shear rate-controlled programme was selected and the shear rate range was set to 0.0001 to 1 s^{-1} and the nominal force was set to 0.1. The rSpace software then measured the torque and angular velocity. The viscosity vs log shear rate was computed by application of the following equations [283]:

$$\nu = \frac{\sigma}{\dot{\gamma}} \tag{3.15}$$

Where,

$\nu =$ viscosity (Pa.s),

$\sigma =$ stress (Pa),

$\dot{\gamma} =$ shear rate (s^{-1})

The stress was calculated from the torque:

$$\sigma = MK_{\sigma} \tag{3.16}$$

Where,

$\sigma =$ stress (Pa),

$M =$ torque (N.m),

$K_{\sigma} =$ stress constant (geometry dependent factor)

The shear rate was computed by,

$$\dot{\gamma} = K_{\gamma}\Omega \tag{3.17}$$

Where,

$\dot{\gamma} =$ shear rate (s^{-1}),

$K_{\gamma} =$ strain constant (geometry dependent factor) ,

$\Omega =$ angular velocity (rad s^{-1})

3.2.8 Attenuated total reflectance - Fourier transform infrared spectroscopy (ATR-FTIR)

ATR-FTIR is used a non-destructive, qualitative analysis technique for the chemical characterisation of a material [284]. Infrared light (IR), over a range of 4000–500 cm^{-1}, is directed onto an optically dense crystal with a high refractive index. Internal reflectance creates an evanescent wave that extends beyond the surface of the crystal and into the sample held in contact (ATR). The degree of IR absorption within the sample is proportional to the molecular concentration. The detector outputs a time domain interferogram to which the software applies a Fourier Transform to output a

frequency domain spectrum. The relationship between energy (E), wavelength (λ), and frequency (ν) is given by [285]:

$$E = h\nu = \frac{hc}{\lambda} \tag{3.18}$$

$$c = h\nu \tag{3.19}$$

where,

- h is Planck's constant (6.626 $\times$ 10^{-34} J s),
- c is the speed of light (3.00 $\times$ 10^{8} m s^{-1})

The absorption (A) is given by the following formulae which involves the ratio of the intensity of light that is passing through a sample (I) to the intensity of light before it passes through (I_o), which is known as transmittance (%T):

$$A = -log(\%T) \tag{3.20}$$

The different functional groups within the sample will absorb IR differently. As a molecule absorbs IR light, electric dipole moments of vibrating functional groups undergo changes, the frequency of the radiation must match the natural vibrational frequency of the molecules present in the sample and this results in a change in the amplitude of the vibration [285].

Uncoated PA12 powders and PA12-nHA powders used in Formiga P100, which utilises a CO_2 laser operating within the infrared region (IR), were analysed. The absorptive properties of the powder were studied via attenuated total reflectance - Fourier transform infrared spectroscopy (ATR-FTIR) on a VERTEX 70/70v spectrophotometer (Bruker). Scanning was performed at a resolution of 8 cm^{-1} with a scan time of 1 minute per sample over a range of 4000–500 cm^{-1}. Samples were scanned 3 times and the spectrum was acquired using the Bruker OPUS software.

3.2.9 UV-Vis spectroscopy

PA12 and PLA powders containing MWCNT and MWCNT-nHA, intended to be used on the Sintratec, which utilises a 455 nm laser in the visible light spectrum, were analysed via UV-Vis spectroscopy. The working principle for UV-Vis is similar to that of FTIR, in this case visible light, between 200 and 800 nm is used. The absorption of quantised light energy within the visible - UV spectrum excites a molecule from a low lying electronic state to a higher energy electronic state. The wavelength position of the peaks corresponds to the energy required for a specific transition. The analysis was performed using a DU640 UV/Vis spectrophotometer (Beckman). Powder samples were loaded into the sample holder and a silica window was placed over the top of the holder to prevent the sample from spilling out. The spectrometer was controlled using the supplied WinUV software. The machine was set to absorbance mode and wavelength between 200 and 800 nm. A baseline calibration was performed prior to scanning of the samples which was achieved using a black steel plate. The powders were analysed three times and the results were acquired on the WinUV software.

3.2.10 X-ray diffraction

X-ray diffraction allows for the study of crystal structures and atomic spacing. X-rays are generated using a cathode ray tube which are then filtered and directed onto the sample. The incident rays with the sample produces constructive interference when conditions satisfy Bragg's Law [286].

$$n\lambda = 2d\sin\theta \tag{3.21}$$

where,

- n is a positive integer,
- λ is the wavelength of the incident X-ray,

- d is the distance between lattice planes in the crystal,
- θ is the Bragg angle (half the scattering angle 2θ).

The sample is scanned through a range of 2θ angles and the diffracted X-rays are counted. All possible diffraction directions of the lattice are obtained due to the random orientation of the powdered material [286]. The inbuilt software converts the diffraction peaks to d-spacings which are used to screen the pattern against a database to identify the mineral.

To assess the crystallographic properties of the powders before and after coating and laser sintering, X-ray diffraction (XRD) studies were carried out on the PA0, PA1H powders and on a PA1H sample produced on the Formiga P100 laser sintering machine. Furthermore, PLA based powders were also assessed with PL0, PL1M and PL1M5H powders in their un-processed state, in addition to PL0, PL1M and PL1M5H powders which had undergone a typical pre-heating cycle (150°C for 2 h) within the Sintratec. This was to assess what effect pre-heating had on the crystallographic properties of the PLA powders. This study was conducted using a Siemens D500 diffractometer using Cu Kα radiation source (K = 1.54 Å). The samples were recorded in 2θ from 15° to 100° with a step size of 0.5°. The resulting diffraction spectrum was then analysed using the Bruker EVA software.

3.2.11 Scanning Electron Microscopy - Powder morphology

The morphology of the powder particles and degree of surface coverage achieved using the coating method was visually assessed via SEM. Briefly, an electron gun generates an electron beam which is focused by a series of electromagnetic lenses and apertures onto the sample surface. The beam of high energy electrons is rastered over a conductive sample and as the electrons interacts with the sample, secondary electrons are produced which are picked up by a detector to form an image.

A thin layer of carbon dag was spread over the top of an aluminium SEM stub, powder was then sprinkled over the stub and was then left to dry overnight in a fume hood.

The following day, excess powder was blown off the stub using a cannister of HFC free compressed air. The nHA and MWCNT particles were also viewed under SEM and were prepared using a similar method. In this case, a drop of NP slurry was used and the SEM stubs were dried in an oven at 50°C for 2 h, before being left overnight in a fume hood. Prior to observation, the samples were sputter coated with a thin, 5 nm, layer of platinum using a Polaron SC7640 coater at 0.8V twice, at 90 s. Due to machine availability samples were examined on either the Philips XL30 FEG ESEM or the JEOL 7100F FEG SEM with an accelerating voltage of 10.0 - 30.0 kV, working distance of 10.0 mm and spot size 3 - 4 mm.

3.2.12 Scanning Electron Microscopy - Fractured samples

The fracture surfaces of the tensile test pieces were examined under SEM. The fractured ends were cut to 10 mm in length using carbon dag, and the pieces were stuck onto the SEM stubs in a vertical position. The samples were then coated with a thin layer of platinum, as described in section 3.2.11 and viewed on either the Philips XL30 FEG ESEM or the JEOL 7100F FEG SEM, using the same settings described in section 3.2.11.

3.2.13 Scanning Electron Microscopy - Biological samples

Following cytoxicity and bioactivity assessment (section 3.4) the laser sintered nanocomposite samples were washed three times in warm PBS (37°C), after the third wash a 3% Glutaraldehyde solution in 0.1M Na cacodylate buffer (fixative) was used to cover the samples for 30 min. This was then replaced with 7% sucrose solution in 0.1M Na cacodylate buffer for a further 30 min. This was then removed and washed three times for 5 min in 0.1M Na cacodylate buffer. Following the third wash, the samples were exposed to 1% osmium tetroxide. After 45 min the osmium was removed. Dehydration was then carried out with successive washings with ethanol at incremental concentrations from 20 - 100%. Hexamethyldisilazane (HDMS) replaced the 100% ethanol wash and was left to air dry overnight. The next day samples were removed

from the well plates and sputter coated with platinum and viewed under SEM using the settings described in section 3.2.11.

3.2.14 Transmission Electron Microscopy

The nano HA rods were viewed under transmission electron microscopy (TEM). Imaging was conducted using a JEOL 2000 FX TEM. The nHA particles were diluted to 0.01% in ethanol and subjected to 20 min of sonication. After this, a drop of nHA suspension was placed onto Holey copper grids (Agar Scientific) and left to dry, to deposit the nHA onto the grids. The samples were placed into the TEM and imaged at 120 kV and spot size of 1 mm.

3.3 Laser Sintering of Nano-coated Powders

3.3.1 Determination of Powder Bed Temperature

Prior to processing the coated powders, the processing bed temperature was first determined by heating the powder close to the onset of melting, as determined by DSC analysis. The temperature was then raised at 1°C intervals and held for 5 min, this was repeated until the powder bed surface started to show signs of agglomeration, or turning darker, due to overheating. For PA0, PA1H, PA1.5H and PA2H this was performed in the commercial laser sintering system (Formiga P100), between 170 – 180°C. In the consumer laser sintering system (Sintratec) PA05M, PA05M2H and PA05M5H powders were tested at 170 – 180°C. The PL1M, PL1M2H and PL1M5H powders were also tested in the Sintratec at 160 – 170°C.

3.3.2 Processing Parameters (Formiga P100)

The description of the laser sintering process can be found in Chapter 2. In this work, the processing window is defined as the parameter ranges that enable the production

TABLE 3.2: Overview of the parameters used for the testing of nHA coated PA12 powders in the Formiga P100.

Formiga P100: Parameters
Laser Power: 2 -25 W
Scan Speed: 800 - 3000 mm/s
Scan Spacing: 0.25 mm
Layer Height: 0.1 mm
Chamber Temperature: 176 -178°C

of completed parts with an average dimensional error of the final part being $\leq$10% of the target dimension (good shape definition) and which the parts can be removed from the powder bed without falling apart (good handleability). The settings used to determine the processing window for PA0, PA05H, PA1H and PA1.5H are presented in Table 5.2. A 15 x 15 x 1 mm sample was attempted by varying the laser power and scan speed until samples that visually displayed a low degree of curling and provided good shape definition were achieved. Shape definition was deduced by measuring the X, Y and Z dimension of the rectangular samples using digital vernier callipers. The dimensional errors were averaged, and samples scoring an average error above 10% of the target size were rejected, any sample scoring an average error of $\leq$10% were deemed to have good shape definition.

Based on the optimum parameters selected, tensile test specimens were then produced in accordance with ASTM standard [287] with a gauge length of 25 mm, width of 6 mm, radius fillet of 6 mm, overall length of 100 mm and width of grip section of 10 mm; in addition to 10 x 1 mm disks for cellular testing.

3.3.3 Processing Parameters (Sintratec)

As the laser power was fixed at 2.3 W, 10 x 10 x 1 mm samples were attempted by varying the scan spacing and laser speed until samples that visually displayed a low degree of curling and provided good shape definition were achieved. Good shape definition was defined by using the method described in 3.3.2. The parameters used for determining the processing windows for PA05M, PA05M2H and PA05M5H powders are summarised in Table 3.3.

TABLE 3.3: Overview of the parameters used for the testing of PA05M, PA05M2H and PA05M5H powders.

Sintratec: Parameters (PA12 powders)
Laser Power: 2.3 W
Scan Speed: 100 - 1000 mm/s
Scan Spacing: 0.01 - 0.1 mm
Layer Height: 0.1 mm
Chamber Temperature: 176 -178°C

TABLE 3.4: Overview of the parameters used for testing of the coated PLA powders.

Sintratec: Parameters (PLA powders)
Laser Power: 2.3 W
Scan Speed: 100 - 1000 mm/s
Scan Spacing: 0.01 - 0.1 mm
Layer Height: 0.1 mm
Chamber Temperature: 165 -166°C

The parameters used for determining the processing windows for PL1M, PL1M2H and PL1M5H are summarised in Table 3.4.

Based on the optimum parameters selected, tensile test specimens were produced in accordance with ASTM standard [287] with a gauge length of 25 mm, width of 6 mm, radius fillet of 6 mm, overall length of 100 mm and width of grip section of 10 mm. Cylinders measuring 20 x 30 mm were also produced for compression testing and specimens measuring 15 x 5 x 1 mm for PLA based nanocomposites, in addition to 10 x 1 mm disks for cellular testing.

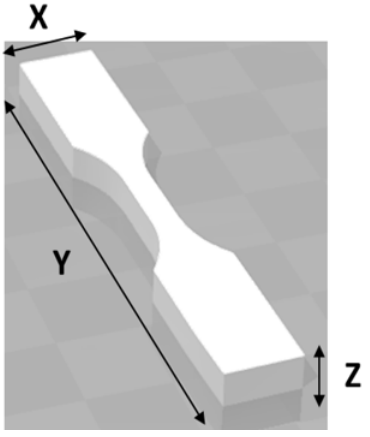


FIGURE 3.4: Fusion 360 CAD images of the tensile test pieces produced on the Sintratec.

3.3.4 Heat Treatment of PLA nanocomposites

Due to the processing difficulties experienced in the Sintratec, to improve the final part densities and mechanical properties additional PL1M, PL1M2H and PL1M5H samples were subjected to a heat treatment cycle. This consisted of heating the samples to 164°C, from room temperature using a digitally controlled laboratory oven (ThermoFisher). The samples were held isothermally for 4 hours, to provide sufficient time to consolidate the under-sintered particles within the bulk. The samples were then left to cool back to room temperature. The length, width and thickness of the samples was then measured using a digital vernier calliper.

3.3.5 Tensile Testing

Tensile testing was conducted to determine the Young's modulus, ultimate tensile strength (UTS) and elongation at break (EOB) for PA0, PA05H, PA1H and PA1.5H, which were processed in the Formiga P100, and PA05M, PA05M2H, PA05M5H, PL1M, PL1M2H and PL1M5H, which had been processed in the Sintratec. An Ingstron Unaxial tensile tester with a 50 kN load cell for PA12 based samples and a 10 kN load cell for PLA based samples was used to perform the test. Dog-bone shaped samples were prepared via laser sintering, using the parameters determined via the method described in sections 3.3.2 and 3.3.3, in accordance with ASTM standard [287]. Five samples of each composition were tested using a strain rate of 1 mm s^{-1}, and a video strain gauge was used to record the EOB. The modulus, UTS and EOB was then calculated using the Bluehill software and extracted from the data tables provided.

3.3.6 Compression Testing of PLA Nanocomposites

The compressive modulus and compressive strength of PL1M, PL1M5H and PL1M5H, in addition to PL1M HT, PL1M2H HT and PL1M5H HT samples, was measured using an Instron uniaxial tensile tester with a 50 kN load cell and a strain rate set to 1 mm s^{-1}. Five cylindrical samples of each composition measuring 20 x 30 mm were

TABLE 3.5: Overview of the parameters used for DMA testing.

Dynamic Mechanical Analysis: Parameters
Frequency: 1 s^{-1}
Strain Amplitude: 0.05 mm
Initial Temp: 25°C
Final Temp: 180°C
Heating Rate: 2°C min^{-1}

prepared via laser sintering in the Sintratec. Initially, variable differential transformer (LVDT) sensors were used to measure the strain. However, due to the processing issues encountered, (discussed in 5) the top surfaces of the samples had slight deformities and were not flat; therefore, the LVDT could not accurately measure the strain and the modulus was therefore omitted. The compressive strength was calculated on the Bluehill software and the values were extracted from the data tables.

3.3.7 Dynamic Mechanical Analysis

Dynamic Mechanical Analysis was used to explore the stiffness and external dampening behaviour of heat treated PLA samples. Rectangular specimens measuring 15 x 5 x 1 mm were fabricated on the Sintratec. Five heat treated specimens of PL1M HT and PL1M5H HT, in addition an un-heat treated PL1M sample used as a comparison, were used for the analysis. An un-heat treated PL1M5H was initially included as a comparison for PL1M5H HT, however the samples were too fragile for DMA testing and were thus omitted. The DMA analysis was performed using a PerkinElmer DMA 800, using auto tension mode and a tensile clamp set on the drive shaft. An overview of the parameters used can be seen in Table 3.5. The DMA applied an oscillatory force, on the sample, at a set frequency. The Pyris software calculated the storage modulus (G$\prime$), related to elastic "in-phase response" to applied oscillatory stress, and the loss modulus (G$\prime\prime$) which was related to the viscous "out of phase" sample response to applied oscillatory stress. The software also calculated the ratio of G$\prime\prime$ to G$\prime$ which gave the dampening coefficient (Tan δ), which was related to the energy dissipation of the sample. These were plotted as a function of temperature.

3.3.8 Density Measurements

The density of the laser sintering nanocomposites was assessed using a gas displacement method (Micrometrics AccuPyc 1330 helium pycnometer). Specimens used for the density measurement were taken from the end grip sections of the tensile test specimens, following tensile testing. Samples were placed into a sealed chamber of known volume, and H_2 gas was then injected into the chamber. Once equilibrium was reached the gas within the sample chamber was then discharged into a second chamber. The pressures observed upon filling the sample chamber and discharging into the secondary chamber allowed the pycnometer to calculate the sample solid phase volume. The density of the sample was then calculated by dividing the sample volume by the sample mass. Prior to testing, the machine was calibrated using a standard which consisted of a steel ball of known volume, mass and density. Samples were measured three times and the average of the three was taken.

3.4 Cell Study

The cyctotoxicity of the nHA, MWCNT and a mixture of MWCNT-nHA particles were tested, in addition to the laser sintered nanocomposites produced on the Formiga P100 and Sintratec. The MG-63 osteosarcoma cell line was used as they possess osteoblastic features and are routinely used as osteoblastic models. These cells have a high proliferation rate and are relatively straightforward to cultivate, when compared to primary cells, thus making them valuable for high throughput cytotoxicity testing. Furthermore, an immortalised version of the Human Mesenchymal Stem Cell (hiMSCs) was cultured directly onto the surface of the samples. The use of hiMSCs allows for the assessment of the osteoconductive properties of the laser sintered nanocomposites. Again, the immortalised version of the cell line was used due to their high proliferative capacity and relative ease of culture. The details of the culturing conditions and assays used for each test are detailed in the following section.

3.4.1 Defrosting of cells

An ampoule of frozen MG-63 osteosarcoma cells, passage 10, (European Collection of Authenticated Cell Cultures) was removed from the liquid nitrogen store. The ampoule was defrosted using a hot water bath set to 37°C, the ampoule was held in the bath for 2 min, ensuring that the lid did not contact the water. Once defrosted the amoule was sprayed with 70% industrial methylated spirit (IMS), wiped dry and transferred into a class II hood (Triple Red). The contents of the ampoule were aspirated and transferred into a 20 ml polystyrene universal tube (ThermoFisher Scientific). Afterwards, 10 ml of pre-warmed (water bath, 37°C) Dulbeco's Modified Eagles Medium (DMEM), supplemented with 10% foetal bovine serum (ThermoFisher Scientific), 1% L-Glutamine, 1% penicillin/streptomycin, 1% non-essential amino acids, 1% HEPEs buffer (ThermoFisher Scientific) and 75 mg ascorbic acid (Sigma Aldrich), was added drop wise to prevent osmotic shock. The cryo-preservative was then removed by centrifuging the tube at 1200 rpm for 4 min (Jouan CR422). The fluid was carefully aspirated and the cells were re-suspended in warm cell culture medium. The contents were then transfered into a 25 cm^2 flask (Corning) and incubated at 37°C, 5% CO_2 (Triple Red, incubator).

An ampoule of hiMSCs, passage 70 (donated by Dr. Virginie Sottile, University of Nottingham, Faculty of Medicine and Health Sciences), was removed from the liquid nitrogen store and the ampoule was defrosted using the same protocol as described above. However, the hiMSC cell culture medium did not contain HEPES buffer or ascorbic acid.

3.4.2 General Cell Maintenance

Both the MG-63 and hiMSCs were cultured in an incubator (Triple Red, incubator) at 37°C, 5% CO_2, with a copper sulphate water bath to provide humidity. Every other day the flasks were transferred into the class II hood, the cell culture medium was aspirated and discarded, the cells were then washed three times with pre-warmed

(water bath, 37°C) phosphate buffer saline (PBS) and replaced with fresh cell culture medium. The flasks were then placed back into the incubator.

The cell cultures were also checked visually at the time of feeding using an inverted microscope (Nikon Eclipse TS100). Once cells reached 80% confluency they were passaged. In a class II hood, the culture media was aspirated from the flasks and washed with three times with PBS. A 1.5 ml solution of 0.02% Trypsin/EDTA with HEPES buffer solution was added and the flasks were transferred back into the incubator for 60 s. The bottom of the flasks was tapped to dislodge the cell monolayer (confirmed via inverted microscope). In the class II hood, 10 ml of cell culture medium was added to the flask, to neutralise the trypsin, and the contents were transferred into a 25 ml universal tube. The tubes were centrifuged at 1200 rpm for 4 min; and the presence of the cell pellet was confirmed visually. The cell culture media was then aspirated and the cells re-suspended in fresh, pre-warmed media. The contents of the tube were then split into three, new, 25 cm^2 flasks. The cells were continually cultured following the method described above. By the start of the experiments the MG-63 cells were at passage 13 and the hiMSCs were at passage 72.

3.4.3 Cell Seeding

To determine if there were enough viable cells to carry out the experiments, the number of viable cells was counted. The cells were removed from the flasks and pelletised using the methods described in section 3.4.2. The cells were then re-suspended in 1 ml of their respective mediums. Using a pipette, a 50 μl suspension of cells was transferred into a 1 ml eppendorf. An equal volume of 0.008% solution of trypan blue dye (Sigma-Aldrich) was added to the eppendorf and left for 1 min at room temperature, giving time for the dead cells to take up the trypan blue dye. A drop of the cell/trypan blue mixture was transferred to a haemocytometer and the number of viable cells was counted using the inverted microscope at x 10 magnification. The cells were counted three times and then averaged. The viable cell count was calculated using the following formula:

$$\textit{Viable cell count per ml} = \left(\frac{\textit{average viable cells counted}}{\textit{suspension volume}} \right) \times \textit{dilution factor} \times n \times 10^4 \tag{3.22}$$

where, n = ratio of volume of media removed for cell count to suspension media volume.

3.4.4 Sample Preparation

Disc shaped samples measuring with a 10 mm diameter x 1 mm thickness were produced on the Formiga P100 and Sintratec laser sintering machines. The compositions evaluated were: PA0, PA05H, PA1H, P1.5H, PA05M, PA05M2H, PA05M5H, PL1M, PL1M2H and PL1M5H. Prior to the day of commencing the cell culture experiments, the samples were cleaned by sonicating for 5 min in isopropyl alcohol (IPA), and rinsed with de-ionised water to remove contaminants and un-sintered particles from the surface. Following washing, the samples were dried in a drying cabinet set, to 50°C, overnight. On the day of the experiment the samples were removed from the drying cabinet and placed into the class II hood. The samples were laid flat inside the hood, in addition to 48-well plates, with the lids removed. The samples and well plates were sterilised using a UV-C lamp. The samples and well plates were exposed to the UV-C light for 20 min, following which the samples were flipped over and exposed for another 20 min. After sterilisation the samples were placed into the well plates and left in the hood to begin preparation for the start of the experiments.

3.4.5 Cytotoxicity study - Alamar Blue Assay (nanoparticles)

Alamar blue is a reagent used for evaluating cellular metabolic activity and is commonly used in high throughput cytotoxicity screening. Alamar blue is a non-toxic compound, the active component, Resaruzin, is reduced in metabolically active cells to produce a bright, red fluorescent compound called Resorufin which can be measured using a plate reader. MG-63 cells were seeded into a 48 well plate (Nunc) at 5,000 cells per

cm^{-2} in 0.5 ml of standard cell culture medium (per well) and allowed to recover for 24 hours. A stock solution of nHA/cell culture medium, MWCNT/cell culture medium and MWCNT-nHA/cell culture medium was prepared at concentrations of 100, 300, 500, 700 and 1000 μg ml^{-1}. Prior to the addition of the culture medium, the solutions were sonicated for 10 min and then vortexed for a further 10 s prior to addition to the wells. Three samples of each concentration were tested in addition to a 0 μg ml^{-1} as a control. The cells were incubated and maintained following the general cell maintenance protocol, as described previously, and were fed every other day with the NP supplemented media. The stock solutions were sonicated and vortexed prior to each feeding. The cells were cultured with the NPs for 7 days and at 24 hours, 72 hours and 7 days, the treated medium was removed and each well was carefully washed three times using warm PBS (37°C). After the third wash a 1:10 solution of Alamar blue concentrate (Biorad) and Hanks balanced salt solution (ThermoFisher) was added to each well (500 μl) in addition to three blanks (Alamar blue solution with no cells). The cells were incubated for 80 min (37°C, 5% CO_2) after which they were wrapped in foil, to prevent light exposure, and shaken on the plate shaker at 150 rpm for 5 min. The contents were transferred back into the class II hood, with the lights off, and 100 μl from each well was aliquoted into a 96 well plate in triplicate. The Fluorescence was then recorded on the FLx-800 plate reader (BioTek) at excitation 560/15 and Emission 590/20. The data was extracted from the KC junior software (BioTek) and the blanks were subtracted. Following the test, the wells were prepared for the following Hoechst 33258 DNA assay by gently washing the wells with warm PBS, to remove the remaining Alamar blue solution. 1 ml of SDW was then added to the plates which were then sealed with the plate cover, using sterile tape, and placed in the -20°C freezer.

3.4.6 Cytotoxicity Study – Hoechst 33258 DNA Assay (Nanoparticles)

Hoeschst 33258 is a fluorescent stain that binds to double stranded DNA, the Hoechst 33258 DNA assay was used to determine cellular proliferation. This test followed on

from the Alamar blue assay. To prepare, the 48 well plates containing the cells and SDW were subjected to a freeze thaw cycle. This consisted of placing the plates in the incubator at 37°C and allowing the SDW to fully defrost before placing the plates back into the -20°C freezer. This was repeated three times to rupture the cell membrane and release their cytoplasmic content. The contents of each well were then aliquoted into 1 ml eppendorfs. Following this, a TNE buffer was prepared by dissolving 0.156 g tris(hydroxymethly)methylamine, 11.72 g NaCl and 0.0372 g EDTA in 100 ml of SDW and pH adjusted to 7.4. The DNA stain was prepared by dissolving Hoechst 33258 stain (Sigma-Aldrich) in 1 ml of sterile distilled water (SDW) and diluted to 1:50 in TNE buffer. This was then sterilised by filtration using a 0.22 μm filter. A 10-point standard curve was prepared using calf thymus DNA solution. The eppendorfs were vortexed to re-suspend the DNA content and 100 μl was aliquoted into a 96 well plate in triplicate, and an equal volume of DNA stain was added to the wells, three additional blanks were included. The absorbance was then read on an FLx-800 plate reader (BioTek) at 360 nm excitation and 460 nm emission. The data was extracted from the KC junior software (BioTek) and the blanks were subtracted. The DNA content was then calculated using the straight-line equation obtained from the standard curve.

3.4.7 Cytotoxicity Study - Alamar Blue (Laser Sintered Nanocomposites)

MG-63 cells were seeded onto the nanocomposite samples at 5,000 cells per cm^{-2} and in a seeding volume of 0.1 ml. The cells were allowed to recover for 24 hours before beginning the experiment. Six samples of each composition were tested in addition to a tissue culture plastic as a control. The cells were incubated for 7 days, washed and fed every other day. At 24 hours, 72 hours and 7 days the cell culture medium was removed and 1:10 volume of Alamar Blue was added following the protocol mentioned in 3.4.5, and the fluorescence was read. Afterwards the wells were washed to remove residual Alamar Blue stain, filled with 1 ml of SDW and stored in the -20°C freezer in preparation for the Hoechst 33258 DNA assay.

3.4.8 Cytotoxicity Study – Hoechst 33258 DNA Assay (Laser Sintered Nanocomposites)

Following the Alamar blue assay conducted on the laser sintered nanocomposites the Hoechst DNA 33258 was also conducted. The protocol followed was the same as that used for the testing of the nanoparticles.

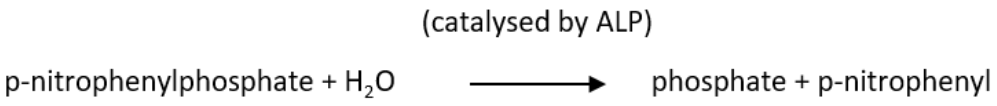
3.4.9 Osteoconductivity studies

A series of experiments to assess the osteoconductivity of the laser sintered nanocomposites was performed using hiMSCs. The hiMSCs were seeded onto: PA0, PA1.5H, PA05M, PA05M5H, PL0, PL1M and PL1M5H, TCP was used as a control. Three samples of each material composition were used for the study and each test was repeated. The cells were seeded onto the material surfaces at a density of 2500 per cm^{-2} and supplemented with osteogenic differentiation media. The cells were incubated for 21 days following the general cell maintenance protocol as described. At 24h, 7d, 14d and 21d the Hoeschst 33258 DNA assay was performed, using the same method as described in the cytotoxicity study. At 7d, 14d and 21d an Alkaline Phosphatase assay (ALP) was performed and at 14d and 21d an Osteocalcin assay was also performed. Alizarin Red was also conducted at 21d. Details of the ALP, Osteocalcin and Alizarin Red assays are described in the following sub-sections.

3.4.10 Osteoconductivity Study - Alkaline Phosphatase Assay

Alkaline phosphatase (ALP) is a glycoprotein, the skeletal isoform is found on the cell membrane of osteoblasts [288]. The accumulation of ALP often precedes bone mineralisation and is therefore commonly used an early marker for osteoblast differentiation [69]. The testing for ALP followed on from the Hoechst DNA assay, and the preparation of the samples followed the same protocol as described in section3.4.6 for the MG-63 cytotoxicity study. The ready to use kit (Randox ALP liquid Assay) was prepared by reconstituting a vial of the ALP substrate (p-nitrophenylphosphate 10

mmol L^{-1}) with 10 ml of Diethanolamine buffer (1 mol L^{-1} at pH 9.8, with $MgCl_2$ 0.5 mmol L^{-1}). The solution was gently inverted several times to dissolve and mix the solution. The samples were aliquoted (50 μl) in triplicate into a 96 well plate to which an equal volume of ALP substrate solution was added. Three blanks consisting of the ALP substrate solution only were also included. The plates were covered and gently shaken on a plate shaker for 30 min and observed for a colour change from clear to yellow, due to the following reaction:



Following gentle shaking the absorbance was measured at 405 nm excitation and 620 nm emission, using the Biotek ELx800 plate reader. The results were extracted from the KC junior software (BioTek) and the blanks were subtracted. The samples were normalised against DNA content.

3.4.11 Osteoinductivity Study - Osteocalcin Assay

Osteocalcin is one of the most abundant forms of non-collagenous proteins present in the bone ECM and is synthesised and secreted exclusively by osteoblastic cells in the late stage of maturation [289][69]. The osteocalcin assay was used as an indicator for late stage differentiation of the osteoblastic phenotype. This was performed using an enzyme linked immunosorbent assay kit (ELISA) (Invitrogen). Monoclonal antibodies coated onto the bottom of a 96 well plate are directed against epitopes of human osteocalcin. A secondary monoclonal antibody, labelled with fluorescent horseradish peroxidase (HRP), is added which binds to the osteocalcin molecules forming a sandwich. The fluorescence can then be read using a plate reader. Prior to conducting the assay, the cell culture media used to feed the cells growing on the laser sintered nanocomposites, was removed and aliquoted into 1 ml eppendorfs at the allocated timepoints, and frozen down. On the day of the assay the frozen samples were defrosted at 37°C. The washing solution was prepared by adding 199 volumes of distilled

water to 1 volume of wash solution (x200) and mixed by magnetically stirring for 10 min. Whilst the wash solution was being mixed, a working solution of anti-OST-HRP conjugate was prepared by adding 40 μl of the concentrated anti-OST-HRP conjugate to 2 ml of conjugate buffer (ready to use, Tris-HCl buffer with bovine serum albumin, bovine casein, EDTA, gentamycin and thymol) and vortexed for 10 s to homogenise the solution.

The standards were prepared ((0 – 75 ng ml^{-1}), human serum, protease inhibitors, benzamin and thymol) by reconstituting the lyophilized standards with 1 ml of SDW and mixing by gentle inversion until completely dissolved. For the assay, 25 μl of each standard, in addition to the samples, was aliquoted into wells coated with monoclonal antibodies. 100 μl of the working anti-OST-HRP conjugate was then added to the wells. The plates were covered with the supplied plate cover and incubated for 2 hours at room temperature. After incubation, the wells were washed three times using the wash solution and 100 μl the Chromogen solution (tetramethylbenzidine) was added to each well followed by another incubation period of 25 min at room temperature. Following the second incubation step 100 μl of stop solution (1N HCl) was added to each well. The side of the plate was tapped to gently mix the solution and a colour change from blue to yellow was observed. The absorbance was read at 405 nm excitation and 620 nm emission using a Biotek ELx-800 plate reader. The osteocalcin concentration was calculated from the straight-line equation obtained from the standard curve.

3.4.12 Osteogenesis Study – Alizarin Red Staining

Mineralisation was qualitatively assessed using the Alizarin Red staining. Alizarin Red (Sigma-Aldrich) stains calcium phosphate deposits and can be used to assess the degree of mineralisation of the cells. The following protocol was adapted from Amy Prosser MSC, PhD [290]. At 21 days, the cell culture media was removed from the wells and the samples were washed three times with PBS and fixed with a 4% paraformaldehyde solution, overnight, at 4°C. The following day, the wells were washed three times with PBS before addition of 100 μl of 1% (w/v) Alizarin Red solution. To account for

potential staining of the nHA particles on the surface of the samples, Alizarin Red was also added to nanocomposite samples with no cells. The plates were incubated for 10 min at room temperature with gentle shaking. A de-stain solution was prepared by mixing 20% (v/v) methanol, 10% (v/v) acetic acid and 70%(v/v) distilled water. After the shaking period the wells were further washed with distilled water to remove excess stain and 500μl of de-stain solution was added to each well, in addition to three blanks containing only de-stain solution. The samples were incubated for 15 min with gentle shaking. 100μl from each well was aliquoted into a 96 well plate in triplicate and the absorbance was read using the Biotek ELx800 plate reader at 405 nm. The results were extracted from the KC junior software (BioTek) and the blanks were subtracted, followed by subtraction of the no cell nanocomposite samples.

3.4.13 Cell Culturing on Laser Sintered Nanocomposite Scaffold

A cylindrical 3D scaffold was generated using a trial version of a functional lattice generation software, Flatt Pack (Added Scientific, The University of Nottingham). A Schwarz P minimal surface unit cell was selected and a cylindrical model measuring 11 mm diameter and 12 mm height, created on Fusion 360 (Autodesk), was imported into the software for lattice generation. The resulting scaffold had a pore size of 0.5 mm, this can be seen in Figure 3.5. Three scaffolds each were produced from PA0 powder on the commercial machine (P100) and PL1M5H powder on the consumer machine (Sintratec). The scaffolds were washed with accordance to the sample preparation procedure described in section (3.4.4). The scaffolds were slotted into the wells of a 48 well plate and osteogenic cell culture medium was added to the scaffold and incubated at 37°C for 1 hour to allow the media to wet the surface. Following this, approximately 2 million hiMSC cells, that were left over from the previous assay, were seeded onto the surface of the scaffold at a density of 5,000 cells per cm^2. The cells were maintained for 21 days following the general cell maintenance protocol described previously. At 21 days the culture media was removed and the samples were dehydrated following the SEM sample preparation procedure for biological samples as described in

section3.2.13. The samples were then dissected both horizontally and vertically before mounting onto an SEM stub and sputter coating with platinum. The samples were viewed under SEM using the settings described in section 3.2.13.

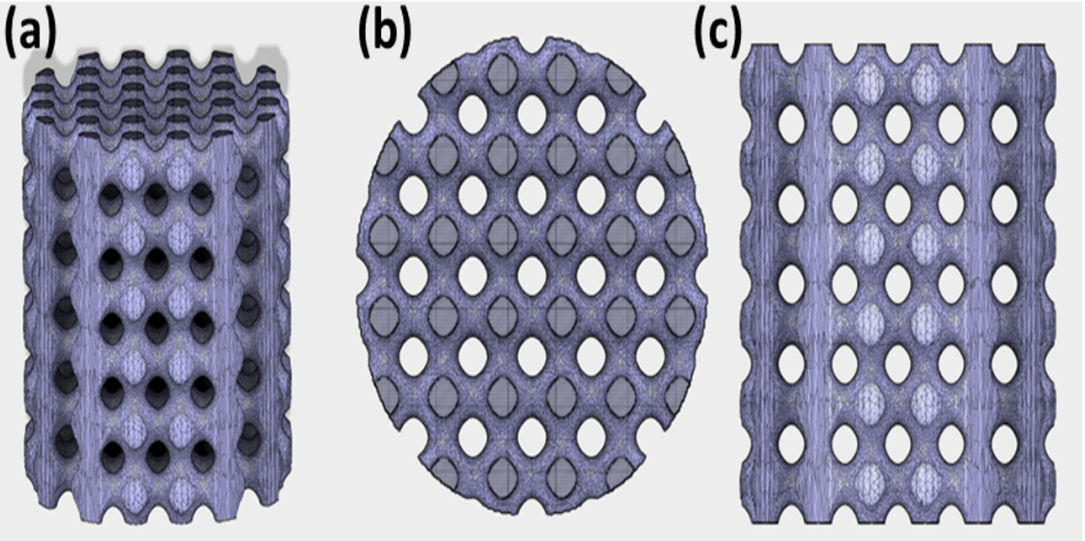


FIGURE 3.5: Fusion 360 CAD images of the scaffold taken from (a) the projected view, (b) top plane and (c) front facing plane.

3.4.14 Statistics

The results for the powder characterisation, and mechanical testing on the nanocomposite samples, were analysed in Prism (GraphPad) using One-way ANOVA with Tukey's post-hoc analysis and a significance level of 0.05.

For cellular testing, each of the assays were repeated with three technical replicates performed per sample (n). The results were analysed in Prism (GraphPad) using Two-way ANOVA with Tukey's post-hoc analysis. One-way ANOVA with Tukey's post-hoc analysis was performed on the results of the Osteocalcin and Alizarin Red assays. A significance level of 0.05 was selected.

In the following chapters the results of each of the experiments are presented and discussed. Chapter 4 assesses the method used for coating the polymer powders with nHA and MWCNT and how the nanocoating may influence powder performance during laser sintering. Chapter 5 examines how the nanocoated powders behave during laser

sintering in the Formiga P100 and Sintratec. Chapter 6 examines how the presence of NPs and the different laser sintering parameters used affects the final part properties of the nanocomposite. Chapter 7 examines the suitability of the resulting nanocomposites for use as a bone substitute material via cellular examination.

Chapter 4

Powder Characterisation

In this chapter, the nanocoated powders produced using the adapted powder production method (as described in Chapter 3) was assessed for its effectiveness in depositing alternative NPs, such as nHA and MWCNT-nHA, on both PA12 and PLA. And to determine what influence the nanocoating may have on the laser sintering performance of the powders. The hypothesis, as described in 2, is that the addition of nHA to the outer surface of PA12 and PLA particles will not significantly impact upon the overall size and morphology of the powder. However, the increased surface roughness may increase the inter-particle friction and decrease the ease at which particles can pass over one another leading to a less densely packed powder bulk, and higher degree of porosity in laser sintered sample. The addition of nHA on the surface of the powder will not alter the melting temperature, however, the temperature at which re-crystallisation occurs will be reduced and the crystallisation rate of the polymer melt will increase as a result of the nHA. To test the hypothesis, Section 4.2 examines the size distribution of the coated powders via laser diffraction to determine if the addition of NPs on the surface affects the overall size of the powder particles. In Section 4.3, SEM was used to examine the morphology of the powders and assess the degree of surface coverage achieved by the coating method used. How the powder flows has a significant impact on the ability to deposit thin layers of powder in the LS machine. Therefore, the flow characteristics of the powder was quantitatively assessed using an FT4 Powder Rheomteter in Section 4.4. As LS involves the melting and recrystallisation of the

polymer powder, the thermal characteristics of the powders was examined using DSC in Section 4.5, this will also aid in determining the LS powder bed temperatures. As LS relies upon flow of the polymer melt to achieve consolidation the zero shear viscosity is an important factor to consider. This was, therefore, assessed in Section 4.6. A key criteria for LS is the ability for the powder to absorb the incoming laser, therefore, the influence that NP have on the optical properties of the powders were assessed via FTIR and UV-VIS in section 4.7.

4.1 Nanoparticle morphology and sizing - nHA

Transmission Electron Microscopy was used to assess the diameter and size of the nHA rods as-received from Promethean Particles. Figure 4.1 shows TEM images of nHA rods that have been in a 0.01% solution in ethanol and sonicated for 10 min prior to deposition onto TEM copper girds. From the images it is clear that sonication did not disperse the particles sufficiently. Agglomerates of the nano rods makes distinguishing individual nHA particles difficult. However, the individual rods are visible at the edges of agglomerates and using the sizing tool on the TEM's software an individual nano rod was measured to be 371 nm long and 35 nm wide.

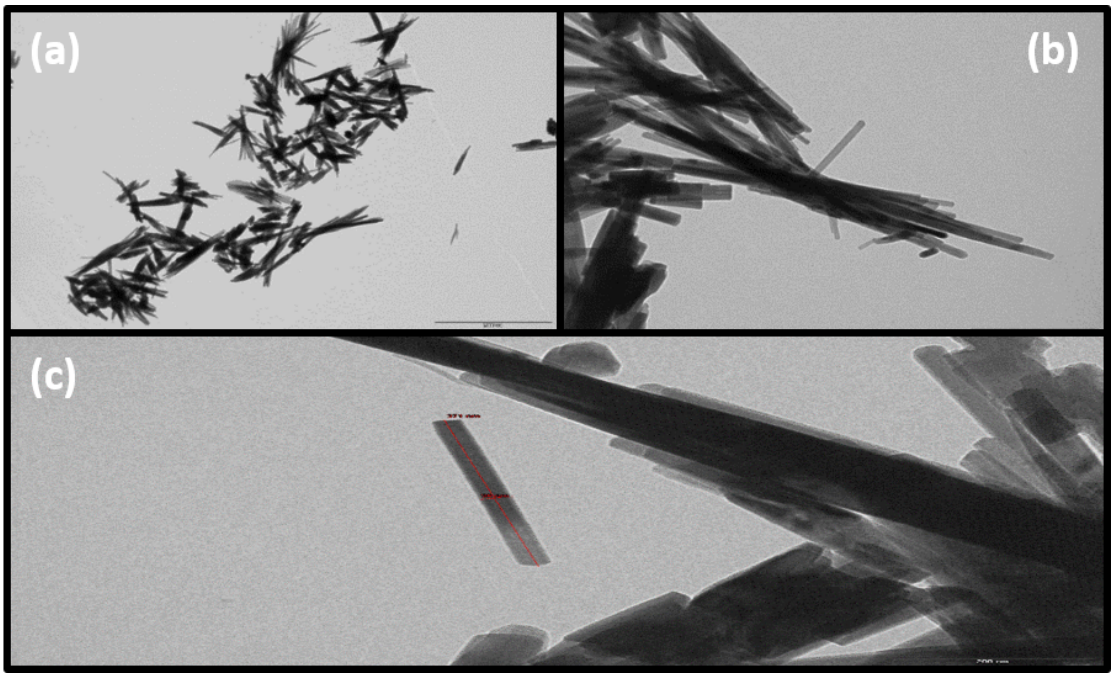


FIGURE 4.1: TEM images of nano HA rods taken at 200 kV, spot size 1 mm (a) and (b) show nano HA rods agglomerated. The scale bar in Figure (a) represent 2000 nm. In Figure (b), a single nano HA rod protruding from the fringes of the agglomerate. Scale bar represents 500 nm. In Figure (c), a single rod visible and sized using TEM software length 371 nm and width 35 nm. Scale bar represents 200 nm.

4.2 Particle Sizing

The size distribution curve for coated PA12 and PLA powders was obtained from the mastersizer 3000, as detailed in Chapter 3. The results are given in the following section.

4.2.0.1 Particle sizing - PA12-nHA powders

As can be seen in Table 4.1, the addition of nHA and MWCNT-nHA had no significant ($P>0.05$, as detailed in Chapter 3) impact on the overall size of the powder particles following coating, as expected. The narrow size distribution of the as-received PA12 was maintained for PA4H and PA05M5H powders, and falling within the reported optimum particle size range for laser sintering powders [41]. This was also reflected in the size distribution curve, as seen in Figure 4.2.

TABLE 4.1: Table showing the particle size distribution of PA12 powders coated with nHA and MWCNT-nHA. Reported as standard error.

Material	Dx(10)	Dx(50)	Dx(90)
PA0	34.9 $\pm$1.8 μm	53.7 $\pm$3.3 μm	82.3 $\pm$2.6 μm
PA4H	35.4 $\pm$1.1 μm	54.7 $\pm$1.5 μm	84.24 $\pm$2.4 μm
PA05M5H	34.2 $\pm$1.7 μm	54.1 $\pm$4.6 μm	83.3 $\pm$5.3 μm

The limited impact that NP coating had on the PA12 powder was also reflected in the size distribution curve. As seen in Figure 4.2, the size distribution curves for each powder composition overlaps one another, indicating no significant affect on the overall size distribution of the powders. As the PA4H and PA05M5H powders did not significantly alter the overall particle size, the: PA05H, PA1H, PA1.5H, PA2H and PA05M2H powders were excluded from further analysis.

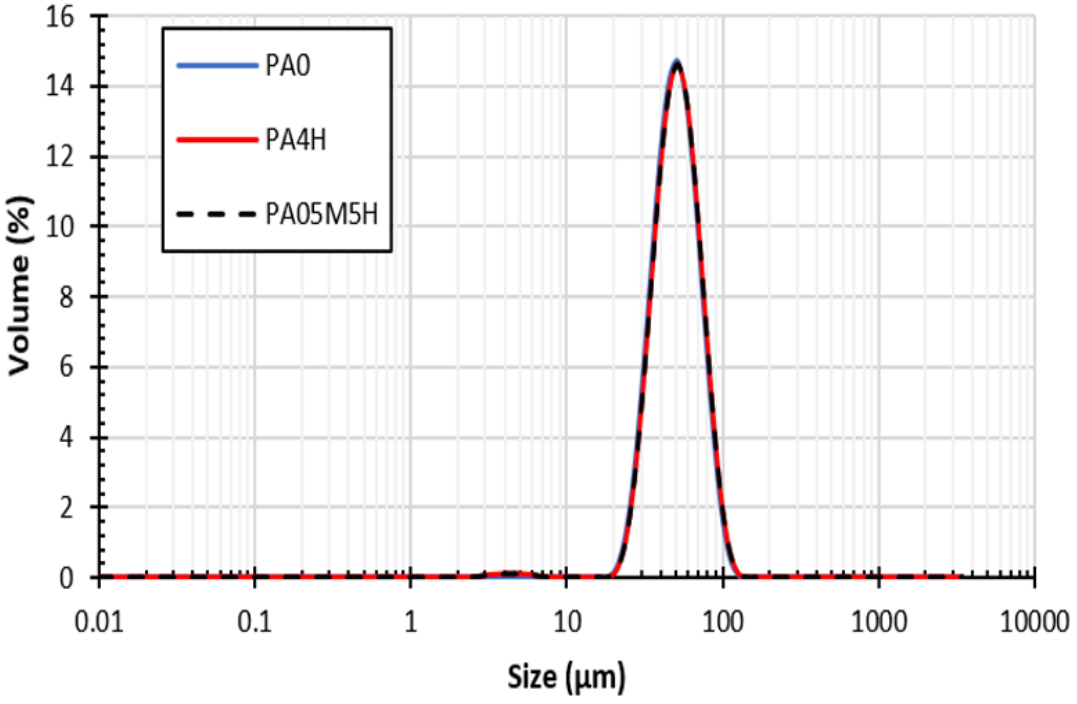


FIGURE 4.2: Particle size distribution curves of PA0, PA4H, PA05M5H. The addition of NPs caused no significant change to to the overall particle size distribution. Reported as standard error n = 10.

TABLE 4.2: Table showing the particle size distribution of PLA powders coated with nHA MWCNT and MWCNT-nHA. Reported as standard error

Material	Dx(10)	Dx(50)	Dx(90)
PL0	62.3 $\pm$1.8 μm	145.1 $\pm$1.3 μm	336.3 $\pm$2.0 μm
PL0 (150 μm sieve)	59.7 $\pm$0.6 μm	107.4 $\pm$0.3 μm	182.8 $\pm$1.4 μm
PL1M	61.5 $\pm$3.4 μm	147.1 $\pm$2.5 μm	339.6 $\pm$2.5 μm
PL1M5H	56.8 $\pm$1.3 μm	135.1 $\pm$1.5 μm	308.3 $\pm$1.2 μm

4.2.0.2 Particle sizing - PLA-MWCNT-nHA powders

As can be seen in Table 4.2, the as-recieved PL0 powder recorded a relatively wide particle size distribution. The PL0 powders were passed through a 150 μm sieved to reduce the particle size to a range more suitable for laser sintering. After sieving, the size distribution narrows significantly, indicated by a significant reduction in Dx(10), Dx(50) and Dx(90) values, as show in Table 4.2. However, this was still higher than the reported optimum range [41] but significantly lower than the, as received, PL0 powder. Despite a reduction in particle size it was noted that passing the as-received PL0 powder though the 150 μm sieve was time consuming and resulted in a low yield of usable powder. Furthermore, the poorer flow properties that the sieved PL0 exhibited, which will be discussed further in section 4.4, led to the decision to coat the as received PL0 powder as opposed to sieving it through a 150 μm sieve prior to coating. The particle size distribution of the PL1M and PL1M5H powders remained relatively similar to the distribution of as-received PL0 powder as they were within the error of measurement. Although the PL1M5H displayed a slightly lower distribution, there was no statistical difference between them. Therefore, similar to the PA12, the coating process conducted on PLA powders also had no significant effect on the overall particle size distribution of the powders.

As seen in Figure 4.3, the distribution curves for as-received PL0, PL1M and PL1M5H powders was relatively wide and remained similar after NP coating with a Dx(50) of 145.1 $\pm$1.3 μm, 147.1 $\pm$2.5 μm and 135.1 $\pm$1.5 μm respectively. Directly overlapping curves can be seen for each of these powder compositions. The distribution curve for the sieved PL0 powder can be seen to significantly narrow from 145.1 $\pm$1.3 μm to 107.4 $\pm$0.3 μm at Dx(50).

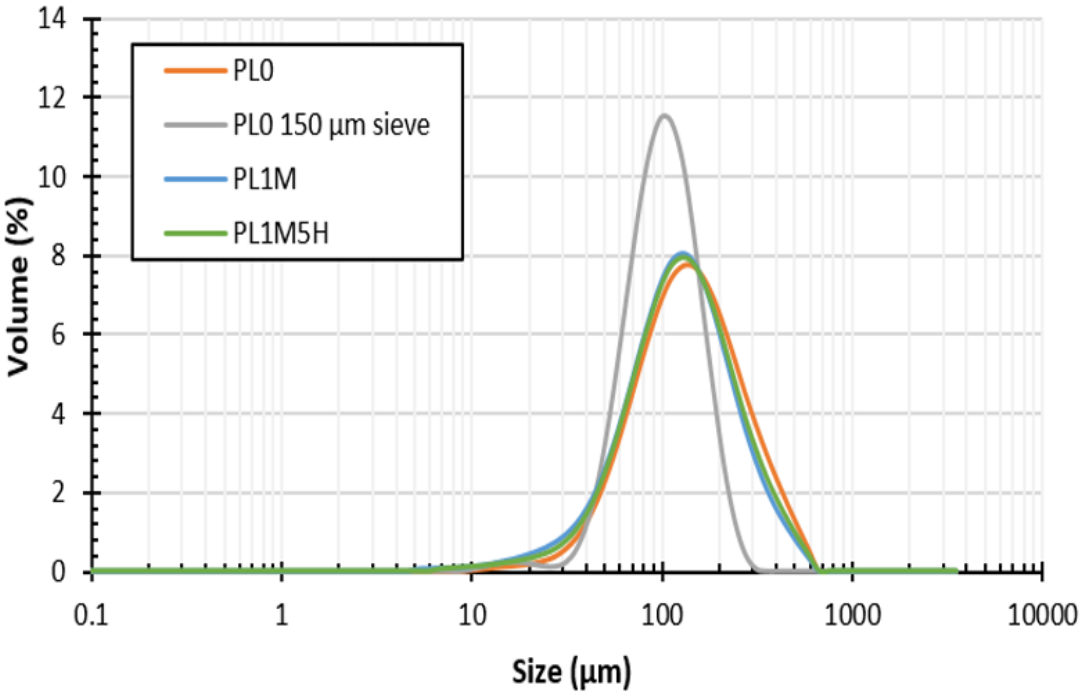


FIGURE 4.3: Particle size distribution curves of as received PL0, PL0 passed through a 150 μm sieve, PL1M and PL1M5H powders, n = 10.

4.3 Powder morphology and surface coverage

4.3.0.1 Powder Morphology and Surface Coverage - PA12-nHA and PA12-MWCNT-nHA powders

The PA0 particles had a near-spherical morphology which can be seen in Figure 4.4 (a). After coating with nHA, this near-spherical morphology was maintained with no noticeable alteration to the particle size and shape when compared to the original, as shown in Figure 4.4(b).

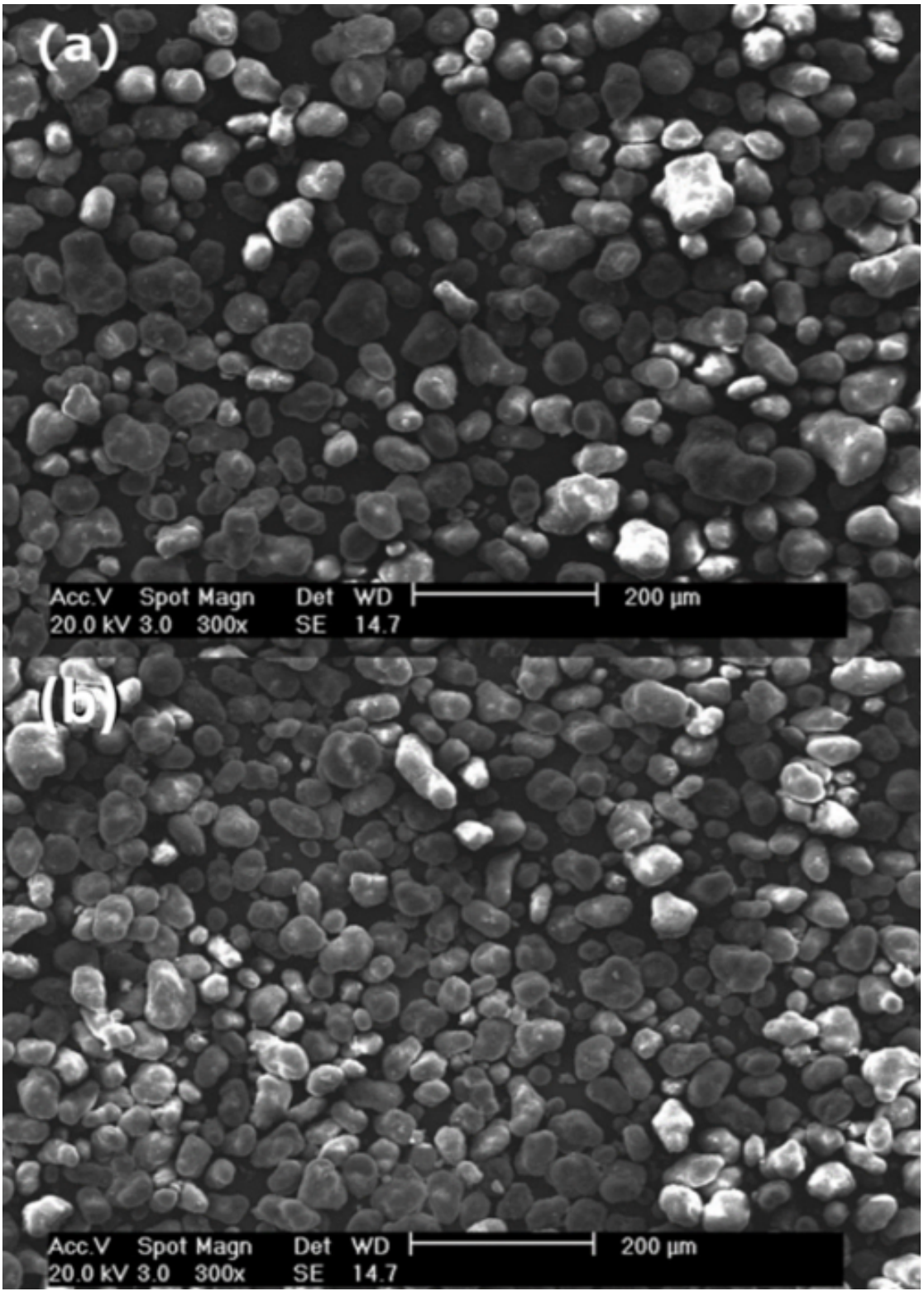


FIGURE 4.4: SEM images of (a) PA0 powder particles and (b) PA4H powder particles at low magnification (x300).

The coating method also provided a high degree of coverage of well-dispersed nHA on the surface of the particles (Figure 4.5). Furthermore, the level of particle coverage

could be significantly increased with a higher nHA loading as shown in Figure 4.5(a), (b), (c) and (d), which are of magnified SEM images of the PA0, PA1H, PA4H and PA10H powders respectively.

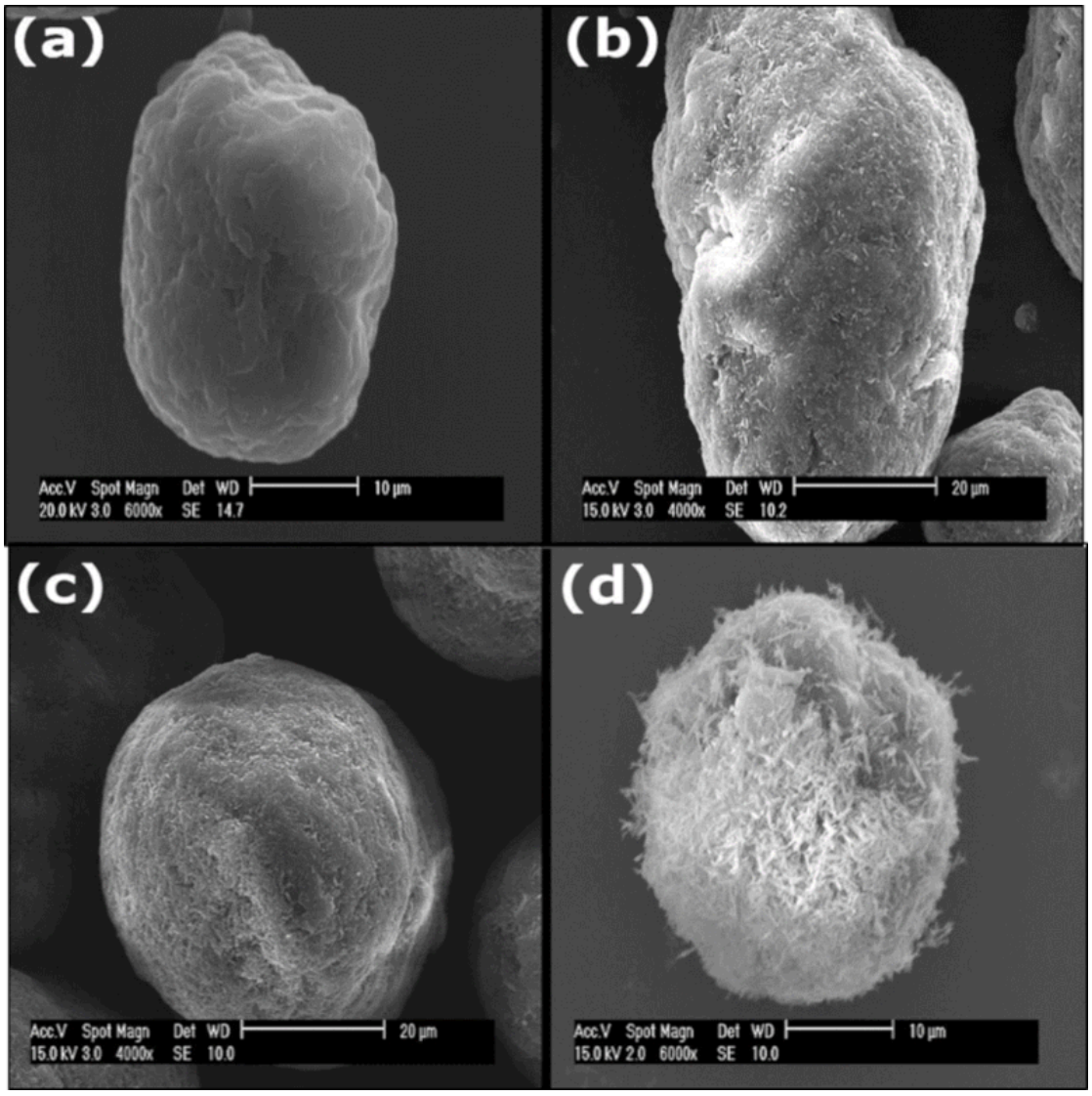


FIGURE 4.5: Magnified SEM images of individual (a) PA0, (b) PA1H (c) PA4H and (d) PA10H particles. The white strands seen on the surface of the particles is nHA. Note the increased surface coverage as the nHA loading is increased.

The Sintratec utilises a laser diode in the visible light spectrum. To enable the powders to absorb the laser they needed to be dark in colour. Therefore MWCNTs, in addition to nHA, were also applied to PA12 using the same coating procedure, as seen in Figure 4.6. The application of two different types of NPs yielded similar results to the PA12-nHA system, with a high degree of surface coverage on the particle.

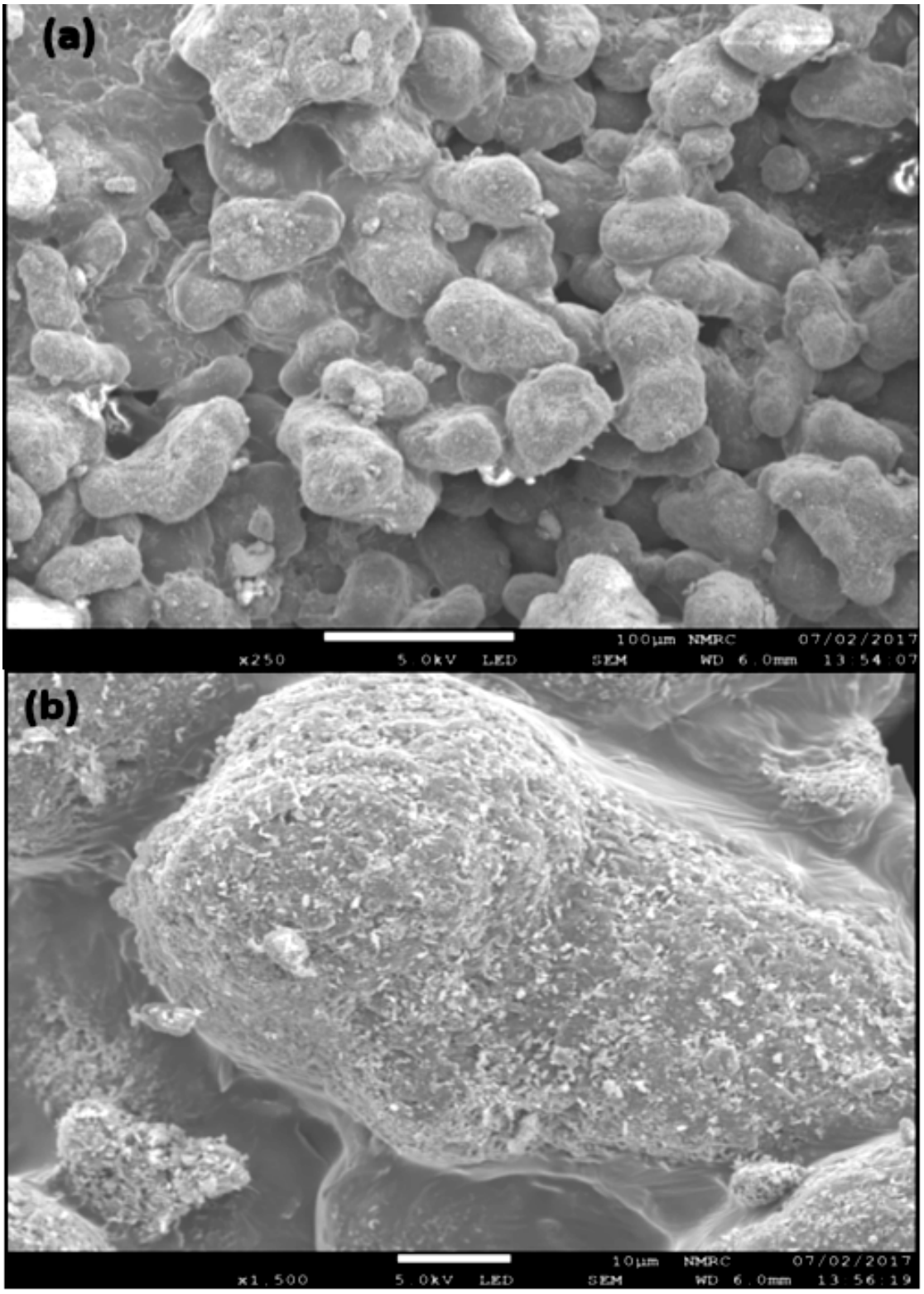


FIGURE 4.6: (a) SEM image of a PA05M5H particles and (b) magnified image of a single PA05M5H particle. A high degree of surface coverage has been achieved using two different NPs. Note that the particles in these images appear more "fused" due to excessive carbon dag used to adhere the particles onto the SEM stub.

Observations made on the PA12-nHA powder at higher magnifications, as seen in Figure 4.7, revealed that the nHA attached lying in various orientations to the surface, some with the flatter surfaces of the NP perpendicular whilst others are flatter or end on to the surface of the PA12 particle. A relatively small loading of 1 wt% nHA showed an even distribution of nHA with a relatively low degree of agglomerates on the surface, indicating that the coating method was able to disperse the nHA particles.

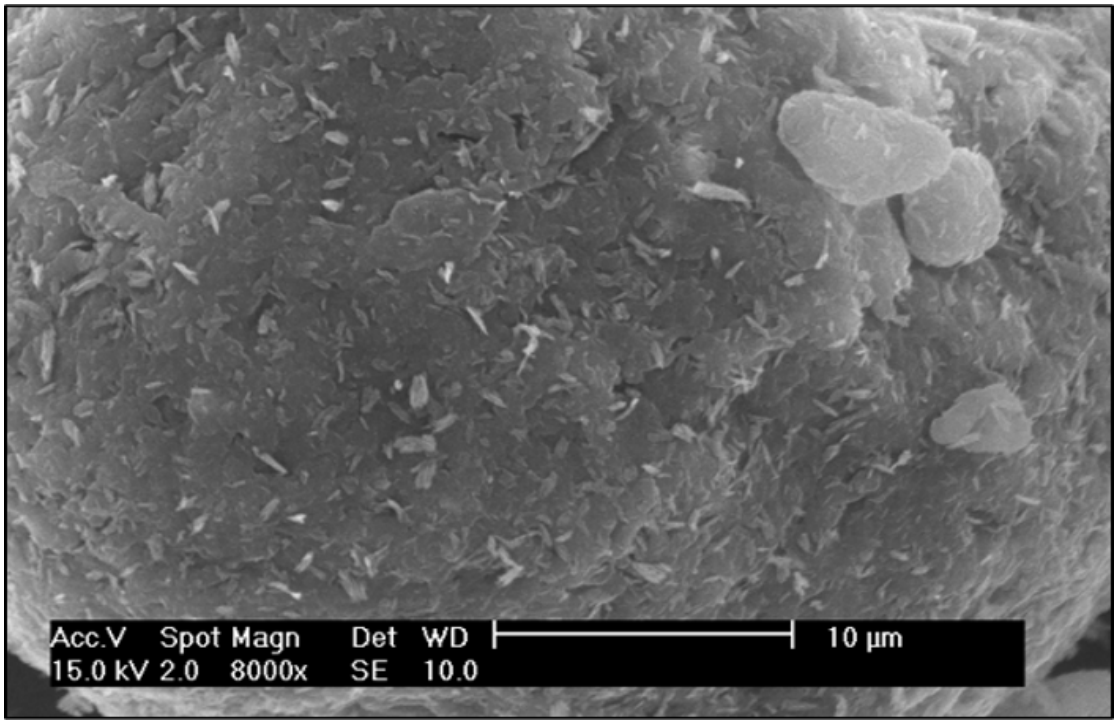


FIGURE 4.7: SEM image taken at x8000 magnification of a PA1H particle showing good surface coverage of nHA with a relatively low degree of agglomerates.

The PA05M powder, as seen in Figure 4.8, also showed a good dispersion of MWCNT on the surface of PA12 which often conformed to the surface undulations.

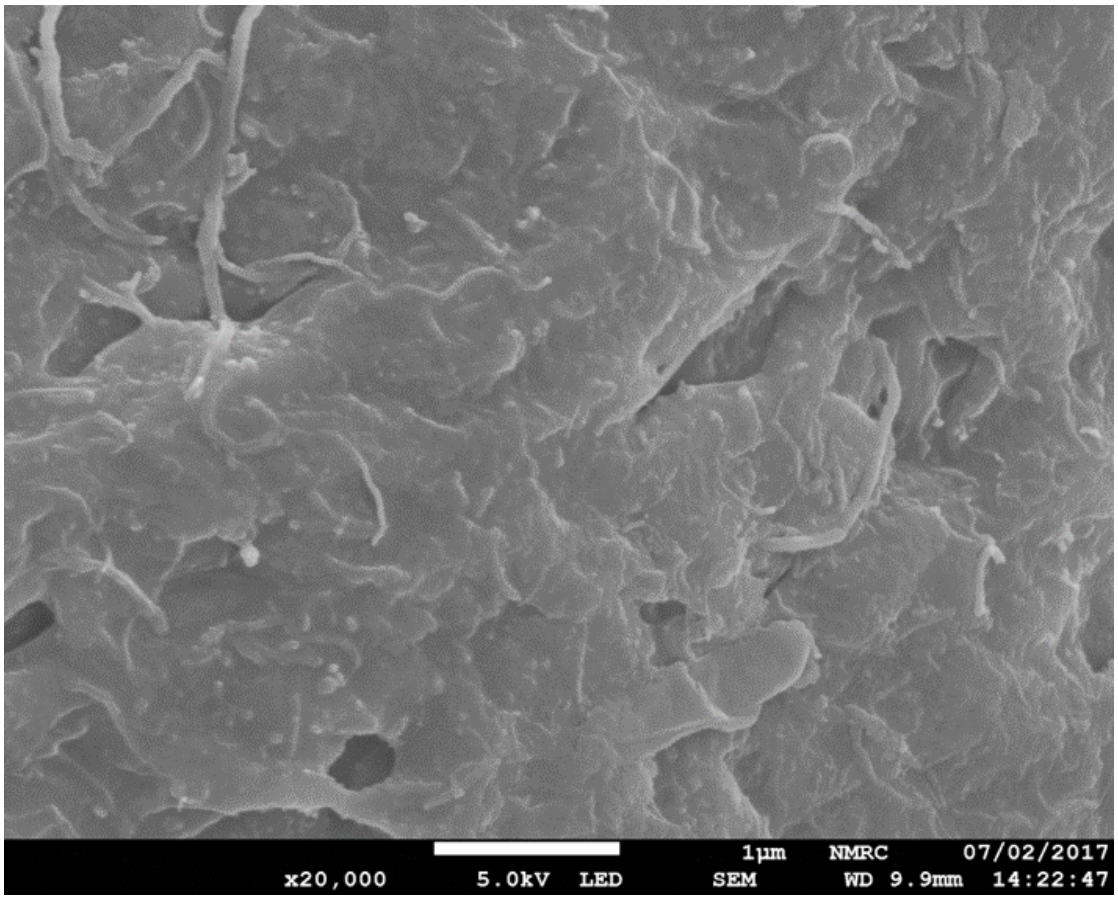


FIGURE 4.8: Magnified SEM image, taken at x20000 of the surface of a PA05M particle. Individual MWCNT strands can be seen attached to the surface.

Due to their surface area to volume ratio, NPs have a high tendency to form agglomerates. Upon increasing the NP loading to 2 wt%, the surface coverage by nHA increased significantly, however, more visible signs of nHA agglomerates can be seen, as shown in Figure 4.9 (a). Similarly, in Figure 4.9 (b), the addition of 0.5% MWCNT and 5% nHA also led to the formation of agglomerates ($<$500 nm in size) indicating that increased NP loading made it significantly more difficult to disperse the particles effectively.

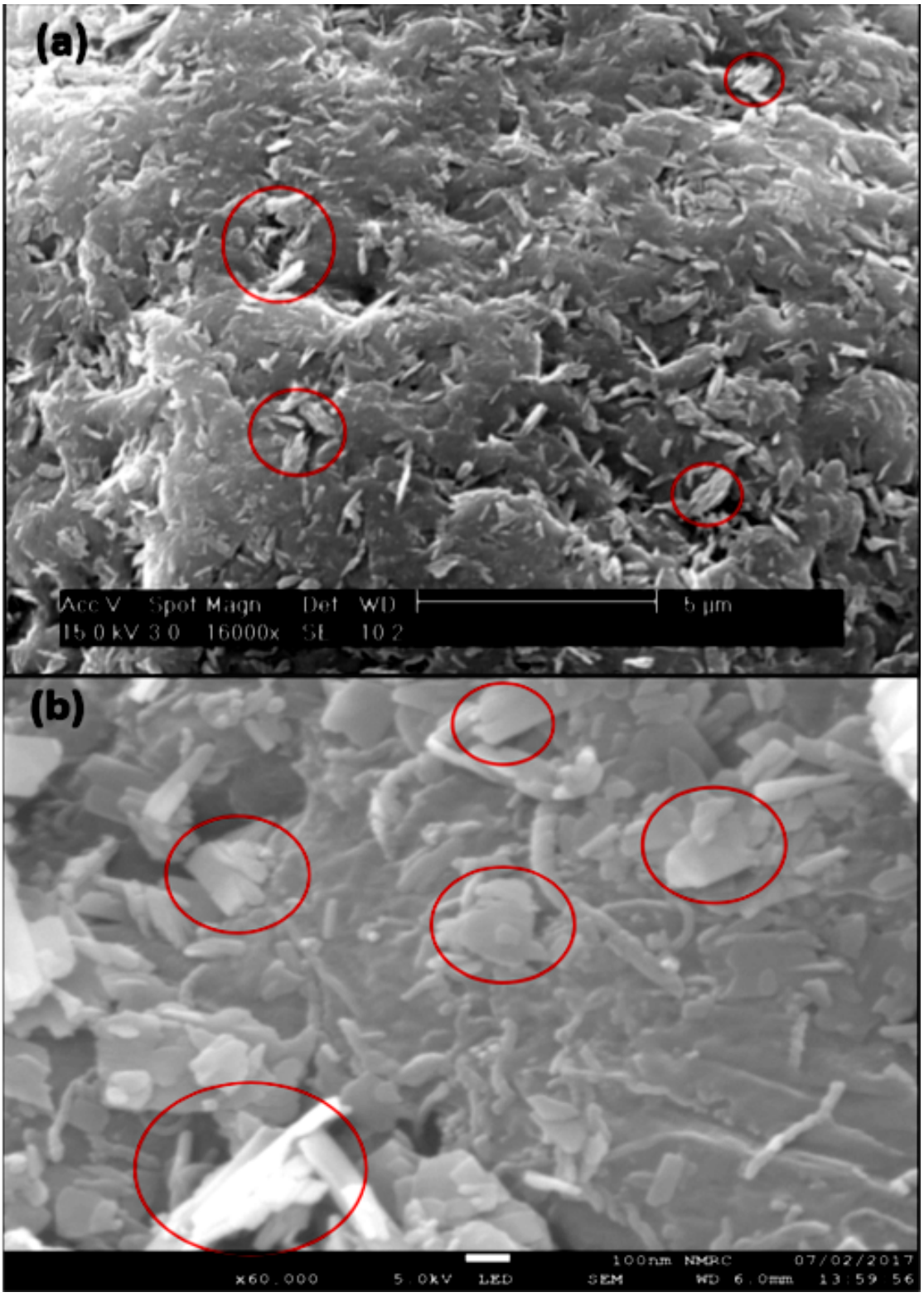


FIGURE 4.9: SEM image of the surface of (a) PA2H taken at x16000 and (b) PA05M5H taken at x60000. The particle surface shows clear signs of agglomerated nHA, as highlighted by the circles, with resemblance to platelet-like structures.

4.3.0.2 Powder Morphology and Surface Coverage - PLA-MWCNT-nHA powders

The as-received PLA powder was prepared via a cryogenic milling process, carried out by A. Schulman, Inc. The neat PL0 powder possessed a wide range of particle sizes with irregular morphologies. The large angular particles were interspersed with smaller flattened particles, this can be seen in Figure 4.10. The surface texture of the PLA particles also appeared rough, with jagged outcrops, in comparison to the smoother, near-spherical, PA12 powders and this is likely due to fracturing of the bulk PLA material through the cryogenic milling process.

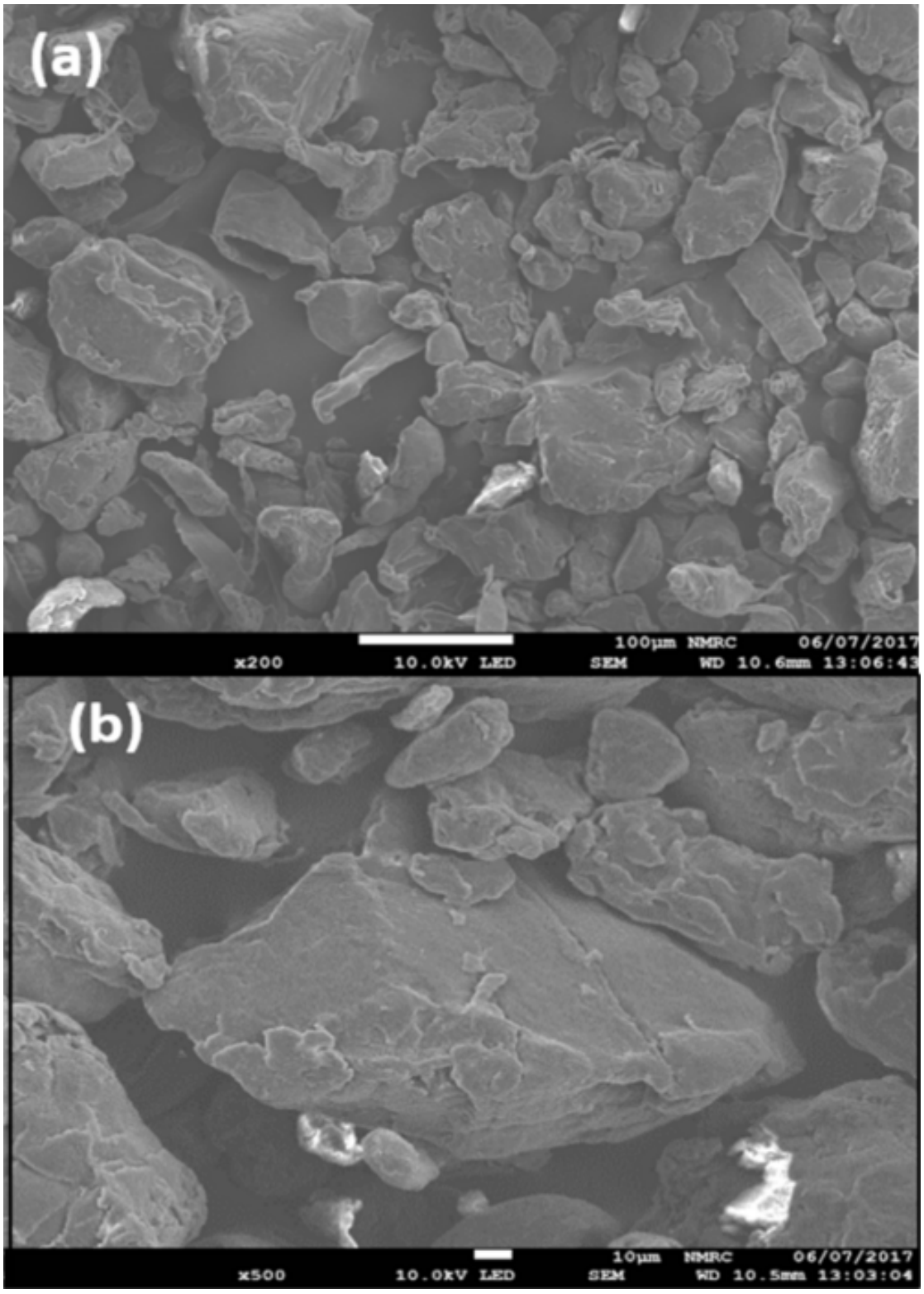


FIGURE 4.10: SEM images of as received PL0 powder taken at (a) x200 and (b) x500. The cryogenically milled powder has an angular morphology with a wide range of particle sizes. The smaller particles appear to possess a more flattened morphology

The same coating method already adopted for the PA12 powders was also used to coat the PLA. Due to the larger size of the PLA particles, a higher loading of 1 wt% MWCNT was required to sufficiently absorb enough of the laser energy to melt the PLA. Furthermore, based on laser sintering experience with coated PA12, it was decided that a relatively high loading of 5 wt% nHA was to be used in an effort to maximise the osteogenic response to the material. At 1 wt% loading of MWCNT, the coating procedure, once again, provided a high degree of surface coverage with most of the surface occupied by MWCNT and with very few agglomerated particles visible, as seen in Figure 4.11 (a) and (b). Once again, the MWCNT adopted a flattened configuration lying horizontally across the particle surface.

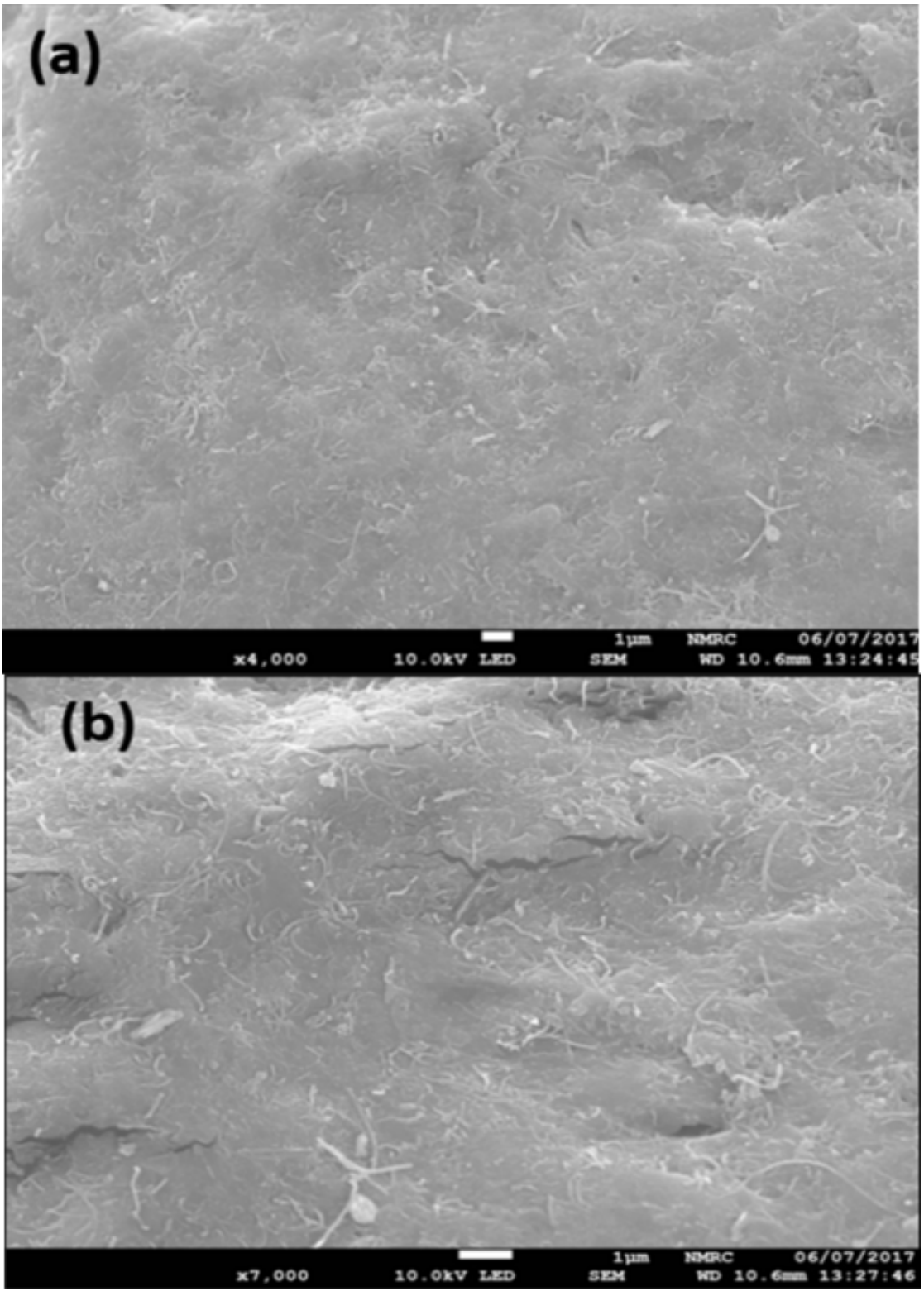


FIGURE 4.11: SEM images of PL1M particle surface taken at (a) x4000 and (b) x7000. White strands on the surface are MWCNTs, a good surface coating was achieved with very few particle agglomerates being visible.

However, the addition of 1 wt% MWCNT and 5 wt% nHA did lead to visible signs of

larger, agglomerated nHA on the surface of the PLA particles, which can be seen in Figure 4.12. Images taken at higher magnification (Figure 4.12 (b)) showed a mixture of nHA interwoven with MWCNT; the nHA in this case appeared to have adopted a platelet-like morphology as opposed to discrete clumps on the surface. Using the in-built measuring tool on the FEG-SEM, an example of a nHA "platelet" was measured and the X, Y and diameter were recorded as 382, 494 and 624 nm respectively; this can be seen in Figure 4.13.

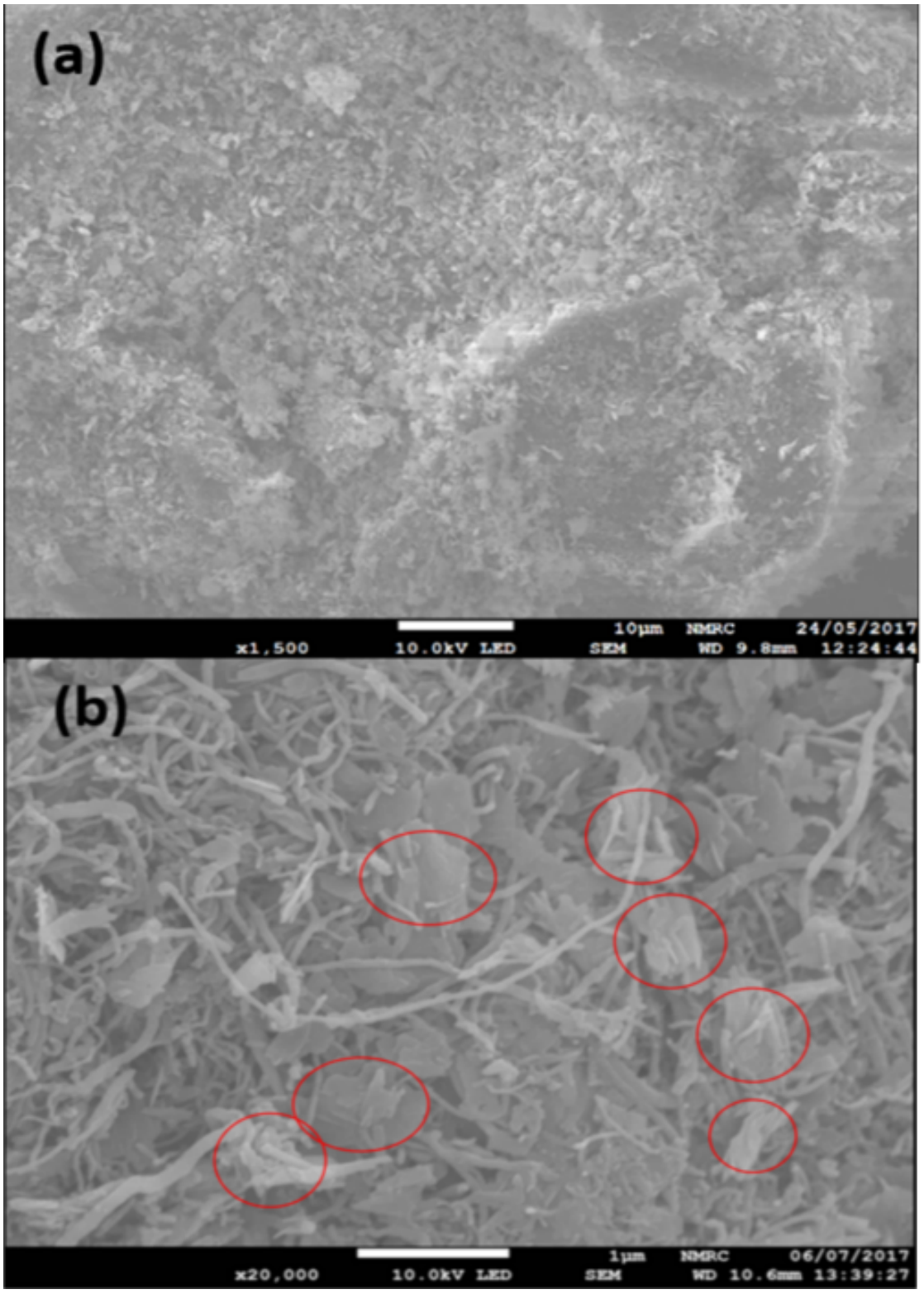


FIGURE 4.12: SEM images of a PL1M5H particle surface taken at (a) x1500 and (b) x20000. A high degree of surface coverage was achieved, however, nHA appears agglomerated on the surface.

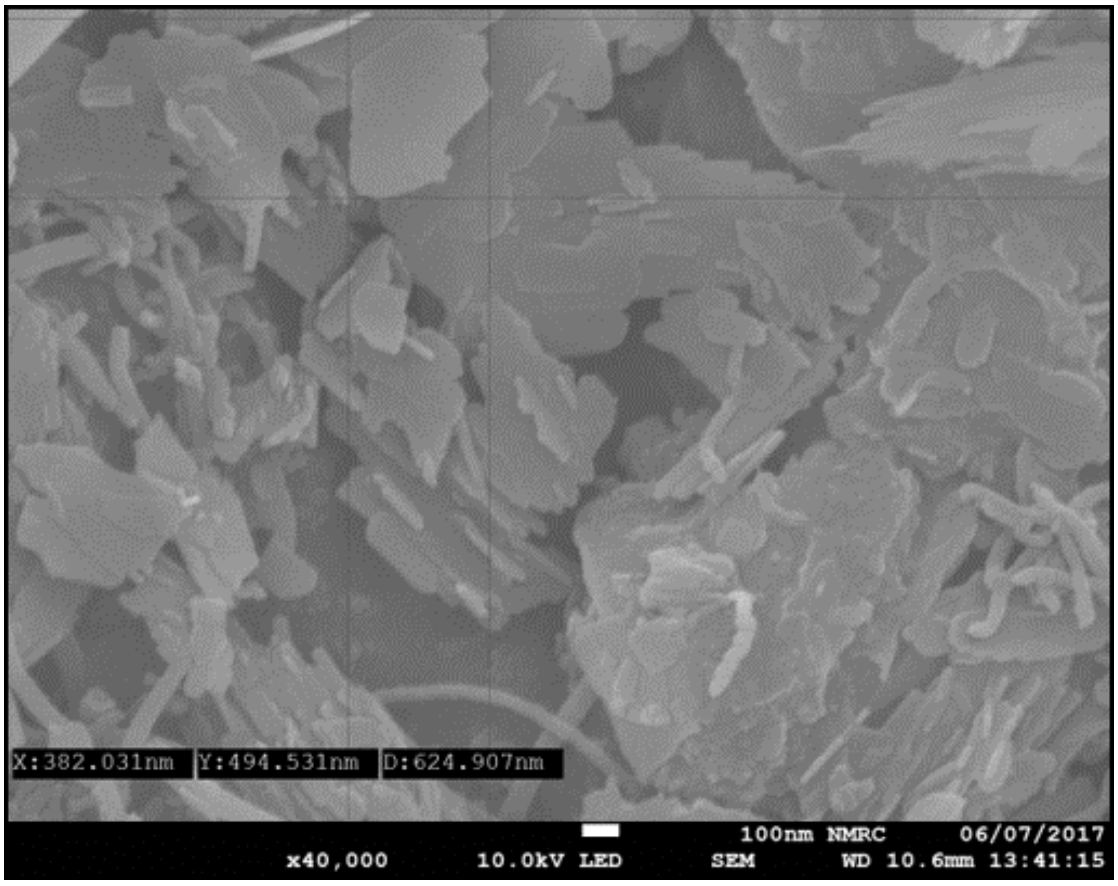


FIGURE 4.13: High magnification SEM image of the surface of a PL1M5H particle, with clear signs of nHA agglomerates.

4.4 Powder Flowability and Powder Bulk Properties

The ability to achieve a smooth and consistent, well deposited, well packed, powder bed can impact upon the surface finish and mechanical properties of laser sintered parts. Therefore powder flowability is an important aspect for consideration in the development of powders. The following section details the results of the powder flowability tests conducted on coated PA12 and PLA powders.

4.4.1 Specific Energy - PA12-nHA and PA12-MWCNT-nHA Powders

For the PA12 powders, the addition of nHA caused the unconfined low stress flow behaviour (denoted as specific energy or SE) to decrease as nHA content was increased. This can be seen in Figure 4.14, suggesting that the presence of nHA had a lubricating affect and reduced the inter-particle friction forces. The PA2H powder recorded an average SE of 5.6 $\pm$ 0.2 mJ g^{-1}, a decrease of 19% compared to the PA0 powder which recorded a SE of 6.9 $\pm$ 0.4 mJ g^{-1}. A higher loading of nHA leads to further reduction in the specific energy with PA4H recording an average of 5.1 $\pm$ 0.3 mJ g^{-1}, a 27% decrease compared to PA0. The addition of nHA caused a reduction in the cohesive nature of the powder.

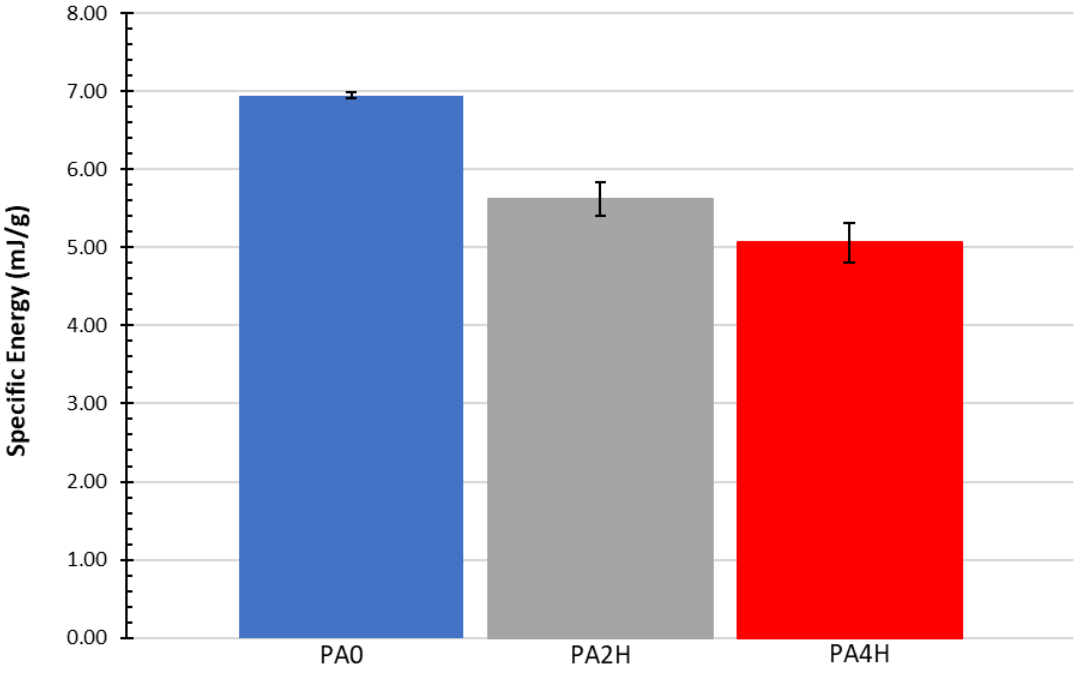


FIGURE 4.14: Chart showing the specific energy recorded on FT4 under the stability and variable flow rate programme for PA0, PA2H and PA4H powders. The error bars represent standard error, n = 3.

4.4.2 Specific Energy - PLA-MWCNT-nHA powders

Due to the larger size and irregular morphology, the PLA powders on the whole recorded a significantly higher average SE compared to the PA12 powders, this can be seen in Figure 4.15. In this case, the as-received powder (asPL0) recorded the second highest average SE at 7.1 $\pm$ 0.1 mJ g^{-1}. The reduction of larger particles through sieving lead to a dramatic increase in SE for the PL0 150μm powder to 7.2 $\pm$ 0.1 mJ g^{-1}, representing a 1.4% increase in SE compared to the asPL0. This is likely caused by the increasing degree of irregular particles with a flattened morphology. This smaller, irregular morphology contributed to higher surface area and thus increased mechanical interlock and inter-particle friction requiring more energy to induce powder flow. The presence of 1 wt% MWCNT provided a lubricating effect with the PL1M powders recording a drop in SE to 6.7 $\pm$ 0.1 mJ g^{-1}. The addition of MWCNT and 5 wt% nHA led to an even greater lubricating effect with the PL1M5H powder recording a SE of 6.1 $\pm$ 0.1 mJ g^{-1}, a decrease of 13% compared to the asPL0 powder.

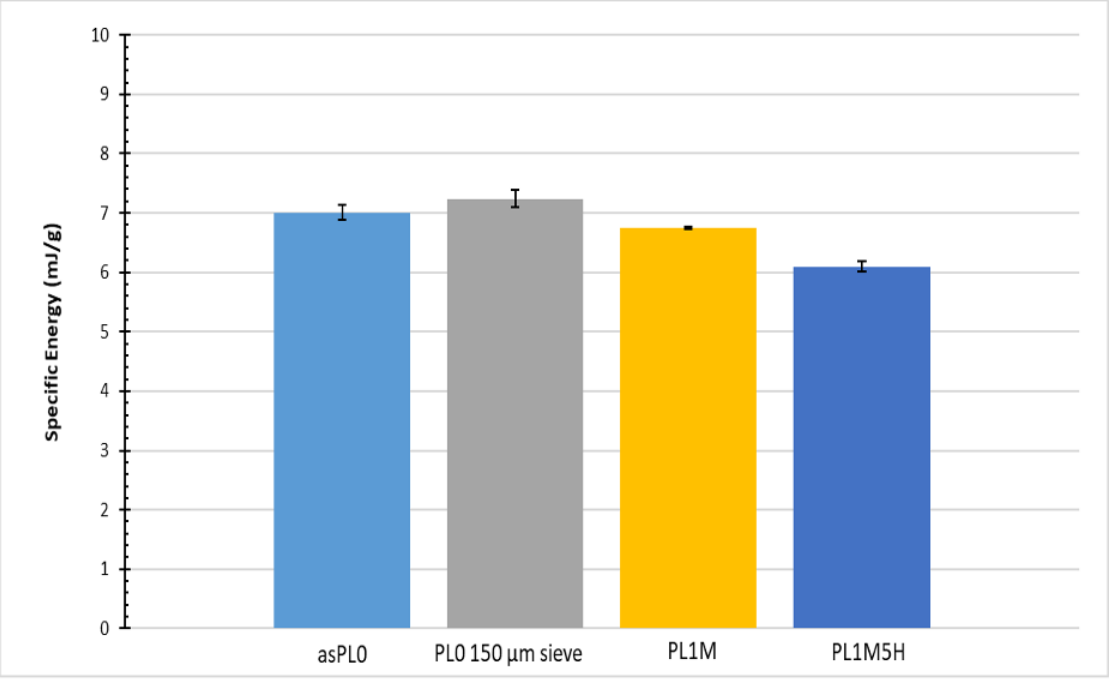


FIGURE 4.15: Chart showing the specific energy recorded on FT4 under the stability and variable flow rate programme for asPL0, PL0 sieved, PL1M and PL1M5H powders. The error bars represent standard error, n = 3. The irregular morphology of PLA powders contributed to a relatively high SE, this increased as the powders were passed through a sieve. The addition of MWCNT and nHA led to improved flow performance of the powders in a low stress, unconfined testing regime.

4.4.3 Aeration - PA12-nHA Powders

As the spaces between powder particles, in a powder bulk, is occupied by air, how the powders interact with air also affects the ability of powders to flow. This is important for gravitational fed process such as powder spreading [281]. As the air flow increased the total energy required to induce powder flow decreased as the particles became more fluidised, this is summarised in Table 4.3. The PA0 powder remains at a higher energy state compared to PA2H and PA4H powders at air velocities from 0-1 mm s^{-1}, in addition to having the lowest AR. The addition of nHA led to increased sensitivity to the presence of air and therefore a less cohesive powder.

TABLE 4.3: Table showing the aerated energy at various air velocities and the aeration ratio for coated PA12 powders. Reported as standard error

	Material Aerated Energy (mJ g^{-1})		
Air Velocity (mm s^{-1})	PA0	PA2H	PA4H
0	135 ±6	87 ±7	86 ±4
0.2	120 ±8	76 ±4	69 ±2
0.4	100 ±7	59 ±2	57 ±1
0.6	86 ±4	47 ±2	42 ±1
0.8	71 ±5	37 ±4	36 ±1
1.0	57 ±4	25 ±4	27 ±1
Aeration Ratio	2.4	3.4	3.1

The recorded total energy or aerated energy (AE) was reported as; 135 ± 6 mJ g^{-1} at 0 mm s^{-1} and 57 ± 4 mJ g^{-1} at 1 mm s^{-1}. The aeration ratio (AR) for the PA0 was also the lowest at 2.4. The addition of 2 wt% nHA reduced the total energy needed to establish flow. The average AE at 0 mm s^{-1} for the PA2H powder was recorded at 87.2 ± 7.1 mJ g^{-1} and at 1 mm s^{-1} the total energy had decreased to 25 ± 4 mJ g^{-1}. The AR value was also slightly higher at 3.43, indicating a higher sensitivity to air flow compared to the PA0 powder. The presence of 4 wt% nHA had a similar energy reading to PA2H powders with an average AE of 86 ± 3 mJ g^{-1} at 0 mm s^{-1} and 27 ± 1 mJ g^{-1} at 1 mm s^{-1}.

In Figure 4.16, the aeration graph shows a significant ($P<0.05$) reduction in the overall aerated energy with PA2H and PA4H showing similar characteristics when compared to the PA12 powders.

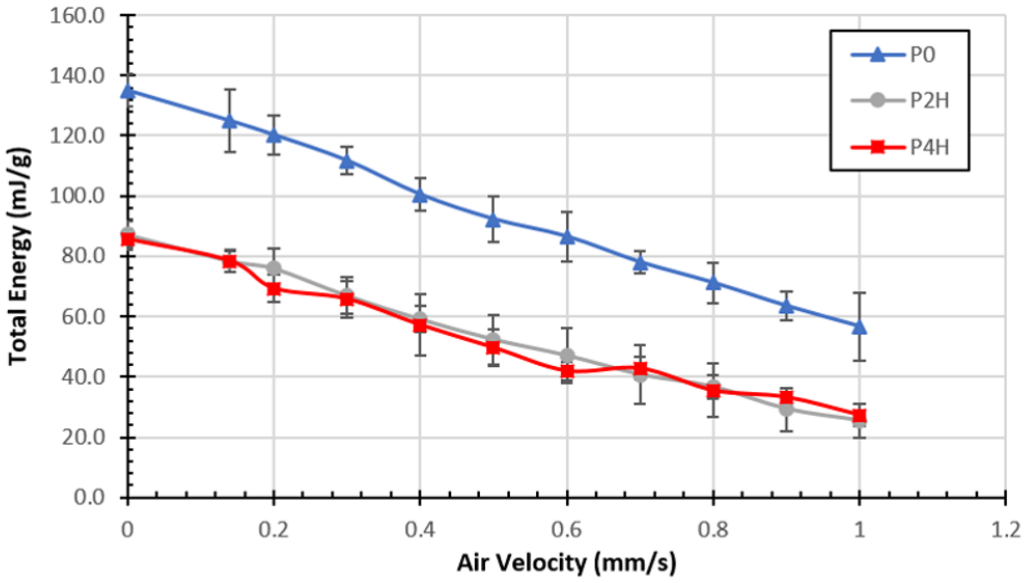


FIGURE 4.16: Aeration test for PA0, PA2H and PA4H powders at air velocity from 0–1 mm s^{-1}. The sensitivity to aeration increases with higher loading of nHA. n = 3, error bars represent standard error.

4.4.4 Aeration - PLA-MWCNT-nHA powders

The cohesivity of the PLA powders was also reflected in the aeration test, as seen in Figure 4.17 (b). The irregular shape and morphology creates a more turbulent flow of air around the particles thus making the powders very sensitive to aeration which is indicated by the steep reduction in total energy as the air velocity increased from 0 to 2 mm s^{-1}. The results are summarised in Table 4.4 and Figure 4.17. The sieved powder, PL0 150 μm, recorded the highest average AE of all the powders, across the air velocity range tested in addition to recording the lowest sensitivity to aeration with the lowest AR value, this indicated that sieving the powder led to a powder which was more cohesive in nature. The addition of MWCNT and MWCNT-nHA led to a higher sensitivity to aeration, when compared to the as-received PL0 powder, however there was no difference between PL1M and PL1M5H.

TABLE 4.4: Table showing the aerated energy at various air velocities and the aeration ratio for coated PLA powders. Reported as standard error.

	Material Aerated Energy (mJ g^{-1})			
Air Velocity (mm s^{-1})	asPL0	PL0 (150 μm sieve)	PL1M	PL1M5H
0	529 ±3	569 ±3	515 ±15	510 ±20
0.3	416 ±3	498 ±4	376 ±14	384 ±14
0.6	333 ±10	441 ±6	287 ±12	280 ±1
0.9	267 ±4	373 ±12	216 ±6	193 ±6
1.2	206 ±6	330 ±5	147 ±1	126 ±3
2.0	89 ±2	245 ±4	40 ±3	56 ±3
Aeration Ratio	5.9	2.3	12.8	9.1

In Figure 4.17, the aeration graph shows a steep decline in aerated energy as air velocity increased, for PL1M and PL1M5H powders, indicative of a higher sensitivity to the presence of air and thus a less cohesive powder when compared to as-received PL0 and sieved powders. Passing the powders through a sieve made the powder more cohesive.

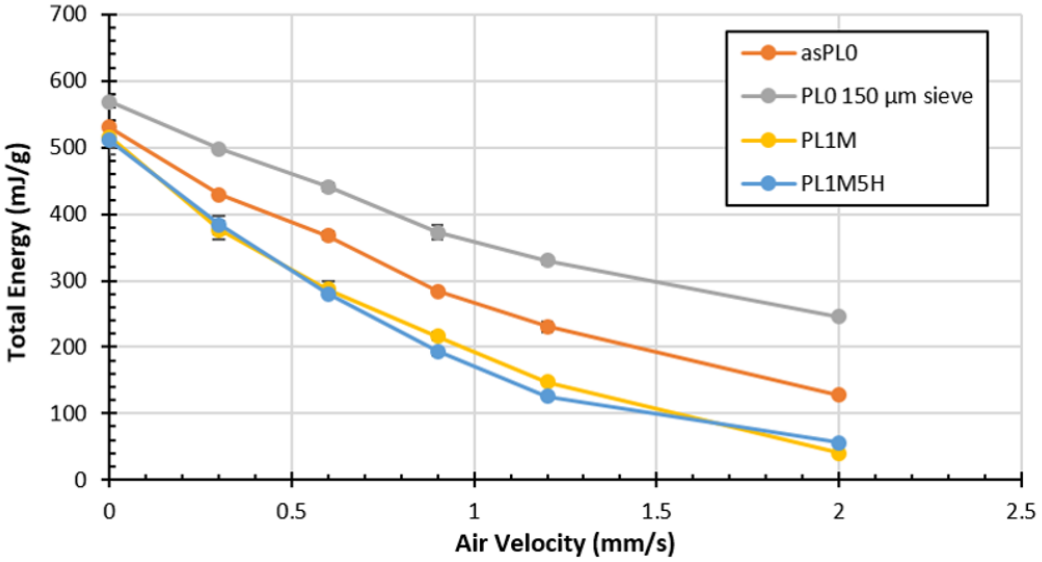


FIGURE 4.17: Aeration test for as-received and coated PLA powders at air velocity from 0–2 mm s^{-1}. n = 3, error bars represent standard error.

4.4.5 Permeability - PA12-nHA powders

The permeability test programme measured the ability of powders to transmit air through its bulk. The PA0 powder exhibited a significantly higher permeability across

the powder bed compared to PA2H and PA4H powders and the results of this can be seen in Figure 4.18. For all powders, the variation in applied stress had little effect on the ability of air to transmit through the powder bulk. For the case of PA0 powders the more cohesive nature led to a larger degree of entrained air within the sample that was forced out of the bulk when load was applied. The addition of 2 and 4 wt% nHA had a similar effect and significantly decreased the amount of entrained air with the sample bulk which was reflected in the low permeability as the more efficient packing state reduced the number of air channels through the powder bulk. The permeability decreased by as much as 20% compared to PA0 powders. These results suggest that the inclusion of nHA improves the ability of the powders to self-assemble more efficiently leading to a higher packing density during powder spreading.

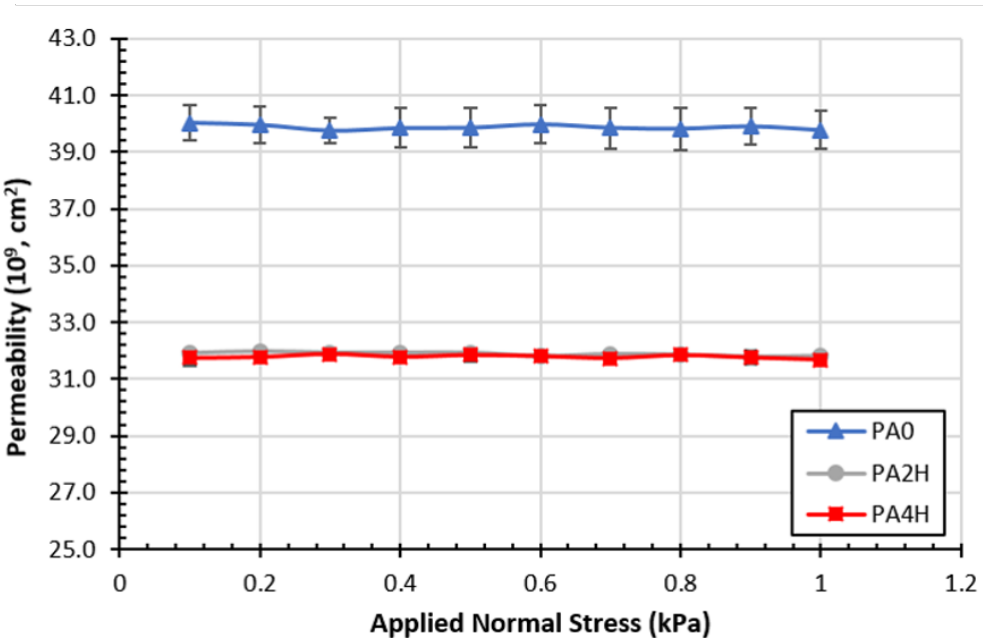


FIGURE 4.18: The permeability test for neat and nHA coated PA12 powder. The increasing addition of nHA a led to a reduction in the permeability of the bulk powder thus indicative of a more efficiently packed powder bulk. Error bars represent standard error n = 3.

4.4.6 Permeability - PLA-MWCNT-nHA powders

In the case of PLA, the permeability test (Figure 4.19) showed that the smaller particle size fraction resulted in a decreasing trend in powder permeability. At 1 kPa, applied normal stress, the asPL0 powder recorded a permeability of 96.7 $\pm$ 0.7 10^9, cm^2. The

PL0 150 μm powder recorded the highest permeability of all the PLA powders tested with a permeability of 97.6 $\pm$ 0.7 10^9, cm^2. Upon the addition of 1 wt% MWCNT, a significant 7% reduction in permeability was recorded at a value of 90.1 $\pm$0.8 10^9, cm^2. Furthermore, the PL1M5H powder also showed a similar to 90.5 $\pm$ 0.7 10^9, cm^2. The decline in permeability for the PL1M and PL1M5H powders indicates that the presence of NPs allowed the powders to pack more efficiently and subsequently there was less air entrained within the powder bulk.

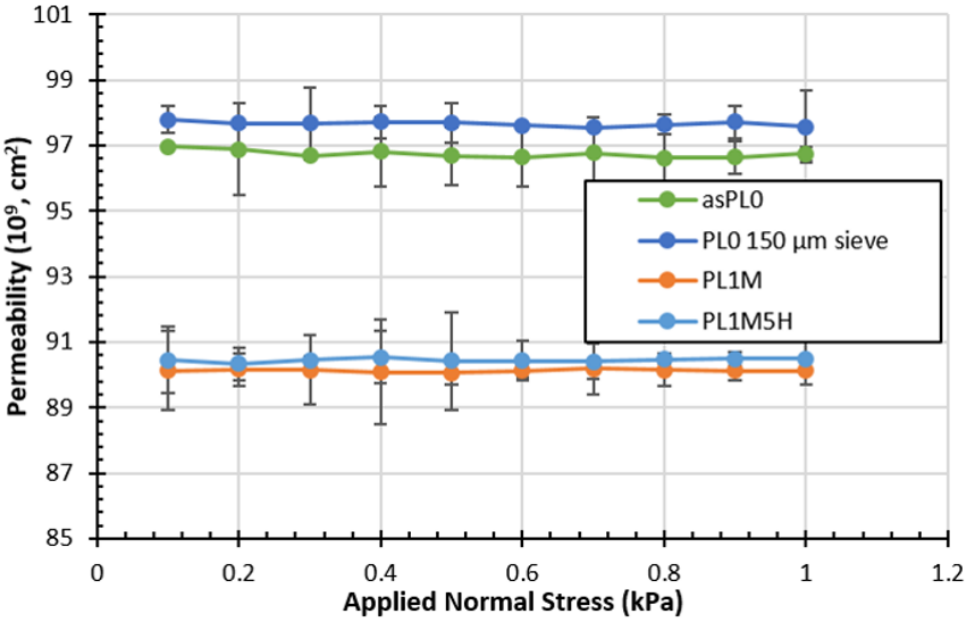


FIGURE 4.19: The permeability test the PLA powders. The addition of MWCNT and MWCNT-nHA decreased the permeability of the bulk powder compared to the asPL0 and PL0 150 μm powders. Error bars represent standard error n = 3.

4.4.7 Compressibility - PA12-nHA powders

The compressibility test programme recorded the density change of the powder as a function of applied normal stress. The results of the compressibility test conducted on the PA12 powders can be seen in Figure 4.20. Across all applied normal stresses, from 0.1-1 kPa, the PA0 powder retained the highest degree of compressibility compared to PA2H and PA4H. At the highest stress of 1 kPa the average % compressibility (CPS) of powder was as follows: 2.9 $\pm$ 0.1%, 2.2 $\pm$ 0.1 % and 2.0 $\pm$ 0.1 % for the PA0, PA2H and PA4H powders respectively. This indicates that the packing efficiency

increases with increased loading of nHA. As the applied normal stress is increased the CPS of the powders also increases as air is forced out of the voids that occupy the space between the particles.

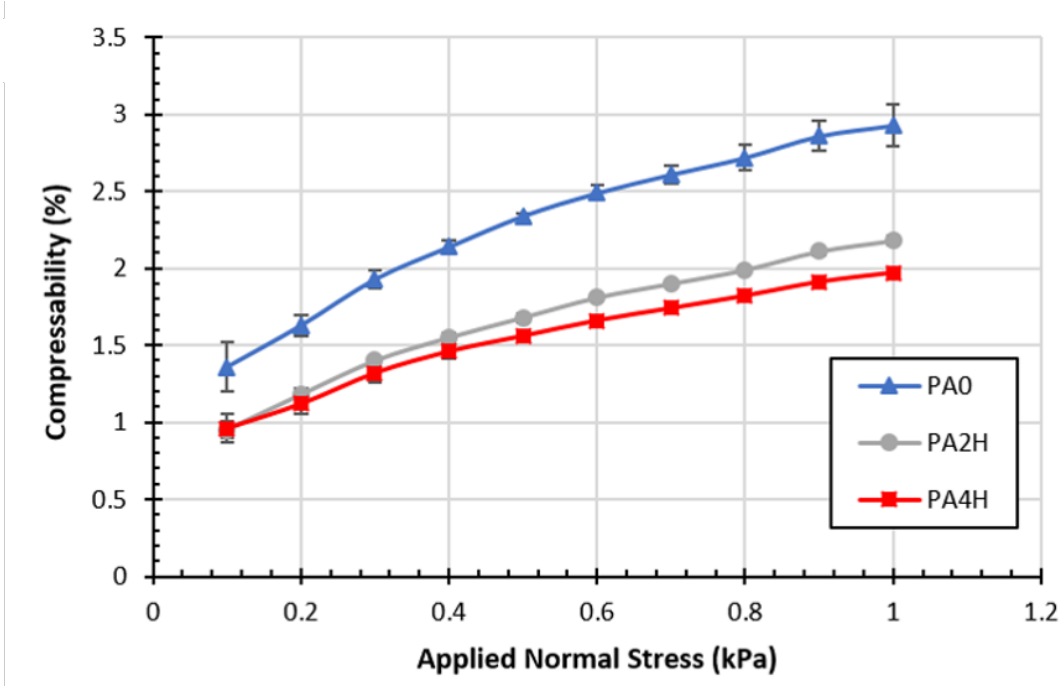


FIGURE 4.20: The results of the compressibility test for neat and nHA coated PA12 powders as a function of applied normal stress. Compressibility reduced with the increasing addition of NPs as a result of more efficient packing. The Error bars represent standard error n = 3.

A more efficiently packed powder bulk is also reflected in a higher conditioned bulk density (CBD), as seen in Figure 4.21. The PA0 displayed a CBD of 0.440 $\pm$ 0.001 g ml^{-1} whereas the PA2H and PA4H powders exhibited a higher CBD of 0.473 $\pm$ 0.001 g ml^{-1} and 0.476 $\pm$ 0.003 g ml^{-1} respectively.

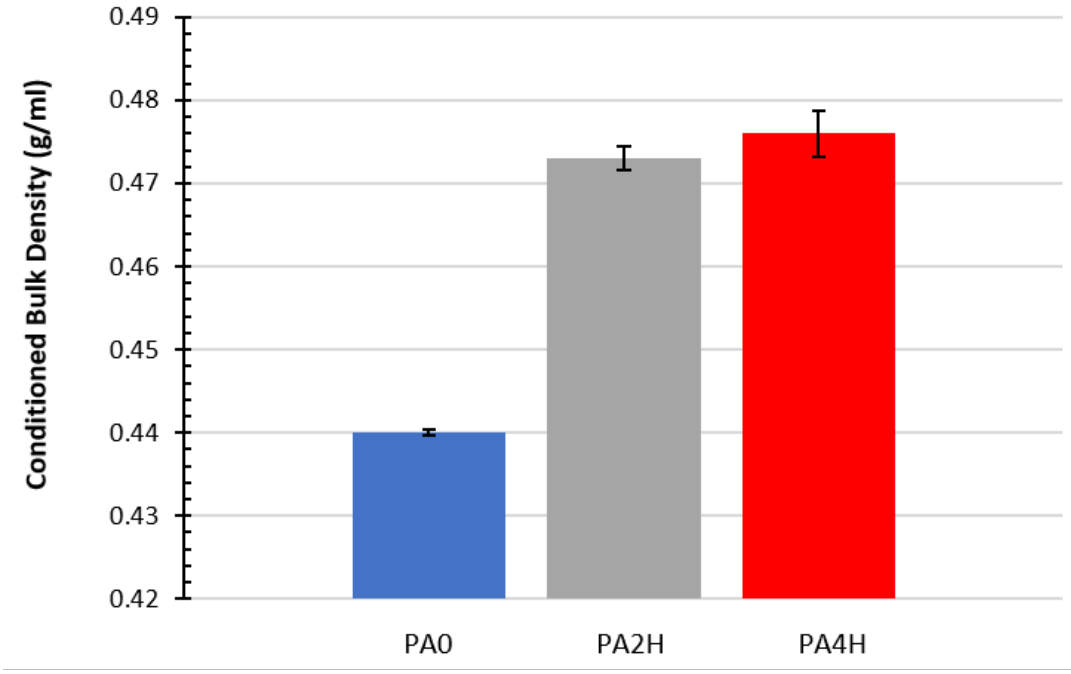


FIGURE 4.21: Conditioned Bulk density measurements from Split-Rep test programme for coated PA12 powders. Increasing nHA content in addition to MWCNT and MWCNT-nHA resulted in a higher CBD for the coated powders. Error bars represent standard error, n = 3.

4.4.8 Compressibility - PLA-MWCNT-nHA powders

For the PLA powders, as seen in Figure 4.22, each of the powders displayed an increase in compressibility with increasing normal stress. The asPL0 powder displayed a moderate degree of compressibility and reached a peak average % compressibility of 3.2 $\pm$ 0.1% at 1 kPa applied stress. The sieved PL0 μm powder displayed a steeper increase in compressibility, relative to all other PLA powders tested, indicating that the powder bulk was very sensitive to compression, and thus contained large amounts of entrained air. The peak CPS value reached at 1 kPa of applied stress was 3.6 $\pm$ 0.1%, the highest peak CPS value of all PLA powders tested, representing a 14% increase in compressibility compared to the asPL0 powder. The PL1M powder displayed a similar profile when compared to the asPL0 powder, however, the degree of compressibility was significantly less. The PL1M powder reached a peak CPS of 2.8 $\pm$ 0.1%, which represented a 12% reduction in compressibility compared to the asPL0 powder. The PL1M5H, on the other hand, displayed the lowest degree of compressibility of all the

PLA powders, and reached a peak CPS of 2.4 ± 0.1%, a 25% decrease in compressibility compared to the asPL0 powder. The results of the compressibility test are in accordance with the permeability test which indicates the presence of NPs improved the overall packing efficiency of the coated powders.

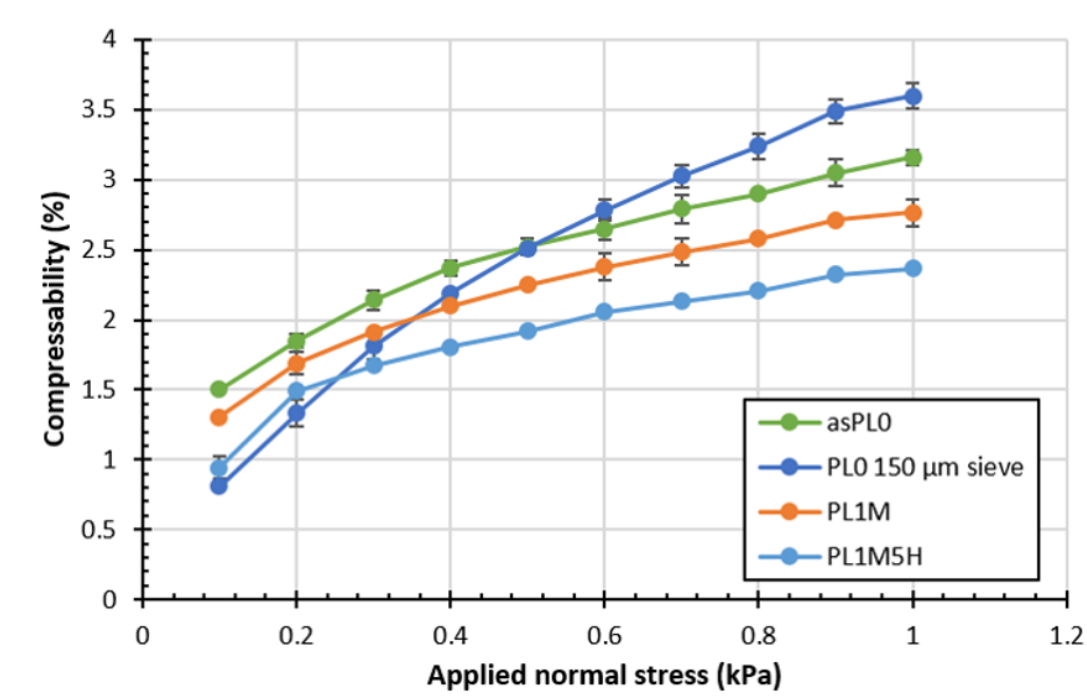


FIGURE 4.22: The compressibility of the PLA powders as a function of applied normal stress. The PL0 150 μm powder exhibited the highest compressibility. Error bars represent standard error n = 3.

The asPL0 powder displayed a peak CBD of 0.57 ± 0.01 g ml^{-1}, following sieving the PL0 powder displayed a significantly lower CBD of 0.52 ± 0.01 g ml^{-1}. The PL1M and PL1M5H powders both displayed the same CBD values of 0.58 ± 0.01 g ml^{-1} and 0.58 ± 0.06 g ml^{-1}.

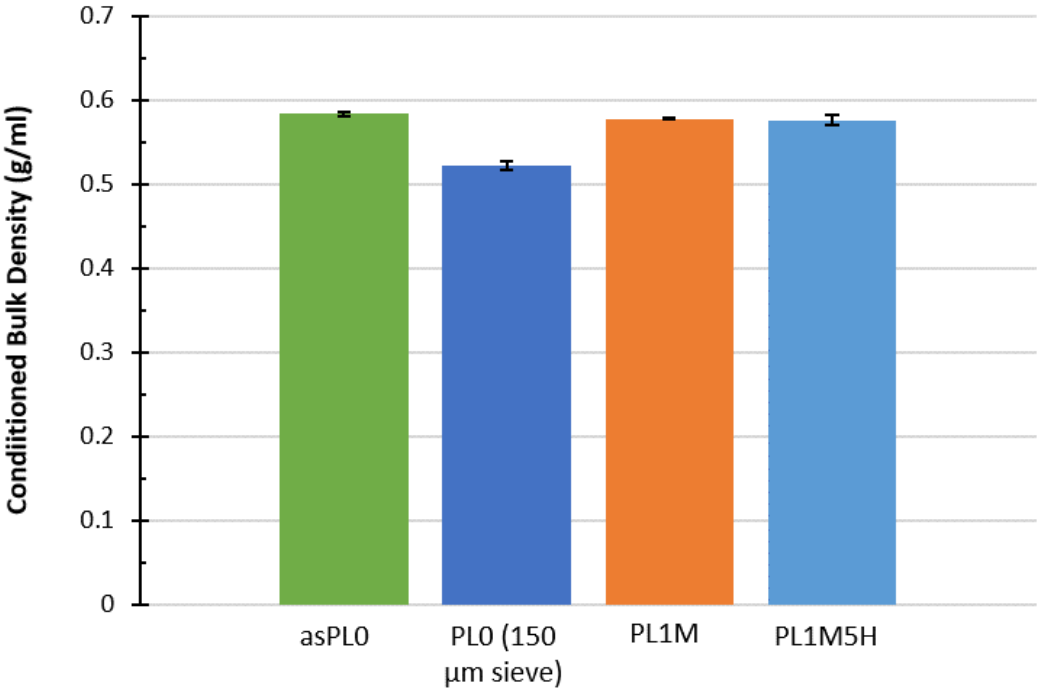


FIGURE 4.23: Conditioned Bulk density measurements from Split-Rep test programme. The prescence of MWCNT and MWCNT-nHA resulted in a higher CBD for coated PLA powders. Error bars represent standard error n = 3.

4.5 Thermal Characterisation

4.5.1 Differential Scanning Calorimetry

4.5.2 Standard DSC - PA12-nHA powders

The DSC curves for PA0, PA05H, PA2H and PA4H can be seen in Figure 4.24 (a). The first heating and cooling cycles for all the powders displayed two distinct, narrow and separated peaks, the endothermic events represent melting and the exothermic events are associated with crystallisation of the polymer. The average peak melting and peak crystallisation temperatures for the neat and coated PA12 can be seen in Table 4.5. As the nHA loading was increased the average peak crystallisation temperature (Tc) increased by 2.9, 6.1 and 8.6°C for PA05H,PA2H and PA4H powders respectively, compared to the PA0 powders. On the other hand, the average melting peak did not show any significant changes.

TABLE 4.5: Averaged DSC data for neat and coated PA12 powders using a scanning rate of 10°C min^{-1}, standard error n = 3.

Material	Tm (°C)	Tc (°C)
PA0	183.6 ±0.9	147.6 ±2.8
PA05H	184.1 ±1.0	149.9 ±1.9
PA1H	183.5 ±1.4	150.5 ±0.2
PA2H	184.9 ±0.6	153.7 ±1.4
PA4H	183.7 ±0.5	156.2 ±0.3

The exothermic crystallisation curves, for the coated PA12 powders can be seen to shift to higher temperatures as the nHA loading is increased.

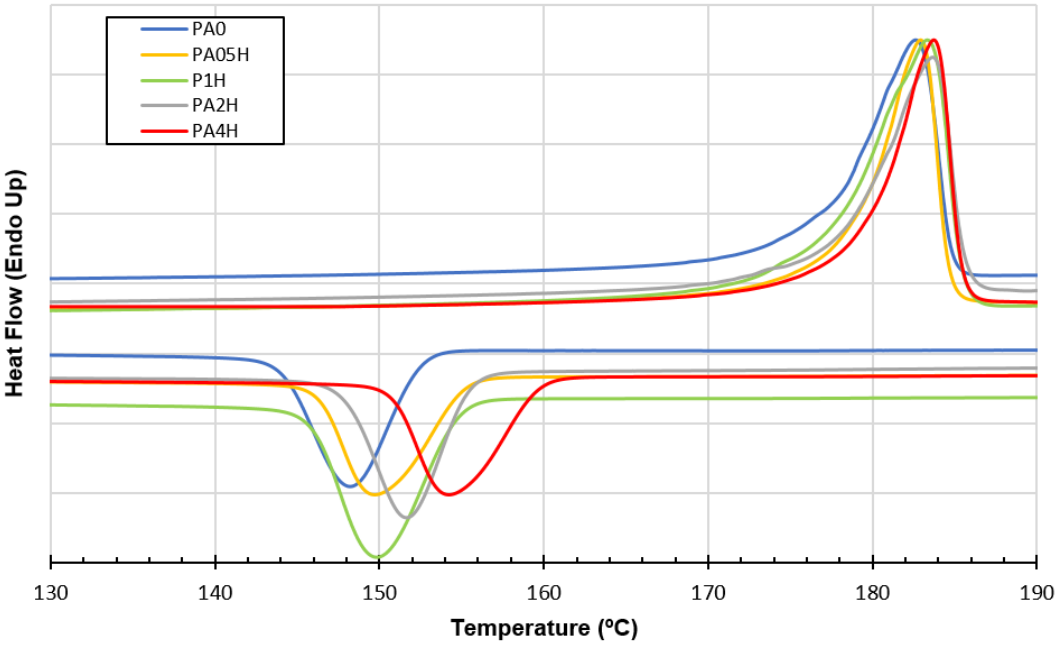


FIGURE 4.24: Graph showing the DSC curve of the endothermic and exothermic phase changes during heating and cooling cycle at 10 °C min^{-1} for PA0, PA05H, PA1H, PA2H and PA4H powders. The curves show the 1st heating and cooling cycles. Peak melting endotherms did not show any significant changes however, the crystallisation exotherms varied with the presence of nHA.

4.5.3 Standard DSC - PLA-MWCNT-nHA powders

A standard heating and cooling cycle was also applied to the PLA powders, as seen in Figure 4.25. The PL0, PL1M and PL1M5H displayed a prominent and narrow melting peak in addition to a separated and slightly broader crystallisation peak. The addition of MWCNT caused a shift of the crystallisation peak for the PL1M powder to a higher

TABLE 4.6: Averaged DSC data for neat and coated PLA powders using a scanning rate of 10°C min^{-1}, standard error n = 3.

Material	Tm (°C)	Tc (°C)
PL0	175.4 ±0.5	109.4 ±0.2
PL1M	175.1 ±0.4	111.6 ±0.1
PL1M5H	174.8 ±0.2	111.6 ±0.1

temperature. The peak Tm, on the other hand, remained unaffected. The PL1M5H powder displayed a very similar heating and cooling curve to the PL1M with a similar increase and narrowing of the crystallisation peak. A smaller melting peak occurring at 114°C could be seen for all powders, this peak was also visible when the PLA powders were subject to different heating and cooling rates (further discussed below) and is consistent with the melting endotherm for lactide monomer and thus suggests the presence of residual lactide within the polymer [291]. The results of the first heat and cooling cycles for PLA can be seen in Table 4.6. The peak melting temperatures for PL0, PL1M and PL1M5H were similar. However, there was a difference between the peak Tc when comparing PL0 against PL1M and PL1M5H. The PL0 powder recorded a peak Tc of 109.4 ± 0.2°C, whereas the PL1M and PL1M5H were higher both recording the same temperature of 111.6 ± 0.1°C.

Multiple heating and cooling cycles were conducted on the PL0 powder which can be seen in Figure 4.26. The second heating curve was conducted following cooling from melt at 10°C min^{-1}. Following the second heating cycle, PL0 was quenched from melt at 80 °C min^{-1} and reheated at 10°C min^{-1}. The presence of a large exothermic peak was observed, with a peak maxima at 91.9 ± 0.5 °C, a clear sign that cold crystallisation had taken place. Thus, the sample was completely amorphous after quenching which is also confirmed by the lack of an exothermic crystallisation peak during cooling at 80°C min^{-1}. Before peak melting was observed a large depression in the heating curve could also be seen at 163°C, indicative of changes to the crystallinity of the sample and a higher proportion of semi-crystalline component. Again, the presence of a small endothermic peak could be seen at 113 ± 2.1 °C during all heating cycles, and suggests the presence of residual lactide monomer as mentioned before.

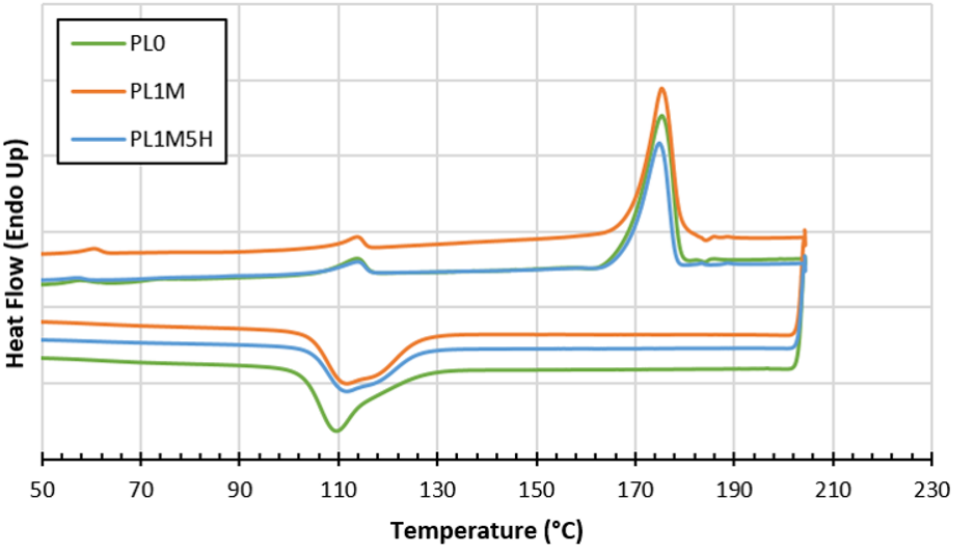


FIGURE 4.25: Graph showing the DSC curve of the endothermic and exothermic phase changes during heating and cooling cycle at 10 °C min^{-1} for PL0, PL1M and PL1M5H powders. The curves show the 1st heating and cooling cycles. Peak melting endotherms did not show any significant changes however, the crystallisation exotherms varied with the presence of increased with the presence of MWCNT and nHA. On this occasion there was not a significant diffrence between the crystallisation peaks of PL1M and PL1M5H. A smaller endothermic peak at approximately 114°C is indicative of residual lactide.

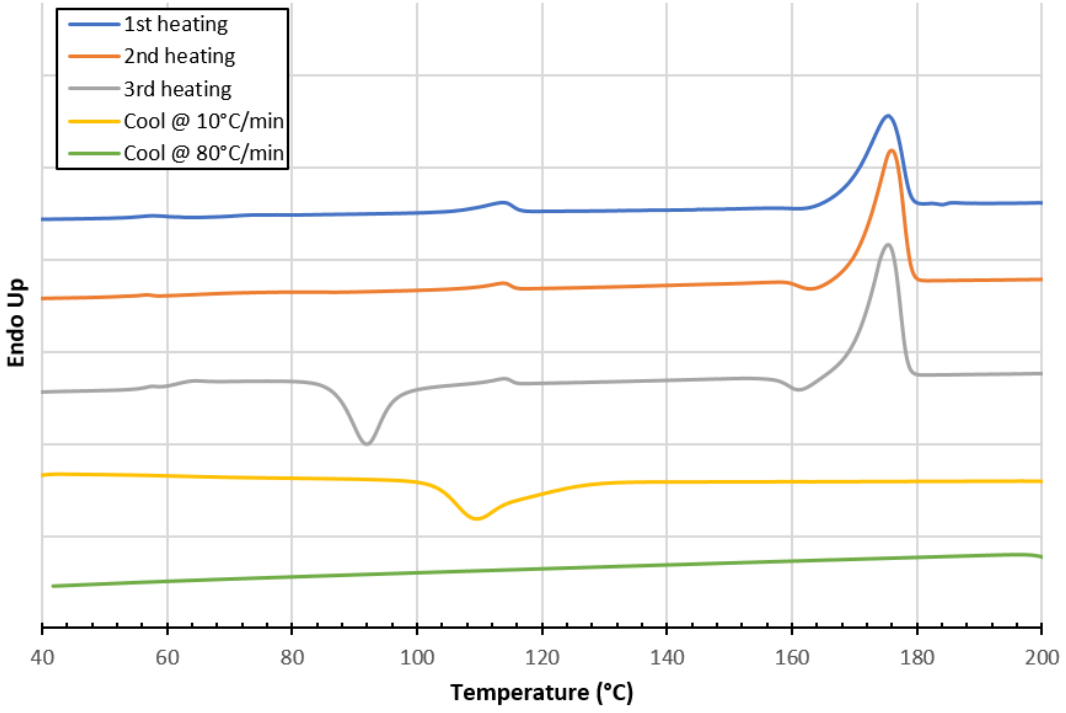


FIGURE 4.26: Graph showing the multiple heating and cooling DSC curves of the endothermic and exothermic phase changes of PL0 powder. Following reheating after quenching from melt a cold crystallisation peak emerges.

4.5.4 The Effect of Different Cooling Rates on PA12-nHA Powders

During laser sintering the powder bed surface remains in a molten state for a long period of time, post laser exposure. Due to thermal gradients experienced at the powder surface in real life conditions, the use of the standard heating and cooling rates of 10 $^{\circ}$C min^{-1} does not truly reflect the thermal conditions that powders experience during processing. Therefore, isothermal and non-isothermal analysis was also conducted on the powders to assess their crystallisation behaviour in response to these temperature differences. During non-isothermal cooling, the different cooling rates affected the temperature at which peak Tc occurred and the rate of crystallisation. Therefore different cooling rates were explored, the non-isothermal DSC curves for the PA0 powders can be seen in Figure 4.27 (a) and PA4H powders in 4.27 (b). It can be seen that, for the PA0 powders, the peak Tc shifts to higher temperatures: 150.3, 154.5, 158.1 and 160.5°C as the cooling rate decreased from 10, 5, 2 and 1 $^{\circ}$C min^{-1} respectively. The coated PA4H powders also displayed a similar shift in the peak Tc to higher temperatures at decreasing cooling rates, as seen in Figure 4.27 (b). However, unlike the PA0 powder, the peak Tc occurred at higher temperatures: 153.3, 161.3, 162.2 and 165.6°C.

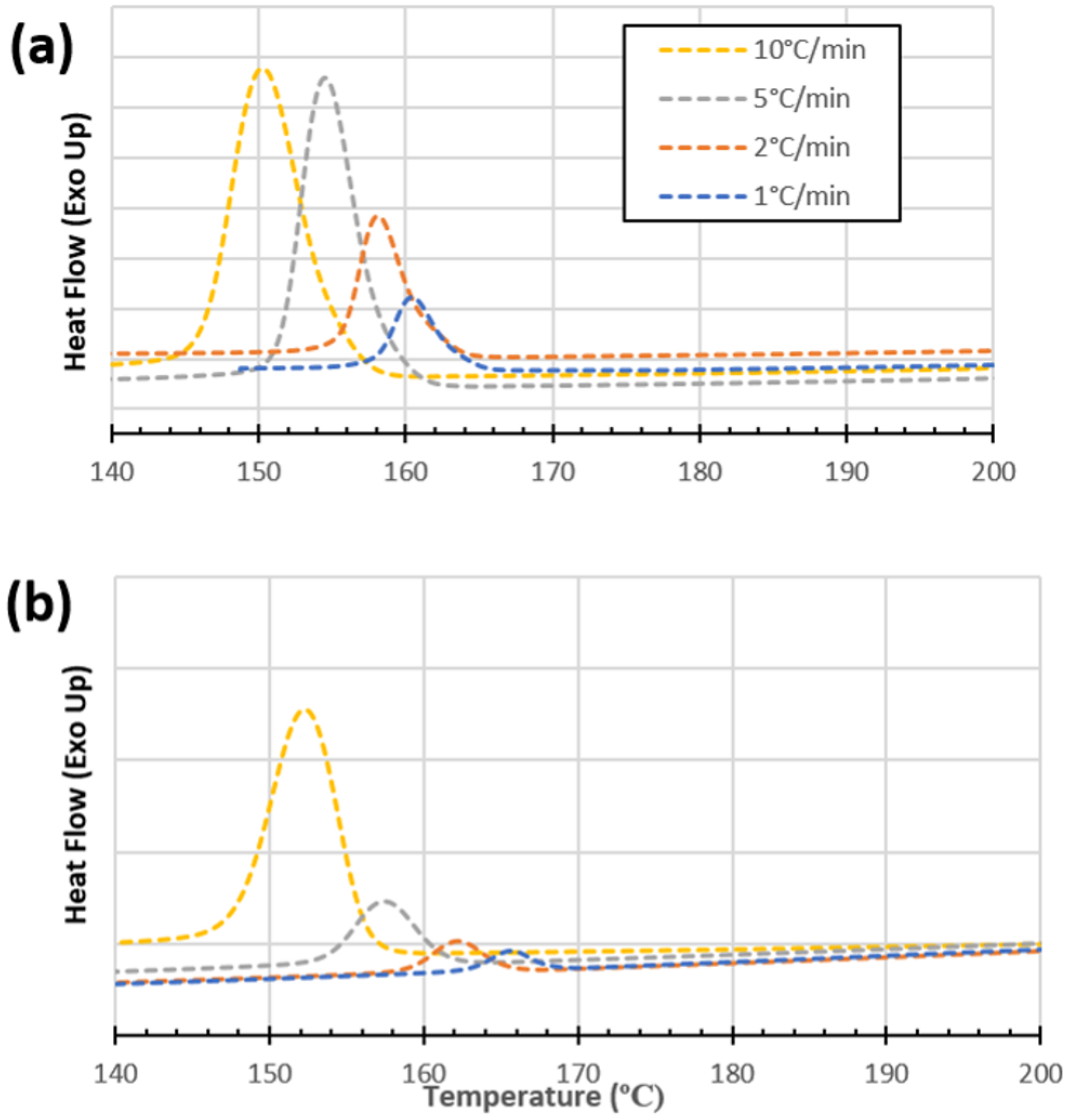


FIGURE 4.27: Non-isothermal crystallisation curves of (a) PA0, (b) PA4H at cooling rates of 10, 5, 2, and 1°C min^{-1}.

4.5.5 The Effect of Different Cooling Rates on PLA-MWCNT-nHA Powders

The effect of different cooling rates was also explored through non-isothermal analysis on the PLA powders. The peak Tc was recorded for PL0, PL1M and PL1M5H powders, which were cooled from melt at a rate of 10, 5, 2 and 1°C min^{-1}. This can be seen in Figure 4.28 (a) which depicts the curve of the as-received PL0 powder, whereas, (b) and (c) represent the PL1M and PL1M5H powders respectively. The PL1M powder

displayed a double peak, similar to that observed during the standard cooling of PL0. However when cooling was decreased further this double peak collapsed into a single peak.

The results of the recorded peak Tc are summarised in Table 4.7. The PL1M5H powders, on average, recorded the highest peak Tc at all cooling rates.

TABLE 4.7: Non-isothermal peak Tc recorded for the coated PLA powders at a cooling rate of 10, 5, 2 and 1°C min^{-1}, standard error n = 3.

	Material Peak Tc (°C)		
Cooling Rate (°C min^{-1})	PL0	PL1M	PL1M5H
10	102.9 ±0.3	106.7 ±0.5	115.8 ±0.9
5	110.8 ±1.1	116.8 ±0.1	123.3 ±1.2
2	118.5 ±0.1	125.0 ±0.1	129.6 ±0.5
1	129.2 ±0.05	129.4 ±0.01	137.7 ±0.1

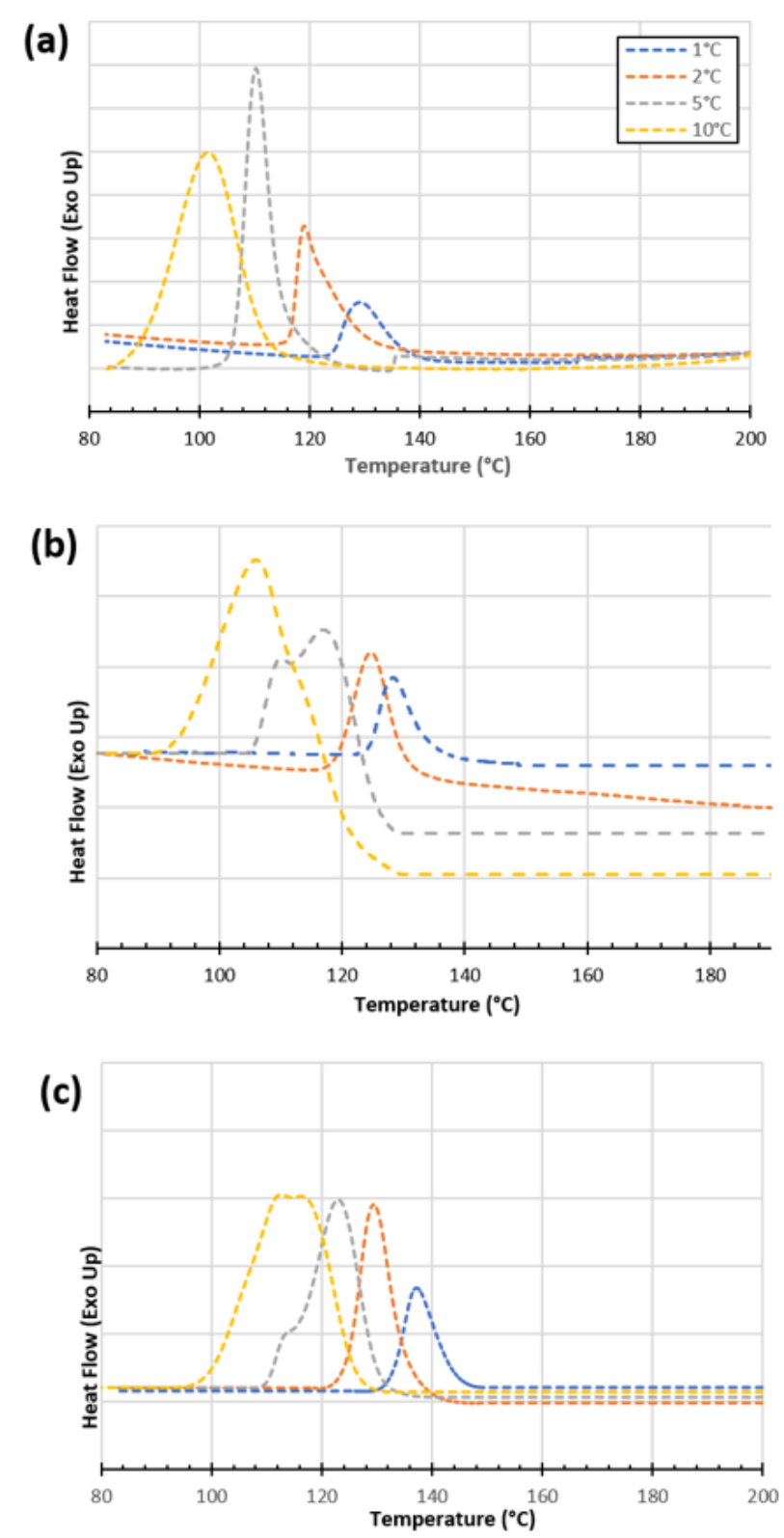


FIGURE 4.28: Crystallisation curves of (a) PL0, (b) PL1M and (c) PL1M5H at cooling rates of 10, 5, 2, and 1°C min^{-1}.

4.5.6 Isothermal DSC - PA12-nHA powders

The isothermal crystallisation of PA0 showed that crystallisation occurred at temperatures from 160–165°C, as seen in Figure 4.29 (a), however for the PA4H powders crystallisation occurred over a slightly wider range of temperatures, from 160–170°C, which can be seen in Figure 4.29 (b). The presence of nHA, however, caused a faster rate of crystallisation for the P4H powder when compared to PA0 this can be seen in Table 4.8.

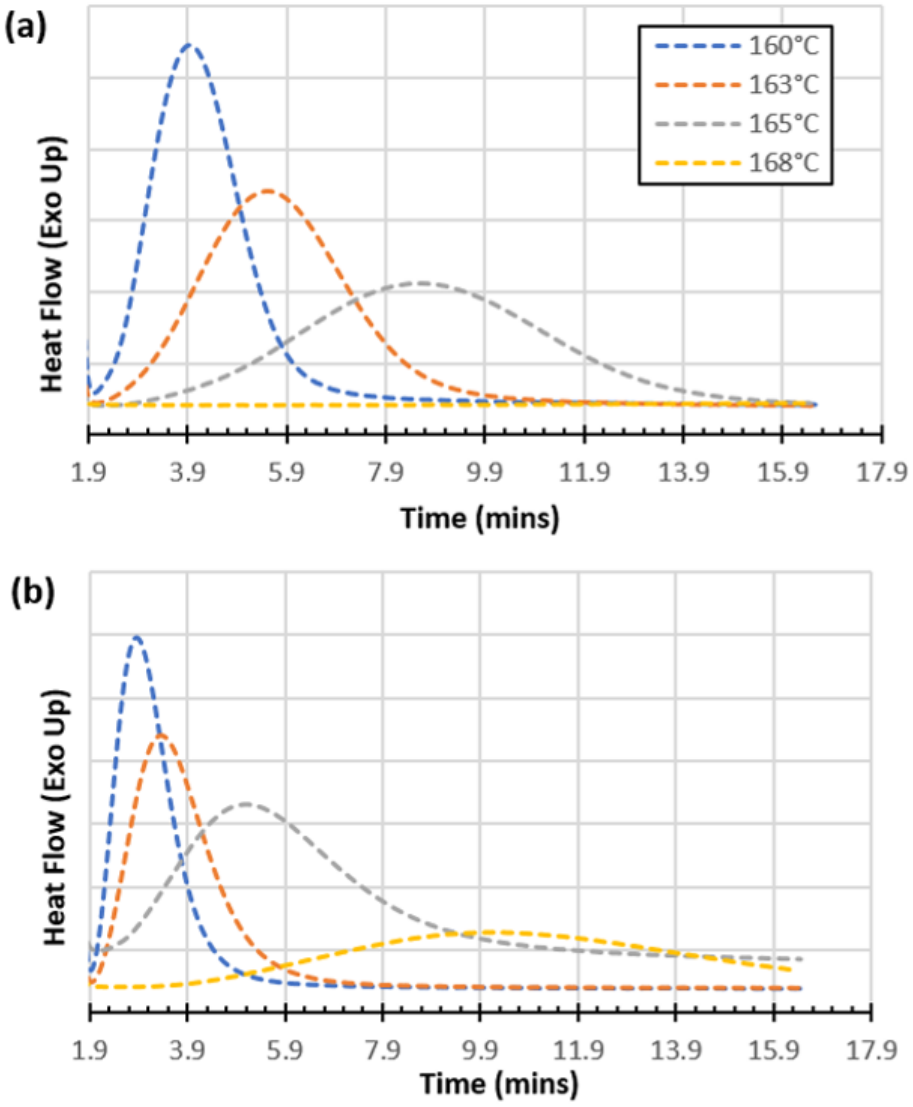


FIGURE 4.29: Isothermal crystallisation peaks of (a) PA0, (b) PA4H powders at various temperatures. The rate of crystallisation was seen to increase significantly with the presence of nHA.

TABLE 4.8: Time taken to reach peak Tc for PA0 and PA4H powders at various isothermal temperatures.

	Material Peak Tc Time (min)	
Isothermal Temperature (°C)	PA0	PA4H
160	2.04	0.96
163	3.36	1.38
165	6.45	5.64
168	-	7.94

4.5.7 Isothermal DSC - PLA-MWCNT-nHA powders

The isothermal study for PL0, PL1M and PL1M5H powders can be seen in Figure 4.30 (a), (b) and (c) respectively. At isothermal temperatures of 123°C, the rate of crystallisation for all powder compositions, was highest, as shown in Table 4.9.

TABLE 4.9: Time taken to reach peak Tc for PL0, PL1M and PL1M5H powders at various isothermal temperatures.

	Material Peak Tc Time (min)		
Isothermal Temperature (°C)	PL0	PL1M	PL1M5H
123	2.87	0.99	0.82
125	3.53	1.16	0.87
127	4.09	1.35	1.04
130	5.22	1.95	1.48
133	6.02	3.12	2.35
135	7.88	4.28	3.37
137	8.81	6.41	4.71
140	11.39	9.56	7.85
143	-	-	11.28

The PL0 reached peak crystallisation in 2.87 min from the onset of crystallisation. As the isothermal temperature was increased, the time taken for crystallisation to occur shifted to longer times and is reflected by the broadening of the exothermic crystallisation peaks, this can be seen in Table 4.9. The addition of MWCNT caused crystallisation to occur more rapidly for the PL1M powder. This indicates the strong nucleating effects that MWCNT had on the PLA. The presence of MWCNT-nHA had a more significant effect on the crystallisation rate of the PLA, with PL1M5H recording the fastest rate of crystallisation across all measured temperatures. At 123°C, peak Tc was reached in 0.82 mins and at 140°C the peak Tc was reached in 7.85 mins.

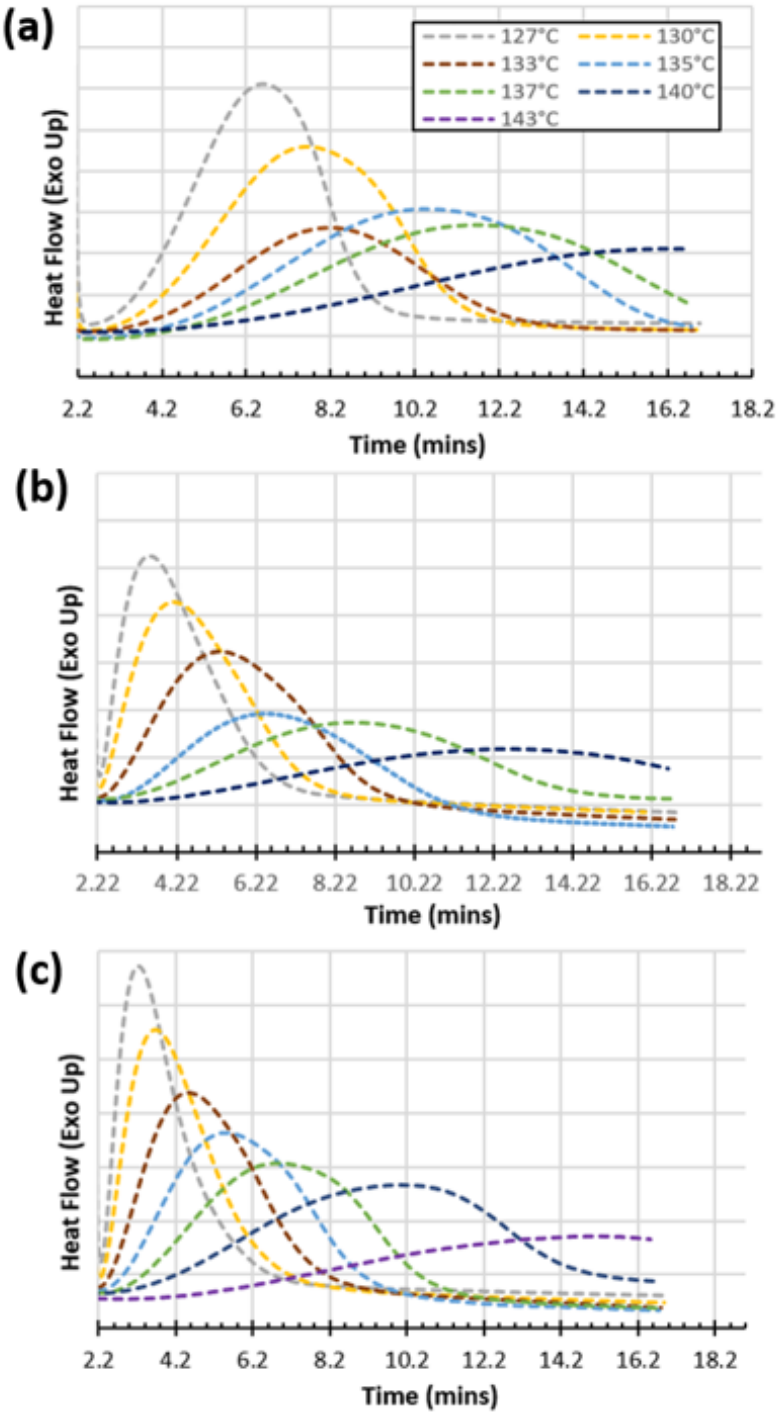


FIGURE 4.30: Isothermal crystallisation peaks of (a) PL0, (b) PL1M and (c) PL1M5H powders at various temperatures. The rate of crystallisation was seen to increase significantly with the presence of NPs.

4.5.8 Crystallisation kinetics - PA12-nHA powders

As shown by the isothermal and non-isothermal tests, crystallisation is significantly influenced by time, temperature, cooling rates and presence of additives. With the assumption that the relative degree of crystallinity of a polymer, cooling from melt, increases with time (t), the isothermal crystallisation curves of the PA12 and PLA powders across the tested temperatures could be represented logarithmically by utilisation of the Avrami model for crystallisation kinetics (Chapter 3). For the PA0 powders this can be seen in Figure 4.31 (a). The PA0 powder displayed parallel lines at the various isothermal temperatures which indicates that the nucleation mechanism and crystal growth geometries remained similar. However, for the PA4H, as seen in Figure 4.31 (b), as the temperature approaches 168°C the curve deviates indicating a change in the crystallisation mechanism.

The application of a linear fit to the data yielded the Avrami constant, n, and by using the Arhhenius relationship (Chapter 3) the Pyris software was able to calculate the activation energy from the gradient of the slope of $lnKvs1/T$, the results of this are shown in Table 4.10 for PA12 powders and the Arrhenius plot is show in Figure 4.32.

TABLE 4.10: Table showing the isothermal temperatures, avrami exponent and activation energy calculated for PA0 and PA4H powders.

Material	Isothermal Temperature (°C)	Exponent, n	Activation energy (J mol^{-1})
PA0	160	2.81	-732.16 ±37.19
	163	3.05	
	165	3.45	
PA4H	160	2.29	-655.20 ±120.35
	163	1.77	
	165	2.44	
	168	3.31	

The addition of nHA caused a reduction in the crystallisation activation energy increases from -932.16 ± 137.19 to -655.20 ± 120.65 kJ mol^{-1}. The n values for PA0

approached the value of 3 which is theoretically associated with three-dimensional spherical growth of homogeneously nucleated spherulites, whereas, the n values for PA4H remained closer to the value of 2 at the lower temperatures and thus exhibited crystallisation components of two-dimensional plane growth with sporadic nucleation [292], this switched at 168°C with the n value approaching 3.

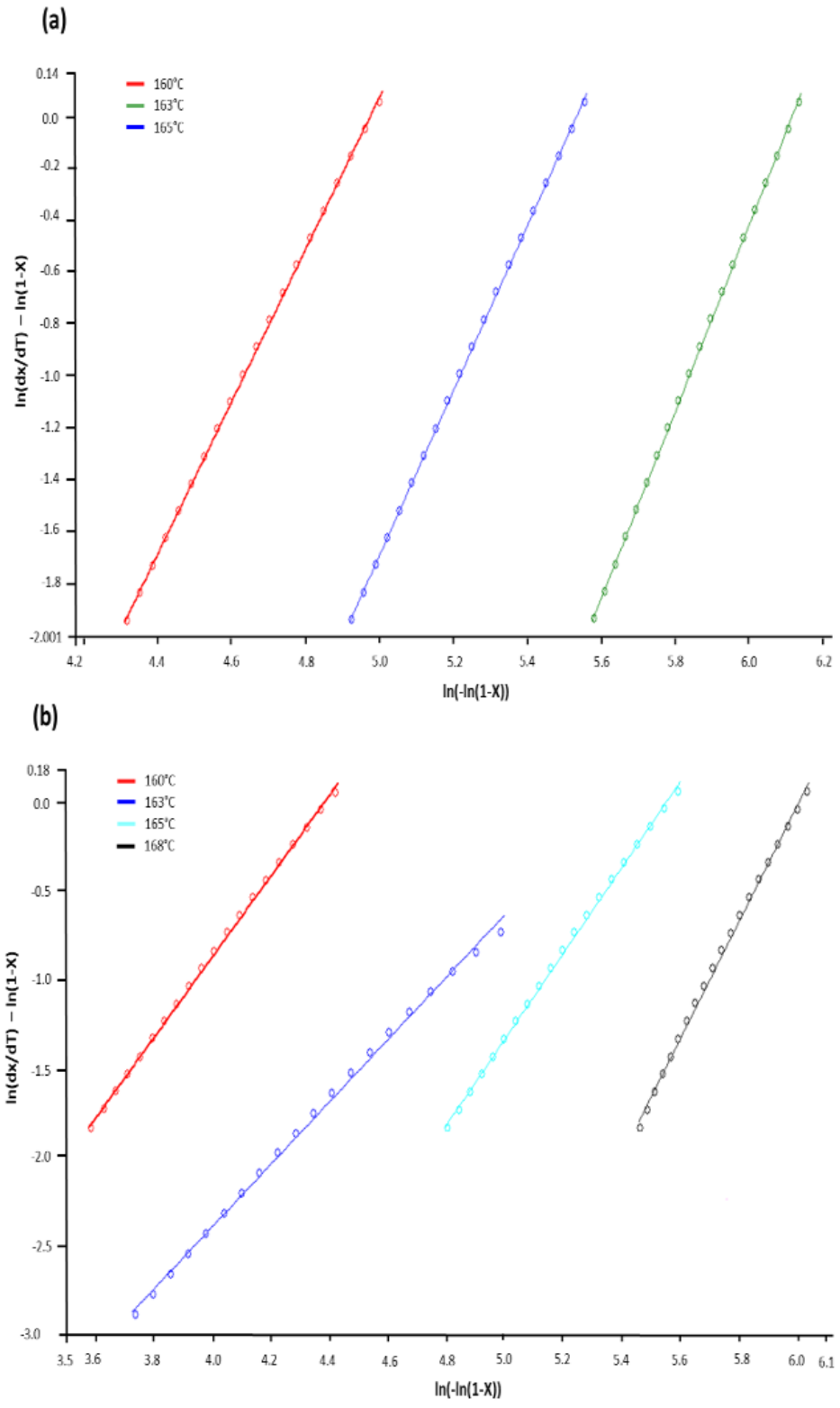


FIGURE 4.31: Avrami plots for (a) PA0 and (b) PA4H powders based on isothermal data taken at various isothermal temperatures.

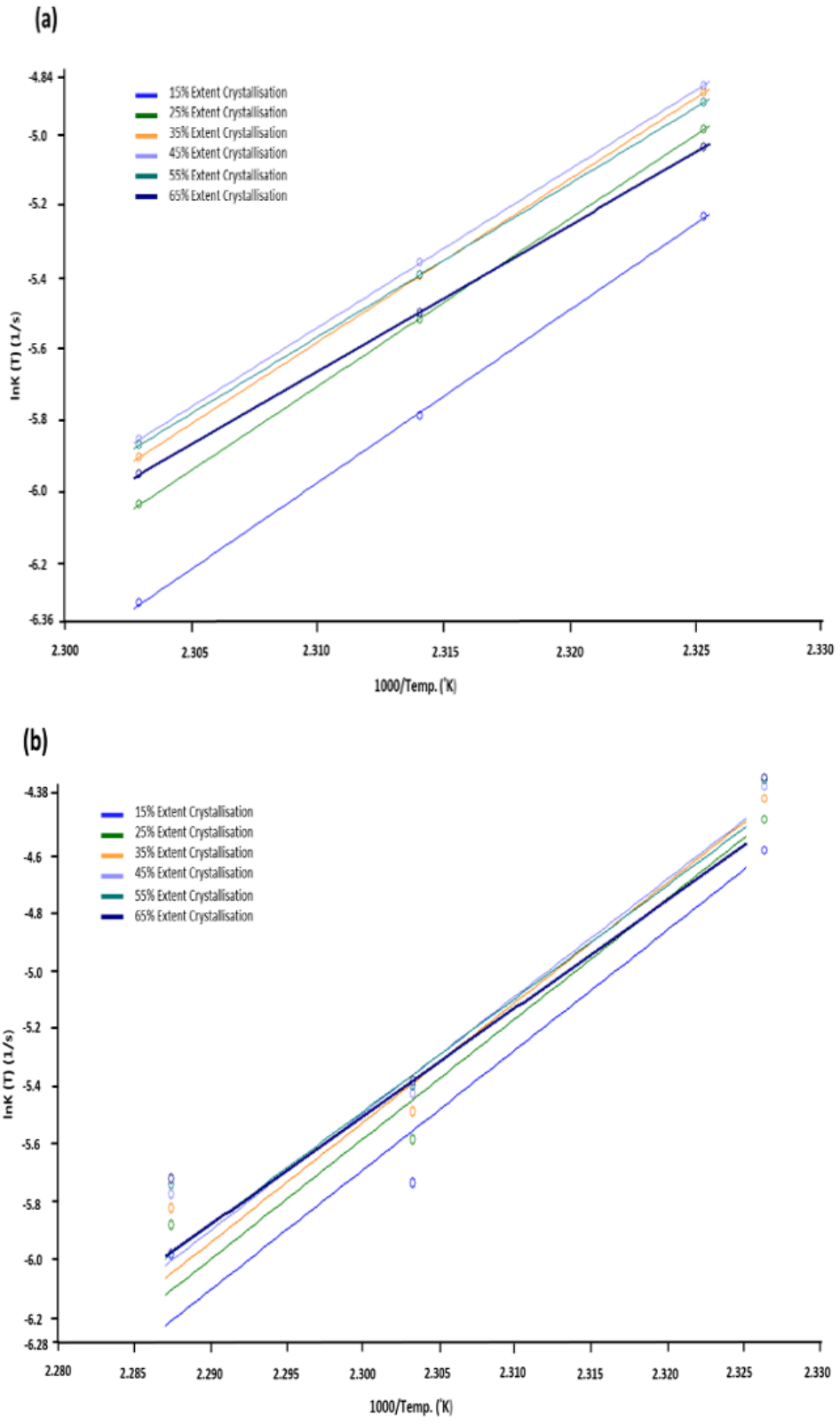


FIGURE 4.32: Arrhenius plots for (a) PA0 and (b) PA4H powders from 15 - 65% extent crystallisation .

4.5.9 Crystallisation kinetics - PLA-MWCNT-nHA powders

The curves for PL0, PL1M and PL1M5H shown in Figures 4.33 (a), (b) and (c) respectively, also displayed parallel lines. However, the PL0 powder shows the two curves, at 123 and 125°C diverging away from each other, indicating a potential shift in crystallisation mechanic as the isothermal temperature surpasses 123°C. Each of the curves displayed a good linear relationship showing that the Avrami model provided a good fit for describing the isothermal crystallisation kinetics of the PLA powders.

TABLE 4.11: Table showing the isothermal temperatures, avrami exponent and activation energy calculated for PL0, PL1M and PL1M5H powders.

Material	Isothermal Temperature (°)C	Exponent, n	Activation energy (J mol^{-1})
PL0	123	4.03	-589.48 ±10.17
	125	3.28	
	127	3.11	
	130	2.60	
PL1M	123	2.27	-426.06 ±57.35
	125	2.06	
	127	2.05	
	130	2.14	
PL1M5H	123	2.25	-378.12 ±26.03
	125	2.10	
	127	2.15	
	130	2.42	

The Avrami exponent and activation energy calculated by Pyris is summarised in Table 4.11 and the Arhhenius plot is given in Figure 4.34. For the PL0, at the isothermal temperature of 123°C, the value of n approached 4 indicating a homogenous, constant nucleation and growth rate through contributions of both three dimensional and one-dimensional growth [293]. At higher temperatures of 125°C, n, approaches the value of 3, indicating a change in crystal growth mechanism. This could be seen on the double logarithmic plot for PL0 with the curves for 123°C and 125°C diverging away from each other and thus transitioning to a predominantly three-dimensional spherulitic growth mechanism which is maintained for the remainder of the test temperatures. For the PL1M and PL1M5H powders, the Avrami exponent approached the value of 2, representing heterogenous nucleation predominantly by a two-dimensional, in-plane, growth mechanism [294]. Once again, the addition of MWCNT and MWCNT-nHA

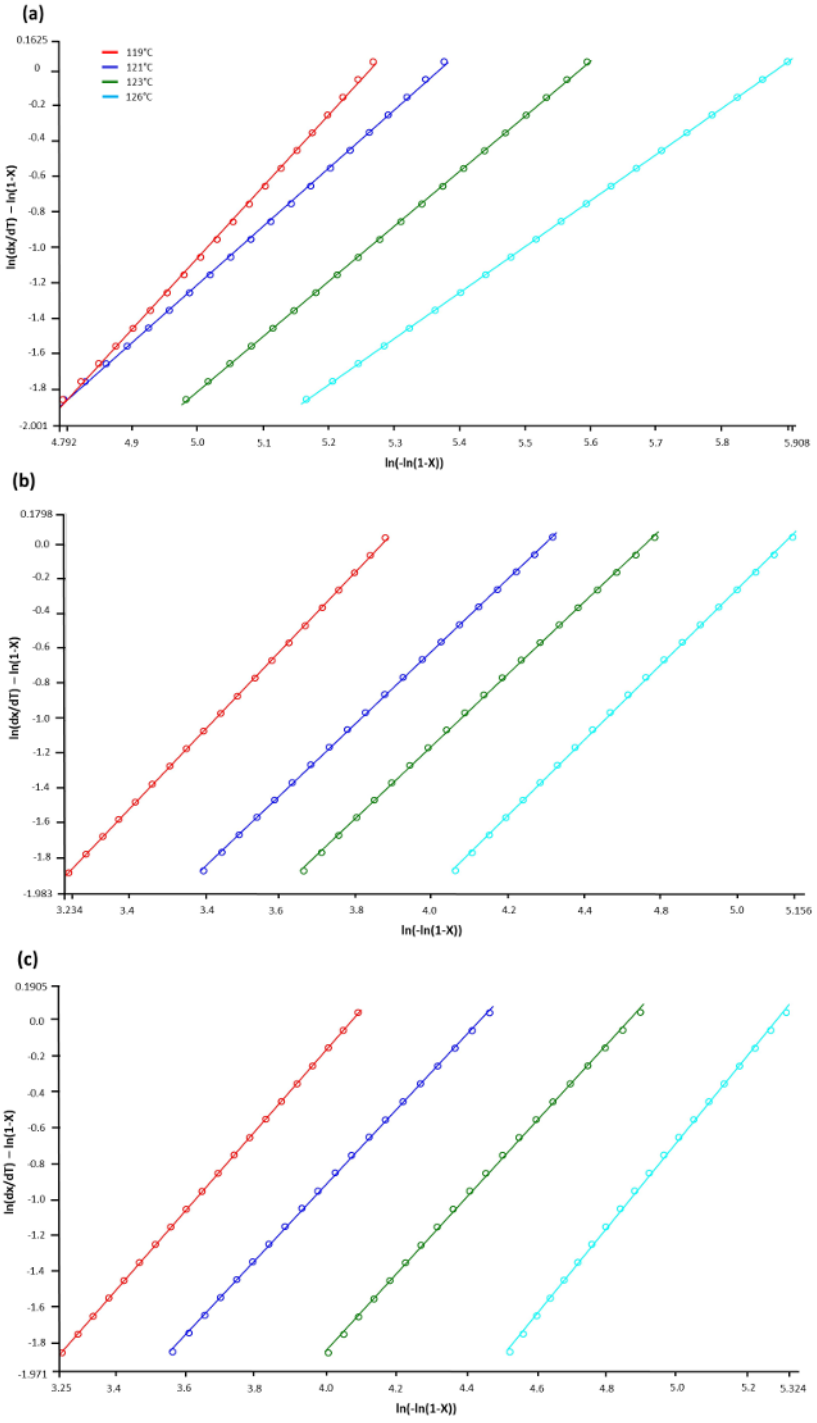


FIGURE 4.33: Avrami plots for (a) PL0, (b) PL1M and (c) PL1M5H powders based on isothermal data taken at various isothermal temperatures.

led to a reduction in the nucleation activation energy from -589.48 ± 10.17 to -426.06 ± 57.35 (PL1M) and -378.12 ± 26.03 kJ mol^{-1} (PL1M5H).

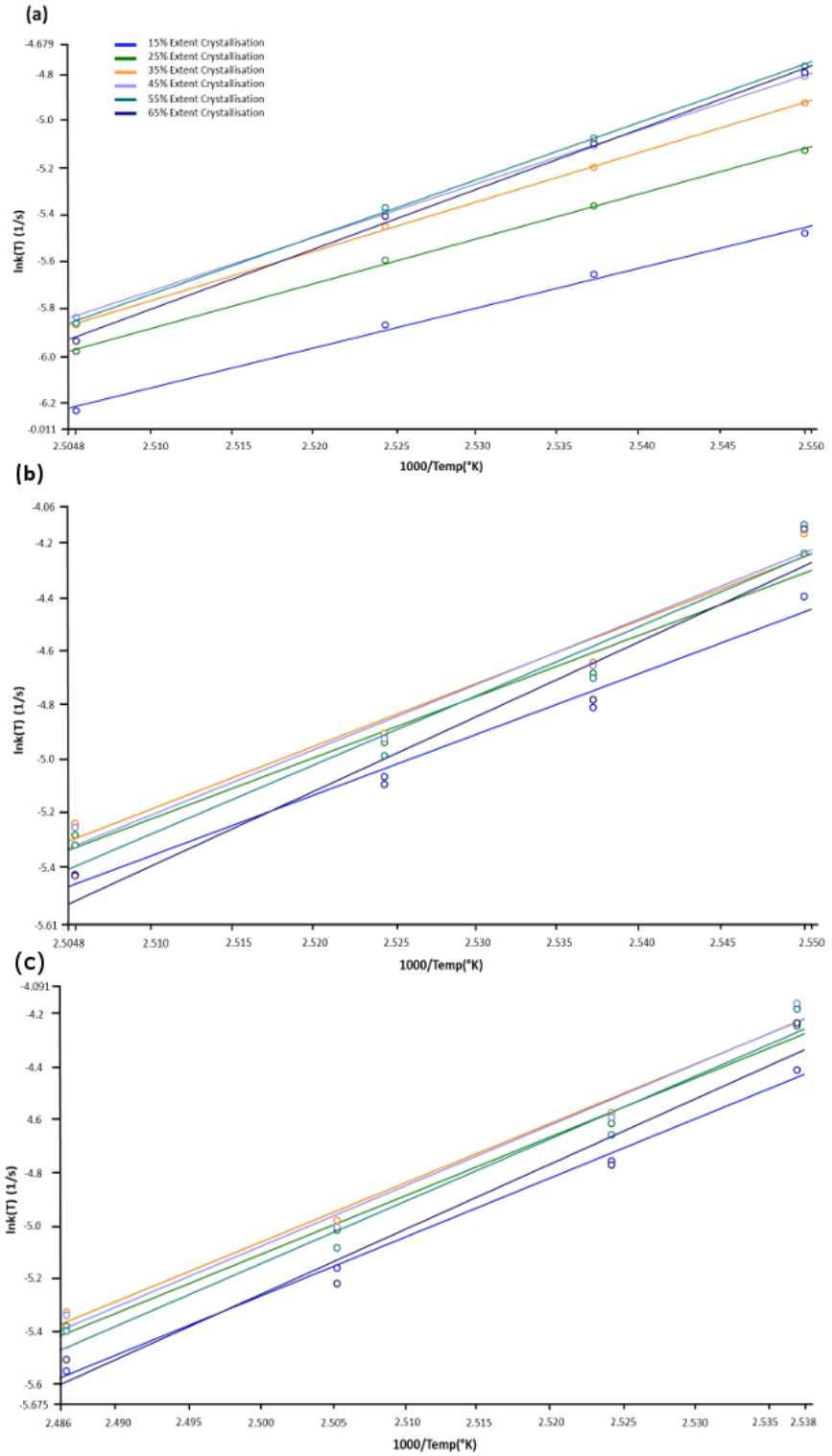


FIGURE 4.34: Arrhenius plots for (a) PL0 and (b) PL1M and (c) PL1M5H powders from 15 - 65% extent crystallisation .

4.6 Melt rheology

The melt rheological properties of the neat and coated PLA powders were studied at low shear rates from 0.0001 to 1 s^{-1} to ascertain the zero shear viscosity of the powder. The results of the test are shown in Figure 4.35. All powders tested displayed a clear plateau region from 1.0x10^{-4} - 3.10x10^{-4} s^{-1} above which the PLA melt transitioned, displaying power law behaviour as shear thinning occurs. The process of shear thinning is caused by the decrease in chain entanglement density as increased shear rates cause polymer chains, relative to each other, to move over at a faster rate. The PL0 possessed the lowest melt viscosity of all the coated powders. The zero shear viscosity was measured to be 1.40x10^{8} Pa.s. The addition of MWCNT caused an upwards shift in the curve for the PL1M melt indicating an increase in melt viscosity to zero shear mealt viscosity was 1.98x10^{8} Pa.s. The addition of MWCNT-nHA had the largest effect on the melt viscosity of the PLA which was indicated by a large upwards shift in the curve, here the zero shear viscosity was recorded at 5.65x10^{8} Pa.s.

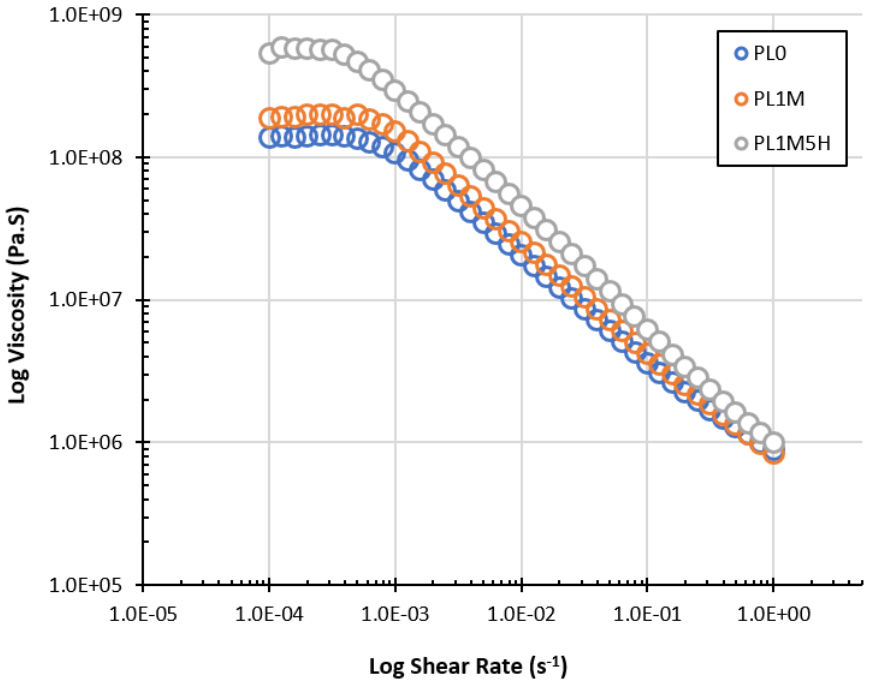


FIGURE 4.35: Shear viscosity for PL0, PL1M and PL1M5H. The shear viscosity significantly increases with increased NP loading.

4.7 ATR-FTIR

ATR-FTIR was conducted on PA0, PA05H, PA1H, PA2H and PA4H powders. The results of this spectrum can be seen in Figure 4.36. Peak assignments can also be seen in Table 4.12. The CO_2 laser used on a commercial laser sintering system, with the wavelength of 10.6 μm, is absorbed by the polymer powder to melt it [295] [296] [297]. With the addition of nHA, the coated powders show an additional peak located at 1032 cm^{-1} and this is reportedly associated with the PO_4^{-3} bending vibration. This is characteristic of hydroxyapatite and the intensity of this peak increases from 0.5 to 4.0 wt% nHA, indicating that nHA may increase the absorption of the CO_2 laser used in the commercial laser sintering system.

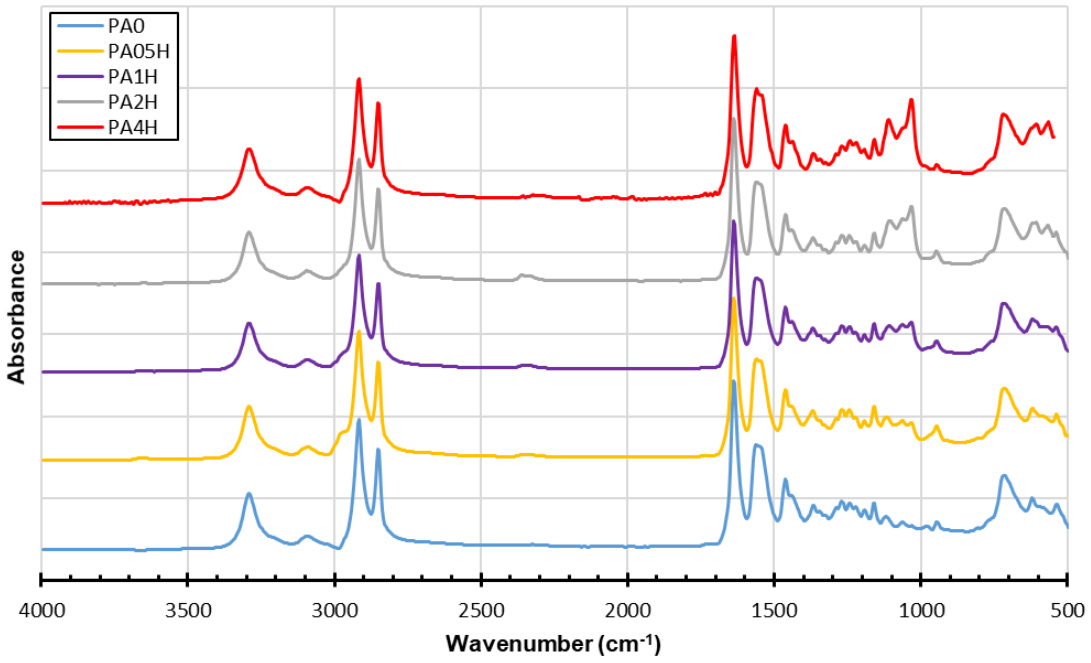


FIGURE 4.36: ATR-FTIR spectrum of PA0, PA05H, PA1H, PA2H and PA4H powders. Peak at 1032 cm^{-1} increases in intensity with higher nHA loading.

TABLE 4.12: Assignment of FTIR spectrum for the PA12 powders [298] [299].

FTIR Peaks (cm^{-1})	Peaks Assignment
3290 and 3094	N-H stretching and Fermi resonance
2917 and 2849	Asymetric and symmetric stretching of CH_2
1638	C=O stretching is related to the amide I absorption band
1550	C-N stretching in addition to C=O in plane bending, collectively associated with the amide II band
1461 and 1368	CH_2 bending and CH bend and CH_2 twisting vibrations
1269	Amide III band due to C-N stretching and C=O in plane bending
1158	Skeletal motion involving CONH
1120	C-C stretching
946 and 716	CONH in plane bending and CH_2 rocking
620 and 538	N-H out of plane bending which is associated with the amide VI band
1032	PO_4^{-3} bending vibration of hydroxyapatite

4.8 UV-Vis Spectroscopy

As the Sintratec uses a laser in the visible light spectrum, in the region of 445 nm, UV-Vis spectroscopy was conducted on PA12 MWCNT-nHA powders. From Figure 4.37, the PA0 powder had recorded the lowest absorption in the region of 420–500 nm. The addition of 0.5 wt% MWCNT led to a substantial increase in absorption, for PA05M powders, across the same region of approximately 60%. The addition of 5 wt% nHA did not significantly affect the absorption which remained at a similar level across the 340–800 nm range when compared to the PA05M powders. To demonstrate that MWCNT could significantly alter the degree of absorption a small sample of PA12 with a 1 wt% MWCNT loading was also examined. As can be seen in 4.37 the PL1M powder recorded significantly higher absorption through-out the spectrum. In the region of 420–500 nm the PL1M powder recorded an increase in absorption by approximately 90% compared to PA0 powders. The intense signal detected in the region below 250 nm for all powders was due to amide bond absorption, which is the shoulder of the -CO-NH- band [300]. The absorption peak maxima at 290 nm suggests the presence of aromatic groups within the chemical structure of PA12, caused by a large transition from the π to π* electronic band [300].

The PLA powders were also subject to UV-VIS analysis as they were to be processed using the Sintratec machine. The absorption spectra for coated PLA powders can be seen in Figure 4.38. The PL0 powders recorded the lowest degree of absorption across the 400–800 nm range. The shoulder of a larger peak located at around 300 nm was observed and this has reportedly been associated with a π-π^* transition of C-O bonds

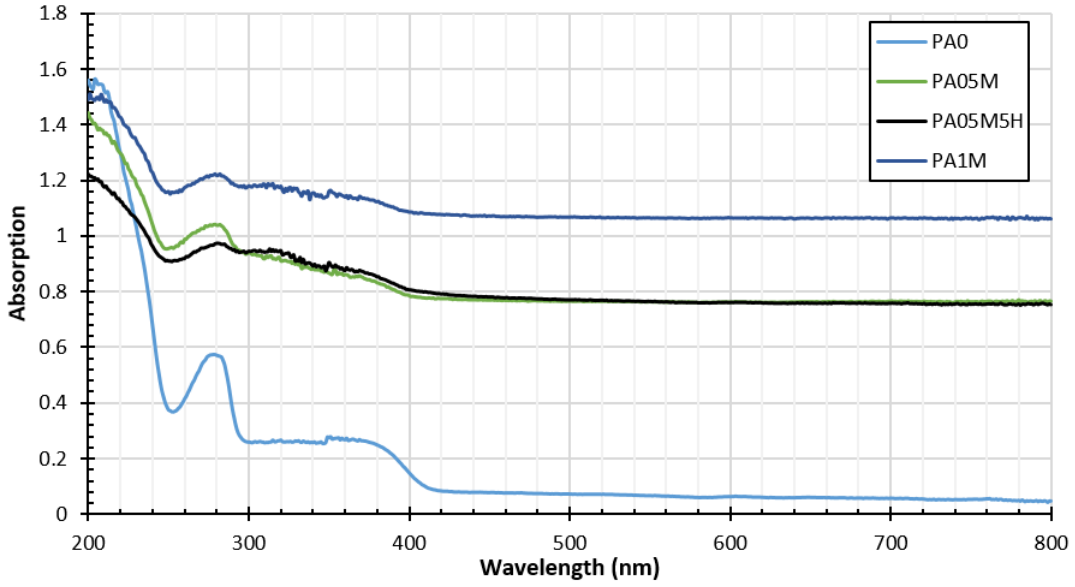


FIGURE 4.37: UV-Vis spectra of PA0, PA05M, PA05M5H and PA1M powders. The absorbance across the entire spectrum increases dramatically with increased loading of MWCNT.

[301] [302]. The addition of MWCNT and MWCNT-nHA led to the absorption spectra for PL1M and PL1M5H to increase significantly between 300–800 nm. The absorption of the PL1M5H can be seen to significantly decrease across the 300–800 nm range when compared to PL1M powder, this is possibly due to masking of the MWCNT by nHA.

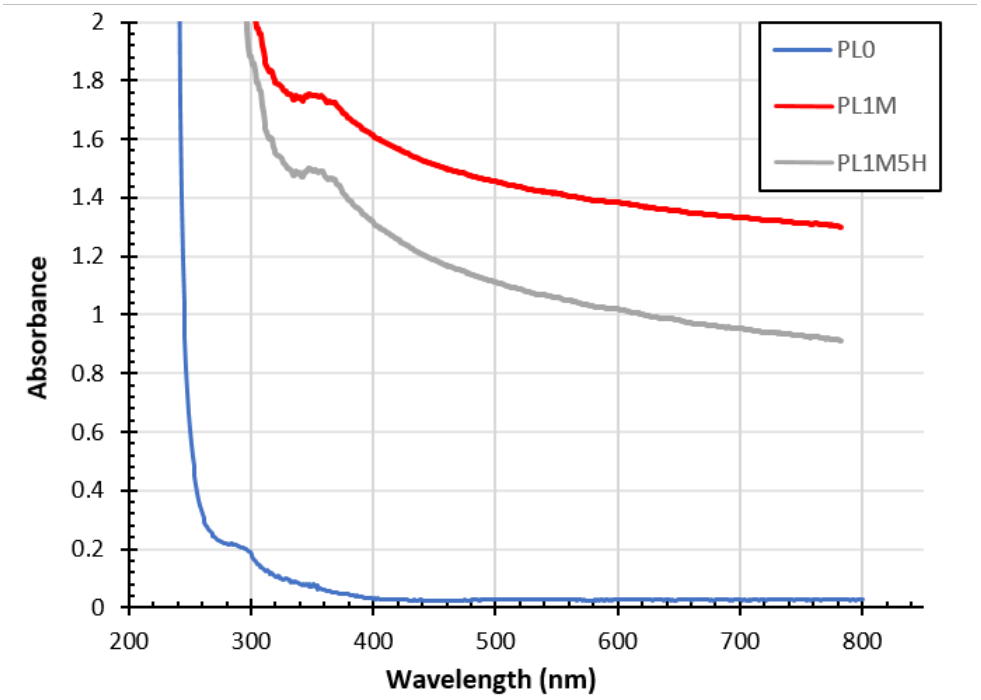


FIGURE 4.38: UV-Vis spectrum of PL0, PL1M and PL1M5H powders. The absorbance across the entire spectrum increased dramatically with increased loading of MWCNT. The addition of nHA caused a reduction in absorption across the spectrum which was possibly due to masking of the MWCNT by nHA particles.

4.9 XRD

4.9.1 XRD - PA12-nHA powders

The XRD patterns for PA0, PA1H, nHA powders in addition to laser sintered PA1H sample are displayed in Figure 4.39. The PA0 powder is a semi crystalline polymer and therefore exhibits two strong crystalline peaks at $2\theta = 21.25°$ and $2\theta = 21.30°$ corresponding to d spacings of 0.412 nm and 0.400 nm respectively. The amorphous humps are also clearly visible appearing at 22° and 42°. The PA1H powder, produced additional diffraction peaks at $2\theta = 25.86°$, $31.78°$, $32.18°$, $32.91°$ and $34.06°$. This corresponds to the (002), (211), (112), (300) and (202) crystal planes which is characteristic of the hydroxyapatite mineral phase [303]. Intense peaks associated with these crystal planes are also visible on the pattern for neat nHA powder with additional characteristic HA peaks at $2\theta = 40.08°$, $46.98°$, $49.78°$ and $53.50°$ corresponding to (130), (222), (213) and (004) planes respectively. The XRD pattern for the PA1H LS

sample showed a single intense peak located at $2\theta = 22.14°$ and a d spacing of 0.421 nm in addition to the faint presence of the (211), (112) and (300) HA crystal planes indicating that upon consolidation the crystal phase changed from a γ'- phase to an α crystal structure.

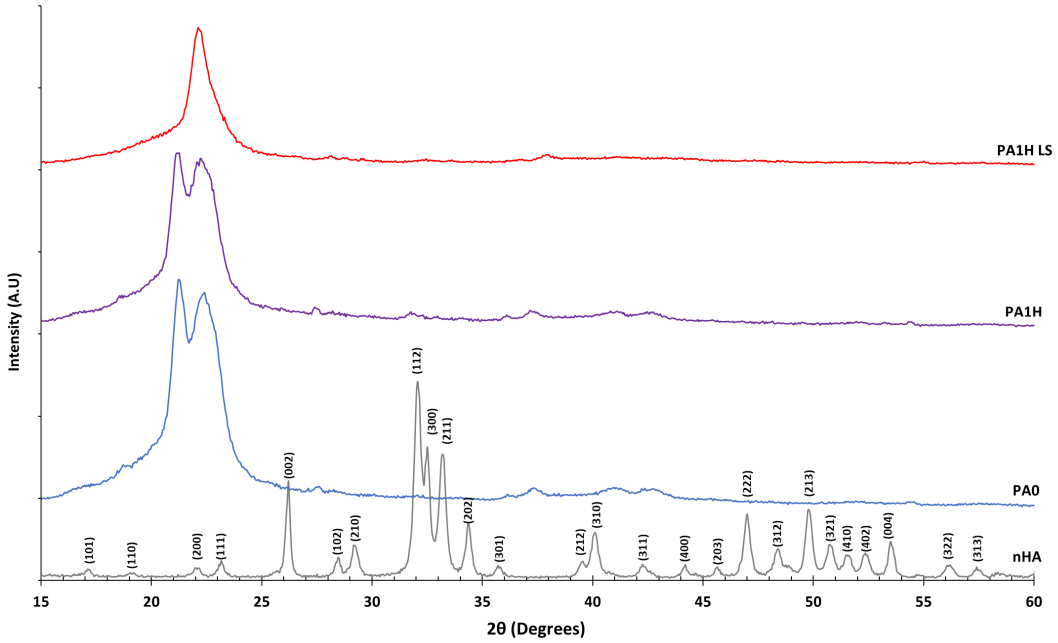


FIGURE 4.39: XRD pattern for PA0, PA1H, nHA powders and PA1H laser sintered sample. The nHA has been indexed giving the (hkl) parameters. The diffraction peaks for PA1H powder at $2\theta = 25.86°$, $31.78°$, $32.18°$, $32.91°$ and $34.06°$, corresponds to the hydroxyapatite mineral phase. The PA1H LS sample showed a single intense peak located at $2\theta = 22.14°$ and a d spacing of 0.421 nm in addition to the faint presence of the (211), (112) and (300).

4.9.2 XRD - PLA-MWCNT-nHA powders

The XRD scans for PL0, PL1M and PL1M5H powders can be seen in Figure 4.40. All sets of powders display two intense peaks that could be seen at $2\theta = 16.8°$ and $18.8°$, these are characteristic peaks associated with PLLA [304]. The peaks located at $2\theta = 16.8°$ can be attributed to the (110) and/or (220) crystal plane, whereas, the reflection at $2\theta = 18.8°$ can be attributed to (203) and/or (213) crystal planes [304]. A weaker peak located at $2\theta = 12.2°$ is conserved for all the powders which is associated with (103)/(104) planes, and is characteristic of the α crystal form which can be formed when the crystallisation temperature is greater than 120°C. This would suggest that

the powder may have been processed at some time above 120°C to allow formation of the α crystal phase [304]. Amorphous humps are also present for the PL0, PL1M and PL1M5H powders indicative of a semi-crystalline polymer. The pattern for PL1M and PL1M5H appeared very similar. A very weak signal detected at $2\theta = 45.25°$ on both PL1M and PL1M5H can be attributed to the (400) reflection of MWCNT [305]. Furthermore, the PL1M5H also contained additional peaks located at $2\theta = 26.25°$ and $2\theta = 32.65°$. These weak peaks were associated with the (002) and (112) reflections of HA, respectively.

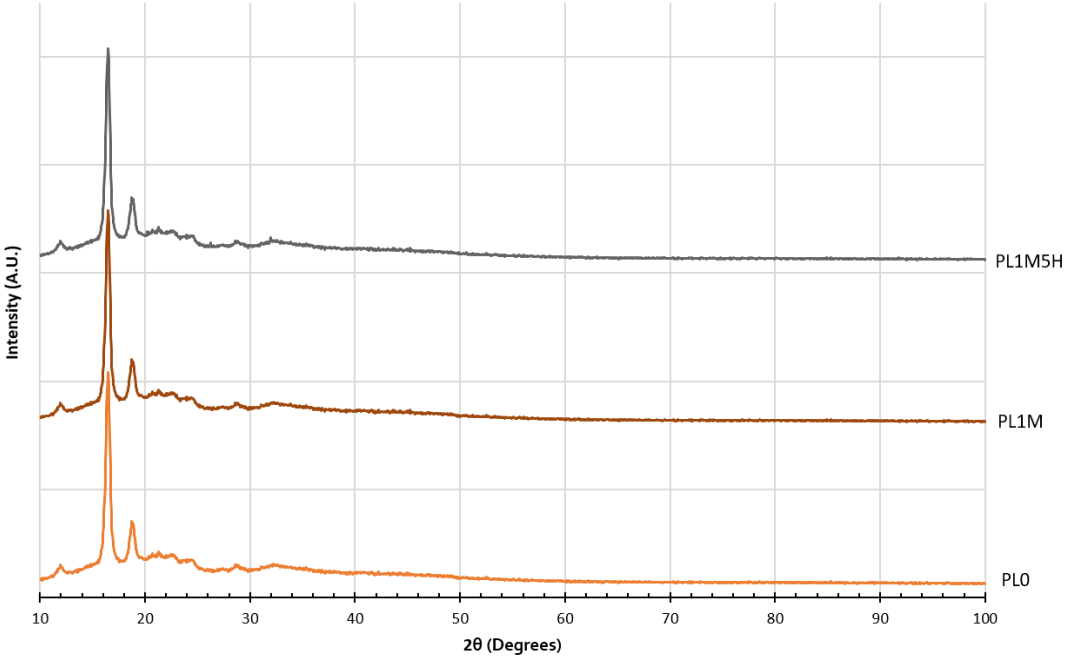


FIGURE 4.40: XRD pattern for PL0, PL1M and PL1M5H powders. Peaks located at $2\theta = 16.8°$ can be attributed to the (110) and/or (220) crystal plane, whereas, the reflection at $2\theta = 18.8°$ can be attributed to (203) and/or (213) crystal planes.Peaks at $2\theta = 12.2°$ is conserved for all the powders which is associated with (103)/(104) planes. Peak at $2\theta = 45.25°$ on both PL1M and PL1M5H can be attributed to the (400) reflection of MWCNT. PL1M5H contained additional peaks located at $2\theta = 26.25°$ and $2\theta = 32.65°$ and are associated with the (002) and (112) reflections of HA.

The mixed phase PLA powders were subjected to preheating conditions of 150°C for two hours to simulate the laser sintering preheating conditions, the change in crystal forms was examined and this can be seen in Figure 4.41. For the PL1M and PL1M5H preheated powders, the amorphous humps were significantly decreased compared to the PL0 powder, and the emergence of various new peaks were seen. The characteristic

peaks at $2\theta = 16.80°$ and $18.80°$, associated with (110)/(220) and (203)/(213) respectively, are still present for all powders. However, for the preheated powders several new peaks emerged. The peak located at $2\theta = 14.95°$, $22.25°$, $23.80°$, $24.75°$, $28.85°$ and $31.3°$ can be associated with; (110), (210), (213), (116), (310)/(020) and (101) crystal planes of an orthrombic α form PLLA crystal which has been reported to only form when isothermal crystallisation temperatures are above 120°C [304]. Therefore, the preheating of the PLA powders was enough to alter the crystal structure of the polymer.

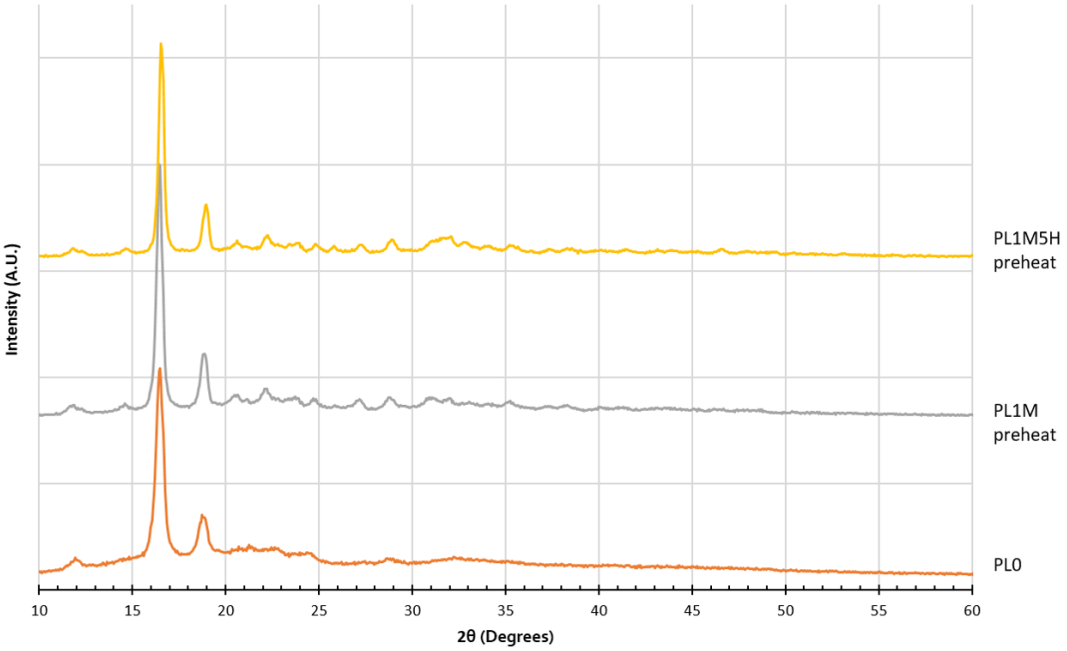


FIGURE 4.41: XRD pattern for PL0 and PL1M and PL1M5H powders that have been preheated inside the Sintratec at 150° for 2 hours. Characteristic peaks at $2\theta = 16.80°$ and $18.80°$, associated with (110)/(220) and (203)/(213) respectively, are still present for all powders. Preheated powders several new peaks emerged. The peak located at $2\theta = 14.95°$, $22.25°$, $23.80°$, $24.75°$, $28.85°$ and $31.3°$ can be associated with; (110), (210), (213), (116), (310)/(020) and (101) crystal planes.

4.10 Discussion

The procedure to coat pure PA12 powder particles was initially developed by Bai et al. [1]. For the first time, this method has been adapted for the production of a single and mixed phase coating of nHA and MWCNT-nHA on the surface of

PA12 and PLA particles. Detailed characterisation of the powder morphology, flow characteristics, powder behaviour during laser sintering (Chapter 5), structural and mechanical properties of the laser sintered nanocomposite (Chapter 6) and the cellular response to the material (Chapter 7) has been conducted.

Commercially available powders for laser sintering, such as PA12, have a near-spherical morphology and by using this coating method, the near spherical morphology of the original powder was maintained whilst also providing a high degree of surface coverage, as seen in Figure 4.4. Maintaining a near-spherical particle morphology has been shown to improve powder flow performance and lead to a more efficient packing density in comparison to cryogenically milled/ground powders which have a more angular morphology [41, 306, 307]. To enable the PA12 powder to be processed in a consumer laser sintering machine (Sintratec), MWCNTs were also added in the form of a mixed phase coating of MWCNT-nHA by the methodology as previously described. The near-spherical morphology and high degree of surface coverage was also maintained and this can be seen in Figure 4.6. The dual coating of MWCNT-nHA was also applied to PLA powder; in this case, the as-received PLA powder did not possess a near-spherical morphology, rather, it had a more irregular and angular shape when compared to the commercial PA12 powder (Figure 4.10). This was due to the cryogenic milling of the PLA to obtain a powdered form. As mentioned, this more irregular morphology impacts negatively upon the flow properties of the powder and will be discussed further below. However, despite the difference in particle morphology, the coating method adopted still provided a high degree of surface coverage, as seen in Figures 4.11 and 4.12. A further advantage of using this coating method was that large quantities of powder could be processed. For example, in the methodology developed here, up to 1 kg could be processed in a batch taking approximately 1 h. Therefore, this adapted method is more commercially viable method of producing other powders in-house, a simple scale up procedure could increase this to 100 kg. Typical methods of mixed phase powder production for laser sintering (discussed in more detail in Chapter 2) can be costly and time consuming [54, 246, 247, 257–259]. Furthermore, achieving good dispersion of NPs is vital as large agglomerates can lead to a reduction of mechanical properties, such as fracture toughness, modulus and UTS, of the final part being produced [1].

From TEM analysis and data provided by Promethean the approximate starting size of nHA particles was 30–40 nm in diameter and approximately 300–400 nm in length. At low concentrations of nHA, of 0.5 and 1 wt%, the degree of agglomeration of nHA on the surface of PA12 was minimal (Figure 4.5 (b)). Furthermore, when PA12 and PLA were coated with only MWCNT at 1.0 wt% (Figure 4.11) the MWCNT was dispersed on the surface of the particles with little to no signs of agglomerates. Due to the large surface energy that nano-phasic materials possess, the tendency to form agglomerates is high [308]. At increased loadings, the nHA became more difficult to disperse with visible signs of larger particle agglomeration on the powder surface, typically 300-400 nm in size, as shown in Figures 4.5 (c) and (d). The magnified images of the surface of the PA2H powder particle (Figure 4.9) showed that the agglomerated nHA appeared as platelets as opposed to rod shaped and were approximately 100 - 400 nm in length and 200 - 300 nm diameter. Bai et al.[1] also noted agglomeration as he increased the loading of MWCNT. However, the platelet like morphology observed at higher loadings of nHA more closely resembles the HA morphology in natural bone [309] [310]. A study by Priya et al. [309] has shown that size and morphology of nHA can have a significant impact on bone formation. It was found that the HOBs cultured on low aspect ratio, platelet like nHA stimulated greater osteogenic effects with higher levels of ALP production and matrix vesicle release compared to the higher aspect ratio of rod shaped morphologies [309]. In this study, the nHA's resemblance to a more platelet-like morphology, at higher loadings of 2.0 and 4.0 wt%, could potentially bring about positive effects regarding osteogenic activity, this is further explored in Chapter 7. It was also observed that the dual mixture of MWCNT and nHA, on both PA12 and PLA at 5.0 wt% nHA loading, led to a high degree of agglomerate formation due to the entanglement of MWCNT fibre like structures with the nHA particles. Therefore, the coating procedure adopted in this thesis is well suited to producing laser sintering powders with a high degree of surface coverage of nHA and MWCNT at relatively low concentrations (0.5 - 1 wt%) however, in regards to achieving highly dispersed NPs when loadings above 1 wt% are used the coating method has shown to be ineffective at achieving this. A lower nHA content may lead to improved mechanical properties of the final part, however, osteogenic responses to the material may not see any benefit.

Therefore, in this work, a compromise must be reached which balances the aspects of nHA distribution, powder processability, mechanical performance, and osteogenic responses, this will be further discussed in Chapters 5, 6 and 7.

Particle size can also affect powder flowability, surface finish, part accuracy and overall density of the part. Too small a particle size can lead to spreading difficulties due to static forces resulting in a more cohesive powder which is less able to flow [256] [41]. Conversely, too large a particle size can lead to poor surface finish and a shift of the processing window, requiring increased laser power to consolidate the particles due to the lower transfer of heat [256] [41]. Therefore, particles should ideally have a relatively narrow size distribution between 45 - 90 μm [256]. The particle size distribution curve in Figure 4.2 (a) showed that the addition of nHA or MWCNT-nHA did not significantly affect the average size of the particle. Even when processed with a relatively high loading of 4.0 wt% nHA, and a combination of 0.5% MWCNT and 5.0% nHA, the method adopted produced coated PA12 particles that maintained a narrow size distribution, with a Dx(10), Dx(50) and Dx(90) of 34.2$\pm$1.7 μm, 54.1$\pm$4.6 μm and 83.3$\pm$5.3 μm respectively, falling well within the reported optimum range. To obtain PLA in powdered form, the PLA was cryogenically milled by A.Schulmans (Figure 4.3 (a)). The as received PLA powder possessed a significantly wider particle size distribution (Dx(10), Dx(50) and Dx(90) of 62.3 $\pm$1.8 μm, 145.1$\pm$1.3 μm and 336.3$\pm$2.0 μm respectively), compared to the PA12 powders. Therefore, it was initially decided to sieve the PLA powder through a 150 μm sieve to obtain a smaller particle size (Figure 4.3 (b)), the Dx(10),Dx(50) and Dx(90) decreased to 59.7$\pm$0.6 μm, 107.4$\pm$0.3 μm and 182.8$\pm$1.4 μm respectively. However, it was noted that passing the asPL0 powder though the 150 μm sieve was time consuming and resulted in a low yield of powder. Furthermore, the poorer flow properties that the sieved PL0 exhibited led to the decision to coat the asPL0 powder as opposed to sieving prior to coating in the knowledge that a greater degree of energy may be required to process the powder. This may be in the form of slower scan speed, decreased scan spacing or an increase in laser power; this will be discussed further in Chapter 5. Upon addition of 1 wt% MWCNT and 1 wt% MWCNT + 5 wt% nHA, to the PLA powder, the resulting particle size did not display any significant deviation from the original asPL0 powder

with direct over lap of the curves. The Dx(10), Dx(50) and Dx(90) of the PL1M powder was reported as 61.5±3.4 μm, 147.1±2.5 μm, 339.6±2.5 μm respectively, whilst the PL1M5H displayed a slightly lower Dx(10), Dx(50) and Dx(90) 56.8±1.3 μm, 135.1±1.5 μm and 308.3±1.2 μm respectively. Therefore, similar to the PA12, the coating process conducted on PLA powders also had little to no effect on the particle size distribution and therefore demonstrated the robustness of the coating technique in obtaining high surface coverage without significantly altering the particle size for different powder types and various different loadings of NPs.

In laser sintering, how the powder flows and packs during layer deposition is crucial to the overall properties of the final part [306]. Frictional forces acting between adjacent particles can significantly influence how powders will flow [281, 311, 312]. During spreading operations in the laser sintering machine, powders experience low stresses and gravity is the main driving force for powder flow. For an unconsolidated powder bulk, the force of gravity must exceed the cohesive forces that exist between the particles in order to flow. As shown in Figure 4.42 for particle 1 to flow away from the others the force of gravity must exceed the cohesive forces that exist between particle 1 and its neighbours [281].

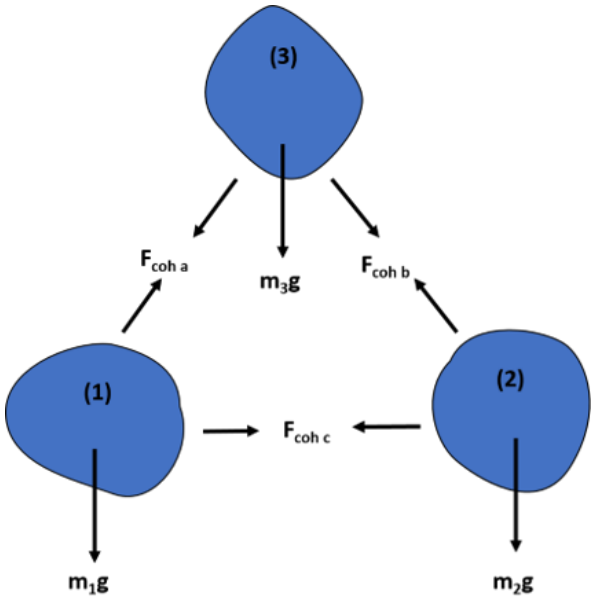


FIGURE 4.42: A force diagram adapted from [281]. For particle 1 to flow away from particles 2 and 3, the force of gravity must overcome the cohesive forces between its neighbouring particles.

Due to the unconfined stress during the upward movement of the rheometer blade the specific energy (SE) is a good descriptor of powder flow in low stress environments. The addition of nHA to the PA12 powders provided a lubricating effect which reduced the frictional forces acting between particles during powder movement. As shown in Figure 4.14 (a), the addition of 2.0 wt% nHA reduced the SE of the PA2H powder by 19% compared to that of the uncoated PA0 powder. Increasing the nHA content further to 4.0 wt% led to a further 27% reduction in SE for the PA4H powder compared to PA0. The cohesive forces existing between dry powder particles can be reduced by increasing the contact distance between them [313]; this is illustrated in Figure 4.43. The use of NPs being added to powder bulks to improve their flow properties has been well documented. Due to their small size and high surface area they adhere strongly to the powder particle surface compared to larger particles and thus a small quantity can lead to significantly improved flow performance [314] [313]. In this study, the presence of NPs on the surface of the powder particles allowed the particles to flow over each other more readily resulting in a less cohesive powder and resulted in a lower recorded SE compared to the uncoated powder.

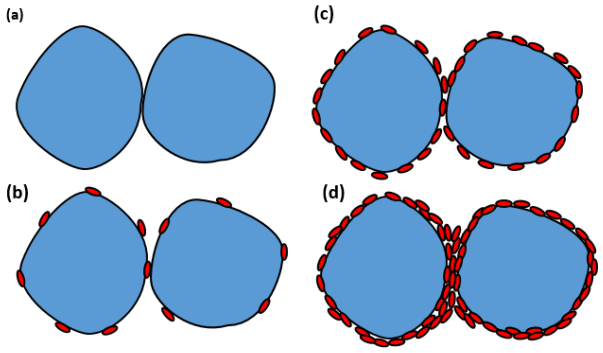


FIGURE 4.43: Illustration depicting PA12 particles (blue) with (a) no nHA and (b-d) increasing levels of surface nHA which results in lower frictional forces between adjacent particles (modified from [281]).

Due to their larger size and irregular morphology, the PLA powders on a whole recorded a significantly higher average SE compared to the PA12 powders, as seen in Figure 4.14 (b). The relatively poorer flow characteristics that the PLA powder exhibited may lead to decreased part density when compared to PA12. However, like the coated PA12 powders, the addition of MWCNT and nHA did provide a lubricating effect on the PLA powders, which improved their flow performance when compared to their neat

counterparts. The PL1M recorded a significant decrease in SE to 6.8 $\pm$ 0.1 mJ g^{-1}, representing a 6.8% reduction in SE, compared to the asPL0 powder which had a SE of 7.1 $\pm$ 0.1 mJ g^{-1}. PL1M5H led to a greater reduction in SE of 6.1 $\pm$ 0.1 mJ g^{-1}, a decrease of 13% compared to asPL0. When the asPL0 powder was sieved the corresponding SE increased to 7.2 $\pm$ 0.1 mJ g^{-1}. This was likely due to the increased presence of small irregular shaped particles, whereby the increased surface area led to higher mechanical friction and inter-lock between the particles resulting in a more cohesive powder and a higher SE.

As air occupies the spaces between powder particles, how the air interacts with it is another factor that can be used to assess the cohesivity of powders through its sensitivity to aeration. The test shown in Figure 4.16 (a) indicates that the addition of nHA causes the PA12 powder to become more sensitive to aeration as less air is required to suspend and separate the powder particles [281]. This was coupled with a drop in AE with less energy required to induce powder flow. The presence of MWCNT and MWCNT-nHA had also led to increased sensitivity to aeration for the PLA powders as seen in Figure 4.17 (b). The irregular shape and morphology of the PLA powders created a more turbulent flow of air around the particles thus making the powders very sensitive to aeration when compared to the PA12 powders. This is indicated by the steep reduction in total energy as the air velocity increased from 0 to 2 mm s^{-1}. The PL1M and PL1M5H recorded the lowest AE at 40 $\pm$ 3 mJ g^{-1} and 56 $\pm$ 3 mJ g^{-1} respectively at the maximum air velocity. This represented a 69% and 56% drop when compared to the asPL0. Due to the higher fraction of irregular, flattened PLA particles, following sieving, the sieved powder recorded the lowest sensitivity to aeration and highest AE of 128 $\pm$ 4 mJ g^{-1}, indicative of a powder displaying a highly cohesive nature which will yield poorer spreading characteristics.

A powder that is less cohesive in nature will be able to self-assemble more efficiently leading to higher packing density with less entrained air within the powder bulk. This was reflected in the compressibility and permeability tests. As the bulk packing state of the PA2H and PA4H was denser compared to the PA0 powders there was less entrained air within the powder bulk and less channels for which the air could escape through, the result of which (Figure 4.20 (a) and (b)) led to a significant decrease in the overall

compressibility for both PA2H and PA4H powders when compared to PA0. The PLA powders, PL1M and PL1M5H, also contained significantly less entrained air within the powder bulk, and thus had a lower compressibility, compared to the asPL0 and sieved PL0 powders. The higher packing efficiency of the coated powders is also supported by the permeability test (Figure 4.18 (a) and (b)) where the PA2H and PA4H are 29% and 36% less permeable compared to uncoated PA0 powders whilst the PL1M and PL1M5H also recorded a reduction in permeability of 7% when compared to the asPL0 powder, this is due to a reduction in air channels through which gas can escape through. This higher packing efficiency was also observed in the conditioned bulk density test (Figure 4.23 (a) and (b)) with coated powders recording, on average, a higher CBD than their neat counterparts. In a study by Cooke et al. [315] fumed silica, with a mean diameter of 12 nm, was added to potato starch (22.1 μm) powders and was seen to influence the dynamic and bulk powder properties. The addition of 0.01% silica dramatically increased the bulk density of potato starch powder by as much as 17%. This was also accompanied by a 50% reduction in permeability. Furthermore, dynamic testing revealed that a 0.05% content decreased interparticle friction resulting in a 18% reduction in SE. Using flow measurements such as these can be a useful predictive tool for powder perfroamnce during laser sintering. For example Lyckfeldt et al. [316], was able to distinguish between stainless steel powders performing differently during selective laser melting despite having similar particle sizes. Dynamic testing showed that the poorest performing powder had a significantly higher SE at 4.84 mJ g^{-1} compared to 2.18 mJ g^{-1} of a powder that performed well. The poorest performing powder also had the lowest sensitivity to aeration and high degree of compressibility indicating that the powder had a higher cohesive nature resulting in poorer flowability and packing densities once deposited [316]. Therefore, the surface coating of nHA and nHA-MWCNT improves the flowability and bulk packing density of the powder by increasing the contact distance between adjacted powder particles and thus decreasing the inter-particle van der Waals forces. This improved flow performance is beneficial for achieving uniform layers during powder deposition, which may translate across to increased and more uniform, densities throughout the final part [317].

In addition to powder morphology and size, the thermal properties of the powder are

an important consideration for laser sintering. Materials for laser sintering, ideally, have a narrow melting range with no overlap of the melting and crystallization peaks [229]. The DSC traces, shown in Figure 4.24 (a), of neat and coated PA12 powders all displayed a prominent melting and crystallisation peak with a clear separation between the two. The exothermic, crystallisation event was a result of the favourable energetic conditions promoting polymer chain mobility and re-ordering. This typically occurs first through formation of parallel arrays, which form a nucleus and is stabilised by secondary valence forces, which is then followed by nuclei growth [318] [319]. The addition of nHA caused the average peak crystallization temperature to shift upwards by 8.6°C from 0 wt% loading to 4.0 wt%. Similarly, the PLA based powders (Figure 4.25 (b)) also displayed two prominent melting and crystallisation peaks and upon addition of MWCNT and MWCNT-nHA the crystallisation curves for the PL1M and PL1M5H shifted upwards by 2.2°C. Both PL1M and PL1M5H displayed identical peak crystallisation temperatures. Yan et al. [240] coated PA12 powders with micron sized aluminium particles and also observed an increase and narrowing of the crystallisation temperature range. Furthermore, Papageorgiou et al. [320] observed this effect when studying PLLA nanocomposites using various inorganic fillers such as Silicone oxide (SiO_2), MWCNT and Montmorillonite (MMT). Similar effects were also seen in nylon 6/clay nano-composites [34] and in PA12/MWCNT powders [260]. This suggests that the presence of the NPs on the surface of the polymer particles provided a strong heterophase nucleation effect which altered the early crystallisation mechanism. This could lead to a more rapid rate of crystallisation from the melt when compared to the neat polymers and would infer a narrowing of the laser sintering window for the coated powders.

The DSC results for PL0, PL1M and PL1M5H, showed a small endothermic peak at $\approx$ 114°C. To gain further insight into the thermal history of the pure PLA powder, PL0 was subjected to multiple heating and cooling cycles as seen in Figure 4.26. During the second heating cycle, a small exothermic depression at 163°C could be observed which was indicative of a slight change to the crystallinity of the sample and a higher proportion of semi-crystalline component [321]. Following melt quenching, after the second heating cycle, a significant change to the third heating curve was

observed. A broad exothermic peak could be observed at 93.0 $\pm$ 0.4°C, a clear sign that cold crystallisation had taken place. Thus, the PLA was completely amorphous after quenching which was also confirmed by the lack of an exothermic, crystallisation peak during quenching. This indicated that the as-received, PLA powder had been thermally heat treated to obtain a relatively high crystalline fraction. Using the reference melting enthalpy of fusion for 100% crystalline PLA (93 J g^{-1} [322]), the % crystallinity was calculated to be 40 $\pm$ 1%. This high degree of crystalline component infers relatively high mechanical stiffness (discussed further in Chapter 6). However, the relatively high % crystallinity of the as-received powder can affect part accuracy during laser sintering caused by crystal shrinkage due to a decrease in specific volume, below the melting temperature, through polymer chain re-organisation [230]. The presence of the small endothermic peak at $\approx$ 114°C was still present during all heating cycles and therefore suggested the presence of residual lactide impurity from the manufacturing of the PLA powder [291] [323]. This was likely from the ring opening polymerisation (ROP) production step used to obtain high molar mass PLA [323]. Residual lactide impurity within the PLA may lead to faster hydrolytic degradation of the PLA [323].

In the studies mentioned previously, a standard heating and cooling rate of 10 - 20°C min^{-1} was used and is an idealised representation of the laser sintering conditions with uniform heating and cooling of the polymers. In reality, the heating and cooling, during and post exposure to the laser is more complicated due to uneven in-process and post-process cooling [324]. As polymer crystallisation is time dependent, the lower cooling rates provide sufficient time for the polymer chains to adopt a less energetic configuration and thus crystals can form at higher temperatures [325]. The crystallisation studies, as seen in Figure 4.28 (a) and (b), showed that the cooling rate had a significant affect on crystallisation. The peak Tc for PA12 and PLA powders shifted to higher temperatures due to the nucleating effect of the NPs. This effect was more pronounced on the coated powders when compared to their neat counterparts. The coated powders, on average, displayed elevated peak Tc at all cooling rates. Drummer et al. [324] also demonstrated this with PA12 powders which were subject to different cooling rates from melt. It was observed that with lower supercooling the crystallisation process occurred well before the assumed crystallisation temperature

was reached, under standard cooling rates of 10 - 20°C min^{-1} [317]. This was also observed by Amado et al. [2] (Figur 4.44). Papageorgiou et al. [320] also noted this effect in their studies in which PLA/MWCNT nanocomposites were shown to possess a significantly higher peak Tc during the non-isothermal studies when compared to neat PLA, demonstrating the effectiveness of MWCNT acting as a nucleating agent [320].

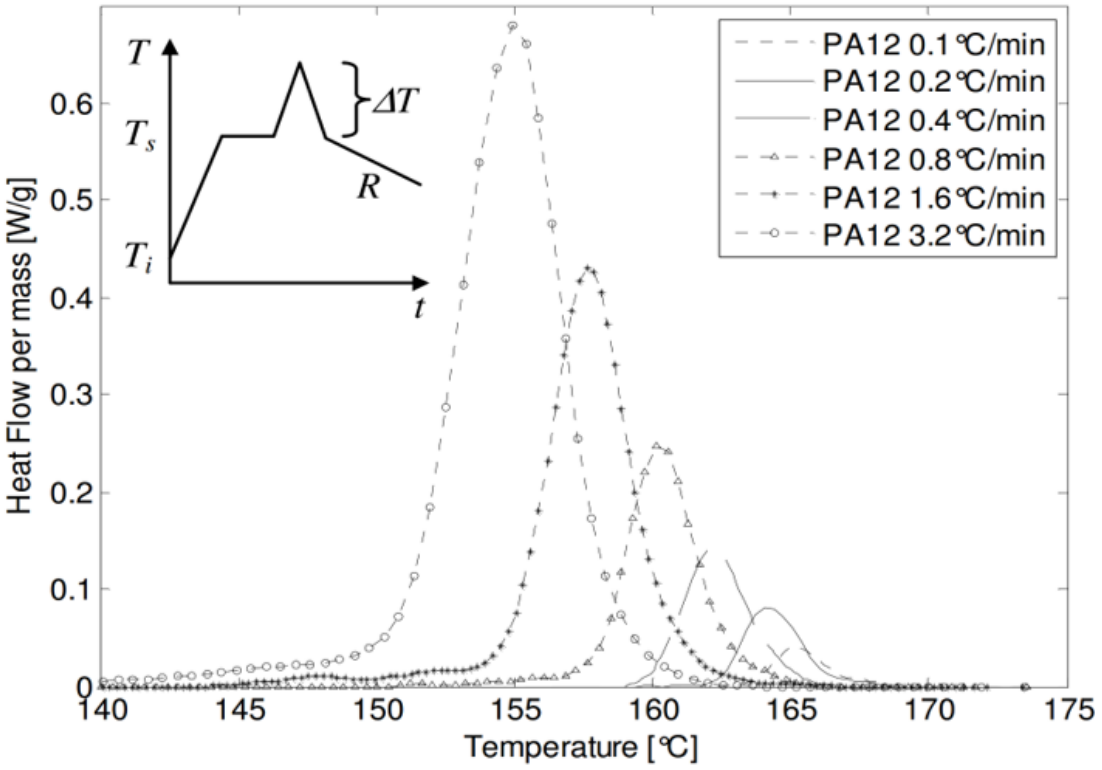


FIGURE 4.44: Non-isothermal curves for PA12 at various cooling rates. Reduction in cooling rate shifts the peak crystallisation to higher temperatures [2]

.

Polymer crystallisation is highly time and temperature dependent, therefore isothermal crystallisation studies were also conducted to assess the impact that nHA and MWCNT had on the early stages of crystallisation. As seen in Figures 4.29 and 4.30 the presence of nHA and MWCNT was found to significantly increase the crystallisation rate of both coated PA12 and PLA powders, with peak crystallisation being achieved sooner across all isothermal temperatures, when compared to the neat powders. As the isothermal temperature was increased, the rate at which crystallisation occurred decreased and in some instances peak crystallisation was not observed within the time frame of the study. The Hoffman-Lauritzen model offers a good description of the

nucleation process. Due to the excessive free energy, as the isothermal temperature is increased towards the melt temperature, the crystal nuclei formation was disrupted before growth could occur, this in turn increases the time taken for the polymer crystallisation to occur. The opposite is true when temperature is decreased towards the Tg [318] [326]. Use of the Avrami model, as described in Chapter 3, the DSC software was able to yield double-log plots, as seen in Figures 4.31 and 4.33, the linear portion of the plot corresponds to the primary stages of crystallisation. Early work by Blundell et al. [327] on carbon-fibre/PEEK composites indicated that crystal nucleation can occur at the fibre interface given the right thermal conditions. It was suspected that the presence of the additives hindered the polymer chain mobility thus making nucleation at the fibre-matrix interface more preferential and thus led to a change in the crystallisation mechanism [327]. This alteration of the crystallisation mechanism has also been observed in other polymer nanocomposites such as PE-CNT [328] and PLLA/nHA [329]; in both systems accelerated crystallisation in addition to a reduction in Avrami exponent has also been reported. In this study, the DSC analysis software applied a linear fit to the data to yield the Avrami exponent (n) which is related to the structure and nature of crystal nucleation [330]. As seen in Table 4.10 and 4.11, the PA0 and PL0 powders tend to a value of ≈ 3 which was indicative of three-dimensional spherical growth of homogeneously nucleated spherulites [293] [294]. Amado et al. [2] also observed this form of crystallisation through his isothermal studies on PA12 and studies by Zhou et al. [329] also noted spherical growth of PLLA crystallites during isothermal analysis with the Avrami exponent approaching the value of 3. The spherical crystal growth was also confirmed by visualisation of PLLA cross sections under polarised light microscopy [329]. The presence of nHA and MWCNT-nHA led to an alternate nucleation mechanism with the Avrami exponent approaching the value of $\approx$ 2, apart from PA4H at 168°C, which may be explained by the additional thermal energy. This corresponded to a two-dimensional, plane growth, crystallisation mechanic [2] and is consistent with the findings reported in the literature above.

For the NP additives to catalyse the nucleation process the polymer must first wet the surface of the NPs, as illustrated in Figure 4.45, where r is the radius of the curvature of the nucleus cap, Y_{s-1} is the solid-liquid interfacial energy, Y_{c-s} is the solid-catalyst

interfacial energy and Y_{c-1} is the liquid-catalyst interfacial energy [331]. In the case of heterogeneous nucleation in the form of a spherical cap, the surface energy of the NP surface, as it is coated by the nucleus, can be expressed as [331]:

$$\Delta G_{surface} = 2\pi r^2(1 - cos\theta)Y_{s-1} + \pi r^2(1 - cos^2\theta)(Y_{c-s} - Y_{c-1}) \tag{4.1}$$

The volumetric Gibbs free energy change can be expressed by the product of the volume of the nucleus cap and the specific free energy change, ΔG_v, in terms of the radius of the curvature and contact angle, taken from [331]:

$$\Delta G_{vol} = \frac{4}{3}\pi r^3 \Delta G_v f(\theta) \tag{4.2}$$

$$f(\theta) = \frac{(2 + cos\theta)(1 - cos\theta)^2}{4} \tag{4.3}$$

$$r^* = -\frac{2Y_{s-1}}{\Delta G_v} \tag{4.4}$$

$$\Delta G^* = \frac{16}{3}\frac{\pi Y_{s-1}^3}{\Delta G_v^2} f(\theta) \tag{4.5}$$

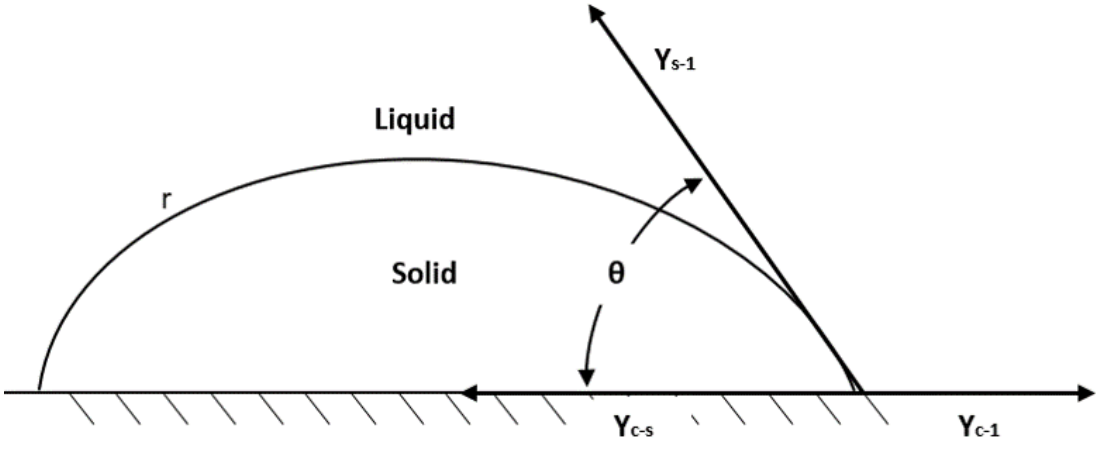


FIGURE 4.45: Illustration of wetting and nucleus cap formation on the surface of the nanoparticle (adapted from [331]).

The critical Gibbs free energy, ΔG^*, is strongly influenced by the wetting that occurs on the NP surface. And by observing the ΔG as a function of radius of curvature

of the nucleus the impact of wetting on the ΔG^* for nucleus formation can be seen (Figure 4.46) [331].

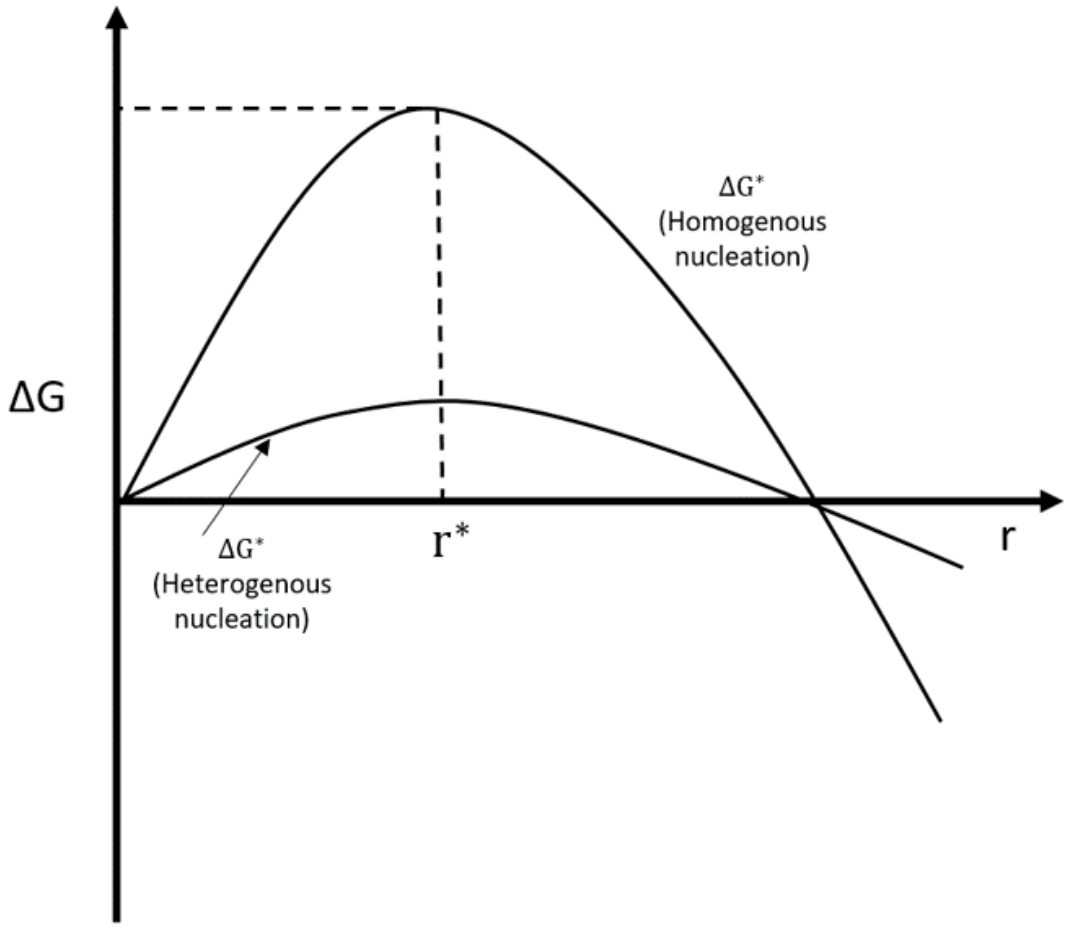


FIGURE 4.46: Plot of ΔG vs r for homogenous and heterogenous nucleation. A decline in ΔG^* through wetting on the surface of nucleating agent reduces the activation energy needed to be overcome for nucleation (adapted from [331]).

The crystallisation activation energy was calculated from plots of $lnK(tc)vs1/T$ (Table 4.10 and 4.11) by application of the Arrhenius equation (Chapter 3) [331]. It showed that the presence of nHA and MWCNT-nHA also led to an increase to the nucleation activation energy of the coated powders. Drummer et al. [324] used the activation energy as a tool for assessing the robustness of a semi-crystalline polymer during laser sintering. When comparing PA12, POM and PEEK powders, PA12 had the lowest activation energy at 332 $\pm$ 216.2 J mol^{-1} whereas POM and PEEK possessed higher activation energies of 986.7 $\pm$ 29.5 and 636.0 $\pm$ 21.3 J mol^{-1} respectively. Thus the POM and PEEK powders were shown to be more sensitive to temperature

gradients near the crystallisation temperature. Polarised light microscopy of the upper surface of microtome cuts made from laser sintered samples of PA12, POM and PEEK showed that PA12 had molten particles at the interface between the part and the surrounding powder bed whereas the POM and PEEK had orientated crystals on the upper surface which indicated that crystallisation took place before particles of the next layer could be molten [324]. Zhou et al. [54] also observed an increase in the activation energy in PLLA/HA compososites when compared to neat PLA and linked this observation to the increase in crystallisation rate observed for the PLLA/HA composite. In this work, due to the strong nucleating properties that NPs possess, their presence as a coating on the surface of the polymer powders had a significant impact on the crystallisation behaviour of the PA12 and PLA. The reduction in the nucleation activation energy is consistent with the rapid increase in crystallisation rate observed during the isothermal studies and is consistent with observations made on other polymer nanocomposite systems in literature [332]. Therefore, the coated powders may respond differently during laser sintering, compared to their neat counterparts. This will be further examined in Chapter 5.

Due to the absence of external shear forces acting on the polymer melt during laser sintering, the zero-shear viscosity (η_0) is an important rheological parameter for the consolidation of polymer particles, as discussed in Chapter 2. Thus the melt rheological properties of the coated PLA powders were studied at low shear rates (1x10^{-4}-1.0 s^{-1}) to more accurately reflect the laser sintering conditions. PA12 powders were omitted from this test due to difficulties in removing PA12 residue from the equipment. The addition of NPs led to a significant rise in the melt viscosity; as seen in Figure 4.35, the zero shear viscosity increased substantially. The PL1M and PL1M5H powders led to a rise in zero-shear viscosity by 41% and 75% respectively, when compared to PL0. In a study conducted by Hyun et al. [333], it was found that the mass content of organclay nanoparticles, in a poly(ethylene oxide)/organoclay nanocomposite, had a significant influence on the rheological properties. The addition of 2 wt% and 5 wt% organoclay saw a substantial 97% and 233% increase in zero shear viscosity [333]. Similarly, Yang et al. [334] observed the melt flow behaviour of isotatctic polyethylene/CNT nanocomposite systems and observed a progressive increase in the

shear viscosity properties of the nanocomposites with increasing CNT loading from 0 - 5 wt%. The degree of shear thinning behaviour also increased with CNT content suggesting that the CNTs became aligned along the flow direction as shear rate was increased. The increase in shear thinning response observed for the PL1M and PL1M5H would also point to this phenomenon occurring for these powders. For micron-sized spherical fillers, the viscosity of pure polymer melts is expected to increase and is predicted by the Einstein-Batchelor law [335] [336]. However, when dealing with low aspect ratio nanoparticles, viscosity can either increase or decrease relative to the pure polymer and is dependent on filler-filler and filler-polymer interaction [336]. The Kregier-Dougherty model [337] predicted a 10-fold increase in polystyrene/silica nanocomposite at 50 wt% silica loading; due to the highly-dispersed nature of the silica particles and their small size of 16 nm. However, a 0.2 - 0.3% decrease in viscosity was actually observed [336]. Due to the high surface area that high aspect ratio nanoparticles possess, the attraction forces between them is high. For the PLA powders studied in this work, the formation of locally or globally connected structures between the NPs, as evidenced by the SEM images in Section 4.3, in the polymer matrix through attractive interactions contributed to the rise in viscosity of the polymer melt. This has also been observed in PLA/graphene nanoocomposites with high aspect ratio graphene particles at loadings between 1 - 14 wt% [338] and in PLA/nanoclay composites with observed increase in viscosity due to formation of stacks of intercalated layers which were randomly orientated within the polymer matrix forming a connected 3D network [339]. Thus the interaction between the NPs within the polymer matrix affects the polymer's melt flow behaviour through hindrance of polymer chain mobility and internal friction between the NPs themselves. The zero-shear viscosity has a strong influence on dimensionless neck formation between adjacent polymer particles during laser sintering and is governed by the Frenkel-Eshelby equation (Chapter 2). The increase in viscosity is likely to lead to greater generation of pore formation and less consolidation between the polymer particles, this in turn will impact upon the mechanical properties of the final part. As mentioned in Chapter 2, Shi et al. [239] investigated the processability of PS powders with different melt viscosities (MFI of 3 cm^3/10 min and 8 cm^3/10 min respectively) and found that PS powders with a higher viscosity resulted in structures

that were less dense and had a higher degree of porosity when compared to PS powders of lower viscosity. PA12 is reported to have a melt viscosity of 100 Pa.s and is capable of achieving full consolidation [340]. In this work, a significantly higher viscosity for PLA and coated PLA powders was observed. This substantial increase in the viscosity of the powders may lead to difficulties in establishing good consolidation between particles at higher scan rates, thus determination of the laser speed will be important in achieving good consolidation between particles.

CO_2 lasers are commonly employed in commercial laser sintering systems. The Formiga P100 used in this study has a CO_2 laser operating at 10.6 μm. HA has been shown to strongly absorb at this particular wavelength and this property of HA has been explored in the field of dentistry with the treatment of hypersensitive teeth caused by exposed dentin tubules using nHA pastes [341]. This was confirmed in the FTIR results, given in Figure 4.36, where the addition of nHA resulted in a new peak located at 1032 cm^{-1}. The intensity of which increased with higher nHA content. This can be associated with the PO_4^{-3} bending vibration which is characteristic to HA. Therefore the surface coating of nHA should act to increase the absorption of the incoming CO_2 laser. Similarly, from the UV-Vis data seen in Figure 4.37, the presence of MWCNT also increased the laser absorption of the powder at 445 nm, which corresponds to the wavelength of laser used in the consumer Sintratec machine. An increase in absorption could be seen for the PA05M powders compared to PA0 powders, which have no processability in the Sintratec. Similarly, the PLA powders also saw an increase in absorption across the 300 - 800 nm range following the addition of 1 wt% MWCNT. The addition of nHA did not affect the absorption at wavelengths between 420 - 500 nm due to the entanglement of nHA particles with MWCNT from the coating procedure, this was also the case for the PL1M5H powder. For the PA12 powders, a large absorption peak was seen at 250 nm for all powders and this was due to amide bond absorption, which is the shoulder of the -CO-NH- band [300]. The absorption peak maxima at 290 nm caused by a large transition from the π to π* electronic band suggests the presence of aromatic groups within the chemical structure of PA12 which may be involved in controlling the thermal characteristics of the powder [300]. These series of peaks share a similar UV-Vis profile to proteins which also possess aromatic side groups and peptide bonds

[342]. The presence of this strong absorption peak suggests that alternative lasers in the 280 - 220 nm region could potentially be used for laser sintering of uncoated PA12 powders. The shoulder of a C-O peak caused by π-π^* transition could be observed for the PL0 powder at 290 nm, however PL1M and PL1M5H displayed red shifting of this peak to 350 nm suggesting some interaction between the PLA matrix and NP coating perhaps through hydrogen bonding [301].

X-ray diffraction studies on the coated PA12 powders before and after laser sintering, as seen in Figure 4.39, show the appearance of two distinct peaks at $2\theta = 21.25^\circ$ and 21.30° for the un-sintered powder. These reflections have been reported to correspond to an unstable, monoclinic, α-phase [343] [203]. Upon laser sintering, this double peak collapses into a single intense peak at $2\theta = 22.14^\circ$ and has been attributed to a more thermally stable γ-phase [343] [203]. This transition from an unstable α-phase to a stable γ-phase (hexagonal) has been observed in other studies when observing the crystal structure of PA12 from melting to cooling [344] [345]. This gamma phase reportedly provides toughness, to melt processed PA12, as it is believed to be more ductile and less stiff compared to the α-phase and thus influences much of the mechanical behaviour of the laser sintered parts [346], this is discussed further in Chapter 6. Furthermore, characteristic peaks associated with HA can also be seen, on both the coated PA12 powder and sintered discs, at $2\theta = 25.86^\circ$, 31.78° , 32.18° , 32.91° and 34.06° corresponding to (002), (211), (112), (300) and (202) crystal planes [303]. These peaks are also present on the pattern for neat HA although the intensity is significantly higher compared to the coated powder due to the relatively low amount of nHA used to coat the PA12 particles. It is also evident on the pattern for the laser sintered discs that the localised temperature of the laser acting on the powder particles did not decompose nHA to tri-calcium phosphate and therefore nHA was not affected by the laser sintering and remained phase pure [347]. The XRD scans for the PLA powders can also be seen in Figure 4.40. The prepared powders display characteristic peaks associated with PLLA. The peaks located at $2\theta = 16.8^\circ$ is associated with the (110)/(220) crystal plane whereas the peak at 18.8° is associated with the [203]/[213] planes [304]. A weaker peak located at $\theta = 12.2^\circ$ is conserved for all the powders which is associated with (103)/(104) planes, which is characteristic

of the α crystal form which can be formed when the crystallisation temperature is greater than 120°C this would suggest that the powder may have been processed at some time above 120°C to allow formation of the α crystal phase [304]. The pattern for PL1M and PL1M5H appeared very similar to the PL0 powder, however, a very weak signal detected at $2\theta = 45.25°$ on both PL1M and PL1M5H can be attributed to the (400) reflection of MWCNT. Powders used for laser sintering are typically preheated to temperatures $\approx$ 10°C below their material melting point and held isothermally for 2 hours to ensure the powder is at a homogeneous temperature. For PLA powders, this preheat temperature is generally around 150°C. The coated PLA powders were subjected to preheating conditions of 150°C for 2 hours and the change in crystal forms was also examined, this can be seen in Figure 4.41. For the PL1M and PL1M5H preheated powders, the amorphous hump is significantly decreased compared to the PL0 powder, and the emergence of various new peaks could be seen. The characteristic peaks at $2\theta = 16.80°$ and 18.80°, associated with (110)/(220) and (203)/(213) respectively, are still present for all powders. However, for the preheated powders several new peaks emerged which are associated with (110), (210), (213), (116), (310)/(020) and (1010) crystal planes of an orthrombic α form PLLA crystal which is has been reported to only form when isothermal crystallisation temperatures are above 120°C [304]. Therefore, the preheating of the PLA powders was enough to alter the crystal structure of the polymer.

Following coating and characterisation of PA12 powders with NPs, the powders were then processed by laser sintering in the Formiga P100 and Sintratec machines. The parameter windows for each of the powder compositions was initially determined before producing laser sintered parts for cellular and mechanical assessment. This is reported in the following chapter.

Chapter 5

Laser Sintering of nano-coated powders

This chapter explores the processing of coated PA12 and PLA powders in both a commercial (Formiga P100) and consumer (Sintratec) laser sintering system. Laser sintering parameters such as powder bed temperature, scan speed and scan spacing were explored to gain a better understanding of how these parameters affect powder fusion, part warping (curl) during the build and assess what further impact the addition of nanoparticles on the surface of the polymer particles have on processing. It was hypothesised the nHA coating will affect the laser sintering parameters, requiring a greater input of energy density to fuse the powder particles, due to the nHA acting as a thermal barrier and reducing the thermal transfer through the powder bulk. Due to the effect that nHA has on polymer re-crystallisation it was also hypothesised that the coated powders may be more sensitive to powder curl, but not significant enough to cause build failure. Therefore, in Sections 5.1, 5.2 and 5.3 establishes the powder bed temperature and laser sintering parameter window for each of the powder compositions. Visual observations based on curl development, dimensional accuracy (average dimensional error of the final part being $\leq$10% of the target dimension, Chapter 3) and handleability were semi-quantified leading to the selection of the final parameters used for the production of mechanical and cellular test pieces. Section 5.4, details the SEM analysis performed on monolayers to assess the degree of particle fusion of

PA12-MWCNT-nHA and PLA-MWCNT-nHA powders that were processed in the Sintratec. Section 5.5 presents an overall discussion on the results obtained from the laser sintering of nanocoated powders.

5.1 Processing of PA12-nHA in the Formiga P100 laser sintering machine

5.1.1 Determination of the powder bed temperature of PA12-nHA powders

During laser sintering, the powder is preheated and held isothermally to minimise thermal gradients, as detailed in Chapter 3 [41]. To determine the optimum powder bed temperature for processing, the powder was spread across the build platform and heated until agglomeration or darkening of the powder bed surface occurred. The results of this test can be seen in Table 5.1.

TABLE 5.1: The results from the spreading test for the neat PA12 and coated PA12 powders conducted in the Formiga P100. ✓denotes good, even spreading of the powder across the build platform. × denotes powder bed clumping and caking occurring across the build platform. The addition of nHA causes the maximum spreading temperature to increase slightly.

Temperature (°C)	PA0	PA05H	PA1H	PA1.5H	PA2H
170	✓	✓	✓	✓	✓
171	✓	✓	✓	✓	✓
172	✓	✓	✓	✓	✓
173	✓	✓	✓	✓	✓
174	✓	✓	✓	✓	✓
175	✓	✓	✓	✓	✓
176	✓	✓	✓	✓	✓
177	✓	✓	✓	✓	✓
178	×	×	×	✓	✓
179	×	×	×	×	×
180	×	×	×	×	×

The optimum temperature for laser sintering should be set as high as possible without causing the powder bed to agglomerate as this can have adverse effects on powder

spreading. Thus, the laser merely acts to tip the material over its melting point. For PA0, PA05H, PA1H and PA1.5H these were 183.6 $\pm$ 0.9°C, 184.1 $\pm$ 1.0°C, 183.5 $\pm$ 1.4°C, 184.9 $\pm$ 0.6°C respectively. For the PA0 powder, the maximum temperature before caking was observed to be 176°C; with the addition of 0.5 wt% nHA the PA05H powder had a slightly higher maximum processing temperature of 177°C. The PA1H powder also recorded a maximum temperature of 177°C. However, increasing the nHA loading further led to a higher powder bed temperature of 178°C for both the PA1.5H and PA2H powders. An example of the powder bed beginning to cake can be seen in Figure 5.1. Early signs of powder bed agglomeration can be seen for the PA05H powder, as the temperature exceeded 177°C, with the powder bed surface appearing rough and chapped at the front left corner of the build platform.

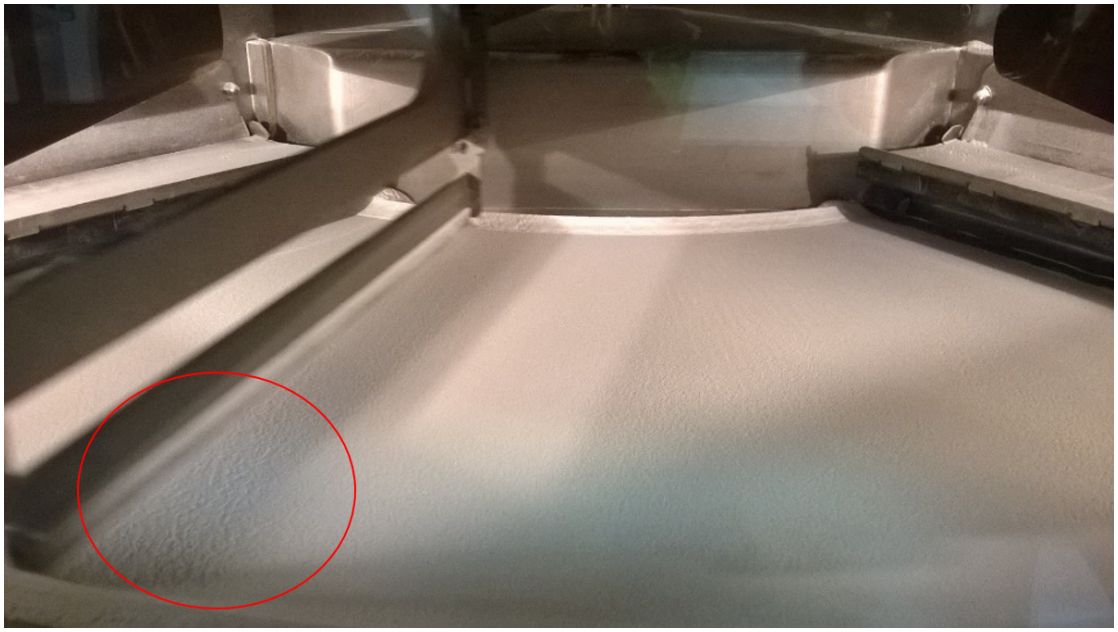


FIGURE 5.1: Image taken of PA05H powder being spread across the build platform of the Formiga P100 at 178°C. Early signs of powder caking can be seen in the lower left corner, as highlighted by the red circle.

5.1.2 Laser sintering parameters for PA12-nHA powders

For the processing of pure PA12 powder in the Formiga P100, the typical processing parameters used are a laser powers of 21 - 25 W, scan speed of 2500 mm s^{-1} and a scan spacing of 0.25 mm. Based on this knowledge, the powders developed in this

work were tested at varying laser powers of 2 - 25 W and varying laser speeds of 800 - 3000 mm s^{-1}. This covered a range of parameters that represented the higher and lower end of energy densities compared to what is typically used to process pure PA12 (0.033 J mm^{-2}) in the Formiga P100. To minimise the number of settings used, the scan spacing and layer height were fixed at 0.25 mm and 0.1 mm respectively, and from the results of the bed temperature test, the processing parameters were tested at 176 - 178°C. The parameters used during testing are summarised in Table 5.2.

TABLE 5.2: Parameters used for the testing of nHA coated PA12 powders in the Formiga P100.

Formiga P100: parameters
Laser Power: 2 - 25 W
Scan Speed: 800 - 3000 mm s^{-1}
Scan Spacing:0.25 mm
Layer Height: 0.1 mm
Powder bed temperature: 176 - 178°C

It was observed that the PA0 powders possessed a significantly wider processing window than the coated PA12 powders. The results of this test can be seen in Figure 5.2. Based on visual observations, parts that were completed, with no signs of warping and had good dimensional accuracy (as defined in Chapter 3) were deemed successful. For the PA0 powders, successful builds were possible within the energy density (ED) range of 0.1 - 0.005 J mm^{-2}. Below an ED of 0.005 J mm^{-2}, the edges of the specimens distorted and warped upwards after consecutive layers were built, which caused the re-coater blade to catch on the raised edges and drag the build off the platform resulting in a failed build. By decreasing the ED further the parts became very fragile due to insufficient fusion between the particles, and fell apart upon removal from the build platform. Above 0.1 J mm^{-2}, visible signs of over sintering and polymer degradation were detected with white plumes of polymer vapour being emitted along the laser scan path, this became worse as the ED was increased further. The addition of 0.5 wt% nHA caused a narrowing of the overall processing window when compared to PA0 (Figure 5.2 (b)). For the PA05H powder, the ED range at which successful builds could be accomplished was determined to be between 0.08 - 0.0057 J mm^{-2}. Again, above the upper ED limit, polymer degradation and warping occurred and below the ED limit, parts were either distorted or fragile. When the nHA loading was increased further, to

1.0 wt%, the PA1H powder displayed a significant reduction in the processing window making the ability to produce successful builds challenging (Figure 5.2 (c)). Successful builds were only possible between an ED range of 0.032 - 0.008 J mm^{-2}. Above 0.032 J mm^{-2}, the powder exhibited significant curling around the edges of the part whilst the laser was scanning. Unlike the curl development witnessed for the PA0 and PA05H powders, which occurred gradually after consecutive layers of powder was deposited, this form of curling occurred instantaneously and led to the re-coater blade catching and pulling the part off the build platform. At a loading of 1.5 wt% nHA (Figure 5.2 (d)) the processing window for PA1.5H was again significantly reduced. The ability to produce successful parts was restricted to an ED range between 0.016 - 0.0032 J mm^{-2}. Similar to the curling phenomenon that occurred for PA1H, at ED greater than 0.016 J mm^{-2}, the PA1.5H powder significantly curled around the edges of the part.

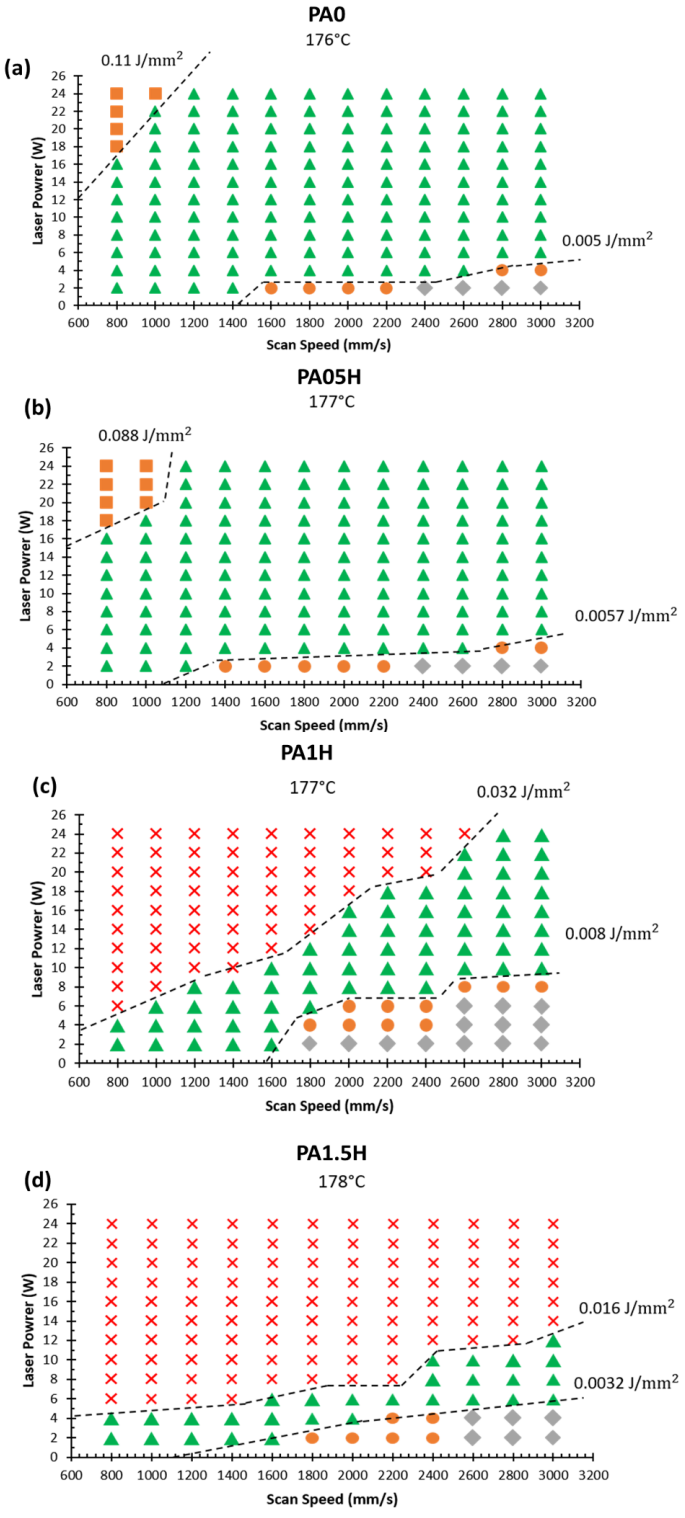


FIGURE 5.2: Graphs showing laser power vs scan speed and the resulting laser sintering processing windows for (a) PA0 powder processed at 176°C, (b) PA05H powder processed at 177°C, (c) PA1H powder processed at 178°C and (d) PA1.5H powder processed at 178°C. Symbol X represents instantaneous curling of the initial layer, square represents gradual curl development after 5-10 successive layers resulting in part failure and diamond represents under sintered parts that either shifted on the powder bed or were too fragile to handle. Note that as the nHA content increased the laser sintering processing window narrowed significantly.

The PA1H, PA1.5H powders predominately failed due to excessive curling around the edges during laser scanning. In Figure 5.3, substantial curling around the edges of the part can be seen which led to the re-coater blading catching and pulling the part off the build platform.

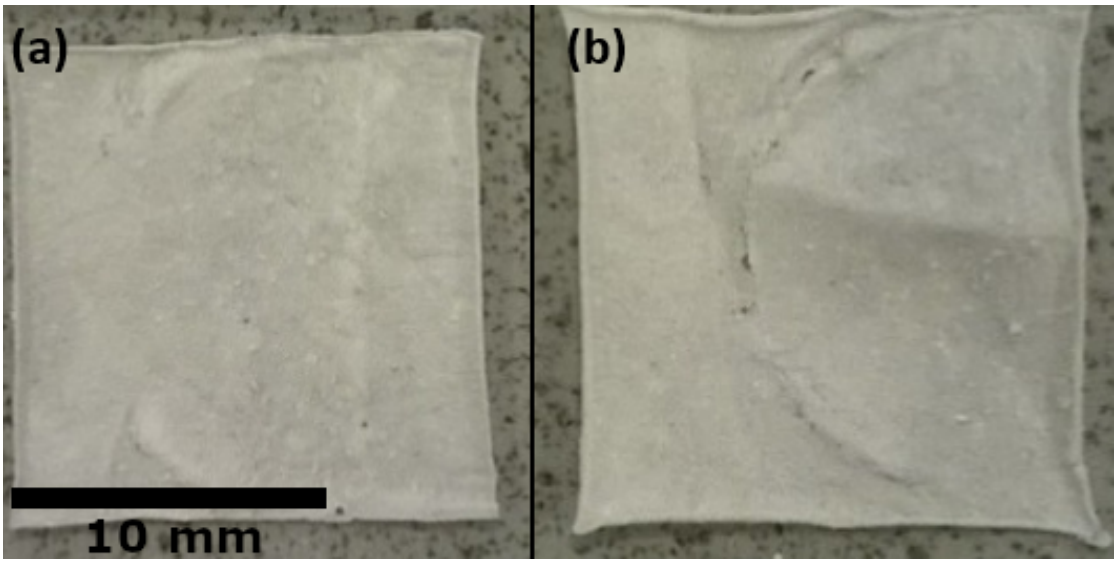


FIGURE 5.3: Recovered failed builds of specimens processed using PA1.5H powder at (a) 10 W at 2600 mm s^{-1} and (b) 18 W at 2600 mm s^{-1}. Curling was more prominent at higher energy densities.

When processing the PA2H powder, at all combinations of laser power and scan speeds tested, no successful parts could be achieved. Once again substantial curling led to the part being pulled off the build platform by the re coater blade and if the ED was lowered the parts could not be handled. Therefore, the PA2H powder did not have a processing window (as defined in Chapter 3) and was omitted from the remaining tests.

It was generally observed that as the laser power was increased and scan speed was reduced the subsequent increasing energy density resulted in more instantaneous warping of the part. Reducing the energy density generally led to a reduction in curling. However, this was not enough to offset part failure caused by shifting of the layers during the re-coating process due to a lack of particle fusion which resulted in highly distorted parts. If decreased too much the parts also gradually warped after consecutive layers of powder were deposited and were too fragile to handle.

Based on visual observations, the parameters that produced successful builds with the least amount of curling and provided with good shape definition for the P05H, P1H, P1.5H powders, were a laser power of 20 W, 16 W and 10 W respectively and a scan speed of 2500 mm s^{-1}, this was determined from Figure 5.5, showing the average dimensional error of the samples produced. These parameters were used to produce tensile test specimens and small disc shaped samples as illustrated in Figure 5.4.

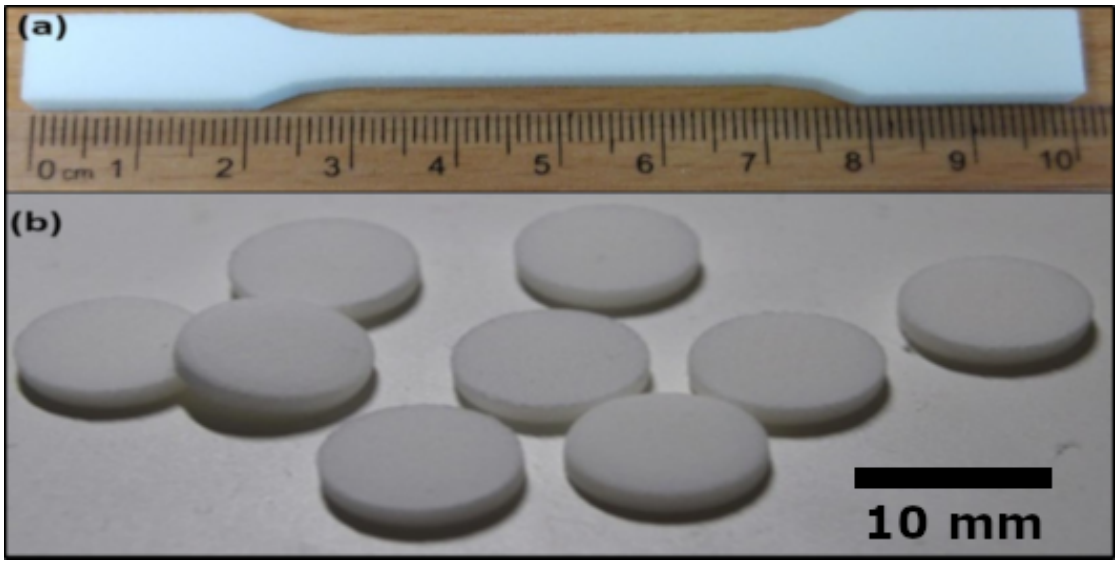
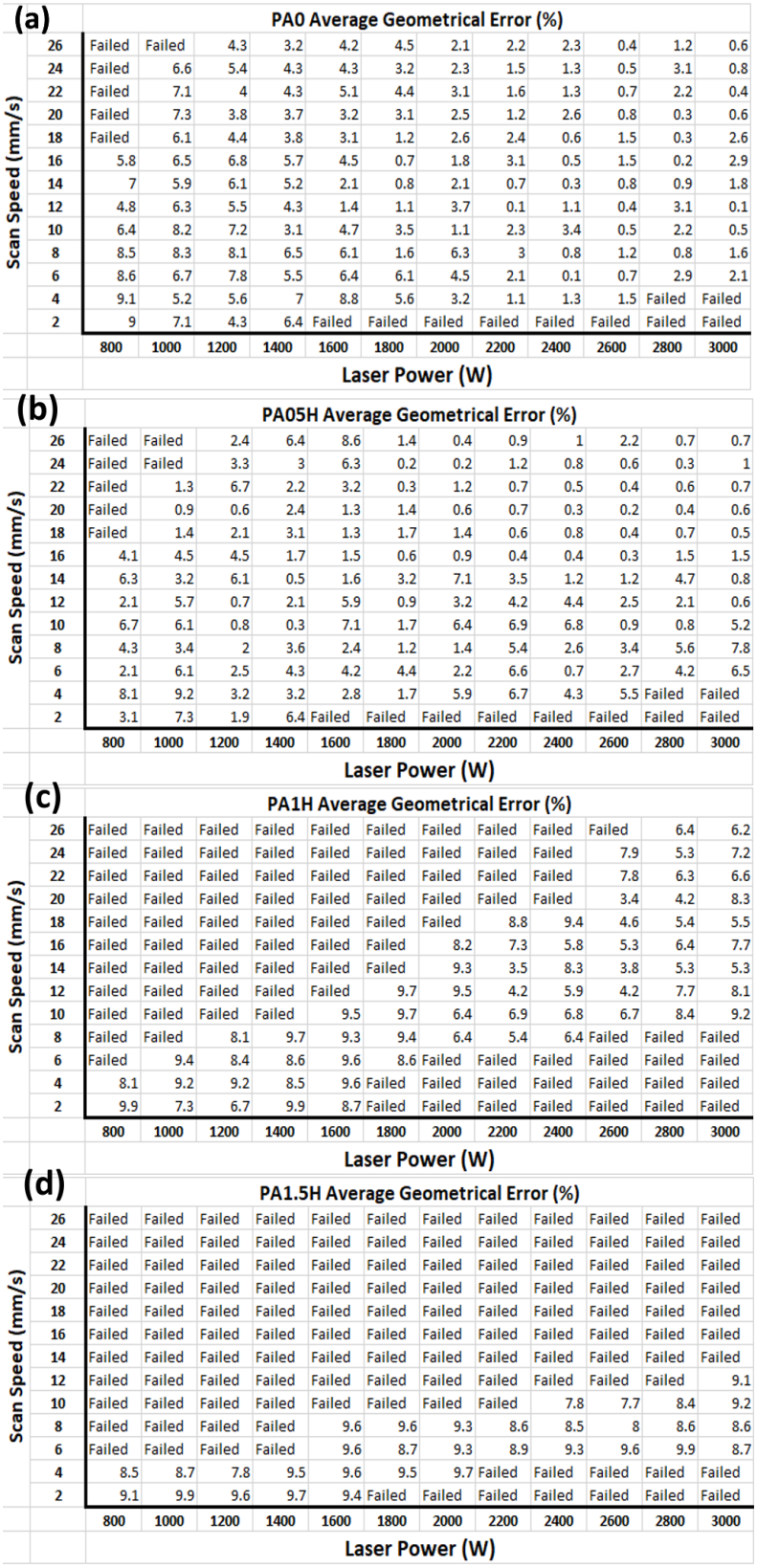


FIGURE 5.4: An example of (a) a tensile test piece and (b) 10 mm diameter discs for cell culture produced from P05H powder at 20 W, 2500 mm s^{-1} and a corresponding energy density of 0.032 J mm^{-2} on the Formiga P100.



(a) PA0 Average Geometrical Error (%)

Scan Speed (mm/s)	800	1000	1200	1400	1600	1800	2000	2200	2400	2600	2800	3000
26	Failed	Failed	4.3	3.2	4.2	4.5	2.1	2.2	2.3	0.4	1.2	0.6
24	Failed	6.6	5.4	4.3	4.3	3.2	2.3	1.5	1.3	0.5	3.1	0.8
22	Failed	7.1	4	4.3	5.1	4.4	3.1	1.6	1.3	0.7	2.2	0.4
20	Failed	7.3	3.8	3.7	3.2	3.1	2.5	1.2	2.6	0.8	0.3	0.6
18	Failed	6.1	4.4	3.8	3.1	1.2	2.6	2.4	0.6	1.5	0.3	2.6
16	5.8	6.5	6.8	5.7	4.5	0.7	1.8	3.1	0.5	1.5	0.2	2.9
14	7	5.9	6.1	5.2	2.1	0.8	2.1	0.7	0.3	0.8	0.9	1.8
12	4.8	6.3	5.5	4.3	1.4	1.1	3.7	0.1	1.1	0.4	3.1	0.1
10	6.4	8.2	7.2	3.1	4.7	3.5	1.1	2.3	3.4	0.5	2.2	0.5
8	8.5	8.3	8.1	6.5	6.1	1.6	6.3	3	0.8	1.2	0.8	1.6
6	8.6	6.7	7.8	5.5	6.4	6.1	4.5	2.1	0.1	0.7	2.9	2.1
4	9.1	5.2	5.6	7	8.8	5.6	3.2	1.1	1.3	1.5	Failed	Failed
2	9	7.1	4.3	6.4	Failed	Failed	Failed	Failed	Failed	Failed	Failed	Failed

Laser Power (W)

(b) PA05H Average Geometrical Error (%)

Scan Speed (mm/s)	800	1000	1200	1400	1600	1800	2000	2200	2400	2600	2800	3000
26	Failed	Failed	2.4	6.4	8.6	1.4	0.4	0.9	1	2.2	0.7	0.7
24	Failed	Failed	3.3	3	6.3	0.2	0.2	1.2	0.8	0.6	0.3	1
22	Failed	1.3	6.7	2.2	3.2	0.3	1.2	0.7	0.5	0.4	0.6	0.7
20	Failed	0.9	0.6	2.4	1.3	1.4	0.6	0.7	0.3	0.2	0.4	0.6
18	Failed	1.4	2.1	3.1	1.3	1.7	1.4	0.6	0.8	0.4	0.7	0.5
16	4.1	4.5	4.5	1.7	1.5	0.6	0.9	0.4	0.4	0.3	1.5	1.5
14	6.3	3.2	6.1	0.5	1.6	3.2	7.1	3.5	1.2	1.2	4.7	0.8
12	2.1	5.7	0.7	2.1	5.9	0.9	3.2	4.2	4.4	2.5	2.1	0.6
10	6.7	6.1	0.8	0.3	7.1	1.7	6.4	6.9	6.8	0.9	0.8	5.2
8	4.3	3.4	2	3.6	2.4	1.2	1.4	5.4	2.6	3.4	5.6	7.8
6	2.1	6.1	2.5	4.3	4.2	4.4	2.2	6.6	0.7	2.7	4.2	6.5
4	8.1	9.2	3.2	3.2	2.8	1.7	5.9	6.7	4.3	5.5	Failed	Failed
2	3.1	7.3	1.9	6.4	Failed	Failed	Failed	Failed	Failed	Failed	Failed	Failed

Laser Power (W)

(c) PA1H Average Geometrical Error (%)

Scan Speed (mm/s)	800	1000	1200	1400	1600	1800	2000	2200	2400	2600	2800	3000
26	Failed	Failed	Failed	Failed	Failed	Failed	Failed	Failed	Failed	Failed	6.4	6.2
24	Failed	Failed	Failed	Failed	Failed	Failed	Failed	Failed	Failed	7.9	5.3	7.2
22	Failed	Failed	Failed	Failed	Failed	Failed	Failed	Failed	Failed	7.8	6.3	6.6
20	Failed	Failed	Failed	Failed	Failed	Failed	Failed	Failed	Failed	3.4	4.2	8.3
18	Failed	Failed	Failed	Failed	Failed	Failed	Failed	8.8	9.4	4.6	5.4	5.5
16	Failed	Failed	Failed	Failed	Failed	Failed	8.2	7.3	5.8	5.3	6.4	7.7
14	Failed	Failed	Failed	Failed	Failed	Failed	9.3	3.5	8.3	3.8	5.3	5.3
12	Failed	Failed	Failed	Failed	Failed	9.7	9.5	4.2	5.9	4.2	7.7	8.1
10	Failed	Failed	Failed	Failed	9.5	9.7	6.4	6.9	6.8	6.7	8.4	9.2
8	Failed	Failed	8.1	9.7	9.3	9.4	6.4	5.4	6.4	Failed	Failed	Failed
6	Failed	9.4	8.4	8.6	9.6	8.6	Failed	Failed	Failed	Failed	Failed	Failed
4	8.1	9.2	9.2	8.5	9.6	Failed	Failed	Failed	Failed	Failed	Failed	Failed
2	9.9	7.3	6.7	9.9	8.7	Failed	Failed	Failed	Failed	Failed	Failed	Failed

Laser Power (W)

(d) PA1.5H Average Geometrical Error (%)

Scan Speed (mm/s)	800	1000	1200	1400	1600	1800	2000	2200	2400	2600	2800	3000
26	Failed	Failed	Failed	Failed	Failed	Failed	Failed	Failed	Failed	Failed	Failed	Failed
24	Failed	Failed	Failed	Failed	Failed	Failed	Failed	Failed	Failed	Failed	Failed	Failed
22	Failed	Failed	Failed	Failed	Failed	Failed	Failed	Failed	Failed	Failed	Failed	Failed
20	Failed	Failed	Failed	Failed	Failed	Failed	Failed	Failed	Failed	Failed	Failed	Failed
18	Failed	Failed	Failed	Failed	Failed	Failed	Failed	Failed	Failed	Failed	Failed	Failed
16	Failed	Failed	Failed	Failed	Failed	Failed	Failed	Failed	Failed	Failed	Failed	Failed
14	Failed	Failed	Failed	Failed	Failed	Failed	Failed	Failed	Failed	Failed	Failed	Failed
12	Failed	Failed	Failed	Failed	Failed	Failed	Failed	Failed	Failed	Failed	Failed	9.1
10	Failed	Failed	Failed	Failed	Failed	Failed	Failed	Failed	7.8	7.7	8.4	9.2
8	Failed	Failed	Failed	Failed	9.6	9.6	9.3	8.6	8.5	8	8.6	8.6
6	Failed	Failed	Failed	Failed	9.6	8.7	9.3	8.9	9.3	9.6	9.9	8.7
4	8.5	8.7	7.8	9.5	9.6	9.5	9.7	Failed	Failed	Failed	Failed	Failed
2	9.1	9.9	9.6	9.7	9.4	Failed	Failed	Failed	Failed	Failed	Failed	Failed

Laser Power (W)

FIGURE 5.5: Average dimensional error of samples produced on the Formiga P100 at varying laser sintinerg parameters for (a) PA0, (b) PA05H, (c) PA1H and (d) PA1.5H. Samples that could not be measured due to build failure, sample fragility or the average dimensional error exceeded 10% were denoted "Failed".

5.2 Processing of PA12-MWCNT-nHA in the Sintratec laser sintering machine

As the Sintratec utilises a laser diode operating at 445 nm, a low cost alternative to a CO_2 laser used on commercial machines, the powders are required to absorb the laser energy and heat the powder. MWCNTs were therefore added, resulting in PA12-MWCNT-nHA mixed phase powders. The use of MWCNT as a coating for PA12 laser sintering has been previously investigated by Bai et al. [1] and has been shown to absorb across the visible light spectrum, as discussed in Chapter 4. Furthermore, literature has shown that MWCNT has a positive impact on stimulating osteogenesis [348–350]. A further advantage to using the Sintratec is the significant reduction in the quantity of powder required for parameter testing due to the smaller build volume.

5.2.1 Determination of the powder bed temperature of PA12-MWCNT-nHA powders

Similar to previous testing conducted on the Formiga P100, the powder bed temperature was first established by spreading the powder across the surface of the build platform at temperatures ranging from 170 - 180°C. As the nHA content increased, the maximum temperature at which powder could be spread increased from 176°C to 178°C for PA05M and PA05M5H, respectively. The results of this test can be seen in Table 5.3.

TABLE 5.3: Results of the powder temperature test for PA05M, PA05M2H and PA05M5H in the Sintratec. The powders loaded with nHA are able to be processed upto 2°C higher than the PA05M powder.

Temperature (°C)	PA05M	PA05M2H	PA05M5H
170	✓	✓	✓
171	✓	✓	✓
172	✓	✓	✓
173	✓	✓	✓
174	✓	✓	✓
175	✓	✓	✓
176	✓	✓	✓
177	×	✓	✓
178	×	✓	✓
179	×	×	×
180	×	×	×

An example of the powder bed agglomerating can be seen in Figure 5.6 of PA05M5H heated at (a) 178 °C, (b) 179°C and (c) 180°C. The powder bed began to show signs of darkening and eventually, when the temperature was high enough (180°C) the powder particles agglomerated and were dragged along the bed as a solid mass, rather than being deposited as a uniform layer.

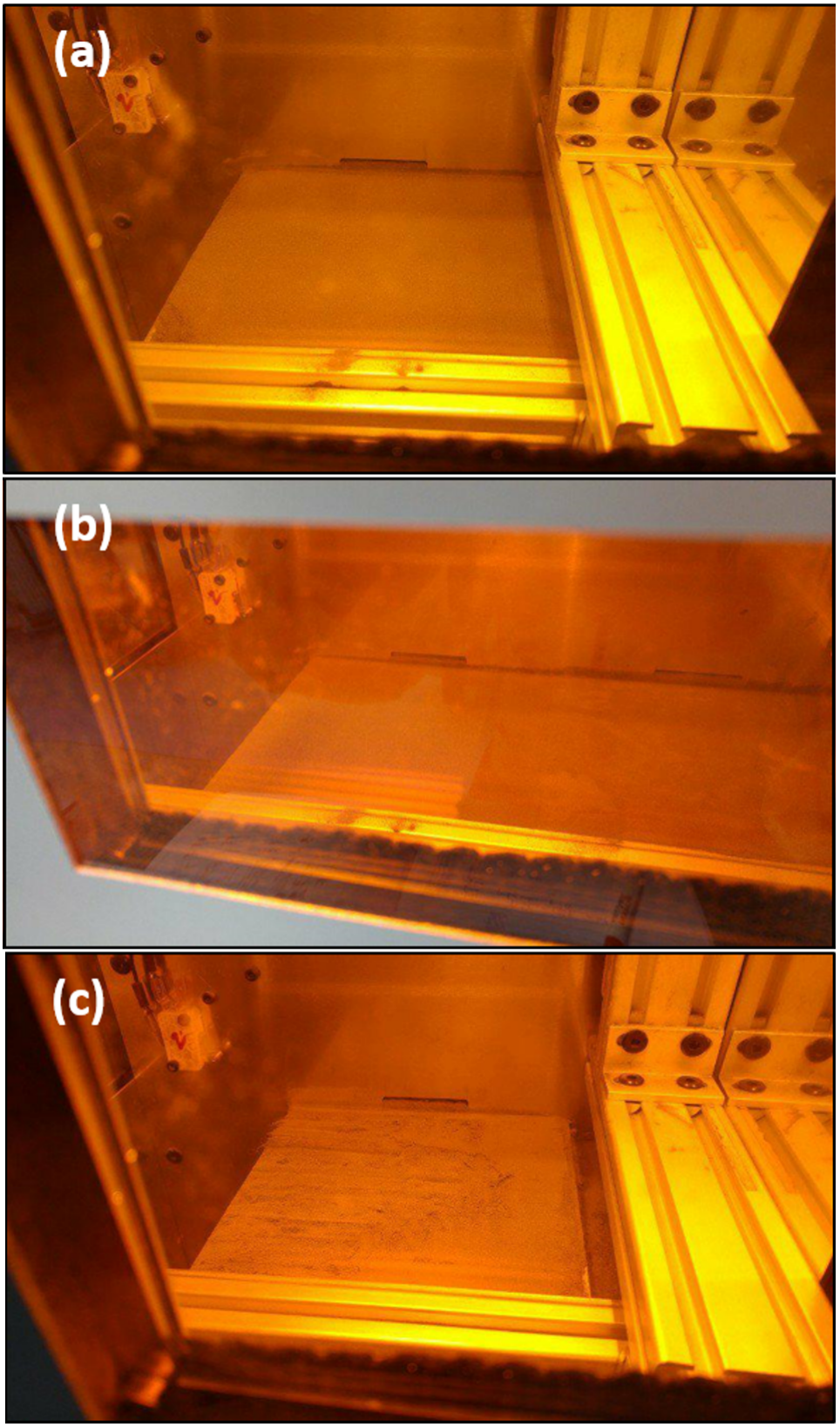


FIGURE 5.6: Images taken of PA05M5H powder heated at (a) 178°C, (b) 179°C and (c) 180°C. Over heating of the powder bed surface occurs above 178°C.

5.2.2 Laser sintering parameters for PA12-MWCNT-nHA powders

As the laser power on the Sintratec is fixed at 2.3 W, to vary the imparted energy density on the powder bed surface, the scan speed and hatch spacing was varied whilst the layer height was fixed, as detailed in Chapter 3. An overview of the parameters used in the Sintratec can be seen in Table 5.4.

TABLE 5.4: Parameters used for the testing of PA05M, PA05M2H and PA05M5H powders.

Sintratec: parameters
Laser Power: 2.3 W
Scan Speed: 100 - 1000 mm s^{-1}
Scan Spacing:0.01 - 0.1 mm
Layer Height: 0.1 mm
Powder bed temperature: 176 - 178°C

The PA05M powder possessed the largest processing window, with successful builds being possible at an ED range between 0.19 - 0.046 J mm^{-2} (Figure 5.7 (a)). Above 0.19 and up to 0.28 J mm^{-2}, the powder showed signs of degradation with significant plumes of white vapour being emitted as the laser scanned. Furthermore, fusion of particles beyond the perimeter of the parts could be seen due to excessive heat causing particles outside and, adjacent to the laser scan path to fuse together. The parts, however, did achieve a completed status but, due to the decomposition of the powder as determined by the degree of vapour being emitted, were deemed unacceptable. At EDs above 0.28 J mm^{-2}, significant warping around the edges could be seen and, parts subsequently failed. At ED below 0.046 J mm^{-2}, part warping, after 1-4 layers into the build, was seen. When the ED was decreased further, the parts became too fragile to handle. The addition of nHA saw a reduction of the processing window for the PA05M2H powder, as seen in Figure 5.7 (b). In this case, successful builds were only possible from 0.16 - 0.053 J mm^{-2}. Above 0.16 J mm^{-2}, powder degradation was seen and by 0.28 J mm^{-2} excessive curling caused parts to fail. At EDs below 0.053 J mm^{-2} parts were either distorted during the build process or were too fragile to handle as the ED was reduced further. The PA05M5H powder (Figure 5.7 (c)) also saw a further reduction in the processing window. Successful builds were only possible

from 0.12 - 0.065 J mm^{-2}. Again, raising the energy density above 0.12 J mm^{-2}, by decreasing scan speed and hatch spacing, led to powder degradation and excessive curling. Below 0.065 J mm^{-2}, the samples experienced distortion as they were being built and became too fragile to handle as the ED was decreased further.

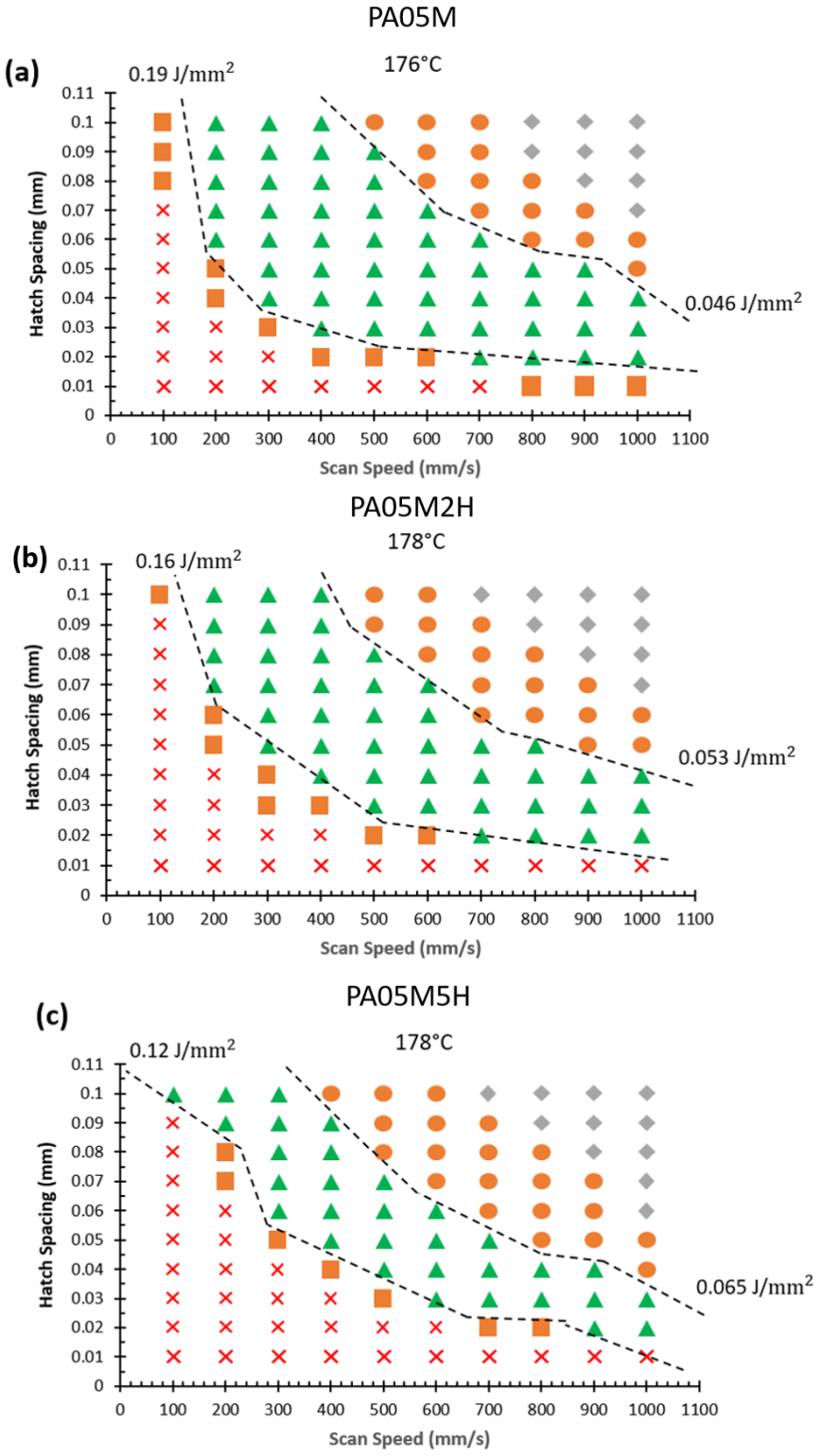


FIGURE 5.7: The Laser sintering processing windows for (a) PA05M processed at 176°C, (b) PA05M2H processed at 178°C and (c) PA05M5H processed at 178°C. PA05M possessed a relatively wide processing window, however, this continually narrowed as the nHA content was increased. Symbol X represents instantaneous curling of the initial layer, square represents gradual curl development after 1 - 5 successive layers resulting in part failure and diamond represents under sintered parts that either shifted on the powder bed or were too fragile to handle.

A reduction in laser speed and/or reduction in hatch spacing led to a corresponding increase in energy density imparted on the powder bed surface. As seen in Figure 5.8 (a) of PA05M2H powder processed at 200 mm s^{-1} and 0.04 mm hatch spacing, the high energy led to over-sintering of the part with excessive particle fusion beyond the perimeter of the scan path. This negatively impacted the dimensional accuracy the part. Figure 5.8 (b) is of the same powder processed at 500 mm s^{-1} and 0.05 mm hatch spacing and showed good shape definition with a good degree of particle fusion. On the other hand, Figure 5.8 (c) shows PA05M2H powder processed at 900 mm s^{-1} and a hatch spacing of 0.07 mm. The lighter sintering region on this layer and slight curling around the edges of the part, indicated that not enough ED was imparted which resulted in distorted and fragile parts.

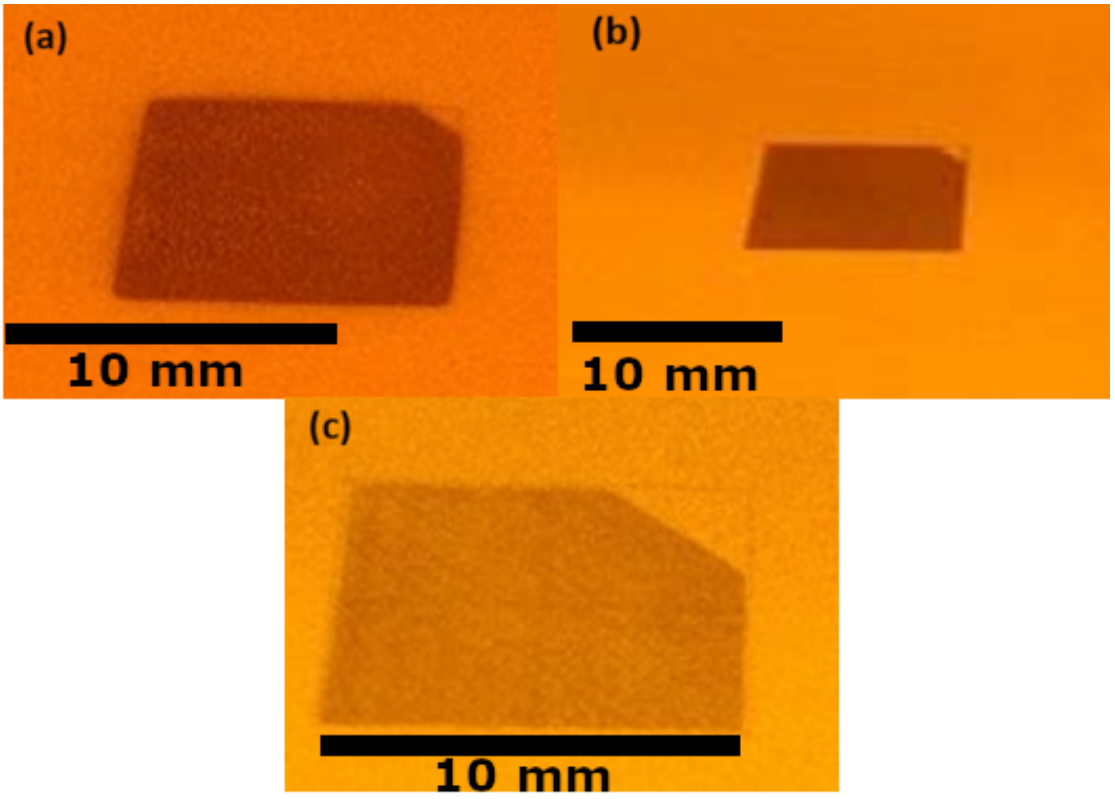


FIGURE 5.8: Images taken of the powder bed surface of PA05M2H processed at (a) 200 mm s^{-1} and 0.04 mm hatch spacing, (b) 4500 mm s^{-1} and 0.05 mm hatch spacing and (c) 900 mm s^{-1} and a hatch spacing of 0.07 mm. Excessive particle fusion can be seen beyond the perimeter of the laser scan path at low speeds, whereas too high a laser speed results in insufficient particle fusion as indicated by the lighter colour of the sintering region.

The further addition of nHA led to a significant reduction in the processing window

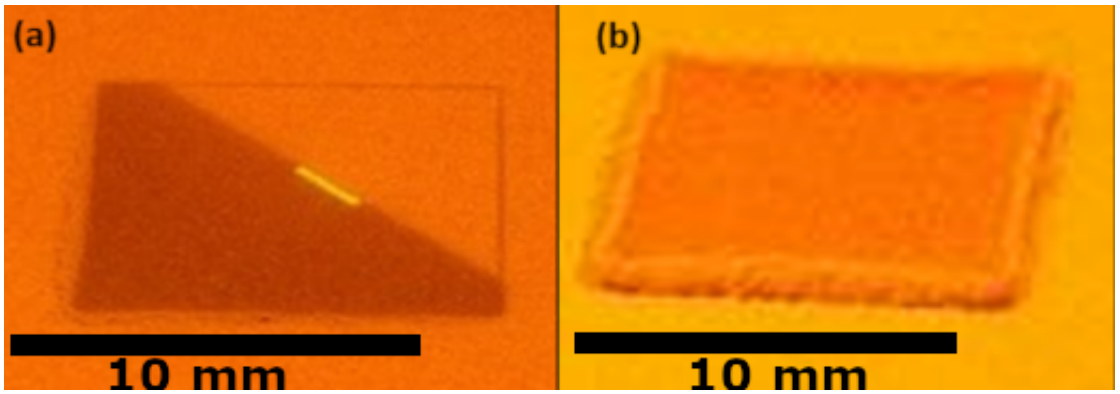


FIGURE 5.9: Image taken of (a) PA05M5H mid way through layer scanning and shows signs of curl development on bottom left corner and edges of the part, whilst (b) is the same layer but at the end of the scan, the curl development was rapid and significant to cause the build to fail.

and increased susceptibility to curling. Figures 5.9 (a) and (b) show PA05M5H powders mid-way through the layer scanning process and at the end of layer scanning respectively. The powder was processed at 200 mm s^{-1} and a hatch spacing of 0.04 mm; it can be seen that curling occurred rapidly and by the end of the layer scanning the curling was significant and caused the build to fail.

Based on visual observations of curl, dimensional accuracy and handlability, as presented in Figure 5.10, the parameters selected for the production of tensile and cellular test samples were: 500 mm s^{-1} at 0.05 mm hatch spacing for PA05H, 500 mm s^{-1} at 0.06 mm hatch spacing for PA05M2H and 500 mm s^{-1} at 0.06 mm hatch spacing for PA05M5H.

It was also noted that during laser sintering of PA05M, PA05M2H and PA05M5H powders, each of the different materials displayed a different visual appearance as the layers were scanned by the laser. This can be seen in Figure 5.11. When each layer of the PA05M powder was processed, it had a glossy sheen after exposure to the laser, which was due to consolidation of the particles through a high degree of melt flow (Figure 5.11 (a)). The PA05M2H and PA05M5H powders (Figures 5.11 (a) and (b)) had a duller, more matted appearance on the surface of the scanned layers. This is likely due to a combination of increased melt viscosity by the presence of the NPs and insufficient ED for complete melting of the particles.

(a) PA05M Average Geometrical Error (%)

Hatch Spacing (mm)	100	200	300	400	500	600	700	800	900	1000
0.11	Failed	8.8	7.6	6.6	Failed	Failed	Failed	Failed	Failed	Failed
0.1	Failed	7.5	7.5	5.4	7.8	Failed	Failed	Failed	Failed	Failed
0.09	Failed	6.7	6.4	7.5	8.5	Failed	Failed	Failed	Failed	Failed
0.08	Failed	6.1	6.4	8.8	6.4	Failed	Failed	Failed	Failed	Failed
0.07	Failed	9.5	5.9	6.5	4.9	8.8	Failed	Failed	Failed	Failed
0.06	Failed	8.4	5.4	5.1	4.9	8.8	9.4	Failed	Failed	Failed
0.05	Failed	Failed	5.5	4.8	5.6	7.5	9.5	9.6	10	Failed
0.04	Failed	Failed	7.9	6.5	6.4	8.9	9.8	9.4	9.4	10
0.03	Failed	Failed	Failed	4.1	9.5	9.5	8.8	8.7	9.7	9.1
0.02	Failed	Failed	Failed	Failed	Failed	Failed	9.5	7.8	9.9	8.9
0.01	Failed	Failed	Failed	Failed	Failed	Failed	Failed	Failed	Failed	Failed

Laser Power (W)

(b) PA05M2H Average Geometrical Error (%)

Hatch Spacing (mm)	100	200	300	400	500	600	700	800	900	1000
0.11	Failed	7.9	8.6	7.9	Failed	Failed	Failed	Failed	Failed	Failed
0.1	Failed	7.4	7.5	7.2	Failed	Failed	Failed	Failed	Failed	Failed
0.09	Failed	8.5	8.2	6.4	8	Failed	Failed	Failed	Failed	Failed
0.08	Failed	7.5	6.5	7.5	8	9.1	Failed	Failed	Failed	Failed
0.07	Failed	8.6	5.7	5.5	7.4	8.2	Failed	Failed	Failed	Failed
0.06	Failed	8.4	7.6	5.4	6.5	8.8	7.5	Failed	Failed	Failed
0.05	Failed	Failed	7.1	5.4	5.9	7	9.7	7.6	Failed	Failed
0.04	Failed	Failed	Failed	7	7.1	6.3	9.5	8.2	9.8	10
0.03	Failed	Failed	Failed	Failed	6.8	6.8	9	9.5	8.6	9.8
0.02	Failed	Failed	Failed	Failed	Failed	Failed	9.5	9.1	10	10
0.01	Failed	Failed	Failed	Failed	Failed	Failed	Failed	Failed	Failed	Failed

Laser Power (W)

(c) PA05M5H Average Geometrical Error (%)

Hatch Spacing (mm)	100	200	300	400	500	600	700	800	900	1000
0.11	Failed	9.5	9.5	Failed	Failed	Failed	Failed	Failed	Failed	Failed
0.1	Failed	9.8	9.8	9.5	Failed	Failed	Failed	Failed	Failed	Failed
0.09	Failed	Failed	9.8	7.9	Failed	Failed	Failed	Failed	Failed	Failed
0.08	Failed	Failed	9.9	8.8	8	Failed	Failed	Failed	Failed	Failed
0.07	Failed	Failed	9.8	9.6	8.7	8.2	Failed	Failed	Failed	Failed
0.06	Failed	Failed	9.9	9.3	7.7	8.8	Failed	Failed	Failed	Failed
0.05	Failed	Failed	Failed	8	7.7	8.5	9.5	Failed	Failed	Failed
0.04	Failed	Failed	Failed	Failed	8.3	8.8	9.5	8.1	9.1	Failed
0.03	Failed	Failed	Failed	Failed	Failed	9.3	9.5	9.3	9.7	9.9
0.02	Failed	Failed	Failed	Failed	Failed	Failed	Failed	Failed	9.6	10
0.01	Failed	Failed	Failed	Failed	Failed	Failed	Failed	Failed	Failed	Failed

Laser Power (W)

FIGURE 5.10: Average dimensional error of samples produced on the Sintratec at varying laser sintering parameters for (a) PA05M, (b) PA05M2H, (c) PA05M5H. Samples that could not be measured due to build failure, sample fragility or the average dimensional error exceeded 10% were denoted "Failed".

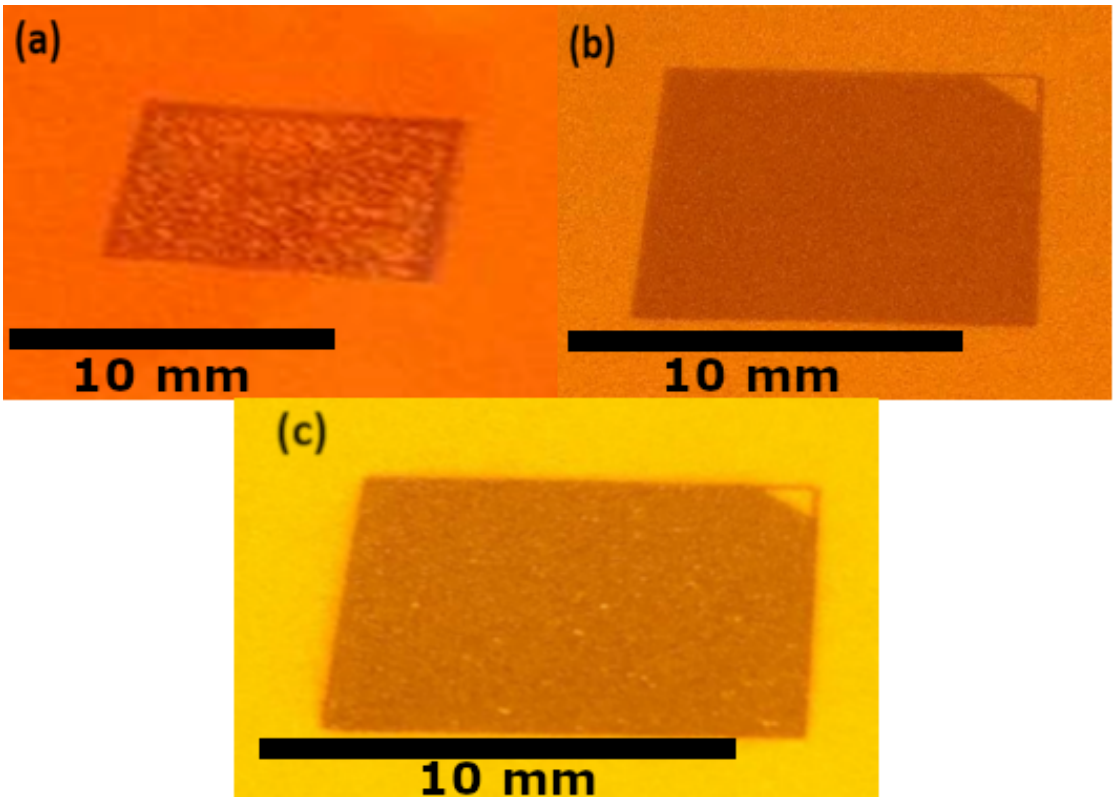


FIGURE 5.11: Image taken of (a) PA05M during layer scanning, at 500 mm s^{-1} and 0.05 mm hatch spacing, and shows the glossy appearance of the scanned layer through viscous flow of the polymer. Image (b) is of PA05M2H and (c) PA05M5H powders processed at 500 mm s^{-1} and 0.06 mm hatch spacing. The appearance of these layers is duller with more matte like appearance due to increased viscosity of the melt and insufficient time for the melt to flow.

5.3 Processing of PLA-MWCNT-nHA in the Sintratec laser sintering machine

As the effects of laser sintering and the application of nanoparticles was established with laser sintering powder (PA12), the attention switched to PLA. As PLA is a biodegradable polymer, its application in orthopaedics is very attractive. The PLA powder supplied was of limited quantity, therefore, use of a consumer system for testing low quantities of PLA powder was favourable. Thus, the dual phase mixture of MWCNT-nHA was also applied to PLA powders and subject to the same rounds of testing as the PA12 powders in the Sintratec.

5.3.1 Determination of the powder bed temperature of PLA-MWCNT-nHA powders

The powder bed temperature test was conducted by spreading the coated PLA powder over the build platform and raising the temperature from 160 to 170°C, this temperature range was selected based on the melting temperature established in Chapter 4, which was 175.4 ± 0.5°C for PL1M, 175.1 ± 0.4°C for PL1M2H and 174.8 ± 0.2°C for PL1M5H powders. The powder bed was observed for any signs of overheating which was typically darkening of the powder bed and agglomeration of the particles during powder spreading. The results of this tests can be seen in Table 5.5. The maximum processing temperature for the PL1M powder was 165°C, above which the powder bed displayed signs of over heating. Both PL1M2H and PL1M5H powders displayed a higher maximum processing temperature of 166°C.

TABLE 5.5: Results of the powder spreading test for PL15M, PL1M2H and PL1M5H powders at various temperatures in the Sintratec LS machine. The addition of nHA increases the maximum temperature by 1°C for PL1M2H and PL1M5H powders.

Temperature (°)	PL1M	PL1M2H	PL1M5H
160	✓	✓	✓
161	✓	✓	✓
162	✓	✓	✓
163	✓	✓	✓
164	✓	✓	✓
165	✓	✓	✓
166	×	✓	✓
167	×	×	×
168	×	×	×
169	×	×	×
170	×	×	×

5.3.2 Laser sintering parameters for PLA-MWCNT-nHA powders

For determination of the coated PLA processing window, the laser scan speed and hatch spacing were varied to adjust the imparted energy acting on the powder bed surface. The parameters used for testing the PLA powders, in the Sintratec, are summarised in Table 5.6.

TABLE 5.6: Overview of the parameters used for testing of the coated PLA powders.

Sintratec: parameters
Laser Power: 2.3 W
Scan Speed: 100 - 1000 mm s^{-1}
Scan Spacing:0.01 - 0.1 mm
Layer Height: 0.1 mm
Powder bed temperature: 165 - 166°C

At energy densities between 0.76 - 0.10 J mm^{-2}, builds were successfully completed with good handleability and shape definition, as seen in Figure 5.13 (a) and Figure 5.15. However, it was evident during the build that there was some degradation of the powder in the form of vapour emitted from the powder bed surface during laser scanning which could not be eliminated, as seen in Figure 5.12.

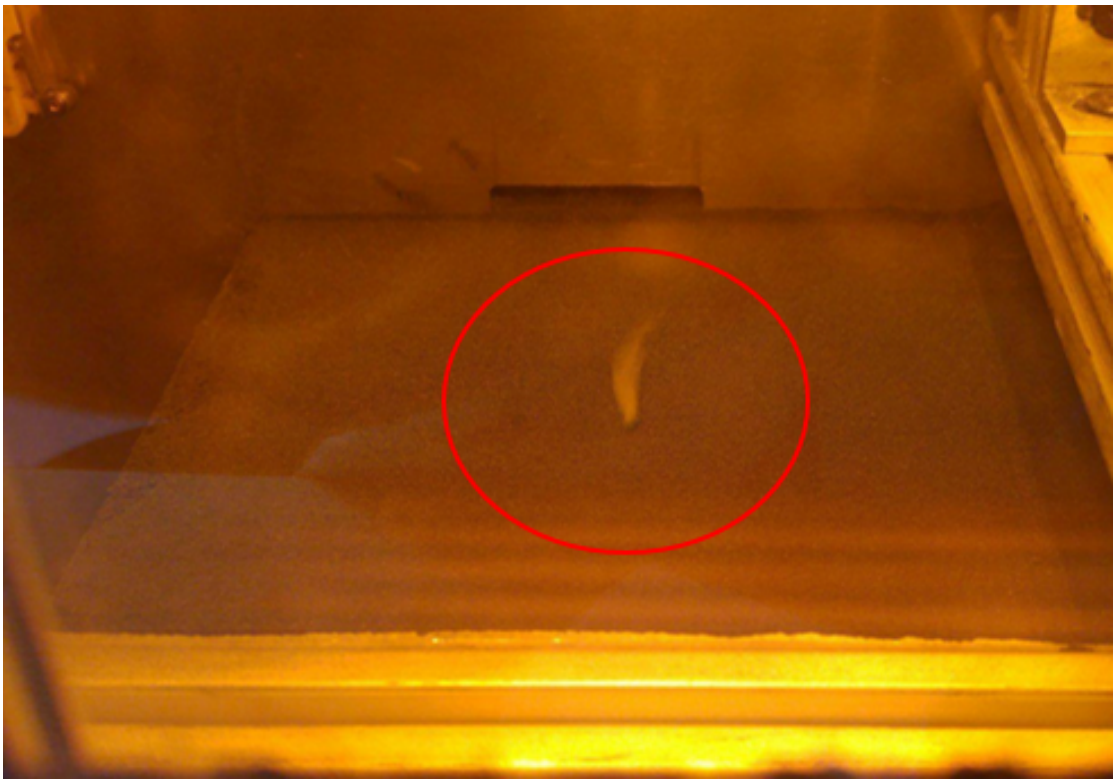


FIGURE 5.12: Image taken of the PL1M powder during initial laser scanning at 400 mm s^{-1} and 0.04 mm hatch spacing. The red circle highlights the smoke formation occurring due to degradation of the powder.

Reducing the energy density did decrease the amount of degradation with a reduction in vapour observed, however, at ED below 0.10 J mm^{-2}, the parts showed signs of warping and were fragile. Above 0.76 J mm^{-2}, warping was observed during laser scanning. The addition of 2 wt% nHA led to a reduction in the processing window as shown in Figure 5.13 (b). The PL1M2H powder had a processing window from 1.15 - 0.12 J mm^{-2}. Above 0.15 J mm^{-2} the initial layer underwent severe curling, by which the edges of the layer warped upwards by as much as 5 mm leading to the re-coater blade catching the part and pulling it off the powder bed. At ED under 0.12 J mm^{-2}, the edges of the layers began warping upwards, this occurred after multiple layers were processed the warping continued until the re-coater blade catches the part, pulling it off the bed. At lower ED, the powder particles did not fuse. It was also noted that, despite successful builds being achieved within the ED range of 0.15-0.12 J mm^{-2}, all parts developed a slight degree of warping during the post cool down process. The PL1M5H powder displayed a further narrowing of the processing window (Figure 5.13 (c)) with successful builds being achieved at an ED range between 1.15 - 0.19 J mm^{-2}.

Similar to the PL1M2H powders, the PL1M5H powders developed post-build warping, as seen in Figure 5.14 (b).

Similar to the PA12 powders tested, the scanned layers of the coated PLA powders appeared to be more matted in colour compared to the glossy sheen of the PL1M powder layers. Again this may be due to an increase in the viscosity of PLA powder by the presence of both MWCNT and nHA. Based on the processing map combined with visual observation and dimensional accuracy testing of the samples, presented in Figure 5.15, the parameters chosen to produce tensile test pieces and discs for cell studies were as follows: 400 mm s^{-1} and 0.03 mm hatch spacing for PL1M, 300 mm s^{-1} and 0.04 mm hatch spacing for PL1M2H, 200 mm s^{-1} and 0.04 mm for PL1M5H.

In addition to 2D discs for cell studies, a 3D scaffold was also produced from PL1M and PL1M5H powder, as shown in Figure 5.14 (a) for further cellular testing.

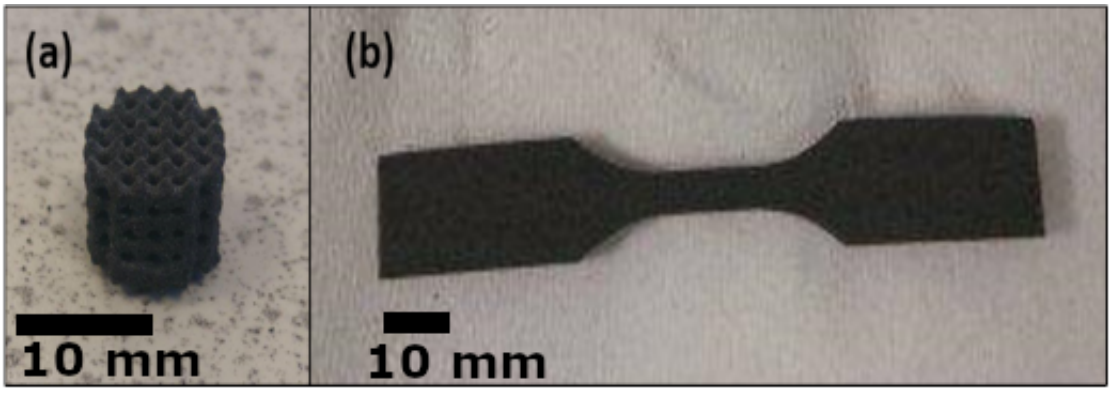


FIGURE 5.14: Image taken of a PL1M5H scaffold for cellular studies (a) and a tensile test piece (b). Both were produced with a scan speed of 200 mm s^{-1} and 0.04 mm hatch spacing. Due to the increased sensitivity of PL1M5H to warping, the flat sections of the tensile piece warped upwards by 4 - 5 mm.

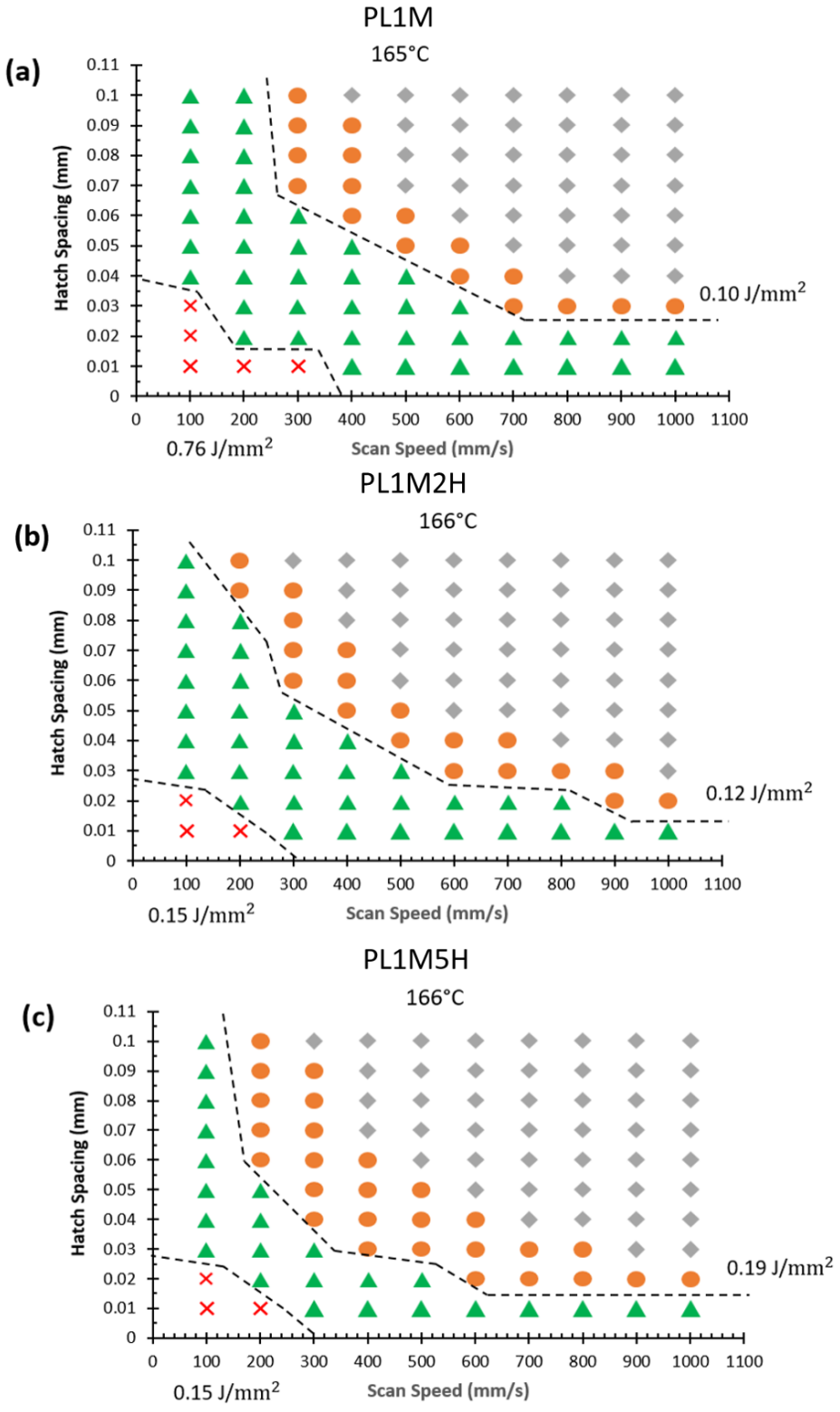


FIGURE 5.13: The processing windows for (a) PL1M processed at 165°C, (b) PL1M2H processed at 166°C and (c) PL1M5H processed at 166°C. All powders possessed a relatively narrow processing window, however this was made significantly worse by the addition of nHA. Symbol X represents instantaneous curling of the initial layer, square represents gradual curl development after 1-5 successive layers resulting in part failure and diamond represents under sintered parts that either shifted on the powder bed or were too fragile to handle.

(a) PL1M Average Geometrical Error (%)

Hatch Spacing (mm)	100	200	300	400	500	600	700	800	900	1000
0.11	7	8.4	Failed	Failed	Failed	Failed	Failed	Failed	Failed	Failed
0.1	7.5	8.5	Failed	Failed	Failed	Failed	Failed	Failed	Failed	Failed
0.09	8.1	7.1	Failed	Failed	Failed	Failed	Failed	Failed	Failed	Failed
0.08	7.5	7.4	Failed	Failed	Failed	Failed	Failed	Failed	Failed	Failed
0.07	6.9	8.9	Failed	Failed	Failed	Failed	Failed	Failed	Failed	Failed
0.06	8.6	7.3	7.8	Failed	Failed	Failed	Failed	Failed	Failed	Failed
0.05	8.6	6.9	7.5	7.1	8.2	Failed	Failed	Failed	Failed	Failed
0.04	6.9	6.9	7.1	6.7	8.3	8.1	Failed	Failed	Failed	Failed
0.03	Failed	8.4	7.1	6.6	7	7.6	Failed	Failed	Failed	Failed
0.02	Failed	8.8	8.3	6.6	7.5	8.5	9.6	8.8	9.7	9.8
0.01	Failed	Failed	Failed	7.1	8.3	8.5	9.5	7.9	9.4	9.4

Laser Power (W)

(b) PL1M2H Average Geometrical Error (%)

Hatch Spacing (mm)	100	200	300	400	500	600	700	800	900	1000
0.11	8.8	Failed	Failed	Failed	Failed	Failed	Failed	Failed	Failed	Failed
0.1	8.5	Failed	Failed	Failed	Failed	Failed	Failed	Failed	Failed	Failed
0.09	9.6	8.5	Failed	Failed	Failed	Failed	Failed	Failed	Failed	Failed
0.08	9.4	8.3	Failed	Failed	Failed	Failed	Failed	Failed	Failed	Failed
0.07	9.3	8.7	Failed	Failed	Failed	Failed	Failed	Failed	Failed	Failed
0.06	8.5	7.4	Failed	Failed	Failed	Failed	Failed	Failed	Failed	Failed
0.05	7.9	8.1	7.8	Failed	Failed	Failed	Failed	Failed	Failed	Failed
0.04	8.1	8.4	7.3	8.5	Failed	Failed	Failed	Failed	Failed	Failed
0.03	8.1	7.5	7.3	8.5	9.1	Failed	Failed	Failed	Failed	Failed
0.02	Failed	7.6	7.9	9.1	9.6	10.0	9.5	9.6	Failed	Failed
0.01	Failed	Failed	7.6	8.8	10	9.6	9.1	9.5	10	10

Laser Power (W)

(c) PL1M5H Average Geometrical Error (%)

Hatch Spacing (mm)	100	200	300	400	500	600	700	800	900	1000
0.11	9.5	Failed	Failed	Failed	Failed	Failed	Failed	Failed	Failed	Failed
0.1	9.6	Failed	Failed	Failed	Failed	Failed	Failed	Failed	Failed	Failed
0.09	8.8	Failed	Failed	Failed	Failed	Failed	Failed	Failed	Failed	Failed
0.08	8.8	Failed	Failed	Failed	Failed	Failed	Failed	Failed	Failed	Failed
0.07	9.6	Failed	Failed	Failed	Failed	Failed	Failed	Failed	Failed	Failed
0.06	9.5	Failed	Failed	Failed	Failed	Failed	Failed	Failed	Failed	Failed
0.05	8.9	8.9	Failed	Failed	Failed	Failed	Failed	Failed	Failed	Failed
0.04	8.9	8.7	Failed	Failed	Failed	Failed	Failed	Failed	Failed	Failed
0.03	9.7	8.7	9.8	Failed	Failed	Failed	Failed	Failed	Failed	Failed
0.02	Failed	9.3	9.8	9.9	9.9	Failed	Failed	Failed	Failed	Failed
0.01	Failed	Failed	10	10	9.6	10	10	10	8.9	8.4

Laser Power (W)

FIGURE 5.15: Average dimensional error of samples produced on the Sintratec at varying laser sintering parameters for (a) PL1M, (b) PL1M2H, (c) PL1M5H. Samples that could not be measured due to build failure, sample fragility or the average dimensional error exceeded 10% were denoted "Failed".

5.4 SEM of single layers from the Sintratec machine

To compare the degree of particle consolidation during laser sintering, the PA05M and PA05M5H were processed at the same energy density of 0.076 J mm^{-2}, using a scan speed of 300 mm s^{-1} and 0.03 mm hatch spacing. The same was also done for PL1M and PL1M5H powders at 0.46 J mm^{-2}, using speeds of 100 mm s^{-1} and hatch spacing of 0.05 mm. A square section measuring 15 x 15 mm was processed using these parameters. The scan was then interrupted just before completion of the first layer. This layer was then removed for SEM imaging, the results of this can be seen in Figure 5.16.

The PA05M and PL1M layers (Figure 5.16 (a) and (c)) have a relatively smooth appearance with few visible signs of pores on the surface due to incomplete fusion between the particles. This was more evident on the PL1M layer, perhaps due to the insufficient ED and/or increased viscosity of the polymer melt. From Chapter 4, the zero shear viscosity of PL1M was 41% higher compared to the pure PL0 powder. When comparing the powders to their nHA loaded counterparts, the PA05M5H and PL1M5H (Figure 5.16 (b) and (d) respectively) layers displayed a significant degree of open pores on the surface and a large degree of incomplete fusion between particles, despite being processed at higher settings (0.46 J mm^{-2}, using speeds of 100 mm s^{-1}). The presence of nHA at a 5 wt% loading clearly affected the degree of particle consolidation that could be achieved, again, this could be a combination of increased viscosity and nHA acting as a barrier to fusion, through increased contact distance between the particle and by the absorption of thermal energy. From Chapter 4, the zero shear viscosity of PL1M5H was 303% higher than the pure PL0 powder.

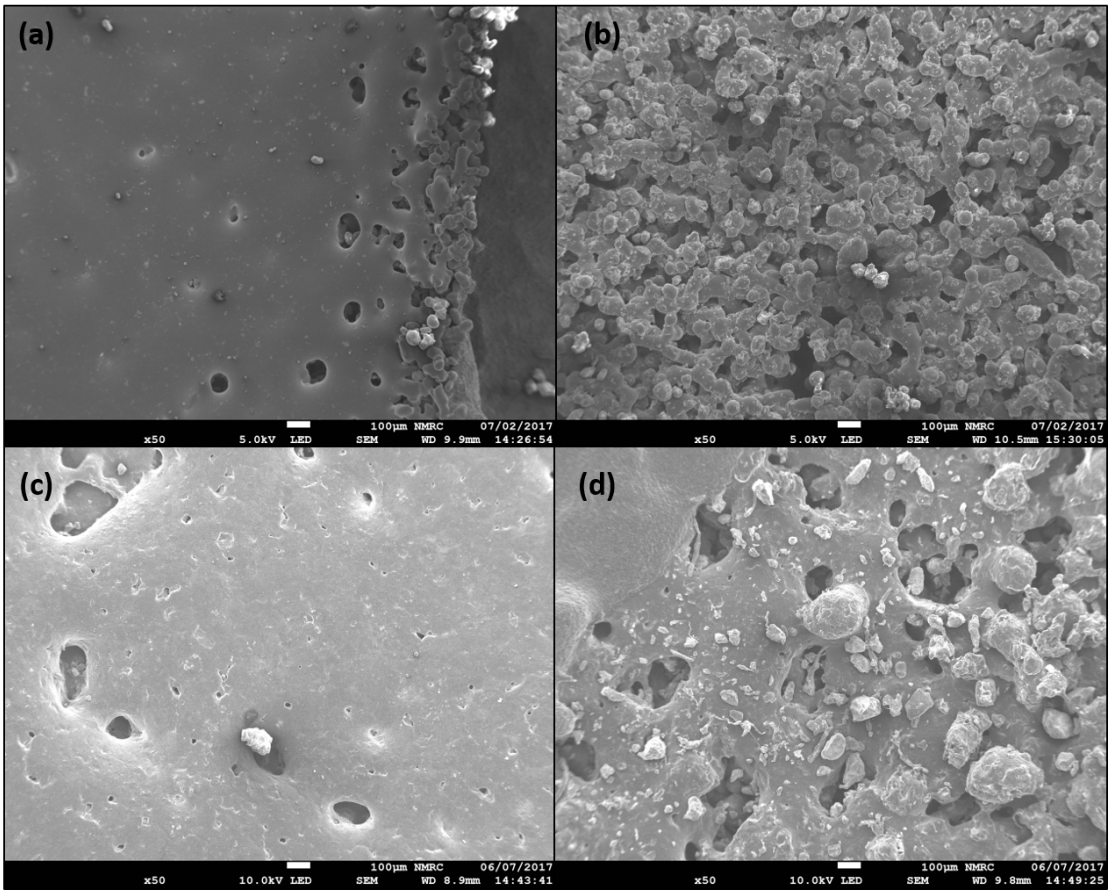


FIGURE 5.16: SEM images of single layers of (a) PA05M (b) PA05M5H (c) PL1M and (d) PL1M5H. The degree of particle consolidation for the PA05M and PL1M powders was significantly greater than that of the PA05M5H and PL1M5H powders.

5.5 Discussion

The uncoated PA0 powders, in the commercial laser sintering system had a wide processing window typically covering ED range of 0.11 - 0.005 J mm^{-2}, completed builds were possible at almost all combinations of laser power and scan speeds tested (within the range of 2 - 25 W and 800 - 3000 mm s^{-1}). The addition of nHA, beyond 0.5 wt%, led to an increased sensitivity to curling, which resulted in build failures at higher energy densities, thus, there was a continued reduction in the processing window from PA1H to PA1.5H. At 2.0 wt% nHA, the PA2H powders could not be successfully processed at any combination of laser power and scan speed tested, due to significant in-build curling which led to parts being dragged off the build platform during re-coating. Due to the large size of the commercial Formiga P100 laser sintering system, a considerable amount of powder was required for basic parameter testing; at

least 1.5 kg of powder was consumed for each composition of powder tested. This rate of powder throughput was unsustainable for the project. Therefore, the need to switch over to a smaller laser sintering system that consumed significantly less powder was needed.

HA is known to greatly absorb CO_2 lasers, owing to the PO_4^{-3} bending vibrations which coincides with the operational wavelength of the laser (10.6 μm). This phenomenon has been applied in the field of dentistry for the treatment of hypersensitive teeth caused by dentin tubules [341]. Tests conducted on human molars, with dentin tubules, showed that exposure of nHA pastes to CO_2 lasers, at a power density of 129.33 W cm^{-2}, for 6 cycles at 5 s bursts, could generate localised heating of the nHA paste. The local temperature of the surrounding tooth only increased slightly by an average of 2.33 ± 0.56°C; this was well below the temperature limit at which the underlying tooth pulp could have become damaged. This localised heating of the nHA led to heating and melting of the paste which occluded the dentin tubules, this was confirmed through SEM and dye penetration tests [341].

The addition of HA has been known to influence laser sintering in a variety of different HA/polymer composite systems. For example Hao et al. [247] found that the level of HA content had a significant effect on the degree of consolidation between HA/HDPE composite powders, which wee made by twin screw compounding and milling. When powders were processed using a CO_2 laser with the same parameters (2 - 10 W laser power and scan speed of 1200 mm s^{-1}), the powders containing 30 wt% produced a thicker monolayer compared to powders containing 40 wt% HA. For example, when the powders were processed at 8 W the single layer of the 30 wt% HA powder was approximately 22% thicker than the layer containing 40 wt% HA. This, in combination with the poor handleability of the 40 wt% HA powder and SEM of the single layers revealing a significantly larger amount of pores and unfused particles indicated that the HA was reducing the processing window of the powder. In another study involving HA/PA composite powders, made using the same technique by Savalani et al. [351]; it was found that HA also had a significant impact on the processability of the powders, showing a similarity in the reduction of fusion between polymer particles as a function of increased HA loading. Studies into laser sintering of HA/PLLA powders (10 wt%),

by Zhou et al. [352] also noted a reduction in consolidation between the particles with the presence of HA. It was concluded that the large disparity in the molar specific heat capacity of HA (694 $\pm$68 J mol^{-1} K^{-1}) and PLA (145-156 J mol^{-1} K^{-1}) resulted in HA acting as a heat sink, thus, less heat was available to system leading to less consolidation between the particles.

From the examples mentioned, the HA content that could be successfully processed was significantly higher than the loadings used in this study. The aforementioned studies utilised micron sized HA with twin-screw compounding/milling and, S/O/W emulsion/solvent evaporation methods to produce composite powders for laser sintering, therefore, the HA was encapsulated within the polymer and not on the surface thus the encapsulated HA did not have much interaction with the incoming laser. Methods of powder production that involve deposition of nHA on the outer surface of the particles, such as dry blending, will result in increased exposure to the incoming laser, and localised heating of the nHA. An example of this can be seen in the work by XiaoHui et al. [353]. This study involved the production of aliphatic polycarbonate/nHA powders. SEM observation noted an increase in surface coverage as the nHA content increased, from 5 to 15 wt%. However, following laser sintering the final part porosity increased significantly from 53 to 82%, due to poorer consolidation between the particles. Wiria et al. [354] also noted the difference in processability between the use of coarse and fine HA particles in HA/PCL powder blends (10-30 wt%). It was found that using fine HA particles led to a higher degree of surface coverage of PCL particles, but required increased energy input to sinter particles together, compared to blends containing coarser HA particles, at the same loadings. As noted by Zhou et al. [352], the high molar specific heat capacity of HA (694 $\pm$68 J mol^{-1} K^{-1}) resulted in a localised heating of the HA when exposed to the CO_2 laser. The study by Al-maliky et al. [341], mentioned above, demonstrated this notion, where exposure of nHA to a CO_2 laser generated localised heating of the nHA, without significantly raising the temperature of the surrounding tooth. However, the dry blending method of powder production, used by XiaoHui [353] and Wiria [354], generally lead to greater levels of NP agglomerates on the surface of the particles. This was observed in both studies, thus affecting the surface coverage. In this study, the coating method developed

resulted in a high degree of surface coverage. The theoretical surface coverage as calculated using the formula detailed in Chapter 3, approximated the surface coverage of PA0.5H, PA1H and PA1.5H as being 20%, 40% and 60%. For PA12 powders used in the Sintratec, which had up to 5.5 - 6.0 wt% NPs, the theoretical coverage was over 100%. The high degree of surface coverage achieved in this wprk was confirmed via SEM images as shown in Chapter 4, of the particle surfaces. Therefore, a combination of localised laser absorption by nHA and a increase of the specific heat capacity of the coated powder, due to the presence of HA, may have resulted in poor heat transfer between the powders needed for particle fusion and large thermal gradients which contributed to the development of curl. Furthermore, the high surface coverage provided by the coating method may have also acted as a barrier to fusion by increasing the contact distance between polymer particles thus also contributing to a reduction in the degree of particle fusion at higher nHA loadings [351]. This is further evidenced by the fact that as the nHA content was reduced from 2 wt% down to 0.5 wt%, the laser sintering processing window became wider and the powder was less susceptible to curling. What was also noted from the aforementioned studies was the use of a roller mechanism for dispensing of new layers of powders, as opposed to the wiper blade which is used on the Formiga P100 and Sintratec. The advantage that a roller mechanism has over a wiper blade, is that layers are compressed during spreading operations, thus any warping around the edges of the layers are squashed back down which aids in a successful build. Thus, powders which are more sensitive may be less likely to significantly impact upon the powder processability via this mechanism for powder spreading.

The laser system used in the consumer machine (Sintratec) was reliant upon the visible light spectrum which operated at 445 nm, as opposed to the CO_2 system operating in the infrared spectrum at 10.6 μm. On it's own pure PA12 and PLA powder could not be processed in the Sintratec. As observed from the UV-Vis spectrum from Chapter 4, the powders had close to 0% absorption at 445 nm. Therefore a decision was made to coat PA12 and PLA powders with a dual phase mixture of MWCNT-nHA. Due to widespread use of PA12 powder, it served as a good test candidate for trialling the mixed phase coating before application to PLA.

The PA05M2H and PA05M5H powders processed in the Sintratec did have a processing window, albeit a narrow one. The EDs ranged from 0.16 - 0.053 J mm^{-2} and 0.12 - 0.065 J mm^{-2}, respectively. As mentioned, due to the differences such as laser systems, temperature control, size and volume, direct comparison between the Formiga P100 and Sintratec laser sintering systems is not appropriate. However, the powders used in the Sintratec did experience a narrowing of the processing window, and increased susceptibility to curling from 2 wt% to 5 wt% nHA, similar to the trend observed in the Formiga P100.

With limited processability of PA12- MWCNT-nHA in the Sintratec machine, PLA-MWCNT-nHA powders were also investigated in the Sintratec. Preliminary testing showed that a 0.5 wt% MWCNT loading was insufficient for the consolidation of the PLA powders, even at slow laser sintering speeds (100 - 300 mm s^{-1}) and low hatch spacing (0.01 - 0.03 mm); owing to their larger particle size range (Dx(10) 56.8 $\pm$1.3 μm, Dx(50) 135.1 $\pm$1.5 μm and Dx(90) 308.3 $\pm$1.2 μm for PL1M5H powders) when compared to PA12, as discussed in Chapter 4. This larger particle size required a greater input of energy to melt the particles within a sufficient time period for laser sintering [227] [41]. Thus, a 1 wt% loading of MWCNT was selected to improve absorbence. The addition of 2 - 5 wt% nHA, again, led to a substantial narrowing of the processing window with PL1M2H and PL1M5H becoming very sensitive to curling which was similar to the observations made on the PA12-nHA and PA12-MWCNT-nHA powders in processed in the Formiga P100 and Sintratec.

Currently, there is very limited literature available that investigates the usage and effects of coated powders in a consumer laser sintering systems such as the Sintratec. Contrary to studies mentioned before that used systems with a CO_2 laser, the Sintratec utilises a laser diode operating at 445 nm. Absorption by nHA, at this wavelength, is minimal as shown in Figure 4.37 and 4.38 from Chapter 4. MWCNT is an excellent thermal conductor arising from its perfect crystalline structure for free phonon and electron transport [355]. Bai et al. [1] has demonstrated the added benefit that small amounts of MWCNT (0.1 wt%) can have on processing and final part densities on PA12. At ED of 0.046 - 0.19 J mm^{-2} for PA05M and 0.10 - 0.76 J mm^{-2} for PL1M, the samples that were produced had good shape definition ($<$ 10% average error),

and had good handleability. Once again, the presence of nHA resulted in processing difficulties. On this occasion, the entanglement of the MWCNT with nHA, arising from the powder production step, meant that there was less surface contact between MWCNT and the polymer, this can be seen in Figure 4.12, from Chapter 4. This entanglement of the MWCNT with the nHA may have also blocked some of the laser energy from reaching the MWCNT. Thus, the heat energy transfer to the polymer was affected. This will have also contributed to the reduction of processing window observed for PA12-MWCNT-nHA and PLA-MWCNT-nHA powders. From PA05M to PA05M2H and PA05M5H the reduction in processing window was 30% and 89% respectively. Whereas from PL1M to PL1M2H and PL1M5H, the processing window reduced by approximately 180%.

Similar to observations made on the PA12 powders, in the Formiga P100, and of other polymer composite powders mentioned in the literature [351–354], the increasing presence of nHA did lead to decreased fusion between the particles as seen in Section 5.4. When the PA05M, PA05M5H, PL1M and PL1M5H powders were processed using the same respective parameters and observed visually, the duller appearance of PA05M5H and PL1M5H layers was apparent. It was noted that pausing the print and waiting 10-15 seconds after the first layer was scanned did provide sufficient time for the polymer to melt and flow which led to a glossy appearance of the layer, similar to that seen in Figure 5.11 (a) of the PA05M layer. However, curling around the edges of the layer also developed over this time. This would suggest increased viscosity of the polymer melt, due to the presence of NPs, which was also indicated by the melt rheological testing performed in Chapter 4. PL1M5H powders recorded a 303% increase in zero shear viscosity when compared to the PL0 powder. The increase in viscosity may have also contributed to the reduction in particle fusion. Finer control over laser dwell time could provide sufficient time for the polymer particles to flow, however, this would add significantly to the build time, and due to non uniform heat loss during the dwell, curling is also likely to occur. Increased ED input for the nHA coated powders may lead to improved fusion between the particles, however as observed during testing, the powders were very sensitive to in build curling as ED was increased from 0.023 to 2.3 J mm^{-2}.

It was evident from the powder processing maps (Figures 5.2, 5.7 and 5.13) that curling of the layers during laser sintering, which caused the build to fail as the re-coater blade catches on the part, became significantly worse and more difficult to control as the nHA loading was increase. Control over the build chamber temperatures and other parameters such as laser power or scan speed and hatch spacing can help mitigate high thermal gradients and eliminate curl. However this approach became ineffective for powders with greater than 1.5 wt% nHA in the Formiga P100 and at 5 wt% nHA in the Sintratec. Curling/warping is due to premature crystallisation and volumetric shrinkage which leads to the build up of residual stresses within the component and results in distortion of the final part [317] [292] [356]. The DSC results from Chapter 4 revealed that nHA and MWCNT acted as strong heterogeneous nucleators, and that the activation energy for crystal nucleation was reduced, indicating that the powders maybe more sensitive to temperature fluctuations which may cause premature crystallisation of the polymer. However, the processing temperatures for all powder compositions tested was set well above the onset Tc temperature for each powder, as determined by standard DSC and by isothermal DSC testing. The powders were also preheated and held at their processing temperatures for 2 hours prior to initiating the build to allow for a homogeneous temperature equilibrium across the build platform. However, in reality, the powder bed surface temperature is likely to vary. This temperature variation is more significant towards the outer edges of the the build platform where the IR heating system does not completely cover the bed. The degree of temperature variation is likely to vary across machines. In most cases, laser sintering machines are not closed systems, with heat loss occurring through non sealed openings and radiation through the walls of the machine. The Sintratec machine, is received as a DIY kit, the quality of the assembly is dependent on the skill and accuracy of the individual performing the assembly. An internal study looking into the temperature variation at the build surface of the Sintratec, revealed large temperature variations towards the front of the build platform compared to the rear, as seen in Figure 5.17 [357].

The most stable temperature is found towards the back left of the machine, here, the temperature fluctuation is less than -2°C. Towards the centre of the platform the

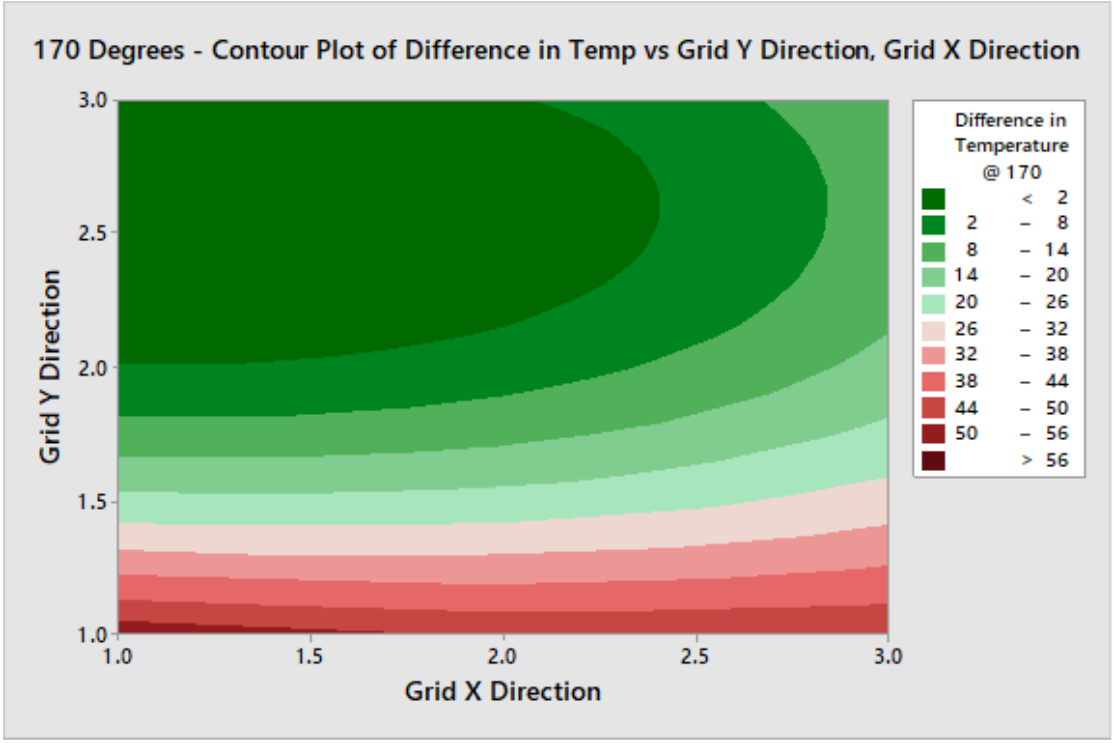


FIGURE 5.17: Contour map displaying the temperature variation across the build platform at 170°C. Test was performed by James Davis, MSc. The temperature is most stable in the top left corner of the build platform and becomes progressively worse towards the front of the build platform where temperatures drop by as much as 50-56°C [357].

temperature fluctuation was more drastic with up to -14-20°C of variation. The front of the platform, closest to the chamber door, had the most significant reduction of up to -50-56°C. The temperature profile of the platform at 170°C is consistent with the layout of the Sintratec machine and observations made during the powder temperature spreading tests (Figure 5.18). Temperature fluctuations of 20°C or over would place PL1M5H powders within the onset of crystallisation (145°C) according to isothermal DSC results in Chapter 4. It is important to note that fresh powder that is deposited over sintered layers is held in an unheated reservoir and thus is significantly cooler than the powder on the build surface. The freshly deposited powder requires heating by the lamps which takes time, this may exacerbate warping issues for materials that are more sensitive to temperature fluctuations.

The front door panel of the machine also had a 5 mm wide gap which ran up the length of the machine providing a route for heat loss. The consequence of the heating arrangement and insufficient sealing led to the large temperature fluctuations seen

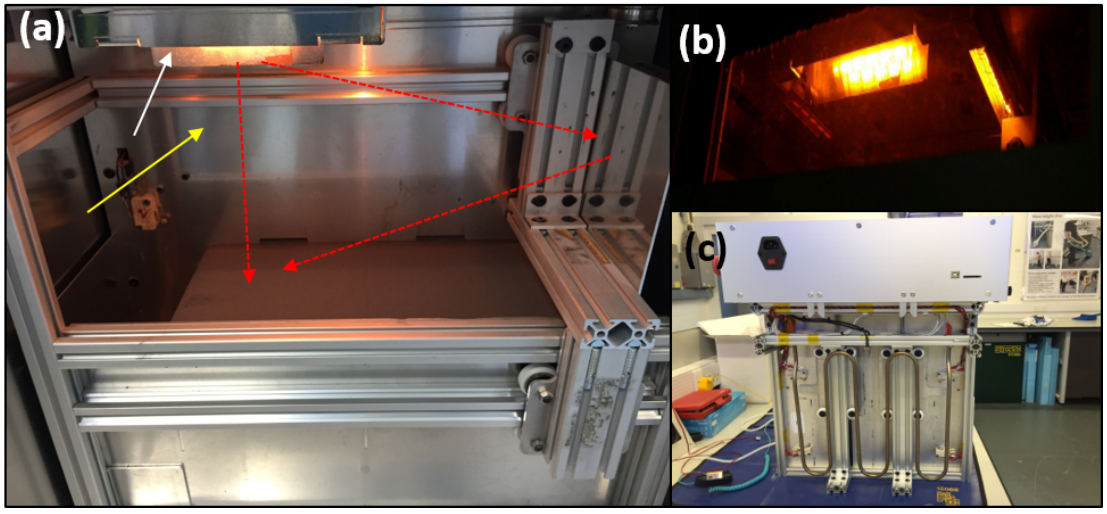


FIGURE 5.18: Image taken of (a) the build chamber; white arrow indicate the active IR lamp that performs heating of the powder bed surface. The red arrows show the general light path for heating the bed and the yellow arrow indicates the position of the heating elements which are behind the back the chamber wall. (b) shows the heat lamp actively heating during laser sintering and (c) is of the rear of the build chamber which shows the chamber heating elements that lie closest to the rear of the build platform.

in the study by James Davis [357]. This was also consistent to observations made during the powder temperature tests, where overheating of the powder surface initially occured in the back left corner of the machine before gradually progressing across the rest of the build surface. Therefore, positioning of parts on the build platform may have serious implications on the overall build success and final part properties. These factors may have contributed towards the significant processing difficulties encountered with the PA05M5H and PL1M5H powders. Inhomogeneous temperature distribution across the build platform is a significant issue found in laser sintering and even commercial machines suffer from it [1] [41] [358]. Figure 5.19, shows the temperature distribution in a commercial EOS P390 laser sintering machine. Studies have shown that parts built in the centre were significantly different, up to $\pm$583 MPa, than those built towards the corners of the machine [41].

The resulting thermal gradient resulted in a build up of residual stress within the layers of the part due to crystallisation. This build up of stress resulted in the warping of the layers and was most evident during the initial few layers of the build. The observations made in this work correlated with the work by Amado et al. [2] [292] who utilised

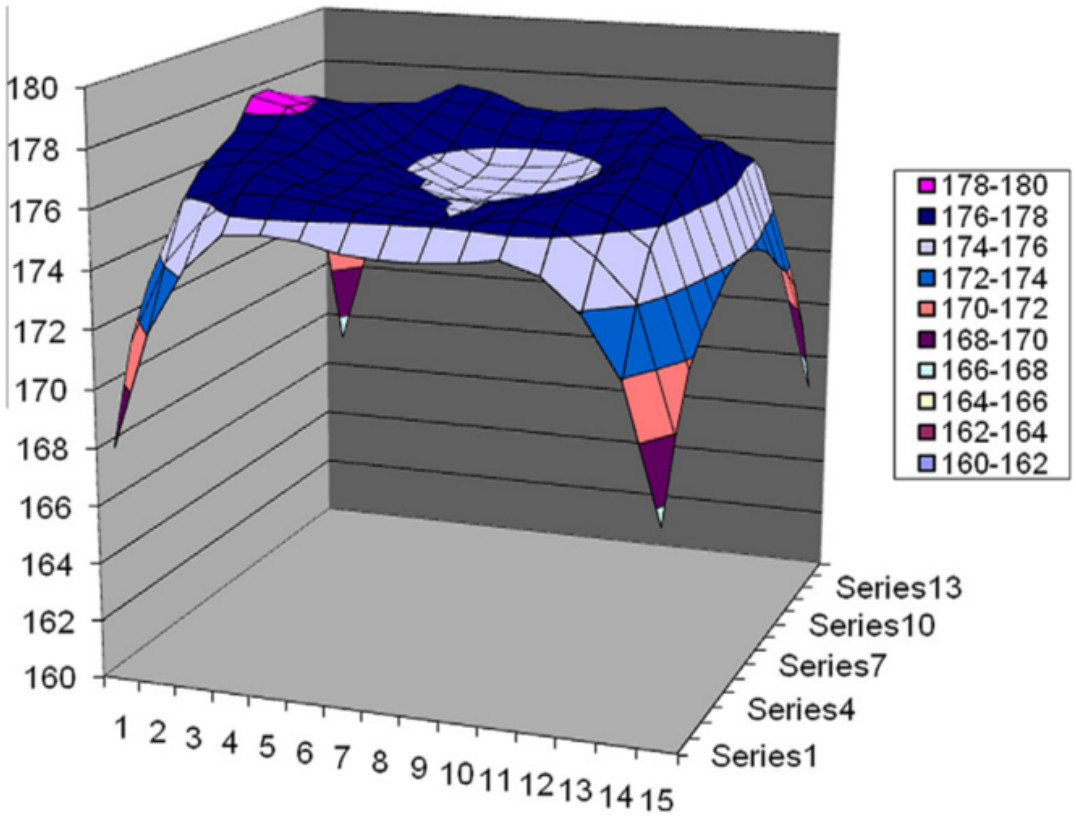


FIGURE 5.19: Graph of the temperature distribution inside the build chamber of an EOS P390 commercial laser sintering machine. Temperature shows significant fluctuations towards the corners of the build area taken from [41].

a transient finite element model (FEM) to simulate the warpage effect that develops during the processing of icoPP (polypropylene) powder and compared that to standard PA12. The powder bed surface temperature of the first 10 layers of deposited powder was monitored by the IR sensors on the machine and recorded. As seen in Figure 5.20, it was evident that there was a steep temperature gradient along the Z orientation during initial powder deposition. The initial temperature drop from for PA12 was recorded to be from 176°C to 130°C and for icoPP from 117°C to 95°C. This data was then used for the simulation which started with the deposition of powder over the first melted layer. As predicted, with each new layer that was added the temperature of the layer below was reduced.

For PA12, the simulation predicted an average cooling rate 0.23°C min^{-1}. In the case of icoPP, this was slightly less, with an average cooling rate 0.18°C min^{-1}. The slower cooling rate is known to raise the temperature over which crystallisation can be

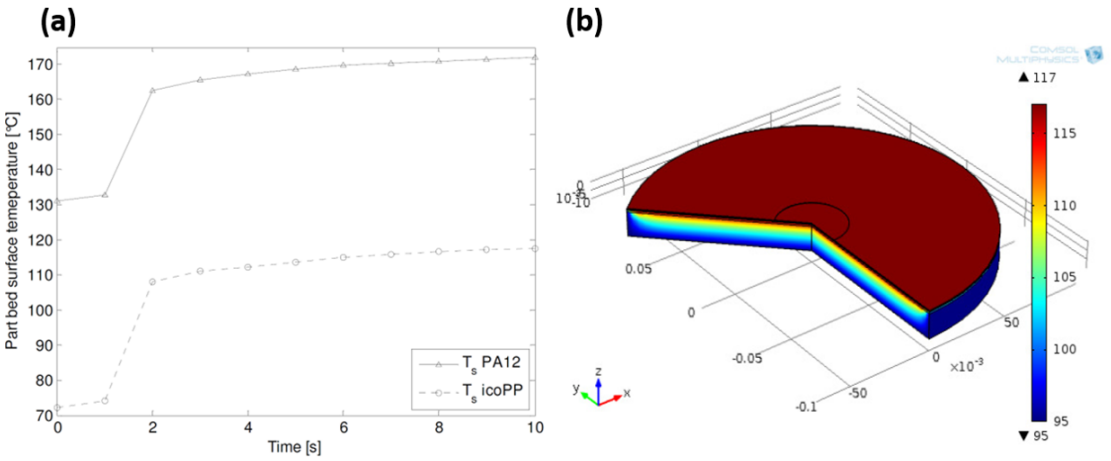


FIGURE 5.20: Image (a) shows the measured surface temperature change of PA12 and icoPP powders with time (b) shows the temperature distribution of the icoPP powder after deposition of the first 10 layers [2].

observed, during non-isothermal crystallisation studies as discussed in the Chapter 4. In Amado's study, this temperature variation occurred in a cyclical manner and, based on isothermal and non-isothermal DSC data, the cumulative degree of crystallisation was calculated. The results of this was the emergence of a "stair-stepping" pattern, across the build sequence. The first, steep, crystallisation change was noted to be induced by the deposition of fresh powder at each new layer, as mentioned before, the fresh powder stored in the reservoir is not directly heated by the heating elements and is cooler than the powder on the build platform. The result of this significant under cooling affect was a steep increase in the degree of crystallisation for the initial few layers. A constant rate of crystallisation occurred during the holding period before the powder bed surface was reheated. Thus, the outcome of the initial layers appear to be the most crucial in achieving successful builds. The method of utilising sacrificial parts to combat this effect is commonly employed in commercial machines. Sacrificial parts provides initial heat input and may aid in the mitigation of thermal and stress gradients during the processing of the first few layers [224].

As seen in Figure 5.21, the "stair-stepping" effect was most significant during the first few layers; before eventually stabilising due to the transfer of heat energy to the subsequent layers which slightly raised the temperature and inhibited crystallisation. Crystallisation can cause inhomogeneous stress distribution between the layers which significantly influences warping and the geometrical properties of the part. The initial

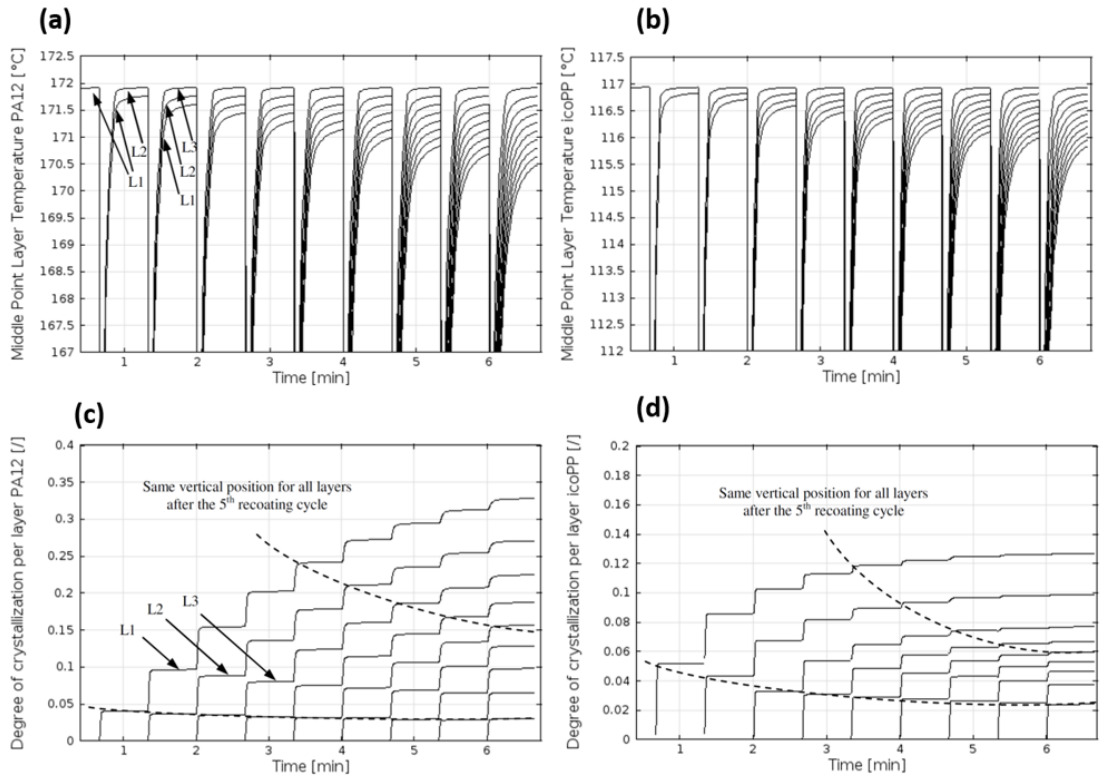


FIGURE 5.21: Graphs showing the simulated temperature variation of (a) PA12 and (b) icoPP at the centre of each layer during. L1, L2 and L3 denote layer number. Whilst graphs (c) and (d) show the cumulative degree of crystallisation for PA12 and for icoPP respectively. Note the cyclical manner of the temperature variation and "stair-step" pattern of crystallisation. Adapted from [2].

simulation by Amado et al. [2] was validated in situ by monitoring the laser sintering of icoPP in a commercial system. The model developed by Amado et al. [292] correlated with their experimental observations, as the development of curl occurred 640 s into the build. At that point the degree of crystallisation was above 50%. The stress distribution between the layers was highly inhomogeneous which was associated with the different crystallisation degree along the build direction. The difference recorded between the stress distribution after the first layer and at the end of the crystallisation phase was more than 100 times.

Thus, the following factors all affected the ability to process nanocoated powders in this work: high surface coverage of nHA affected the heat-transfer between particles; the entanglement of MWCNT-nHA blocked some the laser interaction between MWCNT and the polymer particle; the increase in viscosity reduced particle fusion; the alteration to the crystallisation mechanism of the polymer by the NPs and by poor thermal

management within the machine itself. Despite some of these limitations, there was a narrow processing window in which successful parts could be achieved. The next chapter will explore some of the mechanical properties of the laser sintered samples produced on both the commercial and consumer laser sintering systems.

Chapter 6

Characterisation of Laser Sintered Nanocomposites

This chapter examines what effect the laser sintering parameters, used for each of the PA12 and PLA powder compositions, and the presence of nHA and MWCNT-nHA, had on the final part properties of the nanocomposites, for their suitability as a bone substitute material. It was originally hypothesised that the addition of NP would increase the tensile properties of the nanocomposite. However, due to the processing difficulties encountered in the Chapter 5, a decline in tensile properties was expected with nanocomposites containing the highest loading of MWCNT and nHA. To test the hypothesis analysis of part density via helium pycnometer, in Section 6.2; tensile testing using the Ingstron Unaxial Tensile tester, in Sections 6.2.2 and 6.6.1; and compression testing in Section 6.6.3. Due to the processing issue encountered for the PLA-MWCNT-nHA powders which led to severe warping of the final parts, a heat treatment process was explored (Section 6.4) in an effort to improve the bulk density and thus mechanical performance of the PLA based nancomposites. These heat-treated samples were also subject to density measurements and tensile testing, in addition to compression testing and dynamic mechanical analysis. The microstructure of the PA12-nHA, PA12-MWCNT-nHA and PLA-MWCNT-nHA nanocomposites were also examined, via SEM of the fracture surfaces in Section 6.3 and 6.7.1 and to assess whether the microsturcture of the PLA based nancomposites had changed due

TABLE 6.1: Summary of the processing parameters used for PA12-nHA and PA12-MWCNT-nHA powders.

Material	Laser Power (W)	Laser Speed (mm s^{-1})	Spot Size (mm)	Machine
PA0	21	2500	0.25	Formiga P100
PA05H	20	2500	0.25	Formiga P100
PA1H	16	2500	0.25	Formiga P100
PA1.5H	10	2500	0.25	Formiga P100
PA05M	2.3	500	0.05	Sintratec
PA05M2H	2.3	500	0.06	Sintratec
PA05M5H	2.3	500	0.06	Sintratec

to the heat treatment process. Due to the dynamic loading of natural bone, in real life conditions, the visocelastic properties of the PLA based nancomposites were also explored via DMA, in Section 6.7. Section 6.8 offers an overall discussion of the results.

6.1 Characterisation of PA12 Laser Sintered Nanocomposite Samples

The parameters used to process PA12-nHA and PA12-MWCNT-nHA powders were selected based on powder processability, dimensional accuracy and handleability, as defined in Chapter 3 and discussed in Chapter 5. A summary of the parameters used in both the Formiga P100 and Sintratec can be seen in Table 6.1.

6.2 Density Measurements of PA12 Nanocomposites Processed In a Commercial Machine (Formiga P100)

Specimens used for the density measurements were taken from the end grip sections of the tensile test specimens following tensile testing. Density measurements were conducted on the PA0, PA05H, PA1H and PA1.5H nanocomposite samples and the

results are summarised in Table 6.2. Statistical analysis did not show any signifcant difference between PA1H, PA05H and PA0. However, PA1.5H did record the lowest density, which was signficantly different compared to the other samples tested. This could be due to the reduction in consolidation between the polymer particles; this is further evidenced by SEM images taken of the fracture surfaces as seen in section 6.3.

TABLE 6.2: Density measurements taken for PA0, PA05H, PA1H and PA1.5H nanocomposite samples, which were produced in the Formiga P100, SE n = 5.

Material	**Density (g mm^{-3})**
PA0	0.91 ±0.03
PA05H	0.92 ±0.04
PA1H	0.89 ±0.05
PA1.5H	0.63 ±0.02

6.2.1 Density Measurements of PA12 Nancomposites Processed In a Consumer Machine (Sintratec)

Density measurements on PA05M, PA05M2H and PA05M5H nanocomposite samples, produced in the Sintratec are presented in Table 6.3. The PA05M2H recorded a lower average part density compared to PA05M and this difference was statistically significant ($P<0.05$, as detailed in Chapter 3). The PA05M5H samples recorded the lowest average part density. This may be due to a reduction in the consolidation between the polymer particles, which resulted in a greater number of pores throughout the structure; this can been seen in SEM images of the fracture surfaces taken for these samples which are presented in section 6.3. However, despite the large difference in density recorded between PA05M2H and PA05M5H powders this was shown not to be statistically significant due to a higher degree of variation amongst the PA05M5H samples, presumably as a result of the increased processing difficulties associated with the powder which resulted in samples with varying internal structures.

TABLE 6.3: Density measurement taken for PA05M, PA05M2H and PA05M5H, nanocomposite samples which were produced in the Sintratec.

Material	Density (g mm^{-3})
PA05M	0.97 ±0.05
PA05M2H	0.71 ±0.05
PA05M5H	0.59 ±0.12

6.2.2 Tensile Measurements of PA12 Nanocomposites Processed In a Commercial Machine (P100)

The tensile properties for the PA0, PA05H, PA1H and PA1.5H samples processed in the Formiga P100 are presented in Table 6.4. The tensile test results obtained for the PA05H samples were significantly different when compared to the PA0 samples, with PA05H showing improved tensile properties. The PA1H samples, which were made using a slightly lower laser power of 16 W compared to the 21 W of the PA0, also showed significantly improved mechanical properties, when compared to PA0 powders with an increase in modulus and UTS of 13% and 9% respectively. Similar to the observations made for PA05H samples the EOB also declined significantly, by 44%. The PA1.5H samples, which was the highest composition that could be processed in the Formiga P100, required an even lower laser power of 10 W; this resulted in PA1.5H having the lowest, average, mechanical properties with a significant reduction in modulus and UTS of 66% and 104% respectively. The PA1.5H samples also recorded the lowest EOB with an 84% reduction when compared to the PA0 samples. This could be due to the higher degree of porosity associated with the PA1.5H samples as a result of the lower laser power used to process the powder due to the narrowing of processing window. This was evident in the SEM analysis of the fracture surfaces as presented in section 6.3.

TABLE 6.4: Tensile test data for PA0, PA05H, PA1H and PA1.5H samples, processed in the Formiga P100, SE n = 5.

Material	Young's Modulus (GPa)	Ultimate Tensile Strength (MPa)	Elongation at Break (%)
PA0	1.43 ±0.16	40.70 ±0.23	23.58 ±3.52
PA05H	1.72 ±0.02	46.76 ±0.38	12.58 ±1.84
PA1H	1.63 ±0.02	44.30 ±0.50	13.19 ±1.42
PA1.5H	0.72 ±0.09	12.91 ±1.90	3.89 ±3.94

6.2.3 Tensile Measurements of PA12 Nanocomposites Processed In a Consumer Machine (Sintratec)

The tensile properties of PA05M, PA05M2H and PA05M5H samples, processed in the consumer laser sintering machine (Sintratec) are summarised in Table 6.5. The PA05M2H samples recorded a 9% and 10% decrease in modulus and UTS, in addition to a substantial decrease of 76% in the EOB when compared to the PA05M sample. The PA05M5H samples, recorded the highest reduction in the tensile properties with a 42%, 56% and 84% reduction in modulus, UTS and EOB, respectively. Once again, the EOB decrease recorded for all samples containing nHA was lower, by a factor of four, when compared to PA05M. This could be attributed to the greater free volume within the structure of the sample as a result of poorer consolidation of the particles, as evidenced by the density measurements (Table 6.3).

TABLE 6.5: Average tensile test data for PA05M, PA05M2H and PA05M5H samples, processed in the Sintratec, SE n = 5.

Material	Young's Modulus (GPa)	Ultimate Tensile Strength (MPa)	Elongation at Break (%)
PA05M	1.83 ±0.23	46.70 ±0.40	12.65 ±0.15
PA05M2H	1.68 ±0.23	42.20 ±0.60	3.10 ±1.05
PA05M5H	1.06 ±0.40	20.60 ±0.04	2.03 ±1.21

6.3 SEM of Fracture Surfaces

Following tensile testing of the PA12-nHA (processed in the P100) and PA12-MWNCT-nHA nanocomposites (processed in the Sintratec), the fractured ends of the samples were recovered and examined under SEM.

6.3.1 SEM of PA12 Nanocomposites Processed In a Commercial Machine

Following tensile testing, the fractured ends of the PA12 and PA12-nHA samples that were processed in the P100 were recovered and analysed under SEM. In figure 6.1 had

a rough, angular surface texture which was indicative of a brittle mode of failure. Some small pores can be seen where particles have not completely consolidated. Micro-pits caused by particle de-bonding can also be seen. In figure 6.3 (a), the PA05H also had a roughened fracture surface with no significant signs of plastic deformation; there was also some visible signs of porosity within the structure.

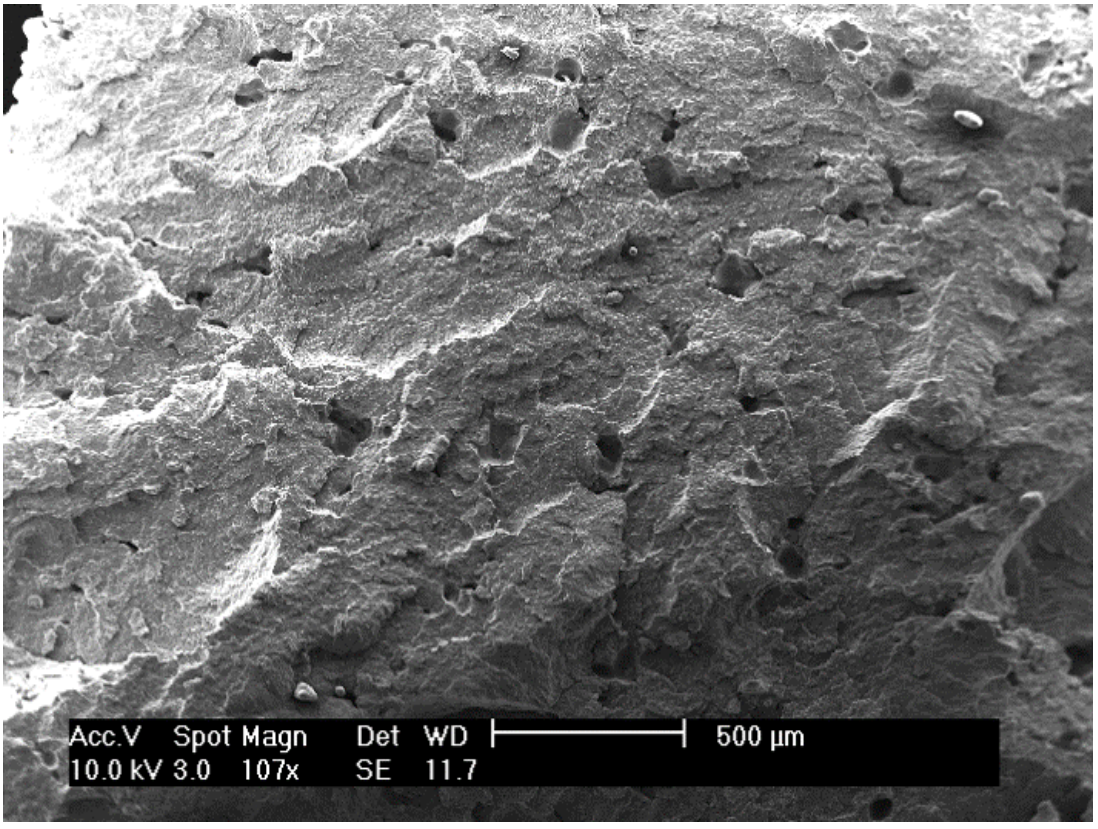


FIGURE 6.1: SEM image of the fracture surface of a PA0 sample.

Increased magnification of the same surface, as seen in Figure 6.3 (b), again revealed a roughed, granular-like, surface texture orientated approximately 50 degrees to the image plane with no visible signs of extensive plastic deformation. The surface of the PA1H sample, in Figure 6.3 (c), had a similar surface texture to the PA05H fracture surface. However, there were clear signs of partially sintered particles, with micro-pits, caused by particle de-bonding. The higher magnification image, as seen in Figure 6.3 (d), showed the surface with more randomly orientated ridges with non-uniform heights, suggesting a slightly more ductile element of fracture occurred compared to the PA05H sample. The fracture surface of the PA1.5H sample, as seen in Figure 6.3 (e), also showed clear signs of partially sintered particles leading to a large volume of

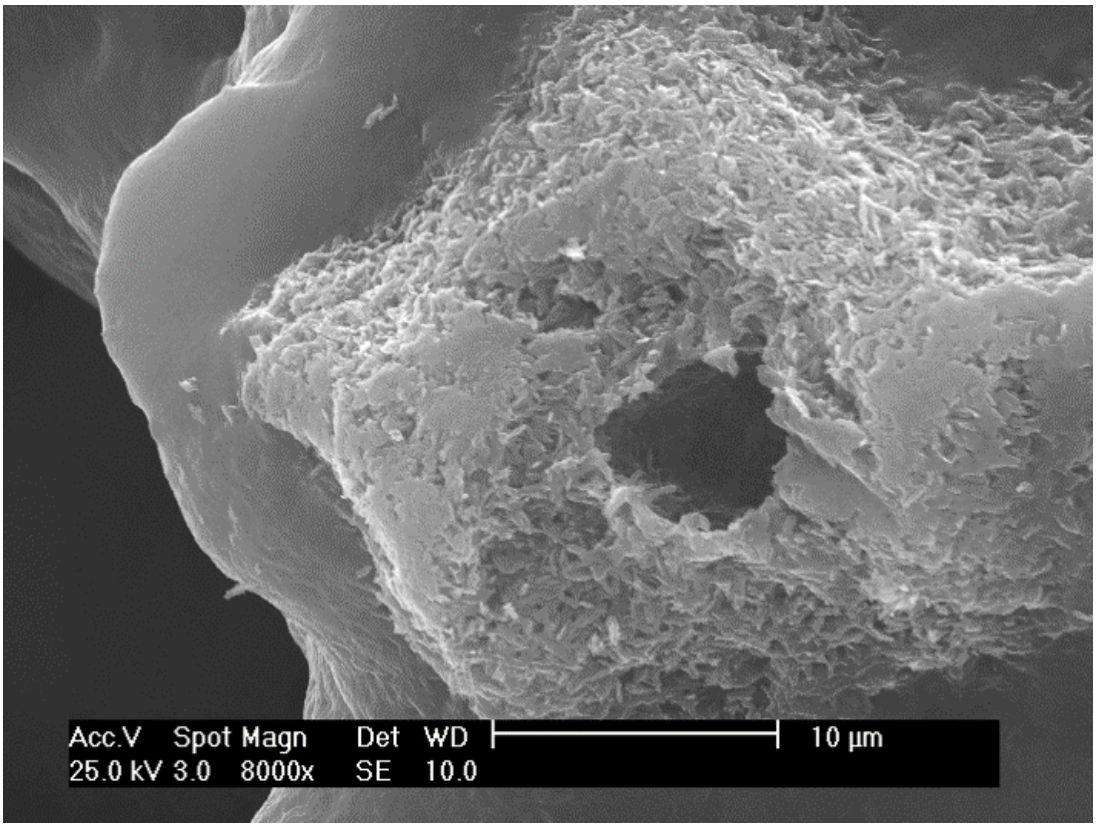


FIGURE 6.2: Close up of the fracture surface of a PA1.5H sample. Debonding of particle has a occurred leaving behind a region with highly agglomerated nHA.

voids present between the layers. The higher magnification image, in Figure 6.3 (f), showed signs of brittle fracture between the sintering necks on the partially sintered particles with large voids; all indicative of insufficient laser power to fully fuse the particles together during laser sintering.

Figure 6.2, shows a close up of the fracture surface of a PA1.5H sample. The debonding of a particle has occurred which has left behind a region high with agglomerated nHA. This indicates that the region between two coated polymer particles have a high concentration of nHA.

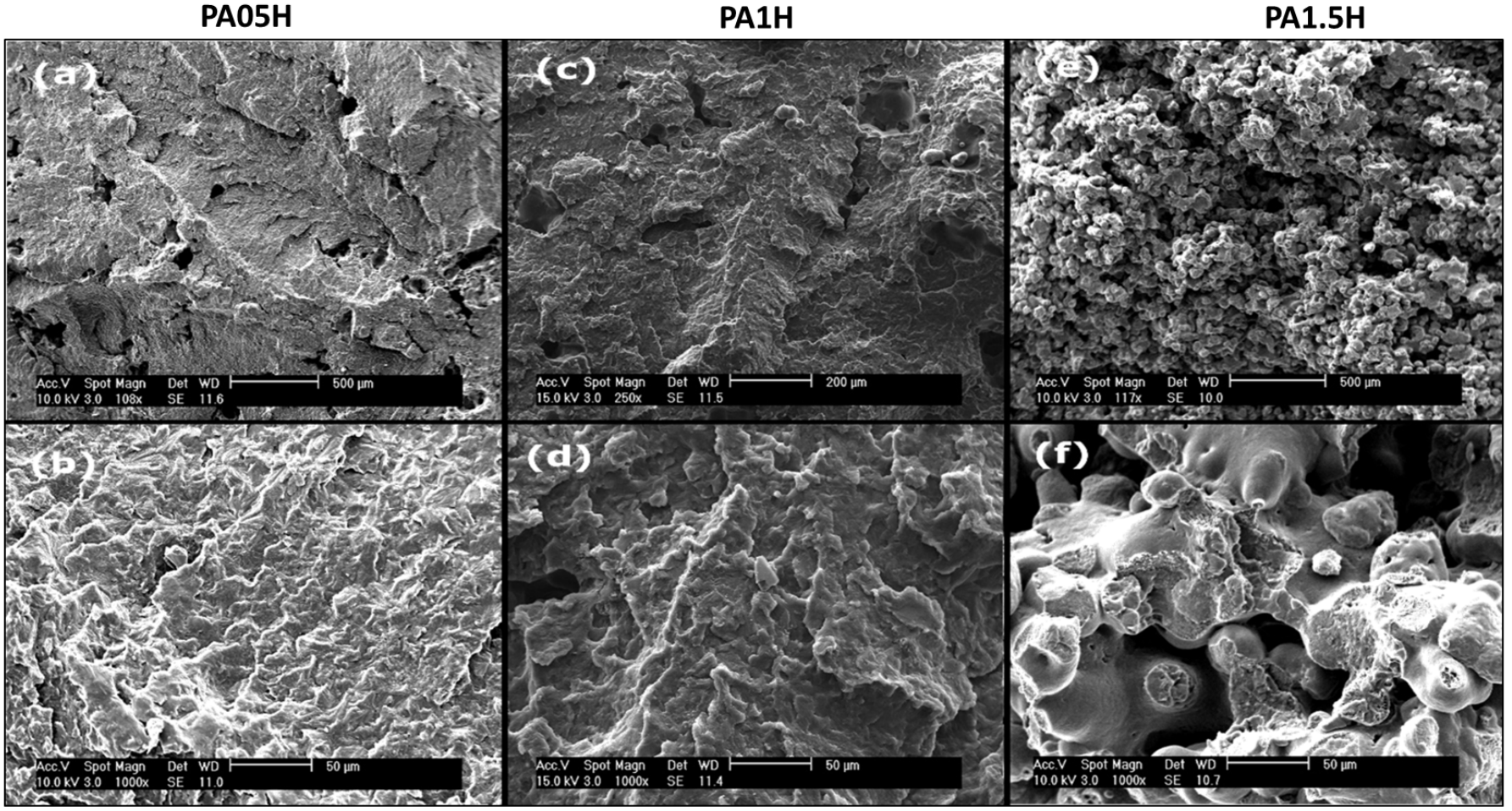


FIGURE 6.3: SEM images of the fracture surfaces of (a) and (b) PA05H, (c) and (d) of PA1H and (e) and (f) PA1.5H nanocomposites taken at low and high magnification.

6.4 Characterisation of PLA Based Nanocomposite Samples

The different PLA powder compositions were processed using parameters based on ease of processing, dimensional accuracy and handleability. A summary of the parameters used in the consumer laser sintering machine (Sintratec) can be seen in Table 6.6. As the laser power is fixed at 2.3 W, in the Sintratec system, the scan speed and hatch spacing was varied.

TABLE 6.6: Summary of the Sintratec parameters used for each composition of coated PLA powder.

Material	Laser Power (W)	Laser Speed (mm s^{-1})	Spot Size (mm)	Machine
PL1M	2.3	400	0.03	Sintratec
PL1M2H	2.3	300	0.04	Sintratec
PL1M5H	2.3	200	0.04	Sintratec

6.5 Density Measurements of PLA Nanocomposites Processed In a Consumer Machine (Sintratec)

Density measurements on PL1M, PL1M2H and PL1M5H nanocomposites are presented in Table 6.7. The PL1M2H sample recorded a 21% lower average part density compared to PL1M, this was reported to be significantly different. The PL1M5H recorded the lowest average density of all samples with a decrease of 37% compared to PL1M, this was also reported as being significantly different. Despite a large difference in density between the PL1M5H and PL1M2H samples no statistical difference between the average densities was reported. This reduction in final part density can, again, be attributed to reduction in particle consolidation during laser sintering when compared to PL1M samples.

TABLE 6.7: Density measurements taken for PL1M, PL1M2H and PL1M5H nanocomposite samples produced in the Sintratec, SE n = 5.

Material	**Density (g mm^{-3})**
PL1M	0.83 ±0.80
PL1M2H	0.61 ±0.04
PL1M5H	0.52 ±0.07

6.5.1 Density Measurements of the Heat Treated PLA Nanocomposite Samples

In an effort to improve the final part densities of the PLA nanocomposites, and thus aid in improving the final part mechanical properties, the PLA samples were subject to a heat treatment process. Samples were placed in a preheated oven and held at 164°C, just within the onset of melting, and held isothermally for 4 hours to provide sufficient time to consolidate the under-sintered particles within the bulk of the samples.

The average part density of the heat treated samples are presented in Table 6.8. The heat treatment process increased the average part density for all the samples. The PL1M HT samples recorded a 37% increase compared to untreated PL1M samples, which was significantly different. The PL1M2H HT and PL1M5H HT samples recorded an increase in average part density of 78% and 92% respectively, when compared to their untreated counterparts. These results were significantly different. However, when comparing just heat treated samples between each other, there was no significant difference between the average densities.

TABLE 6.8: Density measurements taken for PL1M HT, PL1M2H HT and PL1M5H HT nanocomposite samples, SE n = 5.

Material	**Density (g mm^{-3})**
PL1M HT	1.13 ±0.03
PL1M2H HT	1.08 ±0.02
PL1M5H HT	1.01 ±0.03

6.6 Dimensional Change of PLA Samples Following Heat Treatment

Following the heat treatment of the PLA nanocomposites, the resulting samples experienced shrinkage as the free volume within the sample was reduced. This was due to consolidation of the polymer particles within the structure of the material. This was evident when comparing the SEM images of the fracture surfaces of heat treated and non-heat treated samples in section 6.7.1. The X, Y and Z dimensions (Figure 3.4 in Chapter 3) were measured using digital vernier callipers and the % shrinkage was reported. The results of this can be seen in Figure 6.4.

The average % shrinkage in the X dimension was recorded as 1.9 $\pm$1.5%, 2.2 $\pm$2.3% and 1.7 $\pm$1.4% for the PL1M HT, PL1M2H HT and PL1M5H HT samples respectively. However, the Y dimension recorded the most significant shrinkage of 18.6 $\pm$4.0%, 23.5 $\pm$6.1% and 20.7 $\pm$5.7%. The Z dimension recorded the second highest, average, shrinkage of 7.3 $\pm$1.2%, 4.0 $\pm$3.1% and 5.3 $\pm$2.0%.

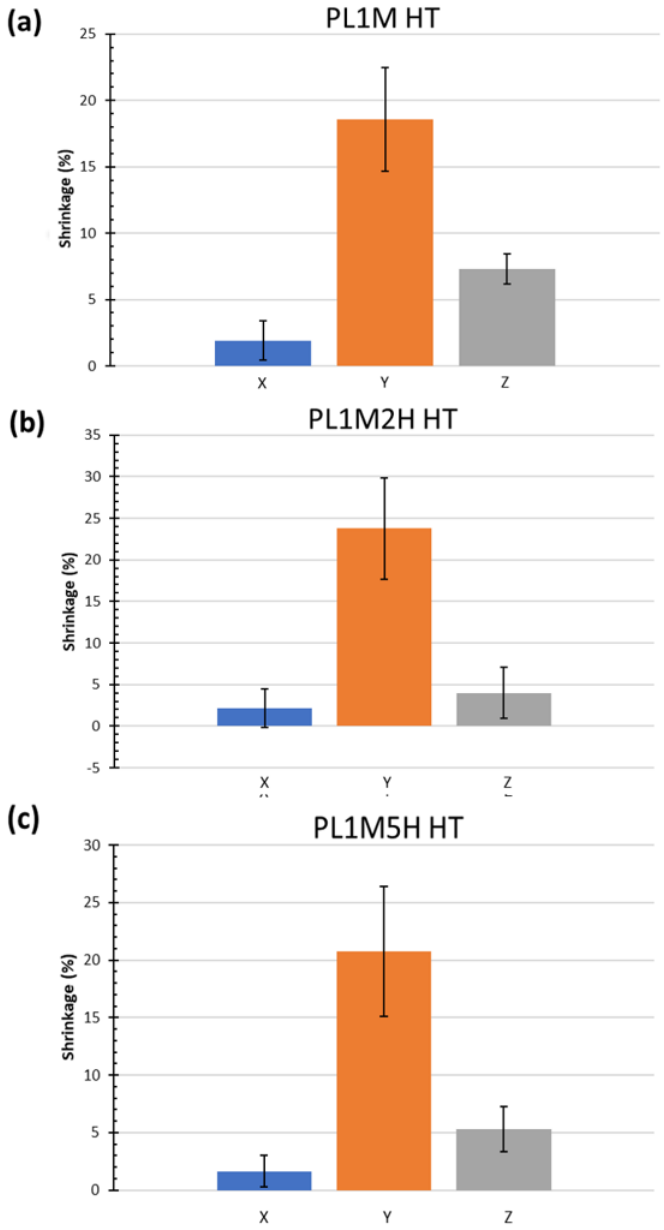


FIGURE 6.4: A series of charts showing the average % shrinkage measured in the X, Y and Z dimensions of (a) PL1M HT (b) PL1M2H HT and (c) PL1M5H HT samples. The image in figure (d) displays the CAD drawing of the tensile specimen. The largest dimensional error was recorded in the Y direction following heat treatment.

6.6.1 Tensile Measurements of PLA Nanocomposites Processed In a Consumer Machine (Sintratec)

The tensile properties of PL1M, PL1M2H and PL1M5H samples are summarised in Table 6.9. The PL1M2H sample recorded a reduction in tensile properties of 17%,

23% and 88% in modulus, UTS and EOB respectively when compared to PL1M. The PL1M5H samples possessed the lowest tensile properties with a drop of 110%, 125% and 98% in modulus, UTS and EOB respectively. The significant decline in properties can be attributed to reduced part density and greater levels of pores within the final sample as seen in the SEM images of the fracture surfaces presented in 6.7.1.

TABLE 6.9: Average tensile test data for PL1M, PL1M2H and PL1M5H samples, processed in the Sintratec, SE n = 5.

Material	Young's Modulus (GPa)	Ultimate Tensile Strength (MPa)	Elongation at Break (%)
PL1M	2.28 ±0.20	26.50 ±1.10	3.84 ±1.01
PL1M2H	1.92 ±0.16	21.20 ±1.10	0.48 ±0.29
PL1M5H	0.66 ±0.13	6.10 ±0.90	0.16 ±0.01

6.6.2 Tensile Measurements of Heat Treated PLA Nancomposite Samples

The tensile properties of PL1M HT and PL1M2H HT and PL1M5H HT are summarised in Table 6.10.

TABLE 6.10: Average tensile test data for PL1M HT, PL1M2H HT and PL1M5 HT samples, SE n = 5.

Material	Young's Modulus (GPa)	Ultimate Tensile Strength (MPa)	Elongation at Break (%)
PL1M HT	2.84 ±0.12	23.59 ±0.16	1.13 ±0.05
PL1M2H HT	2.77 ±0.12	19.82 ±3.58	0.68 ±0.12
PL1M5H HT	2.57 ±0.15	17.14 ±4.45	0.24 ±0.05

The heat treated PL1M HT samples reported a small 13% improvement in modulus compared to their non heat-treated equivalent. However the UTS declined by 24%; furthermore, the EOB decreased substantially following heat-treatment, dropping by 71%. The PL1M2H HT also saw an increase in modulus of 44%. However, on this occasion, the PL1M2H HT samples reported a decline in UTS, dropping by 7%. The EOB increased significantly by 42% due to an increase in final part density. The PL1M5H HT samples saw the most significant improvement in tensile properties, due to increased consolidation within the bulk. The modulus increased by 327%. The UTS also increased by 181% in addition to the EOB increasing by 50%. The heat-treatment

improved the stiffness of the samples, however some of the load handling capabilities declined when compared to the untreated counterparts, whereas the PL1M5H HT samples saw an increase in all measured tensile properties.

In Figure 6.5, a series of charts comparing the heat-treated samples to their non heat-treated counterparts can be seen. Heat-treatment provided an effective way of improving the stiffness of the samples through improved final part density.

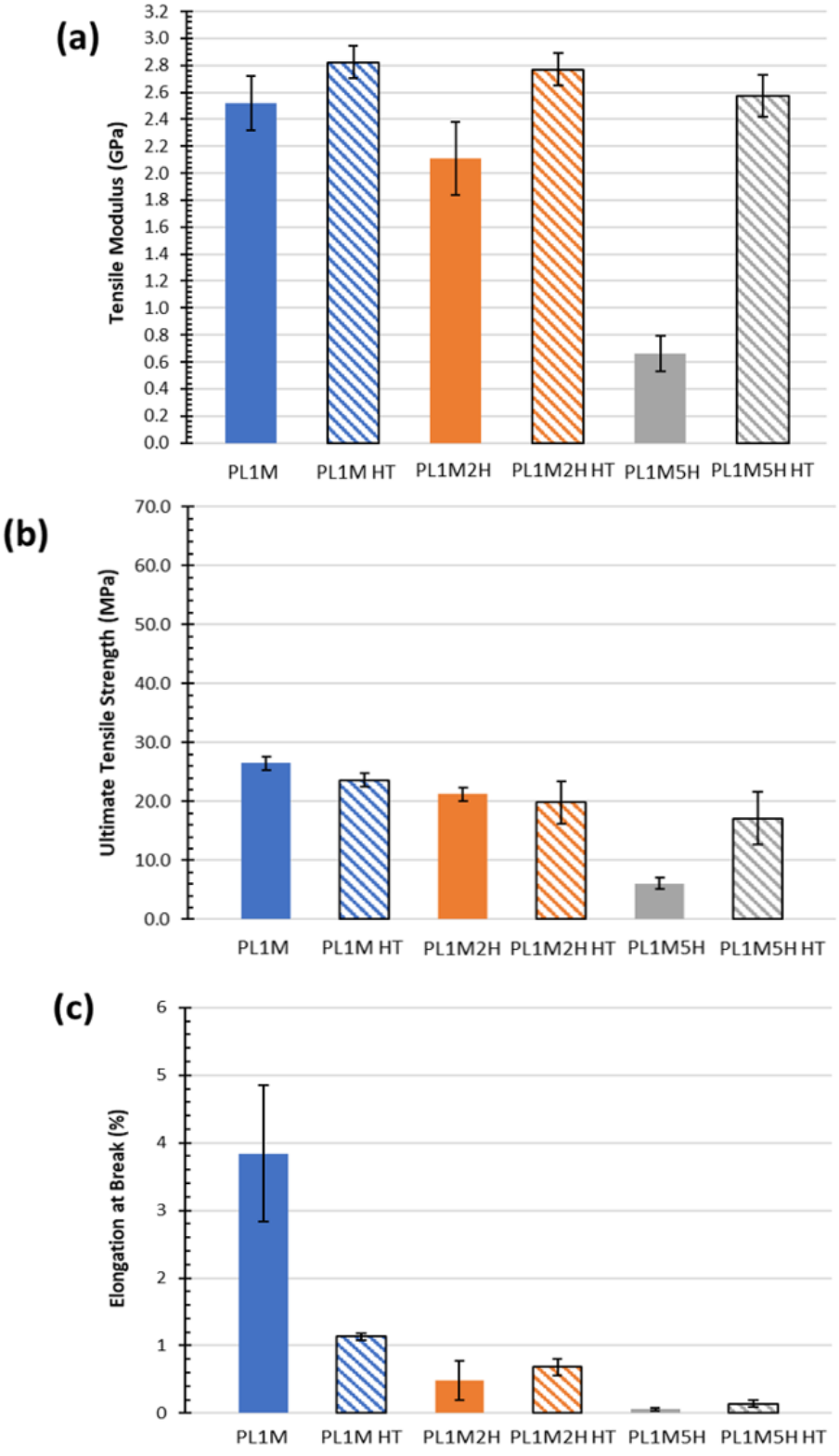


FIGURE 6.5: A series of charts comparing the tensile properties of heat-treated PLA nanocomposites and the non heat-treated PLA nanocomposites. Chart (a) is of tensile modulus, (b) ultimate tensile strength and (c) elongation at break. The heat treatment process increased the modulus, most notably for the PL1M5H HT samples, due to the reduction in the free volume within the sample bulk. The UTS for PL1M HT and PL1M2H HT declined whereas the PL1M5H HT reported an increase when compared to non heat-treated equivalent. The EOB for PL1M HT samples declined substantially when compared to its non heat-treated counterpart. Standard error n=5.

6.6.3 Compression Testing of PLA Nanocomposite Samples

The compressive properties of the PLA samples were also tested. Cylindrical samples measuring 20 mm in diameter and 30 mm in height were subject to the test. The results are resented in Table 6.11. However, due to warping issues encountered during processing of PL1M2H and PL1M5H powders, the top face of the samples had slight deformities and were not flat; therefore, the linear variable differential transformer (LVDT) sensors used for the compression testing could not accurately detect strain. The compressive modulus for PL1M2H and PL1M5H was therefore omitted from the results and only compressive stress is reported for these samples.

The compressive strength of PL1M2H and PL1M5H samples was significantly worse than PL1M by 32% and 93% respectively. Following heat-treatment the compressive strength for all samples improved. The compressive strength and modulus of PL1MHT improved by 5% when compared to PL1M. However, this difference was not significant. The compressive strength of PL1M2H HT improved by 45% when compared to PL1M2H. The PL1M5H HT samples saw the most significant improvement in average compressive strength of 208% when compared to PL1M5H.

TABLE 6.11: Average compressive properties of untreated and heat treated PLA-MWCNT-nHA samples, SE n = 5.

Material	**Compressive Strength (MPa)**	**Compressive Modulus (MPa)**
PL1M	90.2 ±10.3	130.1 ±9.6
PL1M2H	65.1 ±7.9	-
PL1M5H	32.9 ±5.5	-
PL1M HT	95.0 ±3.3	137.7 ±8.7
PL1M2H HT	94.7 ±5.0	-
PL1M5H HT	101.4 ±5.0	-

6.7 Dynamic Mechanical Analysis of PLA Nanocomposite Samples

DMA analysis was conducted on the PL1M, PL1M HT and PL1M5H HT samples to determine the viscoelastic properties of the nanocomposites. The results for PL1M5H were omitted, this was due to their brittle and weak nature which resulted in all samples failing mid-way though DMA testing. The storage modulus (G′), loss modulus (G″) and tan δ are reported in Figures 6.6, 6.7 and 6.8.

The storage modulus is shown in Figure 6.6. The PL1M sample possessed a G′ of 1.45x10^{-9} Pa at 40°C, and showed a significant decline in modulus as the temperature was increased beyond the Tg. The PL1M HT sample possessed a significantly higher storage modulus compared to both PL1M and PL1M5H HT samples. The G′, at 40°C, was recorded at 2.49x10^{-9} Pa, an increase of 72%. The sample also showed a rapid decline in modulus as the temperature increasedas shown in Figure 6.6. The PL1M5H HT displayed a lower storage modulus when compared to the PL1M HT samples with an average G′ of 2.09x10^{-9} Pa, at 40°C, representing a difference of 57% compared to the PL1M HT samples. Thus the ability to store deformation energy in an elastic manner was greatest for the PL1M HT sample compared to PL1M5H HT and PL1M samples.

The loss modulus represents the viscous response of the material [359] and is therefore a measure of energy dissipation within the material in response to an applied load [360]. As seen in Figure 6.7, the G″ increased as the temperature was raised from 40°C. This indicated segmental movement of the polymer chains within the amorphous region of the polymer matrix [1].

In this case, the PL1M HT samples possessed the greatest G″ peak, indicating that much of the molecular segmental motion was dissipated as heat, arising from internal friction between MWCNT and the polymer matrix, thus restricting molecular motion [1] [361]. The PL1M5H HT possessed a lower peak G″ which may be attributed to agglomeration of the nHA within the matrix.

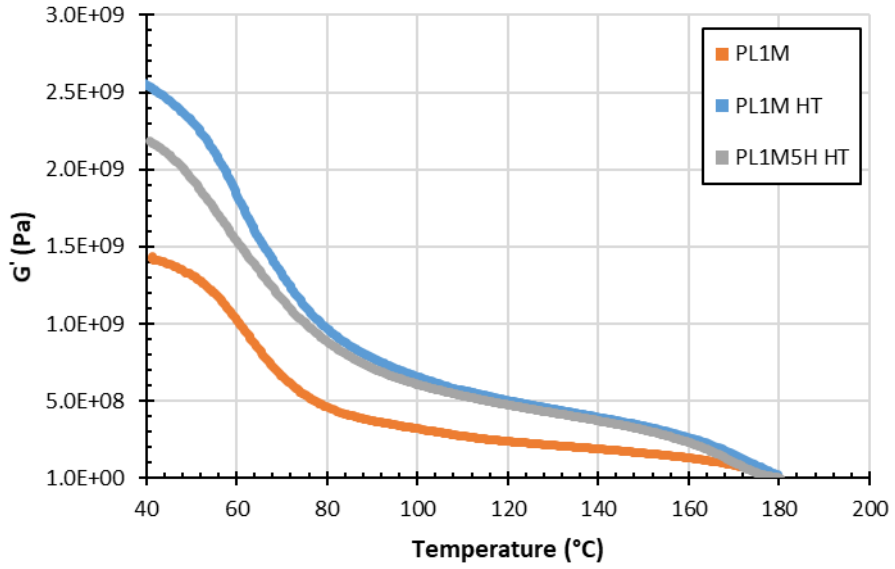


FIGURE 6.6: Graph showing the storage modulus of the heat treated PL1M HT and PL1M5H HT samples and a non-heat treated PL1M sample. The storage modulus of the heat treated samples was significantly higher than that of the non treated PL1M. The stiffness of the samples decreased as the temperature increased beyond Tg.

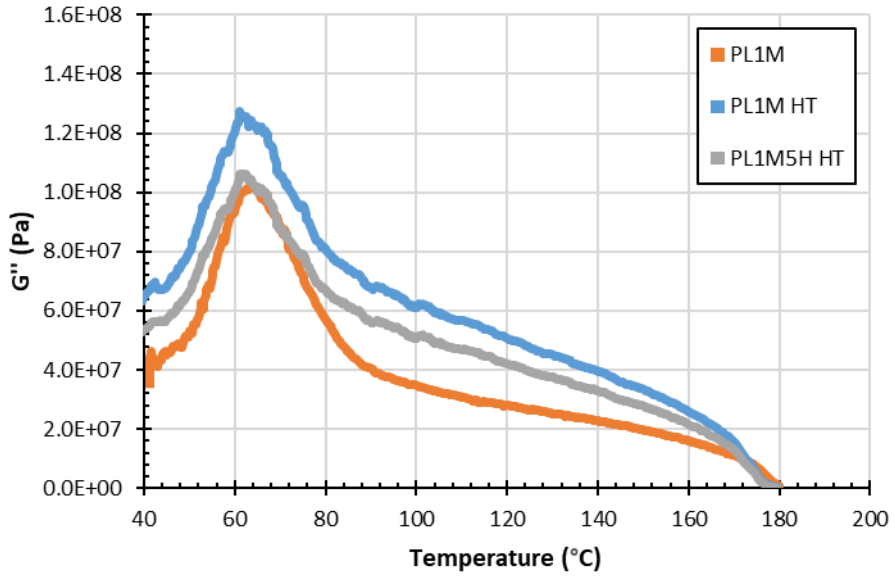


FIGURE 6.7: Graph showing the loss modulus of PL1M, PL1M HT and PL1M5H HT samples. PL1M HT possessed the highest loss modulus peak at approximately 64°C. The loss modulus for the PL1M5H HT samples was significantly lower, with a slight decreasing shift in Tg.

The Tan δ, which is the ratio of the G″/G′, provided information on the energy dissipative nature of the nanocomposites. The results of this can be seen in Figure

6.8. The Tan δ of the PL1M samples displays a prominent peak, which is significantly larger than the peaks obtained for both PL1M HT and PL1M5H HT samples. As the temperature increased beyond 70°C, the Tan δ decreased and then plateaued as the temperature was increased further. In contrast, the curves for the PL1M HT and PL1M5H HT displayed a significantly lower curve, indicative of a more elastic response to applied loading. This response was maintained even as the temperature was increased, indicated by the lack of a steep drop off in Tan δ, but rather a small one. This indicated that the energy dissipative potential of the PL1M samples was greater than that of the heat-treated samples, with PL1M HT and PL1M5H HT possessing a greater elastic response to applied loading.

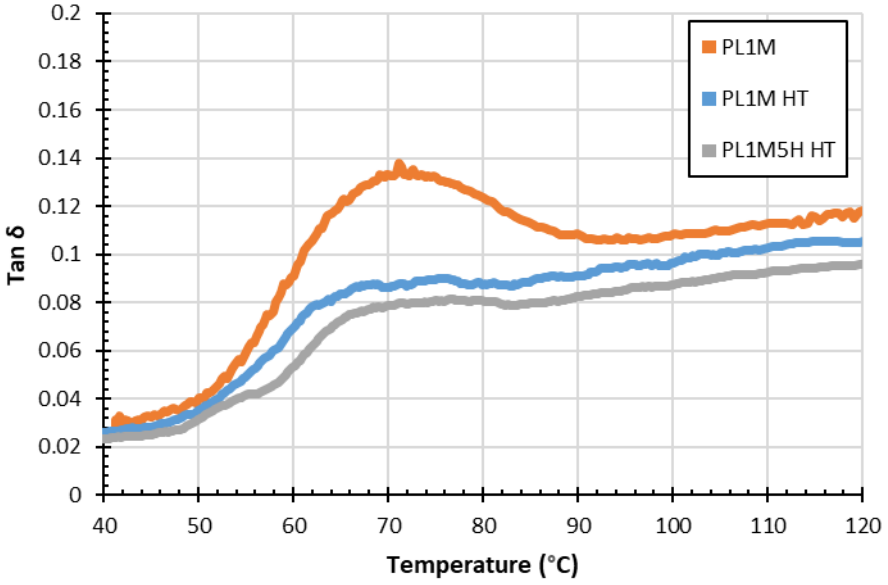


FIGURE 6.8: Chart showing the Tan delta of PL1M, PL1M HT and PL1M5H HT samples. The dampening potential of the PL1M sample was significantly higher than that of the heat treated PLA samples. PL1M5H HT displayed the lowest dampening potential of all the samples.

6.7.1 SEM of PLA Nanocomposites Processed In a Consumer Machine (Sintratec)

The PL1M fracture surface, as seen in Figure 6.9 (a) and (b), appeared to have a roughened, granular-like surface texture which was indicative of a more brittle mode of fracture. High magnification of the fracture surface, as seen in Figure 6.9 (b), revealed

small fibril like structures which could be caused by the de-bonding of the MWCNT, leading to interlamellar failure. The PL1M2H fracture surface, Figure 6.9(c), showed a greater degree of porous voids due to reduced particle fusion. However, similar to the PL1M surface, there was a roughened, granular-like surface texture, indicative of a more brittle mode of failure. Higher magnification images of the surface also revealed fibril like structures. The PL1M5H fracture surface revealed a more substantial degree of porosity within the sample, as seen in 6.9 (e). The surface, once again, had a granular surface texture. Increased magnification (6.9 (f)) showed a more undulating surface, due to de-bonding of non-fused particles.

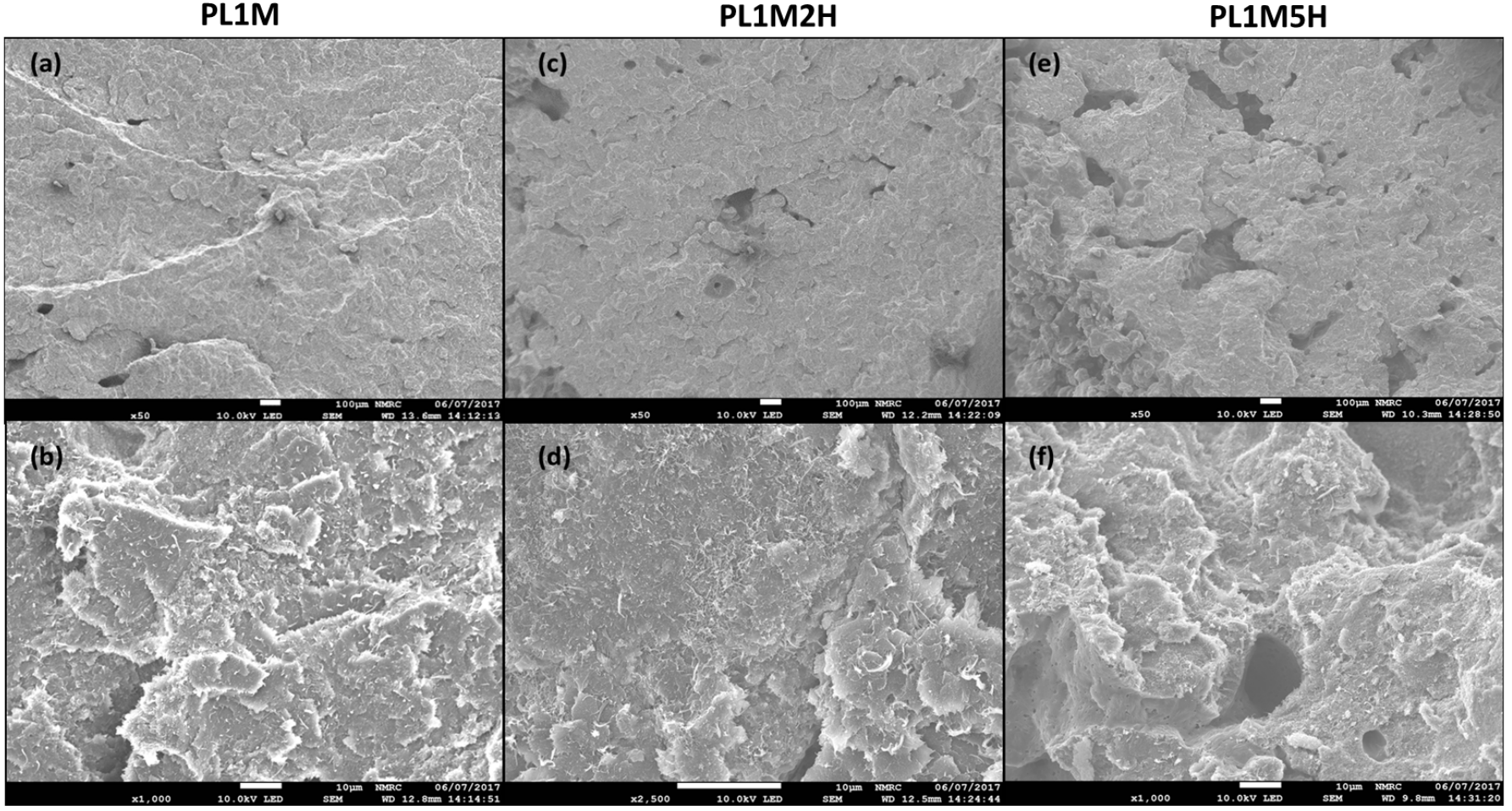


FIGURE 6.9: SEM images of the fracture surfaces of (a) and (b) PL1M, (c) and (d) of PL1M2H and (e) and (f) PL1M5H nano-composites taken at low and high magnification.

6.7.2 SEM of Heat-Treated PLA Nanocomposite Samples

The fracture surfaces of PL1M5H HT samples were also examined, as seen in Figure 6.10 (a) and (b). When compared to the non heat-treated PL1M5H samples, as seen in Figures 6.9 (e) and (f), the heat-treated samples, when viewed at low magnification (Figure 6.10 (a)), had fewer voids visible. The surface of the heat treated samples, once again, had a granular surface texture indicative of a brittle mode of failure. On this occasion, the higher magnification revealed less signs of fibrillation of the surface. The heat treatment may have allowed for a greater degree of consolidation and a reduction in the plastic element of deformation.

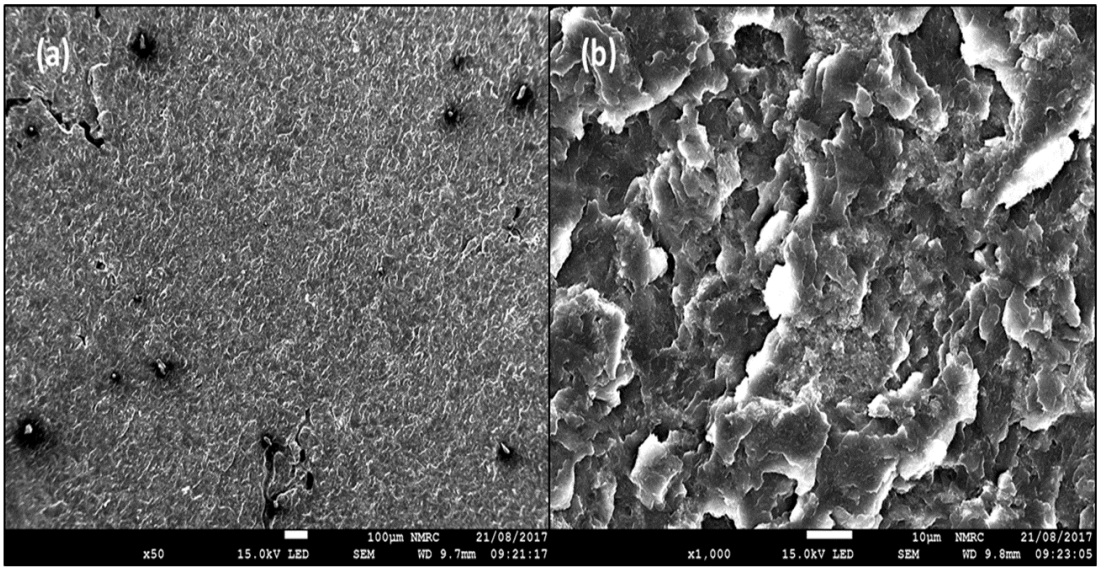


FIGURE 6.10: SEM images of the fracture surfaces of PL1M5H HT samples at (a) low (x50) and (b) high (x1000) magnification. Heat treatment, greatly reduced the porosity with the sample bulk. The appearance of fibril like structures were also less visible after heat treatment.

6.8 Discussion

The results showed that using a relatively low amount of MWCNT increased the mechanical properties of the nanocomposites, produced through laser sintering.

For a low concentrations a NP additives, a simple rule of mixtures can be applied based on randomly orientated discontinuous fibre composites given by [362]:

$$E_{cd} = KE_fV_f + E_mV_m \tag{6.1}$$

Where E_{cd} corresponds to the final modulus of the nanocomposite, E_f and E_m correspond to the modulus of the fibre and matrix, respectively. V_f and V_m correspond to the volume fraction of fibre and matrix, whilst K is the fibre efficiency parameter (0.6 [363]). The reinforcement of the resulting nanocomposite can be approximated. In this case, the modulus of PA12 and PLA matrix can be assumed to be 1.7 GPa [363] and 3.5 GPa [364] respectively, whilst the modulus of MWCNT and nHA can be assumed to be 1.7 TPa [365] and 54 GPa [366]. Due to the significantly higher surface-to-volume ratio that NPs possess the interfacial surface area and surface energy difference between the NP filler and matrix is significantly higher compared to their macro-scale counterparts (For surface energy of pristine MWCNT ≈120 mJ m^{-2} [367] compared to ≈40 mJ m^{-2} for PLA surface [368]) therefore the reinforcement is also expected to be significantly greater than macro-scale reinforcing particles/fillers.

In Bai's work [1, 260], a 0.1 wt% loading of MWCNT increased the elastic modulus and tensile strength by 54% and 6% respectively without decreasing the elongation at break. This was a significantly higher than the expected 16% increase by the rule of mixtures.

In this work, the processing of nHA coated PA12 powders, in a commercial laser sintering machine, also led to an increase in both modulus and UTS. This improvement in Young's modulus and UTS was observed from 0.5-1.0 wt% nHA, the most significant of which was for the PA05H samples which recorded an improvement of 20 and 15% increase, respectively. This was also significantly higher than the expected 9% improvement predicted using the rule of mixtures. The average part density of the PA05H samples was higher than the PA0 samples by 6% although marginal, this will have contributed toward the higher tensile properties than expected. This notion is supported by the observations made in Bai's study who's PA12-MWCNT samples had, on average, 4.1% higher density when compared to pure PA12. Therefore, the increase in final part density observed in this work may have contributed to the higher observed tensile modulus than predicted. The PA1H samples displayed a lower reinforcement of

13% and 9%, for modulus and UTS, compared to the predicted 18% increase. When comparing the average density, the PA1H samples also displayed a slightly lower density compared to PA0 and PA05H samples, thus suggesting that the reinforcement was predominantly due to the presence of nHA. The PA1.5H samples, on the other hand, recorded a significant decline in Young's modulus and UTS of 50% and 70% respectively. When compared to PA0 samples, it was evident from the observations made during laser sintering (reported in the Chapter 5), that the addition of 1.5 wt% nHA resulted in a significant narrowing of the processing window in the Formiga P100. The processing window was defined in Chapter 3, as the set of parameter ranges that enabled the production of completed parts with an average dimensional error of the final part being $\leq$10% of the target dimension (good shape definition) and which can removed from the powder bed without falling apart (good handleability). This decreased processing window led to poor consolidation between the polymer particles, which was also reflected by the significantly lower final part density of 31%, when compared to the PA0, PA05H and PA1H samples. This is shown in Figures 6.3. The decline in processing window and reduction in particle fusion with the presence HA has been extensively discussed in Chapter 5. SEM observations of the fracture surfaces also showed a significant degree of under-sintering associated with the PA1.5H samples, which suggested insufficient energy to achieve adequate consolidation between the particles. The significant decline in modulus, UTS and EOB observed for the remaining samples processed in the consumer machine (PA05M2H, PA05M5H, PL1M2H and PL1M5H) also correlated with the observations made for the PA1.5H samples with a reducing processing window as nHA loading was increased, a decline in final part density, and under-sintering, which could be seen when samples were observed under SEM.

Despite the increase in modulus and UTS observed for PA05H and PA1H samples, a significant decline in EOB of 47% and 44% was observed respectively. A lack of particle fusion was not the cause in this case. It is commonly reported that nanocomposites made by laser sintering see a notable decline in the elongation at break. This could be a result of localised heating of the polymer during laser scanning, resulting in polymer degradation. For example, Salmoria et al. [369], who also produced

PA/MWCNT nanocomposite by laser sintering at 0.5 wt% loading, observed a 9% and 31% improvement in modulus and UTS respectively. However, the elongation at break decreased by 18%. Similar observations were made by Warnakula et al. [370], who produced PA12/nano Al_2O_3 nanocomposites at loadings of 3, 5 and 10 wt%, via laser sintering. The nanocomposites showed significantly improved UTS compared to neat PA12, however, the elongation dropped sharply by around 60–77%. Koo et al. [371] also observed significant reductions in the elongation at break for PA11/ nanoclay and PA12/nanoclay in addition to PA11/carbon nanofibers and PA12/carbon nanofibers. In another study, Rietzel et al. [372] explored laser sintering processing of polyoxymethylene powders (POM) filled with aluminium (up to 30 wt%). An increase in modulus and strength was also observed, however, they also experienced significantly lower elongation at break. Yan et al. [373] also observed a decline of 20, 36 and 65% for PA12/Al composites containing 10, 30 and 50 wt% Al respectively. This was also reflected with a reduction to the impact strength. If a reduction in EOB was a result of polymer degradation, then the observations of nanocomposites produced via different methods such as dissolution would not see this phenomenon. However, this is not always the case. For example Liu et al. [374], who explored the production of PLGA/nHA and PLGA/nano-titania nanocomposites via casting methods, also observed a reduction in the EOB. It was suggested that, at the microstructural level, the volume of the ductile PLGA phase may have been confined by the surrounding, brittle, NPs which restricted the local deformation under stress, thus leading to a reduction in the elongation at break. Similarly, Saputri et al. [375], also observed a 56% reduction in the EOB for solvent casted films made from a polysaccharide matrix and zinc oxide NPs. Furthermore, contrary to these studies, Bai et al. [1] observed a significant increase in tensile and impact properties with no reduction in the elongation at break. Again, this indicates that the reduction of EOB was not caused by polymer degradation.

In this study, both the PA05H and PA1H samples recorded a large decline in UTS of 47 and 44%. This was likely due to insufficient dispersion of the NPs within the matrix which acted as defects [376]. It is important to note that the NP loading used was 10-60 times higher than that used in Bai's study. Despite the NPs being relatively well

dispersed on the surface of the polymer particles, prior to laser sintering, the likelihood of NPs on the surfaces of adjacent polymer particles being in close proximity or even contacting each other is high. Once the powder was exposed to the laser, the polymer particles coalesced forming necks between adjacent particles. Due to their tendency to form aggregates, once the powder was melted by the laser the flow of material may have provided the opportunity for the NPs to reduce their surface energy by coalescing and forming agglomerates. Therefore, the boundaries between the polymer particles, or sintering border, may therefore have had a high concentration of agglomerated NPs. This was seen in the high resolution SEM image of the PA1.5H fracture surface in Figure 6.2. An overall mechanism for this is depicted in Figure 6.11.

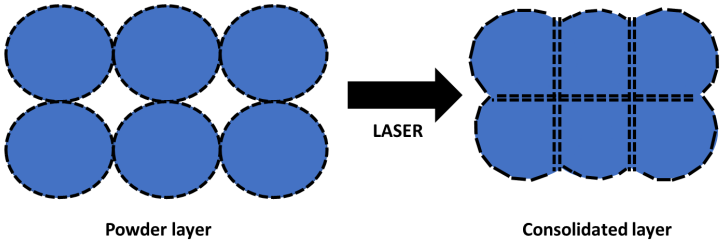


FIGURE 6.11: Schematic showing consolidation of a powder layer. The dashed lines represents NPs. After laser energy is applied the polymer particles coalesce and fuse together. At the sintering borders a high concentraion of NPs can be seen, it likely that the NPs within these regions will be agglomerated.

This could have contributed to the reduction of the elongation at break by acting as defect sites when the final part was subjected to tensile loads [376]. TEM cross sectional analysis of PA12/MWCNT composites conducted in Bai's study [1] may support this notion. His study revealed a high density of MWCNT at the sintering borders between PA12/MWCNT particles. The high loading of nHA used may therefore have exacerbated the issue. However, maximising the nHA content that can be processed is desirable for achieving positive osteogenic and osteoinductive cellular responses to the material, this is discussed further in Chapter 7. In Bai's work, 0.1 wt% may have been below the loading threshold which would create sufficient agglomeration to negatively impact on the final part properties and higher loadings of 0.2 and 0.4 wt% were seen to be agglomerating. Achieving high dispersion within the bulk matrix is still a significant hurdle to overcome when trying to realise the full mechanical benefit that NPs can

provide. However, this work does open further avenues for investigation of methods to maintain NP dispersion during laser sintering in order to process higher NP loadings.

Tensile testing has shown that the PL1M5H samples possessed substantially weaker mechanical properties due to the highlighted processing issues. The decision was taken to subject the PL1M5H samples to a heat treatment process in order to further consolidate the sample. The samples were placed in a preheated oven at 164°C, just within the onset of melting, and held for 4 hours, then allowed to cool down to room temperature. The thermal degradation of the material was expected to be minor <10% of its mass, according to Figure6.12 [377].

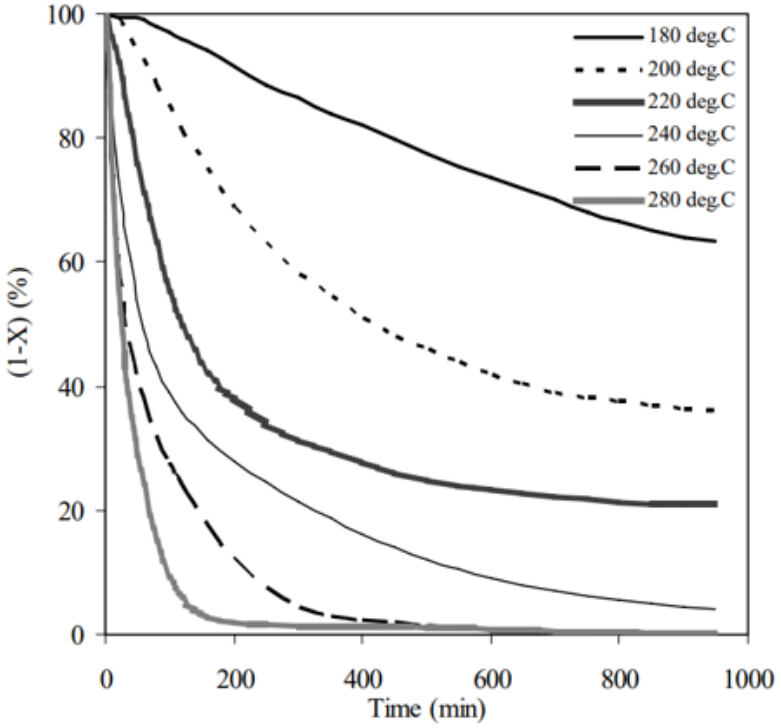


FIGURE 6.12: Graph showing the weight loss of PLA at different isothermal temperatures, adapted from [377].

The PL1M and PL1M2H samples were also subject to the same treatment as a comparison. Following heat-treatment, the stiffness of the samples increased significantly, however the PL1M HT and PL1M2H HT samples saw a significant decline in UTS. Furthermore, all the heat treated samples experienced a significant decline in ductility, which was reflected by a reduction in the EOB. Another effect which may have contributed to the reduction in ductility post-heat treatment was the resulting crystallinity change. Generally, when undrawn semicrystalline polymers are subjected to a constant

time-heat treatment, this can lead to an increase in tensile modulus, yield stress and a decline in ductility [362]. As discussed in Chapter 4, crystallinity is significantly influenced by time and temperature, the long heating and cooling times may have led to an increase in crystalline fraction. The molecular chains of crystalline regions are closely packed and ordered in a parallel arrangement. Secondary bonding between these ordered chain regions is significantly prevalent compared to the surrounding amorphous regions, therefore, crystalline regions deform less under applied tensile loads. As a consequence, as crystallinity increases, the tensile modulus and strength is expected to increase significantly whilst the ductility declines [362]. However, the observed drop in UTS did not follow the expected trend and suggests that agglomeration of NPs within the polymer matrix and poor matrix-NP interaction may have led to this decline by acting as defects within the bulk of the matrix. The dynamical mechanical analysis conducted on the heat-treated samples also pointed to this notion.

Re-heating the nanocomposites to temperatures above the onset melting point, and isothermally holding for a prolonged period allowed the un-melted particle cores to consolidate. This in turn reduced the free volume within the sample bulk and allowed for increased chain entanglement between the MWCNT and nHA. This was explored further by studying the viscoelastic properties of the heat-treated samples via DMA. The storage modulus (G′) represented the elastic response of a material to rapid stresses at a low loading [378]. The heat-treatment significantly increased the nanocomposite stiffness and is confirmed by the observations made during tensile testing. The loss modulus (G″) for the PL1M HT remained consistently the highest, when compared to both the PL1M and PL1M5H HT samples, across the whole temperature range tested. A study by Ahmed et al. [361], which explored the reinforcement of natural rubber with MWCNTs at 1,3,5 and 7 wt%, found that the G′ was mainly dependent on the MWCNT content. Thus as the loading increased from 1 to 7 wt%, the corresponding stiffness also increased. However, the loss modulus displayed a different trend. At first the G″ increased as the MWCNT loading was increased from 1 to 3 wt%, beyond which the G″ declined. It was proposed that in loadings of 3 wt% and less, the MWCNT were more uniformly dispersed throughout the polymer matrix and, therefore, the interfacial area was larger leading to strong interactions between the matrix and

MWCNTs. When the composite was subject to external stresses, the friction generated between the interaction of matrix-MWCNT and MWCNT-MWCNT led to energy being dissipated, which resulted in a high G″. However, when the loading increased beyond 3 wt%, the MWCNTs were more difficult to disperse. These agglomerations acted as defects, which allowed the polymer chains to move more readily, relative to each other, resulting in less energy dissipation and a lower G″. This was accompanied by a decline in the observed Tg under DMA testing [361]. In this work, there was an appreciable decline in G″ for the PL1M5H HT samples. Given the tendency of NPs to agglomerate, the relatively high loading of 5 wt% nHA was difficult to disperse effectively during the powder production stages; this was evident from the SEM images taken of the PL1M5H powders which showed agglomerated nHA on the surface of the particles. The drop in G″ would suggest the presence of a higher degree of agglomerated particles within the matrix of the PL1M5H HT samples. The observed decrease in Tg would also support this, and would also align with the observations made in Ahmed's study [361]. This also aligns with observations made on the Tan δ, which is the ratio of viscous to elastic response (G″/G′) and therefore represents the energy dissipative potential, or damping behaviour, of the material [359]. PL1M HT and PL1M5H HT both possessed a lower dampening potential, and thus displayed more of an elastic response, when compared to the untreated PL1M samples. This is a common observation made for a variety of polymer composites. For example, Shakoor et al. [379] explored the reinforcement of PLA with hemp fibres at 10, 20 and 30 wt% loadings. The composites were processed by compression moulding and DMA analysis showed that the increasing addition of hemp fibres led to a stiffer composite. At 30 wt% loading the storage modulus, at 40°C, had doubled, from 2.18 GPa to 4.55 GPa. The result of this increased stiffness was a reduction in the dampening behaviour with a declining Tan δ as the hemp loading increased. Rostami et al. [380] also observed this trend when exploring PLA/MWCNT and PLA/graphene nanocomposites. The highest loading of 1 wt% MWCNT led to the highest G′, but lowest Tan δ, and it was cited that the high degree of dispersion resulted in a greater restriction in the polymer chain mobility. Chen et al. [381] explored the use of MWCNT and nHA to produce a PP/MWCNT/nHA nanocomposite for bone tissue engineering applications.

However, on this occasion, the nanocomposites containing 1 wt% MWCNT and 5 wt% nHA had a lower G′ compared to the neat PP. When comparing the density of the samples, it was observed that the samples containing MWCNT and nHA had a greater volume of pores, owing to the sintering production method. However, the addition of the nHA led to a greater decrease in the overall Tan δ, which once again aligns with the observations made in this thesis. It was noted that the stiffer nature of the PP/MWCNT/nHA material may be beneficial for tissue implant applications, such as in intervertebral disc replacements, where high dimensional stability under cyclic loads is required [381].

Thus heat-treatment may provide an effective method to improve the density and stiffness of nanocomposites produced from powders that are difficult to process, however this is at the cost of ductility. Finer control over the heat-treatment process to tune the crystallinity may also offer further control over the mechanical properties.

In table 6.12, the mechanical properties of cortical and trabecular bone are displayed alongside those of PA12 based composites and biodegradable polymer nanocomposites for bone substitute / bone tissue engineering applications, as tested in other studies and in the current work. In this study, the neat PA12 samples produced via laser sintering displayed slightly lower tensile properties than those reported in literature (1.7 GPa Modulus and 58 MPa UTS [363]). A direct comparison to a similar approach for producing nanocomposites, such as the work conducted by Bai et al. [1, 260], showed that the PA12-nHA and PA12-MWCNT-nHA nanocomposites also possessed lower mechanical properties compared to the PA12/MWCNT produced in Bai's work. The processing issues encountered for powders with NP loading of > 1 wt%, resulted in samples which were mechanically weaker. This was also the case for PLA based powders. Therefore, parameters which balanced dimensional accuracy and handleability were chosen. The nanocomposites produced in this work also did not match the tensile properties of injection moulded (IM) samples of the same material, which is the general case when comparing laser sintered and IM produced methods, as seen in the Table. However, when compared to conventional production methods, such as solvent casting, the mechanical properties are superior. In their current state the PLA-MWCNT-nHA composites produced by laser sintering possess compressive strength

within the upper range of cortical bone, and are among the highest reported in the available literature. They may therefore serve as a suitable replacement material when loaded principally under compression, such as in the vertebral body [5]. As a replacement material for trabecular bone, both tensile and compressive properties are within the high to mid-range, and may have the structural rigidity to serve as a suitable candidate for the treatment of trabecular bone diseases. Despite lacking the same mechanical properties of IM parts, this is offset by the greater geometric complexity that can be achieved using laser sintering, which is highly advantageous when producing structures for bone regeneration.

In the following chapter the cellular response to the laser sintering manufactured nanocomposite materials will be explored in greater detail.

Material	Processing Method	Tensile Modulus (MPa)	Tensile Strength (MPa)	Compressive Modulus (MPa)	Compressive Strength (MPa)	Reference
Cortical Bone	-	17500 - 18900	124 - 152	-	-	[382]
		-	-	3 - 30000	130 - 180	[383]
Cancellous Bone	-	25-240	0.22 - 10.44	-	-	[384]
		-	-	20 - 500	4 - 12	[383]
PA12	Laser Sintering	1700	50	-	-	[363]
		1586	43	-	-	[385]
		2373	50	-	-	[1]
		1430	40.7	-	-	current work
		-	-	1403	63.30	[386]
PA12/MWCNT	Laser Sintering	3524	54	-	-	[1]
		18300	46.7			current work
PA12/nHA	Laser Sintering	720 - 1720	12.91-40.70	-	-	**current work**
PA12/MWCNT/nHA	Laser Sintering	1006 - 1680	20.6 - 42.2	-	-	**current work**
PLA/HA	Laser Sintering	-	-	17.2 - 40.8	2.4 - 4.6	[387]
PLA/MWCNT	Laser Sintering	2280	26.5	130	90 - 98	**current work**
PLA/MWCNT/nHA	Laser Sintering	660 - 2770	6.1 - 21.2	-	28 - 144	**current work**
PLA//$beta$-TCP	Laser Sintering	-	-	-	16.5 - 17.7	[388]
PLA/carbonated-HA	Laser Sintering	-	-	5.9 - 6.0	0.55 - 0.63	[389]
PVA	Laser Sintering	-	-	-	0.1 - 0.3	[390]
PVA/$CaSiO_3$	Laser Sintering	-	-	1.1 - 1.6	140 - 215.5	[248]
PHBV/Ca-P	Laser Sintering	-	-	6.5	0.50 - 0.55	[389]
nHA	two step Laser Sintering	-	-	18700	246	[391]
Graphene/nano-bioglass 58S	Laser Sintering	-	30 - 48.7	-	-	[392]
PP/MWCNT/nHA	microwave sintering	-	-	-	-	[381]
PA66/HA	Injection Moulding	-	-	232-442	9.3-9.8	[393]
PEEK/HA	Injection Moulding	4000 - 14500	48-68	-	-	[394]
PA66/HA/CF	Melt extrusion	2900 - 5800	109-181	-	116-212	[395]
PLA/CF/nHA	Compression Moulding	1400 - 30000	150 - 425	-	-	[396]
PEEK/HA	Fused Deposition Modelling	-	-	1600-2500	80-100	[397]
PLA	Fused Deposition Modelling	3300 - 3600	54-59	-	-	[398]
PLGA/nHA	solvent casting	6 - 13	0.5 - 1.1	5 - 9	-	[399]
PLGA/TiO_2	solvent casting	1 - 2	0.2 - 0.21	2 - 4	-	[399]
PCL	solvent casting	245	11	-	-	[400]
PCL/Wollsonite	solvent casting	310 - 375	12 - 22	-	-	[400]
PLA/nHA	Phase Seperation	-	-	-	4.5 - 8.3	[401]
PA66/nHA	Foaming	-	-	-	2-10	[402]
PLGA/MWCNT	Electrospun	176.8 - 303.5	5.8 - 9.1	-	-	[253]

TABLE 6.12: A table showing the tensile and compressive properties of various polymer composites/ nanocomposites for bone tissue engineering applications from literature, made by a variety of different processing methods.

Chapter 7

Cellular Assessment of Nano-Particles and Laser Sintered Nanocomposites

As discussed in Chapter 2, a material which is intended to be implanted must be biocompatible. However, for the material to successfully integrate with the bone tissue, it must extend beyond being solely passive in nature, but it must also possess bioactive properties which will encourage the migration, proliferation and differentiation of osteoprogenitor cells. It was hypothesised that the nHA, MWCNT and MWCNT-nHA, when in free suspension and when immobilised onto the surface of PA12 and PLA, will be cytocompatible with osteosarcoma cell lines. Furthermore, the addition of nHA on the surface of the powders will increase the osteogenic response of human mesenchymal stem cells to the laser sintered material when compared to the base polymer. The increased osteogenic response will be partly due to the cells' ability to directly interact with the nHA. Therefore, this Chapter explores the nanocomposites suitability as bone substitute material by way of cytocompatibility and assessment of their osteoconductive properties. As NPs are exposed on the surface and are expected to be released during the degradation of the material in- situ, the cytotoxic effects of both nHA and MWCNT in free suspension, and when immobilised on the surface of the laser sintered nanocomposites, was assessed via cellular metabolic activity (Alamar Blue

Assay) and cellular proliferation (DNA Hoechst 33258 DNA Assay), in Sections 7.1 and 7.2 respectively. To determine if the presence of NPs improved the osteoconductive properties of the material, immortalised human mesenchymal stem cells (hiMSCs) were cultured on the nanocomposite materials across a 21 day period. In Section 7.3, the early and late stage markers for osteoblast differentiation, such as Alkaline Phosphatase (ALP) and Osteocalcin were conducted, in addition to mineralisation assessment using Alizarin Red staining. In Section 7.4, SEM imaging was conducted to gain insight into the morphological state of hiMSCs cultured on the 2D laser sintered nancomposites and on 3D scaffolds at various time-points to assess cytocompatibility and osteoconduction. Section 7.5 offers a discussion of the results.

7.1 Cytotoxicity of Nano-Particles

Due to the potential for NPs to dislodge from the surface of the nanocomposites the cytotoxicity of free nHA, MWCNT and a mixture of MWCNT/nHA (1:5) was assessed by in-vitro testing using the MG-63 osteosarcoma cell line. The assays used for the assessment included Alamar Blue, to measure metabolic activity, and Hoechst 33258 DNA assay, to measure the degree of cellular proliferation, over a period of 7days. Full details of the test method can be found in section 3.

7.1.1 nHA Alamar Blue

The results of the Alamar Blue assay, conducted over a 7-day period, can be seen in Figure 7.1. At 24h, the cell culture media containing no nHA (control) had the highest average RFU value compared to cells supplemented with 100 – 1000 μg ml^{-1}. Statistical analysis showed that the control was significantly higher($P<0.05$, as detailed in Chapter 3) when compared to cells supplemented with 300 – 1000 μg ml^{-1}. Although cells incubated with 100 μg ml^{-1} did record a lower average RFU when compared to the control, this difference was not reported to be statistically significant. As the nHA concentration increased, the average RFU declined from 305.32 $\pm$74.39, reported for

the control, to 182.24 $\pm$81.53 for cells incubated with 1000μg ml^{-1}. By 72 h, all samples showed an increase in average RFU, except for cells exposed to 1000 μg ml^{-1}. The control maintained the highest RFU compared to all other concentrations, which was reported to be significant. As nHA concentration increased, the average RFU became progressively lower. This was reported to be significant when each concentration was compared to the control. When nHA was increased from 300 to 700 and 1000 the RFU decrease was statistically significant. When nHA was increased from 500 to 1000 μg ml^{-1}, the decrease in average RFU recorded was also reported to be significant. At 7d, all samples again showed a significant rise in average RFU values. The control sustained the highest average RFU when compared to all other concentration levels, and this result was shown to be statistically significant. As the nHA concentration was increased the average RFU declined, similar to the observations made at the 24h and 72h time-points. Cells incubated with 1000 μg ml^{-1} recorded the lowest RFU value. No statistical significance was reported between 100 and 300 μg ml^{-1}, despite cells incubated with 300 μg ml^{-1} recording a lower RFU. A similar decline in average RFU was also observed when the concentration was increased from 300 to 700 and 1000 μg ml^{-1}. The decline in average RFU observed as nHA concentration was increased from 500 to 700 and 1000 μg ml^{-1} was also significantly different. The dashed lines on Figure7.1, represents 70% of the control at each timepoint. At 24h and 72h nHA concentrations above 100 μg ml^{-1} can be considered as cytotoxic. However, by 7d the concentration at which a cytotoxic effect can be seen increases to above 300 μg ml^{-1}.

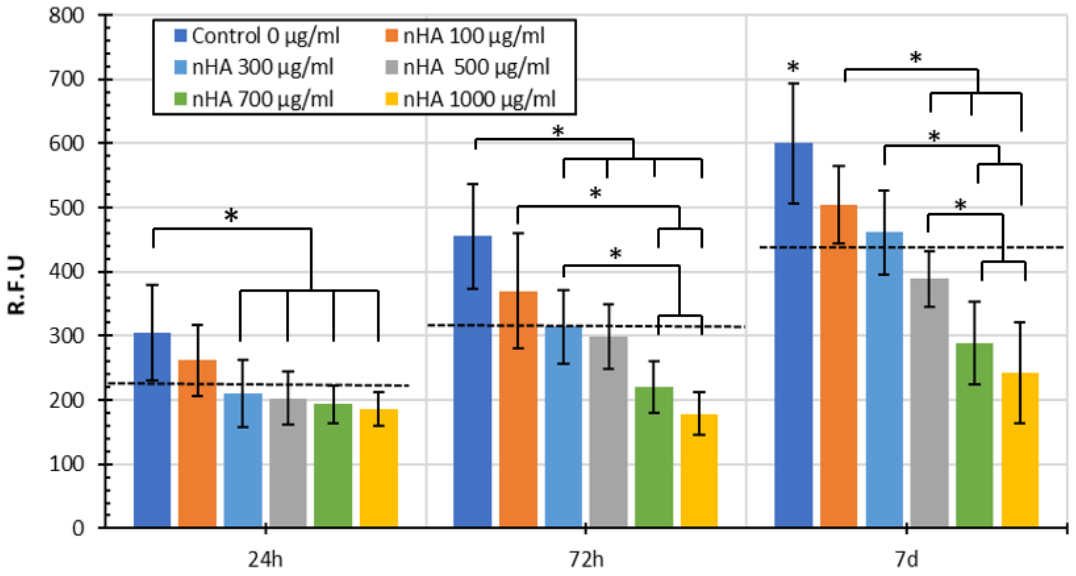


FIGURE 7.1: Graph of Alamar Blue results for MG-63 cells incubated with nHA at concentration from 0 - 1000 μg ml^{-1}. Metabolic activity displayed a dose sensitive response across the 24h, 72h and 7d time-points. The average RFU declined as nHA concentration increased. The control consistently demonstrated higher average RFU, whereas cells incubated with 1000 μg ml^{-1} consistently demonstrated the lowest average RFU. The dashed lines represent 70% of the control. n = 9, error bars represent standard deviation. Asterisk represents statistical significance.

7.1.2 nHA Hoechst 33258 DNA Assay

The cellular proliferation of MG-63 cells exposed to free nHA was assessed using the Hoechst DNA 33258 assay and the results of this can be seen in Figure 7.2. At 24h the control group, which were not exposed to any nHA particles, had the highest average DNA concentration at 0.98 $\pm$0.14 μg ml^{-1}. This was significantly higher than cells exposed to 100 – 1000 μg ml^{-1} nHA. As nHA loading increased the DNA concentration showed a progressive decline. The lowest average DNA concentration was recorded for cells exposed to 1000 μg ml^{-1}. Statistical analysis showed that there was a significant difference between cells incubated at 100 μg ml^{-1} and cells incubated with 500 μg ml^{-1}, 700 μg ml^{-1} and 1000 μg ml^{-1}. By 72 h the average DNA concentration for all samples had increased. The trend observed was similar to that seen at 24h with increased nHA loading resulting in a decline in average DNA concentration. Once again the control displayed the highest DNA concentration and this was significant. Statistical analysis also reported that the differences observed between cells incubated

with 100 μg ml^{-1} and 500 μg ml^{-1}, 700 μg ml^{-1} and 1000 μg ml^{-1} were statistically significant. Samples incubated with 700 and 1000 μg ml^{-1} displayed similar levels of DNA concentration, with an average of 0.42 $\pm$0.1 μg ml^{-1} and 0.40 pm0.22 μg ml^{-1}, respectively. However there was no statistical significance between these values. At day 7, the proliferative activity, and thus DNA content, had further increased. This pattern of DNA concentration increase across the time-points, was maintained. Once again, the control was significantly higher than all other samples and DNA concentration decreased in relation to increasing nHA. However, statistical analysis only recorded a significant difference between cells incubated with 100 and 700 μg ml^{-1} nHA and 1000 μg ml^{-1}. Once again, concentrations above 100 - 300 μg ml^{-1}, appeared to be cytotoxic as highlighted by the dashed lines on the graph.

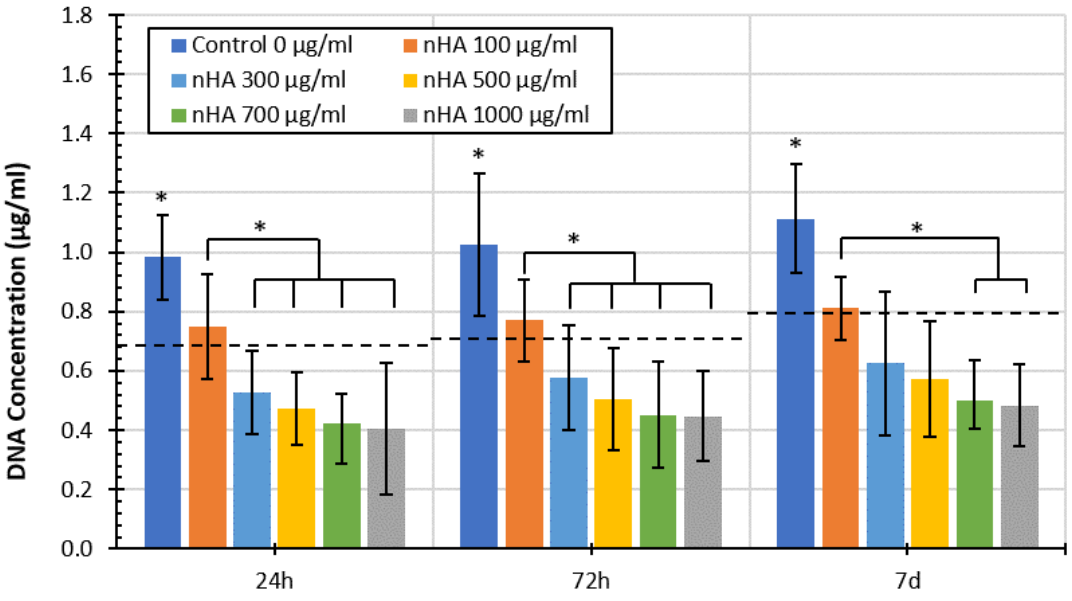


FIGURE 7.2: Graph showing the results of the Hoechst 33258 DNA assay on MG-63 cells incubated with nHA at concentrations from 0 - 1000 μg ml^{-1}. Similar to trends observed during the Alamar Blue assay, DNA content decreased as nHA content increased. The control consistently demonstrated higher average DNA content, whereas cells incubated with 1000 μg ml^{-1}, consistently demonstrated the lowest average RFU. The dashed lines represent 70% of the control for each time point. n = 9, error bars represents standard deviation. Asterisk represents statistical significance.

7.1.3 MWCNT Alamar Blue

Cells incubated with MWCNT were also subject to the Alamar Blue assay and the results of this can be seen in Figure 7.3. At 24h the cells incubated with 100 - 300 μg ml^{-1} reported slightly lower RFU values to that of the control. However these differences were not reported as being statistically significant. Cells incubated with 500, 700 and 1000 μg ml^{-1} also reported progressively lower RFU values, these differences were reported to be significantly lower. As MWCNT concentration was increased from 100 to 1000 μg ml^{-1} the average RFU become progressively lower, and this decline was reported to be significant. No statistical difference was recorded between 700 and 1000 μg ml^{-1} despite cells incubated at 1000 μg ml^{-1} possessing a lower average RFU. At 72h, the average RFU recorded for each of the samples increased which was similar to the observations made at 24h. As MWCNT concentration increased from 0 to 1000 μg ml^{-1}, the average RFU progressively decreased, reaching the lowest value of 201 $\pm$31.67. Despite cells incubated with 100 μg ml^{-1} displaying a slightly lower average RFU compared to the control, this difference was not significant. Differences between 300 and 500 μg ml^{-1}, in addition to 700 and 1000 μg ml^{-1} were also reported as not significant. Again, at 7d all samples reported a rise in average RFU values, and all differences recorded between the concentrations and control were reported as significant apart from: 300 and 500 μg ml^{-1}, 300 and 700 μg ml^{-1},and 500 and 700 μg ml^{-1}. The dashed lines on Figure 7.3 represents 70% of the control. At 24h and 72h, MWCNT concentration above 300-500 μg ml^{-1} could be regarded as being slightly cytotoxic. At 7d the cytoxic effect can be observed at concentrations above 100 μg ml^{-1}.

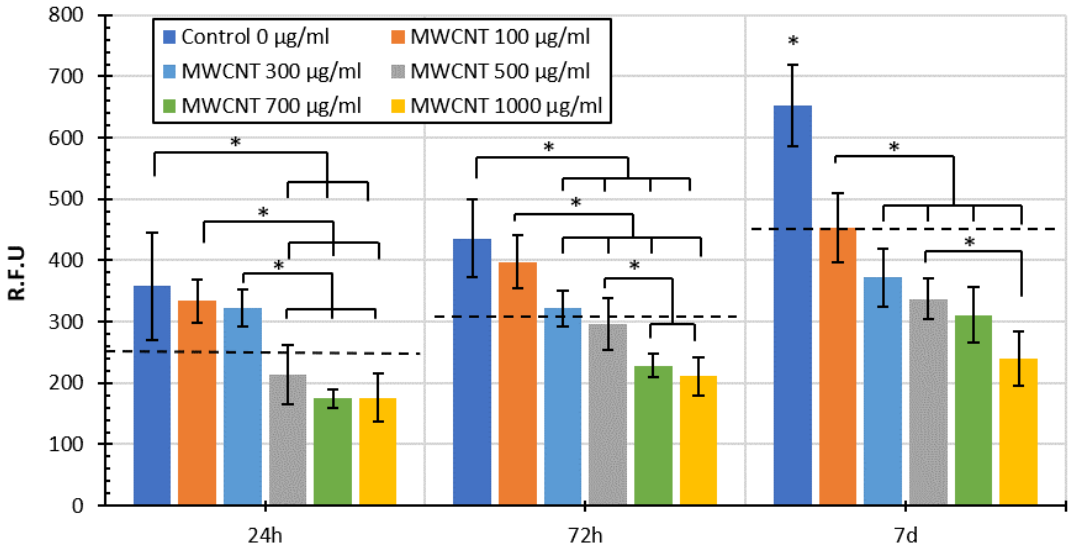


FIGURE 7.3: Graph of Alamar Blue results for MG-63 cells incubated with MWCNT at concentration from 0 - 1000 μg ml^{-1}. Metabolic activity displayed a dose sensitive response across the 24h, 72h and 7d time-points. The average RFU declined as nHA concentration increased. The control consistently demonstrated higher average RFU, whereas cells incubated with 1000 μg ml^{-1}, consistently demonstrated the lowest average RFU. The dashed lines represent 70% of the control value for each time point. n = 9, error bars represents standard deviation. Asterisk represents statistical significance.

7.1.4 MWCNT Hoechst 33258 DNA Assay

DNA quantification, as seen in Figure 7.4, displayed a decreasing trend across all samples as the MWCNT concentration increased from 24h to 7d. This trend was similar to that observed for nHA. At 24h the control displayed the highest DNA concentration and was recorded at 1.03 $\pm$0.19 μg ml^{-1}. Statistical analysis showed that there was no significant difference between the control and cells incubated with 100 μg ml^{-1}, despite these cells displaying a lower DNA content of 0.80 $\pm$0.19 μg ml^{-1}. However, statistical significance was recorded when comparing the control to all other concentrations. Statistical significance was recorded when comparing cells incubated with 100 μg ml^{-1} to 500 μg ml^{-1}, 700 μg ml^{-1} and 1000 μg ml^{-1}. No other significance was recorded despite the decreasing trend. At 72h the average DNA content for all samples increased slightly. Once again the control possessed the highest DNA concentration, which was significantly different compared to all other samples. Further statistical significance was recorded when comparing cells incubated with 100 μg ml^{-1} to cells incubated with

500 μg ml^{-1}, 700 μg ml^{-1} and 1000 μg ml^{-1}. By 7d, cellular DNA content reached a maximum for each of the MWCNT concentrations. The control group maintained a significantly higher DNA content compared to all other samples. Significant differences were also recorded when comparing cells incubated with 100 μg ml^{-1} to cells incubated with 500 μg ml^{-1}, 700 μg ml^{-1} and 1000 μg ml^{-1}. The dashed lines in Figure 7.4 represents 70% of the control, this again highlights the cytotoxicity at concentrations above 100 - 300 μg ml^{-1}.

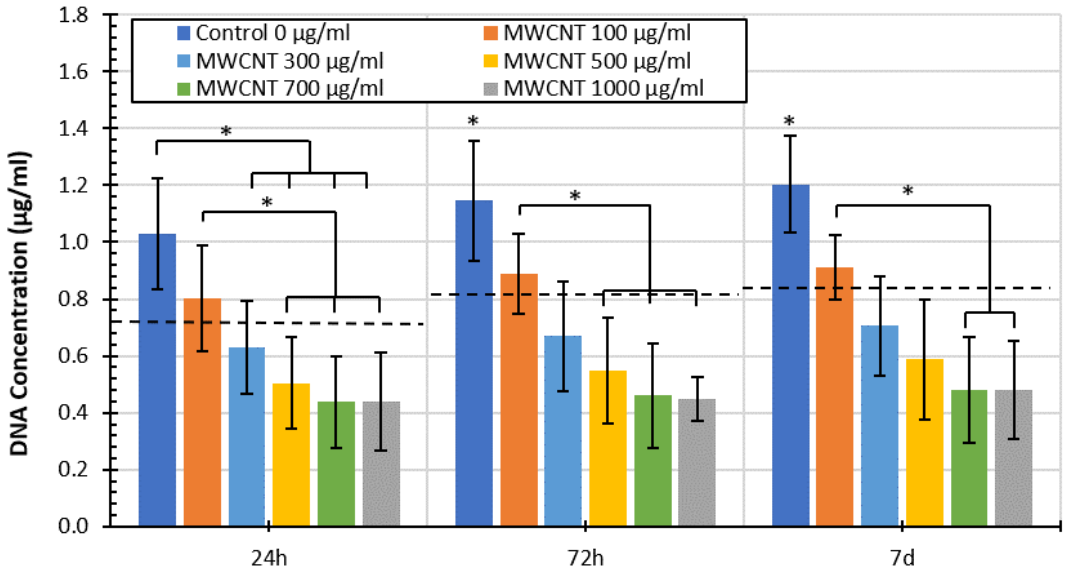


FIGURE 7.4: Graph showing the results of the Hoechst 33258 DNA assay on MG-63 cells incubated with MWCNT at concentrations from 0 - 1000 μg ml^{-1}. Similar to trends observed during the Alamar Blue assay, DNA content decreased as nHA content increased. The control consistently demonstrated higher average DNA content, whereas cells incubated with 1000 μg ml^{-1}, consistently demonstrated the lowest average DNA content. The dashed lines represent 70% of the control value for each time point. n = 9, error bars represent standard deviation. Asterisk represents statistical significance.

7.1.5 MWCNT-nHA Alamar Blue

A mixture of MWCNT and nHA, at a ratio of 1:5, was also evaluated for cytotoxicity using the Alamar Blue test, as seen in Figure 7.5. Across the 7day period the average RFU value, and thus cell number, increased. Cells were exposed to concentrations ranging from 0 - 1000 μg ml^{-1} and as the MWCNT/nHA concentration increased, the average RFU values declined. At 24h the control samples recorded the highest average

RFU value, at 352 $\pm$75.63. This decreased to 303.07 $\pm$81.42 at 100 μg ml^{-1}, however this difference was not reported as being significant. At 300 μg ml^{-1}, the average RFU recorded was slightly higher than that recorded for cells incubated with 100 μg ml^{-1} however this difference was also not significantly different. As concentration increased to 500 μg ml^{-1} the decline in average RFU was reported as statistically significant when compared to the control. However this was not significant different when comparing the RFU to cells incubated with 100 and 300 μg ml^{-1}. As the concentration increased to 700 μg ml^{-1}, the decline in RFU was again reported as being significantly different when compared to the control samples and cells treated with 300 μg ml^{-1}, but not significantly different when compared against samples incubated with 500 μg ml^{-1}. The cells exposed to 1000 μg ml^{-1} possessed the lowest average RFU compared to all other samples at 174.01 $\pm$30.95. This result was significantly lower compared to all other concentrations tested, except for cells incubated with 700 μg ml^{-1}. At 72 h the trend remained the same across the concentrations levels with the RFU value decreasing as MWCNT-nHA concentration increased from 0 – 1000 μg ml^{-1}. Once again, by 7d, the trend observed was similar to previous time-points with a decline in RFU as MWCNT-nHA concentration was increased. No statistical significance was reported when comparing cells incubated with: 300 and 500 μg ml^{-1}, 500 and 700 μg ml^{-1}, 500 and 1000 μg ml^{-1}, 700 and 1000 μg ml^{-1}. By 7d cells metabolic activity increased further. The control once again remained the highest and was significantly different when compared to all other concentrations. A significant difference was also recorded when cells incubated with 100 μg ml^{-1} was compared to cells incubated with 500 μg ml^{-1}, 700 μg ml^{-1} and 1000 μg ml^{-1}. Concentrations above 500 μg ml^{-1} appeared to show potential cytotoxicity at 24h and 72h, this decreased to concentrations of 100 μg ml^{-1} and below by 7d.

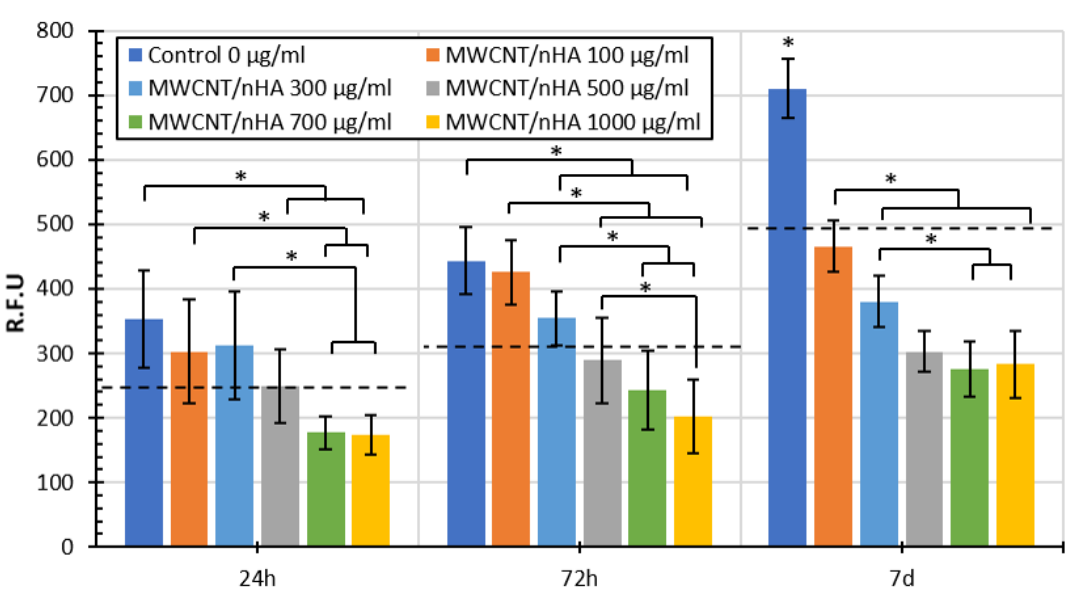


FIGURE 7.5: Graph of Alamar Blue results for MG-63 cells incubated with a mixture of MWCNT-nHA (1:5) at concentration from 0 - 1000 μg ml^{-1}. Metabolic activity displayed a dose sensitive response across the 24h, 72h and 7d time-points. The average RFU declined as MWCNT-nHA concentration increased. The control consistently demonstrated higher average RFU, where as cells incubated with 1000 μg ml^{-1}, consistently demonstrated the lowest average RFU. The dashed lines represent 70% of the control value for each time point. n = 9, error bars represent standard deviation. Asterisk represents statistical significance.

7.1.6 MWCNT-nHA Hoechst 33258 DNA Assay

The DNA assay, as seen in Figure 7.6, also displayed a gradual increase in DNA content across the 7day test period at all concentrations. The trends observed were similar to those of cells incubated with nHA and MWCNT, whereby increasing NP content resulted in a gradual decline in DNA and cellular proliferation, reaching the lowest point at a concentration of 1000 μg ml^{-1}. At 24h the control group recorded the highest DNA content. However, despite the decline in DNA concentration as MWCNT-nHA content increased; a significant difference was only reported when comparing the control to cells incubated with 500 μg ml^{-1} and to cells incubated with 700 μg ml^{-1} and 1000 μg ml^{-1}. At 72 h the control was again significantly higher, than all other samples except for 100 μg ml^{-1}. A significant difference was also recorded when comparing cells incubated with 100 μg ml^{-1} to cells incubated with 500 μg ml^{-1}, 700 μg ml^{-1} and 1000 μg ml^{-1}. Overall, concentrations above 100 - 300 μg ml^{-1}

appeared most cytotoxic, falling below the 70% of control as shown by the dashed lines in Figure 7.5.

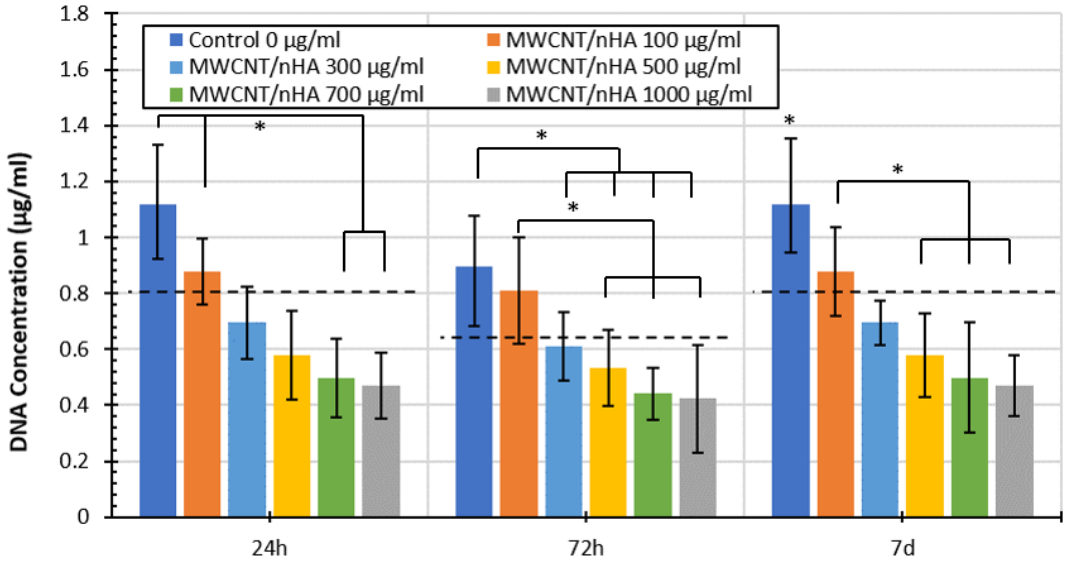


FIGURE 7.6: Graph showing the results of the Hoechst 33258 DNA assay on MG-63 cells incubated with MWCNT-nHA (1:5) at concentrations from 0 - 1000 μg ml^{-1}. Similar to trends observed during the Alamar Blue assay, DNA content decreased as MWCNT-nHA content increased. The control consistently demonstrated higher average DNA content, where as cells incubated with 1000 μg ml^{-1}, consistently demonstrated the lowest average DNA content. The dashed lines represent 70% of the control value for each time point. n = 9, error bars represent standard deviation. Asterisk represents statistical significance.

7.2 Cytotoxicity of Laser Sintered Nanocomposites

Cytotoxicity experiments were also carried out on the disc-shaped, laser sintered nanocomposite samples produced on the P100 and Sintratec machines. The same assays, Alamar Blue and Hoechst 33258 DNA, were used to assess the potential cytotoxicity when polymer and NPs are used in conjunction .

7.2.1 Cytotoxicity of PA12-nHA Nanocomposite - Alamar Blue

Results of the Alamar Blue assay conducted on the PA12-nHA based nanocomposites can be seen in Figure 7.9. Across the 7-day test period all samples displayed increasing

RFU values. At 24h the TCP control displayed the highest average RFU value of 225.27 ± 32.00. Statistical analysis showed that there was a significant difference between the TCP control and cells grown on the PA12/nHA nanocomposite discs. Of the PA12-nHA nanocomposites tested, the PA1H samples recorded the highest RFU of 172.94 ±57.87 and this was found to be significantly the higher. By 72 h, the TCP control once again recorded the highest average RFU at 370.17 ±50.82 and was significantly higher than the PA12-nHA nanocomposites. Of the laser sintered samples produced, the PA0 recorded the highest average RFU at 262.50 ±40.98, this result was shown to be significantly higher than the PA05H and PA1H samples. The PA1.5H samples reported an RFU value of 258.16 ±30.00 and was significantly higher than the PA05H and PA1H samples. By 7d, the TCP recorded the highest RFU value, at 505.50 ±40.23 however this difference was not significantly different. All of the PA12-nHA nanocomposites recorded higher average RFU values compared to the neat PA0 samples and were found to be significantly higher. However, between PA05H, PA1H and PA1.5H there was no significant difference between the recorded RFU values. By 7d all samples displayed an average RFU value that was above 70% of the control, thus indicating that the materials were cytocompatible.

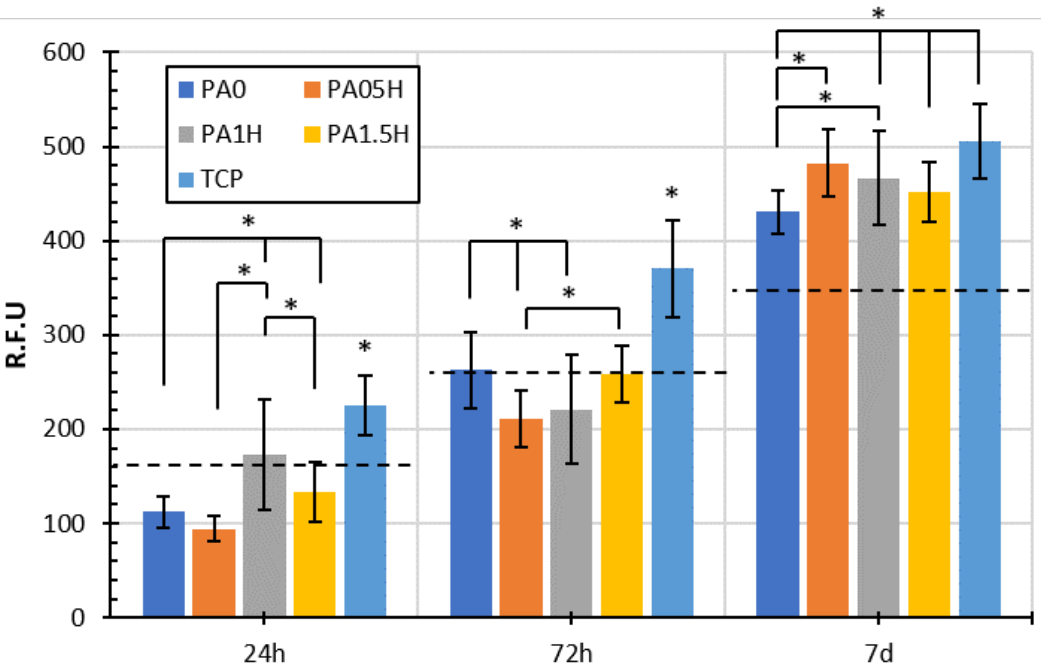


FIGURE 7.7: Graph showing results of the Alamar Blue assay on PA12-nHA based nanocomposites, processed on a commercial laser sintering machine. MG-63 cells displayed a gradual increase in metabolic activity across the 7d period. Cells cultured on the TCP showed consistently higher average RFU at all time-points. At 7d PA05H displayed the highest RFU value when compared to the other laser sintered samples. However no significant difference was detected between any of the laser sintered samples. Dashed line represents 70% of the the control value for each time point. n = 18, error bars represent standard deviation. Asterisk represents statistical significance.

7.2.2 Cytotoxicity of PA12-nHA Nanocomposite - Hoechst 33258 DNA Assay

DNA analysis, as seen in Figure 7.8, showed that the DNA content for all samples tested increased across the 7-day period. At 24h the TCP control recorded a significantly higher DNA content (2.74 $\pm$0.61 μg ml^{-1}) when compared to the laser sintered samples. There was no statistical difference between: PA0, PA05H, PA1H and PA1.5H samples. At 72h the TCP control had the highest average DNA content of 4.46 $\pm$0.70μg ml^{-1} and this difference was significant. However, statistical analysis showed that there was no significant difference between PA0, PA05H, PA1H and PA1.5H samples. At 7d the TCP once again recorded the highest DNA content at 5.71 $\pm$1.26 μg ml^{-1}, this was significantly higher than all the other tested samples

except for PA1.5H samples. The PA1.5H nanocomposite samples recorded the next highest RFU value of 5.44 $\pm$1.44 μg ml^{-1} and was found to be significantly higher than the PA0, PA05H and PA1H samples. There was no significant difference between the average RFU values of PA0, PA05H and PA1H.

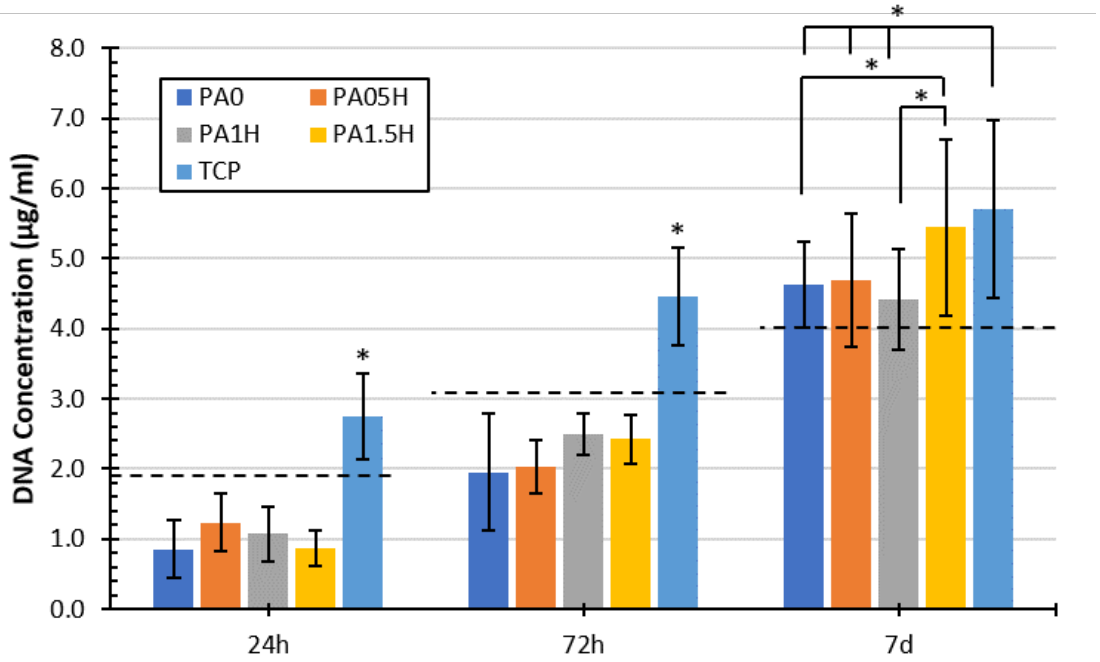


FIGURE 7.8: Graph showing the results of the Hoechst 33258 DNA assay of MG-63 cells cultured on the PA12-nHA based nanocomposites. TCP consistently demonstrated higher DNA content. By 7d PA1.5H displayed the highest average DNA content when compared to all other laser sintered samples, this difference was shown to be significant. Dashed line represents 70% of the the control value for each time point. n = 18, error bars represents standard deviation. Asterisk represents statistical significance.

7.2.3 Cytotoxicity of PA12-MWCNT-nHA Nanocomposite - Alamar Blue

The Alamar Blue assay, conducted on PA12-MWCNT-nHA nanocomposite discs fabricated in the consumer laser sintering machine, can be seen in Figure 7.9. Results showed that the average RFU values for all compositions increased across the 7-day period. However, at 24h the average TCP control recorded a significantly higher average RFU compared to cells grown on the nanocomposite discs. Statistical analysis showed no significant difference between the nanocomposite samples, despite PA05M2H and

PA05M5H displaying slightly lower RFU when compared to PA05M. At 72 h the average RFU values for all samples increased. However, cells grown on the TCP control remained significantly higher compared to cells grown on the nanocomposite discs (370.17 ±50.81) and this result was shown to be significant. The nanocomposite samples displayed similar RFU values. The PA05M2H and PA05M5H were slightly lower than PA05M, however this was not a significant difference. By 7d, all samples approached similar average RFU values. Cells grown on TCP controls remained the highest (472.16 ±76.97), however statistical analysis did not record any significant difference between any nanocomposites and controls tested. By day 72 h all samples displayed an average RFU value that was above 70% of the control, thus indicating that the materials were cytocompatible.

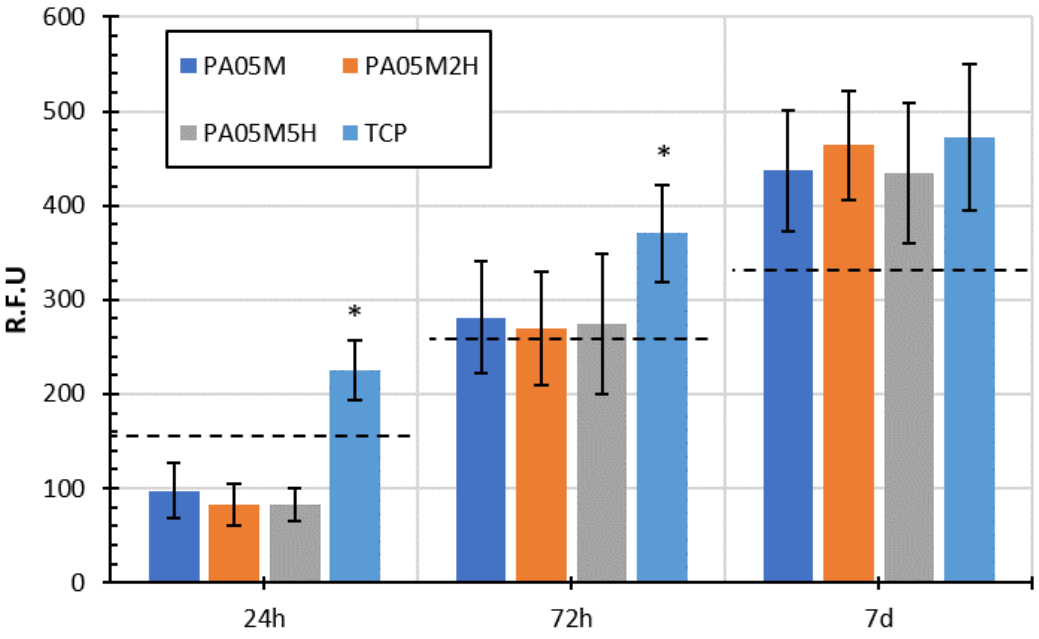


FIGURE 7.9: Graph showing results of the Alamar Blue assay conducted on PA12-MWCNT-nHA based nanocomposites, processed on a consumer laser sintering machine. MG-63 cells displayed a gradual increase in metabolic activity across the 7d period. Cells cultured on the TCP showed consistently higher average RFU at all time-points. At 7d PA05M5H displayed the highest RFU value when compared to the other laser sintered samples, however no significance was detected between any of the laser sintered samples and the control. Dashed line represents 70% of the the control value for each time point. n = 18, error bars represent standard deviation. Asterisk represents statistical significance.

7.2.4 Cytotoxicity of PA12-MWCNT-nHA Nanocomposite - Hoechst 33258 DNA Assay

The DNA content also showed an increasing trend across the 7-day period for all samples and controls tested. At 24h the TCP control recorded the highest average DNA content at 2.75 $\pm$0.61μg ml^{-1}. This was shown to be significantly higher than the nanocomposite samples. Statistical analysis showed no difference between the average DNA concentration values of cells grown on the nanocomposites, despite PA05M5H displaying a slightly higher DNA concentration. By 72 h the DNA content for all samples increased. The TCP control samples remained higher than the nanocomposites with an average DNA content of 4.66 $\pm$0.69 μg ml^{-1}. This was again significantly higher than the nanocomposite discs. The nanocomposites, again, displayed a very similar DNA content with no significant difference reported between the samples. By 7d all cells showed increased levels of DNA content. Once again, the TCP controls recorded a significantly higher DNA content (5.71 $\pm$1.26 μg ml^{-1}) when compared to the nanocomposite discs. Of the nanocomposite discs the PA05M5H displayed the highest DNA content followed by PA05M2H and PA05M. However no significant difference was recorded between the samples.

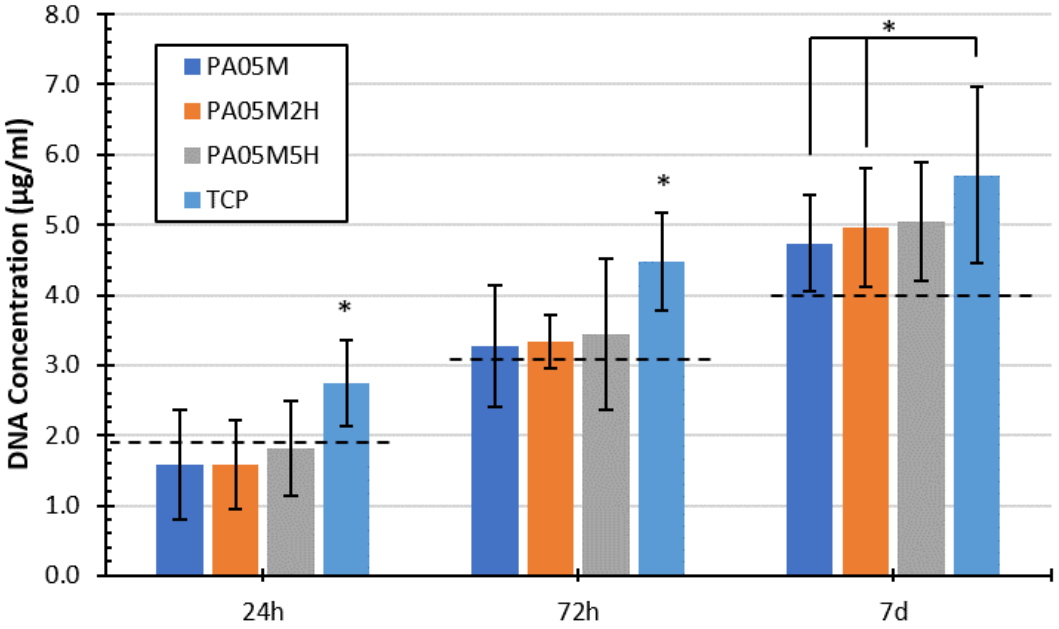


FIGURE 7.10: Graph showing the results of the Hoechst 33258 DNA assay of MG-63 cells cultured on the PA12-MWCNT-nHA based laser sintered nanocomposites. TCP consistently demonstrated higher DNA content. By 7d, PA05M5H displayed the highest average DNA content when compared to all other laser sintered samples, however this difference was not shown to be significant. Dashed line represents 70% of the the control value for each time point. n = 18, error bars represents standard deviation. Asterisk represents statistical significance.

7.2.5 Cytotoxicity of PLA-MWCNT-nHA Nanocomposite - Alamar Blue

Results of the Alamar Blue assay, conducted on PLA-MWCNT-nHA nanocomposites produced in the consumer laser sintering machine, are displayed in Figure 7.11. At 24h the PL1M5H samples displayed the highest average RFU (266 ±66.68), however statistical analysis showed no significant difference between any of the nanocomposite samples and TCP control. By 72 h, the average RFU had increased for all samples. The PL1M sample recorded the highest RFU value (371.72 ±46.67), which was significantly higher when compared to the PL1M2H sample. The PL1M5H was also significantly higher than PL1M2H samples with an average RFU of 362.50 ±47.49. However, when compared to PL1M samples and TCP control, there was no significant difference. By 7d all samples, once again, recorded an increase in average RFU. On this occasion, the TCP control recorded the lowest RFU value (505.50 ±40.23) whilst the nanocomposite

samples remained the highest. The PL1M samples recorded the highest average RFU of 616.11 ±52.26, when compared to PL1M2H and PL1M5H. However, there was no significant difference between the samples. All samples displayed an average RFU value that was above 70% of the control, thus indicating that the materials were cytocompatible.

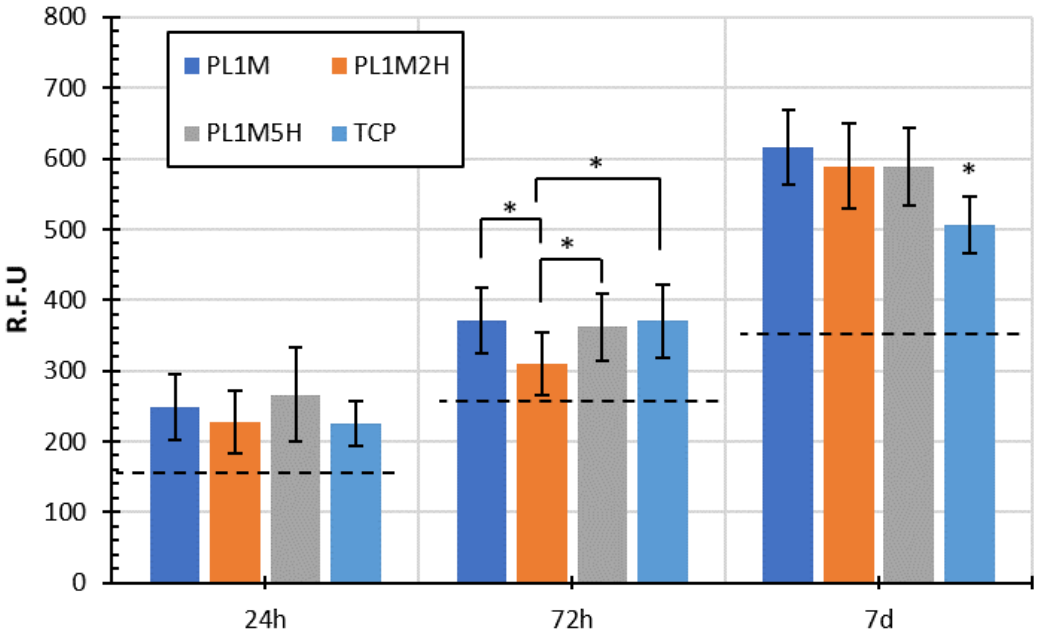


FIGURE 7.11: Graph showing results of the Alamar Blue assay conducted on PLA-MWCNT-nHA based nanocomposites, processed on a consumer laser sintering machine. MG-63 cells displayed a gradual increase in metabolic activity across the 7d period. Cells cultured on the TCP showed consistently higher average RFU at all time-points. At all time-points PL1M, PL1M2H and PL1M5H samples displayed similar RFU values when compared to the TCP control. At 7d, the average RFU values exceeded that of the TCP control. PL1M, PL1M2H and PL1M5H were found to be significantly higher, however between the samples no significance was detected. Dashed line represents 70% of the the control value for each time point. n = 18, error bars represent standard deviation.

7.2.6 Cytotoxicity of PLA-MWCNT-nHA Nanocomposite - Hoechst 33258 DNA Assay

The DNA content (Figure 7.12) of the nanocomposites by 24h was significantly lower than the TCP control (2.74 ±0.61 μg ml^{-1}). PL1M5H displayed the lowest DNA content and this was followed by PL1M. The PL1M2H samples on the other hand

displayed the highest DNA content. However, differences between the nanocomoposite samples were not reported as being significant. By 72h, the DNA content of all samples increased, but the TCP control remained significantly higher than all other test samples (4.46 $\pm$0.70 μg ml^{-1}). Of the nanocomposite samples, the PL1M5H recorded the highest DNA content (2.95 $\pm$0.83 μg ml^{-1}) when compared to PL1M and PL1M2H. This result was shown to be significant. The average DNA content for cells grown on PL1M2H (2.66 $\pm$0.82 μg ml^{-1}) was also significantly higher than PL1M (2.52 $\pm$0.86 μg ml^{-1}). At 7d all samples displayed increased levels of DNA content. On this occasion the PL1M5H samples recorded the highest average DNA content at 5.79 $\pm$1.60μg ml^{-1}, however, statistical analysis revealed no significant difference between all samples and controls tested.

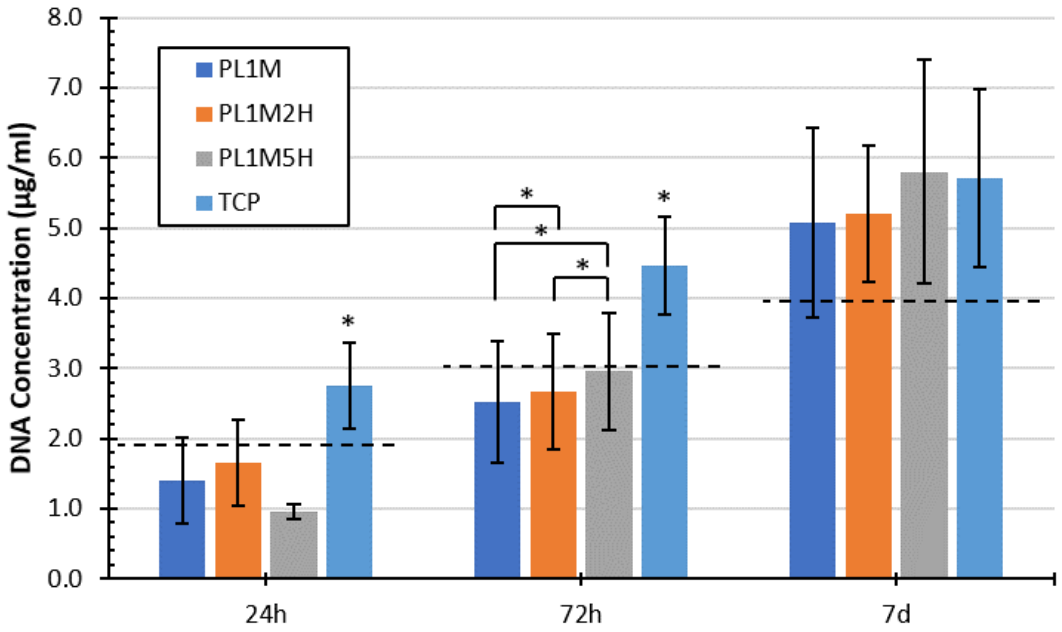


FIGURE 7.12: Graph showing the results of the Hoechst 33258 DNA assay of MG-63 cells cultured on the PLA-MWCNT-nHA based laser sintered nanocomposites. By 7d PL1M5H samples displayed the highest average DNA content when compared to all other laser sintered samples and controls, however this difference was not shown to be significant. Dashed line represents 70% of the the control value for each time point. n = 18, error bars represents standard deviation. Asterisk represents statistical significance.

7.3 Bioactivity Assessment of laser sintered Nanocomposite Materials

To determine the osteoconductive potential that the laser sintered nanocomposites (PA0, PA1.5H, PA05M5H, PL0, PL1M, PL1M5H) possess, hiMSCs were cultured on the surface of the samples and were subjected to a series of DNA, ALP, Osteocalcin Assays, in addition to Alizarin Red staining. Tissue culture plastic (TCP) was used as the control. During the test the hiMSCs were incubated with osteogenic media, the full details of these tests can be seen in Chapter 3.

7.3.1 Bioactivity of Nanocomposite Samples - Hoechst 33258 DNA Assay

A DNA assay was conducted across a 21-day period to determine the proliferative behaviour of cells cultured on the materials, this can be seen in Figure 7.13. At 24h the DNA concentration of all samples under testing remained similar. The PL1M5H samples and the TCP control displayed a slightly higher average of 0.48 $\pm$0.09 μg ml^{-1} and 0.52 $\pm$0.20 μg ml^{-1} respectively. However, statistical analysis did not reveal any significant differences between the two, nor did it detect a difference between the other samples tested. By 7d all samples recorded a higher DNA content and on this occasion the TCP control had a substantially higher DNA content (3.92 $\pm$0.17 $\pm$0.20 μg ml^{-1}) compared to the other test samples. Of the laser sintered samples, PL1M5H possessed the highest average DNA content at 2.17 $\pm$0.57 $\pm$0.20 μg ml^{-1}. Although displaying the highest DNA content, statistical analysis did not deem this difference to be significant. Furthermore, despite the fluctuations in DNA content between the rest of the samples, once again, no statistical significance was recorded. At 14d the DNA content of all samples, and the control, increased again. The DNA content of PA0, PL0, PA1.5H and PL1M samples approached similar levels to that recorded for the TCP control (4.49 $\pm$0.94 μg ml^{-1}) and no statistical difference between these samples was recorded. The PA05M5H and PL1M5H samples, on the other hand, recorded the

lowest DNA content of 3.31 $\pm$0.31 μg ml^{-1} and 3.37 $\pm$0.30 μg ml^{-1} respectively. The DNA content of these samples was reported to be significantly different when compared to the rest of the samples tested. By 21d all samples showed a significant decline in DNA content, whereas the TCP control increased further to 6.05 $\pm$0.60 μg ml^{-1}. Of the laser sintered samples tested PA05M5H displayed the lowest DNA content (2.89 $\pm$0.51 μg ml^{-1}), however no significant difference between any of the samples was observed.

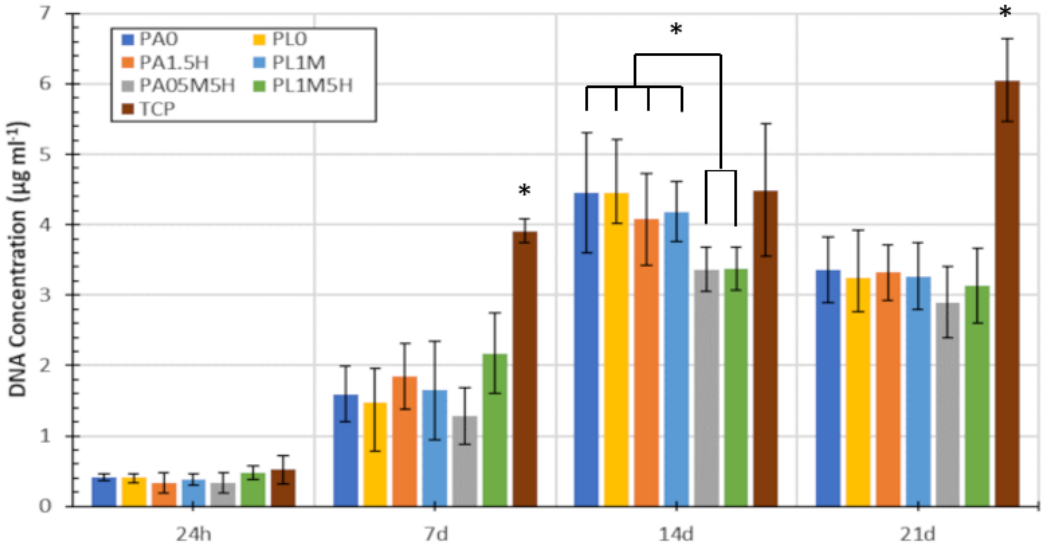


FIGURE 7.13: Graph showing the results of the Hoechst 33258 DNA Assay conducted on hiMSCs cultured on neat PA12 and PLA materials, in addition to PA12-nHA , PA12-MWCNT-nHA and PLA-MWCNT-nHA laser sintered nanocomposite samples, from 24h to 21d. At 24h all samples displayed similar DNA concentrations. PL1M5H and TCP control displayed a slightly higher average DNA content, however no significant difference was detected between any sample. At 72h DNA for TCP control rose sharply, PA05M5H samples displayed the lowest DNA content, however no significant difference was recorded between any of the laser sintered samples. At 14d peak DNA content for the laser sintered samples increased further, both PA05M5H and PL1M5H samples displayed the lowest DNA content compared to the other samples. A significant difference was reported when comparing PA05M5H and PL1M5H to PA0 and PL0 samples. PL1M5H was also reported to be significantly lower when compared to PL1M. At 21d, all samples, excluding the TCP control, showed a decline in DNA concentration. PA05M5H and PL1M5H recorded the lowest values, however no significance was recorded between the samples. n = 9, error bars represent standard deviation. Asterisk represents statistical significance.

7.3.2 Bioactivity of the Nanocomposite Samples - Alkaline Phosphatase Assay

Figure 7.14 shows ALP normalised to DNA concentration. The results recorded at 7d showed that the average ALP activity was highest for the TCP control (0.29 $\pm$0.04). Of the samples tested, cells cultured on PL0 and PL1M recorded higher ALP activity at 0.22 $\pm$0.04 and 0.15 $\pm$0.14 respectively. Statistical analysis revealed no significant difference between PL0, PL1M and TCP control. The ALP activity of the TCP control was, however, significantly higher than PA0, PA1.5H, PA05M5H and PL1M5H samples. The ALP activity recorded for all samples and the control reached peak levels by 14d. Of all the samples, PA05M5H samples recorded the highest ALP activity at 0.70 $\pm$0.74; this was followed by PL1M5H (0.63 $\pm$0.08) and TCP control (0.62$\pm$0.22). Between these samples, statistical analysis showed no significant difference. However, the ALP activity of these samples was significantly higher than PA0, PL0, PA1.5H and PL1M samples. At 21d the average ALP activity for all samples dropped. However, the normalised ALP activity of PA05M5H (0.66 $\pm$0.18) and PL1M5H (0.62 $\pm$0.19) samples remained the highest when compared to all other samples and control. Statistical analysis showed that PA05M5H and PL1M5H were significantly higher than all other samples however, between the two, no significant difference was recorded. All other samples showed similar normalised ALP activity to that of the TCP control (0.41 $\pm$0.04).

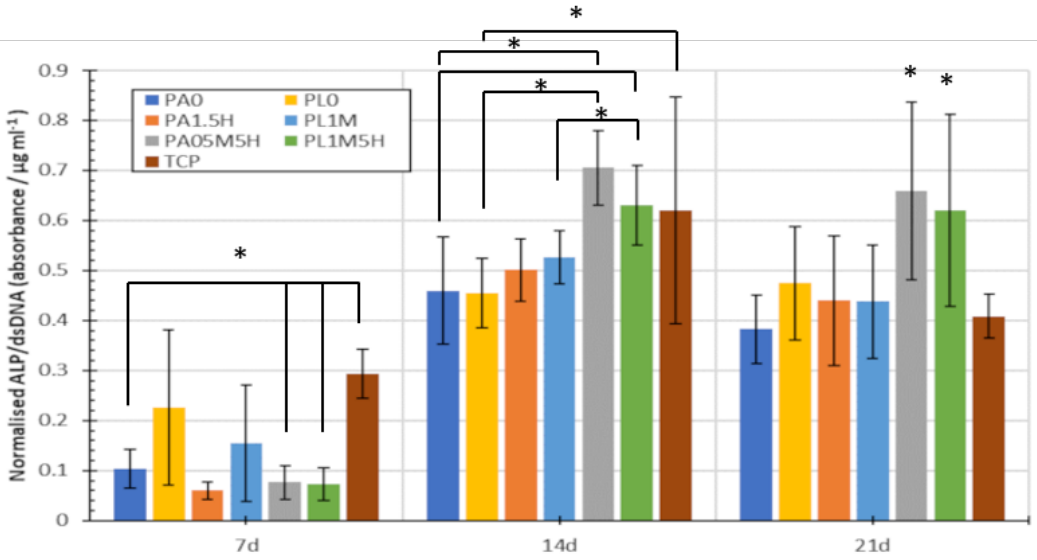


FIGURE 7.14: Graph showing ALP normalised to DNA at 7d, 14d and 21d time-points. PL0 and PL1M displayed high ALP activity at 24h, however these differences were not significant when compared to the other laser sintered samples. At 14d the ALP activity for all samples reached a peak. PA05M5H and PL1M5H samples displayed the highest ALP activity, compared to all samples. These results were reported as being significant. Between the two,these differences were not significant. The TCP control displayed similar ALP activity to PL1M5H samples with no significance recorded between the two. At 21d all samples displayed a decline in ALP activity, however PA05M5H and PL1M5H remained consistently higher when compared to the other samples and this was reported to be significant. n = 9, error bars represents standard deviation. Asterisk represents statistical significance.

7.3.3 Bioactivity of Nanocomposite Samples - Osteocalcin Assay

Cell culture media was extracted off the samples after 21d of cell culture and used for the assessment of Osteocalcin (OCN). The media was extracted from each of the samples at 21d, and the results were normalised to DNA content. This test can be seen in Figure 7.15. PA0 samples recorded an average OCN expression of 6.32 $\pm$1.25 , while the PL0 sample recorded a slightly lower expression of 6.08 $\pm$1.94 a difference of 4%. Statistical analysis using one-way ANOVA did not reveal any significant difference between the two materials. The media obtained from wells containing hiMSCs, grown on PA1.5H samples, displayed a higher average OCN concentration when compared to both PA0 and PL0 samples. The average OCN expression was recorded at 7.03 $\pm$1.05, an increase of 10.09% and 13% respectively. One-way ANOVA did indicate a

significant difference when comparing the average OCN expression of PA1.5H samples to the PL0. However, no significant difference was detected when comparing PA1.5H to PA0 samples. The PL1M samples recorded a lower OCN expression of 6.34 $\pm$1.98. Statistical analysis showed no significant difference between PL1M and PA1.5H, PL0 and PA0 samples. The PA05M5H samples recorded an average OCN expression of 9.46 $\pm$2.01 and, when compared to the other samples tested, a significant difference was recorded. The average OCN expression was also 61% higher than the TCP control which was statistically significant. The PL1M5H samples also recorded a relatively high OCN expression at 9.06 $\pm$2.45, a 59% increase when compared to the TCP control. Statistical analysis did not record any significant difference between PA05M5H and PL1M5H samples, however a significant difference was noted when this was compared to all other samples. The TCP control recorded the lowest OCN expression at 3.72 $\pm$0.54. However, this difference was not significant when compared to PA0, PA1.5H and PL1M. The difference between PL0 samples and the TCP control on the other hand was significantly different.

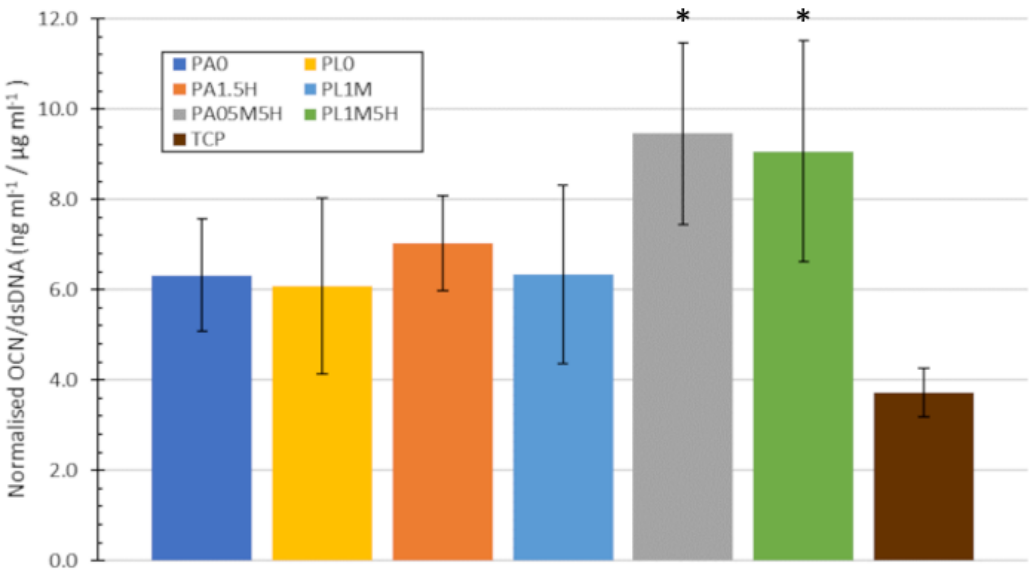


FIGURE 7.15: Graph showing the Osteocalcin assay conducted at 21d for the laser sintered nanocomposite samples. PA05M5H and PL1M5H samples displayed the highest Osteocalcin content compared to the other samples. One-Way ANOVA reported that this result was significant. n = 9, error bars represents standard deviation. Asterisk represents statistical significance.

7.3.4 Bioactivity of Nanocomposite Samples - Alizarin Red Assay

Qualitative analysis of bone mineralisation was conducted using the Alizarin Red assay. The results of this test can be seen in Figure 7.16. The PA0 recorded an absorbance value of 1.87 $\pm$0.21, the PL0 sample recorded a slightly lower absorbance of 1.74 $\pm$0.18, however no significant difference was recorded. The PA1.5H samples recorded a similar absorbance value of 1.70 $\pm$0.50 and statistical analysis also showed no significant difference between these samples. The PL1M samples recorded the lowest average absorbance value (1.66 $\pm$0.20) when compared to all samples and control. Once again, the statistical analysis showed no significant difference between PL1M, PA1.5H, PL0, PA0, PA05M5H and TCP control. The PA05M5H samples recorded a higher absorbance value of 2.013 $\pm$0.25, but once again no significant difference was observed when comparing PA05M5H to the other samples. The PL1M5H samples recorded the highest average absorbance value when compared to all tested samples and control. Compared to the TCP control the absorbance was 23% higher. Statistical analysis showed a significance when compared to PA1.5H, PL0 and TCP control and significance.

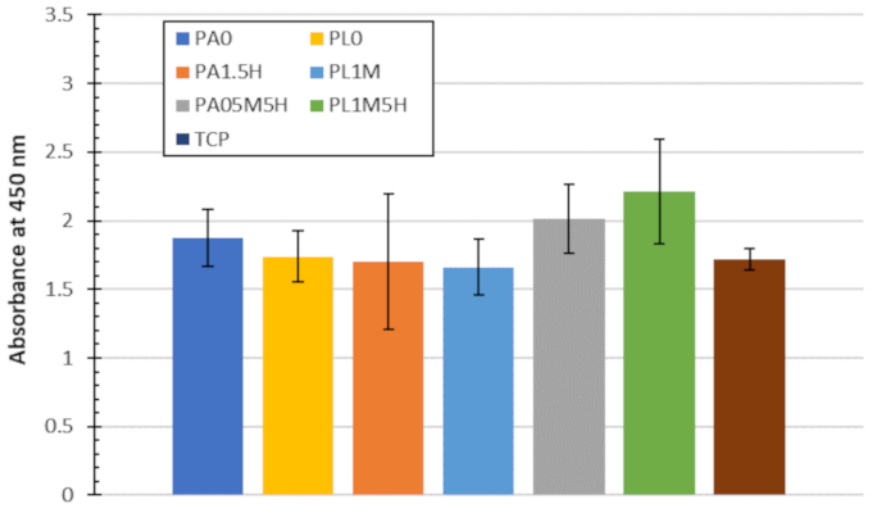


FIGURE 7.16: Graph showing the Alizarin Red assay conducted at 21d for the LS nanocomposite samples. PA05M5H and PL1M5H samples displayed the highest Osteocalcin content compared to the other LS samples. One-Way ANOVA did not report any significance when comparing PA05M5H to LS samples, however PL1M5H was reported to be significantly higher when compared to PA1.5H, PL1M, PL1M5H and TCP control. n = 9, error bars represents standard deviation.

7.4 SEM Imaging

The morphology of the hiMSCs cultured on the 2D, laser sintered nanocomposite samples and 3D scaffolds was visualised via SEM imaging. The samples were imaged at 24h, 7d and 21d.

7.4.1 SEM Imaging of hiMSC Cultured on PA12-MWCNT-nHA Nanocomposite Samples

SEM images, taken at 24h, 7d and 21d time-points, of hiMSC cells grown on the PA0, PA1.5H and PA05M5H samples can be seen in Figure 7.17. At 24h hiMSCs grown on the PA1.5H (7.17 (b)) and PA05M5H samples (7.17 (c)) adopted a flattened, spread, morphology with lamellipodia and filopodia extensions at the leading edges of the cell with no clear preferential direction. The hiMSC identified on the PA0 sample (7.17 (a)), at 24h, adopted a more elongated, spindle like, morphology which spanned across multiple ridges along the surface. From these images, the porous nature of the surface of the laser sintered samples was also apparent. At 7d the cells cultured on

all samples appeared to be merging together, bridging over narrow gaps and making connections between different surface topographical features. The cells also displayed a more flattened, polygonal morphology with a low degree of filopodia at the leading edges and appeared to be approaching confluency. The cells growing on PA05M5H samples ((7.17 (c)) appeared to have a significantly higher surface coverage when compared to PA0 and PA1.5H samples. The SEM image of the cells on the PA0 samples (7.17 (g)) displayed a localised collection of spherical nodules on the right side of the image. The PA1.5H samples (7.17 (h)) displayed a more extensive degree of early bone mineralisation with spherical nodules apparent throughout the image. SEM images of cells grown on the PA05M5H sample (7.17 (i)) also appeared to show extensive signs of mineralisation with a higher degree of agglomerated spherical nodules when compared to PA0 and PA1.5H samples. These cells also appeared flattened and spread across the surface of the material.

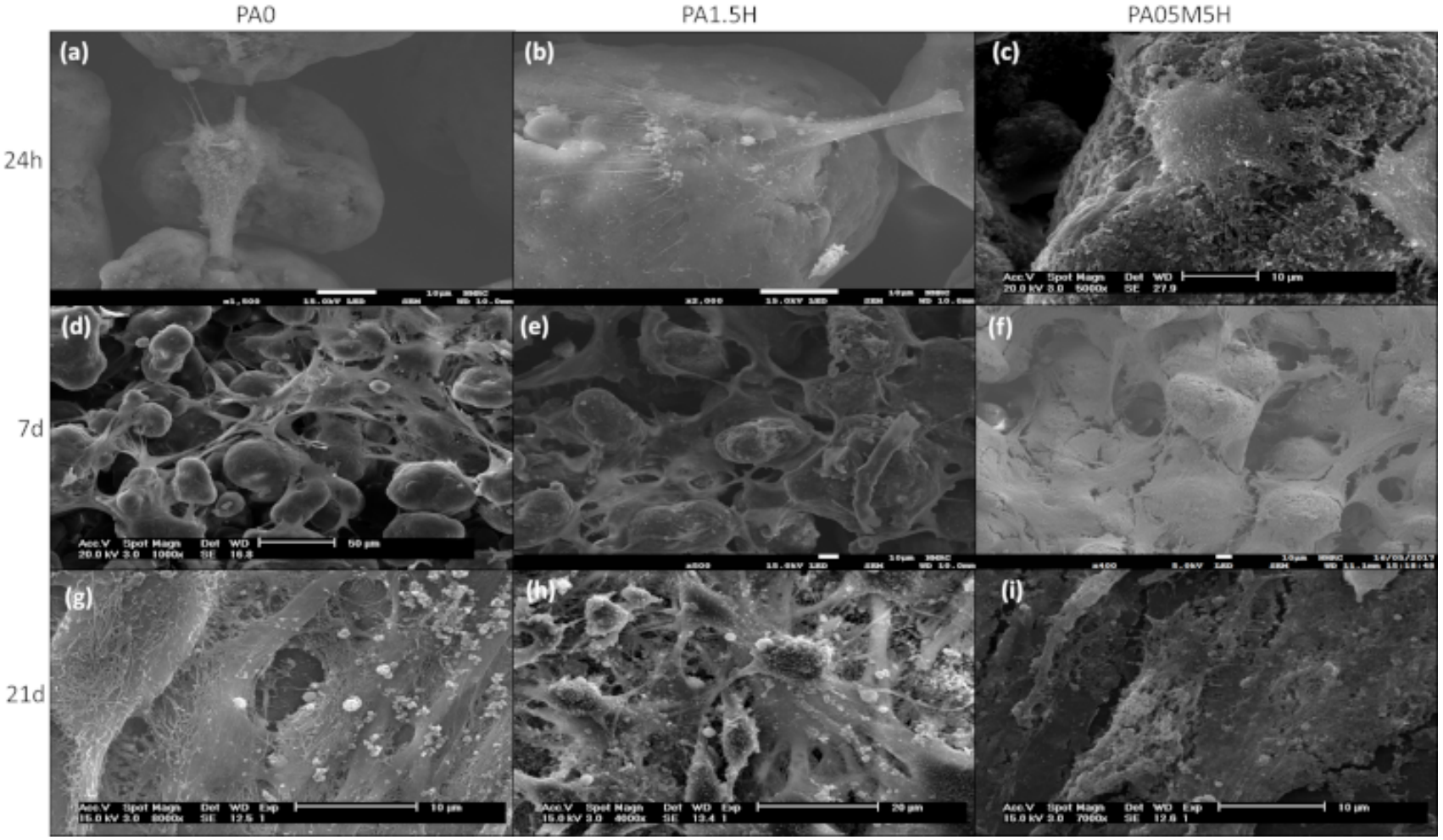


FIGURE 7.17: SEM images of hiMSC cells cultured on PA0(a, d and g), PA1.5H (b, e and f) and PA05M5H (c, f and i) samples, taken at 24h, 7d and 21d time-points. At 24h, cells grown on PA1.5H (b) and PA05M5H (c) display flattened morphology with extended lamellipodia and filopodia at the leading edges of the cell. The cell seen on the PA0 (a) sample adopted a more elongated, spindle like morphology. At 7d, cells appear to be extensively covering the surface of the materials, and are approaching confluence. By 21d, white spherical nodules can be seen on all cells cultured on all samples, indicative of mineralisation.

7.4.2 SEM Imaging of hiMSC Cultured on PLA-MWCNT-nHA Nanocomposite Samples

SEM images were also taken for hiMSCs grown on PLA based laser sintered samples at 24h, 7d and 21d, and can be seen in Figure 7.18. At 24h the hiMSCs grown on PL1M and PL1M5H samples (7.18 (b) and (c)) adopted a spreaded morphology with lamellipodia and filopodia extensions at the leading edges of the cell. The cells grown on the PL1M5H sample clearly showed the lamellipodia and filipodia contacting the NPs on the surface of the material. The cell observed on the PL1M sample, appeared to be bridging the narrow gaps. On the other hand, the cell identified on the PL0 sample (7.18 (a)) adopted a more rounded morphology, with no extensive filipodia and lamellipodia at the leading edges of the cell. By 7d the cells grown on each of the samples appeared to have spread and formed connections, spanning across multiple surface topographical features. Similar to cells grown on the PA12 based samples, the cells also adopted a more flattened, polygonal morphology and appear to be approaching confluency. The surface coverage of the PL1M5H sample appeared to be slightly higher when compared to the PL0 and PL1M images. By 21d there are signs of mineralisation. The cells on the PA0 sample (7.18 (g)) displayed mineralisation at the edges of the cell, identified by the spherical, white, nodules. Cells grown on the PL1M and PL1M5H samples (7.18 (h) and (i)) also displayed extensive signs of mineralisation. Signs of highly agglomerated nodules are extensive on the surface of the cells, and is obvious on both images.

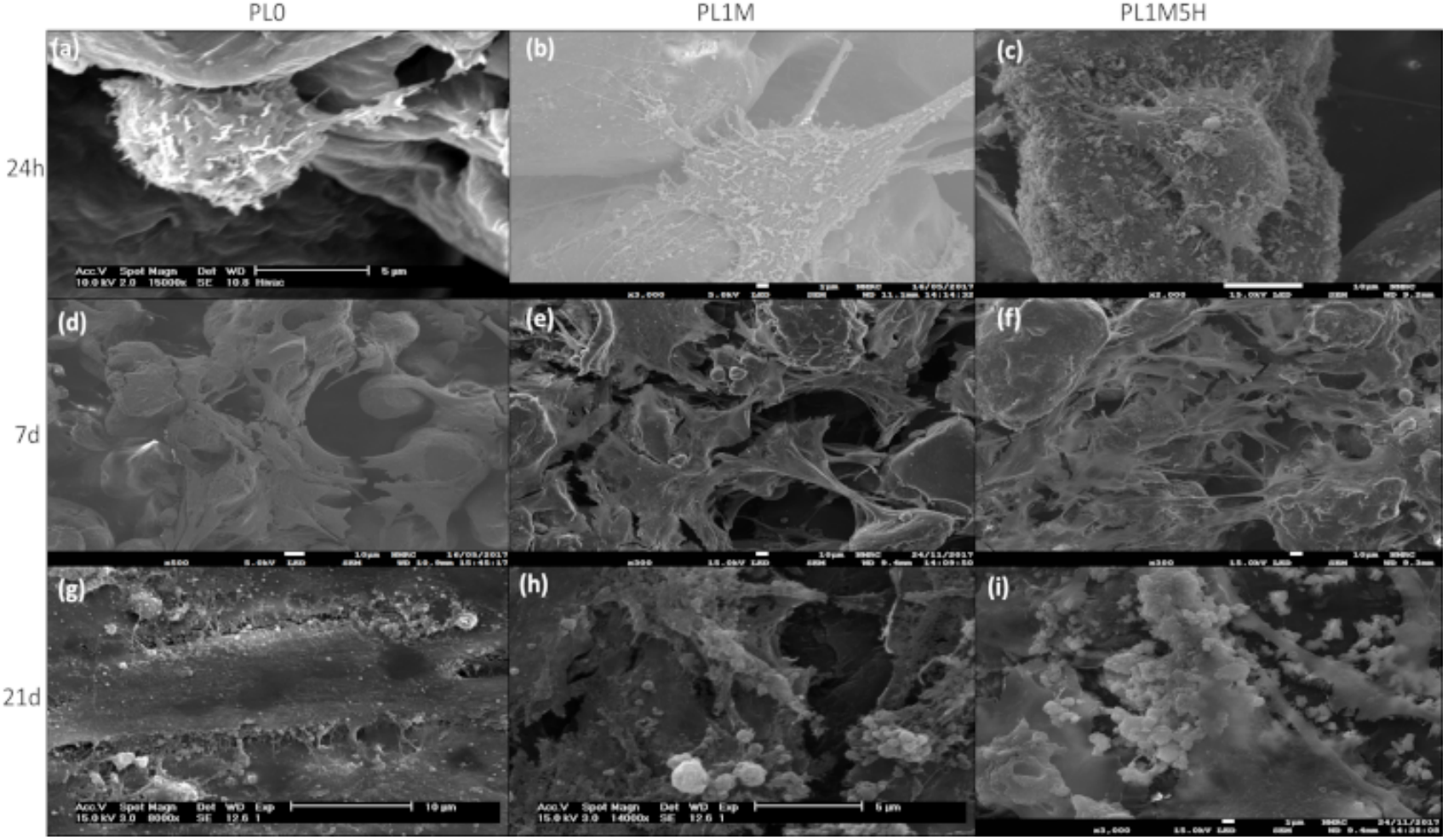


FIGURE 7.18: SEM images of hiMSC cells cultured on PL0(a, d and g), PL1M (b, e and f) and PL1M5H (c, f and i) samples, taken at 24h, 7d and 21d time-points. At 24h, cells grown on PL1M (b) and PL1M5H (c) displayed a more flattened morphology with extended lamellipodia and filopodia at the leading edges of the cell. The cell seen on the PA0 (a) sample adopted a more spherical morphology. At 7d, cells appear to be extensively covering the surface of the materials, and are approaching confluence. By 21d, white spherical nodules can be seen on all cells cultured on all samples, indicative of mineralisation.

7.4.3 SEM Imaging of hiMSC Cultured on a Nanocomposite Scaffold

Following analysis of the cells grown on 2D discs, the cells were then observed growing on a 3D scaffold made from PA0 and PL1M5H. This can be seen in Figure 7.19. In Figure 7.19 (a) and (d) the surface topography of the PA0 and PL1M5H scaffold can be seen. The unfused particles on the outer surface created a porous surface texture. The more jagged and angular morphology of the PLA particles made the surface texture on the PL1M5H scaffold appear rougher in comparison. Close up images, as seen in Figure 7.19 (b) and (e), show cells that had spread across the surface of the scaffold, forming bridges across the gaps between the poorly fused particles. This was particularly evident in the PL1M5H scaffold (7.19 (e)), where cells can be seen bridging a gap approximately 100 μm in length. Figure 7.19 (c) and (f) are magnified images of 7.19 (b) and (e) respectively. The cells in Figure 7.19 (c) appear polygonal in morphology, with few signs of large cellular filipodia extensions at the cell edges. The surface of the cells also displayed spherical nodules, an indication of potential cell maturation and mineralisation. Figure 7.19 (f) showed the cells appearing more striated and spread, and less flat in morphology. A high degree of cell filipodia can be seen forming connections with adjacent cells. Due to the large degree of poorly fused particles on the PL1M5H scaffolds larger gaps between the particles are apparent. The morphologies of the cells observed are likely due to the bridging of larger gaps, as more time is required to establish a confluent cell morphology as displayed in Figure 7.19(c). Spherical nodules can also be seen on the outer edges of the cells, which is indicative of mineralisation.

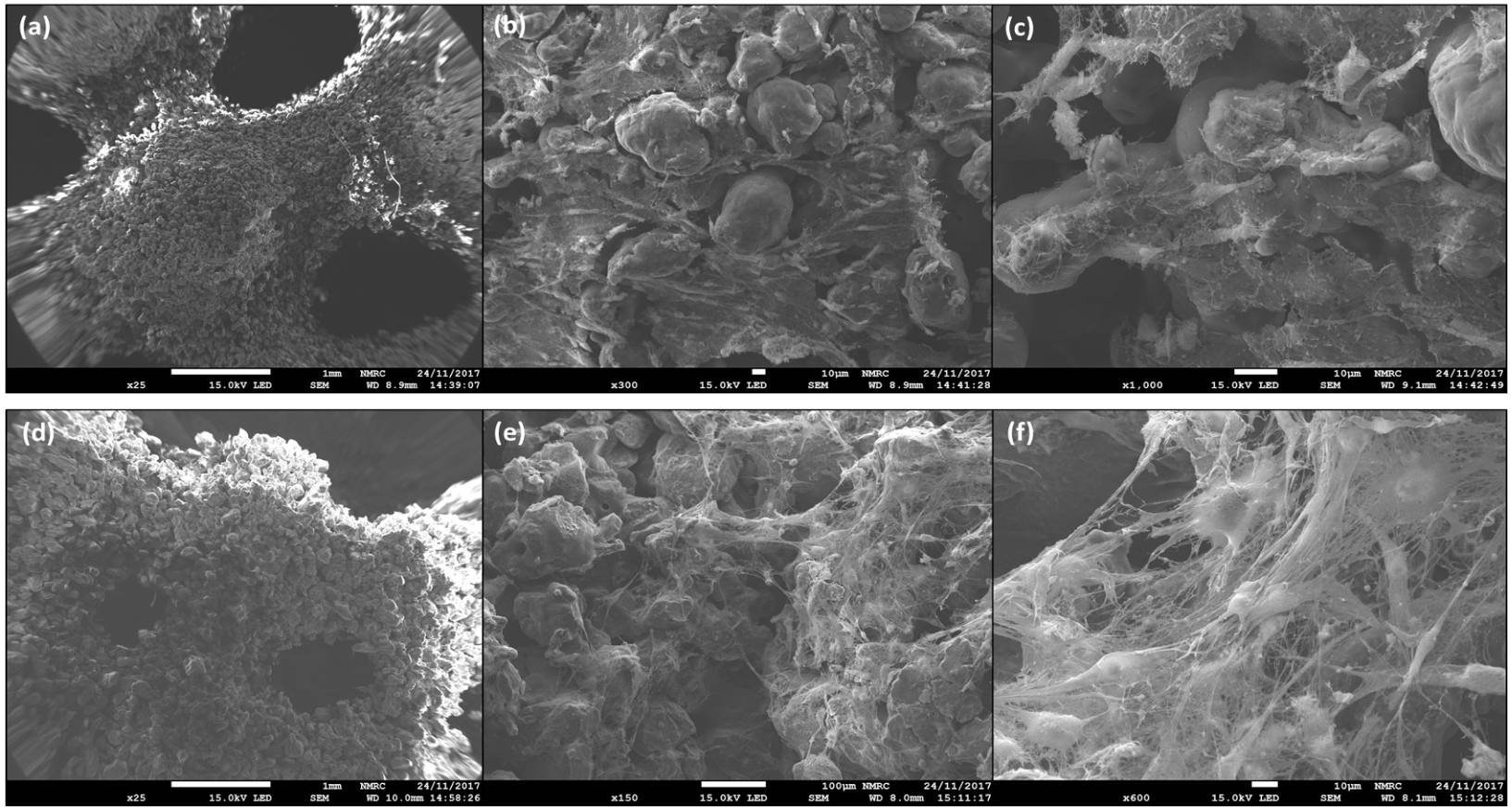


FIGURE 7.19: SEM images of hiMSCs cultured on of PA0 scaffolds (a, b and c) and PL1M5H scaffolds (d, e and f) taken at 21d. Images (a) and (d) show the surface of the scaffolds, unfused particles create a porous outer surface, the large PL1M5H particles appear rougher in comparison.s figure (b) shows hiMSC cells extensively covering the surface of the PA0 scaffold surface, and approaching confluence. The larger, more jagged PL1M5H particles creates larger gaps for the cells to span across. Figure (e) shows hiMSC cells bridging large gap approximately 100 μm in length. Figure (c) and (f) are magnified images of (b) and (e), respectively. Cells seen in (f) appear more striated in comparison to (c), this is likely due to the more extensive bridging. Spherical nodules can be seen on both (c) and (f), indicative of bone mineralisation occurring.

7.5 Discussion

It is important to consider the intended use of the material under investigation. In this work its intended use is as a bone substitute material where, MWCNT and nHA are attached to the surface of the polymer and are not free floating. The results displayed in this work demonstrate that the use of MWCNT and nHA separately, and in combination, for the fabrication of a polymer nanocomposite, are cytocompatible. Direct contact tests, with MG-63 cultured directly onto PA-nHA, PA-MWCNT, PA-MWCNT-nHA, PLA-MWCNT and PLA-MWCNT-nHA nanocomposites, exhibited increasing cellular metabolic activity, cell number and cellular proliferation across the 7d test period. This was confirmed using the Alamar Blue and DNA assays. Furthermore, SEM imaging of the hiMSC cells grown on the laser sintered samples also demonstrated cytocompatibility, with cells approaching confluency on the material surfaces by 7d. These results are in line with observations made in the literature. One of the first studies of culturing osteoblasts on HA/CNT surfaces was conducted by Balani et al. [403]. In this study HA powder was blended with 4 wt% MWCNT and this powder feedstock was plasma sprayed onto the surface of Ti-6Al-4V substrate. Human osteoblasts (HOBs) were cultured on the HA/MWCNT coating. SEM analysis demonstrated unrestricted cell growth at regions containing high levels of CNT after 24h thus demonstrating cytocompatibility. Similarly, Lobo et al. [404] demonstrated that L929 mouse fibroblasts, cultured on MWCNT films, displayed good cytocompatibility through MTT assay and cell adhesion testing. SEM showed that cells cultured on the film adopted a flattened morphology on the MWCNT filament structures. Similarly, in a study by Yun et al. [405] fluorescent imaging of 3T3 fibroblasts cultured on MWCNT substrates demonstrated good adhesion of the 3T3 cells with no significant toxic effects observed. Kalbacova et al. [406] noted that the metabolic activity of a SAOS-2 human osteoblast like cell line culture on SWCNT film decreased by 15-20% and determined that the film demonstrated cytocompatibility. Giannona et al. [407] observed CAL-72 osteoblast like cells cultured on arrays of vertically aligned MWCNT. It was reported that cellular attachment and spreading process on the vertically aligned MWCNTs was significantly enhanced. Liao et al.

[408] produced PA66/nHA in addition to PA66/MWCNT/nHA based nanocomposites (0.1 wt% MWCNT loading), via melt blending, and demonstrated that L929 cells cultured on the MWCNT/nHA nanocomposite exhibited uninhibited cell growth indicating that the presence of MWCNT had negligible effect on cytocompatibility when compared to PA66/nHA samples. Constanda et al. [409] also observed good cytocompatibility with human osteoblasts (HOBs) cultured on a CNT/HA nanocomposite that was produced via co-precipitation. Loadings of 5 and 10 wt% MWCNT were used in the fabrication of the nanocomposites. MTT assays showed that cell viability was not decreased, furthermore reactive oxygen species (ROS) were also measured, with induction of oxidative stress occurring after 2 days of exposure. Osteoblast proliferation on electrically stimulated PLA/MWCNT nanocomposites with 10, 15 and 20% MWCNT, by Supronowicz et al. [410] displayed increased proliferation in addition to enhanced extra-cellular calcium deposition compared to control samples. Correa-Duarte et al. [411] demonstrated that L929 mouse fibroblasts cultured on MWCNT surfaces grown on silicone substrates, produced a healthy, confluent, layer of cells which had grown across the surface after 7days.

However, as discussed in Chapter 2, one must still consider the toxicological effects of free NPs within the body. Dislodgement of particles from the material surface is likely through normal use and/or through biodegredation of the PLA material and it is this aspect that is yet to be thoroughly studied. The conjunction of cytotoxicity testing of free NPs and testing of laser sintered nanocomposites, where the NPs are attached to the surface, may therefore provide a greater understanding of the potential toxicological effects that these nanocomposites may possess. In this work, the MG-63 incubated with rod shaped nHA did display dose dependent inhibition. The Alamar Blue assay which measured cellular metabolic activity, and provided a measure of cell number, showed that MG-63 cells incubated with increasing amounts on nHA concentrations from 100 - 1000 μg ml^{-1} displayed decreasing levels of cellular metabolic activity and a reduction in cell numbers, when compared to the control, across the 7day test period. When compared to the control group containing no NPs, the DNA content, which is indicative of cellular proliferation also reduced with increasing nHA concentration across the 7d period, and mirrored the trend obtained for the Alamar Blue results.

A potential reason as to why a decline in cell number was observed could be due to the increased calcium ion loading associated with high concentrations of NP uptake by cells. Ca^{2+} plays a key role in mediating cell survival since it has a major role as a secondary messenger, therefore, cellular Ca^{2+} concentrations are tightly regulated. Significant deviations from the carefully controlled balance can induce apoptosis [412]. The key mechanism in lowering cytosolic calcium ions is extrusion via the plasma membrane by Ca^{2+} pumps and by Na^{+} /Ca^{2+} exchangers. In addition, the endoplasmic and sarcoplasmic reticulum also act as the major intracellular Ca^{2+} reservoir and can be mobilised in the homeostasis of intracellular Ca^{2+} [413]. Organised increases in cytoplasmic, mitochondrial and nuclear matrix Ca^{2+} is a commonly used intracellular signalling mechanism. However, prolonged changes can trigger numerous cascades that ultimately lead to cell death [412]. One such mechanism involves the mitochondria, whereby sustained elevation of cytoplasmic Ca^{2+} activates a Ca^{2+} uniporter on the inner mitochondrial membrane leading to a membrane potential driven uptake of Ca^{2+} into the mitochondrial lumen. Excessive mitochondrial Ca^{2+} may stimulate the release of apoptosis promoting factors such as cytochrome c, Smac/Diablo, AIF, EndoG and pro-caspases from the intermembrane space to the cytoplasm [414]. Furthermore, mitochondria is the major source of reactive oxygen species (ROS), such as superoxide anions which are formed as a by-product from complexes I and III with 1%–2% of total electrons flowing through the respiratory chain leaking to produce ROS [415]. Excessive Ca^{2+} has been reported to increase ROS production and thus exacerbate the production of apoptosis promoting factors.

Other studies have also demonstrated a nHA does dependent response. For example, Liu et al. [416] demonstrated a low concentration toxicity effect when culturing short, rod shaped, nHA with MG-63 cells for 5 days. Concentrations of 5, 15 and 25 μg ml^{-1} were used in the study. Immunofluorescence microscopy showed cells possessing a de-polymerised and disordered actin cytoskeleton in the presence of nHA. The apoptotic rate of cells also increased with increasing nHA concentration from 1.85% to 2.29%. Furthermore, the total intracellular DNA content decreased as the concentration of nHA increased. However, the ALP marker for early osteoblast differentiation showed no significant difference across the concentration range. It was speculated that the

small size of the nHA, 10-20 nm in diameter and 40-60 nm in length, could have been phagocytosed by the cells which may have led to adverse effects on cellular viability and proliferation. Similarly, Xu et al. [417] demonstrated that nHA particles (10-20 nm), when cultured on primary rat osteoblasts at concentrations of 20, 40, 60, 80 and 100 μg ml^{-1}, led to inhibition of cellular metabolic activity and increasing cellular apoptosis. MTT and Flow Cytometry indicated a maximum inhibition rate and apoptosis of 47.7 and 17.22% respectively when cultured with 100 μg ml^{-1} nHA. Results observed by Fu et al. [418] (nHA 20–40 nm in diameter) and Motskin et al. [419] (nHA aspect ratio of 4.51 $\pm$1.55 nm) also demonstrated concentration dependent toxicity of nHA particles from 50-500 μg ml^{-1}. However, this contradicts the observations made in another study by Albrecht et al. [420], who observed the effects of nHA, of different sizes and morphologies such as needle, dull-needle, rod and plate-like morphologies, on Rat NR8383 and primary alveolar macrophages. When exposed at concentrations of up to 3000 μg ml^{-1}, lactate dehydrogenase (LDH) assays conducted on the NR8383 cells reported no cytotoxicity at all concentrations, whilst dull-needle shaped nHA did display a significant difference at the highest concentration. Primary cells also showed no cytotoxicity at all concentrations tested. It was concluded that the nHA at all concentrations exhibited good cytocompatibility. Similarly, a study by Cai et al. [421] incubated bone marrow mesenchymal stem cells (MSCs) and osteosarcoma cells (U2OS) with HA and nHA particles ranging from 20 $\pm$5, 40 $\pm$10 and 80 $\pm$12 nm in diameter. On this occasion, greater cell viability and proliferation was observed on MSCs incubated with nHA compared to micron sized counter parts. However, the osteosarcoma cell lines displayed inhibited cellular proliferation, particularly when incubated with the smallest, 20 nm, particles. These results suggest that cell type and size of particles played a crucial role in determining cytocompatibility. A study conducted by Pezzatini et al. [422] demonstrated good cytocompatibility of nHA incubated on endothelial cells. Biochemical markers such as nitric oxide synthase and cyclooxygenase-2 demonstrated that microvascular endothelial cells cultured in the presence of nHA, at a concentration of 1 mg ml^{-1}, exhibited good cytocompatibility. Although HA is widely recognised as a biocompatible material, and has been/is still

being extensively explored for use in orthopaedic applications which has been thoroughly discussed in the literature review in Chapter 2; the current literature available regarding the potential cytotoxic effects of free nano-phasic materials is conflicting. As discussed above, factors such as size, morphology and cell type tested can affect the type of cellular response observed.

Although MWCNTs are becoming a popular choice of material for use in medical applications due to their unique physiochemical properties [423] there is still a lack of information regarding any cytotoxic effects that free MWCNT may possibly have. Therefore, MWCNTs obtained from the supplier were also subject to the same cytotoxicity examination as the nHA particles. Similar to the observations made for nHA, there was also a dose dependent response. The Alamar Blue and Hoechst 33258 DNA assay indicated that cellular metabolic activity and cell number had declined in response to increasing MWCNT concentration. The DNA content also reflected these observations with a significant decline in DNA content in response to increasing MWCNT concentration. This was also demonstrated when MWCNT and nHA was used in conjunction, at a ratio of 1:5, as the same dose-dependent inhibition was produced as when nHA and MWCNT were used separately. In a study by Patolla et al. [423] the cellular response of normal human dermal fibroblasts (NHDF) to MWCNT, measuring 15-20 μm in length and 15-30 nm in diameter, at concentrations of 40, 200 and 400 μg ml^{-1}, was examined. Following exposure to the MWCNT, MTT tests showed that cells experienced significant loss of viability through a reduction in cellular metabolic activity. LDH leakage also showed cellular membrane damage with a reduction in cell viability of almost 50% at 400 μg ml^{-1} over a 96 hour period. DNA damage was also detected through comet assays and the extent of the damage was shown to increase as MWCNT concentration increased. Riviere et al. [424] also observed cytotoxic effects when exposing human epidermal keratinocytes (HEK) to MWCNTs at 0.1, 0.2 and 0.4 mg ml^{-1}. TEM examination revealed that MWCNT was present in the cytoplasmic vacuoles of the HEK at all time points of 1, 2, 4, 8, 12, 24 and 48h. MWCNT also stimulated the release of proinflammatory cytokine interleukin 8 from the HEKs. Neutral red assays indicated a decline in cell viability as concentrations increased from 0.1 mg to 0.4 mg ml^{-1}. Muller et al. [425] also demonstrated cytotoxic effects caused

by MWCNT in epithelial cells exposed to 10, 25, 50 ,100 and 150 μg ml^{-1}. MTT and LDH leakage showed a dose dependent inhibition of metabolic activity and a reduction in cell viability with increasing cell membrane damage.

To assess any potential osteoconductive properties that the laser sintered nanocomposites may possess, various assays were conducted. Alkaline phosphatase (ALP) is a glycoprotein, and its skeletal isoform is found on the cell membrane of osteoblasts [288]. The accumulation of ALP often precedes bone mineralisation and is therefore commonly used an early marker for osteoblast differentiation [426]. When ALP was normalised to DNA content, the hiMSC cultured on the PA05M5H and PL1M5H consistently demonstrated the highest ALP content from 14d and 21d. This ability of PA05M5H and PL1M5H to elicit increased differentiation of osteoblastic lineage was also confirmed when assessing osteocalcin levels. Osteocalcin is one of the most abundant forms of non-collagenous proteins present in the bone ECM and is synthesised and secreted exclusively by osteoblastic cells in the late stage of maturation [289] [426]. Osteocalcin is often used as an indicator of osteoblast differentiation and is believed to play a role in controlling the nucleation of HA crystals [289] [427]. The Osteocalcin levels recorded for PA05M5H and PL1M5H were significantly higher than all other samples at 21d. SEM analysis of the hiMSCs cultured on the PA05M5H and PL1M5H samples also confirmed the observations made above. The materials demonstrated good cytocompatibility with cells approaching confluency on the materials' surfaces by 7d. It was also evident that cells cultured on these materials displayed a greater number nodule formation at the fringes of the cell borders which is indicative of mineralisation, when compared to images taken of neat PA12 and PLA taken at the same timepoint of 21d. This was also supported by Alizarin Red staining, a common assay used for identifying calcium deposits. In this case it was highest for PA05M5H and PL1M5H samples. Kroustalli et al. [428] showed that hMSCS cultured on MWCNT substrates exhibited decreased cell numbers but an accelerated progression towards the osteogenic phenotype which was indicated by early and elevated levels of ALP, Osteocalcin and Osteopontin. A study by Ha et al. [429] noted that sustained gene expression changes when comparing synthesised nHA rods, with a length of 100 nm, and spherical silica NPs with a similar hydrodynamic volume and a diameter of 100

nm. Close examination of the ALP promoter region determined that nHA stimulated DNA methylation. The authors also noted that bone sialoprotein was tightly coordinated with ALP suggesting that nHA generated signals that could coordinate cellular behaviour.

The cellular response to a material is greatly determined by the intrinsic nature of the surface. The presence of the MWCNT and nHA on the surface of the nanocomposites produced by laser sintering, in this thesis, may have imparted sufficient roughened surface topography to elicit elevated osteoblastic phenotype in hiMSC cells. As evidenced in Figure 7.18 and SEM images presented in Chapter 4 and Chapter 5. The surface tography of laser sintered parts had a mico-scale surface texture which were also covered with NPs which also imparted an additional nano-scale surface texture, the nHA platelet like structures on the surface measured approximately 624 nm in diameter and these platelets were composed of individual nHA rods which were approximately 371 nm long and 35 nm wide. Khang et al. [430] stipulated that the enhancement of early cellular function, may be influenced by fibronectin adsorption and the nanoscale surface roughness is considered as a key factor for leading enhanced fibronectin adsorption and may induce unique conformational changes. In their study they found that α_1 and α_V integrin expression was enhanced on hMSC cultured on nano-roughened Ti surfaces. There was a direct correlation between the integrin expression and the promotion of proliferation and differentiation of osteoprogenitor cells. A nanoscale height of just 2-4 nm was enough to trigger rapid cytoskeleton re-organisation on the Ti surfaces. This selective activation of integrin receptors and the following cyclin expression can greatly affect the behaviour of osteopregenitor cells. Klein et al. [431] also noted that the nanoscale topography of the surface can greatly dictate the differentiation of osteoblastic cells. His studies demonstrated this effect when comparing osteoblasts cultured on nano and micro-roughened Ti surfaces. Osteoblast proliferation on nano-roughened surfaces was seen to reduce, however differentiation was significantly enhanced. These results were in line with the observations made by Webster et al. [52] who also observed this effect on surfaces containing nanoscale particles such as: alumina (24 nm), titania (39 nm) and HA (67 nm), compared to their macroscale counterparts. Protein analysis also revealed that the surfaces containing nanoparticles had greater levels of adsorbed

vitronectin and fibronectin which corresponded to enhanced adhesion of osteoblasts. Oh et al. [279] attempted to determine an optimum nano-dimension for enhanced osteogenic response. In their study, it was found that small (30 nm diameter) nanotubes promoted hBMSC adhesion but with no noticeable differentiation differences, whereas larger diameters of 70 to 100 nm elicited a selective differentiation towards the osteogenic lineage.

As discussed before in the Literature Review, calcium phosphate based ceramics and their derivatives are the most popular choice for use as bioactive bone substitute materials and have been used extensively since the 1960s. The use of nHA in nanocomposite materials has been demonstrated to enhance osteoinductive properties, and its use has been extensively explored in the fabrication of polymer nanocomposites made via traditional manufacturing routes and via additive manufacturing. Further to this, the use of nano-carbon structures has recently garnered significant interest and has recently been used in conjunction with nHA for providing enhanced osteoinductive properties of polymeric materials. For example, Chan et al. [432] demonstrated that Human Osteoblasts (HOBs) cultured on a PEEK nanocomposite containing both 15% nHA and 1.9% carbon nanofiber, fabricated via melt blending and injection moulding, displayed enhanced ALP activity compared to neat material. Similarly, Oyefusi et al. [433] grafted HA to CNT to produce nanosheets and cultured Human Fetal Osteoblast Cells (hFOB) on the material. Through western blot analysis, the cells cultured on the double HA/CNT nanosheets displayed early expression of osteocalcin after the third day of incubation, and a notable increase in expression after 12 days. Hahn et al. [434] also observed higher ALP activity for MCT3-E1 pre-osteoblasts cultured on HA-CNT composite coatings, compared to those cultured on bare Ti. As the MWCNT loading was increased from 1 to 3 wt% the ALP activity and cellular proliferation was significantly higher when compared to pure HA coatings. This suggested that the presence of MWCNT further enhanced the osteoinductive response of the material. Furthermore, Raucci et al. [435] demonstrated that human bone marrow derived mesenchymal stem cells (MSCs) cultured on gels dispersed with MWCNT and strontium doped HA displayed significantly improved osteogenic differentiation. ALP and Osteocalcin levels were found to be significantly upregulated. Rajesh et al.

[436] developed a tricomponent composite scaffold, containing oxidised MWCNT/alginate/HA and constructed using a freeze-drying method. In-vitro cell studies using MG-63 cells demonstrated increased cellular proliferation, when assessed by MTT and Hoechst 3342 assay. Fluorescent imaging showed good cellular attachment throughout the scaffold, furthermore ALP activity on was found to increase significantly from 2 to 4 days' culture. The authors claimed that the results confirmed that the prepared tricomponent scaffold enabled better cell differentiation.

The literature discussed demonstrate that MWCNT used in conjunction with nHA in polymer nanocomposites or coating could provide enhanced osteoinductive properties compared to neat polymers. These results observed in literature are in line with the in-vitro results observed in this work. Furthermore, the results for the in-vitro cell testing presented in this work, for PA12-MWCNT-nHA sand PLA-MWCNT-nHA nanocomposites fabricated via laser sintering is a first and expands our knowledge within this area. The results observed in this work also demonstrate that the enhanced osteoconductive and osteoinductive properties can be achieved through this method of nanocomposite production.

Chapter 8

General Discussion,Conclusion and Suggestions for Future Work

8.1 General Discussion

In this work nanoparitcles of HA with a typical size of 370 nm in length and 30 nm in diameter in addition to MWCNT with a typical size of $>$ 10 - 20 μm in length and $>$ 50 nm diameter was deposited on the surface of two types of polymer particles. The two polymers used were PA12 owing to its wide use in laser sintering and PLA due to the large body of work surrounding it's usage in orthopaedic applications. It was discovered that the NPs could be relatively well dispersed on the surface of the particles when a low loading was used (0.5 - 1 wt%). Compared to conventional methods of composite powder production, such as oil in water / emulsion or melt blending, the method adopted in this study was capable of producing large quantities of coated powder over a relatively short period of time (1 h per 1 kg batch) and is a more economically viable option for powder production which can be easily scaled up to produce larger quantities. As discussed in Chapter 2. A further advantages of having NPs coated on the surface of the powder particle is that the final nanocomposite will have the NPs present on the outer surface without the need for further post processing. Regarding biomedical applications, this can be beneficial for guiding cell-material interactions as

the cellular response is highly influenced by the surface topographical, physical and chemical properties, this was discussed in Chapter 2. The surface coating of NPs also improved the flow properties of the base polymer powders by creating a "lubricating" effect. Improvements to specific energy, bulk packing density and an overall lower powder cohesiveness was observed for nano coated particles compared to powders without NPs. The coating method may provide an effective means of improving the flow properties of other milled powders for use in laser sintering.

The addition of NPs was seen to alter the nucleation mechanism and reduce the nucleation activation energy. This resulted in an increased rate in re-crystallisation at an elevated temperature. There was a clear link between the effects observed during the thermal analysis studies and the laser sintering performance of the powders. The alteration of the crystallisation mechanisms of the powder, due to the NPs, was found to significantly influence powder processability with increased processing difficulties being observed. Part warping became more pronounced as the NP loading was increased. The overall effect was an increased narrowing of the processing window as a result of premature crystallisation of the layer. It was possible to minimise the effects of curling by reducing the overall energy density imparted on the powder bed. However, this had an impact on the mechanical properties of the final part. Therefore, a trade-off between NP loading, powder processability and final part properties existed. This phenomenon has not been previously reported in other studies where significantly higher loadings of HA and nHA composite powders were being successfully processed by laser sintering. This was discussed further in the Chapter 5. However, it was identified that the powder production methods used in these studies commonly had the NPs encapsulated within the polymer particles. The high surface coverage of nHA and MWCNT-nHA achieved in this study affected laser absorption and acted as a thermal barrier. This, in combination with the observed increase in melt viscosity and alteration to crystallisation mechanism, contributed to the processing difficulties experienced on both the commercial (Formiga P100) and consumer (Sintratec) laser sintering machines. The observations made during laser sintering of nano-coated PA12 and PLA powders in this study clearly demonstrate a link between the crystallisation and thermal effects observed and the impact that NPs, such as nHA and MWCNT, can

have on the processability of PA12 and PLA powders. The observations made in other studies discussed in Chapter 5 clearly support this notion. This also opens up further possibilities to explore the impact of different NPs on the laser sintering process. In addition, the results of this study indicate the importance of exploring alternative thermal management systems, the effectiveness of laser absorption and thermal conductivity between NPs and the polymer particles and different processing strategies for powders which are more susceptible to warping during laser sintering.

For the first time, the processing of nanocoated powders was also explored in a consumer laser sintering machine (Sintratec). The major advantages of using consumer machines is price. Commercial machines can cost in the region of £250,000 - £1 million, whereas the Sintratec costs in the region of £4,500, up to 220 times less than the commercial systems. The space required to house and operate a consumer machine is also significantly less than that of commercial systems, which often require dedicated rooms with specific ventilation requirements and the need for inert gas systems and servicing contracts. The Sintratec is a desktop machine and may allow for easier adoption in a small research lab or a hospital / healthcare clinic. As of 2014, 12 NHS hospitals had adopted the use of additive manufacturing to support surgical procedures [437]. The Phoenix Children's Hospital, veterans hospitals in the U.S., the Royal Brisbane and Women's Hospital in Australia have invested in dedicated additive manufacturing units [438]. More recently a £500,000 investment was announced for the creation of a 3D printing innovation hub at Alder Hey Children's Hospital [438]. According to Sculpteo's 4th Annual State of 3D Printing survey, 70% of hospital respondents had increased their investments in additive manufacturing in 2017 [439]. Therefore, consumer machines, like the Sintratec, make additive manufacturing far more accessible for bespoke and highly personalised solutions in the healthcare sector. However, the major downside of the Sintratec is that the machine is bought as a kit which requires assembly. The quality of the build is dependent on the user and build consistency can differ between machines. Furthermore, the machine is not a sealed system, and gaps between side panels allow heat to escape from the build chamber. These factors ultimately led to processing inconsistency with poor thermal management, which may

have exacerbated the processing issues encountered for the nanocoated powders. However, newer generation of consumer machines have recently emerged. For example, the Formlabs Fuse 1, has the same operational capabilities of the Sintratec machine, but functions within a fully enclosed system. Thus the thermal management within this system is far superior than the Sintratec [3]. Similarly, the Sinterit Lisa 1 also offers a fully enclosed system [4]. The nanocoated powders may therefore perform differently within the newer generation of consumer laser sintering machines and offer a further avenue of research to compare the laser sintering consistency between these machines.

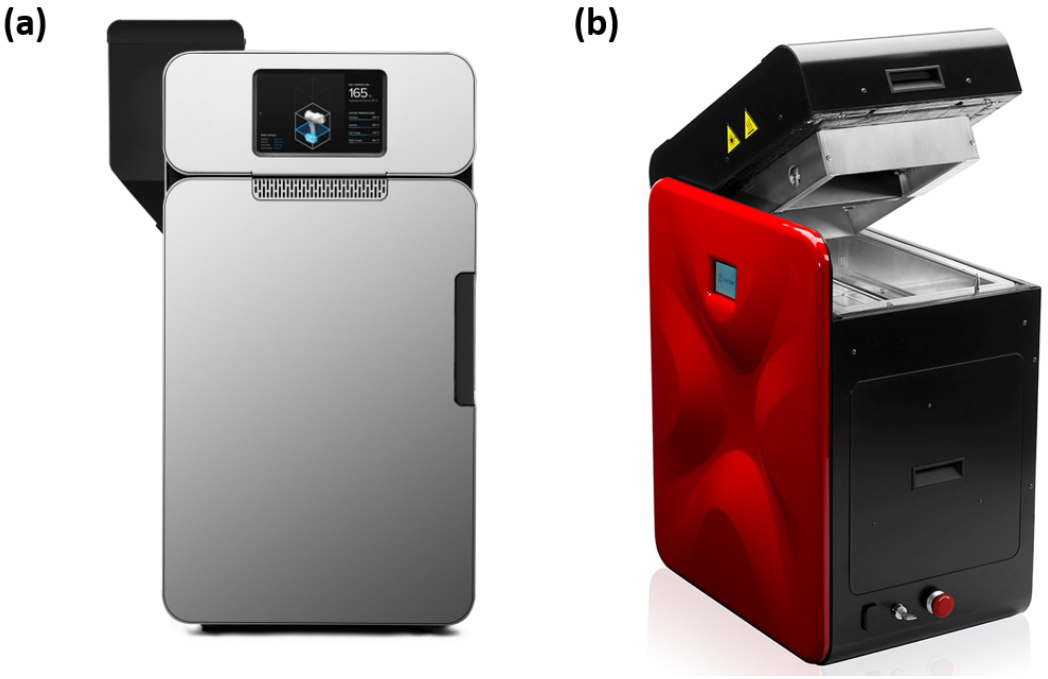


FIGURE 8.1: Image showing (a) Formlabs Fuse 1 and (b) SinterIt Lisa, consumer laser sintering machines which both feature a fully enclosed design [3] [4].

When observed under SEM, the nanocomposite samples containing a higher loading of NPs, and thus requiring a lower energy density input to achieve successful build, had a significantly more porous structure compared to samples containing a lower NP content. This was also confirmed through gas displacement density analysis. Tensile testing showed that the addition of 0.5 and 1.0 wt% nHA did increase the Young's modulus and UTS by 18% and 3% respectively for PA05H samples. The PA1H samples observed an increase of 13% and 8%, respectively. However, PA1.5H saw a significant decline of 66% and 104% respectively. This was a direct result of low final part density due to a reduced laser sintering processing window. Similarly, PA05, PA05M2H and

PA05M5H and PL1M, PL1M2H and PL1M5H samples, processed in the Sintratec, observed a similar trend in tensile properties due to the reasons defined above. Heat-treatment of the PLA samples was trialled, which did improve density and tensile properties. This may be an effective post processing method for powders which are more difficult to process and require lower energy densities for laser sintering. However, unlike results the observed in Bai's work [1], the resultant laser sintered samples all displayed a significant reduction in the elongation at break which was likely a result of a higher degree of agglomeration at the sintering borders between adjacent polymer particles. The PA12 and PLA based nancomposites featured in this thesis, in their current state, possess the compressive strength within the upper range of cortical bone. They may therefore serve as a suitable replacement material when loaded principally under compression, such as the vertebral body [5]. However, the tensile properties of the nanocomposites are still lacking and do not meet the properties of cortical bone. On the other hand, as a replacement for cancellous bone, both tensile and compressive properties are within the high to mid-range and, combined with their osteoinductive inductive properties (as discussed in Chapter 7), may serve as a suitable candidate for the treatment of cancellous bone diseases.

Due to the more porous nature of cancellous bone and its occupation within the marrow cavity it is not an efficient weight-bearing structure when considered alone. However, it does provide a significant mechanical function which is, principally, a means for directing imposed stresses onto the stiffer cortical bone. An analogy of this can be seen in the supporting struts of a bar stool, the presence of connecting struts and cross bracing allows for effective load transfer. Absence of the supporting struts reduces the load transfer between the legs of the stool, which can lead to collapse [440]. Literature has shown that complete loss of cancellous bone can reduce the stiffness of the overall long bone by two to three times. Of the chronic bone abnormalities osteoporosis is one of the most prominent, and cases of such bone diseases are set to increase with an ageing population. Osteoporosis is characterised by low bone density and microarchitectural deterioration of the bone tissue. An example of this can be seen in Figure 8.2 [441]. Therefore, people suffering from osteoporosis are at greater risk of fracturing their bones, particularly in regions that are high in cancellous bone

such as the vertebral bodies and proximal femur. Osteoporosis is the cause of more than 8.9 million fractures annually worldwide and ranks highly amongst diseases that cause people to become bed ridden with serious complications [441] [440]. Typical osteoporotic vertebral fractures can lead to height reduction of the anterior vertebral body whilst leaving the posterior vertebral wall intact. This collapse and bowing of the vertebral body (Figure 8.2) can lead to an increase in kyphosis deformity; the magnitude of which can increase with the degree of multiple vertebral fractures. The fracture risk of neighbouring elements has also been shown to increase fivefold compared to healthy vertebrae [442].

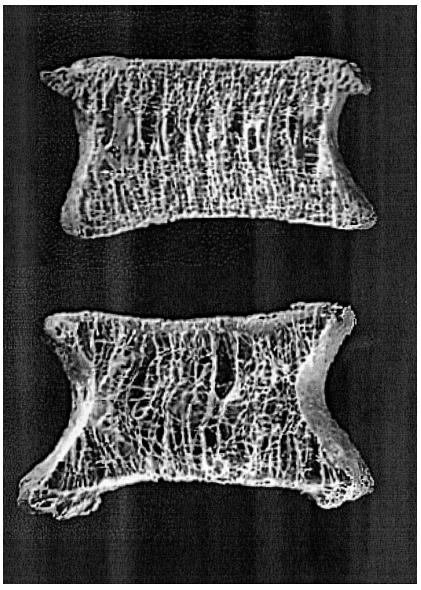


FIGURE 8.2: Top image shows a cross section of a normal, healthy, vertebrae where as the image underneath is of an osteoporotic. Note the reduction in cancellous bone density and inwards bowing of the osteoporotic vertebrae [5].

The cytotoxicity studies showed that both nHA and MWCNT had a dose dependent metabolic and proliferative inhibition on MG-63 cells. However, when compared to nanocomposite samples where the NPs are adhered onto the surface, cytotoxic effects were not observed on both the PA12 and PLA based nanocomposites. When MWCNT and nHA are used in combination for the fabrication of a polymer nanocomposite, the resultant samples were found to be cytocompatible. Direct contact testing with MG-63 cultured directly onto the following nanocomposites exhibited increasing cellular metabolic activity, cell number and cellular proliferation, across the 7d test

period: PA/nHA, PA/MWCNT, PA/MWCNT/nHA, PLA/MWCNT and PLA/MWCNT/nHA. This was confirmed using the Alamar Blue and DNA assays in addition to SEM imaging. The PA05M5H and PL1M5H consistently demonstrated the highest ALP content from 14d and 21d. This ability of PA05M5H and PL1M5H to elicit increased differentiation of osteoblastic lineage was also confirmed when assessing osteocalcin levels. This demonstrated that when a sufficient amount of nHA was used an improvement in osteogenic response could be observed. However, as demonstrated, a balance must be reached with respect to NP content in terms of powder processability, mechanical properties and cellular response to the material. The degradable nanocomposites produced in this work may provide sufficient structural integrity during the restoration of healthy bone tissue and may serve as a suitable alternative, given some of the downsides, to other bone graft materials which as discussed in Chapter 2.

8.2 Conclusion

Based on the original research objectives the following conclusions are summarised below:

- Adapt the coating method adopted by Bai et al. [1], for the coating of PA12 and PLA powders with alternative nano-particles such as nHA, and investigate how different loadings of nHA may impact the powder morphology, flowability and thermal characteristics of the coated powders, what influence may this have on powder processability during laser sintering?

It was possible to coat individual PA12 and PLA particles with nHA and MWCNT-nHA. Based on SEM analysis the optimal loading to maintain good dispersion of the nHA on the surface of the powders was between 0 - 1 wt%. The coating method did not significantly alter the overall particle size distribution of the PA12 and PLA particles, even when a relatively high loading of 4 wt% nHA (PA12) and 5 wt% nHA (PLA) was used. The increased NP loading led to a reduction in the cohesive properties of nanocoated powders, which was assessed through powder rheometery. This

improvement in flow characteristics was significant for the the larger, more angular PLA particles. Standard DSC revealed that there was a sufficiently large temperature separation between the melting and crystallisation peaks for the coated powders, thus indicating that the coated powders had a processing window for laser sintering. However, through isothermal and non-isothermal analysis the addition of NP had an affect on the early stages of the crystallisation mechanism and the nucleation activation energy was altered by presence of the NPs. Different cooling rates also revealed the temperature at which the onset of crystallisation occurred was significantly higher than the standard DSC, which indicated that under real-word conditions the processing window for the powders was significantly narrower than initially suggested. These effects may have contribute towards a higher sensitivity to part warping (curling) during laser sintering. A higher zero-shear melt viscosity was also observed with increasing addition of NPs for the coated PLA powders, suggesting a higher degree of energy input may be required for sufficient coalescence of the powder particles. The presence of the NPs also affected the optical properties of the powder. The increased loading of nHA led to a higher absorption within the operating wavelength of the CO_2 laser used in the commercial LS machine thus indicating localised absorption of the incoming laser by the nHA. The addition of MWCNT enabled the absorption of the incoming laser used in the consumer LS machine, thus allowing for the material to be processed, the degree of absorption could be controlled by varying the loading of MWCNT. A higher MWCNT loading may allow for a faster laser scan speed to be used.

- Investigate the feasibility of processing the nHA coated powders in a commercial (EOS Formiga P100) and consumer laser sintering system (Sintratec). Determine the optimum laser sintering parameters needed to successfully process the coated powders for the production of nanocomposites for mechanical and cellular testing. Assess whether the presence of nHA at different loadings affects the laser sintering performance of the powders, if so how?

At loadings above 1.5 wt%, the nanocoated PA12 powders became increasing difficult to process. A significant reduction of the processing window was observed. Part warping became more significant as the nHA loading was incrementally increased from 0.5

to 2.0 wt%. Above 1.5 wt% nHA the PA12-nHA powders could not be successfully processed in the commercial laser sintering machine due to significant part warping. To reduce powder consumption, a consumer laser sintering machine was used to process PA12-MWCNT-nHA and PLA-MWCNT-nHA powders. In this case 0.5 to 1.0 wt% MWCNT and 2.0 and 5.0 wt% nHA could be processed. However, similarly to observations made in the commercial machine for PA12-nHA powders, part warping became more pronounced and this was accompanied by a significant reduction of the processing window. This effect had not been observed in other studies which had used laser sintering to process other nanocomposite powders. When single layers were viewed in a SEM, powders containing higher nHA loading, which were processed using the same laser sintering parameters, displayed a higher degree of porosity. It was a determine that a range of factors affected the processability of the coated powders, these included: the high surface coverage of NP which affected the heat-transfer between particles; the increase in viscosity reduced the inter-particle fusion; the strong heterogenous nucleating effect of the NPs and poor thermal management within the LS machine itself contributed towards significant part warping. Despite some of these limitations, there was a narrow processing window in which successful parts could be achieved, thus it was feasible to process the coated powders via laser sintering in both a commercial and consumer machine.

- Assess whether the nancomposites produced on the commercial and consumer laser sintering systems are suitable as a bone substitute material by way of examination of the mechanical properties of the nanocomposite and the behaviour that osteoblast-like cells exhibit when cultured directly onto the surface of the material.

Powders produced using a higher loading of nHA had significantly lower final part density and tensile properties when compared to nanocomposites produced with a lower nHA content, owing to the reduced laser sintering processing window for these powders. However, for PA05H and PA1H a large increase in tensile modulus and strength was observed. The relatively low nHA content did not significantly alter the processing window and, as such, the nHA provided a reinforcing effect. However, the elongation

at break had reduced significantly, possibly as a result of agglomeration of the nHA at the sintering borders between the particles, after laser consolidation. Through a heat treatment process the properties of the PL1M2H and PL1M5H nanocomposites could be recovered and the tensile modulus exceeded that of the PL1M samples. Heat treatment may provide an effective means of post processing powders which are sensitive to warping during laser sintering. However, the elongation was significantly reduced as a result of the increased consolidation of the polymer particles. Further investigation will be required to assess whether this may result in lower impact properties of the final part. In their current state, the PA12 and PLA nanocompsites do not meet the mechanical properties for cortical bone, however, the compressive properties are within the mid to high range of cancellous bone. These nanocomposites could therefore serve as a suitable replacement when principally loaded under compression. However, other properties such as impact strength, fracture toughness and flexural strength are yet to be assessed.

Cytotoxicity assays indicated a dose dependent inhibition of cellular metabolic activity when MG-63 cells were cultured with free nHA and MWCNT particles. This is an important consideration for the degradable PLA based nanocomposites. In future, degradation experiments for the PLA nancompoites will need to be conducted to ascertain the NP release rate. Alamar Blue and Hoechst 33258 DNA analysis showed that all samples had a good cytocompatibility across the 7 day test period. However, no clear distinction could be made between samples with and without NPs. A higher osteoconductive response for hiMSCs cultured directly onto PA05M5H and PL1M5H with osteogenic media was observed when compared to all other nanocomposite samples after 21 days. This was evaluated though ALP and Osteocalcin assays. This indicated that a relatively high loading of nHA was more beneficial in directing osteoprogenitor cells to differentiate into osteoblasts. Alizarin Red assay indicated higher osteogenesis when hiMSCs were cultured onto PL1M5H samples, however this was not statistically significant, hiMSCs were also cultured directly onto scaffolds produced from PA0 and PL1M5H powders using the commercial and consumer laser sintering machines for each powder respectively. SEM analysis showed that the cells had spread across the surface of the scaffolds and displayed signs of nodule formation after 21 days which

was indicative of mineralisation. Therefore, the nanocomposites produced by laser sintering in this work were sufficient in supporting cellular proliferation, and indicated that the materials containing the highest NP loading could facilitate an improved osteoconductive response.

8.3 Suggestions for Future Work

Unanswered questions in relation to how the NPs affect laser absorption and heat transfer through the powder bulk are yet to be explored. Laser sintering is a heat transfer process; one experiment which could shed some light on this is to pulse a CO_2 laser or a diode laser, to simulate a commercial machine or a consumer machine respectively, on the surface of a powder bed and measure the local temperature change at the laser spot either optically or via temperature probe. The rate of temperature change for powders coated with and without nano-particles, and at different loadings, may offer insight into how the presence of NPs affects heat-transfer and laser absorption. Thermal conductivity experiments to study what effect NPs have on the powder thermal conductivity and thermal diffusivity could also be performed. This will help establish a link between re-crystallisation, heat transfer and laser absorption effects which can offer a more complete picture of how the presence of NPs on the surface of the powder can affect laser sintering performance.

The nanocoated powders produced in this work were sensitive to warping during laser sintering. This suggested that a tightly controlled thermal management system may be needed in order to process powders which are more sensitive to warping. Generally, both commercial and consumer laser sintering machines are controlled by proprietary firmware in which the heating strategy is non-alterable by the end-user. Hardware modification and open source firmware may offer the ability to explore and optimise non-standard thermal management strategies for laser sintering. Most fused deposition modelling machines are commonly controlled using open source firmware such as Marlin, which utilises a widely used numerical programming language, g-code. This offers limitless capabilities to alter machine settings. There are documented cases of

experimental laser sintering machines utilising open source software for the control of the machine [443]. For laser sintering, special attention could be paid to the heating regime during and post laser exposure in order to mitigate or control temperature fluctuations, which could improve the success of processing nanocoated powders and other powders more prone to warping.

As discussed in Chapter 2, for a bone substitute material to successfully integrate with natural bone the physical properties of the material must closely resemble that of its natural counterpart. Therefore, mechanical testing was essential to assess the suitability of the resulting nanocomposite for use as a bone substitute material. Due to the nature of the sample geometries and powder quantity required, the mechanical properties of PA12 and PLA based nanocomposites were primarily explored through tensile, compressive and dynamic mechanical analysis testing. However, other properties such as flexural and impact properties are also important, and the study of these properties would offer a more complete basis from which to assess the suitability of the material to be able to perform as desired. Furthermore, repeating the mechanical testing on heat-treated samples, would also need to be conducted to fully assess the reproducibility of this post-processing method. The degradation properties of the PLA based nanocomposites should also be investigated to see what effect the presence of NPs has and whether the presence of NPs can be used to control the rate of degradation with the aim of allowing bone regeneration to match the rate of nanocomposite material loss. This will then lead to investigations into different structural geometries to see how different structures will affect the mechanical properties of the final part, and how different geometries and pore sizes will influence osseointegration with the material. Furthermore, with consideration of device development for future commercialisation, the mechanical properties pre and post sterilisation would need to be assessed.

In this work, the cytotoxicity assessment of free nHA and MWCNT suggested a dose dependent cytotoxic effect on osteosacroma cell lines. Although the nanocomposites produced by laser sintering, with NPs adhered onto the surface, did not elicit a cytotoxic response; a further investigation exploring the concentration of NPs released during nanocomposite degradation under simulated in-vivo conditions, is needed to better

evaluate the biocompatibility of the material. Progressing from this, in-vivo testing followed by histological examination would be needed to fully assess the biocompatibility of the nanocomposite material produced using these methods. As discussed in Chapter 2, the surface topology can also have a profound effect on the cellular response of mesenchymal stem cells to the material. A roughened surface texture is commonly employed on implantable devices such as artificial hip stems and acetabular cups to promote osseointegration with the implant which aids in the prevention of aseptic loosening. Future experiments which investigate how the surface roughness of the laser sintered nanocomposites is affected by the presence of NPs, laser sintering parameters and post processing would be needed to further evaluate to what extent the surface topology and / or the presence of NPs has an effect on the cellular response to the nanocomposite.

There was evidence to suggest that the presence of nHA, at a loading of 5 wt%, on the surface of the nanocomposite material did elicit an osteoinductive response with an observed increase in ALP, osteocalcin and calcium deposition for mesenchymal stem cells. Additional testing using primary cells cultured in basal media will provide a clearer picture of the affects that the nanocomposite material has on the cellular response. Whether the effects translates across in-vivo is yet to be seen. Therefore, an animal study may need to be conducted by implantation of the nanocomposite material into a bone defect site and observation of the response to the material via histological examination. Although nodule formation was observed on the nanocomposite samples, which may indicate mineralisation, further examination via energy dispersive X-ray (EDX) analysis is required to confirm that the nodules observed contained calcium-phosphate. This in conjunction with testing with Alizarin Red will provide further supporting evidence of bone mineralisation. The combination of these experiments will provide further insight into the overall biocompatiblity of the nanocomposite material for its intended use, as a temporary bone substitute material.

Appendix A

Publications

Hui, D., Goodridge, R.D., Scotchford, C.A. and Grant, D.M., 2018. Laser sintering of nano-hydroxyapatite coated polyamide 12 powders. Additive Manufacturing, 22, pp.560-570. DOI: 10.1016/j.addma.2018.05.045

Bibliography

[1] Jiaming. Bai. Development of a Polyamide12/Carbon nanotube nanocomposite for laser sintering. `https://dspace.lboro.ac.uk/2134/13909`, 2014. Accessed: 10-12-2017.

[2] A Amado, K Wegener, M Schmid, and G Levy. Characterization and modeling of non-isothermal crystallization of polyamide 12 and co-polypropylene during the sls process. In *5th International Polymers & Moulds Innovations Conference*, pages 207–216, 2012.

[3] Fuse 1 Tech Specs. `https://formlabs.com/3d-printers/fuse-1/tech-specs/`. Accessed:10-06-18.

[4] SinterIt Lisa1. `https://www.sinterit.com/sinterit-lisa/`. Accessed:10-06-18.

[5] Stephen J Ferguson and Thomas Steffen. Biomechanics of the aging spine. *European Spine Journal*, 12(2):S97–S103, 2003.

[6] Olga P. Coutinho Salgado, António J. and Rui L. Reis. Bone tissue engineering state of the art and future trends. *Macromol Biosci*, 4(8):743–765, 2004.

[7] Dietmar W. Hutmacher. Scaffolds in tissue engineering bone and cartilage. *Biomaterials*, 21(24):2529–2543, 2000.

[8] Peter X. Ma. Scaffolds for tissue fabrication. *Materials Today*, 7(5):30–40, 2004.

[9] Joshua L. Simon John L. Ricci E. Dianne Rekow Van P. Thompson Roy, Tithi Dutta and J. Russell Parsons. Performance of degradable composite bone repair products made via three-dimensional fabrication techniques. *Journal of Biomedical Materials Research Part A*, 66A(2), 2003.

[10] J. D. Bobyn M. Tanzer G. J. Stackpool J. J. Krygier Harvey, E. J. and S. A. Hacking. Effect of flexibility of the femoral stem on bone-remodeling and fixation of the stem in a canine total hip arthroplasty model without cement. *J Bone Joint Surg Am.*, 81(1):93–107, 1999.

[11] Joost Dick de Bruijn C. E. Wilson F. C. Oner C. A. Van Blitterswijk A. J. Verbout Kruyt, M. C. and W. J. A. Dhert. Viable osteogenic cells are obligatory for tissue-engineered ectopic bone formation in goats. *Tissue Eng.*, 9(2):327–336, 2003.

[12] H. Takita D. Kobayashi E. Tsuruga M. Inoue M. Murata N. Nagai Y. Dohi Kuboki, Y. and H. Ohgushi. Bmp-induced osteogenesis on the surface ofhydroxyapatite with geometrically feasible and nonfeasiblestructures: Topology of osteogenesis. *Journal of Biomedical Research Part A*, 39(2): 190–199, 1998.

[13] Hiroko Takita Hideaki Itoh Yuichi Wakisaka Tsuruga, Eichi and Yoshinori Kuboki. Pore size of porous hydroxyapatie as the cell-substratum controls bmp-induced osteogenesis. *J. Biochem*, 121(2):317–324, 1997.

[14] Amy J. Thorsen Lisa A. Czerwonka Yuan Bao Robert Langer Douglas N. Winslow Mikos, Antonios G. and Joseph P. Vacanti. Preparation and characterization of poly(l-lactic acid) foams. *Polymer*, 35(5):1068–1077, 1994.

[15] Georgios Sarakinos Susan M. Leite Joseph P. Vacanti Mikos, Antonios G. and Robert Langer. Laminated three-dimensional biodegradable foams for use in tissue engineering. *Biomaterials*, 14(5):323–330, 1993.

[16] Gouping Chen Takashi Ushida Satoshi Gojo Kaoru Segawa Hitoshi Tai Kenju Ueno et al. Ochi, Kensuke. Use of isolated mature osteoblasts in abundance

acts as desired-shaped bone regeneration in combination with a modified poly-dl-lactic-co-glycolic acid (plga)-collagen sponge. *J Cell Physiol*, 194(1): 45–53, 2003.

[17] So Yeon Kim Kang, Hyun Goo and Young Moo Lee. Novel porous gelatin scaffolds by overrun/particle leaching process for tissue engineering applications. *J Biomed Mater Res B Appl Biomater*, 79(2):388–397, 2006.

[18] Soung Gon Kang Eun Seok Kim Sang Ho Cho Oh, Se Heang and Jin Ho Lee. Fabrication and characterization of hydrophilic poly(lactic-co-glycolic acid)/poly(vinyl alcohol) blend cell scaffolds by melt-molding particulate-leaching method. *Biomaterials*, 24(22):4011–4021, 2003.

[19] Ivan Martin Shastri, Venkatram Prasad and Robert Langer. Macroporous polymer foams by hydrocarbon templating. *PNAS*, 97(5):1970–1975, 2000.

[20] Daniel F. Baldwin Nam P. Suh Joseph P. Vacanti Mooney, David J. and Robert Langer. Novel approach to fabricate porous sponges of poly(d,l-lactic-co-glycolic acid) without the use of organic solvents. *Biomaterials*, 17(14):1417–1422, 1996.

[21] Jun Jin Yoon and Tae Gwan Park. Degradation behaviors of biodegradable macroporous scaffolds prepared by gas foaming of effervescent salts. *J Biomed Mater Res*, 55(3):401–408, 2001.

[22] Robert G. Dennis Joel L. Kileny Murphy, William L. and David J. Mooney. Salt fusion: an approach to improve pore interconnectivity within tissue engineering scaffolds. *Tissue Eng*, 8(1):43–52, 2002.

[23] Patrick B. O'Donnell and James W. McGinity. Preparation of microspheres by the solvent evaporation technique. *Advanced Drug Delivery Reviews*, 28(1): 25–42, 1997.

[24] J. H. Aubert and R. L. Clough. Low-density, microcellular polystyrene foams. *Polymer*, 26(13):2047–2054, 1985.

[25] Kevin E. Kinzer Lloyd, Douglas R. and H. S. Tseng. Microporous membrane formation via thermally induced phase separation. i. solid-liquid phase separation. *Journal of Membrane Science*, 52(3):239–261, 1990.

[26] Kazuro L. Fujimoto Michael S. Sacks Guan, Jianjun and William R. Wagner. Preparation and characterization of highly porous, biodegradable polyurethane scaffolds for soft tissue applications. *Biomaterials*, 26(18):3961–3971, 2005.

[27] V. La Carrubba S. Piccarolo Pavia, F. Carfì and V. Brucato. Polymeric scaffolds prepared via thermally induced phase. *Journal of Biomedical Materials Research Part A*, 86A(2), 2007.

[28] John W. Haycock. 3d cell culture: a review of current approaches and techniques. *Methods Mol Biol.*, 695:1–15, 2011.

[29] Shaofeng Wang. Polyethylene nanocomposites. *Biomaterials*, 24:2133, 2003.

[30] M. A. Shokrgozar S. Sh Homaeigohar M. Hosseinalipour A. Khavandi Sadi, A. Yari and J. Javadpour. The effect of partially stabilized zirconia on the biological properties of ha/hdpe composites in vitro. *J. Mater.Sci. Mater. Med*, 17(5):407–412, 2006.

[31] C. K. Chua K. F. Leong M. W. Naing Tan, K. H. and C. M. Cheah. Fabrication and characterization of three-dimensional poly(ether- ether-ketone)/-hydroxyapatite biocomposite scaffolds using laser sintering. *Proc Inst Mech Eng H.*, 219(3):183–194, 2005.

[32] D. Pohle H. Münstedt T. Rechtenwald K. A. Schlegel Petrovic, L. and S. Rupprecht. Effect of betatcp filled polyetheretherketone on osteoblast cell proliferation in vitro. *J. Biomed Sci*, 13(1):41–46, 2006.

[33] Mohammed Naffakh José M. González-Domínguez Alejandro Ansón Yadienka Martínez-Rubi M. Teresa Martinez Benoit Simard Díez-Pascual, Ana M. and Marián A. Gómez. High performance peek/carbon nanotube composites compatibilizes with polysulfones-1. structure and thermal properties. *Carbon*, 48(12):3485–3499, 2010.

[34] Tongxin Wang Laurence C. Chow Mingshu Yang Liu, Xingxun and James W. Mitchell. Effects of inorganic fillers on the thermal and mechanical properties of poly(lactic acid). *International Journal of Polymer Science*, 2014:8, 2014.

[35] Rafael Auras Yuzay, Isinay E. and Susan Selke. Poly(lactic acid)/aluminum oxide composites fabricated by sol-gel and melt compounding processes. *Macromolecular Materials and Engineering*, 295(3):283–292, 2010.

[36] R. L. Reis M. B. Claase-Dirk W. Grijpma Azevedo, M. C. and Jan Feijen. Development and properties of polycaprolactone/hydroxyapatite composite biomaterials. *J. Mater. Sci. Mater. Med.*, 14:103, 2003.

[37] Samira Gharehkhani Mehdi Mehrali Hooman Yarmand Hendrik Simon Cornelis Metselaar-Nahrizul Adib Kadri Shirazi, Seyed Farid Seyed and Noor Azuan Abu Osman. A review on powder-based additive manufacturing for tissue engineering: selective laser sintering and inkjet 3d printing. *Science and Technology of Advanced Materials*, 16(3), 2015.

[38] Susmita Bose, Sahar Vahabzadeh, and Amit Bandyopadhyay. Bone tissue engineering using 3D printing. *Materials Today*, 16(12):496–504, dec 2013. ISSN 1369-7021. doi: 10.1016/J.MATTOD.2013.11.017. URL `https://www.sciencedirect.com/science/article/pii/S136970211300401X`.

[39] Michele Lanzetta Franco, Alessandro and Luca Romoli. Experimental analysis of selective laser sintering of polyamide powders: an energy perspective. *Journal of Cleaner Production*, 18(16–17):1722–1730, 2010.

[40] P. E. McHugh Caulfield, Brian and S. Lohfeld. Dependence of mechanical properties of polyamide components on build parameters in the sls process. *Journal of Materials Processing Technology*, 182(1–3):477–488, 2007.

[41] R.D. Goodridge, C.J. Tuck, and R.J.M. Hague. Laser sintering of polyamides and other polymers. *Progress in Materials Science*, 57(2):229–267, 2012.

[42] Jim. Banks. Adding value in additive manufacturing: researchers in the united kingdom and europe look to 3d printing for customization. *IEEE Pulse*, 4(6), 2013.

[43] C. Lee. Ventola. Medical applications for 3d printing: Current and projected uses. *P T*, 39(10):704–711, 2014.

[44] Stephanie. Bartlett. Printing organs on demand. *The Lancet Respiratory Medicine*, 1(9):684, 2013.

[45] Hod. Lipson. New world of 3-D printing offers "completely new ways of thinking": Q and A with author, engineer, and 3-D printing expert hod lipson. *IEEE Pulse*, 4(6):12–14, 2013.

[46] T Briggs. Getting it right first time: improving the quality of orthopaedic care within the national health service in england. 2015.

[47] US Markets Orthopedic Implant. Reconstruction, and trauma products. *LSI website* `http://www.lifescienceintelligence.com/market-reports-page.php`.

[48] TH Smit, Tom AP Engels, Serge HM Söntjens, and LE Govaert. Time-dependent failure in load-bearing polymers: a potential hazard in structural applications of polylactides. *Journal of Materials Science: Materials in Medicine*, 21(3):871–878, 2010.

[49] Lin Xiao, Bo Wang, Guang Yang, and Mario Gauthier. Poly (lactic acid)-based biomaterials: synthesis, modification and applications. In *Biomedical science, engineering and technology*. InTech, 2012.

[50] Shuko Suzuki and Yoshito Ikada. *Biomaterials for surgical operation*. Springer Science & Business Media, 2011.

[51] Xian Jiang and Lawrence T Drzal. Properties of injection molded high density polyethylene nanocomposites filled with exfoliated graphene nanoplatelets. In *Some Critical Issues for Injection Molding*. InTech, 2012.

[52] Thomas J Webster, Celaletdin Ergun, Robert H Doremus, Richard W Siegel, and Rena Bizios. Specific proteins mediate enhanced osteoblast adhesion on nanophase ceramics. *Journal of Biomedical Materials Research Part A*, 51(3): 475–483, 2000.

[53] Luigi Ambrosio. *Biomedical Composites*. Woodhead Publishing Limited,, 1 edition, 2010.

[54] Siu Hang Lee Min Wang Wai Lam Cheung Zhou, Wen You and Wing Yuk Ip. Selective laser sintering of porous tissue engineering scaffolds from poly(l-lactide)/carbonated hydroxyapatite nanocomposite microspheres. *Journal of Materials Science: Materials in Medicine*, 19(7):2353, 2008.

[55] Michael J. Yaszemski John M. Powers Thomson, Robert C. and Antonios G. Mikos. Hydroxyapatite fiber reinforced poly(alpha-hydroxy ester) foams for bone regeneration. *Biomaterials.*, 19(21):1935–1943, 1998.

[56] Szem J.W. Kumta P.N. DiMilla P.A. Marra, K.G. and L.E. Weiss. In vitro analysis of biodegradable polymer blend/hydroxyapatite composites for bone tissue engineering. *Journal of Biomedical Materials Research: An Official Journal of The Society for Biomaterials, The Japanese Society for Biomaterials, and The Australian Society for Biomaterials and the Korean Society for Biomaterials.*, 47(3):324–335, 1999.

[57] R. Zhang and P.X. Ma. Poly(alpha-hydroxyl acids)/hydroxyapatite porous composites for bone-tissue engineering. i. preparation and morphology. *Journal of Biomedical Materials Research: An Official Journal of The Society for Biomaterials, The Japanese Society for Biomaterials, and The Australian Society for Biomaterials.*, 44(4):446–455, 1999.

[58] John C. Middleton and Arthur J. Tipton. Synthetic biodegradable polymers as orthopedic devices. *Biomaterials*, 21(23):2335–2346, 2000.

[59] D. K. Gilding and A. M. Reed. Biodegradable polymers for use in surgery—polyglycolic/poly(lactic acid) homo-and copolymers: 1. *Polymer*, 20 (12):1459–1464, 1979.

[60] Bart Clarke. Normal bone anatomy and physiology. *Clinical journal of the American Society of Nephrology*, 3(Supplement 3):S131–S139, 2008.

[61] Russell S Taichman. Blood and bone: two tissues whose fates are intertwined to create the hematopoietic stem-cell niche. *Blood*, 105(7):2631–2639, 2005.

[62] Patrick Garnero. The role of collagen organization on the properties of bone. *Calcified tissue international*, 97(3):229–240, 2015.

[63] Adele L Boskey. Mineralization of bones and teeth. *Elements*, 3(6):385–391, 2007.

[64] G.N. Ramachandran and C.M. Venkatachalam. The stability of the two-bonded collagen triple helix. *Biochimica et Biophysica Acta*, 120(3):457–458, 1996.

[65] Ewa M Spiesz, Werner Kaminsky, and Philippe K Zysset. A quantitative collagen fibers orientation assessment using birefringence measurements: calibration and application to human osteons. *Journal of structural biology*, 176(3):302–306, 2011.

[66] Timothy G Bromage, Haviva M Goldman, Shannon C McFarlin, Johanna Warshaw, Alan Boyde, and Christopher M Riggs. Circularly polarized light standards for investigations of collagen fiber orientation in bone. *The Anatomical Record Part B: The New Anatomist: An Official Publication of the American Association of Anatomists*, 274(1):157–168, 2003.

[67] Kambiz Farbod, M Reza Nejadnik, John A Jansen, and Sander CG Leeuwenburgh. Interactions between inorganic and organic phases in bone tissue as a source of inspiration for design of novel nanocomposites. *Tissue Engineering Part B: Reviews*, 20(2):173–188, 2013.

[68] Yan Chen, BS Bal, and JP Gorski. Calcium and collagen binding properties of osteopontin, bone sialoprotein, and bone acidic glycoprotein-75 from bone. *Journal of Biological Chemistry*, 267(34):24871–24878, 1992.

[69] Aiman I Al-Qtaitat and Saed M Aldalaen. A review of non-collagenous proteins; their role in bone. *American J Life Sci*, 2:351–5, 2014.

[70] H Sun, F Ye, J Wang, Y Shi, Z Tu, J Bao, M Qin, H Bu, and Y Li. The upregulation of osteoblast marker genes in mesenchymal stem cells prove the osteoinductivity of hydroxyapatite/tricalcium phosphate biomaterial. 40(8): 2645–2648, 2008.

[71] Amina F Zebboudj, Minori Imura, and Kristina Boström. Matrix gla protein, a regulatory protein for bone morphogenetic protein-2. *Journal of Biological Chemistry*, 277(6):4388–4394, 2002.

[72] Alexandrine During, Guillaume Penel, and Pierre Hardouin. Understanding the local actions of lipids in bone physiology. *Progress in lipid research*, 59: 126–146, 2015.

[73] Patricia S. Wolfe Koyal Garg Jennifer M. McCool Isaac A. Rodriguez Sell, Scott A. and Gary L. Bowlin. The use of natural polymers in tissue engineering: A focus on electrospun extracellular matrix analogues. *Polymers*, 2(4):522–553, 2010.

[74] Liliana Polo-Corrales, Magda Latorre-Esteves, and Jaime E Ramirez-Vick. Scaffold design for bone regeneration. *Journal of nanoscience and nanotechnology*, 14(1):15–56, 2014.

[75] Geerling EJ Langenbach Vincent Everts Willems, Nop MBK and Andrej Zentner. The microstructural and biomechanical development of the condylar bone: a review. *Eur J Orthod.*, 36(4):479–485, 2014.

[76] Anko Antabak Augustin, Goran and Slavko Davila. The periosteum. part 1: Anatomy, histology and molecular biology. *Injury*, 38(10):1115–1130, 2007.

[77] M. Martiniakova, M. Vondrakova, and R. Omelka. Manual preparation of thin sections from historical human skeletal material. *Timisoara Medical Journal*, 1, 2006.

[78] Gerard J. Tortora and Bryan Derrickson. *Introduction to the Human Body: The Essentials of Anatomy and Physiology.* John Wilson and Son's, Inc., 2003.

[79] Patitapabana Parida, Ajit Behera, and Subash Chandra Mishra. Classification of biomaterials used in medicine. *International Journal of Advances in Applied Sciences*, 1(3):125–129, 2012.

[80] William H Eaglstein and Vincent Falanga. Tissue engineering and the development of apligraf®, a human skin equivalent. *Clinical therapeutics*, 19 (5):894–905, 1997.

[81] Michael J Yaszemski, Richard G Payne, Wilson C Hayes, Robert Langer, and Antonios G Mikos. Evolution of bone transplantation: molecular, cellular and tissue strategies to engineer human bone. *Biomaterials*, 17(2):175–185, 1996.

[82] Subrata Pal. *Design of the Total Artificial Heart*. Springer, 2014.

[83] MAK Liebschner and MA Wettergreen. Optimization of bone scaffold engineering for load bearing applications. *Topics in tissue engineering*, 1, 2003.

[84] Elise F Morgan and Tony M Keaveny. Dependence of yield strain of human trabecular bone on anatomic site. *Journal of biomechanics*, 34(5):569–577, 2001.

[85] Arnav Sanyal, Atul Gupta, Harun H Bayraktar, Ronald Y Kwon, and Tony M Keaveny. Shear strength behavior of human trabecular bone. *Journal of biomechanics*, 45(15):2513–2519, 2012.

[86] David F Williams. On the mechanisms of biocompatibility. *Biomaterials*, 29 (20):2941–2953, 2008.

[87] Alexander R Vaccaro. The role of the osteoconductive scaffold in synthetic bone graft. *Orthopedics*, 25(5):S571–S578, 2002.

[88] Susmita Bose, Mangal Roy, and Amit Bandyopadhyay. Recent advances in bone tissue engineering scaffolds. *Trends in biotechnology*, 30(10):546–554, 2012.

[89] Zeeshan Sheikh, Corneliu Sima, and Michael Glogauer. Bone replacement materials and techniques used for achieving vertical alveolar bone augmentation. *Materials*, 8(6):2953–2993, 2015.

[90] FG Draenert, D Huetzen, A Neff, and WEG Mueller. Vertical bone augmentation procedures: basics and techniques in dental implantology. *Journal of Biomedical Materials Research Part A*, 102(5):1605–1613, 2014.

[91] Rahul Seth, Neal D Futran, Daniel S Alam, and P Daniel Knott. Outcomes of vascularized bone graft reconstruction of the mandible in bisphosphonate-related osteonecrosis of the jaws. *The Laryngoscope*, 120(11): 2165–2171, 2010.

[92] Todd Boyce, Jean Edwards, and Nelson Scarborough. Allograft bone: the influence of processing on safety and performance. *Orthopedic Clinics*, 30(4): 571–581, 1999.

[93] William W Tomford. Transmission of disease through transplantation of musculoskeletal allografts. *JBJS*, 77(11):1742–1754, 1995.

[94] Centers for Disease Control and Prevention. Update: allograft-associated bacterial infections—united states. *MMWR Morb Mortal Wkly*, 51:207–210, 2002.

[95] Centers for Disease Control and Prevention. Septic arthritis following anterior cruciate ligament reconstruction using tendon allografts—florida and louisiana. *MMWR Morb Mortal Wkly*, 50:1081–1083, 2000.

[96] Aldo R Boccaccini and Peter X Ma. *Tissue engineering using ceramics and polymers*. Elsevier, 2014.

[97] H Minakawa, MH Stone, BM Wroblewski, JG Lancaster, E Ingham, and J Fisher. Quantification of third-body damage and its effect on uhmwpe wear with different types of femoral head. *The Journal of bone and joint surgery. British volume*, 80(5):894–899, 1998.

[98]

[99] Satyavrata Samavedi, Abby R Whittington, and Aaron S Goldstein. Calcium phosphate ceramics in bone tissue engineering: a review of properties and their influence on cell behavior. *Acta biomaterialia*, 9(9):8037–8045, 2013.

[100] Ji Hye Lee, Nae Gyune Rim, Hyun Suk Jung, and Heungsoo Shin. Control of osteogenic differentiation and mineralization of human mesenchymal stem cells on composite nanofibers containing poly [lactic-co-(glycolic acid)] and hydroxyapatite. *Macromolecular bioscience*, 10(2):173–182, 2010.

[101] Hamid Mirzadeh Yossef Mohamadi Eslaminejad, Mohamadreza Baghaban and Aghbibi Nickmahzar. Bone differentiation of marrow-derived mesenchymal stem cells using beta-tricalcium phosphate-alginate-gelatin hybrid scaffolds. *1*, 6:417–424, 2007.

[102] Qinghong Hu, Zhou Tan, Yukan Liu, Jinhui Tao, Yurong Cai, Ming Zhang, Haihua Pan, Xurong Xu, and Ruikang Tang. Effect of crystallinity of calcium phosphate nanoparticles on adhesion, proliferation, and differentiation of bone marrow mesenchymal stem cells. *Journal of Materials Chemistry*, 17(44): 4690–4698, 2007.

[103] Petra J Ter Brugge, Joop GC Wolke, and John A Jansen. Effect of calcium phosphate coating composition and crystallinity on the response of osteogenic cells in vitro. *Clinical oral implants research*, 14(4):472–480, 2003.

[104] Huipin Yuan, Hugo Fernandes, Pamela Habibovic, Jan de Boer, Ana MC Barradas, Ad de Ruiter, William R Walsh, Clemens A van Blitterswijk, and Joost D de Bruijn. Osteoinductive ceramics as a synthetic alternative to autologous bone grafting. *Proceedings of the National Academy of Sciences*, 107(31):13614–13619, 2010.

[105] Garima Tripathi and Bikramjit Basu. A porous hydroxyapatite scaffold for bone tissue engineering: Physico-mechanical and biological evaluations. *Ceramics International*, 38(1):341–349, 2012.

[106] Daniele Cristina Do Prado Ribeiro, Luanda de Abreu Figueira, JoÃO Paulo Mardegan Issa, Cesar Adriano Dias Vecina, Fernando JosÉDias, and Marcelo Rodrigues Da Cunha. Study of the osteoconductive capacity of hydroxyapatite implanted into the femur of ovariectomized rats. *Microscopy research and technique*, 75(2):133–137, 2012.

[107] Kug-Sun Hong Hyuk-Joon Youn Hyun-Seung Ryu Sung-Soo Chung Chang, Bong-Soon and Kun-Woo Park. Osteoconduction at porous hydroxyapatite with various pore configurations. *Biomaterials*, 2000.

[108] Landon S Pryor, Earl Gage, Claude-Jean Langevin, Fernando Herrera, Andrew D Breithaupt, Chad R Gordon, Ahmed M Afifi, James E Zins, Hal Meltzer, Amanda Gosman, et al. Review of bone substitutes. *Craniomaxillofacial trauma & reconstruction*, 2(3):151, 2009.

[109] Larry Leroy Hench, R J_ Splinter, WC Allen, and TK Greenlee. Bonding mechanisms at the interface of ceramic prosthetic materials. *Journal of biomedical materials research*, 5(6):117–141, 1971.

[110] Larry L Hench. Bioceramics: from concept to clinic. *Journal of the american ceramic society*, 74(7):1487–1510, 1991.

[111] Vidya Krishnan and T Lakshmi. Bioglass: A novel biocompatible innovation. *Journal of advanced pharmaceutical technology & research*, 4(2):78, 2013.

[112] Julian R Jones. Review of bioactive glass: From hench to hybrids. *Acta biomaterialia*, 23:S53–S82, 2015.

[113] Pilar Sepulveda and Larry L Hench. Bioactive hierarchical structures for genetic control of bone morphogenesis. *Materials Research*, 5(3):243–246, 2002.

[114] Kevin R Rust, George T Singleton, June Wilson, and Patrick J Antonelli. Bioglass middle ear prosthesis: long-term results. *The American journal of otology*, 17(3):371–374, 1996.

[115] Stuart B Goodman, Zhenyu Yao, Michael Keeney, and Fan Yang. The future of biologic coatings for orthopaedic implants. *Biomaterials*, 34(13):3174–3183, 2013.

[116] Kelly Alvarez and Hideo Nakajima. Metallic scaffolds for bone regeneration. *Materials*, 2(3):790–832, 2009.

[117] Felicia Suska, Lena Emanuelsson, Anna Johansson, Pentti Tengvall, and Peter Thomsen. Fibrous capsule formation around titanium and copper. *Journal of Biomedical Materials Research Part A: An Official Journal of The Society for Biomaterials, The Japanese Society for Biomaterials, and The Australian Society for Biomaterials and the Korean Society for Biomaterials*, 85(4): 888–896, 2008.

[118] Allison A Campbell. Bioceramics for implant coatings. *Materials Today*, 6(11): 26–30, 2003.

[119] C.J. Rhodes-J. Moncol M.-Izakovic M. Mazur M., Valko. Free radicals, metals and antioxidants in oxidative stress-induced cancer. *Chemico-Biological Interactions.*, 160(1):1–40, 2006.

[120] Moreira L.M.-Santos V.J. Ramos-A.S. Lyon J.P.-Soares C.P. Gomes, C.C. and F.V. Santos. Assessment of the genetic risks of a metallic alloy used in medical implants. *Genetics and molecular biology*, 34(1):116–121, 2011.

[121] Osbjorn M. Pearson and Daniel E. Lieberman. The aging of wolff's "law": ontogeny and responses to mechanical loading in cortical bone. *American journal of physical anthropology.*, 125(39):63–99, 2004.

[122] Dankai Wu-Min Luo Piao, Chengdong and Hongshun Ma. Stress shielding effects of two prosthetic groups after total hip joint simulation replacement. *Journal of Orthopaedic Surgery and Research*, 9(71), 2014.

[123] Solehuddin Shuib A. Y. Hassan A. A. Shokri Ridzwan, M. I. Z. and MN Mohamad Ibrahim. Problem of stress shielding and improvement to the hip implant designs: A review. *Journal of Medical Sciences*, 7:460–467, 2007.

[124] Susmita Bose and eds. Amit Bandyopadhyay. *Materials and Devices for Bone Disorders*. Academic Press, 2016.

[125] Edward KS Chan Sunil Gupta Arora, Manit and Ashish D. Diwan. Polymethylmethacrylate bone cements and additives: A review of the literature. *World Journal of Orthopaedics.*, 4(2):67–74, 2013.

[126] John. Charnley. Anchorage of the femoral head prosthesis to the shaft of the femur. *The Journal of bone and joint surgery*, 42B:28–30, 1960.

[127] Faramarzi R. Jungwirth F. Kleffner B.V. Mumme T. Weber M. Marx, R. and D.C. Wirtz. Silicate coating of cemented titanium-based shafts in hip prosthetics reduces high aseptic loosening. *Zeitschrift fur Orthopadie und Unfallchirurgie*, 147(2):175–182, 2009.

[128] Mrinal K. Musib. A review of the history and role of uhmwpe as a component in total joint replacements. *International Journal of Biological Engineering*, 1 (1):6–10, 2011.

[129] Alessandro Bistolfi Pierangiola Bracco Del Prever, Elena Maria Brach and Luigi Costa. Uhmwpe for arthroplasty: past or future? *Journal of Orthopaedics and Traumatology.*, 10(1):1–8, 2009.

[130] William H. "Wear Harris and periprosthetic osteolysis: the problem. Wear and periprosthetic osteolysis: the problem. *Clinical Orthopaedics and Related Research.*, 393:66–70, 2001.

[131] Raptor Biomedicine. *Raptor Biomedicine*, volume 1. University of Minnesota Press, 1 edition, 1993.

[132] Elvidio de Paula Silva and Orlando Ayrton de Toledo. Tissue repair after orbital reconstruction using polypropylene mesh implants: A histological study in dogs. *Revista Odonto Ciencia Journal of Denal Science*, 24(4), 2009.

[133] M. Wang, C.Y. Yue, and B. Chua. Production and evaluation of hydroxyapatite reinforced polysulfone for tissue replacement. *J Mater Sci Mater Med.*, 12(9):821–826, 2001.

[134] A. James Jose and M. Alagar. Development of bioactive polysulfone nanocomposites for bone tissue replacement. *ICCM-18 International Conferences on Composite Materials*, 2011.

[135] Malte Winnacker. Polyamides and their functionalization: recent concepts for their applications as biomaterials. *Biomaterials science*, 5(7):1230–1235, 2017.

[136] Laurence W McKeen. *The effect of creep and other time related factors on plastics and elastomers*. Elsevier, 2009.

[137] Manfred F Maitz. Applications of synthetic polymers in clinical medicine. *Biosurface and Biotribology*, 1(3):161–176, 2015.

[138] Matthew D. Shoulders and Ronald T. Raines. Collagen structure and stability. *Annual review of biochemistry.*, 78:929–958, 2009.

[139] Norio Amizuka Masayoshi Nakadate Hideo Ohnishi Noritaka Fujii Kimimitsu Oda Shuichi Nomura Taguchi, Yuya and Takeyasu Maeda. A histological evaluation for guided bone regeneration induced by a collagenous membrane. *Biomaterials*, 26(31):6158–6166, 2005.

[140] Pinholt E. M. Madsen J. E Zhao, S and K. Donath. Histological evaluation of different biodegradable and non-biodegradable membranes implanted subcutaneously in rats. *Journal of Cranio-Maxillofacial Surgery*, 28(2): 116–122, 2000.

[141] Xiaoxue Xu Sabir, Muhammad Iqbal and Li Li.. A review on biodegradable polymeric materials for bone tissue engineering applications. *Journal of Materials Science*, 44(21):5713–5724, 2009.

[142] Piergiorgio Gentile Valeria Chiono Ferreira, Ana Marina and Gianluca Ciardelli. Collagen for bone tissue regeneration. *Acta biomaterialia.*, 8(9):3191–3200, 2012.

[143] S. A. Mengi Meena, C. and S. G. Deshpande.. Biomedical and industrial applications of collagen. *Proceedings of the Indian Academy of Sciences - Chemical Sciences*, 111(2):319–329, 1999.

[144] Auger F.A. Grandbois E. Guignard R. Giasson M. Boisjoly H. Germain, L. and S.L Guérin. Reconstructed human cornea produced in vitro by tissue engineering. *Pathobiology*, 67(3):140–147, 1999.

[145] Luc Avérous and Eric Pollet. Biodegradable polymers. *Environmental Silicate Nano Biocomposites*, page 450, 2012.

[146] N. Sharif Razak, Saifullzwan Abd and W. A. W. A. Rahman. Biodegradable polymers and their bone applications: A review. *International Journal of Basic and Applied Sciences*, 12(1):31, 2012.

[147] Mike Jenkins. *Biomedical Polymers*. Woodhead Publishing Limited, 2007.

[148] N. Bitinis E. Fortunati S. Mattioli N. Rescignano R. Verdejo M. A. Lopez-Manchado Armentano, I. and J. M. Kenny. Multifunctional nanostructured pla materials for packaging and tissue engineering. *Progress in Polymer Science*, 28(1):1720–1747, 2013.

[149] Lakshmi S. Nair and Cato T. Laurencin. Biodegradeable polymers as biomaterials,. *Progress in Polymer Science*, 39(8):762–798, 2007.

[150] Ricardo Bernhardt Dieter Scharnweber Wolfgang Schneiders Stefan Rammelt Rentsch, Barbe and Claudia Rentsch. Embroidered and surface coated polycaprolactone-co-lactide scaffolds: a potential graft for bone tissue engineering. *Biomatterials.*, 2(3):158–165, 2012.

[151] Annalia Asti and Luciana Gioglio. Natural and synthetic biodegradable polymers: different scaffolds for cell expansion and tissue formation. *The International journal of artificial organs*, 37(3):187–205, 2014.

[152] Tanahashi K. Fisher J.P. KKasper, F.K. and A.G. Mikos. Synthesis of poly (propylene fumarate). *Nature protocols.*, 4(4):518–525, 2009.

[153] Lichun Lu Wang, Shanfeng and Michael J. Yaszemski. Bone-tissue-engineering material poly(propylene fumarate): correlation between molecular weight, chain dimensions, and physical properties. *Biomacromolecules*, 7(6):1976–1982, 2006.

[154] Joseph D. Gresser Donald L. Wise Lewandrowski, Kai-Uwe and Debra J. Trantolo. Bioresorbable bone graft substitutes of different osteoconductivities: a histologic evaluation of osteointegration of poly(propylene glycol-co-fumaric acid)-based cement implants in rats. *Biomaterials.*, 21(8):757–764, 2000.

[155] Venkatram R. Shastri Anseth, Kristi S. and Robert Langer. Photopolymerizable degradable polyanhydrides with osteocompatibility. *Nature Biotechnology.*, 17(2):156–159, 1999.

[156] Amy K. Burkoth Muggli, Dina Svaldi and Kristi S. Anseth. Crosslinked polyanhydrides for use in orthopedic applications: degradation behavior and mechanics. *Journal of Biomedical Materials Research: An Official Journal of The Society for Biomaterials, The Japanese Society for Biomaterials, and The Australian Society for Biomaterials.*, 46(2):271–278, 1999.

[157] Rashmi Ghai Reddy, C. S. K. and V.C. Kalia. Polyhydroxyalkanoates: an overview. *Bioresource Technology*, 87(2):137–146, 2003.

[158] Guo-Qiang Chen and Qiong Wu. The application of polyhydroxyalkanoates as tissue engineering materials. *Biomaterials*, 26(33):6565–6578, 2005.

[159] Iftikhar Ali and Nazia Jamil. Polyhydroxyalkanoates: Current applications in the medical field. *Frontiers in Biology*, 11(1):19–27, 2016.

[160] Superb K. Misra Aldo R. Boccaccini Valappil, Sabeel P. and Ipsita Roy. Biomedical applications of polyhydroxyalkanoates: an overview of animal testing and in vivo responses. *Expert Rev Med Devices.*, 3(6):853–868, 2016.

[161] M. V. Kayser W. Bonfield Dalby, M. J. and L. Di Silvio. Initial attachment of osteoblasts on an optimised hapex topography. *Biomaterials*, 23:681–690, 2002.

[162] Saunders L.S. Ward I.M G. W. Davies M. WangK. E. Tanner W. Bonfield Bonner, M. Anisotropic mechanical properties of orientated hapex. *Journal of Materials Science*, 37(2):325–334, 2002.

[163] Hervé Guezenoc Peter Davies Baral, Nicolas and Christophe Baley. High modulus carbon fibre composites: Correlation between transverse tensile and mode i interlaminar fracture properties. *Materials Letters*, 62(6–7):1096–1099, 2008.

[164] Blanchfield J.P. Bloom L.D. Coburn B.H. Elkington M. Fuller J.D. Gilbert M.E. Muflahi-S.A. Pernice M.F. Rae S.I. Scholz, M.S. and J.A. Trevarthen. The use of composite materials in modern orthopaedic medicine and prosthetic devices: A review. *Composites Science and Technology*, 71(16):1791–1803, 2011.

[165] Zdero R. Dubov A. Shah S. Khurshid S. Bougherara, H. and E.H. Schemitsch. A preliminary biomechanical study of a novel carbon-fibre hip implant versus standard metallic hip implants. *Medical engineering and physics.*, 33(1): 121–128, 2011.

[166] K. M. Herbert Attawia, M. A. and C. T. Laurencin. Osteoblast-like cell adherance and migration through three-dimensional porous polymer matrices. *Biochemical and Biophysical Research Communications*, 213(2):639–644, 1995.

[167] Lucy. Di Silvio. *Cellular response to biomaterials*. Woodhead Publishing Limited,, 2009.

[168] B. Pukanszky and Voros G. Mechanism of interfacial interactions in particulate filled composites. *Composite Interfaces*, 1:411–427, 1993.

[169] Xi-Qiao Feng Bernd Lauke Fu, Shao-Yun and Yiu-Wing Mai. Effects of particle size, particle/matrix interface adhesion and particle loading on mechanical properties of particulate– polymer composites. *Composites Part B: Engineering,*, 39(6):933–961, 2008.

[170] Landon Onyebueke Hu, Hurang and Ayo Abatan. Characterizing and modeling mechanical properties of nanocomposites-review and evaluation. *Journal of Minerals and Materials Characterization and Engineering*, 9(4):275–319, 2010.

[171] Javad Rafiee Zhou Wang Huaihe Song Zhong-Zhen Yu Rafiee, Mohammad A. and Nikhil Koratkar. Enhanced mechanical properties of nanocomposites at low graphene content. *ACS Nano.*, 3(12):3884–2890, 2009.

[172] Valeria Pettarin J. Viana António Pontes A. Pouzada Costantino, Alejandra and P. Frontini. Microstructure of pp/clay nanocomposites produced by shear induced injection moulding. *Procedia Materials Science*, 1:34–43, 2012.

[173] Xiuqian Lv Zhijie Sun Lu, Xili and Yufeng Zheng. Nanocomposites of poly(l-lactide) and surface grafted tio2 nanoparticles : synthesis and characterisation. *European Polymer Journal*, 44:2476–2481, 2008.

[174] Xiaodong Wang Yongzhi Song Wu, Dezhen and Riguang Jin. Nanocomposites of poly(vinyl chloride) and nanometric calcium carbonate particles: Effects of chlorinated polyethylene on mechanical properties, morphology, and rheology. *Journal of Applied Polymer Science*, 92(4):2714—2723, 2004.

[175] Nadir Kchit Catherine Billotte François Trochu Bensadoun, Farida and Edu Ruiz. A comparative study of dispersion techniques for nanocomposite made with nanoclays and an unsaturated polyester resin. *Journal of Nanomaterials*, 2011:12, 2011.

[176] F. Hild P. W. Dunne K. Walton-D. M. Grant Derek J. Irvine Gimeno-Fabra, M. and E. H. Lester. Continuous synthesis of dispersant-coated hydroxyapatite plates. *CrystEngComm*, 17:6175–6182, 2015.

[177] Chandana Mohanty Anju Harilal Uma K. Maheswari Sanjeeb Kumar Sahoo Mitra, Moutushy and Subramanian Krishnakumar. A novel in vitro three-dimensional retinoblastoma model for evaluating chemotherapeutic drugs. *Molecular Vision*, 18:1361–1378, 2012.

[178] Mohamed A. Attawia Hoda E. Elgendy Laurencin, Cato T. and Kelly M. Herbert. Tissue engineered bone-regeneration using degradable polymers: the formation of mineralized matrices. *Bone*, 19(1):93–99, 1996.

[179] Mohamed A. Attawia Devin, Jessica E. and Cato T. Laurencin. Three-dimensional degradable porous polymer-ceramic matrices for use in bone repair. *J Biomater Sci Polym Ed*, 7(8):661–669, 1996.

[180] Preparation, characterization and in vivo evaluation of 120-day poly(d,l-lactide) leuprolide microspheres.

[181] V. Sardinha JL Escobar Ivirico J. F. Mano Cruz, DM García and JL Gómez Ribelles. Gelatin microparticles aggregates as three-dimensional scaffolding system in cartilage engineering. *J Mater Sci Mater Med*, 24(2):503–513, 2013.

[182] S. F. El-Amin Mohamed Attawia Borden, Mark and Cato T. Laurencin. Structural and human cellular assessment of a novel microsphere-based tissue engineered scaffold for bone repair. *Biomaterials*, 24(4):597–609, 2003.

[183] Yoon Sung Nam and Tae Gwan Park. Biodegradable polymeric microcellular foams by modified thermally induced phase separation method. *Biomaterials*, 20(19):1783–1790, 1999.

[184] Jianqing Feng Jianxin Wang Xingdong Zhang Yubao Li Huang, Mei and Yonggang Yan. Synthesis and characterization of nano-ha/pa66 composites. *J. Sci. Mater. Med.*, 14:655, 2003.

[185] Yubao Li Wei, Jie and Kin-Tak Lau. Preperation and characterisation of a nanoapatite/polyamide 6 bioactive composite. *composites Part B*, 38:301, 2007.

[186] T. Wohlers, T. Caffrey, and R.I. Campbell. Wohlers report 2016. *Wohlers Associates, Inc.*, 2016.

[187] Spencer O. Onuh and Yahaya Y. Yusuf. Rapid prototyping technology: applications and benefits for rapid product development. *Journal of Intelligent Manufacturing*, 10(3):301–311, 1999.

[188] T. Wohlers, T. Caffrey, and R.I. Campbell. Wohlers report 2012. *Wohlers Associates, Inc.*, 2016.

[189] Sharon LN. Ford. Additive manufacturing technology: Potential implications for u.s. manufacturing competitiveness. *United States International Trade Commision Journal of International Commerce and Economics*, 2014.

[190] Simon Ford and Mélanie Dspeisse. Additive manufacturing and sustainability: an exploratory study of the advantages and challenges. *Journal of Cleaner Production*, 137(20):1573–1587, 2016.

[191] Royal Academy of Engineering. Additive manufacturing: opportunities and constraints. *A summary of a roundtable forum hosted by the Royal Academy of Engineering*, 2013.

[192] G. Tromans and D. Wimpenny. Rapid manufacturing. proc. 4th european conference on rapid prototyping and manufacturing. pages 27–41, 1995.

[193] Mark C. Van Langeveld Schubert, Carl and Larry A. Donoso. Innovations in 3D printing: a 3D overview from optics to organs. *British Journal of Ophthalmology*, 98(2):159–161, 2014.

[194] Matthew B. . Hoy. 3D printing: making things at the library. *Med Ref Serv Q.*, 32(1):94–99, 2013.

[195] Yi Lu Klein, Geraldine T. and Michael Y. Wang. 3d printing and neurosurgery–ready for prime time? *World Neurosurg.*, 80(3–4):233–235, 2013.

[196] ASTM International. Standard terminology for additive manufacturing technologies. 12a, 2012.

[197] *Cost Efficient Planning for Additive Manufacturing Technologies*, 2016. Verlag nicht ermittelbar.

[198] Make A Difference, official website. `http://catalogue.a-difference-in-making.com/skull-implant/`. Accessed:12-05-17.

[199] Sara M. Gaytan Edwin Martinez Frank Medina Murr, Lawrence E. and Ryan B. Wicker. Next generation orthopaedic implants by additive manufacturing using electron beam melting. *Int J Biomater.*, 2012:14, 2012.

[200] Iwan Zein, Dietmar W Hutmacher, Kim Cheng Tan, and Swee Hin Teoh. Fused deposition modeling of novel scaffold architectures for tissue engineering applications. *Biomaterials*, 23(4):1169–1185, 2002.

[201] Bina Rai, Jane L Lin, Zophia XH Lim, Robert E Guldberg, Dietmar W Hutmacher, and Simon M Cool. Differences between in vitro viability and

differentiation and in vivo bone-forming efficacy of human mesenchymal stem cells cultured on pcl–tcp scaffolds. *Biomaterials*, 31(31):7960–7970, 2010.

[202] Arash Khojasteh, Hossein Behnia, Fatemeh Sadat Hosseini, Mohammad Mehdi Dehghan, Pegah Abbasnia, and Fatemeh Mashhadi Abbas. The effect of pcl-tcp scaffold loaded with mesenchymal stem cells on vertical bone augmentation in dog mandible: A preliminary report. *Journal of Biomedical Materials Research Part B: Applied Biomaterials*, 101(5):848–854, 2013.

[203] Fang Xu, Chunze Yan, Yat-Tarng Shyng, Hong Chang, Yongde Xia, and Yanqiu Zhu. Ultra-toughened nylon 12 nanocomposites reinforced with if-ws2. *Nanotechnology*, 25(32):325701, 2014.

[204] Jayda L. Erkal Sarah Y. Lockwood Chengpeng Chen Gross, Bethany C. and Dana M. Spence. Evaluation of 3d printing and its potential impact on biotechnology and the chemical sciences. *Analytical Chemistry*, 86(7): 3240–3253, 2014.

[205] Anh-Vu Do, Behnoush Khorsand, Sean M Geary, and Aliasger K Salem. 3d printing of scaffolds for tissue regeneration applications. *Advanced healthcare materials*, 4(12):1742–1762, 2015.

[206] Malcolm N Cooke, John P Fisher, David Dean, Clare Rimnac, and Antonios G Mikos. Use of stereolithography to manufacture critical-sized 3d biodegradable scaffolds for bone ingrowth. *Journal of Biomedical Materials Research Part B: Applied Biomaterials*, 64(2):65–69, 2003.

[207] Claudia Dworak. Biocompatible phosphorus containing photopolymers. In *Biomedical Engineering-Frontiers and Challenges*. InTech, 2011.

[208] Kytai Truong Nguyen and Jennifer L West. Photopolymerizable hydrogels for tissue engineering applications. *Biomaterials*, 23(22):4307–4314, 2002.

[209] S. CK Chua N. Sudarmadji Leong, K. F. and W. Y. Yeong. Engineering functionally graded tissue engineering scaffolds. *J Mech Behav Biomed Mater.*, 1(2):140–152, 2008.

[210] Xigeng Miao and Dan Sun. . Graded/gradient porous biomaterials. *Materials*, 3(1):26–47, 2010.

[211] Guoyuan Li, Lei Wang, Wei Pan, Fei Yang, Wenbo Jiang, Xianbo Wu, Xiangdong Kong, Kerong Dai, and Yongqiang Hao. In vitro and in vivo study of additive manufactured porousTi6Al4V scaffolds for repairing bone defects. *Scientific reports*, 6:34072, 2016.

[212] S Hallmann, P Glockner, C Daniel, V Seyda, and C Emmelmann. Manufacturing of medical implants by combination of selective laser melting and laser ablation. *Lasers in Manufacturing and Materials Processing*, 2(3): 124–134, 2015.

[213] Fraunhofer-Gesellschaft. Manufacturing of individual titanium implants using selective laser melting slm. Technical Document.

[214] Anatoliy Popovich, Vadim Sufiiarov, Igor Polozov, Evgenii Borisov, and Dmitriy Masaylo. Producing hip implants of titanium alloys by additive manufacturing. *International Journal of Bioprinting*, 2(2), 2016.

[215] Daniel VC Stoffelen, Koen Eraly, and Philippe Debeer. The use of 3d printing technology in reconstruction of a severe glenoid defect: a case report with 2.5 years of follow-up. *Journal of shoulder and elbow surgery*, 24(8):e218–e222, 2015.

[216] Huiwu Li, Liao Wang, Yuanqing Mao, You Wang, Kerong Dai, and Zhenan Zhu. Revision of complex acetabular defects using cages with the aid of rapid prototyping. *The Journal of arthroplasty*, 28(10):1770–1775, 2013.

[217] Yin Qingfeng, Liu Wenguang, and Wang Shaojin. Application of customized augments fabricated by rapid prototyping for severe bone defects of the knee, 2014.

[218] Domenick J Sisto and Vineet K Sarin. Custom patellofemoral arthroplasty of the knee. *J Bone Joint Surg Am*, (2 suppl 2):214–225, 2007.

[219] Shalin Shaunak. Innovations in trauma and orthopaedic surgery: 3d printing. 2016.

[220] Sculpteo, official website. Accessed:12-05-17.

[221] A. Stwora and G. Skrabalak. Influence of selected parameters of selective laser sintering process on properties of sintered materials. *Journal of Achievments in Materials and Manufacture Engineering*, 61(2), 2013.

[222] James Christian Nelson. *Selective laser sintering: a definition of the process and an empirical sintering model*. PhD thesis, University of Texas at Austin, 1993.

[223] John Williams, David Miller, and Carl Deckard. Selective laser sintering part strength as function of andrew number, scan rate and spot size. In *Proceedings of Solid Freeform Fabrication Symposium 1996*, pages 549–557, 1996.

[224] Ming C Leu, Shashwatashish Pattnaik, and Gregory E Hilmas. Optimization of selective laser sintering process for fabrication of zirconium diboride parts. In *Proceeding of International Solid Freeform Fabrication Symposium, Austin, TX*, 2010.

[225] R. A. Paggi G. V. Salmoria Beal, V. E. and A. Lago. Statistical evaluation of laser energy density effect on mechanical properties of polyamide parts manufactured by selective laser sintering. *Journal of applied polymer science*, 113(5):2910–2919, 2009.

[226] Luke N Carter, Xiqian Wang, Noriko Read, Raja Khan, M Aristizabal, Khamis Essa, and Moataz M Attallah. Process optimisation of selective laser melting using energy density model for nickel based superalloys. *Materials Science and Technology*, 32(7):657–661, 2016.

[227] Jean-Pierre Kruth, X Wang, Tahar Laoui, and Ludo Froyen. Lasers and materials in selective laser sintering. *Assembly Automation*, 23(4):357–371, 2003.

[228] KG Prashanth, S Scudino, T Maity, J Das, and J Eckert. Is the energy density a reliable parameter for materials synthesis by selective laser melting? *Materials Research Letters*, pages 1–5, 2017.

[229] G. Levy R. Schindel Tom Craeghs Kruth, Jean-Pierre and Evren Yasa. Consolidation of polymer powders by selective laser sintering. *Inspire*, 2008.

[230] Ian Gibson and Dongping Shi. Material properties and fabrication parameters in selective laser sintering process. *Rapid Prototyping Journal*, 3(4):129–136, 1997.

[231] Pavan Suri German, Randall M. and Seong Jin Park. Review: liquid phase sintering. *Journal of Materials Science*, 44(1):1–39, 2009.

[232] Peter Mercelis J. Van Vaerenbergh Ludo Froyen Kruth, Jean-Pierre and Marleen Rombouts. Binding mechanisms in selective laser sintering and selective laser melting. *Rapid Prototyping Journal*, 11(1):26–36, 1995.

[233] Randall M German. *Powder Metallurgy Science*. Metal Powder Industries Federation, New Jersey, 2 edition, 1994.

[234] Nico Kamperman Bart van de Vorst Moeskops, Eef and R. Knopppers. Creep behaviour of polyamide in selective laser sinterin. *roceedings of the Solid Freeform Fabrication Symposium on Creep Behaviour of Polyamide in Selective Laser Sintering, University of Texas in Austin, Texas, USA*, 2004.

[235] Neil Hopkinson N. F. Kamperman Zarringhalam, Hadi and J. J. De Vlieger. Effects of processing on microstructure and properties of sls nylon 12. *Materials Science and Engineering: A*, 435–436(5):172–180, 2006.

[236] M. K. Bisaria Bellehumeur, C. T. and J. Vlachopoulos. An experimental study and model assessment of polymer sintering. *Polymer Engineering and Science*, 36(17):2198–2207, 1996.

[237] O. Pokulda, C.T. Bellehumeur, and J. Vlachopoulos. Modification of frenkel's model for sintering. *AIChE Journal*, 43(12):3253–3256, 1997.

[238] Jean-Pierre Kruth. nternational institution for production engineering research (general assembly). *Consolidation phenomena in laser and powder-bed based layered manufacturing, Paris*, 2007.

[239] Z. Li H. Sun S. Huang Shi, Y. and F. Zeng. Effect of the properties of the polymer materials on the quality of selective laser sintering parts. *Proceedings of the Institution of Mechanical Engineers, Part L: Journal of Materials: Design and Applications*, 218(3), 2004.

[240] Y. Shi Yan, C. and L. Hao. Investigation into the differences in the selective laser sintering between amorphous and semi-crystalline polymers. *International Polymer Processing*, 26(4):416–423, 2011.

[241] American Society for Testing and Materials. Standard test method for melt flow rates of thermoplastics by extrusion plastometer1. *ASTM International*, page 16, 2013.

[242] Electro optical systems (eos). eos official website, . Accessed:12-05-17.

[243] 3d systems. 3d systems official website. Accessed:12-05-17.

[244] Advanced laser materials (alm). alm official website. Accessed:12-05-17.

[245] L. Hao M. M. Savalani Russell A. Harris L. Di Silvio Zhang, Y. and K. E. Tanner. In vitro biocompatibility of hydroxyapatite-reinforced polymeric composites manufactured by selective laser sintering. *Journal of biomedical research part A*, 91A(4), 2008.

[246] K. F. Leong K. H. Tan F. E. Wiria Chua, C. K. and C. M. Cheah. Development of tissue scaffolds using selective laser sintering of polyvinyl alcohol/hydroxyapatite biocomposite for craniofacial and joint defects. *J Mater Sci Mater Med*, 15(10):1113–1121, 2004.

[247] M. M. Savalani Y. Zhang K. E. Tanner Hao, Liang and R. A. Harris. Selective laser sintering of hydroxyapatite reinforced polyethylene composites for bioactive implants and tissue scaffold development. *Proc Inst Mech Eng H.*, 220(4):521–531, 2006.

[248] Ci-jun Shuai, Zhong-zheng Mao, Zi-kai Han, and Shu-ping Peng. Preparation of complex porous scaffolds via selective laser sintering of poly (vinyl alcohol)/calcium silicate. *Journal of Bioactive and Compatible Polymers*, 29 (2):110–120, 2014.

[249] Eleftherios Vairaktaris Dirk Pohle Thomas Rechtenwald Rainer Lutz Helmut M′unstedt Garrit Koller et al. von Wilmowsky, Cornelius. Effects of bioactive glass and beta-tcp containing three-dimensional laser sintered polyetherketone composites on osteoblasts in vitro. *Journal of Biomedical Materials Research Part A*, 87A(4), 2008.

[250] Dermot Brabazon Stefan Lohfeld Eosoly, Szilvia and Lisa Looney. Selective laser sintering of hydroxyapatite/poly-epsilon-carprolactone. *Acta Biomaterialia*, 6(7):2511–2517, 2009.

[251] Senan Cahill Valerie Barron Peter McHugh Lutz D′urselen Ludwika Kreja Christine Bausewein Lohfeld, Stefan and Anita Ignatius. Fabrication, mechanical and in vivo performance of polycaprolactone/tricalcium phosphate composite scaffolds. *Acta Biomater*, 8(9):3446–3456, 2012.

[252] Panyu Zhou Xiaosong Cheng Yang Xie Chong Liang Chao Li Xia, Yan and Shuogui Xu. Selective laser sintering fabrication of nano-hydroxyapatite/poly-epsilon-caprolactone scaffolds for bone tissue engineering applications. *Int J Nanomedicine*, 8(4):4197–4213, 2013.

[253] Fu Rong Liu Zhang, Qiang and Ji Min Chen. Development of porous scaffolds using selective laser sintering of polylactic acid/ hydroxyapatite for bone tissue engineering. *Advanced Materials Research*, 291–294:1399–1404, 2011.

[254] Sayed-Hadi Mirmalek-Sani Neil A. Hanley Alexander L. Ivanov John JA Barry Clare Upton Kevin M. Shakesheff et al. Kanczler, Janos M. Biocompatibility and osteogenic potential of human fetal femur-derived cells on surface selective laser sintered scaffolds. *Acta Biomaterialia*, 5(6):2063–2071, 2009.

[255] P.J.D.S. Bartolo et al. Proc. 6th international conference on advanced research in virtual and rapid prototyping. *Leiria, Portugal*, 2013.

[256] K. W. Dalgarno Goodridge, R. D. and D. J. Wood. Indirect selective laser sintering of an apatitemullite glassceramic for potential use in bone replacement applications. *Proceedings of the Institution of Mechanical Engineers, Part H: Journal of Engineering in Medicine 1*, 220:57–68, 2006.

[257] M. Wang W. Y. Zhou Duan, B. and W. L. Cheung. Synthesis of ca–p nanoparticles and fabrication of ca–p/phbv nanocomposite microspheres for bone tissue engineering applications. *Applied Surface Science*, 255(2):529–533, 2008.

[258] Valeria Chiono Caterina Cristallini Niccoletta Barbani Arti Ahluwalia Giovanni Vozzi Antonino Previti Giovanni Tantussi Ciardelli, Gianluca and Paolo Giusti. Innovative tissue engineering structures through advanced manufacturing technologies. *Journal of Materials Science: Materials in Medicine*, 15(4): 305–310, 2004.

[259] Md Saidin Wahab. *Selective laser sintering of polymer nanocomposites*. PhD thesis, The University of Leeds, 2008.

[260] Ruth D. Goodridge Richard JM Hague Bai, Jiaming and Mo Song. Improving the mechanical properties of laser sintered polyamide 12 through incorporation of carbon nanotubes. *Polymer Engineering and Science*, 53(9):1937–1946, 2013.

[261] Eric L Crump. Economic impact analysis for the proposed carbon black manufacturing neshap. *US Environmental Protection Agency. Office of Air Quality Planning and Standards. Innovative Strategies and Economics Group. Durham: US Environmental Protection Agency (EPA)*, 2000.

[262] Ann Don Porto Carero, PHM Hoet, L Verschaeve, G Schoeters, and Benoit Nemery. Genotoxic effects of carbon black particles, diesel exhaust particles, and urban air particulates and their extracts on a human alveolar epithelial cell line (a549) and a human monocytic cell line (thp-1). *Environmental and molecular mutagenesis*, 37(2):155–163, 2001.

[263] Jong Gwan Lee, Won Jun Noh, Hwa Kim, and Moo-Yeol Lee. Generation of reactive oxygen species contributes to the development of carbon black cytotoxicity to vascular cells. *Toxicological research*, 27(3):161, 2011.

[264] V Stone, J Shaw, DM Brown, W MacNee, SP Faux, and K Donaldson. The role of oxidative stress in the prolonged inhibitory effect of ultrafine carbon black on epithelial cell function. *Toxicology in vitro*, 12(6):649–659, 1998.

[265] Annike I Totlandsdal, Magne Refsnes, and Marit Låg. Mechanisms involved in ultrafine carbon black-induced release of il-6 from primary rat epithelial lung cells. *Toxicology in Vitro*, 24(1):10–20, 2010.

[266] Peter A Valberg, Christopher M Long, and Sonja N Sax. Integrating studies on carcinogenic risk of carbon black: epidemiology, animal exposures, and mechanism of action. *Journal of occupational and environmental medicine*, 48 (12):1291–1307, 2006.

[267] Boris Z Simkhovich, Michael T Kleinman, and Robert A Kloner. Air pollution and cardiovascular injury: epidemiology, toxicology, and mechanisms. *Journal of the American College of Cardiology*, 52(9):719–726, 2008.

[268] Robert D Brook, Sanjay Rajagopalan, C Arden Pope, Jeffrey R Brook, Aruni Bhatnagar, Ana V Diez-Roux, Fernando Holguin, Yuling Hong, Russell V Luepker, Murray A Mittleman, et al. Particulate matter air pollution and cardiovascular disease: an update to the scientific statement from the american heart association. *Circulation*, 121(21):2331–2378, 2010.

[269] Qinghua Sun, Xinru Hong, and Loren E Wold. Cardiovascular effects of ambient particulate air pollution exposure. *Circulation*, 121(25):2755–2765, 2010.

[270] European Parliament. Regulation (EU) 2017/745 of the European Parliament and of the Council of 5 April 2017 on medical devices, amending Directive 2001/83/EC, Regulation (EC) no 178/2002 and Regulation (EC) no 1223/2009 and repealing Council Directives 90/385/EEC and 93/42/EEC

(Text with EEA relevance.). https: //eur-lex.europa.eu/legal-content/EN/TXT/?uri=CELEX:32017R0745. Accessed: 11-05-2018.

[271] International Standards Organisation. BS EN ISO 10993 -1:2009, Biological evaluation of medical devices – Part 1: Evaluation and testing within a risk management process. https://www.iso.org/standard/44908.html, . Accessed: 05-03-2018.

[272] Ahmad Aqel, Kholoud MM Abou El-Nour, Reda AA Ammar, and Abdulrahman Al-Warthan. Carbon nanotubes, science and technology part (i) structure, synthesis and characterisation. *Arabian Journal of Chemistry*, 5(1):1–23, 2012.

[273] Michael J O'connell. *Carbon nanotubes: properties and applications*. CRC press, 2006.

[274] Prabhakar R Bandaru. Electrical properties and applications of carbon nanotube structures. *Journal of nanoscience and nanotechnology*, 7(4-5): 1239–1267, 2007.

[275] Valentin N Popov. Carbon nanotubes: properties and application. *Materials Science and Engineering: R: Reports*, 43(3):61–102, 2004.

[276] Yit Thai Ong, Abdul Latif Ahmad, Sharif Hussein Sharif Zein, and Soon Huat Tan. A review on carbon nanotubes in an environmental protection and green engineering perspective. *Brazilian Journal of Chemical Engineering*, 27(2): 227–242, 2010.

[277] Peter Newman, Andrew Minett, Rutledge Ellis-Behnke, and Hala Zreiqat. Carbon nanotubes: their potential and pitfalls for bone tissue regeneration and engineering. *Nanomedicine: Nanotechnology, Biology and Medicine*, 9(8): 1139–1158, 2013.

[278] Sung Young Park, Sun Young Park, Seon Namgung, Byeongju Kim, Jiwoon Im, Ji Youn Kim, Kyung Sun, Kyu Back Lee, J-M Nam, Yongdoo Park, et al.

Carbon nanotube monolayer patterns for directed growth of mesenchymal stem cells. *Advanced Materials*, 19(18):2530–2534, 2007.

[279] Seunghan Oh, Karla S Brammer, YS Julie Li, Dayu Teng, Adam J Engler, Shu Chien, and Sungho Jin. Stem cell fate dictated solely by altered nanotube dimension. *Proceedings of the National Academy of Sciences*, 106(7): 2130–2135, 2009.

[280] Rowena McBeath, Dana M Pirone, Celeste M Nelson, Kiran Bhadriraju, and Christopher S Chen. Cell shape, cytoskeletal tension, and rhoa regulate stem cell lineage commitment. *Developmental cell*, 6(4):483–495, 2004.

[281] *Freeman Technology FT4, User manual*.

[282] PerkinElmer. Pyris - Help guide - Kinetics Theory. In softwarel, .

[283] F Neil Cogswell. *Polymer melt rheology: a guide for industrial practice*. Elsevier, 1981.

[284] Tristan Petit and Ljiljana Puskar. Ftir spectroscopy of nanodiamonds: Methods and interpretation. *Diamond and Related Materials*, 2018.

[285] Alfred Conklin Jr, Michael J Goldcamp, and Jacob Barrett. Determination of ethanol in gasoline by ft-ir spectroscopy. *Journal of Chemical Education*, 91(6): 889–891, 2014.

[286] Honghui Cheng, Chen Lu, Jingjing Liu, Yongke Yan, Xingbo Han, Huiming Jin, Yu Wang, Yi Liu, and Changle Wu. Synchrotron radiation x-ray powder diffraction techniques applied in hydrogen storage materials-a review. *Progress in Natural Science: Materials International*, 27(1):66–73, 2017.

[287] American Society for Testing and Materials. Standard test method for tensile properties of plastics. *ASTM International*, page 16, 2013.

[288] Per Magnusson, Lasse Larsson, Martin Magnusson, Michael WJ Davie, and Christopher A Sharp. Isoforms of bone alkaline phosphatase: characterization and origin in human trabecular and cortical bone. *Journal of Bone and Mineral Research*, 14(11):1926–1933, 1999.

[289] MONNIPHA Sila-Asna, Ahnond Bunyaratvej, Sakan Maeda, Hiromichi Kitaguchi, and NARONG Bunyaratavej. Osteoblast differentiation and bone formation gene expression in strontium-inducing bone marrow mesenchymal stem cell. *Kobe J Med Sci*, 53(1-2):25–35, 2007.

[290] Amy Prosser. *Enhanced differentiation of mesenchymal stem cells for osteochondral constructs*. PhD thesis, University of Nottingham, 2015.

[291] Cynthia D'Avila Carvalho Erbetta, Ricardo José Alves, Jarbas Magalhães Resende, Roberto Fernando de Souza Freitas, and Ricardo Geraldo de Sousa. Synthesis and characterization of poly(d,l-lactide-co-glycolide) copolymer. *Journal of Biomaterials and Nanobiotechnology*, 3(2):208–225, Apr 2012. ISSN 2158-7027.

[292] Manfred Schmid Amado, Antonio and Konrad Wegener. Simulation of warpage induced by non-isothermal crystallization of co-polypropylene during the sls process. *AIP*, 1664(1), 2015.

[293] Laurence A Belfiore. Crystallization kinetics via spherulitic growth. *Physical Properties of Macromolecules*, pages 287–327, 2010.

[294] Jianglei Qin, Shiqi Zhang, and Zhiting Li. Melting behavior and isothermal crystallization kinetics of polypropylene/metallocene-catalyzed polyethylene elastomer blends. *Journal of applied polymer science*, 110(5):2615–2622, 2008.

[295] Zhi Cao Han, Jie and Wei Gao. Remarkable absorption properties of polyamide 12 microspheres for a broad-spectrum antibacterial (triclosan) in water. *Journal of Materials Chemistry A*, 1(16):4941–4944, 2002.

[296] Sangkeun Rhee and James L. White. Crystal structure and morphology of biaxially oriented polyamide 12. *Journal of Polymer Science Part B*, 40(12): 1189–1200, 2002.

[297] Yorio Itoh Matsubara, Ikuo and Masayasu Shinomiya. Lower-frequency infrared spectra (800-200 cm.1) and structures of polyamides. *Journal of Polymer Science Part B*, 4(1):47–53, 1966.

[298] Jie Han, Zhi Cao, and Wei Gao. Remarkable sorption properties of polyamide 12 microspheres for a broad-spectrum antibacterial (triclosan) in water. *Journal of Materials Chemistry A*, 1(16):4941–4944, 2013.

[299] Suresh Sagadevan, Arivuoli Dakshnamoorthy, et al. Synthesis and characterization of nano-hydroxyapatite (n-hap) using the wet chemical technique. *International Journal of physical sciences*, 8(32):1639–1645, 2013.

[300] A. Mele Liquori, A. M. and V. Carelli. Ultraviolet absorption spectra of polyamides. *Journal of Polymer Science Part A*, 10(5):510–512, 1953.

[301] Zhe Zhang, Huihui Chen, Chunyan Xing, Mingyi Guo, Fugang Xu, Xiaodan Wang, Hermann J Gruber, Bailin Zhang, and Jilin Tang. Sodium citrate: A universal reducing agent for reduction/decoration of graphene oxide with au nanoparticles. *Nano Research*, 4(6):599–611, 2011.

[302] C Rodríguez-González, HE Cid-Luna, P Salas, and VM Castaño. Hydroxyapatite-functionalized graphene: a new hybrid nanomaterial. *Journal of Nanomaterials*, 2014:113, 2014.

[303] Gérrard Eddy Jai Poinern Brundavanam, Ravi Krishna and Derek Fawcett. Modelling the crystal structure of a 30 nm sized particle based hydroxyapatite powder synthesised under the influence of ultrasound irradiation from x-ray powder diffraction data. *American Journal of Materials Science*, 3(4):84–90, 2013.

[304] Jingqing Li, Peitao Xiao, Hongfei Li, Yao Zhang, Feifei Xue, Baojing Luo, Shaoyong Huang, Yingrui Shang, Huiying Wen, Jesper de Claville Christiansen, et al. Crystalline structures and crystallization behaviors of poly (l-lactide) in poly (l-lactide)/graphene nanosheet composites. *Polymer Chemistry*, 6(21): 3988–4002, 2015.

[305] Andrew M Baker, Liang Wang, Suresh G Advani, and Ajay K Prasad. Nafion membranes reinforced with magnetically controlled fe 3 o 4–mwcnts for pemfcs. *Journal of Materials Chemistry*, 22(28):14008–14012, 2012.

[306] Paulo Jorge da Silva Bártolo, Ana Cristina Soares de Lemos, and António Mário Henriques et al., editors. *Proc. 6th International Conference on Advanced Research in Virtual and Rapid Prototyping, Leiria, Portugal,*, 2013. CRC Press 2013.

[307] Sasan Dadbakhsh Michael Van den Eynde Jean-Pierre Kruth Bart Goderis Verbelen, Leander and Peter Van Puyvelde. Characterization of polyamide powders for determination of laser sintering processability. *European Polymer Journal*, 75:163–174, 2016.

[308] S. Rothenbacher M. Kirchhoff H-J. Schmid-G. Kasper Seipenbusch, M. and A. P. Weber. Interparticle forces in silica nanoparticle agglomerates. *Journal of Nanoparticle Research*, 12(6):2037–2044, 2010.

[309] Gema Vizcay-Barrena Jian Ping Fan Alice Warley Lucy Di Silvio Kalia, Priya and Jie Huang. Nanohydroxyapatite shape and its potential role in bone formation: an analytical study. *J R Soc Interface.*, 11(93), 2014.

[310] AV Kuznetsov, AS Fomin, AG Veresov, VI Putlyaev, IV Fadeeva, and SM Barinov. Hydroxyapatite of platelet morphology synthesized by ultrasonic precipitation from solution. *Russian Journal of Inorganic Chemistry*, 53(1):1–5, 2008.

[311] John W Carson and Brian H Pittenger. Bulk properties of powders. 2013.

[312] Takehiko Horio, Masatoshi Yasuda, and Shuji Matsusaka. Effect of particle shape on powder flowability of microcrystalline cellulose as determined using the vibration shear tube method. *International journal of pharmaceutics*, 473 (1):572–578, 2014.

[313] Jürgen Tomas and Sebastian Kleinschmidt. Improvement of flowability of fine cohesive powders by flow additives. *Chemical engineering & technology*, 32 (10):1470–1483, 2009.

[314] D Schulze. Powders and bulk solids: Behavior, characterization, storage and flow. 2008, 2003.

[315] Reg Freeman and J Cooke. The flowability of powders and the effect of flow additives. In *World Congress on Particle Technology, Orlando*, 2006.

[316] Ola Lyckfeldt. Powder rheology of steel powders for additive manufacturing. In *International Powder Metallurgy Congress and Exhibition, Euro PM 2013*. European Powder Metallurgy Association (EPMA), 2013.

[317] Manfred Schmid, Antonio Amado, Konrad Wegener, and Sadhan C Jana. Polymer powders for selective laser sintering (sls). In *AIP Conference Proceedings*, volume 1664, page 160009. AIP Publishing, 2015.

[318] Luke Harris. *A Study of the crystallisation kinetics in PEEK and PEEK composites*. PhD thesis, University of Birmingham, 2011.

[319] JGC Mc Kenzie and G Cowie. Polymers: Chemistry &physics of modern materials. *Nelson Thornes, Cheltenham*, 1991.

[320] GZ Papageorgiou, DS Achilias, S Nanaki, T Beslikas, and D Bikiaris. Pla nanocomposites: effect of filler type on non-isothermal crystallization. *Thermochimica Acta*, 511(1):129–139, 2010.

[321] Racha Al-Itry, Khalid Lamnawar, and Abderrahim Maazouz. Improvement of thermal stability, rheological and mechanical properties of pla, pbat and their blends by reactive extrusion with functionalized epoxy. *Polymer Degradation and Stability*, 97(10):1898–1914, 2012.

[322] Daniele Battegazzore, Sergio Bocchini, and Alberto Frache. Crystallization kinetics of poly (lactic acid)-talc composites. *Express Polymer Letters*, 5(10): 849–858, 2011.

[323] Saara Inkinen, Minna Hakkarainen, Ann-Christine Albertsson, and Anders Soodergard. From lactic acid to poly (lactic acid)(pla): characterization and analysis of pla and its precursors. *Biomacromolecules*, 12(3):523–532, 2011.

[324] Dietmar Drummer, Dominik Rietzel, and Florian Kühnlein. Development of a characterization approach for the sintering behavior of new thermoplastics for selective laser sintering. *Physics Procedia*, 5:533–542, 2010.

[325] Estevão Freire, Otavio Bianchi, Johnny N Martins, Elisabeth EC Monteiro, and Maria Madalena C Forte. Non-isothermal crystallization of pvdf/pmma blends processed in low and high shear mixers. *Journal of Non-Crystalline Solids*, 358 (18):2674–2681, 2012.

[326] Stephen ZD Cheng and Bernard Lotz. Enthalpic and entropic origins of nucleation barriers during polymer crystallization: the hoffman–lauritzen theory and beyond. *Polymer*, 46(20):8662–8681, 2005.

[327] DJ Blundell, RA Crick, B Fife, J Peacock, A Keller, and A Waddon. Spherulitic morphology of the matrix of thermoplastic peek/carbon fibre aromatic polymer composites. *Journal of materials science*, 24(6):2057–2064, 1989.

[328] Eric D Laird and Christopher Y Li. Structure and morphology control in crystalline polymer–carbon nanotube nanocomposites. *Macromolecules*, 46(8): 2877–2891, 2013.

[329] Wen You Zhou, Bin Duan, Min Wang, and Wai Lam Cheung. Isothermal and non-isothermal crystallization kinetics of poly (l-lactide)/carbonated hydroxyapatite nanocomposite microspheres. In *Advances in Diverse Industrial Applications of Nanocomposites*. InTech, 2011.

[330] Jiao Yang, Benjamin J McCoy, and Giridhar Madras. Distribution kinetics of polymer crystallization and the avrami equation. *The Journal of chemical physics*, 122(6):064901, 2005.

[331] Miray Çelikbilek, Ali Erçin Ersundu, and Süheyla Aydın. Crystallization kinetics of amorphous materials. In *Advances in crystallization processes*. InTech, 2012.

[332] Tomoo Shiomi. Crystallization in multiphase polymer systems. *Sen'i Gakkaishi*, 55(3):P87–P91, 1999.

[333] Yang H Hyun, Sung T Lim, Hyoung J Choi, and Myung S Jhon. Rheology of poly (ethylene oxide)/organoclay nanocomposites. *Macromolecules*, 34(23): 8084–8093, 2001.

[334] Jingjing Yang, Yaqiong Zhang, Zhigang Wang, and Peng Chen. Influences of high aspect ratio carbon nanotube network on normal stress difference measurements and extrusion behaviors for isotactic polypropylene nanocomposite melts. *RSC Advances*, 4(3):1246–1255, 2014.

[335] Jagannathan T Kalathi, Gary S Grest, and Sanat K Kumar. Universal viscosity behavior of polymer nanocomposites. *Physical review letters*, 109(19):198301, 2012.

[336] Michael E Mackay, Tien T Dao, Anish Tuteja, Derek L Ho, Brooke Van Horn, Kim Ho-Cheol, and Craig J Hawker. Nanoscale effects leading to non-einstein-like decrease in viscosity. *Nature materials*, 2(11):762, 2003.

[337] S Mueller, EW Llewellin, and HM Mader. The rheology of suspensions of solid particles. In *Proceedings of the Royal Society of London A: Mathematical, Physical and Engineering Sciences*, page rspa20090445. The Royal Society, 2009.

[338] Mohammad Sabzi, Long Jiang, and Nasser Nikfarjam. Graphene nanoplatelets as rheology modifiers for polylactic acid: graphene aspect-ratio-dependent nonlinear rheological behavior. *Industrial & Engineering Chemistry Research*, 54(33):8175–8182, 2015.

[339] Jinghua Chen and Wei Zheng. The effects of nano-clay on the rheological properties of polylactic acid.

[340] THC Childs and AE Tontowi. Selective laser sintering of a crystalline and a glass-filled crystalline polymer: experiments and simulations. *Proceedings of the Institution of Mechanical Engineers, Part B: Journal of Engineering Manufacture*, 215(11):1481–1495, 2001.

[341] M.A. Al-maliky, A.S. Mahmood, and S. et al. Al-karadaghi. The effects of co2 laser with or without nanohydroxyapatite paste in the occlusion of dentinal tubules. *The Scientific World Journal*, 2014, 2014.

[342] ELTE TTK, official website. `http://elte.prompt.hu/sites/default/files/tananyagok/IntroductionToPracticalBiochemistry/ch04s06.html/`. Accessed:30-05-17.

[343] Kazuo Inoue and Sadao Hoshino. Crystal structure of nylon 12. *Journal of Polymer Science: Polymer Physics Edition*, 11(6):1077–1089, 1973.

[344] Lon J Mathias and C Greg Johnson. Solid-state nmr investigation of nylon 12. *Macromolecules*, 24(23):6114–6122, 1991.

[345] C Ramesh. Crystalline transitions in nylon 12. *Macromolecules*, 32(17): 5704–5706, 1999.

[346] Siddharth Dasgupta, Willis B Hammond, and William A Goddard. Crystal structures and properties of nylon polymers from theory. *Journal of the American Chemical Society*, 118(49):12291–12301, 1996.

[347] Chun-Jen Liao, Feng-Huei Lin, Ko-Shao Chen, and Jui-Sheng Sun. Thermal decomposition and reconstitution of hydroxyapatite in air atmosphere. *Biomaterials*, 20(19):1807–1813, 1999.

[348] Kaveh PourAkbar Saffar, Nima JamilPour, and Gholamreza Rouhi. Carbon nanotubes in bone tissue engineering. In *Biomedical Engineering*. InTech, 2009.

[349] Imelda Olivas-Armendariz, Santos Adriana Martel-Estrada, Mónica E Mendoza-Duarte, Florinda Jiménez-Vega, Perla García-Casillas, and Carlos A Martínez-Pérez. Biodegradable chitosan/multiwalled carbon nanotube composite for bone tissue engineering. *Journal of Biomaterials and Nanobiotechnology*, 4(02):204, 2013.

[350] Lanlan Pan, Xibo Pei, Rui He, Qianbing Wan, and Jian Wang. Multiwall carbon nanotubes/polycaprolactone composites for bone tissue engineering application. *Colloids and Surfaces B: Biointerfaces*, 93:226–234, 2012.

[351] MM Savalani, L Hao, Y Zhang, KE Tanner, and Russell A Harris. Fabrication of porous bioactive structures using the selective laser sintering technique.

Proceedings of the Institution of Mechanical Engineers, Part H: Journal of Engineering in Medicine, 221(8):873–886, 2007.

[352] Wen You Zhou, Min Wang, Wai Lam Cheung, and Wing Yuk Ip. Selective laser sintering of poly (l-lactide)/carbonated hydroxyapatite nanocomposite porous scaffolds for bone tissue engineering. In *Tissue engineering*. InTech, 2010.

[353] Song XiaoHui, Li Wei, Song PingHui, Su QingYong, Wei QingSong, Shi YuSheng, Liu Kai, and Liu WenGuang. Selective laser sintering of aliphatic-polycarbonate/hydroxyapatite composite scaffolds for medical applications. *The International Journal of Advanced Manufacturing Technology*, 81(1-4):15–25, 2015.

[354] FE Wiria, KF Leong, CK Chua, and Y Liu. Poly-ε-caprolactone/hydroxyapatite for tissue engineering scaffold fabrication via selective laser sintering. *Acta biomaterialia*, 3(1):1–12, 2007.

[355] Rodney S Ruoff and Donald C Lorents. Mechanical and thermal properties of carbon nanotubes. *carbon*, 33(7):925–930, 1995.

[356] Antonio F Amado Becker. *Characterization and prediction of SLS processability of polymer powders with respect to powder flow and part warpage*. PhD thesis, ETH Zurich, 2016.

[357] James Davis. Internal report, commissioning of the sintratec laser sintering system.

[358] Alva E Tontowi and THC Childs. Density prediction of crystalline polymer sintered parts at various powder bed temperatures. *Rapid Prototyping Journal*, 7(3):180–184, 2001.

[359] PerkinElmer. Introduction to DMA. `http://www.perkinelmer.co.uk/CMSResources/Images/44-74546GDE_IntroductionToDMA.pdf`, . Accessed: 21-12-2017.

[360] N Saba, M Jawaid, Othman Y Alothman, and MT Paridah. A review on dynamic mechanical properties of natural fibre reinforced polymer composites. *Construction and Building Materials*, 106:149–159, 2016.

[361] Sahrim Hj Ahmad, SY Yahya, Rozaidi Rasid, et al. Reinforced thermoplastic natural rubber (tpnr) composites with different types of carbon nanotubes (mwnts). In *Carbon Nanotubes-Synthesis, Characterization, Applications*. InTech, 2011.

[362] D.W. Callister and D.G. Rethwisch. *Materials science and engineering*, volume 5. John Wiley & Sons NY, 2011.

[363] EOS. PA2200 material data sheet. `https://www.shapeways.com/rrstatic/material_docs/mds-strongflex.pdf`, . Accessed: 21-12-2017.

[364] Majid Jamshidian, Elmira Arab Tehrany, Muhammad Imran, Muriel Jacquot, and Stéphane Desobry. Poly-lactic acid: production, applications, nanocomposites, and release studies. *Comprehensive Reviews in Food Science and Food Safety*, 9(5):552–571, 2010.

[365] Rodney S Ruoff, Dong Qian, and Wing Kam Liu. Mechanical properties of carbon nanotubes: theoretical predictions and experimental measurements. *Comptes Rendus Physique*, 4(9):993–1008, 2003.

[366] K Teraoka, A Ito, K Maekawa, K Onuma, T Tateishi, and S Tsutsumi. Mechanical properties of hydroxyapatite and oh-carbonated hydroxyapatite single crystals. *Journal of Dental Research*, 77(7):1560–1568, 1998.

[367] Xiali Zhang, Dong Yang, Peng Xu, Changchun Wang, and Qiangguo Du. Characterizing the surface properties of carbon nanotubes by inverse gas chromatography. *Journal of materials science*, 42(17):7069–7075, 2007.

[368] Mario H Gutierrez-Villarreal, Francisco J Rodríguez-Gonzalez, and Yibran Perera-Mercado. Estimation of surface free energy of poly (lactic acid) during

uv-grafting with n-vinylpyrrolidone. In *Macromolecular Symposia*, volume 374, page 1600130. Wiley Online Library, 2017.

[369] Gean V Salmoria, Rodrigo A Paggi, Alexandre Lago, and Valter E Beal. Microstructural and mechanical characterization of pa12/mwcnts nanocomposite manufactured by selective laser sintering. *Polymer Testing*, 30 (6):611–615, 2011.

[370] Anthony Warnakula and Sarat Singamneni. Selective laser sintering of nano al2o3 infused polyamide. *Materials*, 10(8):864, 2017.

[371] JH Koo, S Lao, W Ho, K Ngyuen, J Cheng, L Pilato, G Wissler, and M Ervin. Polyamide nanocomposites for selective laser sintering. In *Proc. SFF Symp., Austin*, pages 392–409, 2006.

[372] D Rietzel and E Schmachtenberg. Materials: New thermoplastic powder for selective laser sintering. *Kunststoffe International-Online Magazine for Plastics*, 98(2):42, 2008.

[373] Chunze Yan, Yusheng Shi, Jingsong Yang, and Jinhui Liu. Preparation and selective laser sintering of nylon-12 coated metal powders and post processing. *Journal of Materials Processing Technology*, 209(17):5785–5792, 2009.

[374] Huinan Liu and Thomas J Webster. Mechanical properties of dispersed ceramic nanoparticles in polymer composites for orthopedic applications. *International Journal of Nanomedicine*, 5:299, 2010.

[375] Apriliana Eka Saputri, Danar Praseptiangga, Emma Rochima, Camellia Panatarani, and I Made Joni. Mechanical and solubility properties of bio-nanocomposite film of semi refined kappa carrageenan/zno nanoparticles. In *AIP Conference Proceedings*, volume 1927, page 030040. AIP Publishing, 2018.

[376] Prashant K Jain, Pulak M Pandey, and PVM Rao. Selective laser sintering of clay-reinforced polyamide. *Polymer composites*, 31(4):732–743, 2010.

[377] Cristian-Andi Nicolae, Margareta Anca Grigorescu, and Raluca Augusta Gabor. An investigation of thermal degradation of poly (lactic acid). *Engineering Letters*, 16(4):568–571, 2008.

[378] International Standards Organisation. ISO 6721-1:2011, Plastics Determination of Dynamic Mechanical Properties - Part 1: General Principles, 2011. `https://www.iso.org/standard/57312.html`, . Accessed: 21-12-2017.

[379] A Shakoor, R Muhammad, NL Thomas, and VV Silberschmidt. Mechanical and thermal characterisation of poly (l-lactide) composites reinforced with hemp fibres. In *Journal of Physics: Conference Series*, volume 451, page 012010. IOP Publishing, 2013.

[380] Amir Rostami, Hossein Nazockdast, and Mohammad Karimi. Graphene induced microstructural changes of pla/mwcnt biodegradable nanocomposites: rheological, morphological, thermal and electrical properties. *RSC Advances*, 6 (55):49747–49759, 2016.

[381] Ling Chen, Chak Yin Tang, Harry Siu-lung Ku, Chi Pong Tsui, and Xu Chen. Microwave sintering and characterization of polypropylene/multi-walled carbon nanotube/hydroxyapatite composites. *Composites Part B: Engineering*, 56: 504–511, 2014.

[382] Subrata Pal. Mechanical properties of biological materials. In *Design of Artificial Human Joints & Organs*, pages 23–40. Springer, 2014.

[383] Mahmoud Azami, Fariba Orang, and Fathollah Moztarzadeh. Nanocomposite bone tissue-engineering scaffolds prepared from gelatin and hydroxyapatite using layer solvent casting and freeze-drying technique. In *Biomedical and Pharmaceutical Engineering, 2006. ICBPE 2006. International Conference on*, pages 259–264. IEEE, 2006.

[384] John B Brunski. Mechanical properties of trabecular bone in the human mandible: implications for dental implant treatment planning and surgical placement. *Journal of Oral and Maxillofacial Surgery*, 57(6):706–708, 1999.

[385] Duraform. DuraForm PA material data sheet. `http://www.five-star-plastics.com/DS_DuraForm_PA_US.pdf`.

[386] Cristina Stefana Miron-Borzan, Mircea Cristian Dudescu, and Petru Berce. Bending and compression tests for pa 2200 parts obtained using selective laser sintering method. In *MATEC Web of Conferences*, volume 94, page 03010. EDP Sciences, 2017.

[387] Fernando Cruz. Fabrication of ha/plla composite scaffolds for bone tissue engineering using additive manufacturing technologies. In *Biopolymers*. InTech, 2010.

[388] Defu Liu, Jingyu Zhuang, Cijun Shuai, and Shuping Peng. Mechanical properties' improvement of a tricalcium phosphate scaffold with poly-l-lactic acid in selective laser sintering. *Biofabrication*, 5(2):025005, 2013.

[389] Bin Duan, Min Wang, Wen You Zhou, Wai Lam Cheung, Zhao Yang Li, and William W Lu. Three-dimensional nanocomposite scaffolds fabricated via selective laser sintering for bone tissue engineering. *Acta biomaterialia*, 6(12): 4495–4505, 2010.

[390] Cijun Shuai, Zhongzheng Mao, Haibo Lu, Yi Nie, Huanlong Hu, and Shuping Peng. Fabrication of porous polyvinyl alcohol scaffold for bone tissue engineering via selective laser sintering. *Biofabrication*, 5(1):015014, 2013.

[391] Pei Feng, Man Niu, Chengde Gao, Shuping Peng, and Cijun Shuai. A novel two-step sintering for nano-hydroxyapatite scaffolds for bone tissue engineering. *Scientific reports*, 4, 2014.

[392] Chengde Gao, Tingting Liu, Cijun Shuai, and Shuping Peng. Enhancement mechanisms of graphene in nano-58s bioactive glass scaffold: mechanical and biological performance. *Scientific reports*, 4, 2014.

[393] Song Zhou, Yu-Bao Li, Yan-Ying Wang, Yi Zuo, Shi-Bo Gao, and Li Zhang. Injection-molded porous hydroxyapatite/polyamide-66 scaffold for bone repair

and investigations on the experimental conditions. *Polymer Engineering & Science*, 54(5):1003–1012, 2014.

[394] MS Abu Bakar, MHW Cheng, SM Tang, SC Yu, K Liao, CT Tan, KA Khor, and P Cheang. Tensile properties, tension–tension fatigue and biological response of polyetheretherketone–hydroxyapatite composites for load-bearing orthopedic implants. *Biomaterials*, 24(13):2245–2250, 2003.

[395] Xuesong Zhang, Yonggang Zhang, Xuelian Zhang, Yan Wang, Jiaqi Wang, Ming Lu, and Hong Li. Mechanical properties and cytocompatibility of carbon fibre reinforced nano-hydroxyapatite/polyamide66 ternary biocomposite. *Journal of the mechanical behavior of biomedical materials*, 42:267–273, 2015.

[396] Xiao-Ling Liao, Wen-Feng Xu, Yuan-Liang Wang, JIA Bi, and Guan-Yu Zhou. Effect of porous structure on mechanical properties of c/pla/nano-ha composites scaffold. *Transactions of Nonferrous Metals Society of China*, 19: s748–s751, 2009.

[397] Mohammad Vaezi, Cameron Black, David MR Gibbs, Richard OC Oreffo, Mark Brady, Mohamed Moshrefi-Torbati, and Shoufeng Yang. Characterization of new peek/ha composites with 3d ha network fabricated by extrusion freeforming. *Molecules*, 21(6):687, 2016.

[398] Todd Letcher and Megan Waytashek. Material property testing of 3d-printed specimen in pla on an entry-level 3d printer. In *ASME 2014 International Mechanical Engineering Congress and Exposition*, volume 2, pages 14–22. American Society of Mechanical Engineers, 2014.

[399] Huinan Liu and Thomas J Webster. Mechanical properties of dispersed ceramic nanoparticles in polymer composites for orthopedic applications. *International Journal of Nanomedicine*, 5:299, 2010.

[400] I Kotela, J Podporska, E Soltysiak, KJ Konsztowicz, and M Blazewicz. Polymer nanocomposites for bone tissue substitutes. *Ceramics International*, 35(6):2475–2480, 2009.

[401] Guobao Wei and Peter X Ma. Structure and properties of nano-hydroxyapatite/polymer composite scaffolds for bone tissue engineering. *Biomaterials*, 25(19):4749–4757, 2004.

[402] Yan Xiong, Cheng Ren, Bin Zhang, Hongsheng Yang, Yun Lang, Li Min, Wenli Zhang, Fuxing Pei, Yonggang Yan, Hong Li, et al. Analyzing the behavior of a porous nano-hydroxyapatite/polyamide 66 (n-ha/pa66) composite for healing of bone defects. *International journal of nanomedicine*, 9:485, 2014.

[403] Kantesh Balani, Rebecca Anderson, Tapas Laha, Melanie Andara, Jorge Tercero, Eric Crumpler, and Arvind Agarwal. Plasma-sprayed carbon nanotube reinforced hydroxyapatite coatings and their interaction with human osteoblasts in vitro. *Biomaterials*, 28(4):618–624, 2007.

[404] AO Lobo, MAF Corat, EF Antunes, MBS Palma, C Pacheco-Soares, EE Garcia, and EJ Corat. An evaluation of cell proliferation and adhesion on vertically-aligned multi-walled carbon nanotube films. *Carbon*, 48(1):245–254, 2010.

[405] YeoHeung Yun, Zhongyun Dong, Zongqin Tan, Mark J Schulz, and Vesslin Shanov. Fibroblast cell behavior on chemically functionalized carbon nanomaterials. *Materials Science and Engineering: C*, 29(3):719–725, 2009.

[406] M Kalbacova, M Kalbac, L Dunsch, and U Hempel. Influence of single-walled carbon nanotube films on metabolic activity and adherence of human osteoblasts. *Carbon*, 45(11):2266–2272, 2007.

[407] Suna Giannona, Izabela Firkowska, José Rojas-Chapana, and Michael Giersig. Vertically aligned carbon nanotubes as cytocompatible material for enhanced adhesion and proliferation of osteoblast-like cells. *Journal of nanoscience and nanotechnology*, 7(4-5):1679–1683, 2007.

[408] Jianguo Liao, Yongxiang Zhang, Xiali Guan, Jingxian Liu, Nian Shan, Yanqun Li, Yufen Xie, and Haohuai Liu. Synthesis and characterization of nano-hydroxyapatite/polyamide 66 biocomposites reinforced with multi-walled

carbon nanotubes. *Journal of Biomaterials science, Polymer edition*, 27(16): 1674–1684, 2016.

[409] Sabrina Constanda, Miruna Silvia Stan, Carmen Steluța Ciobanu, Mikael Motelica-Heino, Régis Guégan, Khalid Lafdi, Anca Dinischiotu, and Daniela Predoi. Carbon nanotubes-hydroxyapatite nanocomposites for an improved osteoblast cell response. *Journal of Nanomaterials*, 2016:75, 2016.

[410] PR Supronowicz, PM Ajayan, KR Ullmann, BP Arulanandam, DW Metzger, and R Bizios. Novel current-conducting composite substrates for exposing osteoblasts to alternating current stimulation. *Journal of Biomedical Materials Research Part A*, 59(3):499–506, 2002.

[411] Miguel A Correa-Duarte, Nicholas Wagner, José Rojas-Chapana, Christian Morsczeck, Michael Thie, and Michael Giersig. Fabrication and biocompatibility of carbon nanotube-based 3d networks as scaffolds for cell seeding and growth. *Nano Letters*, 4(11):2233–2236, 2004.

[412] György Hajnóczky, Erika Davies, and Muniswamy Madesh. Calcium signaling and apoptosis. *Biochemical and biophysical research communications*, 304(3): 445–454, 2003.

[413] P Pinton, C Giorgi, R Siviero, E Zecchini, and R Rizzuto. Calcium and apoptosis: Er-mitochondria ca 2+ transfer in the control of apoptosis. *Oncogene*, 27(50):6407, 2008.

[414] Xiaodong Wang. The expanding role of mitochondria in apoptosis. *Genes & development*, 15(22):2922–2933, 2001.

[415] Yuan Yan, Chao-liang Wei, Wan-rui Zhang, He-ping Cheng, and Jie Liu. Cross-talk between calcium and reactive oxygen species signaling. *Acta Pharmacologica Sinica*, 27(7):821, 2006.

[416] Xiaochen Liu, Jie Wei, and Shicheng Wei. Biological effects of osteoblast-like cells on nanohydroxyapatite particles at a low concentration range. *Journal of Nanomaterials*, 2011:41, 2011.

[417] Zheng Li Xu, Jiao Sun, Chang Sheng Liu, and Jie Wei. Effect of hydroxyapatite nanoparticles of different concentrations on rat osteoblast. In *Materials Science Forum*, volume 610, pages 1364–1369. Trans Tech Publ, 2009.

[418] Qiang Fu, Nai Zhou, Wenhai Huang, Deping Wang, Liying Zhang, and Haifeng Li. Effects of nano hap on biological and structural properties of glass bone cement. *Journal of Biomedical Materials Research Part A*, 74(2):156–163, 2005.

[419] M Motskin, DM Wright, K Muller, N Kyle, TG Gard, AE Porter, and JN Skepper. Hydroxyapatite nano and microparticles: correlation of particle properties with cytotoxicity and biostability. *Biomaterials*, 30(19):3307–3317, 2009.

[420] Catrin Albrecht, Agnes M Scherbart, Damien van Berlo, Carola M Braunbarth, Roel PF Schins, and Julia Scheel. Evaluation of cytotoxic effects and oxidative stress with hydroxyapatite dispersions of different physicochemical properties in rat nr8383 cells and primary macrophages. *Toxicology in vitro*, 23(3):520–530, 2009.

[421] Yurong Cai, Yukan Liu, Weiqi Yan, Qinghong Hu, Jinhui Tao, Ming Zhang, Zhongli Shi, and Ruikang Tang. Role of hydroxyapatite nanoparticle size in bone cell proliferation. *Journal of Materials Chemistry*, 17(36):3780–3787, 2007.

[422] Silvia Pezzatini, Raffaella Solito, Lucia Morbidelli, Stefania Lamponi, Elisa Boanini, Adriana Bigi, and Marina Ziche. The effect of hydroxyapatite nanocrystals on microvascular endothelial cell viability and functions. *Journal of Biomedical Materials Research Part A*, 76(3):656–663, 2006.

[423] Anita Patlolla, Brionna Knighten, and Paul Tchounwou. Multi-walled carbon nanotubes induce cytotoxicity, genotoxicity and apoptosis in normal human dermal fibroblast cells. *Ethnicity & disease*, 20(1 Suppl 1):S1, 2010.

[424] Nancy A Monteiro-Riviere, Robert J Nemanich, Alfred O Inman, Yunyu Y Wang, and Jim E Riviere. Multi-walled carbon nanotube interactions with human epidermal keratinocytes. *Toxicology letters*, 155(3):377–384, 2005.

[425] Julie Muller, Ilse Decordier, Peter H Hoet, Noömi Lombaert, Leen Thomassen, François Huaux, Dominique Lison, and Micheline Kirsch-Volders. Clastogenic and aneugenic effects of multi-wall carbon nanotubes in epithelial cells. *Carcinogenesis*, 29(2):427–433, 2008.

[426] Aiman I Al-Qtaitat and Saed M Aldalaen. A review of non-collagenous proteins; their role in bone. *American J Life Sci*, 2:351–5, 2014.

[427] H Sun, F Ye, J Wang, Y Shi, Z Tu, J Bao, M Qin, H Bu, and Y Li. The upregulation of osteoblast marker genes in mesenchymal stem cells prove the osteoinductivity of hydroxyapatite/tricalcium phosphate biomaterial. In *Transplantation proceedings*, volume 40, pages 2645–2648. Elsevier, 2008.

[428] Anthoula A Kroustalli, Souzana N Kourkouli, and Despina D Deligianni. Cellular function and adhesion mechanisms of human bone marrow mesenchymal stem cells on multi-walled carbon nanotubes. *Annals of biomedical engineering*, 41(12):2655–2665, 2013.

[429] Shin-Woo Ha, Hae Lin Jang, Ki Tae Nam, and George R Beck Jr. Nano-hydroxyapatite modulates osteoblast lineage commitment by stimulation of dna methylation and regulation of gene expression. *Biomaterials*, 65:32–42, 2015.

[430] Dongwoo Khang, Jungil Choi, Yeon-Min Im, Youn-Jeong Kim, Je-Hee Jang, Sang Soo Kang, Tae-Hyun Nam, Jonghan Song, and Jin-Woo Park. Role of subnano-, nano-and submicron-surface features on osteoblast differentiation of bone marrow mesenchymal stem cells. *Biomaterials*, 33(26):5997–6007, 2012.

[431] Marcus Oliver Klein, Ana Bijelic, Thomas Ziebart, Felix Koch, Peer W Kämmerer, Marco Wieland, Moritz A Konerding, and Bilal Al-Nawas. Submicron scale-structured hydrophilic titanium surfaces promote early

osteogenic gene response for cell adhesion and cell differentiation. *Clinical implant dentistry and related research*, 15(2):166–175, 2013.

[432] Kai Wang Chan, Cheng Zhu Liao, Hoi Man Wong, Kelvin Wai Kwok Yeung, and Sie Chin Tjong. Preparation of polyetheretherketone composites with nanohydroxyapatite rods and carbon nanofibers having high strength, good biocompatibility and excellent thermal stability. *RSC Advances*, 6(23): 19417–19429, 2016.

[433] Adebola Oyefusi, Opeyemi Olanipekun, Gururaj M Neelgund, Deforest Peterson, Julia M Stone, Ebonee Williams, Laura Carson, Gloria Regisford, and Aderemi Oki. Hydroxyapatite grafted carbon nanotubes and graphene nanosheets: promising bone implant materials. *Spectrochimica Acta Part A: Molecular and Biomolecular Spectroscopy*, 132:410–416, 2014.

[434] Byung-Dong Hahn, Jung-Min Lee, Dong-Soo Park, Jong-Jin Choi, Jungho Ryu, Woon-Ha Yoon, Byoung-Kuk Lee, Du-Sik Shin, and Hyoun-Ee Kim. Mechanical and in vitro biological performances of hydroxyapatite–carbon nanotube composite coatings deposited on ti by aerosol deposition. *Acta Biomaterialia*, 5(8):3205–3214, 2009.

[435] MG Raucci, M Alvarez-Perez, D Giugliano, S Zeppetelli, and L Ambrosio. Properties of carbon nanotube-dispersed sr-hydroxyapatite injectable material for bone defects. *Regenerative biomaterials*, 3(1):13–23, 2016.

[436] Rajendiran Rajesh and Y Dominic Ravichandran. Development of a new carbon nanotube–alginate–hydroxyapatite tricomponent composite scaffold for application in bone tissue engineering. *International journal of nanomedicine*, 10(Suppl 1):7, 2015.

[437] Twelve NHS Hospitals Implement 3D Printing Solutions with Replica 3DM. `https://www.tctmagazine.com/3d-printing-news/twelve-nhs-hospitals-implement-3d-printing-solutions/`. Accessed:10-06-18.

[438] 3D Lifeprints Secures £500,000 To Expand Hospital Based 3D Printer Labs. https://3dprintingindustry.com/news/3d-lifeprints-secures-500000-expand-hospital-based-3d-printer-labs-128118/ Accessed:10-06-18.

[439] 3D-Printed Healthcare: Devices Transforming Hospitals Forever. https://mcalindenresearchpartners.com/2018/05/31/3d-printed-healthcare-devices-transforming-hospitals-forever/. Accessed:10-06-18.

[440] Douglas R Gnepp. *Diagnostic Surgical Pathology of the Head and Neck E-Book*. Elsevier Health Sciences, 2009.

[441] World Health Organization et al. Who scientific group on the assessment of osteoporosis at primary health care level. In *Summary meeting report*, pages 5–7, 2004.

[442] Mary E Jensen, Avery J Evans, John M Mathis, David F Kallmes, Harry J Cloft, and Jacques E Dion. Percutaneous polymethylmethacrylate vertebroplasty in the treatment of osteoporotic vertebral body compression fractures: technical aspects. *American Journal of Neuroradiology*, 18(10): 1897–1904, 1997.

[443] Ian S Kinstlinger, Andreas Bastian, Samantha J Paulsen, Daniel H Hwang, Anderson H Ta, David R Yalacki, Tim Schmidt, and Jordan S Miller. Open-source selective laser sintering (OpenSLS) of nylon and biocompatible polycaprolactone. *PloS one*, 11(2):e0147399, 2016.